

Geographia Technica



Technical Geography
an International Journal for the Progress of Scientific Geography

Volume 17, Geographia Technica No. 2/2022

www.technicalgeography.org

Cluj University Press

Editorial Board

Okke **Batelaan**, Flinders University Adelaide, Australia
Yazidhi **Bamutaze**, Makerere University, Kampala, Uganda
Valerio **Baiocchi**, Sapienza University of Rome, Italy
Gabriela **Biali**, "Gh. Asachi" University of Iasi, Romania
Habib **Ben Boubaker**, University of Manouba, Tunisia
Gino **Dardanelli**, University of Palermo, Italy
Qingyun **Du**, Wuhan University, China
Renata **Dulias**, University of Silesia, Poland
Massimiliano **Fazzini**, University of Ferrara, Italy
Edward **Jackiewicz**, California State University, Northridge CA, USA
Shadrack **Kithiia**, University of Nairobi, Kenya
Jaromir **Kolejka**, Masaryk University Brno, Czech Republic
František **Križan**, Comenius University in Bratislava, Slovakia
Muh Aris **Marfai**, Universitas Gadjah Mada, Yogyakarta, Indonesia
Béla **Márkus**, University of West Hungary Szekesfehervar, Hungary
Jean-Luc **Mercier**, Université de Strasbourg, France
Igor **Patrakeyev**, Kyiv University of Construction and Architecture, Ukraine
Cristian Valeriu **Patriche**, Romanian Academy, Iasi, Romania
Dušan **Petrovič**, University of Ljubljana, Slovenia
Hervé **Quénol**, Université de Rennes 2 et CNRS, France
Sanda **Roșca**, Babes-Bolyai University of Cluj-Napoca, Romania
José J. de **Sanjosé Blasco**, University of Extremadura, Spain
Richard R. **Shaker**, Reyson University, Toronto, Canada
Sarintip **Tantane**, Naresuan University, Phitsanulok, Thailand
Gábor **Timár**, Eötvös University Budapest, Hungary
Kinga **Temerdek-Ivan**, Babes-Bolyai University of Cluj-Napoca, Romania
Yuri **Tuchkovenko**, Odessa State Environmental University, Ukraine
Eugen **Ursu**, Université de Bordeaux, France
Changshan **Wu**, University of Wisconsin-Milwaukee, USA
Chong-yu **Xu**, University of Oslo, Norway

Editor-in-chief

Ionel **Haidu**, University of Lorraine, France

Editorial Secretary

Marcel Mateescu, Airbus Group Toulouse, France
George Costea, Yardi Systemes, Cluj-Napoca, Romania

Online Publishing

Magyari-Sáska Zsolt, "Babes-Bolyai" University of Cluj-Napoca, Romania

Geographia Technica



Technical Geography

an International Journal for the Progress of Scientific Geography

2022 – No. 2

Cluj University Press

ISSN: 1842 - 5135 (Printed version)

ISSN: 2065 - 4421 (Online version)

© 2022. All rights reserved. No part of this publication may be reproduced or transmitted in any form or by any means, electronic or mechanical, including photocopy, recording or any information storage and retrieval system, without permission from the editor.

Babeş-Bolyai University
Cluj University Press
Director: Codruța Săcelean
Str. Hașdeu nr. 51
400371 Cluj-Napoca, România
Tel./fax: (+40)-264-597.401
E-mail: editura@editura.ubbcluj.ro
<http://www.editura.ubbcluj.ro/>

Asociatia Geographia Technica
2, Prunilor Street
400334 Cluj-Napoca, România
Tel. +40 744 238093
editorial-secretary@technicalgeography.org
<http://technicalgeography.org/>

Cluj University Press and Asociatia Geographia Technica
assume no responsibility for material, manuscript, photographs or artwork.

Contents

Geographia Technica

Volume 17, Issue 2, autumn 2022

An International Journal of Technical Geography

ISSN 2065-4421 (Online); ISSN 1842-5135 (printed)

ESTABLISHING SPATIAL DISTRIBUTIONS OF DROUGHT PHENOMENA ON CULTIVATION SEASONS USING THE SWAT MODEL

Haris PRASANCHUM, Nutthasit TUMMA & Worapong LOHPAISANKRIT 1
DOI: 10.21163/GT_2022.172.01

EARLY WARNING SYSTEM BASED ON HISTORICAL COASTAL FLOOD EVENTS IN SEMARANG CITY, INDONESIA

Fitriana Nur Indah SARI, Denny Nugroho SUGIANTO & Kunarso KUNARSO .. 14
DOI: 10.21163/GT_2022.172.02

ESTIMATION OF PARTICULATE MATTER LESS THAN 10 MICRONS VOLUME THROUGH VARIOUS FORMATS OF SPATIAL INTERPOLATION METHODS

Jumpol ITSARAWISUT & Teerawong LAOSUWAN 26
DOI: 10.21163/GT_2022.172.03

A LOW-COST DRONE MAPPING AND SIMPLE PARTICIPATORY GIS TO SUPPORT THE URBAN FLOOD MODELLING

Aditya SAPUTRA, Agus Anggoro SIGIT, Yuli PRIYANA, Andy Muhammad ABROR, Anggraini Noor Lia SARI & Oky NURSETIYANI 35
DOI: 10.21163/GT_2022.172.04

A DIRECT METHOD TO DELIMIT WEIR POOLS

Francesco DONATI 47
DOI : 10.21163/GT_2022.172.05

ANALYSES OF TRENDS IN THE FIRE LOSSES AND THE FIRE-BRIGADE CALL-OUTS IN SOUTH AFRICA BETWEEN 2004 AND 2017

Rennifer MADONDO, Nhamo MUTINGWENDE, Siviwe SHWABABA, Robyn J. BAYNE, Ágoston RESTÁS & Roman TANDLICH 54
DOI : 10.21163/GT_2022.172.06

ACCURACY PERFORMANCE OF SATELLITE-DERIVED SEA SURFACE TEMPERATURE PRODUCTS FOR THE INDONESIAN SEAS

Restu TRESNAWATI, Anindya WIRASATRIYA & Adi WIBOWO 69
DOI: 10.21163/GT_2022.172.07

GIS-BASED ASSESSMENT OF COASTAL VULNERABILITY IN THE JATABEK (JAKARTA, TANGERANG, AND BEKASI) REGION, INDONESIA

Guntur A. RAHMAWAN, Ruzana DHIAUDDIN, Ulung J. WISHA, Wisnu A. GEMILANG, Agung SYETIAWAN, Wiwin AMBARWULAN & Ati RAHADIATI 84
DOI: 10.21163/GT_2022.172.08

HOW THE CLIMATE MIGRATES. CASE STUDY FOR FOUR LOCATIONS IN THE CARPATHIAN-BASIN

Zsolt MAGYARI-SÁSKA 97
DOI: 10.21163/GT_2022.172.09

JOINT DISTRIBUTION AND COINCIDENCE PROBABILITY OF THE NUMBER OF DRY DAYS AND THE TOTAL AMOUNT OF PRECIPITATION IN SOUTHERN SUMATRA FIRE-PRONE AREA

Sri NURDIATI, Mohamad Khoirun NAJIB & Achmad Syarief THALIB 107
DOI : 10.21163/GT_2022.172.10

ALGORITHMS DEVELOPMENT OF THE FIELD MANGROVE CHLOROPHYLL-A BIOMASS, CARBON BASED ON SENTINEL-2A DATA AT CAWAN ISLAND, SUMATERA, INDONESIA

Agus HARTOKO, Aulia RAHIM & Nurul LATIFAH 119
DOI: 10.21163/GT_2022.172.11

TIDAL FLOOD MODEL PROJECTION USING LAND SUBSIDENCE PARAMETER IN PONTIANAK, INDONESIA

Randy ARDIANTO, Aris ISMANTO, Joko SAMPURNO & Sugeng WIDADA . 135
DOI: 10.21163/GT_2022.172.12

DAILY STREAMFLOW FORECASTING USING EXTREME LEARNING MACHINE AND OPTIMIZATION ALGORITHM. CASE STUDY: TRA KHUC RIVER IN VIETNAM

Huu Duy NGUYEN 148
DOI: 10.21163/GT_2022.172.13

HEIGHT MEASUREMENT AND OIL PALM YIELD PREDICTION USING UNMANNED AERIAL VEHICLE (UAV) DATA TO CREATE CANOPY HEIGHT MODEL (CHM)

Nayot KULPANICH, Morakot WORACHAIRUNGREUNG, Katawut WAIYASUSRI, Pornperm SAE-NGOW & Dusadee PINASU 164
DOI: 10.21163/GT_2022.172.14

NIGHTTIME AND DAYTIME POPULATION ESTIMATION FROM OPEN DATA

Nelson MILEU & Margarida QUEIRÓS 179
DOI: 10.21163/GT_2022.172.15

A NEAR FUTURE CLIMATE CHANGE IMPACTS ON WATER RESOURCES IN THE UPPER CHAO PHRAYA RIVER BASIN IN THAILAND

Naphol YOOBANPOT & Weerayuth PRATOOMCHAI 193
DOI: 10.21163/GT_2022.172.16

MAPPING OF SUBAK AREA BOUNDARIES AND SOIL FERTILITY FOR AGRICULTURAL LAND CONSERVATION

Ida Bagus Putu BHAYUNAGIRI & Moh SAIFULLOH 208
DOI: 10.21163/GT_2022.172.17

CATEGORIZING THE CAUSES OF OCCURRENCE OF CHATEAU BROWNFIELDS: A CASE STUDY ON THE CZECH REPUBLIC

Kamila TURECKOVA 220
DOI: 10.21163/GT_2022.172.18

ESTABLISHING SPATIAL DISTRIBUTIONS OF DROUGHT PHENOMENA ON CULTIVATION SEASONS USING THE SWAT MODEL

Haris PRASANCHUM^{1*}, Nutthasit TUMMA², Worapong LOHPAISANKRIT³

DOI: 10.21163/GT_2022.172.01

ABSTRACT:

Due to global climate change, drought phenomena are becoming longer. As a result, water availability is insufficient to meet demand for agriculture during the cultivation seasons and many areas have affected by drought. These can cause difficulties in water resources management. The main objectives of this study were to establish the spatial distribution of drought phenomena at sub-basin scales in the Lam Khan Chu and Lam Nam Chi Part II watersheds, which is the major headwater of the Chi River Basin, Thailand. The Soil and Water Assessment Tool (SWAT) model was used to synthesize streamflow data at the sub-basins of the watersheds. To estimate drought severity, the Streamflow Drought Index (SDI) was computed from the time series of the synthesized streamflow data during 2008 to 2019. The simulated streamflow of the SWAT model was acceptable based on the R^2 , Nash-Sutcliffe Efficiency (NSE) and Percent bias (PBIAS) reaching good levels in both calibration and verification. According to the SDI calculation, the most severe drought in the study period was in the year 2016. During January and April of 2016, the affected areas of about 3%, 30%, 14%, 30 and 23% of the study area were identified as none, mild, moderate, severe and extreme droughts, respectively. The integration of the hydrological model and drought index to monitor drought severity in space and time will be a useful tool for assessing drought severity. Moreover, the results can support managers for water resources management.

Key-words: *drought, Streamflow Drought Index, SWAT, Lam Khan Chu sub-watershed, Lam Nam Chi Part II sub-watershed.*

1. INTRODUCTION

Currently, our world is facing the challenge of climate change, which has become more intense. This challenge leads to water scarcity in many countries, and both rainfall and streamflow vary from normal value (Faiz et al., 2018; Irannezhad et al., 2020; Koo et al., 2020). The average rainfall in Thailand since the 2018 rainy season has been 5% lower than normal value. This circumstance is happening in many areas throughout the country, especially in northeastern Thailand (Rotjanakusol & Laosuwan, 2019). The Royal Irrigation Department is basically responsible for water management at regional level each year by considering seasonal related conditions based on meteorological conditions, streamflow in major rivers flowing into surface water resource, and reservoir operation rule (Llones et al., 2021; Wannasin et al., 2021). The core principle of operation is water allocation according to crop calendar both inside and outside the irrigation areas (Hussainzada & Lee, 2022). To allocate water for different activities through irrigation system, rainfall is the major source in the rainy season that people basically depend on while water stored in reservoir is the major source in the dry season (Takeda et al., 2015). However, measured by streamflow observed stations, the streamflow in rivers is mostly below the average, and water allocation does not go as planned. For this reason, many areas have to be declared as drought-affected, and agriculturists are able to plant only once a

^{1*}Rajamangala University of Technology Isan, Khon Kaen Campus, Department of Civil Engineering, Faculty of Engineering, Khon Kaen, Thailand, Corresponding Author: haris.pr@rmuti.ac.th

²Regional Irrigation Office 6, Khon Kaen, Royal Irrigation Department, tae006@gmail.com

³Khon Kaen University, Department of Civil Engineering, Faculty of Engineering, Khon Kaen, Thailand, woralo@kku.ac.th

year or in the rainy season (Prabnakorn et al., 2019). On the other hand, growing crops with less water is needed during the dry season, or sometimes agriculturists are not able to grow their crops due to raw water shortage (Boonwichai et al., 2018).

According to the aforementioned problem, hydrological drought analysis is a way utilized for obtaining the results that are useful for prediction and decision support on water resource management planning in watershed areas. One of the universally used methods is hydrologic model for analyzing and predicting impacts in the past, present, and future situations (Kumar et al., 2022). The Soil and Water Assessment Tool (SWAT) is one of these commonly used because of its strong point in streamflow analysis, which is associated with size and extent classification of sub-watershed by physical evidence of the area and is able to calculate the streamflow with high reliability (Diriba, 2021; Prasanchum et al., 2020). In analyzing drought severity to integrate between the results obtained from hydrologic model and occurrence of drought, hydrological drought index called Streamflow Drought Index (SDI) was employed in this study. This index can also display severity levels of drought calculated from streamflow data, and it has been also used in many countries around the world (Brouziyne et al., 2020; Jahangir et al., 2020), Southeast Asia (Fung et al., 2019; Linh et al., 2021) including Thailand (Foyhirun & Promping, 2021; Lohpaisankrit & Techamahasaranont, 2021). The process of this study began with classifying the sub-watershed by using SWAT. Then the obtained analytical results of streamflow were measured for SDI value in order to eventually gain a spatial map displaying the severity levels according to the crop calendar of Thailand. For regional watersheds in Thailand, there have been a small number of studies applying SWAT to SDI and presenting spatial map. Therefore, this study has tried to assess the streamflow in watershed areas at the regional level, particularly in the major headwater areas that have been affected by drought. Hopefully, the results of this study will be beneficial to society. For instance, it will be helpful to the authorities concerned in improving their preventive measures in order to reduce any damage. Also, agriculturists will be able to plan for their cultivation in watershed areas and have more efficient way to manage water resources during a drought.

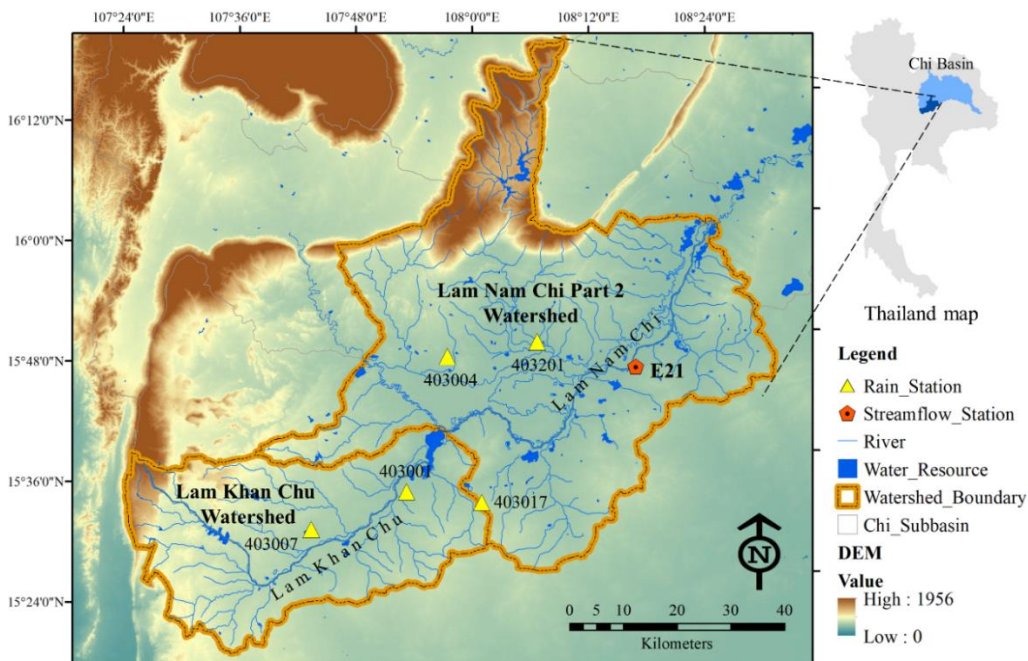
2. STUDY AREA AND DATA COLLECTION

This study area was chosen because it is an upstream forest area in the western part of the Chi River, which is a main river of the northeastern region of Thailand. There are two watersheds selected for this study i.e. Lam Khan Chu and Lam Nam Chi Part II, which is a sub-watershed of the Chi River Basin (1 of 25 major watersheds in Thailand), with a catchment area of 1,733 and 3,795 square kilometers, respectively. In this area, there are the Lam Khan Chu River and the Chi River as the major river flowing from southwest to northeast. The average rainfall is 950 to 1,100 millimeters per year referred from data collected in 5 rainfall gauge stations. The average streamflow per year is between 620 to 1,078 million cubic meters referred from complete data collected from E21 observed station during 2008 to 2019. Moreover, further data also used in the study gathered from many institutes consist of Digital Elevation Model (DEM), river map, land use map, soil type map, meteorological data, and hydrological data, as shown in **Table 1** and **Fig. 1 (a), (b) and (c)**, respectively.

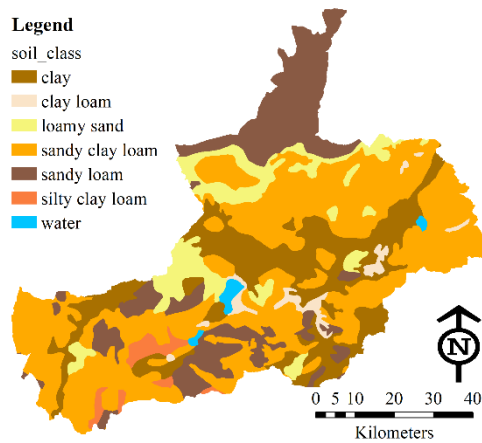
Table 1.

Spatial data and hydrological data

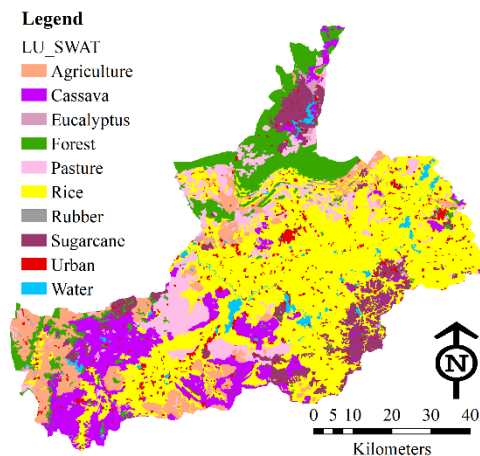
Data type	Period	Scale	Source
Digital Elevation Model (DEM)	2018	30x30 m	Land Development Department
River map	2018	1:50,000	
Soil type map	2018	1:50,000	
Land use map	2018	1:50,000	
Climate and Rainfall data (5 stations)	2008-2019	Daily	Thai Meteorological Department
Observed streamflow data at E21	2008-2019	Monthly	Royal Irrigation Department



(a)



(b)



(c)

Fig. 1. Spatial data of the study area (a) Location of Lam Khan Chu and Lam Nam Chi Part II sub-watersheds, (b) Soil type map, and (c) Land use map.

3. METHOD

3.1. Streamflow simulation

3.1.1. SWAT Model

Soil and Water Assessment Tool (SWAT) is an open source model (Arnold et al., 1998) and also a semi-distributed hydrological model developed to analyze the streamflow (Koua et al. 2021), sediment, and water quality that are affected by climate and land use changes (Prasanchum & Kangrang, 2017). SWAT was applied to processing classification at many levels of river basin such

as creation of sub-basins in a major basin as well as calculation to demonstrate outcome at daily level and long term. A water balance equation was then used for taking into account depending on hydrological process as Eq. (1):

$$SW_t = SW_o + \sum_{i=1}^t (R_{day} - Q_{surf} - E_a - W_{seep} - Q_{gw}) \quad (1)$$

where:

SW_t	-final soil water content (millimeter);
SW_o	-soil water content starting from day i (millimeter);
t	-time (day);
R_{day}	-rainfall amount of day i (millimeter);
Q_{surf}	-surface water amount of day i (millimeter);
E_a	-evapotranspiration amount of day i (millimeter);
W_{seep}	-the amount of water absorbed underground of day i (millimeter);
Q_{gw}	-the amount of underground water running into a river of day i (millimeter)

3.2.1. Model Accuracy Assessment

In assessing the accuracy of results from SWAT, data on monthly streamflow recorded at E21 station from 2008 to 2019 were equated and verified. The process began with sensitivity analysis of hydrological parameters that were related to streamflow defined by Hydrologic Response Unit (HRU), which was developed from the model (Khatun et al., 2018). This process of SWAT has been outstanding and widely accepted due to its efficiency and accuracy in calculation results compared to other semi-distributed models. In this study, a model called SWAT Calibration and Uncertainty Programs (SWAT-CUP) (Djebou, 2018; Faiza et al., 2018) through Sequential Uncertainty Fitting version 2 (SUFI-2) was utilized because it is a technique that requires the smallest number of sensitivity parameters, but it gives optimum outcomes (Malik et al., 2021). In goodness of fit test, calculation results obtained from SUFI-2 were compared to data collected from the measuring station by adjusting sensitivity parameters based on efficiency criteria i.e. Coefficient of Determination (R^2), Nash-Sutcliffe Efficiency (NSE), and Percent bias (PBIAS). The calculation can be done according to Eq. (2) to (4) below:

$$R^2 = \left[\frac{\sum_{i=1}^n [(Q_{obs} - \bar{Q}_{obs})(Q_{sim} - \bar{Q}_{sim})]}{\sqrt{\sum_{i=1}^n (Q_{obs} - \bar{Q}_{obs})^2} \sqrt{\sum_{i=1}^n (Q_{sim} - \bar{Q}_{sim})^2}} \right] \quad (2)$$

$$NSE = 1 - \frac{\sum_{i=1}^n (Q_{obs} - Q_{sim})^2}{\sum_{i=1}^n (Q_{obs} - \bar{Q}_{obs})^2} \quad (3)$$

$$PBIAS = \frac{\sum_{i=1}^n (Q_{obs} - Q_{sim})}{Q_{obs}} \times 100 \quad (4)$$

where:

i	-data order;
n	-total number of data;
Q_{obs}	-value obtained from observed;
\bar{Q}_{obs}	-average of total observed data;
Q_{sim}	-value obtained from model;
\bar{Q}_{sim}	-average of data obtained from all models;
SW_t	-final soil water content (millimeter)

3.2. Standard Drought Index (SDI)

SDI is counted as simple and efficient to drought analysis. It was developed by Nalbantis & Tsakiris (2009) to identify characteristics, analyze hydrological drought, and assess severity as well as causes of drought properly at all levels of area (Abbas & Kousar, 2021). In calculating, monthly data on streamflow volume from the observed station were used as input (Aghelpour et al., 2021). SDI has been widely used in studying and analyzing drought situations such as hydrological drought in river basin areas (Hong et al., 2015; Ozkaya & Zerberg, 2019), drought caused by climate change (Pandhumas et al., 2020), and drought in river basins without an observed station (Lohpaisankrit & Techamahasaranont, 2021). Negative results of SDI reflect hydrological drought with levels represented by number from 0 (mild drought) to -2 (extreme drought). In addition, positive results are also shown to indicate there is no situation of drought, as presented in **Table 2** (Hong et al., 2015; Niaz et al., 2021). In terms of calculating SDI, it was identified according to data on streamflow volume $V_{i,k}$ for each reference range of hydrological year i as seen in Eq. (5) below:

$$SDI_{i,k} = \frac{V_{i,k} - \bar{V}}{s_K} \quad i = 1, 2, \dots, k = 1, 2, 3, 4 \quad (5)$$

where;

V_k and s_k -mean and standard deviation, respectively, of accumulated streamflow of reference time k because these values have a long-term estimate. In this definition, reduction level was defined as V_k although other values could be used.

Table 2.

Drought classification for SDI

Description	Class
Extreme wet	$SDI \geq 2.00$
Severe wet	$1.50 \leq SDI < 2.00$
Moderate wet	$1.00 \leq SDI < 1.50$
Mild wet	$0.00 \leq SDI < 1.00$
Mild drought	$-1.00 \leq SDI < 0.00$
Moderate drought	$-1.50 \leq SDI < -1.00$
Severe drought	$-2.00 \leq SDI < -1.50$
Extreme drought	$SDI \leq -2.00$

3.3 Crop Calendar for Irrigation Area in the Northeast of Thailand

The Royal Irrigation Department (RID) of Thailand, determined a proper way of seasonal cultivation (Prabnakorn et al., 2018). In northeastern Thailand, crop calendar for dry-season farming was defined between January to April. Farmers are suggested to cultivate depending mainly on allocation water from a reservoir, and water distribution stops at the end of April in order that the farmers can harvest their crops. Nevertheless, water allocation during the dry season has its limitation, or it can be managed only in the irrigation area. When the rainy season arrives, between July and October, the farmers have to grow crops. In case that rainfall and streamflow in the reservoir are below the average, which affect water utilized for cultivation, the RID has to allocate water to be sufficient to farmer for their farming including other purposes of water use. However, to assure the risk of reservoir management, the RID needs to specify the end of November as the end of water allocation for growing crops in the rainy season in order that farmers can harvest their crops in December.

4. RESULTS AND DISSCUSSION

4.1 SWAT Accuracy Assessment

4.1.1 Parameter Sensitivity Analysis

The sensitivity analysis used 13 hydrological parameters related to streamflow by using SWAT-CUP for the purpose of optimization in order that the obtained results from the model could demonstrate value as close as possible to observed value. The analysis result has indicated the first five parameters influencing calculation: ALPHA_BF, CN2, ESCO, GW_DELAY, and CH_N2, respectively. These could be seen from statistics through creating a relation equation called "linear regression equation" depending on t -Stat and P-Value for the analysis. When P-Value becomes high (by not considering signs), it means that parameter is highly sensitive to objective function. When P-Value is close to zero, it means that parameter is sensitive to objective function with high significance. The details are shown in **Table 3**.

4.1.2 Model Calibration and Validation

In model calibration and validation, the SWAT-CUP was employed in specifying a cycle of calculation of 500 rounds to compare results to values recorded at E21 observed station from 2008 to 2019 as presented in **Fig. 2**. The calibration results by means of the calculation results from 2008 to 2015 (8 years) compared to observed values indicated $R^2 = 0.86$, $NSE = 0.80$, and $PBIAS = -4.32\%$ while the validation interval demonstrated $R^2 = 0.87$, $NSE = 0.85$, and $PBIAS = -2.55\%$. According to the results, the calculation accuracy of streamflow is very good because R^2 and NSE are higher than 0.80, and $PBIAS$ is lower than 10% (Prasanchum et al., 2021).

Table 3.

Sensitivity parameters and fitted values using SUFI-2 from SWAT-CUP

Ranks	Parameter	Description	Fitted value	t -stat	P-value
1	ALPHA_BF	Baseflow alpha factor	0.218	-31.69	0
2	CN2	SCS runoff curve number	0.108	-21.12	0
3	ESCO	Soil evaporation compensation factor	0.649	11.43	0
4	GW_DELAY	Groundwater delay	5.300	-6.09	0.000000002
5	CH_N2	Channel Manning's coefficient	0.0200	5.76	0.000000015
6	CH_K2	Effective hydraulic conductivity in main channel alluvium	120.508	5.08	0.000000545
7	GWQMN	Threshold depth of water in the shallow aquifer required for return flow to occur	248.500	-5.07	0.000000559
8	REVAPMN	Threshold depth of water in the shallow aquifer for "revap "to occur	466.500	4.32	0.000019147
9	SOL_AWC	Available water capacity of the soil layer	0.661	4.17	0.000035378
10	GW_REVAP	Groundwater "revap "coefficient	0.136	-3.86	0.000127172
11	RCHRG_DP	Deep aquifer percolation fraction	0.623	-3.23	0.001292101
12	LAT_TTIME	Lateral flow travel time	104.580	2.80	0.005379043
13	SLSOIL	Slope length for lateral subsurface flow	63.450	-2.16	0.031036977

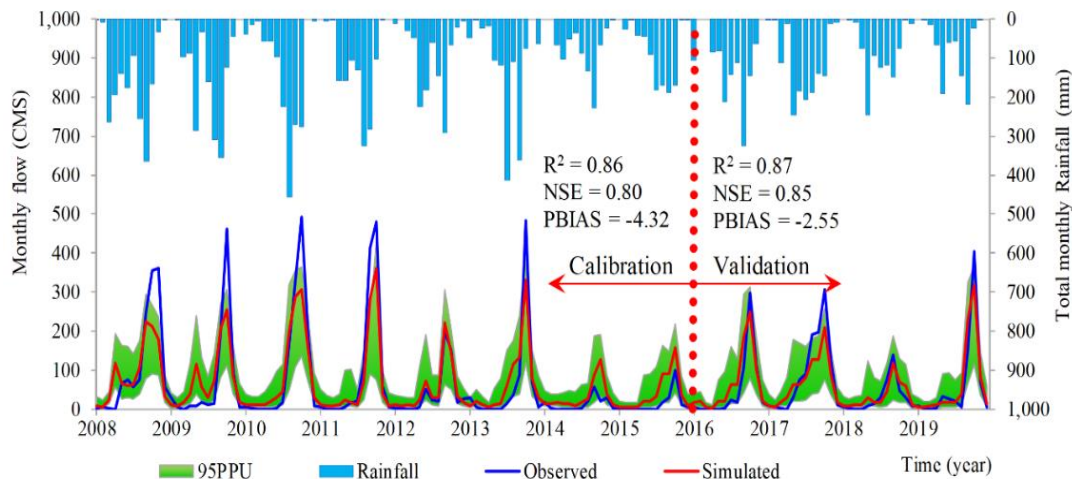


Fig. 2. Calibration and validation of the SWAT-CUP model.

4.2 Monthly SDI from Streamflow Simulation

Drought situations at sub-basin scales in the Lam Khan Chu and Lam Nam Chi Part II watersheds have been monitored based on SDI. To visualize the spatial distribution of SDI, the first step is to simulate the appropriate sub-watershed boundary in the Lam Khan Chu and Lam Nam Chi Part II sub-watersheds based on the DEM data. **Fig. 3** shows 25 sub-watersheds of the study area resulted from watershed delineation techniques of the SWAT model. Then, SWAT calculated monthly streamflow from 2008 to 2019 and yielded results at all 25 sub-watershed levels (the sensitivity parameters were adjusted and fixed to achieve the highest accuracy results as detailed in the previous section). Subsequently, monthly streamflow in each sub-watershed were calculated as monthly SDI and integrated into the GIS model to provide a map of the spatial distribution of drought phenomena in the study area.

Fig. 4 illustrates the results of a 1-month SDI in 25 sub-watersheds during 2008 to 2019. SDI results of SB-7, SB-11 and SB-16 basins were described as examples of the change in time series and position of different areas. The SB-7 basin is located along the main river, whereas the SB-11 and SB-16 basins are located along the Lam Khan Chu River and the Chi River, respectively. SDI values provide information on historical drought events. As shown in the figure, temporal characteristics of drought events among the basins were quite dissimilar. In the SB-7 basin, five months and fourteen months were classified as severe and moderate drought months, respectively. The period of three months between February and April of 2010 was the longest duration of the severe drought event in the basin. The worst drought event in the SB-11 between March and April of 2016 and the SDI values were below -2.0, which were classified as an extreme drought. In the SB-16 basin, it is found that the longest period of drought event was between September, 2014 and April, 2015 and was classified as severe to extreme drought months. The result shows that drought conditions in sub-basins located beside of and far away from the river are different. Drought conditions in basins located far away from the river may mainly rely on precipitation. This finding is consistent with that of Shen et al. (2017) and Peña-Gallardo et al., (2019) who noted that drought is significantly influenced by meteorological factors. Meanwhile, droughts conditions in basins located beside of the river may be influenced by precipitation (Yang et al., 2020) and hydrological conditions (Zhao et al., 2019) of upstream basins.

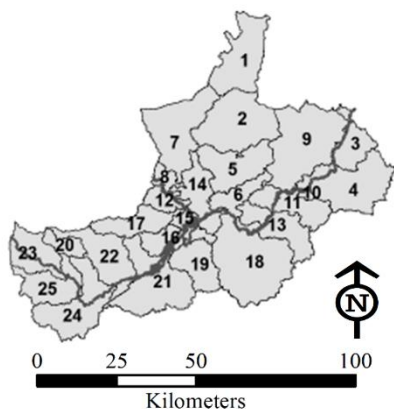


Fig. 3. 25 sub-watersheds of the study area divided from SWAT.

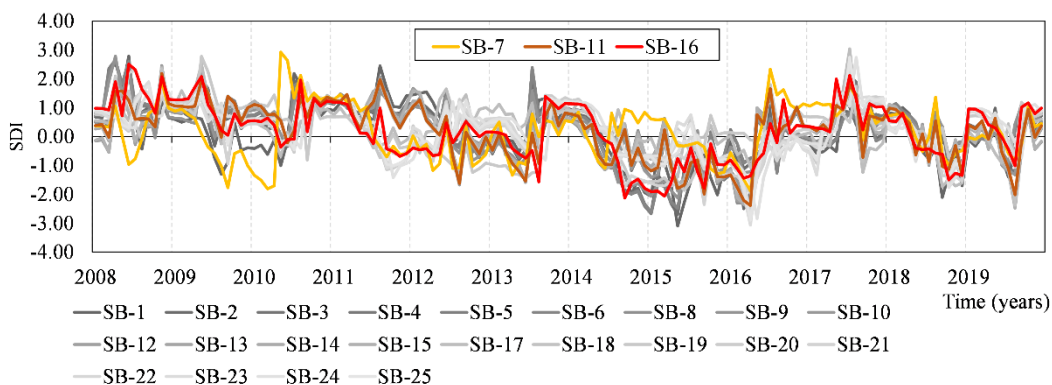


Fig. 4. 1-month SDI in 25 sub-watersheds during 2008-2019.

4.3 Spatial Distribution Area of SDI on Cultivation Seasons

To make an easily understandable presentation on drought severity in the Lam Khan Chu and Lam Nam Chi Part II watersheds, maps of SDI distributions were produced. The SDI was used to determine drought severity conditions on the basis of streamflow deficits. **Fig. 5** presents the spatial distribution of drought phenomena in the dry season between 2008 to 2019 at sub-watershed scales. The results of drought analysis based on SDI show that the drought phenomenon in the year 2016 was the most severe drought event. The SDI values of seven sub-watersheds, namely SB-8, SB-11, SB-12, SB-13, SB-14, SB-15 and SB-18 were found to be ranged from -2.17 to -2.01 during the month of January and April, 2016 indicating the presence of extreme drought. The seven sub-watersheds covered an area of 1,247 square kilometers (23% of the watershed area) as shown in **Table 4**. These results are likely to be related to observed streamflow data at E21 observed station (**Fig. 2**). Since the streamflow for the years 2015 and 2016 was below average during 2008 to 2019 at the station E21, low streamflow conditions in the year 2015 may result in a potential drought situation for the early period of the following year. **Fig. 6** shows the spatial distribution of drought phenomena in the rainy season between 2008 and 2019 in the study area. For example, the 18 sub-watersheds (66% of the watershed area) indicated with the SDI values ranging from -1.79 to -1.05 were determined as moderate to severe droughts in the year 2018 (**Table 4**). The results have pointed out that drought events can occur throughout the year for all regions.

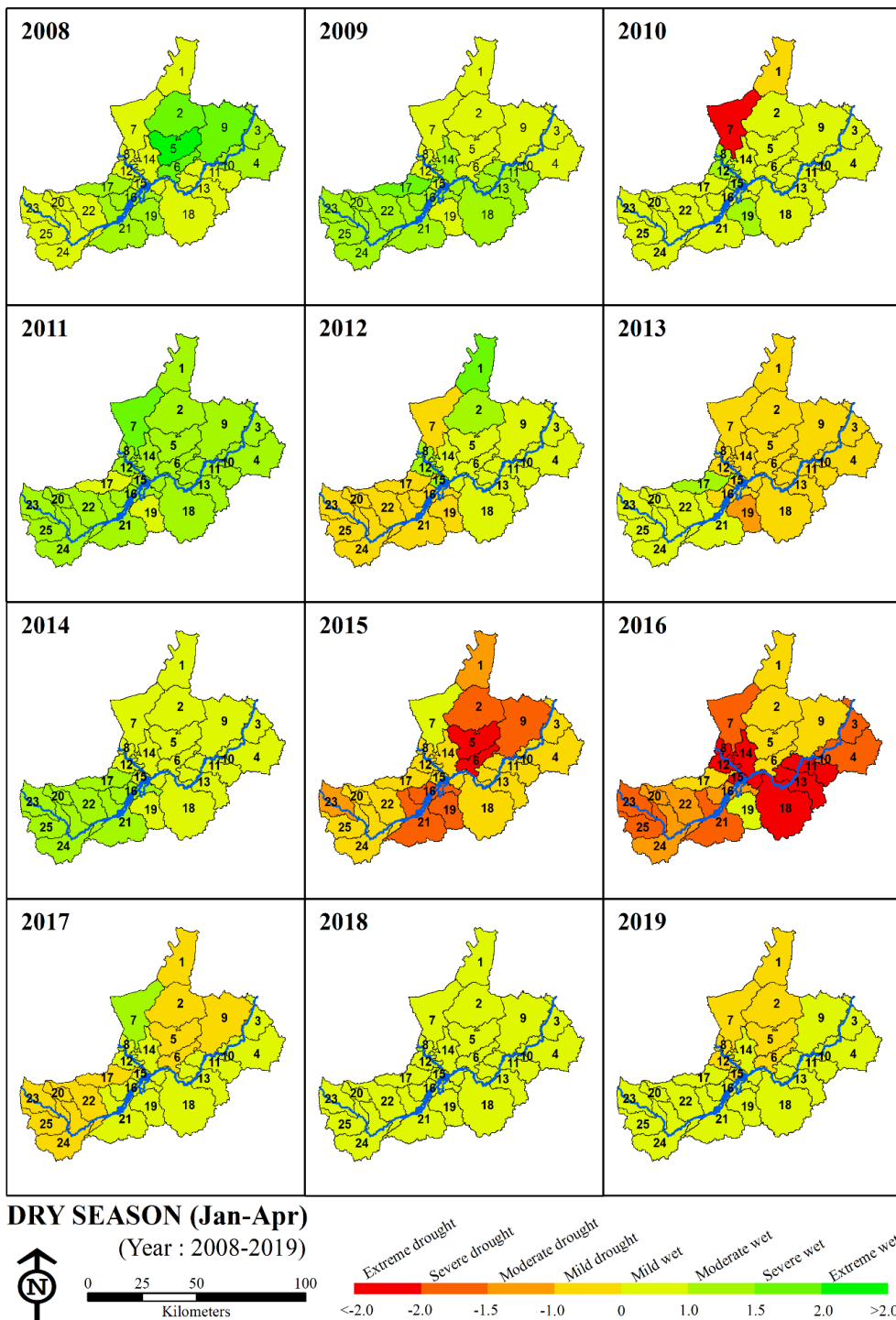


Fig. 5 Spatial distribution of drought phenomena in dry season (January to April) during 2008 to 2019.

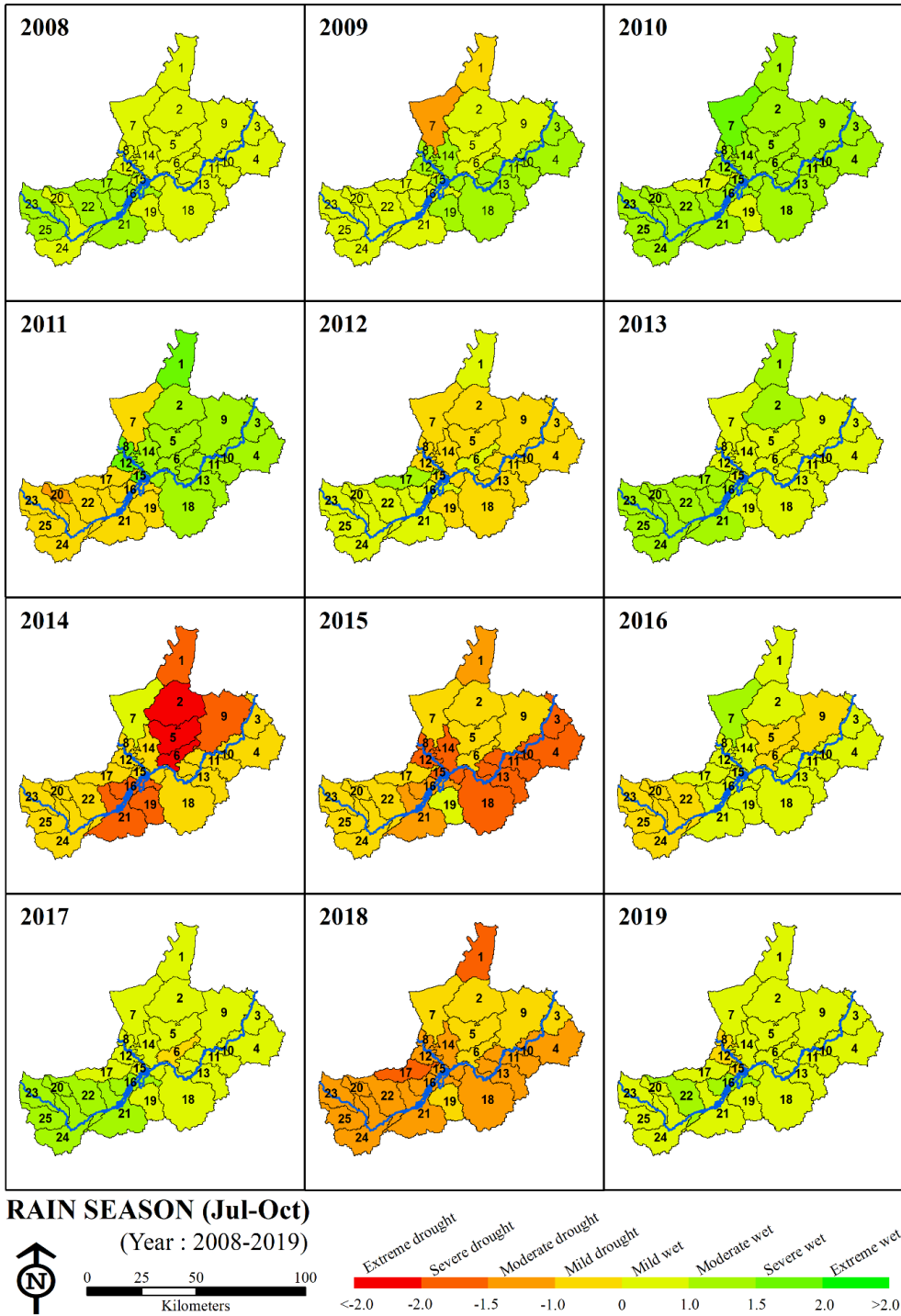


Fig. 6 Spatial distribution of drought phenomena in rainy season (July to October) during 2008 to 2019.

Table 4.

The quantity of area during the year affected by the continuous drought phenomena divided by the SDI level

SDI level		2014		2015		2016		2017		2018	
		Area (km ²)	%	Area (km ²)	%	Area (km ²)	%	Area (km ²)	%	Area (km ²)	%
Dry season	Moderate wet	1,653	30.6	0	0.0	0	0.0	343	6.4	0	0.0
	Mild wet	3,741	69.4	343	6.4	170	3.2	2,436	45.2	5,394	100
	Mild drought	0	0.0	2,726	50.5	1,625	30.1	2,615	48.5	0	0.0
	Moderate drought	0	0.0	472	8.8	757	14.0	0	0.0	0	0.0
	Severe drought	0	0.0	1,505	27.9	1,595	29.6	0	0.0	0	0.0
	Extreme drought	0	0.0	348	6.5	1,247	23.1	0	0.0	0	0.0
Rainy season	Moderate wet	0	0.0	0	0.0	343	6.4	1,496	27.7	0	0.0
	Mild wet	343	6.4	170	3.2	3,257	60.4	3,791	70.3	0	0.0
	Mild drought	2,907	53.9	2,667	49.4	1,794	33.3	107	2.0	1,834	34.0
	Moderate drought	0	0.0	797	14.8	0	0.0	0	0.0	3,112	57.7
	Severe drought	1,423	26.4	1,760	32.6	0	0.0	0	0.0	448	8.3
	Extreme drought	721	13.4	0	0.0	0	0.0	0	0.0	0	0.0

6. CONCLUSIONS

The current study established the spatial distribution of drought phenomena at sub-watershed scales in the Lam Khan Chu and Lam Nam Chi Part II watersheds using SDI for the historical period (2008-2019). The SDI was computed based on streamflow information simulated using the SWAT model. According to the simulated results of the SWAT model in the calibration and validation processes, the model can provide reasonable streamflow data based on R², NSE and PBIAS. Simulated monthly streamflow data obtained from the SWAT model for each sub-watershed outlet was used to compute SDI. In this study, the drought analysis based on SDI was performed in dry and rainy seasons. This SDI was found to be suitable for drought monitoring. Drought events indicated by the SDI seem to be consistent with observed streamflow in the main river. Moreover, the spatial distributions of SDI over the watershed can identify areas, prone to droughts. Further work is required to integrate results of SDI with additional indices related to meteorological and agricultural droughts. The integration can provide useful support for long-term drought mitigation and management.

REFERENCES

- Abbas, S. & Kousar, S. (2021), Spatial analysis of drought severity and magnitude using the standardized precipitation index and streamflow drought index over the Upper Indus Basin, Pakistan. *Environment, Development and Sustainability*, 23, 15314-15340, DOI: 10.1007/s10668-021-01299-y.
- Aghelpour, P., Bahrami-Pichaghchi, H. & Varshavian, V. (2021), Hydrological drought forecasting using multi-scalar streamflow drought index, stochastic models and machine learning approaches, in northern Iran.

- Stochastic Environmental Research and Risk Assessment*, 35, 1615-1635, DOI: 10.1007/s00477-020-01949-z.
- Arnold, A.G., Srinivasan, R., Muttiah, R.S. & Williams, J.R. (1998), Large area hydrological modeling and assessment part I: model development. *Journal of American Water Resource Association*, 34 (1), 73-89.
- Boonwichai, S., Shrestha, S., Babel, M.S., Weesakul, S. & Datta, A. (2018), Climate change impacts on irrigation water requirement, crop water productivity and rice yield in the Songkhram River Basin, Thailand. *Journal of Cleaner Production*, 198, 1157-1164, DOI: 10.1016/j.jclepro.2018.07.146.
- Brouziyne, Y., Abouabdillah, A., Chehbouni, A., Hanich, L., Bergaoui, K., McDonnell, R., & Benaabidate, L. (2020), Assessing hydrological vulnerability to future droughts in a Mediterranean watershed: combined indices-based and distributed modeling approaches. *Water*, 12, 2333, DOI: 10.3390/w12092333.
- Diriba, B.J. (2021), Surface runoff modeling using SWAT analysis in Dabus watershed, Ethiopia. *Sustainable Water Resources Management*, 7, 96 (2021), DOI: 10.1007/s40899-021-00573-1.
- Djebou, D.C.S., (2018), Assessment of sediment inflow to a reservoir using the SWAT model under undammed condition: A case study for the Somerville Reservoir, Texas, USA. *Journal of International Soil and Water Conservation Research*, 6 (3), 222-229.
- Faiz, M.A., Liu, D., Fu, Q., Uzair, M., Khan, M.I., Baig, F., Li, T. & Cui., S. (2018), Stream flow variability and drought severity in the Songhua River Basin, Northeast China. *Stochastic Environmental Research and Risk Assessment*, 32, 1225-1242, DOI: 10.1007/s00477-017-1463-3.
- Faiza, H., Mohamed, M., Gil, M., Salaheddine, A. & Abdelkader, K. (2018), Modeling of discharge and sediment transport through SWAT model in the Cathment of Harraza (Northwest of Algeria). *Journal of Water Science*, 32, 79-88.
- Foyhirun, C. & Promping, T. (2021), Future hydrological drought hazard assessment under climate and land use projections in Upper Nan River Basin, Thailand. *Engineering and Applied Science Research*, 48(6), 781-790.
- Fung, K.F., Huang, Y.F. & Koo, C.H. (2019), Investigation of streamflow as a seasonal hydrological drought indicator for a tropical region. *Water Supply*, 20 (2), 609-620, DOI: 10.2166/ws.2019.192.
- Hong, X., Guo, S., Zhou, Y. & Xiong, L. (2015), Uncertainties in assessing hydrological drought using streamflow drought index for the upper Yangtze River Basin. *Stochastic Environmental Research and Risk Assessment*, 29 (4), 1235-47.
- Hussainzada, W, & Lee, H.S. (2022), Effect of an improved agricultural irrigation scheme with a hydraulic structure for crop cultivation in arid northern Afghanistan using the Soil and Water Assessment Tool (SWAT). *Scientific Reports*, 12, 5186 (2022), DOI: 10.1038/s41598-022-09318-2.
- Irannezhad, M., Liu, J. & Chen, D. (2020), Influential climate teleconnections for spatiotemporal precipitation variability in the Lancang-Mekong River Basin from 1952 to 2015. *Journal of Geophysical Research: Atmospheres*, 125, e2020JD033331, DOI: 10.1029/2020JD033331.
- Jahangir, M.H. & Yarahmadi, Y. (2020), Hydrological drought analyzing and monitoring by using Streamflow Drought Index (SDI) (case study: Lorestan, Iran). *Arabian Journal of Geosciences*, 13, 110 (2020), DOI: 10.1007/s12517-020-5059-8.
- Khatun, S., Sahana, M., Jain, S.K. & Jain, N. (2018), Simulation of surface runoff using semi distributed hydrological model for a part of Satluj Basin: parameterization and global sensitivity analysis using SWAT CUP. *Modeling Earth Systems and Environment*, 4, 1111-1124, DOI: 10.1007/s40808-018-0474-5.
- Koo, H., Chen, M, Jakeman, A.J. & Zhang, F. (2020), A global sensitivity analysis approach for identifying critical sources of uncertainty in non-identifiable, spatially distributed environmental models: A holistic analysis applied to SWAT for input datasets and model parameters. *Environmental Modelling & Software*, 127 (2020) 104676, DOI: 10.1016/j.envsoft.2020.104676.
- Koua, T.J.J., Dhanesh, Y., Jeong, J., Srinivasan, R. & Anoh, K.A. (2021), Implementation of the semi-distributed SWAT (Soil and Water Assessment Tool) model capacity in the Lobo Watershed at Nibéhibé (Center-West of Côte d'Ivoire). *Journal of Geoscience and Environment Protection*, 9, 21-38.
- Kumar, A., Singh, A. & Gaurav, K. (2022), Assessing the synergic effect of land use and climate change on the upper Betwa River catchment in Central India under present, past, and future climate scenarios. *Environment, Development and Sustainability*, DOI: 10.1007/s10668-022-02260-3.
- Linh, V.T., Tram, V.N.Q., Dung, H.M., Phuong, D.N.D., Liem, N.D., Nguyen, L.D., Yin, C., Kortun, A. & Loi, N.K. (2021), Meteorological and Hydrological Drought Assessment for Dong Nai River Basin, Vietnam

- under Climate Change. *Mobile Networks and Applications*, 26, 1788-1800, DOI: 10.1007/s11036-021-01757-x.
- Llones, C., Mankeb, P., Wongtragoon, U. & Suwanmaneepong, S. (2021), Bonding and bridging social capital towards collective action in participatory irrigation management. Evidence in Chiang Rai Province, Northern Thailand. *International Journal of Social Economics*, 49 (2), 296-311.
- Lohpaisankrit, W. & Techamahasaranont, J. (2021), Analysis of precipitation and streamflow data for drought assessment in an unregulated watershed. *Environment and Natural Resources Journal*, 19 (2), 112-121.
- Malik, M.A., Dar, A.Q., & Jain M.K. (2021), Modelling streamflow using the SWAT model and multi-site calibration utilizing SUFI-2 of SWAT-CUP model for high altitude catchments, NW Himalaya's. *Modeling Earth Systems and Environment*, 8, 1203-1213.
- Nalbantis, I. & Tsakiris, G. (2009), Assessment of hydrological drought revisited. *Water Resources Management*, 23(5), 881-897.
- Niaz, R., Hussain, I., Ali, Z. & Fisal, M. (2021), A novel framework for regional pattern recognition of drought intensities. *Arabian Journal of Geosciences*, 14, 1644 (2021), DOI: 10.1007/s12517-021-08097-w.
- Ozkaya, A. & Zerberg, Y. (2019) A 40-Year Analysis of the hydrological drought index for the Tigris Basin, Turkey. *Water*, 11(4), 657, DOI: 10.3390/w11040657.
- Pandhumas, T., Kuntiyawichai, K., Jothityangkoon, C. & Suryadi, F.X. (2020), Assessment of climate change impacts on drought severity using SPI and SDI over the Lower Nam Phong River Basin, Thailand. *Engineering and Applied Science Research*, 47 (3), 326-338.
- Peña-Gallardo, M., Vicente-Serrano, S.M., Hannaford, J., Lorenzo-Lacruzc, J., Svoboda, M., Domínguez-Castro, F., Maneta, M., Tomas-Burguera, M. & Kenawy, A.E. (2019), Complex influences of meteorological drought time-scales on hydrological droughts in natural basins of the contiguous United States. *Journal of Hydrology*, 568, 611-625, DOI: 10.1016/j.jhydrol.2018.11.026.
- Prabnakorn, S., Maskey, S., Suryadi, F.X. & de Fraiture, C. (2018), Rice yield in response to climate trends and drought index in the Mun River Basin, Thailand. *Science of The Total Environment*, 621, 108-119, DOI: 10.1016/j.scitotenv.2017.11.136.
- Prabnakorn, S., Maskey, S., Suryadi, F.X. & Fraiture, C.D., (2019), Assessment of drought hazard, exposure, vulnerability, and risk for rice cultivation in the Mun River Basin in Thailand. *Natural Hazards*, 97, 891-911, DOI: 10.1007/s11069-019-03681-6.
- Prasanchum, H. & Kangrang, A. (2017), Optimal reservoir rule curves under climatic and land use changes for Lampao Dam using Genetic Algorithm. *KSCE Journal of Civil Engineering*, 22, 351-364.
- Prasanchum, H., Phisnok, S. & Thinubol, S. (2021), Application of the SWAT model for evaluating discharge and sediment yield in the Huay Luang Catchment, Northeast of Thailand. *ASM Science Journal*, 14, DOI: 10.32802/asmscj.2020.574.
- Prasanchum, H., Sirisook, P. & Lohpaisankrit, W. (2017), Flood risk areas simulation using SWAT and gumbel distribution method in Yang catchment, Northeast Thailand. *Geographia Technica*, 15 (2), 29-39.
- Rotjanakusol, T. & Laosuwan, T. (2019), An Investigation of drought around Chi watershed during ten-year period using Terra/Modis data. *Geographia Technica*, 14 (2), 74-83.
- Shen, Q., Liang, L., Luo, Li, Y. & Zhang, L. (2017), Analysis of the spatial-temporal variation characteristics of vegetative drought and its relationship with meteorological factors in China from 1982 to 2010. *Environmental Monitoring and Assessment*, 189, 471 (2017), DOI: 10.1007/s10661-017-6187-9.
- Takeda, M., Laphimsing, A. & Putthividhya, A. (2015), Dry season water allocation in the Chao Phraya River basin, Thailand. *International Journal of Water Resources Development*, 32 (2), 321-338, DOI: 10.1080/07900627.2015.1055856.
- Wannasin, C., Brauer C.C., Uijlenhoet, R., van Verseveld, W.J. & Weerts, A.H. (2021), Daily flow simulation in Thailand Part II: Unraveling effects of reservoir operation. *Journal of Hydrology: Regional Studies*, 34 (2021), 100792, DOI: 10.1016/j.ejrh.2021.100792.
- Yang, M., Mou, Y., Meng, Y., Liu, S., Peng, C. & Zhou, X. (2020), Modeling the effects of precipitation and temperature patterns on agricultural drought in China from 1949 to 2015. *Science of The Total Environment*, 711, DOI: 10.1016/j.scitotenv.2019.135139.
- Zhao, P., Lü, H., Yang, H", Wang, W. & Fu, G. (2019), Impacts of climate change on hydrological droughts at basin scale: A case study of the Weihe River Basin, China. *Quaternary International*, 513, 37-46, DOI: 10.1016/j.quaint.2019.02.022.

EARLY WARNING SYSTEM BASED ON HISTORICAL COASTAL FLOOD EVENTS IN SEMARANG CITY, INDONESIA

Fitriana Nur Indah SARI¹, Denny Nugroho SUGIANTO^{2,3} and Kunarso KUNARSO⁴

DOI: 10.21163/GT_2022.172.02

ABSTRACT:

Semarang is the capital city of Central Java located in the Northern Coastal Area of Java which floods have occurred quite often. Apart from the natural causes, the rapid development in the area resulted in worsened land subsidence leading to exacerbation of the flood's occurrence. During the last 10 years, there have been at least 15 flood events occurred in the area that was recorded by National Disaster Management Authority but early warning about these incidents is not given much. By using event data from the last 10 years, floods will then be analyzed to determine the characteristics based on three parameters, which are meteorological parameters (rainfall and wind), oceanographic (tidal wave and waves), and land subsidence in the area to create a threshold for early warning system based on these parameters. The results show that each parameter has significant influence on the occurrence of coastal flooding. Ten occurrences of coastal flood in Semarang happened on rainy season and the others on dry season. In rainy season, tidal height for each occurrence varied from 16.58 – 47.12 cm from Mean Sea Level (MSL) accompanied by heavy-extreme rainfall during or the previous day of the flooding. Rain that occurs at higher plains also affects the incidence of flooding in the coastal area of Semarang. While in dry season, tidal waves have greater influence with 80% of the occurrences have high tides above 45 cm from MSL. Wind direction and mean wave direction comes from Northwest for 46.67% and 80% of the cases. These results can be used as the preliminary threshold to increase level of alert before issuing an early warning. The average of rate of displacement for land subsidence in Semarang City is 8.9 cm/year in 2020, which indicates that if this condition occurs continuously, the potential for coastal flooding will increase regardless of season and tidal height happen in the Semarang area.

Key-words: Coastal flood, Meteorology, Oceanography, Land subsidence, Early warning system.

1. INTRODUCTION

Floods are one of the most frequent natural disasters which can have a significant impact on humans' activities (Nadeem, et al., 2014; Gigovic, et al., 2017; Udin, et al., 2018 in Batista, 2018). Coastal areas are not an exception, in fact most of the major flooding happen in coastal areas (Batista, 2018). Coastal flooding can result from a variety of different causes, such as tidal waves due to tidal activity, high waves due to the influence of strong local winds, incoming swell waves from distant offshore storms (Hoeke, et al., 2013; Smith and Juria, 2019), the rising of sea levels accompanied by high river currents, accelerated sea level rise due to global warming (Marfai & King, 2008), storm surges, and heavy rains (Batista, 2018). Areas that suffer from land subsidence increases the likelihood of coastal flooding and also can experience more severe impact of coastal flooding. The coastal area itself is characterized as an area that has a very diverse ecosystem that is a habitat for various species and also supports various economic activities, which causes high population growth in the area (Bijlsma et al., 1995). The city of Semarang is the capital of the province of Central Java, which is located in the North Coast of Java (Pantura). The Pantura region

¹Diponegoro University, Faculty of Fisheries and Marine Sciences, 50275, Semarang, Indonesia, fitriananur95@gmail.com

²Diponegoro University, Dept. Oceanography, 50275, Semarang, Indonesia, kunarso@lecturer.undip.ac.id

³Center for Coastal Rehabilitation and Disaster Mitigation Studies, Diponegoro University, 50275, Semarang, Indonesia, dennynugrohosugianto@lecturer.undip.ac.id

⁴Indonesian Agency for Meteorology Climatology and Gephysics, 10610, Jakarta, Indonesia

is also one of the coastal areas that has the potential for rapid development, especially in the transportation sector. This caused the Government in the 2020-2024 National Medium-Term Development Planning document to budget 50.8 trillion to provide security in the North Coast of Java due to the vulnerability of this area to the risk of land loss caused by various factors. The priority areas in this development include five large urban areas, namely Jakarta, Semarang, Pekalongan, Demak and Cirebon. In general, coastal security in these five areas aims to overcome the tidal flooding disaster. Semarang as one of the cities located in the Pantura region also has a dense population. Based on data from the Central Bureau of Statistics (Badan Pusat Statistik) in 2020, Semarang City has a population of 1.67 million people with a total area of 373.7 km² with a density of 4,854.54 people/km². Therefore, it is necessary for the vulnerable population to obtain comprehensive early warning information in this region so that losses can be minimized.

Indonesian Agency for Meteorological, Climatological and Geophysics (Badan Meteorologi, Klimatologi, dan Geofisika or simply BMKG) is the official agency in charge of providing early warning to institutions related to disasters caused by meteorological, climatological, and geophysical phenomena. Based on the UN Sendai Framework for Disaster Risk Reduction 2015-2030, the World Meteorological Organization (WMO) issues specific guidelines for providing early warning information based on the impact of meteorological phenomena that occur. This then resulted in a change in the provision of early warning information which was previously only limited to hydrometeorological phenomena that occurred, into providing early warning information based on impacts. Based on the information listed on the website of the Maritime Meteorology Center of the BMKG, it explains that the Standard Operating Procedure (SOP) in providing information on coastal flooding is to use wave and swell data obtained from numerical modeling of SWAN Ina-Forecast Map of Shallow Wave Waters and based on real time data and tidal height forecast in coordination with the Indonesian Navy Hydrography and Oceanography Center as well as Geospatial Information Agency.

Research on flooding in coastal areas has been carried out quite often, including in the Semarang area. Several recent studies regarding flooding in the Semarang area, among others, were carried out by Irawan et al., (2021) who examined the projection of flood events in the coastal area of Semarang until 2050 using the LISFLOOD-FP numerical model in terms of sea level rise and land surface subsidence. Another study was conducted by Widada et al., (2020) which modeled the possible location of tidal inundation in Semarang based on the subsidence factor using the Geographic Information System (GIS) in the area. Unfortunately, the application of these models is still very limited due to the difficulty of data access and limited resources. Therefore, this research will focus on the use of data that can be easily accessed by both disaster-related agencies and the public so that early warning information about coastal flooding can reach various levels of society more easily.

2. STUDY AREA

Semarang City is the capital city of Central Java Province (**Fig. 1**) which located in the North Coast of Java. Lowland and coastal areas in Semarang City are very dynamic and versatile, where it is being used as residential areas, recreation, industrial area, fishing activities and pond areas (Marfai & King, 2008). The morphology of Semarang City is lowlands and hills that have various heights, which are between 0.75 - 348 m above sea level, with a topography consisting of coastal/coastal areas, plains and hills with land slopes ranging from 0% - 45% (Afifah, 2014). The city of Semarang is also traversed by at least 16 rivers which are under the authority of the Semarang Department of Public Works and 22 rivers with non-status authority. The research area will be limited to the coastal area of Semarang City which is determined based on the Law of the Republic of Indonesia No. 1 of 2014 concerning Management of Coastal Areas and Small Islands, where in Article 2 of the Law explains that the scope of the coastal area includes transitional areas between land ecosystem and sea which are affected by changes in land and sea, landward covers the administrative area of the sub-district and towards the sea as far as 12 nautical miles measured

from the coastline. During the last decade, from the National Disaster Management Authority report, at least 15 flooding events occurred in the coastal areas of Semarang as shown in **Table 1**. However, there is also a possibility that there were events that were not recorded by the authorities because historical data collection can be a problem (Smith & Juria, 2019). These 15 flooding occurrences will be used as the sample in this research as coastal flood in the coastal area of Semarang frequently happened and the occurrences are increasing every year.

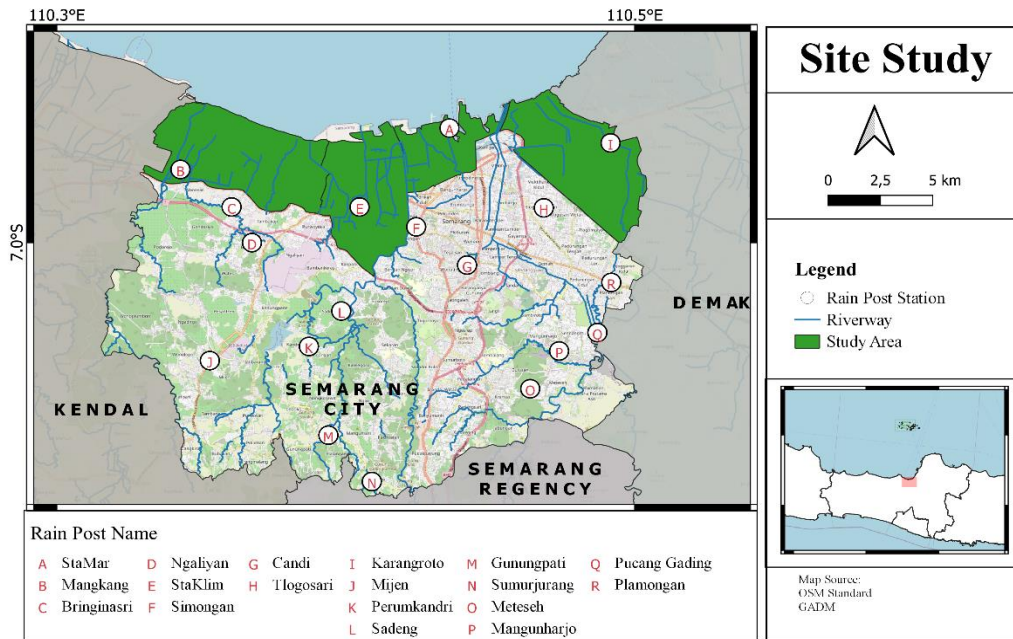


Fig. 1. Map of Semarang City and its sub-districts (green), from left to right, Tugu, West Semarang, North Semarang and Genuk.

Table 1.
Flood events in the coastal areas of Semarang from 2011-2020 recorded by National Disaster Management Authority

Affected district	Date of event
Genuk	October 31, 2020
Semarang Barat	May 2, 2020
Tugu	March 21, 2020
Genuk	March 7, 2020
Tugu	February 6, 2020
Semarang Utara	May 13, 2019
Tugu	April 4, 2019
Genuk	December 14, 2018
Genuk	December 6, 2018
Tugu	March 25, 2018
Semarang Barat	December 13, 2017
Semarang Utara	July 18, 2017
Genuk	February 15, 2017
Genuk	June 18, 2016
Semarang Utara	January 23, 2014
Genuk	January 23, 2014

3. DATA AND METHODS

3.1. Meteorological Parameters

Meteorological parameters used in this study include daily rainfall data (before incident (D-1), on the day of the incident (D-0), and the day after the incident (D+1)) and daily average wind direction and speed at the time of the incident. Both data are obtained from Indonesian Agency for Meteorological, Climatological and Geophysics (BMKG) Semarang in the form of daily total rainfall data from the nearest rain post to the affected area and hourly-observed wind speed and direction data. The result of this data can be seen on **Table 2**.

Table 2.
Analysis of rainfall conditions and wind condition at the time of flooding based on the season.

Affected District	Date of Event	Rainfall intensity (mm/day)			Wind Direction	Wind Speed (m/s)
		D-1	D-0	D+1		
Rainy Season						
Tugu	March 21, 2020	0	31	0	North – North East	1.75
Genuk	March 7, 2020	17	5	6	North West	2.30
Tugu	February 6, 2020	12	5	29	North West - North	2.75
Tugu	April 4, 2019	109	4	0	North East	1.50
Genuk	December 14, 2018	5	67	2	East – South East	1.78
Genuk	December 6, 2018	4	0	45	South East	2.03
Tugu	March 25, 2018	15	69	0	South East	1.91
Semarang Barat	December 13, 2017	0.3	14.5	7.5	North West - North	1.73
Genuk	February 15, 2017	0	14	0	North	2.29
Semarang Utara	January 23, 2014	120.5	36.9	92.8	South West – North West	5.05
Genuk		135	35	87	South West – North West	5.05
Dry Season						
Genuk	October 31, 2020	0	56	8	North	2.0
Semarang Barat	May 2, 2020	72	0	0	South East	1.61
Semarang Utara	May 13, 2019	0	0	0	North East - East	2.06
Semarang Utara	July 18, 2017	0	0	9	South East	3.52
Tugu	June 18, 2016	0	43	0	North East – South East	2.85
Genuk		4	13	1	North East – South East	2.85

3.2. Oceanographic Parameters

Oceanographic parameters analyzed in this study are tidal conditions and wave conditions (direction, significant height, maximum wave height and mean wave period). Tidal data was obtained from the Geospatial Information Agency (BIG). Tidal data will be adjusted to its Mean Sea Level (MSL) condition and also corrected with the detrend analysis to remove any trend from the data, which then will be analyzed based on the maximum tide height at the time of flooding in the coastal area of Semarang. The MSL height is obtained from the processing of the tidal harmonic components which are processed using the Least Square method. Wave conditions were analyzed using InaWAVES High Resolution hindcast data which obtain from BMKG with a horizontal resolution of $0.0625^\circ \times 0.0625^\circ$ ($6 \text{ km} \times 6 \text{ km}$). This hindcast data was then processed using GrADS to determine the significant wave height, maximum wave height, wave direction, and mean wave period at the time of the incident.

3.3. Land Subsidence

Land subsidence data processing was carried out using the DInSAR method by processing Sentinel-I SAR satellite data to identify spatial changes in an area by utilizing coherence in interferometric phase measurements from the same surface (Francis, et al., 1996).

Processing with the DInSAR method was carried out on the SNAP and SNAPHU applications. After obtaining the land subsidence map from the SNAP application, further analysis was carried out on the GIS mapping application to determine the rate of land subsidence in each sub-district on the coast of Semarang. The results obtained from processing with this GIS application include the minimum, maximum, average, and standard deviation rates of land subsidence in each sub-district in the research area.

4. RESULT AND DISCUSSION

4.1. Results on Meteorological Parameters

The results of processing rain data obtained from the Indonesian Agency for Meteorological and Geophysical (BMKG) daily rain post were analyzed according to the criteria specified in the KBMKG Regulation No. 009 of 2010 concerning Standard Operating Procedures for Implementation of Early Warning, Reporting and Socialization of Extreme Weather with the following criteria.

Table 3.

Rainfall Intensity Categories.

Rain Classification	Description
Light	1 – 5 mm/hour or 5 - 20 mm/day
Moderate	5 – 10 mm/hour or 20 – 50 mm/day
Heavy	10 – 20 mm/hour or 50 – 100 mm/day
Extreme	>50 mm/hour or >100 mm/day

Source: Perka KBMKG (2010)

Rainfall conditions of the previous, during and following day of the occurrences also daily average wind data values can be seen in **Table 3**. According to Setiawan (2018), Semarang city is still included in the seasonal zone which is influenced by the monsoon where the rainy season and dry season has clear distinction. Rainy season in monsoon zone active on November until April and dry season active on May until October (Aldrian & Susanto, 2013; Setiawan, 2018). Based on this, the result shows that 10 cases of the flooding happened in rainy season and 5 others in dry season.

In rainy season, 2 cases have heavy rainfall on the day of the incident, 2 cases on the previous day has extreme rainfall and 6 cases with light-moderate rainfall on the day or the previous day of the incident. Due to the condition of the Semarang city area which is close to the highlands and traversed by many rivers, it is very possible that the flooding that occurred in this coastal area was caused by rain that occurred in the highland area which then resulted in increased river water discharge reaching the coastal area. Therefore, for the occurrence in the rainy season, rain post data was added for the higher plains area which is close to the river flow that flows into the coastal area of the flood incident. The rain post location and the riverway across Semarang city can be seen in **Fig 1** and the additional rain post data can be seen in **Table 4**. In dry season, there are 5 occurrences of coastal flood in Semarang area, 1 cases in in October 31, 2020 has heavy rain ocured on the day of the incident, 1 cases in May 2, 2020 has heavy rain ocured on the previous day of the incident and 3 cases with rainfall 0 – 13 mm/day.

Based on the result in **Table 4**, it shows that in rainy season, although the flood-affected areas did not experience any heavy rains, the areas with higher elevations experienced heavy rains. It is assumed that this will result in an increase in river discharge that reaches the coastal area and causes flooding in the coastal area. From 6 cases with light – moderate rain on the location of the flooding area, 4 events indicate that flooding that occurs in coastal areas is indeed influenced by the occurrence of heavy rain that occurs in higher plains.

Table 4.

**Rainfall data from rain post station located in higher plains of the flood-affected areas
(Flood cases during rainy season).**

District	Date Of Event	Rainpost Location			Rainpost Location			Rainpost Location		
		Rain data (D-1)	Rain data (D-0)	Rain data (D+1)	Rain data (D-1)	Rain data (D-0)	Rain data (D+1)	Rain data (D-1)	Rain data (D-0)	Rain data (D+1)
Tugu	March 21, 2020	Mangkang			Bringin Asri			Ngaliyan pp ex rumah dinas		
		0	31	0	1	19	0	0	0	0
Genuk	March 7, 2020	Karangroto			Tlogosari			Plamongan		
		4	15	11	8	8	14	4	15	11
		Pucang Gading			Mangunharjo			Meteseh		
		1	21	13	4	26	13	4	13	17
		Sumurjurang								
		61	76	35						
Tugu	Feb 6, 2020	Mangkang			Bringin Asri			Ngaliyan pp ex rumah dinas		
		12	5	29	3	16	56	65	15	95
Tugu	April 4, 2019	Bringin Asri			Ngaliyan pp ex rumah dinas			Mijen		
		81	48	0	109	4	0	89	14	10
Genuk	Dec 14, 2018	Karangroto			Tlogosari			Plamongan		
		5	67	2	38	75	2	21	42	1
Genuk	Dec 6, 2018	Karangroto			Tlogosari			Plamongan		
		4	0	45	3	0	27	0	0	79
Tugu	March 25, 2018	Bringin Asri			Ngaliyan pp ex rumah dinas					
		15	69	0	11	50	0			
Semarang Barat	Dec 13, 2017	Staklim			Simongan			Sadeng		
		0.3	14.5	7.5	1	126	12	0	62	17
Genuk	Feb 15, 2017	Karangroto			Tlogosari			Plamongan		
		0	14	0	1	23	1	1	39	8
		Mangunharjo			Meteseh			Sumurjurang		
		10	13	12	1	53	23	31	68	23

From the condition of the direction and speed of the wind at the time of the incident, 46.6% of the total flooding events, the wind came from the Northwest – North, 13.3% from North East – East, and the rest came from South East with wind speeds varying from 1.5 – 5.05 m/s. This wind speed condition based on the KBMKG Perka (2010) is not included in extreme conditions. The extreme wind speed conditions based on the KBMKG Perka (2010) are above 12.8 m/s.

4.2. Results on Oceanographic Parameters

Analysis of wave conditions was studied based on significant height, maximum wave height, mean wave direction and also the mean period. The analysis of significant wave heights then was categorized according to the Douglas scale as shown in **Table 5**. The tabulation results between wave conditions and sea level based on tides can be seen in **Table 6**. The significant wave height in the northern waters of Semarang varies between 0 – 1.23 meters. Based on the Douglas scale this altitude is still in the smooth to moderate category. While maximum wave height varies from 0 – 2.07 meters. In the Perka KBMKG (2010), it is stated that the condition of sea waves that need to be disseminated for early warning is significant sea waves with a height greater than or equal to 2 meters. The mean wave period also varies between 2 - 6 seconds in all cases of coastal flooding. According to Holthuijsen (2010), the mean wave period shows that the sea surface is still influenced by the wind, so the waves formed are still in the category of wind-generated waves. As for the direction of the

waves, in line with the definition of wind-generated waves or waves that are still influenced by the wind, the direction of the waves at the time of the flooding incident was 80% from the Northwest. The same thing also happened to the condition of the wind direction which was dominated from the Northwest.

Table 5.
Wave Categories based on Douglas sea scale.

Wave height (m)	Description
0.1 – 0.5	Smooth
0.5 – 1.25	Slight
1.25 – 2.50	Moderate
2.50 – 4.0	Rough
4.0 – 6.0	Very Rough
6.0 – 9.0	High
9.0 – 14.0	Very High

Source: Owens E.H (1982).

Table 6.
Tabulation of wave and sea level data analysis.

Affected District	Date of Event	Mean Period (s)	Significant Wave Height (m)	Maximum Wave Height (m)	Wave Direction (from)	Tidal Height (cm)
Rainy Season						
Tugu	March 21, 2020	4	0.04 – 0.06	0.06 – 0.08	West	34.77
Geluk	March 7, 2020	3 – 4	0.35 – 0.49	0.47 – 0.65	North West	20.04
Tugu	February 6, 2020	3 – 4	0.36 – 0.76	0.53 – 1.11	North West	16.58
Tugu	April 4, 2019	3	0.01 – 0.03	0.02 – 0.04	North West	20.34
Geluk	December 14, 2018	3 – 4	0.05 – 0.17	0.08 – 0.23	North West	47.12
Geluk	December 6, 2018	4	0	0	West – North West	28.27
Tugu	March 25, 2018	3 – 6	0.03 – 0.21	0.04 – 0.28	North West	16.95
Semarang Barat	December 13, 2017	4	0 – 0.16	0 – 0.27	West – North West	38.72
Geluk	February 15, 2017	4	0.37 – 0.47	0.62 – 0.77	West – North	35.09
Semarang Utara	January 23, 2014	4 – 5	0.93 – 1.23	1.58 – 2.07	West - North	20.38
Geluk		4 – 5	0.93 – 1.23	1.58 – 2.07	West - North	20.38
Dry Season						
Geluk	October 31, 2020	4	0.01 – 0.04	0.01 – 0.06	North West	28.58
Semarang Barat	May 2, 2020	2 – 4	0.02 – 0.40	0.02 – 0.52	South West – North West	51.00
Semarang Utara	May 13, 2019	2 – 6	0 – 0.5	0 – 0.5	North East – South East	45.61
Semarang Utara	July 18, 2017	3 – 5	0.03 – 0.07	0.07 – 0.10	South West - West	52.41
Tugu	June 18, 2016	3 – 4	0 – 0.06	0.03 – 0.09	South West - West	56.5
Geluk		3 – 4	0 – 0.06	0.03 – 0.09	South West - West	56.5

There were 4 events with a significant wave height ≥ 0.5 meters and 2 events with a maximum wave height above 1 meter. Nursamsiah, et al (2017) tried to analyze the extreme height of significant wave height in the Northern waters of Semarang area, which the result shows that extreme significant height in this area varies between 0.25 – 1.48 meters depends on the month. The highest extreme condition occurs in January, February, December and March with height 1.48 m, 1.27 m, 0.87 m, 0.80 m respectively. This result is also seen in the results of this study where the wave height is also quite high in these months. The MSL height in Semarang waters which obtained using the Least Square method is 187.63 cm. This value is obtained from the So component of the tidal harmonic analysis. After the observation data was adjusted to the MSL height and eliminated the trend using the detrend analysis, the result can be seen in **Fig. 2**.

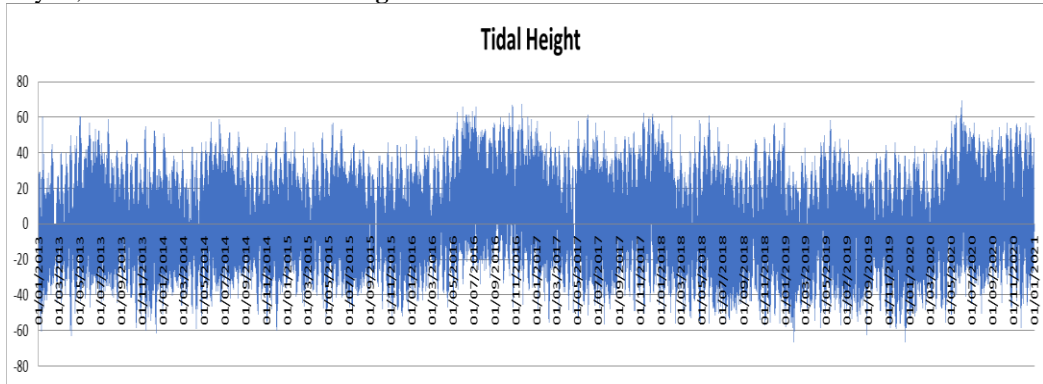


Fig. 2. Historical data of tidal waves on Semarang area in 2013–2020.

Based on the results in **Table 6**, in rainy season, the tidal height varies between 16.58 – 47.12 cm, while in dry season the tidal height varies from 28.58 – 56.5 cm. 4 out of 5 cases of flooding events happened in dry season has tidal height exceeding 45 cm, the case on October 21, 2020 is more likely being affected by the heavy rain as explained in the previous section. Based on this results, it can be concluded that the floods that occur during the dry season are more influenced by high tidal waves. The flooding areas map based on the result of this and previous section can be seen in **Fig. 3**.

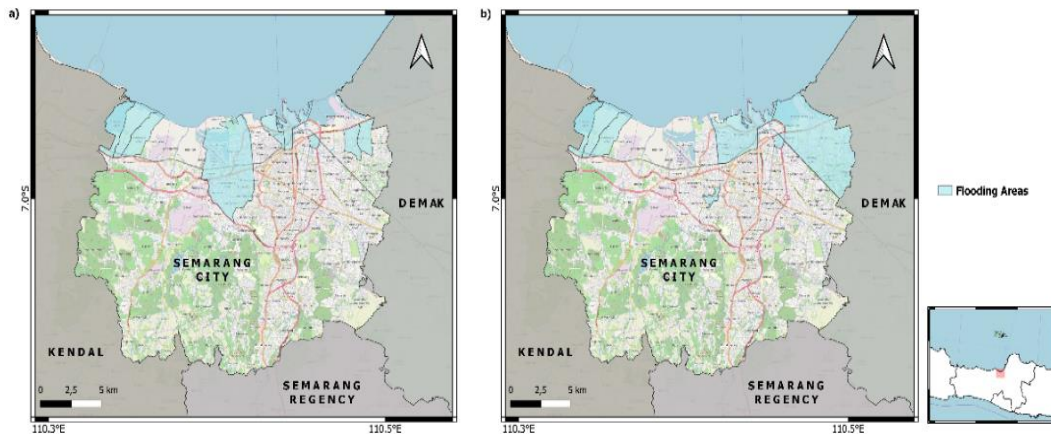


Fig. 3. (a) Flooding areas caused by tidal waves, (b) Flooding areas caused by rainfall

Flooding areas data was obtained from both BNPB and online newspaper, since not all flooding location was mentioned in BNPB records. Verification of the area that affected by the floods in Semarang city is very difficult because there is no field data that can be used to verify it, such as satellite image data or aerial photos during a flood.

4.3. Results on Land Subsidence

Sentinel-I SAR data processing used recorded data from 2021 and 2020 so that the results of land subsidence in this study indicate the rate of land subsidence during 2020. The map of land subsidence resulting from the processing of the DInSAR method can be seen in **Fig. 4**. Processing on the GIS application was carried out to form Regions of Interest (ROIs) to obtain the maximum, minimum, average and standard deviation values for each sub-district in the coastal area of Semarang. The statistical results of ROIs can be seen in **Table 7**

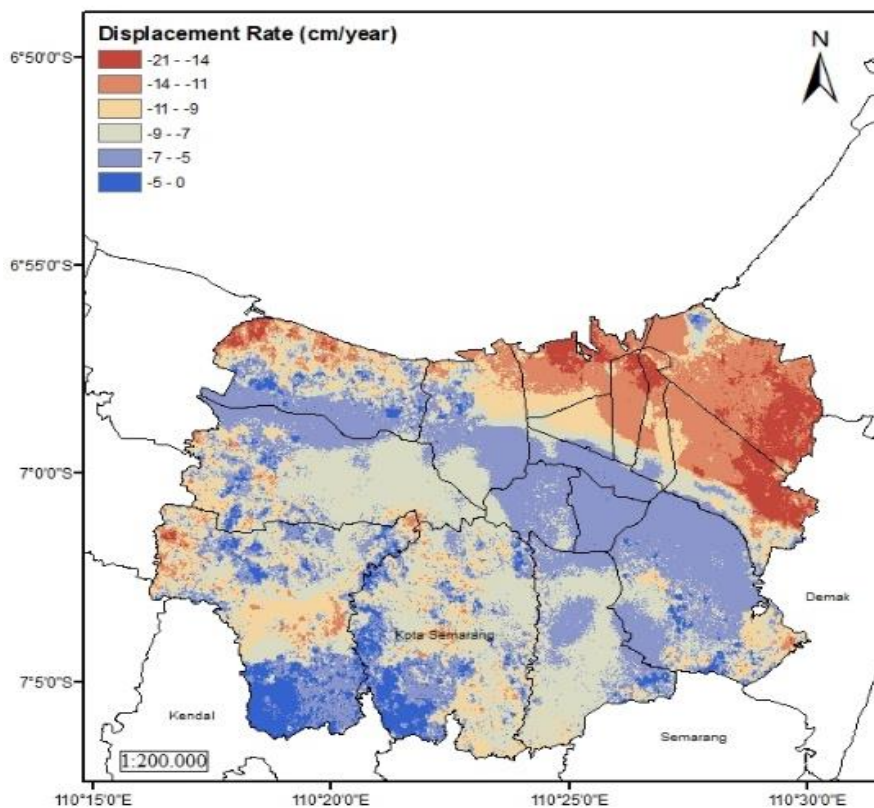


Fig. 4. Map of the land subsidence of Semarang City in 2020.

Table 7.
The rate of land subsidence in Semarang City in 2020 using the DInSAR method.

District	Maximum (m)	Minimum (m)	Average (m)	Standard Deviation
Tugu	-0.19	-0.016	-0.089	0.024
Semarang Barat	-0.16	-0.023	-0.087	0.019
Semarang Utara	-0.21	-0.071	-0.129	0.020
Genuk	-0.21	-0.041	-0.132	0.0186
Semarang (City)	-0.21	+0.018	-0.0899	0.026

Based on the results above, the average land subsidence in the coastal area of Semarang is greatest in the Genuk District, based on a land use map in Semarang according to Agency for Regional Development (Bappeda) (2011) this area is dominated by residential and industrial areas. Research on land subsidence has often been done, with a similar method Fakhri Islam et al., (2017) researching land subsidence in the Semarang area in 2016, the results can be seen in **Table 8** below.

Table 8.
The land subsidence rate of Semarang City in 2016 used the DInSAR method.

District	Maximum (m)	Minimum (m)	Average (m)	Standard Deviation
Tugu	-0.1674	+0.0585	-0.0474	0.0238
Semarang Barat	-0.1463	+0.0113	-0.0411	0.0196
Semarang Utara	-0.1549	-0.0203	-0.0823	0.0158
Genuk	-0.1593	-0.039	-0.1035	0.0186

Source :Fakhri Islam et al., (2017)

By comparing data of land subsidence in 2020 to the result of research done in 2016, it is shown that the rate of land subsidence in all coastal areas of Semarang has increased by 50% or doubled. This condition will greatly affect the tidal conditions that occur. When coastal areas continue to subside, these areas will more easily experience tidal flooding due to sea level that is higher than the land areas that are experiencing land subsidence.

5. CONCLUSION

Based on the results of previous section, it is known that the incidence of flooding in the coastal area of Semarang can be distinguished by the causal factors based on the season. Semarang City which is still included in the monsoon zone has 2 types of seasons, namely the rainy season in November - April and the dry season in May - October. Floods that occur in the rainy season are strongly influenced by the intensity of the rain that occurs. All flood events that occurred in the rainy season have heavy to extreme rain intensity with a value of > 50 mm/day either on the day or the previous day before the incident. Interestingly, in several flood events during rainy season, the incident area did not experience high intensity of rain. However, because this coastal area is also traversed by rivers and the slope of the land in the Semarang area is quite high, then when heavy rains occurred in the higher plains of the Semarang area, it can cause flooding in the coastal areas of Semarang. Thus, monitoring the rain that occurs in the highlands of Semarang is also very necessary. During dry season, tidal wave conditions also need to be monitored. Four out of 5 flood cases during the dry season have high tides above 45 cm. These results of the analysis show that important parameter that can be used in making early warning information for coastal flooding in the coastal area of Semarang is the rainfall and tide wave condition. These parameters can be used to increase the level of vigilance before issuing early warning information. Land subsidence parameters also play an important role in the incidence of coastal flooding. Based on the results of the study, the difference in the rate of land subsidence in the last 5 years has increased significantly. If the condition of the worsened land subsidence is not handled properly, the potential for flooding in this coastal area will likely continue to increase.

ACKNOWLEDGEMENTS

The authors would like to thank the Faculty of Fisheries and Marine Sciences for the opportunity given in the preparation of this research and all parties involved in this research. The authors also thank the Geospatial Information Agency and the Meteorology, Climatology and Geophysics Agency for the data provided to support the smooth running of this research.

REFERENCES

- Afifah, R. S. (2014). Pemetaan Geologi Daerah Semarang Dan Sekitarnya, Kecamatan Gajahmungkur, Sampangan, Kotamadya Semarang, Provinsi Jawa Tengah. *MTG*, 4(2).
- Agency for Regional Department (Bappeda). (2011). *Rencana Tata Ruang Wilayah Kota Semarang Tahun 2011 – 2031*. Peraturan Daerah Kota Semarang Nomor 14 Tahun 2011. Kepala Bappeda. Semarang.
- Aldrian, E., & Dwi Susanto, R. (2003). Identification of three dominant rainfall regions within Indonesia and their relationship to sea surface temperature. *International Journal of Climatology: A Journal of the Royal Meteorological Society*, 23(12), 1435-1452.
- Alifdini, I., Shimada, T., & Wirasatriya, A. (2021). Seasonal distribution and variability of surface winds in the Indonesian seas using scatterometer and reanalysis data. *International Journal of Climatology*, 41(10), 4825–4843. <https://doi.org/10.1002/joc.7101>.
- Batista, C. M. (2018). Coastal flood Hazard mapping. *Encyclopedia of Earth Sciences Series, PartF2*. https://doi.org/10.1007/978-3-319-48657-4_356-1.
- Bijlsma, L., Ehler, C. N., Kulshrestha, S. M., Mclean, R. F., Mimura, N., Nicholls, R. J., Nurse, L. A., Stakhiv, E. Z., Turner, R. K., & Warrick, R. A. (1995). Coastal Zones and Small Islands. *Climate Change 1995: Impacts, Adaptations and Mitigation of Climate Change: Scientific-Technical Analyses*, 289–324.
- Central Bureau of Statistic. (2020). *Statistik Sumber Daya Laut Dan Pesisir*. Katalog BPS / BPS Catalogue : 3312002.
- Fakhri Islam, L. J., Prasetyo, Y., & Sudarsono, B. (2017). Analisis Penurunan Muka Tanah (Land Subsidence) Kota Semarang Menggunakan Citra Sentinel-1 Berdasarkan Metode Dinsar Pada Perangkat Lunak Snap. *Jurnal Geodesi Undip*, 6(2), 29–36.
- Francis, P. W., Wadge, G., & Mouginis-Mark, P. J. (1996). Satellite monitoring of volcanoes. R. Scarpa and R.I. Tilling (eds.) *Monitoring and mitigation of volcano hazards*, SpringerVerlag, 257-298.
- Hoeke, R. K., McInnes, K. L., Kruger, J. C., McNaught, R. J., Hunter, J. R., & Smithers, S. G. (2013). Widespread inundation of Pacific islands triggered by distant-source wind-waves. *Global and Planetary Change*, 108, 128-138.
- Indonesian Agency for Meteorological, Climatological and Geophysics. (2010). *Prosedur Standar Operasional Pelaksanaan Peringatan Dini, Pelaporan, Dan Diseminasi Informasi Cuaca Ekstrim*. Peraturan KBMKG Nomor: 009 Tahun 2010. Kepada Badan Meteorologi, Klimatologi dan Geofisika. Jakarta.
- Irawan, A. M., Marfai, M. A., Munawar, Nugraheni, I. R., Gustono, S. T., Rejeki, H. A., Widodo, A., Mahmudiah, R. R., & Faridatunnisa, M. (2021). Comparison between averaged and localised subsidence measurements for coastal floods projection in 2050 Semarang, Indonesia. *Urban Climate*, 35(May 2020), 100760. <https://doi.org/10.1016/j.uclim.2020.100760>.
- Marfai, M. A., & King, L. (2008). Coastal flood management in Semarang, Indonesia. *Environmental Geology*, 55(7), 1507–1518. <https://doi.org/10.1007/s00254-007-1101-3>.
- Maritime Meteorology Center. (2022). *Peringatan Dini Banjir Rob*. [Online] Available from: <https://peta-maritim.bmkg.go.id/info/19/Peringatan-Dini-Banjir-Rob>. [Accessed 07 January 2022].
- National Development Planning Agency. (2019). *Rencana Pembangunan Jangka Menengah Nasional 2020-2024*. Rancangan Teknokratik. Jakarta.
- National Disaster Management Authority. (2021). *Geoportal Data Bencana Indonesia*. [Online] Available from: <https://gis.bnpb.go.id/>. [Accessed 04 June 2021].
- Nursamsiah, N., Sugianto, D. N., & Suprijanto, J. (2017). Analisis Data Ekstrim Tinggi Gelombang di Perairan Utara Semarang menggunakan Generalized Pareto Distribution. *Proceeding of Annual Seminar of Fisheries and Marine Science VI*, 243 – 253.

- Owens E.H. (1982) *Sea conditions*. In: *Beaches and Coastal Geology*. Encyclopedia of Earth Sciences Series. Springer, New York, NY. https://doi.org/10.1007/0-387-30843-1_397
- Republic of Indonesia (RI). (2014). *Pengelolaan Wilayah Pesisir dan Pulau-Pulau Kecil*. Undang-Undang RI Nomor 1 Tahun 2014. Presiden Republik Indonesia. Jakarta.
- Setiawan, D. (2018). *Pengelompokan Zona Musim di Indonesia Berdasarkan Data Curah Hujan Menggunakan Time Series Based Clustering*. [Online]. Available from: https://repository.its.ac.id/56777/%0Ahttps://repository.its.ac.id/56777/1/062114400000071-Undergraduate_Theses.pdf. [Accessed 20 June 2022].
- Smith, G., & Juria, N. (2019). Diagnosis of historical inundation events in the Marshall Islands to assist early warning systems. *Natural Hazards*, 99(1), 189–216. <https://doi.org/10.1007/s11069-019-03735-9>.
- Widada, S., Zainuri, M., Yulianto, G., Satriadi, A., Jati Wijaya, Y., & Helmi, M. (2020). Mitigation of floodwaters inundation due to land subsidence in the coastal area of Semarang City. *IOP Conference Series: Earth and Environmental Science*, 530(1), 0–6. <https://doi.org/10.1088/1755-1315/530/1/012006>.

ESTIMATION OF PARTICULATE MATTER LESS THAN 10 MICRONS VOLUME THROUGH VARIOUS FORMATS OF SPATIAL INTERPOLATION METHODS

Jumpol ITSARAWISUT¹ ^{*}, Teerawong LAOSUWAN¹ 

DOI: 10.21163/GT_2022.172.03

ABSTRACT:

The problem on air pollution, especially the problem on smoke caused by accumulation of smoke and dust in the air, is considered as one of important problems in Thailand and this problem is currently more serious increasingly. This study aims to study on relationship between Particulate Matter Less Than 10 Microns (PM₁₀) volume in northern area and physical factors of the area as well as estimate PM₁₀ through various formats of Spatial Interpolation Methods and study on appropriateness of each method. The result revealed that mean of 24 hours of PM₁₀ volume throughout 5 years from 2017 – 2021 was in the highest level in March with average volume from all weather stations at 101 μg/m³ followed by February and April. Month with the lowest PM₁₀ volume was July. When analyzing on physical characteristics of areas with high PM₁₀ volume, it was found that northern area had landscape of intermontane plateau with small area. Since it was surrounded by mountain ranges, distribution of dust was poor. In addition, since it was located near some neighboring countries, it was affected by dust from wildfire and open burning that was blown from many areas as well as those neighboring countries. When using data on mean of PM₁₀ volume from 9 weather stations of Pollution Control Department (PCD) to evaluate PM₁₀ volume through various formats of Spatial Interpolation Methods, including Inverse Distance Weight (IDW), Kriging, Spline, and Trend, it was found that IDW was the most suitable method for making map showing distribution of PM₁₀ volume, especially from February to April with the highest volume of dust due to the lowest level of difference between estimated value and measured value. For spatial interpolation by using Spline method, it was found to be improper due to the highest level of difference between estimated value and measured value.

Key-words: Air pollution, PM₁₀, Spatial Interpolation, Geographic Information System

1. INTRODUCTION

Air pollution is air condition with contamination that may not be seen by naked eyes, for example, dust, natural gas, or pollution emitted from exhaust pipe, etc. It is considered as imminent danger causing huge effects and dangers against our health. Air pollution is classified as another important problem of Thailand and this problem is currently more serious increasingly (Junpen et al., 2018). There are 2 major causes of air pollution including: human actions, for example, demands on energy for consuming in households, industries, and agriculture as well as air pollution caused by cars, ships, and planes that causes CO₂, NO₂, and hydrocarbons giving bad effects to human's health directly (Canha et al., 2021; Thai et al., 2021). Combustion of these types of fuel also increase the problems on air pollution every year; natural actions, for example, volcanic eruption causing high amount of dust and ash blowing in the air (Perera, 2018; Mperejekumana et al., 2021), wildfire causing smoke that is dangerous for respiratory system, decomposition of humus and carcass that may cause CO₂, CH₄, and NH₃ in case of chemical reaction (Ray et al., 2019; Junpen et al., 2020); and dust caused by broken objects that would be distributed in the air when they are blown by the wind.

¹Department of Physics, Faculty of Science, Mahasarakham University, Thailand, *Corresponding author, jumpol.i@msu.ac.th, teerawong@msu.ac.th

Although the problem on pollution is unable to be solved but it can be analyzed and monitored continuously in order to control further problems on air pollution (Kim et al., 2014; WHO, 2018).

In each region of Thailand, causes of air pollution are similar and different based on landscape and land utilization (Intarat, 2017; Supasri et al., 2018; Vichit-Vadakan et al., 2011; Suriya et al., 2021). For the problem on haze pollution in the northern part of Thailand, it was found that the major cause was wildfire and open burning in Thailand and neighboring countries. It is a kind of open burning of agricultural wastes for preparing plantation areas for plantation in rainy season, open burning for facilitating puff ball mushrooms and wild sweet leaves collecting, community waste incineration, and firing for warming (Pongkaset et al., 2020). These actions cause the problem on small dust and hazardous gases. This kind of open burning causes the important pollution problem of the northern part of Thailand, i.e., the problem of small dust causing health effects (Choi et al., 2015; Chalvatzaki et al., 2019), especially PM₁₀ is a dust with a particulate matter less than 10 microns produced by fuel combustion, open burning, industrial processes, grinding, milling, or powdering of construction. PM₁₀ may cause effects against body system when it enters our body, for example, coughing, sneezing, and shortness of breath that are the causes of diseases related to respiratory system.

Currently, Geographic Information System (GIS) is used to create spatial model from data on map, image, and other kinds of data (Pradabmook & Laosuwan, 2021). GIS can be applied to various fields (Pradabmook & Laosuwan, 2021; Wiatkowska et al., 2021; Jazdzewska et al., 2022) and used as a part of analysis on areas and distribution of air pollution (Eeftens et al., 2016; when surveying to collect field data, there may be some gaps of data when using data to perform mapping. As a result, it is required to estimate value of such gaps by using Spatial Interpolation Methods, for example, topographic mapping, calculation on density of population and weather. Data must be analyzed to use the results of estimation to study on relationship related to other kinds of data (Goovaerts, 1997; Mitmark & Jinsart, 2017; Goutham et al., 2018; Srivastava et al., 2019).

This study was conducted to study on relationship between PM₁₀ volume in the northern area of Thailand and physical factors of area, to evaluate PM₁₀ volume by using various formats of spatial interpolation methods, and to study on appropriateness of various formats of spatial interpolation methods with evaluation of PM₁₀ volume in the northern part of Thailand by using GIS as the operational tool. The obtained results could be useful for managing and controlling air pollution and used as supporting data of further researches on air pollution in other areas.

2. MATERIALS AND METHODS

2.1 Study Area

The northern part of Thailand (**Fig. 1**) has total area of 96,077 km² consisted of 9 provinces, i.e., Chiang Rai, Chiang Mai, Nan, Phayao, Phrae, Mae Hong Son, Lampang, Lamphun, and Uttaradit (Wikipedia, 2021). Most landscapes are mountain ranges, mountains, valleys, and intermontane plateau with steeps from the northeastern part that gradually slope to lowlands in the southeastern part and central part before getting higher in the eastern part and the northeastern part in Nan province, i.e., Luang Prabang Range. These plateaus are considered as the sources of various rivers and streams that flow to Mekong River from the north to Chao Phraya River in the south before flowing to Salawin River in the west. For climate, it is classified as tropical zone for some seasons (Department of Mineral Resources, 2021).

Climate of most northern areas is Aw, i.e., tropical wet switched with drought. Average yearly temperature is ranged from 24-27°C with 3 seasons including rainy season (May – October), winter (October–February), and summer (February – May). Province with the lowest temperature is Chiang Rai and province with the highest temperature is Uttaradit. Province with heavy rainfall is Chiang Rai whereas province with the lowest rainfall is Lampang with average rainfall of 1,230 mm/y and 110 rainy days. Zone with low rainfall has average rainfall of 800-1,000 mm/y whereas zone with heavy rainfall has the highest rainfall of 2,000 mm/y.

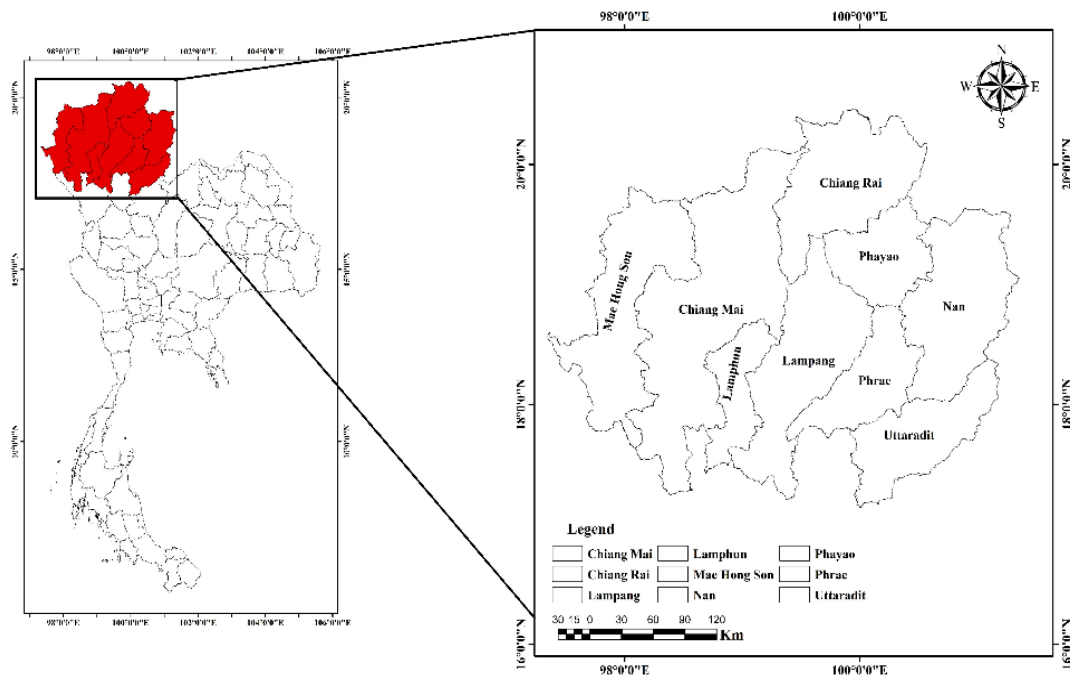


Fig. 1. The northern part of Thailand.

2.2 Collection and Preparation of Data on GIS

This research was conducted to study on methodology and operational guidelines from documents and researches related to distribution of dust and air pollution in Thailand and other countries. Subsequently, data were collected from various sources in order to evaluate PM₁₀ volume in the northern part by using Spatial Interpolation Methods consisted of the following data:

- (1) Data on PM₁₀ volume in the northern part (Source: Pollution Control Department);
- (2) Data on location of weather stations (Source: Pollution Control Department);
- (3) Data on boundary of the northern part and administrative boundaries of provinces in the northern part (Source: Royal Thai Survey Department); and
- (4) Data on height of areas in the northern part (Source: Royal Thai Survey Department)

2.3 Research Tools

- (1) High quality computer for data processing;
- (2) GIS software package, in this study, ArcMap 10.2 was used as the base software; and
- (3) Data on dust volume from Air4Thai website (<http://air4thai.pcd.go.th/webV3/#/Home>)

2.4 Procedures of Data Analysis

The Materials and Methods should be described with sufficient details to allow others to replicate and build on the published results. Please note that the publication of your manuscript implicates that you must make all materials, data, computer code, and protocols associated with the publication available to readers. Please disclose at the submission stage any restrictions on the availability of materials or information. New methods and protocols should be described in detail while well-established methods can be briefly described and appropriately cited.

(1) Collect data on PM₁₀ volume from weather stations of Pollution Control Department, data on location of weather stations, and data on boundary of the northern part and administrative boundaries of provinces in the northern part for inputting into GIS system.

(2) Analysis on relationship between PM₁₀ volume and physical characteristics of area in the northern part consisted of locations, distance from neighboring countries, months with dust distribution, and landscapes in the manner of intermontane plateau with differences on sizes of plateaus and height, etc.

(3) Spatial Interpolation Methods was analyzed by using data obtained from measurement of PM₁₀ volume from 9 weather stations of Pollution Control Department during 2017 – 2021 through 4 Spatial Interpolation Methods including IDW, Kriging, Spline, and Trend. Subsequently, PM₁₀ volume was mapped and Table on Conclusion of Differences of Monthly PM₁₀ Volume Data during 2017-2021 was made. There were 9 weather stations used in analysis through spatial interpolation including:

- 1) Ministry of Natural Resources and Environment in Chiang Rai (No.1), located between the latitude of 19.910 and the longitude of 99.823;
- 2) Public Health Office in Mae Sai District, Chiang Rai (No.2), located between the latitude of 20.427 and the longitude of 99.883;
- 3) Chiang Mai City Hall in Muang District, Chiang Mai (No.3), located between the latitude of 18.925 and the longitude of 98.651;
- 4) Yupparaj Wittayalai School in Muang District, Chiang Mai (No.4), located between the latitude of 18.791 and the longitude of 98.978;
- 5) Nan Municipality Office in Nan District, Nan (No.5), located between the latitude of 18.784 and the longitude of 100.779;
- 6) Phayao Learning Park in Muang District, Phayao (No.6), located between the latitude of 19.168 and the longitude of 99.896;
- 7) Phrae Weather Station in Muang District, Phrae (No.7), located between the latitude of 18.128 and the longitude of 100.162;
- 8) Ministry of Natural Resources and Environment in Mae Hong Son (No.8), located between the latitude of 19.304 and the longitude of 97.971; and
- 9) Sobprad Sub-District Health Promoting Hospital in Mae Moe District, Lampang (No.9), located between the latitude of 18.250 and the longitude of 99.763.

(4) Differences and appropriateness of each Spatial Interpolation Methods were analyzed in order to obtain appropriate methods for mapping the map showing distribution of PM₁₀ volume in the northern part.

3. RESULTS AND DISCUSSION

3.1. Result of Evaluation of PM₁₀ Volume and Relationship with Physical Factors of Area

The result of evaluation of PM₁₀ volume and relationship with physical factors of area from mean of 24 hours of PM₁₀ volume throughout 5 years from 2017 – 2021 obtained from 9 weather stations was shown in **Table 1**.

From **Table 1**, it was found that mean of 24 hours of average PM₁₀ volume throughout 5 years from 2017– 2021 was in the highest level in March with average volume from all weather stations at 101 µg/m³ followed by April and February with volume of 73 and 66 µg/m³, respectively. The lowest volume was in July with average volume from all weather stations at 19 µg/m³ that was similar to June with average volume of 20 µg/m³. When considering on mean of each weather station, it was found that Chiang Mai City Hall in Chiang Mai had the highest mean, i.e., 47 µg/m³ followed by Public Health Office in Mae Sai District, Chiang Rai, and Phrae Weather Station with mean of 43 and 42 µg/m³, respectively. From analyzing on physical characteristics of areas with high volume of small dust, it was found that they were intermontane plateaus with small areas and pressure of cooler air mass in upper atmosphere causing poor distribution of dust. In addition, with landscape surrounded by mountain ranges and neighboring countries like Myanmar and Laos, this area had to encounter with dust problem from wildfire and wind from various sources as well as those from neighboring countries blew open burning that.

Table 1.

Mean of 24 hours of PM₁₀ volume throughout 5 years from 2017 – 2021 (µg/m³).

Weather	Jan	Feb	Mar	Apr	May	Jun	Jul	Aug	Sep	Oct	Nov	Dec	Mean
No.1	34.00	57.20	102.8	80.80	45.20	20.00	17.80	25.00	21.20	22.00	26.8	35.8	40.71
No.2	34.60	55.80	118.20	87.60	46.60	26.80	19.20	16.00	22.00	23.00	29.20	37.80	43.06
No.3	44.80	72.20	105.20	85.20	47.60	23.60	26.80	28.40	29.20	31.40	35.60	44.00	47.83
No.4	45.00	69.20	98.60	78.40	44.20	29.80	31.80	30.80	30.00	32.20	36.60	43.40	47.5
No.5	37.20	59.60	94.00	74.80	41.00	17.80	20.20	20.80	24.60	27.20	29.80	36.60	40.30
No.6	40.00	66.20	98.00	54.80	26.00	10.20	10.20	10.20	12.00	19.00	21.60	31.40	32.45
No.7	48.80	78.00	96.00	66.00	38.20	20.20	19.00	17.80	22.00	27.60	34.40	45.20	42.76
No.8	37.40	68.40	114.20	70.10	38.40	17.20	17.80	16.80	16.60	25.00	27.80	38.40	40.67
No.9	42.20	69.60	86.00	59.40	38.20	16.80	17.00	15.00	16.20	18.40	20.20	34.20	36.1
Mean	40.44	66.24	101.44	73.01	40.60	20.26	19.97	20.42	21.53	25.08	29.11	38.53	41.26

March was considered as the period with no main monsoon that was flown to Thailand, i.e., northeast monsoon and southwest monsoon. Consequently, general climate was swelter and drought. As a result, there was no factor to reduce and distribute density of dust. Therefore, based on data analyzed in this research, it was found that PM₁₀ volume was in the highest level in March.

3.2. Result of Evaluation of PM₁₀ Volume through Spatial Interpolation Methods

Data on mean throughout 5 years from 2017 – 2021 obtained from 9 weather stations were analyzed by 4 Spatial Interpolation Methods including IDW, Kriging, Spline, and Trend. The result was shown in Fig. 2 and Table 2.

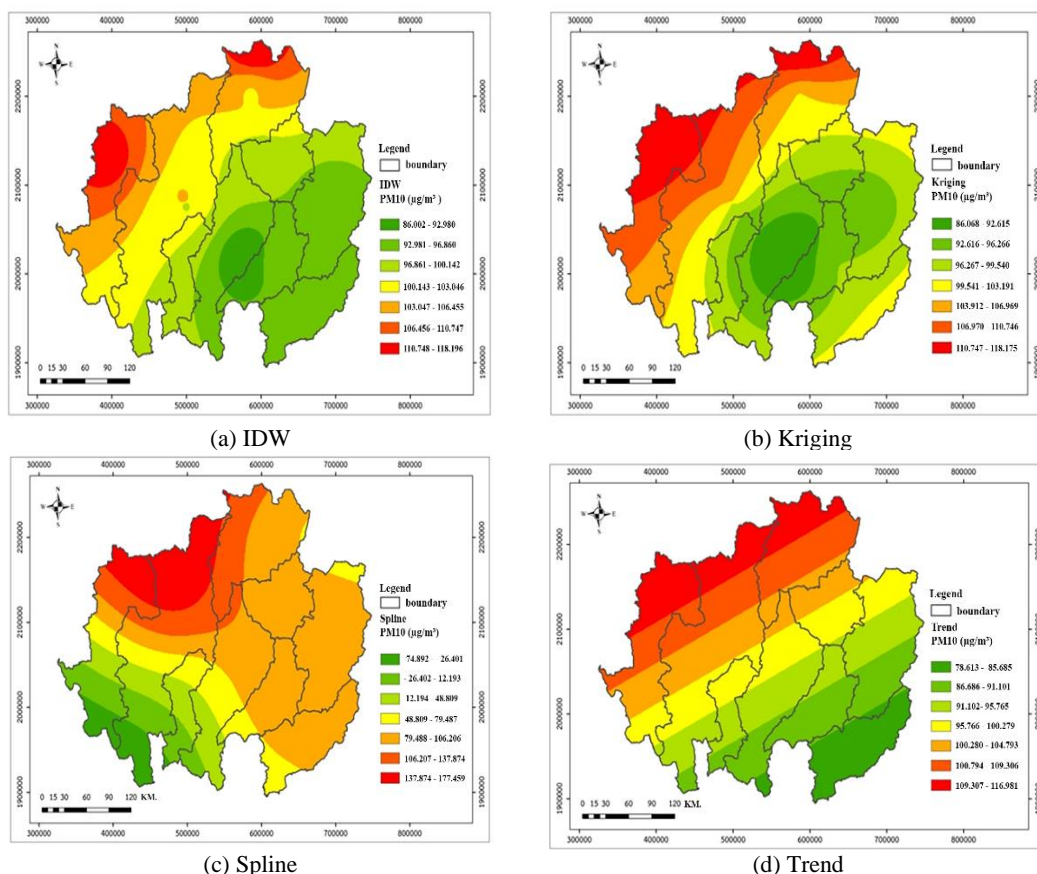


Fig. 2. Spatial Interpolation Methods (a) IDW, (b) Kriging, (c) Spline and (d) Trend.

The result of spatial interpolation of average PM₁₀ volume throughout 5 years from 2017 – 2021 obtained from 9 weather stations revealed that the highest PM₁₀ volume was in March followed by February and April. Similarly, actual measurement revealed that the lowest PM₁₀ volume was in July and September. This was different from mean obtained from actual measure that revealed that the lowest volume was in August.

Table 2.

Month	IDW	Kriging	Spline	Trend	Mean
January	40	40	41	39	40
February	65	66	67	66	66
March	101	100	102	100	101
April	72	72	75	73	73
May	39	39	42	40	40
June	19	19	22	20	20
July	18	18	20	19	19
August	19	19	22	20	20
September	21	21	19	23	21
October	25	25	25	25	25
November	29	29	29	29	29
December	38	38	38	38	38

3.3. Differences between Spatial Interpolation Methods and Actual Measurement

Data on PM₁₀ volume obtained from analysis through 4 methods from 9 weather stations were compared with data obtained from actual measurement. In this research, it was found that each weather station yielded different value of data. In March with the highest PM₁₀ volume, it could represent difference of each method as shown in **Table 3**.

Table 3.

Weather stations	PM ₁₀ from Station	Spatial Interpolation Methods							
		IDW		Kriging		Spline		Trend	
		Spatial Interpolatio	(+/-)	Spatial Interpolatio	(+/-)	Spatial Interpolatio	(+/-)	Spatial Interpolatio	(+/-)
		n		n		n		n	
No.1	102	110	-8	110	-8	110	-8	115	-13
No.2	118	125	-7	125	-7	125	-7	124	-6
No.3	105	115	-10	115	-10	115	-10	110	-5
No.4	98	96	-2	96	-2	96	-2	96	-2
No.5	94	95	-1	95	-1	95	-1	95	-1
No.6	98	100	-2	100	-2	100	-2	105	-7
No.7	96	97	-1	97	-1	97	-1	97	-1
No.8	114	117	-3	117	-3	117	-3	116	-1
No.9	86	90	-4	90	-4	90	-4	88	-2
Total difference			38		38		38		25

From **Table 3**, it was found that when analyzing data on PM₁₀ volume obtained from 9 weather stations of Pollution Control Department in the northern part during 2017 – 2021 in March through 4 Spatial Interpolation Methods including IDW, Kriging, Spline, and Trend, it was found that Trend yielded the lowest differences, i.e., 25, whereas IDW, Kriging, and Spline yielded the highest differences, i.e., 38. Spatial interpolation of each method yielded different value as follows:

Spatial Interpolation Methods through IDW method had the lowest differences at Chiang Mai City Hall in Chiang Mai whereas the highest differences were found at Nan Municipality Office in Nan and Phrae Weather Station in Phrae.

Spatial Interpolation Methods through Kriging method had the lowest differences at Chiang Mai City Hall in Chiang Mai whereas the highest differences were found at Nan Municipality Office in Nan and Phrae Weather Station in Phrae.

Spatial Interpolation Methods through Spline method had the lowest differences at Chiang Mai City Hall in Chiang Mai whereas the highest differences were found at Nan Municipality Office in Nan and Phrae Weather Station in Phrae.

Spatial Interpolation Methods through Trend method had the lowest differences at Nan Municipality Office in Nan District, Nan, Phrae Weather Station in Muang District, Phrae, and Ministry of Natural Resources and Environment in Mae Hong Son.

3.4. Result of Analysis on Monthly Differences of Spatial Interpolation Methods

The result of analysis on monthly differences of 4 Spatial Interpolation Methods based on mean of data of 12 months during 2017–2021 was shown in **Table 4**.

Table 4.

Analysis on Monthly Differences of Spatial Interpolation Methods.

Month	IDW	Kriging	Spline	Trend	PM ₁₀ from Station	Least different	Most different
January	40	40	41	39	40	Trend	Spline
February	65	66	67	66	66	IDW	Spline
March	101	100	102	100	101	Kriging/Trend	Spline
April	72	72	75	73	73	IDW/ Kriging	Spline
May	39	39	42	40	40	IDW/ Kriging	Spline
June	19	19	22	20	20	IDW/ Kriging	Spline
July	18	18	20	19	19	IDW/ Kriging	Spline
August	19	19	22	20	20	IDW/ Kriging	Spline
September	21	21	19	23	21	Spline	Trend
October	25	25	25	25	25	all method	without
November	29	29	29	29	29	all method	without
December	38	38	38	38	38	all method	without

From **Table 4**, it was found that when considering on appropriateness of 4 Spatial Interpolation Methods from 12 months during 2017–2021 including IDW, Kriging, Spline, Trend, spatial interpolation through IDW and Kriging was the appropriate method for mapping the map showing distribution of PM₁₀ volume due to the lowest differences between spatial interpolation and actual measurement of 10 months from 12 months followed by Trend and Spline of 5 months and 12 months.

3.5 Result of Analysis on Seasonal Differences of Spatial Interpolation Methods

Differences of PM₁₀ volume obtained from 4 Spatial Interpolation Methods including IDW, Kriging, Spline, and Trend obtained from actual measurement of 12 months were analyzed in each season with differences of climate during 2017–2021. In this research, it was found that IDW, Kriging, and Trend were the most appropriate methods for analyzing in drought, during January, February, March, and April, with high PM₁₀ volume because it yielded the lowest differences. The method that was improper was Spline because differences were in the highest level in this duration. For rainy season from May to July, August, September, and October, with low PM₁₀ volume, the result revealed that Kriging was the most appropriate method for spatial interpolation during this period of time because it yielded the lowest differences. Improper method was Spline because it yielded the highest differences during this period of time. For inter in November and December with higher PM₁₀ volume, the result revealed that IDW, Kriging, Spline, and Trend were the most appropriate methods for spatial interpolation because it yielded the lowest differences.

4. CONCLUSIONS

For relationship between PM₁₀ volume in the northern part and physical factors of area found from mean of 5 years from 2017–2021, it was found that PM₁₀ was in high level in summer from the end of February to March and April due to lower level of high pressure caused by northeast monsoon. Consequently, temperature was higher causing swelter weather and drought that was generally cause

of wildfire in various areas of the northern part. In addition, weeds were also burnt in summer for facilitating collection of forest products and preparing plantation areas for agriculture in rainy season. Consequently, PM₁₀ was highly increased in summer. In addition, the northern part also had landscape in the manner of intermontane plateaus with small areas surrounded by mountain ranges and neighboring countries therefore lower atmosphere was compressed by cooler air mass than upper atmosphere causing poor dust distribution. Mean of 24 hours of average PM₁₀ volume throughout 5 years from 2017-2021 was in the highest level in March with average volume from all weather stations at 101 µg/m³ followed by April and February with volume of 73 and 66 µg/m³, respectively. The lowest PM₁₀ volume was found in August with average volume from all weather stations at 19 µg/m³. Moreover, when analyzing on data on average PM₁₀ volume through 4 Spatial Interpolation Methods including IDW, Kriging, Spline, and Trend for finding appropriateness, it was also found that IDW was the most appropriate method for mapping the map showing distribution of PM₁₀ volume because differences of value obtained from Spatial Interpolation Methods and actual measurement were in the lowest level, i.e., 10 months, whereas Spline was improper due to the highest differences of value obtained from Spatial Interpolation Methods analysis and actual measurement, i.e., 7 months from 12 months.

ACKNOWLEDGMENTS


This research project was financially supported by Mahasarakham University

REFERENCES

- Adamkiewicz, L., Maciejewska, K., Skotak, K., Krzyzanowski, M., Badyda, A., Juda-Rezler, K., & Dąbrowiecki, P. (2021). Health-Based Approach to Determine Alert and Information Thresholds for Particulate Matter Air Pollution. *Sustainability*, 13(3), 1345.
- Canha, N., Diapouli, E., & Almeida, S.M. (2021). Integrated Human Exposure to Air Pollution. *Int. J. Environ. Res. Public Health*, 18(5), 2233.
- Chalvatzaki, E., Chatoutsidou, S.E., Lehtomäki, H., Almeida, S.M., Eleftheriadis, K., Hänninen, O., & Lazaridis, M. (2019). Characterization of Human Health Risks from Particulate Air Pollution in Selected European Cities. *Atmosphere*, 10(2), 96.
- Choi, H., Melly, S., & Spengler, J. (2015). Intraurban and Longitudinal Variability of Classical Pollutants in Kraków, Poland, 2000–2010. *Int. J. Environ. Res. Public Health*, 12(5), 4967–4991.
- Eeftens, M., Meier, R., Schindler, C., Aguilera, I., Phuleria, H., Ineichen, A., & Künzli, N. (2016). Development of land use regression models for nitrogen dioxide, ultrafine particles, lung deposited surface area, and four other markers of particulate matter pollution in the Swiss SAPALDIA regions. *Environ. Health*, 15(1), 53.
- Department of Mineral Resources. (2021). Thailand Geopark. Available online: https://en.wikipedia.org/wiki/Northern_Thailand (Accessed on 15 October 2021).
- Goovaerts, P. (1997). Kriging vs stochastic simulation for risk analysis in soil contamination. In Geo-ENVI—Geostatistics for Environmental Applications; Soares, A., Gomez-Hernandez, J., Froidevaux, R., Eds., Kluwer Academic Publishers: Dordrecht, The Netherlands, 247–258.
- Goutham, P.M., Jayalakshmi, S., & Samundeeswari, R. (2018). A Study on Comparison of Interpolation Techniques for Air Pollution Modelling. *Indian J.Sci.Res.*, 17(2), pp 58–63.
- Intarat, T. (2011). Geoinformatics Application on Air Quality Assessment: A Case Study in Chon Buri Province. *Burapha Science Journal*, 16(1), 32–40.
- Jazdzewska, I.A., Lechowski, L., & Babuca, D. (2022). GIS-Based Approach for the Analysis of Geographical Education Paths. *ISPRS Int. J. Geo-Inf.*, 11(1), 41.
- Junpen, A., Pansuk, J., Kamnoet, O., Cheewaphongphan, P., & Garivait, S. (2018). Emission of Air Pollutants from Rice Residue Open Burning in Thailand. *Atmosphere*, 9(11), 449.
- Junpen, A., Roemmontri, J., Boonman, A., Cheewaphongphan, P., Thao, P.T.B., & Garivait, S. (2020). Spatial and Temporal Distribution of Biomass Open Burning Emissions in the Greater Mekong Subregion. *Climate*, 8(8), 90.
- Kim, H.H., Lee, G.W., Yang, J.Y., Jeon, J.M., Lee, W.S., Lim, J.Y., Lee, H.S., Gwak, Y.K., Shin, D.C., & Lim, Y.W. (2014). Indoor Exposure and Health Risk of Polycyclic Aromatic Hydrocarbons (PAHs) via Public Facilities PM_{2.5}, Korea (II). *Asian J. Atmos. Environ.*, 8(1), 35–47.

- Levei, L., Hoaghia, M.A., Roman, M., Marmureanu, L., Moisa, C., Levei, E.A., Ozunu, A., & Cadar, O. (2020). Temporal Trend of PM₁₀ and Associated Human Health Risk over the Past Decade in Cluj-Napoca City, Romania. *Appl. Sci.*, 10(15), 5331.
- Mitmark, B., & Jinsart, W. (2017). A GIS Model for PM₁₀ Exposure from Biomass Burning in the North of Thailand. *Applied Environmental Research*, 39(2), 77–87.
- Mperejekumana, P., Li, H., Wu, R., Lu, J., Tursunov, O., Elshareef, H., Gaballah, M.S., Nepo, N.J., Zhou, Y., & Dong, R. (2021). Determinants of Household Energy Choice for Cooking in Northern Sudan: A Multinomial Logit Estimation. *Int. J. Environ. Res. Public Health*, 18(21), 11480.
- Peng, Y., Li, W., Luo, X., & Li, H. (2019). A geographically and temporally weighted regression model for spatial downscaling of MODIS land surface temperatures over urban heterogeneous regions. *IEEE Trans. Geosci. Remote Sens.*, 57(7), pp. 5012–5027.
- Perera, F. (2018). Pollution from Fossil-Fuel Combustion is the Leading Environmental Threat to Global Pediatric Health and Equity: Solutions Exist. *Int. J. Environ. Res. Public Health*, Vol. 15(1), 16.
- Pongkaset, A., Supapwanich, C., & Sonbut, J. (2020). Meteorological Factors related to PM₁₀ and Health Risk Assessment for Resident Exposed to PM₁₀ in Yala City, Yala Province. *The Public Health Journal of Burapha University*, 15(2), 39–49.
- Pradabmook, P., & Laosuwan, T. (2021). The Integration of Geo-informatics Technology with Universal Soil Loss Equation to Analyze Areas Prone to Soil Erosion in Nan Province. *ARPN Journal of Engineering and Applied Sciences*, 16(8), 823–830.
- Pradabmook, P., & Laosuwan, T. (2021). Estimation of PM 10 using Spatial Interpolation Techniques. *International Journal on Technical and Physical Problems of Engineering*, 13(4), 33–39.
- Ray, R.L., Ibrinke, A., Kommalapati, R., & Fares, A. (2019). Quantifying the Impacts of Land-Use and Climate on Carbon Fluxes Using Satellite Data across Texas, U.S. *Remote Sensing*, 11(17), 1733.
- Srivastava, P.K., Pandey, P.C., Petropoulos, G.P., Kourgiyalas, N.N., Pandey, V., & Singh, U. (2019). GIS and Remote Sensing Aided Information for Soil Moisture Estimation: A Comparative Study of Interpolation Techniques. *Resources*, 8(2), 70.
- Supasri, T., Intra, P., Jomjunyong, S., & Sampattagul, S., (2018). Evaluation of Particulate Matter Concentration by Using a Wireless Sensor System for Continuous Monitoring of Particulate Air Pollution in Northern of Thailand. *Journal of Information Technology Research*, 1(2), pp 65–78.
- Suriya, W., Chunpang, P., & Laosuwan, T. (2021). Patterns of relationship between PM₁₀ from air monitoring quality station and AOT data from MODIS sensor onboard of Terra satellite. *Scientific Review Engineering and Environmental Sciences*, 30(2), 236–249.
- Thai, T., Bernatik, A., & Kučera, P. (2021). Air Pollution Associated with Total Suspended Particulate and Particulate Matter in Cement Grinding Plant in Vietnam. *Atmosphere*, 12(12), 1707.
- Vichit-Vadakan, N., & Vajanapoom, N. (2011). Health impact from air pollution in Thailand: current and future challenges. *Environ Health Perspect.*, 119(5), A197–A198, 2011.
- WHO. (2018). First WHO Global Conference on Air Pollution and Health, Geneva, Switzerland, 30 October–1 November 2018; WHO: Geneva, Switzerland.
- Wiatkowska, B., Słodczyk, J., & Stokowska, A. (2021). Spatial-Temporal Land Use and Land Cover Changes in Urban Areas Using Remote Sensing Images and GIS Analysis: The Case Study of Opole, Poland. *Geosciences*, 11(8), 312.
- Wikipedia. (2021). Northern Thailand. Available online: https://en.wikipedia.org/wiki/Northern_Thailand (Accessed on 15 November 2021).
- Zhong, S., Yu, Z., & Zhu, W. (2019). Study of the Effects of Air Pollutants on Human Health Based on Baidu Indices of Disease Symptoms and Air Quality Monitoring Data in Beijing, China. *Int. J. Environ. Res. Public Health*, 16(6), 1014.

A LOW-COST DRONE MAPPING AND SIMPLE PARTICIPATORY GIS TO SUPPORT THE URBAN FLOOD MODELLING

Aditya SAPUTRA^{1*}, Agus Anggoro SIGIT¹, Yuli PRIYANA¹, Andy Muhammad ABROR²,
Angraini Noor Lia SARI² and Oky NURSETIYANI²

DOI: 10.21163/GT_2022.172.04

ABSTRACT:

Obtaining the micro topographic characteristic of river has a decisive role in urban flood mapping and modelling. However, the approachability of high resolution and detail river morphography and micro relief have been often difficult. Furthermore, the variation of spatial and temporal of observation coverage have been often challenging to make the study more low-cost and effective. Nowadays, the advanced of remote sensing technologies can outgrow many of these limitations. the recent development of remote sensing based on small format unmanned drone is capable to produces detail scale of topographic data of the study area. The drone technology is actually a simple system, relatively cheap, effective and well-timed technique in generating high resolution aerial photographs of study area. The objectives of this research were to generate detail land cover and digital elevation by using low-cost drone mapping, also to obtain the historical flood inundation information from local people to support the urban flood mapping in study area. By combining the flood inundation data which was obtained from the participatory GIS process and detail landcover condition, the distribution of flood susceptibility area can be obtained. Further, this data can be used to generate the flood model which is essential for planning, monitoring and controlling the flood in urban area. The results showed that highest flood inundation was 1.7 meter. The most susceptible areas were located between Sungai Pepe and Sungai Kali Gajah Putih especially in ward 1, 2, and 3. Ward 1 is dominated by dense settlement area which is identic to slump. The ward 2 and 3 is dominated by the medium settlement with some agricultural area in between. Furthermore, the risk reduction effort needs to be focused on these wards to reduce the damage and loss when the flood occurs again in study area, by conducting several mitigation programs such as increase the people capacity, establish the evacuation route, and educate the local people.

Key-words: Drone mapping, Structure from Motion, Urban flood, Simple participatory GIS.

1. INTRODUCTION

Urban flood can potentially disturb cities and lead to a major impact both on people and economic. The impact is often amplified by the climate change effect (Hammond et al., 2013) or worse situation such as current pandemic situation of covid-19 (Tripathy et al., 2021). Sufficient preparedness level and adequate disaster management are needed to reduce the risk and loss during the disaster. During the disaster, the evacuation process is one of the critical aspects to minimize the loss of lives (Na et al., 2012). Preparing the evacuation plan is before the flood occurrence is very important and need to involve various criteria including hazard analysis, distribution of inundation area (extent and depth of inundation), accessibility and often social aspect (vulnerability).

¹ Geography Faculty, Universitas Muhammadiyah Surakarta, as105@ums.ac.id, aas278@ums.id, yuli.priyana@ums.ac.id

² GIS Laboratory, Geography Faculty, Universitas Muhammadiyah Surakarta, Andiabr35@gmail.com, laboratoriumgeografi@ums.ac.id, setiyani11@gmail.com

Disaster and risk management of flood can be divided into two major groups; first, the flood hazard and risk analysis or assessment and second, the mitigation aspect. The main purpose of the hazard and risk analysis is to find out where the high flood risk location and where the mitigation actions are mandatory needed. Thus, the core of risk mitigation which means to construct, evaluate, and establish the parameter to reduce the risk in particular area is a comprehensive flood risk analysis and assessment (Meyer et al., 2009).

In term of flood risk analysis and assessment, at least two components must be determined before, i.e., hazard and vulnerability. Hazard talked more about physical characteristic and several aspects of actual flooding such as flood extent and depth of inundation). Vulnerability aspect more focused on the exposure of people, land use type, and various element at risk that might be impacted during the flood event (Schanze et al., 2006; Apel et al., 2009). Landuse and landcover data plays the important role in flood hazard and risk reduction. With this data the accurate damage and loss prediction can be obtained, moreover the evacuation planning can be established precisely. In term of the complexity of the analysis, both hazard and vulnerability assessment have various level of complexity depend on their spatial scale. The detailed analysis should be applied in local spatial scale, meanwhile the less detailed analysis can be applied in regional scale.

Tehrany et al. (2013); Kia et al. (2011); Kuzakis et al. (2015) stated that the flood analysis either at regional or local spatial scale need to identify the location of flood prone area in order to provide early warning system, quick response facilitate, and reduce the impact of potential flood. In general, the prone area of flood can be revealed through several method. Liu et al., 2003 and Forte et al. (2005) generated flood hazard map by super-imposed the geological characteristic and hydrological information in GIS. Furthermore, Dewan et al. (2007) construct the flood inundation map by adding the analysis on the historical data of major flood event in 1998. Multi-Criteria analysis on GIS platform are often used to generate flood hazard zonation. The physical parameters such as elevation, geological and soil characteristic, land use and land cover, hydrological aspect, flood historical data and distance from the river were analysed together by using spatial multicriteria evaluation in GIS platform. The level of important of each parameter were defined clearly on this analysis (Fernandez and Iuts, 2010; Wang et al., 2010; Kourgialas and Karatzas, 2011; Tehrany 2014).

At the local scale, the accuracy of flood hazard zonation especially the extend of flood, is determined by the quality of input data such orthophoto, DEM and hydrological data (Moore et al., 1991). Nowadays, the advanced development of remote sensing technology, the unmanned aerial vehicle (UAV) has gradually replaced the airborne sensing using the manned aero plane. The flexibility, effectivity, relatively rapid return period, and high-resolution results made UAV more popular than the conventional airborne sensing (Saputra, et al., 2019). On the other hand, the community-based flood mapping also very important in disaster risk reduction program since difficult to find the satellite image which recorded the flood events (Joy, J., et al., 2019). Simple participatory GIS, the extend of flood can be obtained effectively by extracting information from people who live in impacted area.

The objective of this research is to bring the low-cost mapping to support the flood hazard assessment. The integrated approach between drone mapping and participatory GIS can provide the detail data of land use-land cover and the extend of historical flood event which is very important for mitigation plan.

2. STUDY AREA

The study area is Sumber Village which part of the famous watershed in Central Java, i.e., Sumber is located in the middle part of Bengawan Solo Watershed. Gajah Putih and Pepe River are tributary of Bengawan Solo River which often drown some part of Sumber Village in rainy season. In general, Sumber Village lies in the temperate climate zone with the average annual rainfall of 800 mm. From the administrative point of view, Sumber village belongs to Banjarsari District, Surakarta City, Central Java, Indonesia. The situation of the study area can be seen in **Fig. 1** below.

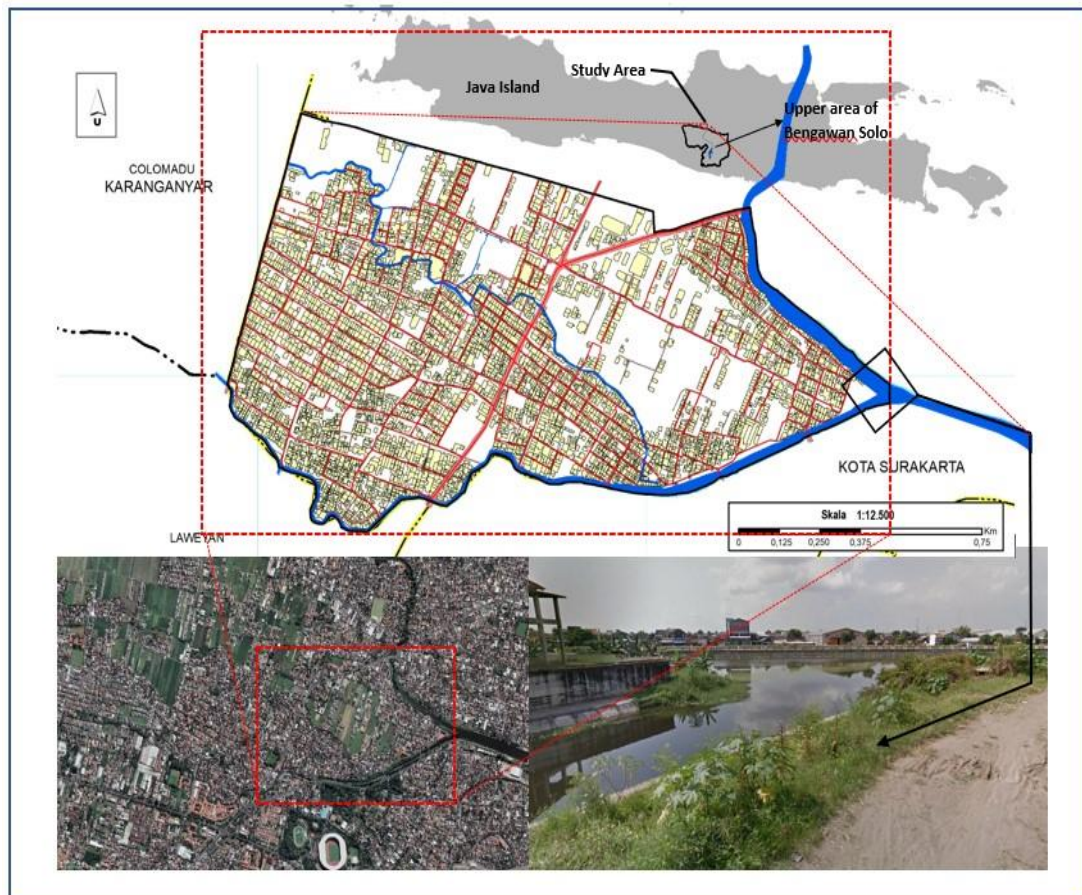


Fig. 1. Study area (above), The orthophoto (left) and the existing condition of the area near the river (Right).

3. METHOD

Given the purpose of the paper, the methods consisted two stages. The first stage was to generate the detail landcover data through the drone mapping. The second stage was to conduct the simple participatory GIS to reveal the extend of the historical flood and the depth of inundation in impacted area.

3.1. Landcover data extraction

Since the high-resolution satellite imagery was not available freely in study area, the drone mapping technique was used to extract the recent and detail landcover in study area. Three main steps need to be conducted such as 1) Data acquisition; 2) Orthophoto process, and 3) Interpretation. Before the drone mapping were implemented, the study area was defined into smaller block with the total area at least 3 hectare and not more than 5 Ha. There is no rule on how to divide the block. The block division was implemented to reduce the risk of loss connected between the drone and controller. The block was established by considering the road at local level and the natural object for instance river. We used the commercial drone of phantom series to conduct the drone mapping in the field. The specification of drone can be seen in **Table 1** below.

Table 1.

The specification of Phantom pro 4 obsidian.

No	Specification	Characteristics
1	Weight (including battery and 4 propellers)	1,375 gram
2	The maximum flight velocity	S-Mode (<i>Sport mode</i>): 72 km/ hour A-Mode (<i>Attitude mode</i>): 58 km/ hour P-Mode (<i>Positioning mode</i>): 50 km/ hour
3	Flight duration (1 battery)	30 minutes
4	Navigation system	GPS/GLONASS
5	Visual record system	<i>forward, backward, dan downward</i> record system
6	Obstacle sensors	Front and back sensors Infrared sensor in left and right wings
7	Camera	1" CMOS,
8	Wind resistance	Max 10 m/s
9	Operational temperature	0-40°C
10	Photo format	JPEG, DNG (RAW), JPEG+DNG
11	Video format	MP4/MOV (AVC/H.264; HEVC/H.265)
12	Battery	LiPo4S
13	<i>Charger</i>	Voltage: 17.4; power: 100W
14	Operational frequency	2.4 GHz/ 5.8 GHz
15	Maximum transmission coverage	4.3 mi (6.9 km)

Source: DJI Forum, 2019.

The orthophoto was generated from the mosaicking process of drone photograph by using Agisoft Photoscan Pro. First the software will align the stereoscopic images. Second, the software will generate the sparse point cloud and dense cloud. The sparse and dense cloud represent the particular point in several photographs which has the same pixel value. The mesh, texture, and orthophoto can be obtained after generating the sparse dan dense. Detail the workflow of drone can be seen in Fig. 2.

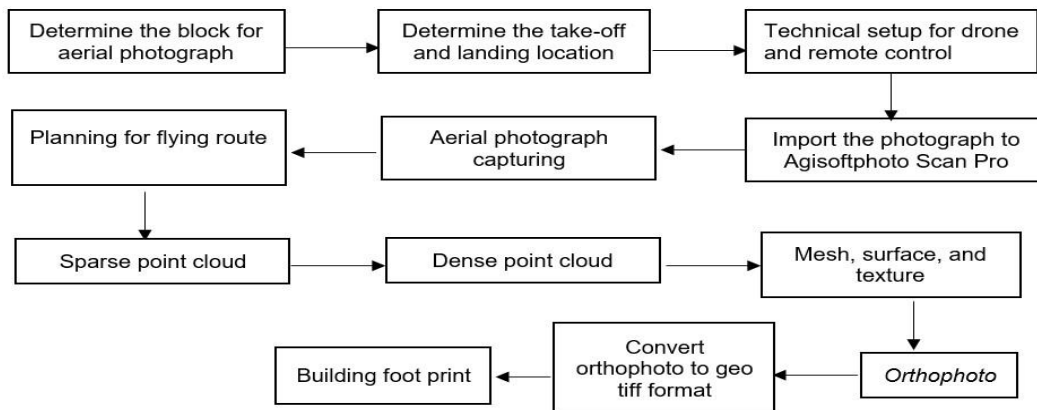


Fig. 2. Research Workflow (landcover extraction).

3.2. Participatory mapping.

Since lack of satellite imagery that recorded on disaster event, the best method to extract the flood extend and inundation depth is to ask the people who live in affected area. Post-flood survey is very important in term of flood hazard analysis. We can get the accurate information about the extent of the flood with relatively simple and effective way. The purposive sampling was used to choose the respondent. We chose the key person live near the river around 250-500 m. We assumed the people who live near the river have better knowledge on flood historical event in this area. The design sample of respondent can be seen in Fig. 3.

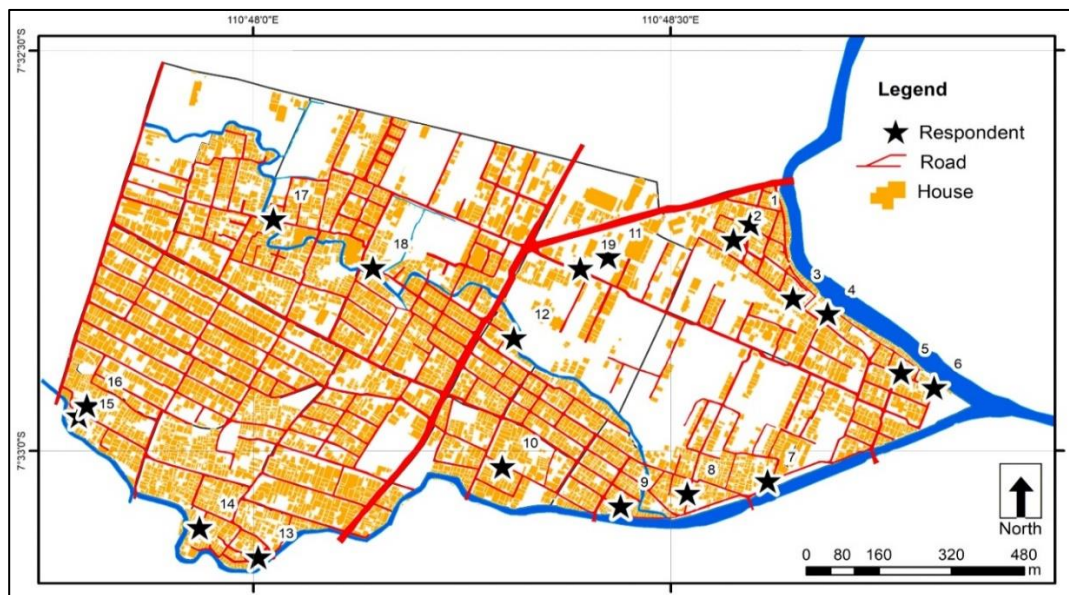


Fig. 3. The respondent distribution.

4. RESULTS

4.1. Block division

Sumber Village is divided into 46 photograph blocks, each of which is approximately 2 to 3 Ha in size. As stated in the introduction, the size of a block photograph plays no specific role. However, due to the radio signal transmission between the aircraft (drone) and the remote control, and for safety reasons, the size of the block photograph was set at least 2 ha and up to 5 ha. When we set up the block photograph more than 5 ha, we frequently experience radio signal transmission loss (drone-remote control is disconnected). When the signal is lost, the drone will automatically hover and return to the take-off position (as default setting in Phantom pro 4 obsidian). As a result, not all photographs will be taken, and the re-launch and image capture process will have to be repeated. The division of block can be seen in the Fig. 4. Based on field experience, two flight parameters that are appropriate for conducting drone mapping in urban areas are as follows: 1) the suggested flight elevation is 50-70 m above sea level. If the drone mapping is done at less than 50 meters of elevation, it will take longer, produce more high-resolution images, and pose a greater risk. If the flight elevation is greater than 100 meters, the resulting orthophoto will have less detail and will be more difficult to interpret visually. Furthermore, flights above 100 m can disrupt commercial flights, particularly in the vicinity of the airport. 2) The side-lap and front-lap (overlapping areas) must be determined to be approximately 65 and 75 percent, respectively. The higher the value of front-lap and side-lap in the flight parameter, the more images will be obtained and the longer the drone will operate. In addition, the image mosaicking process will take longer time because the greater the front-lap and side-lap, the greater the number of photos. The flight parameter that needs to be determined before the drone mapping process can be seen in Table 2 below.

Table 2.

Flight parameter that very important to be set before flight mission.

No	Flight Parameter	Suggestion
1	Flight Altitude	75-100 m
2	Obstacle Avoidance	On
3	Area	2-5 Ha
4	Sidelap	65%
5	Frontlap	75%
6	Take off position	Centre area
7	Take off condition	No obstacle



Fig. 4. Block plan of drone mapping.

4.2. Orthophoto

Orthophoto of every single block was generated through several steps (Fig. 3). The orthophoto generation starts with the alignment process of photograph. The time required on alignment process differs of every block. It depends on the size of block and the number of photographs. By using the photogrammetry software, the photo taken by drone will align automatically based on the location of camera position. For the size area of 2-3 Ha with the 70 flying altitudes will produce around 30-35 photographs. The time requirement for one alignment process is around 4 minutes 48 seconds. The illustration of alignment process and the result are provided in Fig. 5.

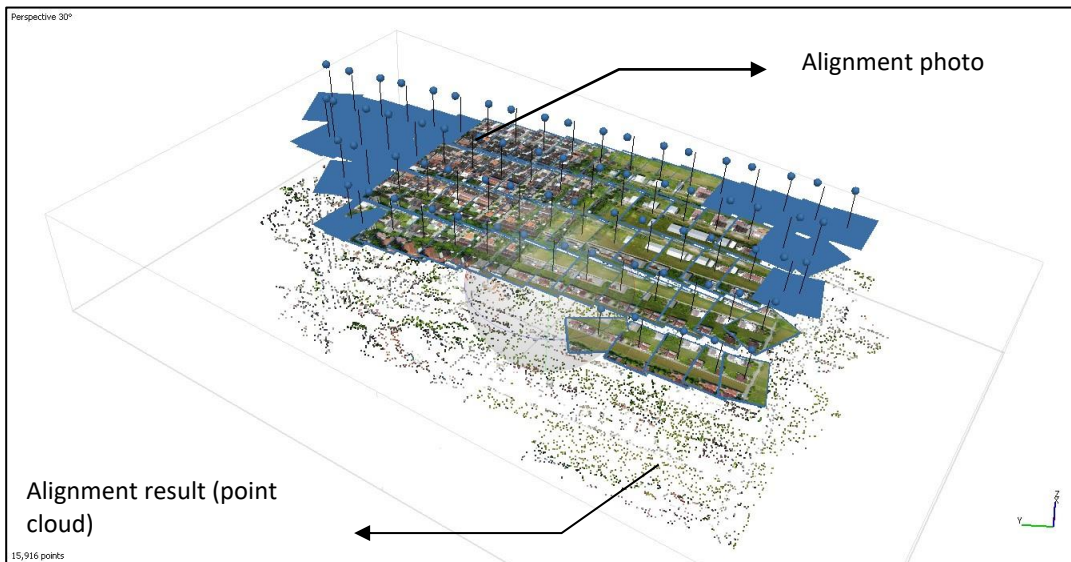


Fig. 5. Illustration of alignment photo and point cloud generation.

Further, the sparse point cloud (the results of align photo) will be derived into dense point cloud. The software tries to extrapolate the sparse point cloud into much more point which is appear in at least two scenes of photos. For instance, in Figure 5 above, the number of points of the area observed are 15,916 points, in the dense point cloud, the number of points increase become, 14,157,740 points. Although, the point is much more than previous process, the dens point cloud generation took faster, i.e. 2 minutes 21 seconds. The example of dense point cloud of block number 8 can be seen in **Fig. 6**.

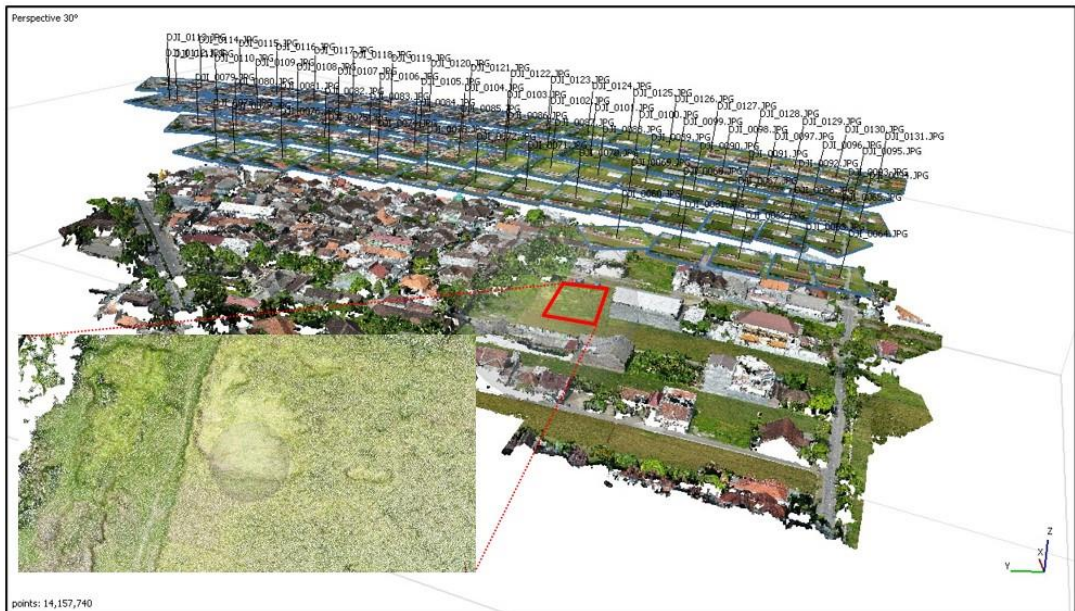


Fig. 6. The dense cloud of block 8.

The last step before DSM extraction is to generate the surface texture. This process was executed by using the dense cloud from the previous process. By using orthophoto mode, mosaic blending mode, and medium quality this process (around 14 million points) can be finished in 1 minutes 42 seconds and produced 308,057 faces and 154,627 vertices. The orthophoto was generated by exporting the textured surface to orthophoto. The example of textured surface of block 8 can be seen in **Fig. 7**, meanwhile the orthophoto can be seen in **Fig. 8**.



Fig. 7. The textured surface of block 8.



Fig. 8. The orthophoto of block 8.

4.3. DSM Generation

The DSM was generated after applied the point classification to the dense cloud. The point classification follows automatically in agisoft photoscan pro classification. There were several classifications such as ground, high vegetation, building, road surface, cars and man-made object. For example, the north part of block 8 has minimum elevation of DSM around 133 m and the highest point around 151 m. Please see **Fig. 9** to check out the DSM of the north part of block 8.

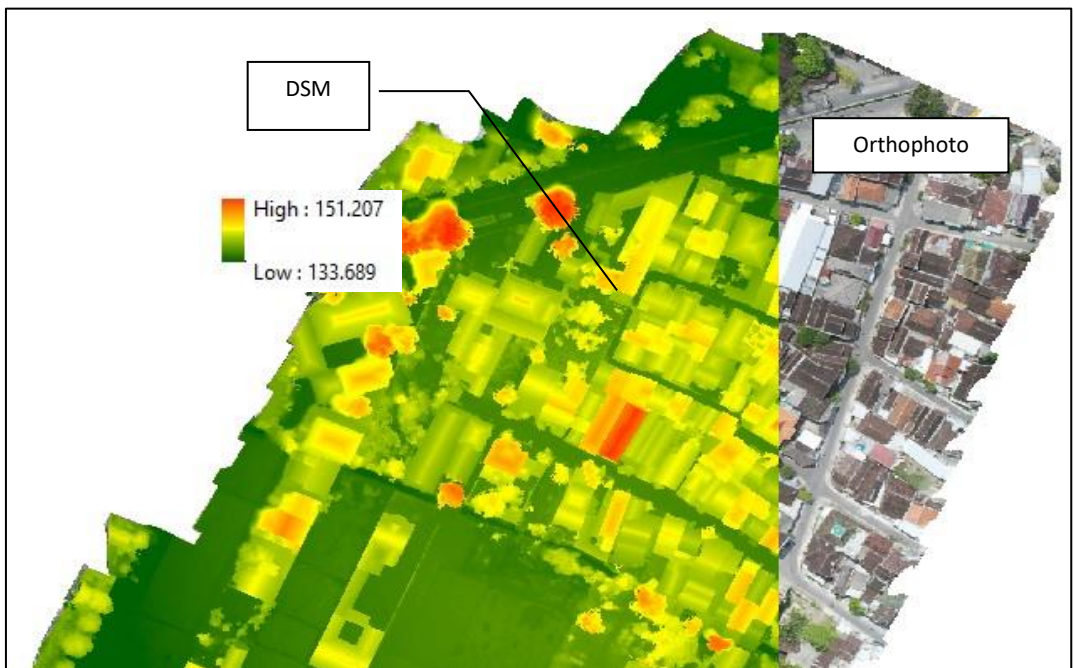


Fig. 9. The DSM and orthophoto of the north part block 8.

5. DISCUSSION

Based on the orthophoto results, the landcover especially the built area can be clearly distinguished. By using the visual interpretation technique land cover in study area can be divided into several major group such as building (House), agricultural vegetation, non-agricultural vegetation, bare land, water body, and road. Those all object can be identified by analyses the colour/tone element and other element such as shape, pattern, association, shadow, and size. The key interpretation of several object can be seen in **Table 3** below.

Table 3.

The example of object identification.

Object	Color/ Tone	shape	pattern	Shadow
Agricultural land	Green to light brown	rectangle	Clustered	non
Building	Brown, green, white	rectangle	Clustered	yes
Water Body	Blue	longwise	longwise	no
Road	Dark gray	longwise	longwise	yes

The building map was extracted from the interpretation results by observing the existence of shadow. Some objects have the similar color with the rooftop of the building, however if there are no shadows around the object then the object was considered as bare land or sports field. The results of the building can be seen in **Fig. 10**, meanwhile the results of orthophoto, landcover and the building map are provided in the **Fig. 11**.

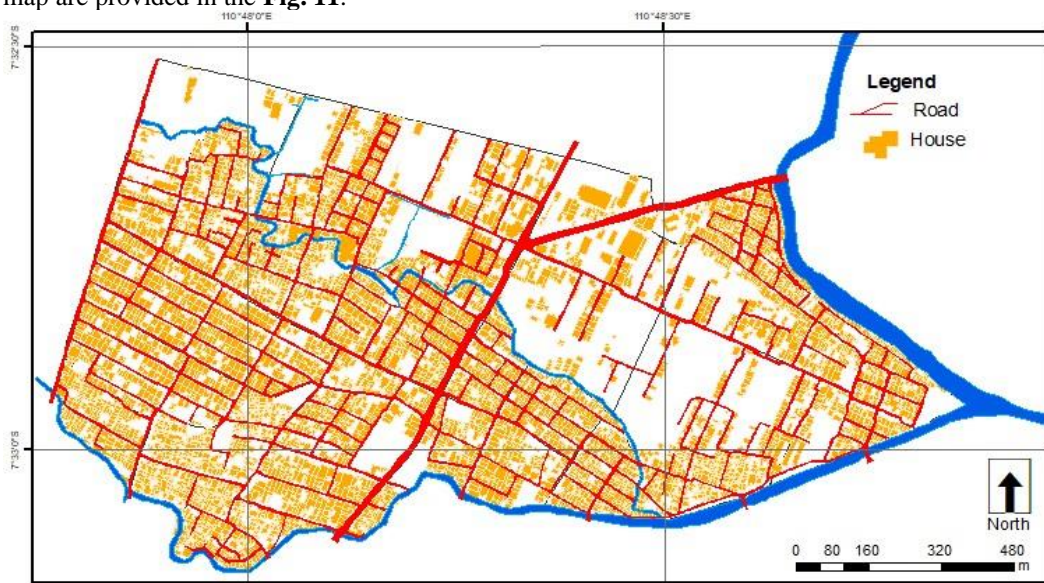


Fig. 10. Building footprint of study area.

Based on the participatory mapping, the worst flood in study area occurred in 2015 with the highest water raise of 170 cm. the depth of inundation on metric scale was generated from the conversion of relative scale by using body parts benchmarking technique. Thus, if the respondent said that the last flood 2015 inundated the house until at least as high as neck of adults, it means the depth of inundation is around 150. This conversion technique used the average height of Indonesian adults which is 162.6 cm.

Based on the participatory mapping from several keyperson, it can be seen that the lowest inundation depth is 10 cm or as high as an adult’s ankle. The most prone area to flood is located in the eastern part of Sumber Village. This prone area covers at least three RT (the lowest administrative units) or neighborhood, i.e., RT 1-3.



Fig. 11. Orthophoto, drone image of block 1-2, and landuse map of study area.

The average flood depth in those areas was 1.5-1.7 m. in term of geomorphology, this area can be classified as flood plain which has fertile and thick soil. However, during the rainy season this area is often inundated by the water as the debit of th river increase. Furthermore, this area is located in ‘hook’ location between Kali Gadjah Putih and Pepe River which can amplify the impact of flood and increase the depth of flood. The distribution of flood inundation Is provided in the **Fig. 12** below.

The advanced technology nowadays allowed us to extract the topographic data by the relatively simple and low-cost method. Drone mapping is able to generate local DSM and DEM or even ectract land use and landcover data in local scale with has flexibility of temporal resolution and rapid acquisition. By combining with the information of depth from the local people by using simple participatory mapping, the model of flood inundation can be generated and can be used for further contingency plan or mitigation. Based on the results, the eastern part of Sumber village has the deepest flood around 1,7 m. with this high It will be inundated everything including road and paddy field except the building. Further to reduce the impact of flood the local government need to make collaboration plan to establish the evacuation planning in the eastern part of Sumber Village. This is important as the most crucial aspect to mitigate the flood. The local government need to plan precisely which neighborhood that need help first during the flood disaster.

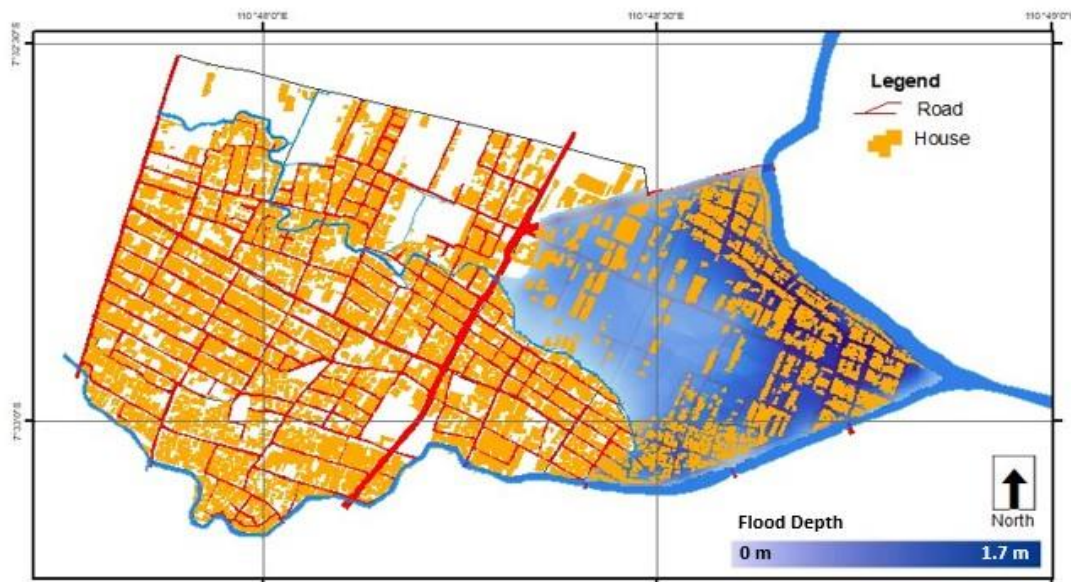


Fig. 12. The flood inundation distribution.

6. CONCLUSION

The most prone area to flood is located in the eastern part of study area especially in RT 1-3. The average depth of inundation in this area around 1.5-1.7 m. Based on the result, it is revealed that the integrated method between the drone mapping and participatory GIS can be an alternative method to support the flood mitigation planning at local level.

ACKNOWLEDGEMENT

The authors are thankful to Universitas Muhammadiyah Surakarta, who has provided funding, adequate tool, equipment and supported this project.

REFERENCES

- Apel H, Aronica GT, Kreibich H, Thielen AH. 2009. Flood risk analyses - how detailed do we need to be? *Nat Hazards*. 49:7998
- Dewan, Ashraf M., Monirul Islam, M., Kumamoto, T., Nishigaki, M., 2007. Evaluating flood hazard for land-use planning in greater Dhaka of Bangladesh using remote sensing and GIS techniques. *Water Resour. Manag.* 21 (9), 1601–1612. <http://dx.doi.org/10.1007/s11269-006-9116-1> (ISSN 09204741).
- DJI Forum. 2019. Introducing DJI Phantom 4 Pro Obsidian, *Forum.dji.com*, <https://forum.dji.com/thread-110999-1-1.html>, (accessed July 1, 2019).
- Fernández, D.S., Lutz, M.A., 2010. Urban flood hazard zoning in Tucumán Province, Argentina, using GIS and multicriteria decision analysis. *Eng. Geol.* 111, 90–98. <http://dx.doi.org/10.1016/j.enggeo.2009.12.006>
- Forte, F., Pennetta, L., and Strobi, R.O. 2005. Historical records and GIS applications for flood risk analysis in the Salento Peninsula (Southern Italy). *Natural Hazard earth system science*, 5(6), 833-844. 10.5194/nhess-5-833-2005

- Hammond, MJ., Chen, AS., Djordjevic, S., Butler, D., Mark, O. 2013. Urban flood impact assessment: A State of the art review. *Urban Water Journal*, V 12 (1), 2015. <https://doi.org/10.1080/1573062X.2013.857421>
- Joy, J., Kanga, S., Singh, S.K.. 2019. Kerala Flood 2018: Flood mapping by participatory GIS approach, Meloor Panchayat. *International Journal on emerging technologies*, 10 (1): 197-205. Doi: 10(1): 197-205(2019)
- Kia, M.B., Pirasteh, S., Pradhan, B., Mahmud, A.R.M., Sulaiman W.N.A., and Moradi, A. 2011. An artificial neural network model for flood simulation using GIS: Johor River Basin, Malaysia. *Environ. Earth Sci.*, 67 (2011), pp. 251-264, 10.1007/s12665-011-1504-z.
- Kourgialas, Nektarios N., Karatzas, George P., 2011. Flood management and a GIS modelling method to assess flood-hazard areas: a case study. *Hydrol. Sci. J.* 56 (2), 212–225. <http://dx.doi.org/10.1080/02626667.2011.555836>
- Kuzakis, N., Kougiass, I., Patsialis, T. 2015. Assessment offlood hazard areas at a regional scale using an index-basedapproach and Analytical Hierarchy Process: Application inRhodope–Evros region, Greece. *Science of the total Environment* 538, 555-563. <http://dx.doi.org/10.1016/j.scitotenv.2015.08.055>
- Liu, Y.B., Gebremeskel, S., De Smedt, F., Hoffmann, L., Pfister, L. 2003. A diffusive transport approach for flow routing in
- Meyer V, Scheuer S, Haase D. 2009. A multicriteria approach for flood risk mapping exemplified at the Mulde river, Germany. *Nat Hazards*. 48:1739
- Moore ID, Grayson RB, Ladson AR. 1991. Digital terrain modelling: a review of hydrological, geomorphological and biological applications. *Hydrol Process*. 5:3_30.
- Na L, Xueyan S and Mingliang Q 2012 A bi-objective evacuation routing engineering model with secondary evacuation expected costs *Syst. Eng. Proc.* 5 1–7
- Saputra, A., Akbar, M., Permadi, A.S., Pratama, B.M., Rudiyanto. 2019. Structure from motion (SfM) technique to support land cover mapping. *Disaster Advances* 12 (9), p 25-33.
- Schanze, Jochen, Zeman, Evzen, Marsalek, Jiri, 2006. Flood riskmanagement: hazards, vulnerability and mitigation measures. 9781402045974 <http://dx.doi.org/10.1007/978-1-4020-4598-1>.
- Tehrany, M.S., Pradhan, B, and Jebur, M.N. 2013. Spatial prediction of flood susceptible areas using rule-based decision tree (DT) and a novel ensemble bivariate and multivariate statistical model in GIS. *J. Hydrol.*, 504 (2013), pp. 69-79, 10.1016/j.jhydrol.2013.09.034
- Tehrany, Mahyat Shafapour, Pradhan, Biswajeet, Jebur, Mustafa Neamah, 2014. Flood susceptibility mapping using a novel ensemble weights-of-evidence and support vector machine models in GIS. *J. Hydrol.* 512, 332–343. <http://dx.doi.org/10.1016/j.jhydrol>.
- Tripathy, SS., Bhatia, U., Mohanty, M., Karmakar, S., and Ghosh, S. 2021. Flood evacuation during pandemic: a multi-objective framework to handle compound hazard. *Environmental research Letters* 16(2021) 034034. <https://doi.org/10.1088/1748-9326/abda70>.
- Wang, Yamei, Li, Zhongwu, Tang, Zhenghong, Zeng, Guangming, 2011. A GIS-based spatial multi-criteria approach for flood risk assessment in the Dongting Lake Region, Hunan, Central China. *Water Resour. Manag.* 25 (13), 3465–3484. <http://dx.doi.org/10.1007/s11269-011-9866-2>

A DIRECT METHOD TO DELIMIT WEIR POOLS

*Francesco DONATI*¹

DOI : 10.21163/GT_ 2022.172.05

ABSTRACT:

Weir pools are one of the most widespread artificial aquatic environments in Europe. In recent years, they draw the attention of scientists and managers, who try to understand how they work and put in place strategies to manage them. However, these studies confront with the difficulty of delimiting the spatial extension of weir pools: to solve this problem, we created a direct technique that permits to identify their perimeter through the measure of the raising of the waterline and the slowing down of the flow generated by weirs. To verify its validity and efficiency we tested it in two weir pools located in France to check whether it can find them. In both cases, the results obtained are convincing and they demonstrate how this methodology can be used to study and manage the spaces that form upstream weirs.

Key-words: Weir, Weir pool, Run-of-river dam, Weir pool perimeter.

1. INTRODUCTION

A weir pool is the space where occurs the raising of the water line and the slowing of the flow caused by weir, a hydraulic structure generally of small dimensions, overflows and transverses to the river bed of a stream (Degoutte, 2012). Over time, this kind of environment became very common in European rivers, especially in countries where industrialization developed in previous times, such as in France, where several thousands of weir pools have been built, mostly to operate water mills (Barraud et al., 2013; Rivals, 2000).

From an ecological point of view, the main characteristic of a weir pool is the flow velocity gradient which develops from upstream to downstream and whose intensity varies according to the time of year, determining the typical hybrid operation of this kind of environment, which cross lotic and lentic features (Donati, 2021; Donati et al., 2019; Donati et al., 2020 a; Donati et al., 2020 b). That can create some environmental impacts, such as the retention of sediments transported by the waters or the formation of thermal stratifications and the consequent warming of the waters downstream of the weirs. For this reason, especially after the promulgation of the Water Framework Directive and the diffusion of the concept of Ecological Continuity, everywhere in Europe weir pools draw the attention of scientists and managers, who try to understand how their work and put in place strategies to manage them (e.g. Malavoi, 2003; Rickard et al., 2003; Anderson et al., 2015).

However, any study about weir pools must be confronted with some practical constraints that they pose: one of these is the delimitation of their spatial extent. Indeed, their perimeter is not immediately recognizable, because weirs do not cause the overflow of the watercourse that they

¹ Science Research Firm « Ecolimneau », 8 Rue René Coty – 85000 La Roche-Sur-Yon, France, fdonati@ecolimneau.fr.

obstruct, unlike other structures which create real waterbodies, for example the dams or the pond's dykes. To overcome this issue, in the scientific literature it is possible to find indirect methods, which are based on geometric calculations made from the height of the structure, the slope of the water line or that of the bed. (e.g. Csiki & Rhoads, 2010; Maniere, 2013; Pearson & Pizzuto, 2015). They have several advantages such as being cheap and less time-consuming, but our experience taught us that they can also be inaccurate and not always reliable. So, we created a direct method that permits to limits a weir pools thanks field measurements and that we consider very efficient. The purpose of this article is to illustrate it, so that scientists can use it in their research and managers as decision support for their action about weir pools.

2. STUDY AREA

To verify the reliability and efficiency of our methodology we tested it in two study area located in Metropolitan France.

2.1. The Saint-Hilaire weir pool

The first site we tested is the Saint-Hilaire weir pool, located in central France, in the Loiret department, to the west of Orléans. It is supplied by the Mauves, a watercourse of approximately 40 km, with an average flow of 1,075 m³/s (Banque Hydro data). It is created by the weir of the homonymous water mill, which is 0,5 meters tall and which is surmounted by a gate.

The peculiarity of this weir pool is that we know its spatial extent. Indeed, in previous times its water level was regulated at a precise height, registered in a local law, in order not to interfere with the operation of the Pantin water mill, which is located upstream. This height is still respected today by the site manager and for this reason we know that the weir pool extends throughout all the space that separates these two ancient factories. Therefore, this study area is ideal for testing the reliability of our methodology, observing whether the results reflect the reality.

2.2. The Baerenthal weir pool

The second site we tested is the Baerenthal weir pool, located in the North-East of France, in the Moselle department, to the South-East of Bitche. It is supplied by the Zinsel du Nord, a river of approximately 40 km with an average flow of 0,596 m³/s (Regional Natural Park of Vosges du Nord data). More precisely, it is supplied by the confluence of this river and an artificial canal that comes from a pond. This study area is characterized by a concrete weir, which is 1 m tall and which is devoid of any moving element.

The peculiarity of this weir pool is that the slowing down of flow caused by the weir forming it cause the deposition of a large quantity of sediment over its bottom. Therefore, this study area is ideal to test the effectiveness of our methodology in a real study, verifying if it permits to bring a better understanding of the phenomena which characterize this type of environment. In this specific case we are observing if the limits that it permits to fix intercept the sectors that are silted up.

3. DATA AND METHODS

The methodology that we created to delimit weir pools is based on the direct observation of the two main effects generated by weirs, that are the raising of the water line and the slowing of the flow. More specifically, it makes possible to set the upstream limit of a weir pool, the downstream one coinciding with the weir.

To do this, first of all it is necessary to select a homogeneous section of river, between the weir that forms the studied weir pools and another hydraulic structure, a confluence, a sudden change in the stream hydromorphology, etc. Second of all, in this sector, from downstream, we position fifteen equidistant transects which will serve as a measuring station, by lining the last one up with the weir. This number of transects was established from other protocols used for rivers study, according to which fifteen measurement stations are sufficient to be able to assess the features of a river section. (e.g. the French protocol CARHYCE, see Onema, 2010). Furthermore, this same number of transects was found to be effective in other studies whose purpose was to study the characteristics of the spaces located upstream of weirs (Bellot, 2014; Donati et al., 2020). In Saint-Hilaire, a transect was placed every 37 meters, between the two water mills that delimit this study area; In Baerenthal, a transect was placed every 24 meters, between the weir and a confluence located a few hundred meters upstream.

On the fifteen transects, the average speed of the flow (m/s) is measured using a current meter. The kind of instrument that is used is established by the conformation of the study area: if from one hand it is possible to prospect it by foot it is possible to use a conventional current meter (helices or doppler), on the other hand if the depth is too great it is possible to use a floating profiler. In this study we used a doppler current meter, the "FlowTracker 2". With this instrument, on each transect of the two-study area, the speed was measured in three verticals: two beside the banks and one in the center of the river. The number and depth of the measurement points were automatically calculated by the current meter, as the average speed of each transect.

On the fifteen transects, the average water depth (m) is also measured. Indeed, at the raising of the water line generated by the weir corresponds a progressive increase in the thickness of the water column, an effect that in Hydraulics we associate to a back water curve designated with the acronym "M1" (Chanson, 2004; Dingman, 2009; Martin, 2013). To measure this, there are several solutions: it is possible to use a graduated staff, the bar of the current meter or the average depth value that the profilers usually give after each measurement. In the first two cases, it is necessary to measure the velocity depth in several verticals and then calculate the average depth for each measuring station.

Finally, we enter the data collected in a Cartesian graph with an abscise axis for the transects and a double ordinate axis for the speed and the average depth of the flow. The intersection between the two curves materializes the upstream limit of the weir pool as the point where these two phenomena begin.

From a temporal point of view, this methodology should be applied during low flows, when the velocity gradient that characterizes the weir pool is stronger and better visible. Rather, it shouldn't be applied during high flows, when the energy gradient is lower, especially during floods when the hydrological effects of the weir can be completely canceled.

4. RESULTS AND DISCUSSIONS

In the two fields of study that we studied/tested, the application of this methodology gave the following results

4.1. The results in Saint-Hilaire weir pool

Regarding the Saint-Hilaire study area, the data that we collected show that the raising of the water line and the slowing of the flow begin at the beginning of the reach upstream the old water mill (**Fig. 1**). More precisely, the curves of these two hydrological parameters intersect at the level of transect number 2, where we fix the upstream limit of weir pool (**Fig. 2**). It has an area of about 0,5 ha, an average width of 8 m and an average depth of 0,54 m. This perimeter corresponds to the information that the manager gave us on this study area before the application of our methodology, that is the weir pool is spread over the entire length of the reach that divide the Saint Hilaire and Pantin water mill.

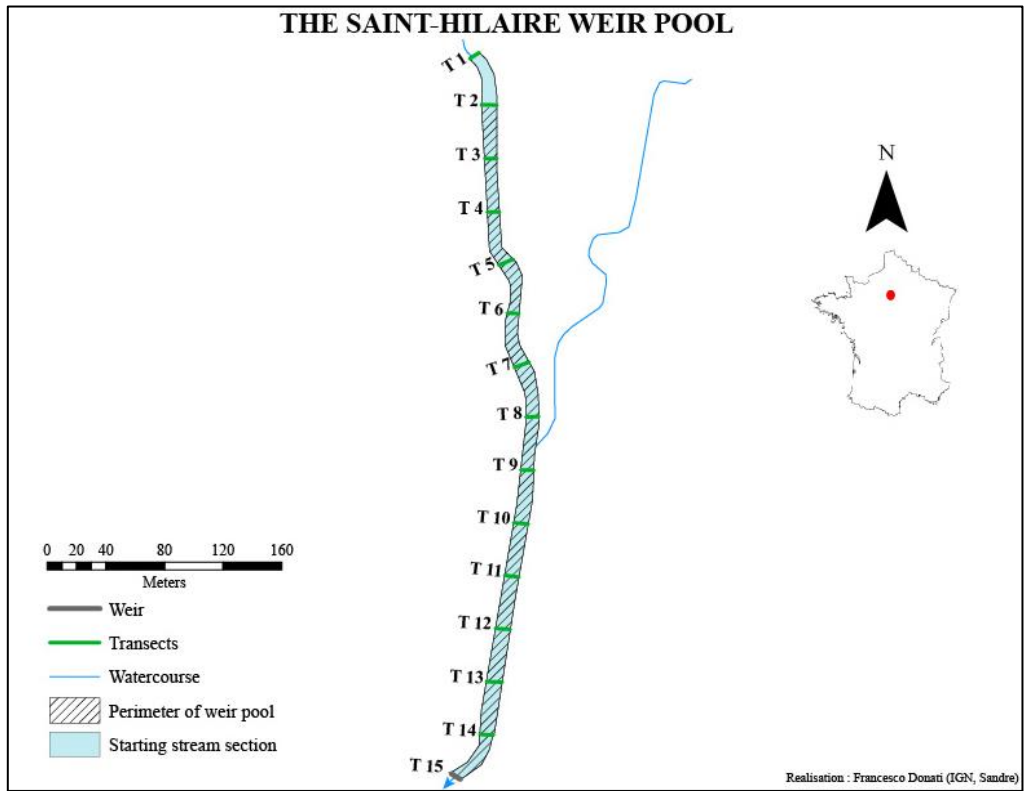


Fig. 1. The extension of Saint-Hilaire weir pool (*Realization: Francesco Donati*).

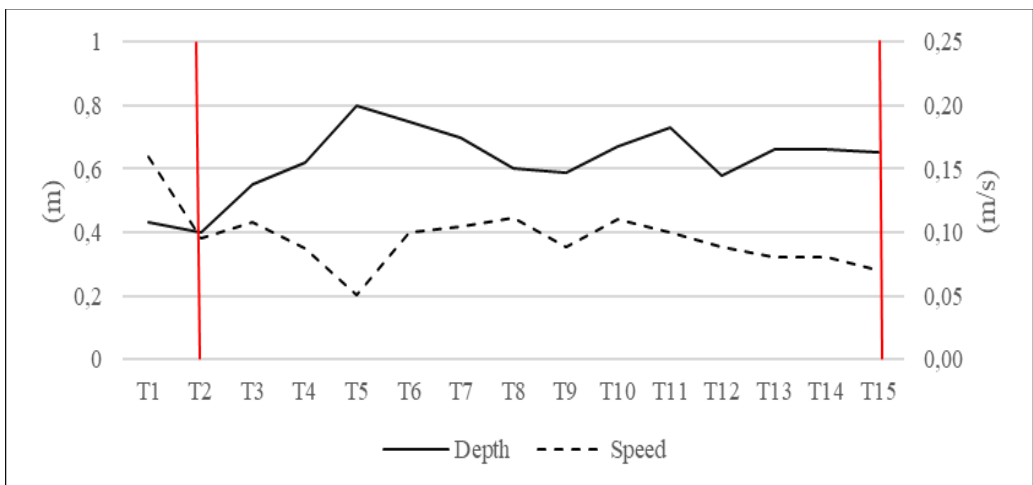


Fig. 2. The evolution of the depth and the speed of the flow in the Saint-Hilaire weir pool; the red bars show the extension of weir pool (*Realization: Francesco Donati*).

4.2. The results in Baerenthal weir pool

Regarding the Baerenthal study area, the data that we collected show that the raising of the water line and the slowing of the flow appear shortly after half of the reach created by the weir (**Fig. 3**). More precisely, the curves of these two hydrological parameters intersect at the level of transect number 9, where fix the upstream limit of weir pool (**Fig. 4**).

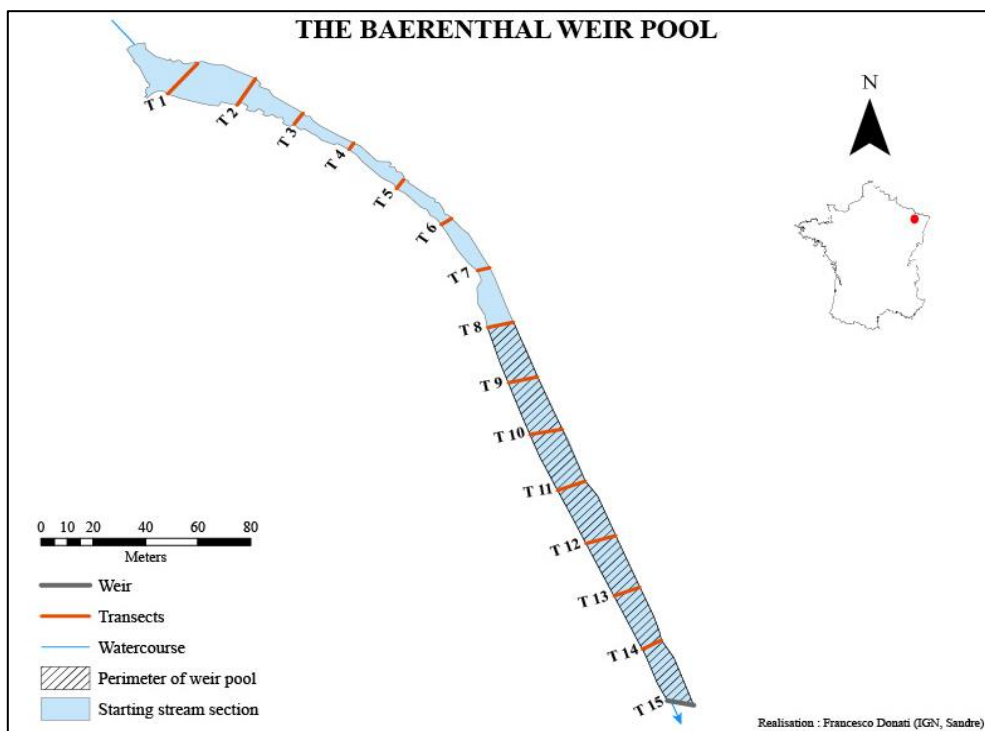


Fig. 3. The extension of Baerenthal weir pool (Realization: Francesco Donati).

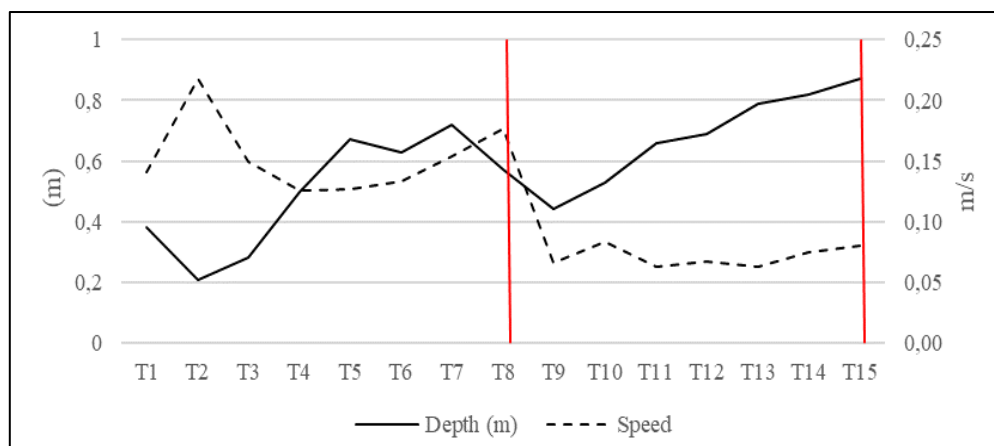


Fig. 4. The evolution of the depth and the speed of the flow in the Baerenthal weir pool; the red bars show the extension of weir pool (Realization: Francesco Donati).

It has an area of about 0,2 ha, an average width of 11 m and an average depth of 0,78 m. As it is possible to see from figure 4, the depth and speed curves also intersect before the transect number 9: this is not due to the effect of the weir, but to the morphology of the site. In fact, between transects 1 and 4, the speed of the water before increases because of the confluence of the two streams that supply this study area, after it decrease due to the widening of the riverbed. On the other hand, between transects 4 and 8, the riverbed suddenly narrows, causing the increase of water depth, while the energy of the flow remains constant.

As we explained above, this study area was selected to verify whether this methodology makes possible to delimit some aspects of the functioning of the weir pool, in this specific case the silting up of the bottom. To study this phenomenon, we collected additional data, using a technique commonly deployed upstream of any type of reservoir (Carlini, 2006; Donati et al., 2020; Maleval & Alain, 2002; Maleval & Pitois, 2017). On each transect used to study the hydrological parameters, the depth of the water and the substrate were measured using a graduated staff, in three verticals.

First of all, we measured the water depth, after which we measured the depth of the substrate: the difference between these two data gives the thickness of the layer of sediment covering the bottom. When we cross these data with those used to determine the extent of the sill reservoir, we observe that the area silted up are included almost perfectly within the perimeter of the weir pool that we identified and they coincide with the sudden change in flow velocity and the consequent decrease in its sediment competence (**Fig. 5**).

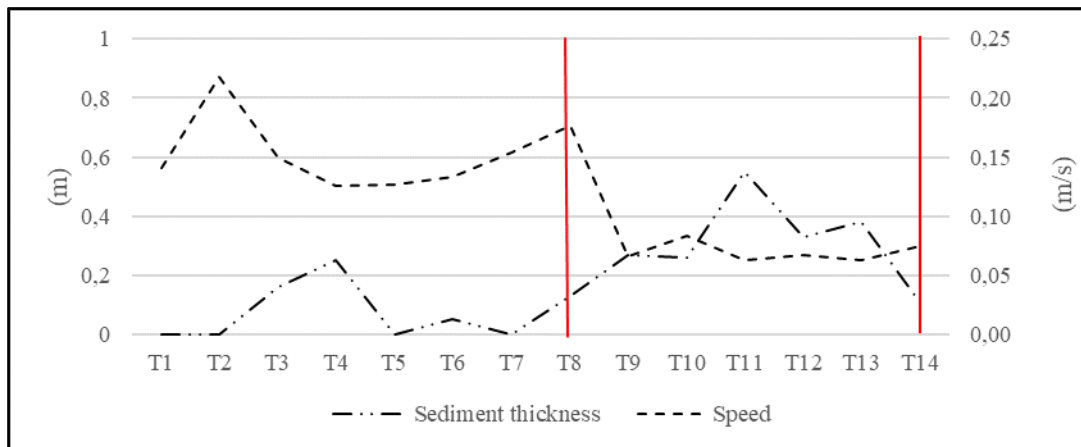


Fig. 5. The evolution of the thickness of sediments and the speed of the flow in the Baerenthal weir pool; the red bars show the extension of weir pool (*Realization: Francesco Donati*).

6. CONCLUSIONS

These results that we obtained seems to demonstrate the reliability of the methodology that we created to delimit weir pools. Indeed, the perimeters that we identified thanks to it reflect the informations we had about the two-study area before its application. So, this technique looks like a valid tool for researchers and technicians, for example during studies about the operation of this kind of environments or projects of river restauration. Of course, compared to indirect methodologies, it requires the use of instruments that can be expensive or the deployment of several people to realize the measurements. However, it allows to avoid generalizations that may be wrong and to better consider the environmental context of each weir pool.

REFERENCES

- Anderson, D., Moggridge, H., Warren, P., & Shucksmith, J. (2015). The impacts of ‘run-of-river’ hydropower on the physical and ecological condition of rivers: Physical and ecological impacts of ROR hydropower. *Water and Environment Journal*, 29(2), pp. 268-276.
- Barraud, R., Lespez, L., Germaine, M.-A., Ballut, C., & Fournier, P. (2013). Moulins à eau et ouvrages hydrauliques, outils de reconstitution et d’interprétation des trajectoires paysagères des fonds de vallées. In *Au fil de l’eau. Ressources, risques et gestion du Néolithique à nos jours* (p. 71-88). Maison des Sciences de l’Homme.
- Carlini, M. (2006). *Morphologie et hydrodynamique des plans d’eau : Le cas des étangs-lacs en Limousin*.
- Chanson, H. (2004). *Hydraulics of Open Channel Flow*. Elsevier.
- Csiki, S., & Rhoads, B. L. (2010). Hydraulic and geomorphological effects of run-of-river dams. *Progress in Physical Geography: Earth and Environment*, 34(6), pp. 755-780.
- Degoutte, G. (2012). *Diagnostic, aménagement et gestion des rivières : Hydraulique et morphologie fluviales appliquées* (2e éd.). Éd. Tec & doc: Lavoisier.
- Dingman, S. L. (2009). *Fluvial Hydraulics*. Oxford University Press.
- Donati F., Touchart L., & Bartout P. (2019). Do rivers upstream weirs have lotics or lentic characteristics? *Geographia Technica*, 14(2), pp. 1-9.
- Donati, F., Touchart, L., & Bartout, P. (2020 a). Les seuils en rivière transforment-ils les milieux lotiques en milieux lenticques ? *Physio-Géo, Volume 15*, pp. 111-131.
- Donati F., Touchart L., Bartout P., & Choffel Q. (2020 b). Anciens et nouveaux écosystèmes aquatiques : Une revue sur leur fonctionnement abiotique. *Dynamiques Environnementales*, 45, pp. 11-21.
- Donati F. (2021). La nature des retenues de seuil : Une question limnologique ? Étude hydrodynamique, thermique et sédimentaire (Loiret, Moselle, Mayenne). Phd thesis, Université d’Orléans, 238 p.
- Malavoi, J.-R. (2003). *Stratégie d’intervention de l’Agence de l’eau sur les seuils en rivière* (N° AFF02011; p. 135). Agence de l’Eau Loire Bretagne.
- Maleval, V., & Alain, J. (2002). La sédimentation dans un lac artificiel. L’exemple de Saint-Pardoux (Massif d’Ambazac, Limousin). *Géomorphologie : relief, processus, environnement*, 4, pp. 307-319.
- Maleval, V., & Pitois, F. (2017). Fonctionnement hydro-sédimentaire et bilan sédimentaire du lac de Saint-Germain-de-Confolens (Charente, France) : Paramètres géomorphologiques à prendre en considération dans la gestion du lac. *Physio-Géo - Géographie Physique et Environnement*, pp. 197-227.
- Maniere, L. (2013). *Mise au point d’un protocole ’évaluation de l’impact des ouvrages transversaux sur la continuité sédimentaire dans le cadre d’une approche multiscalaire*. Université de Lyon 2 - Agence de l’Eau Loire Bretagne.
- Martin, J. L. (2013). *Hydro-Environmental Analysis : Freshwater Environments*. CRC Press.
- Onema. (2010). *Carhyce : Caractérisation hydromorphologique des cours d’eau* (p. 48). Onema.
- Pearson, A. J., & Pizzuto, J. (2015). Bedload transport over run-of-river dams, Delaware, U.S.A. *Geomorphology*, 248, pp. 382-395.
- Rickard, C., Day, R., & Purseglove, J. (2003). *River Weirs—Good Practice Guide* (N° W5B-023/HQP; p. 157). Environment Agency.
- Rivals, C. (2000). *Le moulin et le meunier. Mille ans de meunerie en France et en Europe* (Vol. 1 & 2). Empreinte Éditions.

ANALYSES OF TRENDS IN THE FIRE LOSSES AND THE FIRE-BRIGADE CALL-OUTS IN SOUTH AFRICA BETWEEN 2004 AND 2017

Rennifer MADONDO¹ , Nhamo MUTINGWENDE¹ , Siviwe SHWABABA¹ ,
Robyn J. BAYNE² , Ágoston RESTÁS³  and Roman TANDLICH^{1,4*} 

DOI : 10.21163/GT_2022.172.06

ABSTRACT:

The current study aimed at performing correlation analyses to gain a more detailed systems understanding of the temporal trends in financial losses from fires (disaster impacts) and the fire brigade call-outs (disaster response) in South Africa from the 2004 to 2017 period. The analysis is performed using data on the fire disaster impacts at the national level and the local level (Makana Local Municipality). The data on disaster impacts was extracted from databases and reports published by the Fire Protection Association of Southern Africa and Statistics South Africa. The total number of fire brigade call-outs/fires for the entire territory of South Africa ranged from 26574 in 2010 to 49567 in 2017. There was a direct correlation between the total number of fires and the losses from fires in residential settings in South Africa with time for the studied period. The losses from fire disasters in residential settings accounted for between 21.84 % and 74.06 % of all financial losses in South Africa between 2004 and 2017. On the other hand, call-outs to fire brigades with a residential cause or related to rubbish/bush/grass accounted for an average of 81.7 ± 2.7 % between 2004 and 2007, while it reached 88.5 ± 4.9 % in Makana Local Municipality. This indicates that fires in residential settings or related to rubbish or plant-based fuel account for a significant majority of the time fire brigades spent fighting fires in South Africa between 2004 and 2017. Fuel and waste management, and increasing fire human resilience at the household level, will play a significant role in the fire disaster risk management in South Africa. Vegetation cover and management will play a key role in the fire DRM in South Africa and local municipalities such as Makana.

Key-words: *Brigade, Damage assessment, Financial losses, Fire causes, Fire statistics*

1. INTRODUCTION

Understanding disasters, managing the related risk(s), and decreasing the impacts of the disasters on the affected population is a complex process. It requires the system's understanding to be applied to the disasters under study and the related risks/impacts. Dealing with disaster risks must consider the triggers of a disaster, i.e., hazards and the links to the vulnerability of the human population, assets, or environmental components of the socio-ecological systems to the effects of the disaster in question. At the same time, it is necessary to understand the adaptive capacity of the socio-ecological system to cope with the disaster disruptions through internal perturbations and the human resilience, assets, and environment to the disruptions.

¹ Disaster Management and Ethics Research Group (DMERG), Faculty of Pharmacy, Rhodes University, Grahamstown 6140, South Africa, r.tandlich@ru.ac.za, nmutingwende@gmail.com, siviwe.shwababa@ru.ac.za

² School of Disaster Management, Stenden South Africa, 1 Grand Street, Port Alfred 6170, South Africa, robynjbayne@gmail.com

³ Institute of Disaster Management, National University of Public Service, Ludovika tér. 3, 1441 Budapest Pf. 60, Hungary, Restas.Agoston@uni-nke.hu

⁴ Faculty of Health Sciences, Technical University of Liberec, Studentská 2, 461 17 Liberec, Czech Republic, *corresponding author's email: roman.tandlich@gmail.com

This is a short but holistic picture which many authors have reflected upon, analysed, and developed as part of a theoretical framework in the academic field of Disaster Risk Management (DRM) science. Many of these authors studied the components of this system, i.e., hazards, vulnerability and coping/adaptive capacity, as well as resilience. As pointed out by Becker (2009), understanding the components of disaster risk is not enough to achieve comprehensive DRM. Their interdependencies or links and interplays between the DRM system's components are just as important and must be understood in detail to avoid a 'suboptimisation problem' (Becker, 2009). The suboptimisation problem is the misunderstanding about the cause and effect, i.e., how does the change in the value of one parameter impact the whole system of DRM. This perspective has some aspects in common with the time-person-place perspective from the public health and disease progression, i.e., the interplay of a specific person's (physical) presence at the place where a pathogen can come into contact with them at a time when the pathogen is most virulent/infectious and/or when the individual human can be most susceptible to disease from the pathogen (Boston University School of Public Health, 2020). The complexity of the DRM space and the related considerations will be demonstrated in the example of drought and the links to fires in South Africa and its implications on other disasters, as well as impacts on human wellbeing.

Climate change in South Africa has been linked as the cause/contributing factor to the 2015-2022 El-Niño related drought, which in turn caused the 2018 water delivery problems in the City of Cape Town (Archer et al., 2022). The impacts have extended into the Eastern Cape Province, where agriculture, as one of the primary sources of population income/economic activity, has been impacted (Archer et al., 2022). In addition, the 2015-2022 El-Niño related drought has been causing significant problems in providing safe drinking water to the population (Iheanetu and Tandlich, 2022). Problems in the WASH service delivery by local government have resulted in Natechs occurring (similar to the findings of Hoossein et al., 2016). Natechs or complex disasters here will be those human actions that have led to climate change and that in turn has a negative feedback effect on the proliferation of novel disaster hazards, e.g. increases in the intensity of fires under drought conditions...conditions where component of the system is linked and affected bidirectionally by another (based on the authors' application of the work by Coetzee and van Niekerk, 2012). In this DRM landscape, climate change will thus have cascading effects on resource management and how disaster risk is minimised or managed. In the complex and drought-related DRM space, one of the important considerations will be fires. This will be the result of a combination of the increased availability of dry and combustible fuel, and the decreased volumes of water to fight the fires. Therefore the WASH angle could be extended to other disasters, as a reference viewpoint or a way to interpret the DRM space.

The fuel angle can be demonstrated by the conditions of the fynbos and the invasive pine plantations, as reported for the Knysna fires in 2017 by Kraaij et al. (2018). The decreased water volumes and the fire DRM issues will be similar to the severity to the data reported for the fire-fighting challenges in the California fires during ongoing and severe drought (Wang et al., 2017). Simply put, the decreasing precipitation will contribute to decreased volumes of water being available for human consumption and agriculture. Those uses will (have to) be prioritised in terms of allocation in the use of the existing water resources over fire-fighting and fire DRM, i.e. unless fires happen planning decisions and political will are likely to prefer activities with proven links to human existence over potential disasters. As a result, the water volumes for fire-fighting will likely be negatively impacted by the drought and climate change. Drought has been a contributing factor to the recent fire disasters in South Africa and there has therefore been an ongoing interest and research into the fire DRM, under drought conditions (Kraaij et al., 2018; COGTA, 2020). Similar studies on fire DRM have been conducted in Australia (Haque et al., 2021) and the European Union countries (European Environment Agency, 2021). In more detail for South Africa, several studies in recent years have looked at some of the fire impacts and disaster outcomes.

Strydom and Savage (2016) reported that fires could lead to the release of CO, CO₂ and deposit of black carbon on the surface of the snow, which can, in turn, result in a feedback loop in increasing climate change effects. By the same token, fires can have cascading disaster impacts that increase soil erosion rates, lower ground infiltration and escalate hazards from flash flooding in areas such as the

Eastern Cape Province, South Africa (Strydom and Savage, 2016). The monthly number of fires, as determined based on satellite imagery analysis for the entire territory of South Africa, was reported to range from just under 100 in April to the maximum of just over 700 in August and September in a single calendar year (Strydom and Savage, 2016). Considering the individual provinces in South Africa, Mpumalanga and KwaZulu-Natal were reported to experience most fires in August, while the Western Cape with the City of Cape Town suffered most fires in February between 2003 and 2013 (Strydom and Savage, 2016). The detrimental impacts of veld fires in Mpumalanga and KwaZulu-Natal, according to (Forsyth et al., 2010), can be summarized as follows:

“two South African provinces, i.e. KwaZulu Natal and Mpumalanga lost over 60 000 hectares at some point. Loss of timber worth billions was recorded in South Africa in one veld fire incident. Many people have lost jobs and property, and land damages have been recorded due to veld fires”

At the same time, the three agricultural and more rural provinces of North West Province, Free State and Eastern Cape, along with the economic hub of South Africa...the Gauteng Province, have the peak fire seasons in September (Strydom and Savage, 2016). Finally, the sparsely populated Northern Cape Province was reported to experience the most fires in November (Strydom and Savage, 2016). The threat of fires is also ongoing, and this is demonstrated by the current fire map for some of the Southern African countries in **Fig. 1** below.

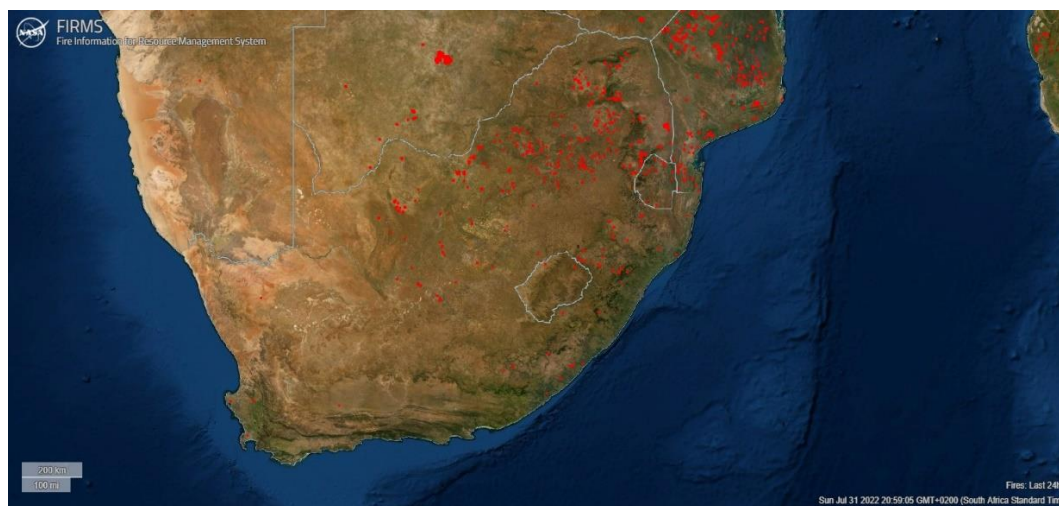


Fig. 1. Geographical distribution of fires in South Africa on 31st July 2022 (figure was adapted from <https://firms.modaps.eosdis.nasa.gov/map/#d:2022-07-30..2022-07-31,2022-07-30;@27.9,-28.8,6z>; no copyright applies; website accessed on 31st July 2022). Red dots represent active fires.

In 2021, a total of 126169 fires were reported countrywide in South Africa and the most affected provinces were the Eastern Cape, the North-West and Mpumalanga (Sgqolana, 2021). Efforts to tackle disaster hazards, vulnerability and manage disaster risk have also been ongoing. Academic examples of such efforts include the study by Ishola et al. (2020), who proposed a quantitative risk assessment for the fires in commercial complexes in South Africa that provides some tools to help manage the fire disaster risk in the country. Xulu et al. (2021) used open-source data from Google and satellite imagery to determine that 37.4% of the area in the Western Cape Province of South Africa was severely burned during the 2018 fires. In the same study, fires contribute to elevated atmospheric concentrations of carbon mono-oxide and black carbon (Xulu et al., 2021).

Based on the text so far, it is clear that the frequency and geographical distribution of fires in South Africa have been studied prior to the current study. To avoid the occurrence of the ‘suboptimisation’ problem with fires in the DRM space, it is necessary to conduct further studies on the impact of fires in South Africa. The impact of fires will be analysed in terms of financial losses

from the destruction of assets, e.g., housing and industrial infrastructure. In South Africa, losses in those assets, changes in the quality of life due to injuries in the aftermath of fires, and the displacement of populations due to loss of housing stock can result in significant disruptions to the functioning of society. More examination of the local data from South African databases is necessary regarding the residential impacts of fires and the potential sources of fuel/fuel load in residential areas, e.g. significance of vegetation and rubbish not collected by local municipalities. A complete and recently updated databases for fire impacts in South Africa should be used as data sources for the analysis.

The authors follow up with the current analysis on the review paper by Madondo et al. (2022). The aim here is to perform a set of correlation analyses and calculations to understand the structure of fire losses and response measures to fires in South Africa. Analyses were performed at the national level and on the example of a small local municipality in the rural Eastern Cape from 2004 until 2017. This local municipality was Makana Local Municipality is rural and has been impacted by problems in service delivery such as provision of drinking water. The authors have experience and ongoing interest in the DRM profile of the municipality and the paper could be looked as a continuation of those efforts. Due to the ongoing drought in South Africa and the breakdown in municipal service delivery, it is the working hypothesis of the current paper that the majority of the fire-fighting resources will be required to fight fires in residential settings. In addition, the authors hypothesise that municipal waste and its rates of its collection will have an impact on the fuel load and the fire-fighting resources that must be committed to fighting the fires in South Africa and in local municipal settings

2. METHODOLOGY

2.1. Evaluation of the temporal trends in fire statistics in South Africa 2004-2017

The first interest of the authors was to gain an understanding about the recent temporal trends in the fire numbers and their impacts/causes in South Africa. Interdependencies between the fire occurrence and the triggers of the fires should be linked to the fire triangle (Madondo et al., 2022). In other words, the monitoring and evaluation of fire statistics should focus on identifying the main type(s) of fuel that drive(s) fires in South Africa.

By the same token, the major assets impacted by the fires should also be identified and impacts quantified to avoid the 'suboptimisation' problem in the fire DRM in South Africa. The relevant data was extracted from the statistics published by the Fire Protection Association of Southern Africa (FPASA; see www.fpassa.co.za for details; website accessed on 4th May 2022). In particular, the authors extracted the total number of fires in a given calendar year in South Africa. Further, the data on the total financial and residential property losses due to fires were also extracted for the 2004-2017 study period. The residential property losses are reported as the sum of the losses from formal and informal dwellings, flats, and the hotel/hostel/boarding accommodation. In addition, the total call-outs for a fire brigade to assist with fire-related issues, i.e. the total number of fires in South Africa, were extracted with the FPASA database for the 2004-2017 time period. As with the fire losses, the number of calls were analysed for those originating from formal dwellings, flats, informal dwellings, and the hotel/hostel/boarding accommodation. At the same time, the fire brigade call-outs for rubbish, bush or grass related fire issues were correlated with time in the 2004-2017 period.

After data extraction, the first step in the quantitative analyses was to calculate the correlation coefficients, namely the Spearman correlation coefficient (see <https://www.socscistatistics.com/tests/spearman/default2.aspx> for details; website accessed on 28th April 2022 and 4th May 2022) and the Pearson correlation coefficient (see <https://www.socscistatistics.com/tests/pearson/default2.aspx> and <https://www.socscistatistics.com/pvalues/pearsondistribution.aspx> for more information; website accessed on 28th April 2022 and 4th May 2022). Calculations of the Spearman and Pearson correlation coefficients were aimed at establishing if there was a direct or indirect proportionality or a lack thereof, between the calendar year as an independent variable and the measure of fire disaster impacts

as the dependent variable. In other words, the correlation evaluations were to establish whether the disaster/fire impacts (financial losses), as well as the fire brigade call-outs (disaster response), were showing a significantly monotonous and/or linear trend in South Africa with time. Such trends could provide insight into the increasing or decreasing fire disaster risk and the South African DRM systems' ability to mobilise, respond and to some extent to cope or not to cope with fires between 2004 and 2017. The correlation coefficients for fire brigade call-outs were calculated for the entire territory of South Africa and for Makana Local Municipality. The reason for the two scales of analysis was two-fold. Firstly, the need to ascertain whether there was a correspondence between the national and local trends in the selected fire statistics or not. This is important to avoid the ecological fallacy of transposing the national trends on the local conditions in a specific area, if not appropriate, in South Africa. In addition, the evaluations of both trends at the national and local levels should also provide more insight into the cause and effect of fires (as disasters), i.e. help avoid the 'suboptimisation' problem in the fire DRM in South Africa.

2.2. Residential losses and the fuels controlling the fire brigade call-outs in South Africa for the 2004-2017 study period

Percentage of financial losses from fires in the residential settings in South Africa were calculated in relation to the total losses from fires in the country. This calculation assessed the fire disaster hazard/risk to the housing stock/residential properties in South Africa. The fraction/percentage of the total financial losses accounted for by the residential fire losses (X) were then calculated on an annual basis using Equation (1).

$$X = 100 \times \frac{Z}{Y} \tag{1}$$

where

Z represents the total financial losses from fires in formal and informal dwellings, flats, hostels and boarding houses extracted from the FPASA database and summed up to represent the residential property in South Africa (see the Results and Discussion section below for details)

Y represents the total financial losses from fires in South Africa in a given calendar year (see the Results and Discussion section below for details).

Finally, the percentage of call-outs for fire brigades in South Africa was recorded for the residential fires and/or by fires related to rubbish/bush/grass. These were calculated as a percentage of the total fire call-outs in South Africa and Makana Local Municipality (*designated as A in further text*). The percentages were calculated as shown in Equation (2).

$$A = 100 \times \frac{B}{C} \tag{2}$$

The terms in Equation (2) are analogical to the terms in Equation (1), except those financial losses were replaced by the number of the fire brigade call-outs in South Africa or Makana Local Municipality. Analysing the call-outs trends can indicate the type of assets most at risk from fires, as well as the potential of fuel control in the management of fires during droughts, and the fires which will require the allocation/use of most of the fire DRM resources in the country. The analyses of that data provide a better understanding of the burden of South African fires, which occur in residential settings. This might, in turn, indicate the potential optimisation of the DRM resource allocation to fires in South Africa, required to decrease the potential disaster impact of fires on the country's population.

If the domestic waste was not collected by local municipalities regularly for the 2004-2017 period, then that could increase the fuel load for the fires across South Africa. A correlation analysis was performed to investigate that point in more detail for the number of fire brigade call-outs due to rubbish/bush/grass and the percentage of South African/Makana households with regular refuse

collection. The raw data for the latter variable was extracted from the General Household Survey by Statistics South Africa, or the Integrated Development Plans of Makana Local Municipality (see the Results and Discussion section for details). The correlation was examined using the Spearman correlation coefficient at a 5 % level of significance, just as with the above-mentioned correlations. The vegetation in the study is looked at as a fuel source and it is not the aim of this study to specifically link the causes of the fire to the vegetation type in a particular part of the country. The vegetation types and classification can be found at the South African National Biodiversity Institute (SANBI, 2022). Briefly, the following biomes are commonly found across South Africa: thicket biome, fynbos biome, grassland savanna biome, desert, Nama-Karoo, and succulent Karoo Biomes (SANBI, 2022). Thicket and fynbos types have also been reported to be present in Makana Local Municipality (Palmer, 2004). Local government services are not only necessary to protect wellbeing of the residents in an area, but the lack of waste collection can increase the fire hazards through the potential for fires spreading through the combustion of loose rubbish. This element will also be investigated in the current paper.

2.3. Prediction of the fire numbers for the 2018-2022 period

Data from the FPASA was used in this paper, as the authors found it to be the most complete and most fit for purpose from the data sources available on fire statistics in South Africa. Other data sources could be used if the level of data disaggregation would be similar to the FPASA database. An example of such data could be the VIIRS system, but the damages and financial information is not the same, as reported in the FPASA database for the 2004-2017 period (Global Forest Watch, 2022). However, the level of detail and the information diversity is limited to a specific aspect of the fires, e.g. the burn intensity and area (Xulu et al., 2021). The FPASA data allows for the evaluation of the resource allocation and potential optimisation at the national and local level across South Africa. That was the main reason that the FPASA fire statistics database was selected by the authors of the current study. However it is clear that the data must be extended beyond 2017. Therefore, the authors attempted to model some aspects of the FPASA data for extrapolation beyond 2017. The total number of fires in South Africa was correlated as an independent, using the multiple linear regression analysis (Past 3.0, Hammer et al., 2001), with the human development index (HDI; Countryeconomy.com, undated; Human Development Report, 2020), the gross national product per capita based on purchasing power parity (GDP_{PPP} in USD; World Bank, 2022) and the interest of the South African public in fires/veld fires/veldfires by extracting total number of yearly searches on Google for the keyword fire through Keywordseverywhere.com (GSKEF in number of searches; Burivalová et al., 2018; Pretorius et al., 2022 and <https://keywordseverywhere.com/>; website accessed on 29th June 2022).

3. RESULTS AND DISCUSSION

3.1. Evaluation of the temporal trends in fires and fire losses/damages in South Africa for the 2004-2017 study period

Data from the FPASA in **Table 1** shows the total number of fire call-outs/fires and fire losses in South Africa from 2004 to 2017. The numbers indicate that the total number of fire brigade call-outs for the entire territory of South Africa ranged from 26574 in 2010 to 49567 in 2017. These are equal to the total number of fires in the given calendar year, with only one insignificant exception that did not have any effect on the results of the correlation analyses (data not shown). There was a direct and statistically significant increase in the total number of fire brigade call-outs/fires with time in South Africa between 2004 and 2017. That conclusion was supported by the value of the Spearman correlation coefficient, which was equal to 0.65385, and that value was statistically significant at 5 % of significance (p -value = 0.01535). At the same time, the directly proportional relationship was likely

linear in nature, as indicated by the value of the Pearson correlation coefficient, which was equal to 0.58440, and that value was statistically significant at 5 % of significance (p -value = 0.03595).

Table 1.
Fire statistics and fire losses in South Africa, as based on the Fire Protection Association of South Africa between 2004 and 2017.

Year	Total losses from fires (ZAR)	TFC ^a (#)	Total residential losses from fires (ZAR)	Residential losses as percentage total (%)	Pages in data source	Website for source document
2004	1211926334	36591	492120909	40.61	Page 15, 17, 19	https://www.fpsa.co.za/images/FireStats/Fire_Stats_2004.pdf
2005	1321494810	42863	350056269	26.49	Page 21	https://www.fpsa.co.za/images/FireStats/Fire_Stats_2005.pdf
2006	2732970948	33499	2023916105	74.06	Pages 12, 18, 21	https://www.fpsa.co.za/images/FireStats/Fire_Stats_2006.pdf
2008	2312573487	35434	504966938	21.84	Pages 28-30	https://www.fpsa.co.za/images/FireStats/Fire_Stats_2008.pdf
2009	2013698822	40481	667102742	33.13	Pages 26-27	https://www.fpsa.co.za/images/FireStats/Fire_Stats_2009.pdf
2010	1323019072	26574	613802753	46.39	Page 20	https://www.fpsa.co.za/images/FireStats/Fire_Stats_2010.pdf
2011	2085522959	37721	728144691	34.91	Page 48	https://www.fpsa.co.za/images/FireStats/Fire_Stats_2011.pdf
2012	3162240443	41481	744278394	23.54	Page 32	https://www.fpsa.co.za/images/FireStats/Fire_Stats_2012.pdf
2013	2158223582	42343	1008867283	46.75	Page 34	https://www.fpsa.co.za/images/FireStats/Fire_Stats_2013.pdf
2014	1847497349	46187	680486831	36.83	Pages 48 and 50	https://www.fpsa.co.za/images/FireStats/Fire_Stats_2014.pdf
2015	2732024282	45784	1186434833	43.43	Pages 30-31 and 36	https://www.fpsa.co.za/images/FireStats/Fire_Stats_2015.pdf
2016	3144851768	41873	1843930163	58.63	Pages 22, 23 and 28	https://www.fpsa.co.za/images/FireStats/Fire_Stats_2016.pdf
2017	5481548883	49567	2773495906	50.60	Pages 18, 19 and 24	https://www.fpsa.co.za/images/FireStats/Fire_Stats_2017.pdf

^a Total number of fires/fire brigade callouts in South Africa between 2004 and 2017. The unit for this parameter is dimensionless or number, marked with # in Table 1.

For the 2004-2017 period, the total financial losses due to fires in South Africa ranged from 1.321 billion ZAR in 2005 to 5.482 billion ZAR in 2017 per year (exchange rate 1 USD = 6.1851-14.8171 ZAR: SARS, 2003-present). At the same time, the financial losses from fires in residential settings ranged, for the 2004-2017 period, from 350.056 million ZAR in 2005 to 2.773 billion ZAR in 2017. There was a direct and statistically significant increase in the financial losses from fires with time in South Africa for the analysed period. For the total financial losses, that conclusion was indicated by the value of the Spearman correlation coefficient, which was equal to 0.62637, and that value was statistically significant at 5 % of significance (p -value = 0.02199).

The directly proportional relationship was likely linear in nature, as indicated by the value of the Pearson correlation coefficient, which was equal to 0.65660, and that value was statistically significant at 5 % of significance (p -value = 0.01478). A similar correlation performed for the residential setting fire losses showed that the Spearman correlation coefficient was equal to 0.70879, and that value was statistically significant at 5 % of significance (p -value = 0.00668). This relationship was monotonous but likely not linear, as indicated by the Pearson correlation coefficient, which was equal to 0.52710, but was not statistically significant at 5 % of significance (p -value = 0.06382). Based on the correlation analysis of the fire loss data from the FPASA, it is clear that the financial

losses from fires have been increasing in absolute terms in South Africa with time between 2004 and 2017. That increase was linear with time. There was an increase in fire losses in housing stock, and it was directly correlated with time, but not in a linear fashion. Losses from fire disasters in residential settings accounted for a significant portion of the financial fire disaster losses, as they accounted for between 21.84 and 74.06 % of all financial losses from fires in South Africa between 2004 and 2017.

3.2. Evaluation of the temporal trends in fire brigade call-outs in South Africa for the 2004-2017 study period

The FPASA data in **Table 2** indicate that the number of fire brigade call-outs for the entire territory of South Africa ranged from 26574 in 2010 to 49567 in 2017. In more detail, the number of fire brigade call-outs, which were related to fires in residential settings, ranged from 7170 in 2006 to 13123 in 2017. Finally, the number of fire brigade call-outs due to rubbish/bush/grass ranged from 16909 in 2010 to 28482 in 2017. For the number of fire brigade call-outs to residential fires, the Spearman correlation coefficient was equal to 0.85165, and that value was statistically significant at 5 % of significance (p -value = 0.00022). This relationship was monotonous and likely linear, as the value of the Pearson correlation coefficient which was equal to 0.82190 and that correlation was statistically significant at 5 % of significance (p -value = 0.00057).

Table 2.
Fire brigade call-outs in South Africa, as based on the Fire Protection Association of South Africa between 2004 and 2017.

Year	<i>TFC</i> ^a (dimensionless)	<i>RFC</i> ^b (dimensionless)	<i>RBGFC</i> ^c (dimensionless)	<i>PRRBGFC</i> ^d (%)	Pages in data source	Website for source document
2004	36591	7505	23367	84.37	Pages 26,27	https://www.fpsa.co.za/images/FireStats/Fire_Stats_2004.pdf
2005	42863	7423	28165	83.03	Pages 22,23	https://www.fpsa.co.za/images/FireStats/Fire_Stats_2005.pdf
2006	33499	7170	19271	78.93	Page 26	https://www.fpsa.co.za/images/FireStats/Fire_Stats_2006.pdf
2008	35434	7207	22228	83.07	Pages 32-33	https://www.fpsa.co.za/images/FireStats/Fire_Stats_2008.pdf
2009	40481	8496	24683	81.96	Page 32-33	https://www.fpsa.co.za/images/FireStats/Fire_Stats_2009.pdf
2010	26574	5391	16909	83.92	Page 22	https://www.fpsa.co.za/images/FireStats/Fire_Stats_2010.pdf
2011	37721	8330	22646	82.12	Page 39	https://www.fpsa.co.za/images/FireStats/Fire_Stats_2011.pdf
2012	41481	9491	23977	80.68	Page 28-29	https://www.fpsa.co.za/images/FireStats/Fire_Stats_2012.pdf
2013	42343	10199	24989	83.10	Page 26-27	https://www.fpsa.co.za/images/FireStats/Fire_Stats_2013.pdf
2014	46187	10514	28482	84.43	Pages 42-43	https://www.fpsa.co.za/images/FireStats/Fire_Stats_2014.pdf
2015	45784	11326	25882	81.27	Pages 26-27	https://www.fpsa.co.za/images/FireStats/Fire_Stats_2015.pdf
2016	41873	10555	20684	74.60	Pages 16-17	https://www.fpsa.co.za/images/FireStats/Fire_Stats_2016.pdf
2017	49567	13123	26866	80.68	Pages 14-15	https://www.fpsa.co.za/images/FireStats/Fire_Stats_2017.pdf

^a Total number of fires/fire brigade callouts in South Africa between 2004 and 2017.

^b Dwellings, informal dwellings, flats and hotels/boarding houses in South Africa between 2004 and 2017.

^c Rubbish, grass and bush fire brigade call-outs in South Africa between 2004 and 2017.

^d Dwellings and rubbish call-outs as percentage of all total call-outs in South Africa between 2004 and 2017.

The correlation analyses were repeated for the number of fire brigade call-outs to fires linked to the rubbish/bush/grass. The relevant Spearman correlation coefficient was equal to 0.28571, and that value was not statistically significant at 5 % of significance (p -value = 0.34400). The respective relationship was not monotonous and likely not linear, as the Pearson correlation coefficient was equal to 0.21350 and, therefore, not statistically significant at 5 % of significance (p -value = 0.48370). Based on the data from the FPASA, it is clear that the number of fire brigade call-outs increased overall in South Africa between 2004 and 2017. An analogical trend was observed for the call-outs to residential fires, but not for fires related to rubbish/bush/grass. For the 2004-2017 study period, the call-outs to fire brigades, which had a residential cause or related to rubbish/bush/grass, accounted for an average of 81.7 ± 2.7 %. This indicates that fires in residential settings, or fires related to rubbish/bush/grass, accounted for a significant majority of the time fire brigades spent fighting fires in South Africa between 2004 and 2017. Fuel and waste management, as well as increasing the fire human resilience at the household level, will play a significant role in the fire DRM in South Africa. This is based on the likelihood that fire DRM resources might become insufficient to fight fires during drought related conditions. The number of fire brigade call-outs between 2004 and 2017 were correlated with the household percentage in South Africa with regular refuse collection. The raw data is shown in **Table 3** below.

Table 3.

Fire brigade call-outs in South Africa due to rubbish/bush/grass, as based on the Fire Protection Association of South Africa, and correlation with the percentage of the South African households with regular municipal refuse collection between 2004 and 2017.

Year	<i>RBGFC</i> ^a (dimensionless)	<i>PHRRR</i> ^a (dimensionless)	General Household survey raw data location	Website for source document
2004	23367	57.1	Figure 28 on page xxxi	https://www.statssa.gov.za/publications/P0318/P03182004.pdf
2005	28165	60.1	Figure 20 on page xxvii	https://www.statssa.gov.za/publications/P0318/P03182005.pdf
2006	19271	60.6	Figure 20 on page xxx	https://www.statssa.gov.za/publications/P0318/P03182006.pdf
2008	22228	60.5	Figure 21 on page 31	https://www.statssa.gov.za/publications/P0318/P03182008.pdf
2009	24683	55.1	Figure 25 on page 32	https://www.statssa.gov.za/publications/P0318/P03182009.pdf
2010	16909	59.1	Figure 26 on page 32	https://www.statssa.gov.za/publications/P0318/P03182010.pdf
2011	22646	61.0	Figure 31 on page 34	https://www.statssa.gov.za/publications/P0318/P03182011.pdf
2012	23977	64.0	Figure 33 on page 35	https://www.statssa.gov.za/publications/P0318/P03182012.pdf
2013	24989	63.5	Table 13 on page 50	https://www.statssa.gov.za/publications/P0318/P03182013.pdf
2014	28482	63.8	Table 13 on page 51	https://www.statssa.gov.za/publications/P0318/P03182014.pdf
2015	25882	63.5	Table 13 on page 48	https://www.statssa.gov.za/publications/P0318/P03182015.pdf
2016	20684	64.9	Table 12 on page 47	https://www.statssa.gov.za/publications/P0318/P03182016.pdf
2017	26866	65.9	Table 13 on page 45	https://www.fpasa.co.za/images/FireStats/Fire_Stats_2017.pdf

^a *Rubbish, grass and bush fire brigade call-outs in South Africa between 2004 and 2017.*

^b *The percentage of households with regular municipal refuse removal in South Africa between 2004 and 2017.*

There was no statistically significant relationship at a 5 % level of significance, as indicated by the value of the Spearman correlation coefficient and the p -value (0.26685; p -values = 0.37814). Therefore, rubbish uncollected by local government is not the only controlling factor, in determining the number of fires/fire brigade call-outs, due to rubbish/bush/grass. As a result, the plant fuel might

play a more significant role in the fire triangle relevant to the fire-prone and drought-stricken areas in South Africa between 2004 and 2017 (Madondo et al., 2022).

To avoid the ecological fallacy of applying national data to the local level, the South African conclusions were compared to those for Makana Local Municipality as an example. Rhodes University is based in Makana Local Municipality, and the area has been impacted by drought since about 2015 (as indicated, for example, by Iheanetu and Tandlich, 2022). Drought will require alteration of the existing fire-fighting approaches, as the volumes of water available for such purpose might not be sufficient or might be decreased to pre-drought status. Therefore, it is necessary to evaluate whether the resources of fire brigades are required for similar or different activities compared to the entire South Africa. Therefore, the FPASA data in **Table 4** show the number of fire brigade call-outs in Makana Local Municipality for the 2004-2017 study period. The number of call-outs, or the total number of fires in the municipality, ranged from 99 in 2015 to 280 in 2016. The number of fire brigade call-outs related to fires in residential settings ranged from 26 in 2014 to 70 in 2016. Finally, the number of fire brigade call-outs between 2004 and 2017, which were related to fires by rubbish/bush/grass in Makana Local Municipality, ranged from 62 in 2015 to 153 in 2005. There was no statistically significant relationship between the number of the total fire brigade call-outs, nor the call-outs to residential fires or fires related to rubbish/bush/grass and time between 2004 and 2017.

Table 4.

Fire brigade call-outs in Makana Local Municipality, as based on the Fire Protection Association of South Africa between 2004 and 2017.

Year	<i>TFC</i> ^a (dimensionless)	<i>RFC</i> ^b (dimensionless)	<i>RBGFC</i> ^c (dimensionless)	<i>PRRBGFC</i> ^d (%)	Pages in data source	Website for source document
2004	159	36	112	93.08	Pages 26,27	https://www.fpasa.co.za/images/FireStats/Fire_Stats_2004.pdf
2005	194	27	153	92.78	Pages 22,23	https://www.fpasa.co.za/images/FireStats/Fire_Stats_2005.pdf
2006	135	42	72	84.44	Page 26	https://www.fpasa.co.za/images/FireStats/Fire_Stats_2006.pdf
2008	218	45	149	88.99	Pages 32-33	https://www.fpasa.co.za/images/FireStats/Fire_Stats_2008.pdf
2009	144	36	82	81.94	Page 32-33	https://www.fpasa.co.za/images/FireStats/Fire_Stats_2009.pdf
2010	145	42	88	89.66	Page 22	https://www.fpasa.co.za/images/FireStats/Fire_Stats_2010.pdf
2011	172	54	98	88.37	Page 39	https://www.fpasa.co.za/images/FireStats/Fire_Stats_2011.pdf
2012	152	36	108	94.74	Page 28-29	https://www.fpasa.co.za/images/FireStats/Fire_Stats_2012.pdf
2013	146	30	86	79.45	Page 26-27	https://www.fpasa.co.za/images/FireStats/Fire_Stats_2013.pdf
2014	144	26	108	93.06	Pages 42-43	https://www.fpasa.co.za/images/FireStats/Fire_Stats_2014.pdf
2015	99	29	62	91.92	Pages 26-27	https://www.fpasa.co.za/images/FireStats/Fire_Stats_2015.pdf
2016	280	70	182	90.00	Pages 16-17	https://www.fpasa.co.za/images/FireStats/Fire_Stats_2016.pdf
2017	136	41	71	82.35	Pages 14-15	https://www.fpasa.co.za/images/FireStats/Fire_Stats_2017.pdf

^a Total number of fires/fire brigade callouts in Makana Local Municipality between 2004 and 2017.

^b Dwellings, informal dwellings, flats and hotels/boarding houses in Makana Local Municipality between 2004 and 2017.

^c Rubbish, grass and bush fire brigade call-outs in Makana Local Municipality between 2004 and 2017.

^d Dwellings and rubbish call-outs as percentage of all total call-outs in Makana Local Municipality between 2004 and 2017.

That conclusion was supported by the value of the Spearman correlation coefficients, which ranged from -0.29711 to 0.01936, for the Makana data. None of the correlations were statistically significant at 5 % of significance (p -values = 0.40941- 0.94994). For the 2004-2017 time period, the call-outs to fire brigades, which had a residential cause or were caused by rubbish/bush/grass, accounted for an average of 88.5 ± 4.9 % of all fire brigade call-outs in Makana Local Municipality. That proportion was statistically significantly different from the analogical proportion for the entire territory of South Africa (t -test at 5 % level of significance, p -value = 0.0001). Therefore, just like for the entire territory of South Africa, fuel/waste management and increasing the fire human resilience at the household level will play a significant role in the fire DRM in Makana Local Municipality. This will be based on the drought and the potential insufficient fire-fighting resources available to fight such fires in South Africa and in Makana Local Municipality. The Integrated Development Plans (IDPs) for Makana Local Municipality could only be found from 2011 until 2017 (see <http://www.makana.gov.za/wp-content/uploads/2013/06/Final-Document-IDP-2016-2017.pdf> for details; website accessed on 19th May 2022). Only the 2001-2011 census figure for the access to regular municipal refuse removal could be found; more specifically the 2011 figure was equal to 89.6 % of all Makana households. Based on this point estimate, vegetation management will, therefore, likely play a significant role in the fire DRM under the conditions of drought in Makana, just like concluded for South Africa. In addition, littering or illegal dumping in non-designated landfills/areas by Makana residents might provide another plausible explanation.

3.3. Prediction of the fire numbers for the 2018-2022 period

The fire call-out were equal to the number of fires in South Africa for the given calendar year between 2004 and 2017. Data on the HDI, GDP_{ppp} and the GSKEF were compiled for the 2004-2017 period, and they are listed in **Table 5** below.

The 2018-2022 period was modelled based on the following reasoning. The number of fires can be expected to be correlated to the level of development of the given country. In other words, the value and number assets at risk from fire disasters can reasonably be expected to be linked to the level of development of the country and wealth/economic value or status in a given country. In addition, the level of education and health/wellbeing of the country's population will be linked to the and the interest of the population in a type of disaster, i.e. fire. Therefore, the authors of the current study attempted to develop an equation that could be used to predict the fire statistics, namely the *TFC* in relation to HDI, GDP_{ppp} and the GSKEF. For this, data from **Table 5** was used and the correlations were performed as the multiple linear regression analysis as shown in Equation (3).

$$TFC = -70815(\pm 24997) + 2.109 \times 10^5(\pm 66527) \times HDI + 3.8151(\pm 1.6507) \times GDP_{ppp} + 0.1513(\pm 0.1013) \times GSKEF; R^2 = 0.7580 \quad (3)$$

For Equation (3), 12 points in the correlation yielded the following statistical data for ANOVA: F -statistic 8.354, $df1 = 3$ and $df2 = 8$ and p -value = 0.0075735. At the same time, the adjusted R^2 value was equal to 0.66729. The *TFC* value for 2010 was removed to increase the R^2 value from around 0.57 to 0.7580.

The Graphpad online outlier calculator (see <https://www.graphpad.com/quickcalcs/grubbs2/> for details; website accessed on 2nd August 2022) was used to assess whether the 2010 value of *TFC* is a statistically significant outlier or not. The Z value for the 2010 value of *TFC*, namely 26574, was equal to 2.21. The critical Z value was equal to 2.462 and p -value was higher than 0.05. Therefore the 2010 value of *TFC* was not statistically significantly an outlier at 5 % level of significance. However, the value was removed to improve the quality of the fit in the multiple linear regression and the justification for this step is based on the following reasons: increase in the R^2 value, the standard deviation of the optimised values of adjustable parameters were mostly below 50 % of the parameter value and the recalculated *TFC* values from Equation (3) were 100 ± 6 % of the actual FPASA values. Therefore, the predictions in the 2004-2017 interval were reliable based on Equation (3). It is,

however, also true that the adjusted R^2 values indicated that the used independent variables were only able cumulatively to account for around 66 % of the variance in the dependent variable. Therefore, other parameters could influence the number of fire brigade call-outs in South Africa. The values of the fire brigade call-outs were extrapolated to the 2018-2022 period and the assumptions made are shown in **Table 5**. The predicted number of fire brigade call-outs ranged from 43064 to 46997. In 2021, a total of 126169 fires were reported countrywide in South Africa and the most affected provinces were the Eastern Cape, the North-West and Mpumalanga (Sgqolana, 2021). Therefore, the prediction from Equation (3) should be multiplied by 2.862 to get the extrapolation close to the real-life data. However, the difference in the data collation methodology might also have to be examined, as a potential source of discrepancy.

Table 5.
Fire brigade call-outs as a function of the level of human development, gross domestic product per capita and the total number of Google searches for fire in South Africa between 2004 and 2017.

Year	HDI ^a (dimensionless)	GDP _{PPP} ^b (USD)	GSKEF ^c (dimensionless)	TFC ^d
2004	0.619	10061.5974	120100	36591
2005	0.622	10790.3306	128370	42863
2006	0.626	11599.1032	115300	33499
2008	0.646	12857.9865	121440	35434
2009	0.655	12565.2928	130690	40481
2010	0.664	12913.5405	126110	26574
2011	0.665	13393.7669	142860	37721
2012	0.675	13215.7087	146965	41481
2013	0.685	13606.9429	138926	42343
2014	0.693	13602.1026	129226	46187
2015	0.701	13701.9454	143326	45784
2016	0.703	13748.4614	127266	41873
2017	0.705	13860.2702	147312	49567
2018	0.707	14207.4329 ^e	125411	43064
2019	0.709	14288.5899 ^e	138404	45143
2020	0.709 ^e	13359.4843 ^f	127236	46997
2021	0.709 ^e	14420.1743 ^f	134663	44075
2022	0.709 ^e	14420.1743 ^f	151266	46587

^a Human Development Index in the given calendar year between 2004 and 2017.

^b Gross domestic product per capita based on purchasing power parity between 2004 and 2017.

^c Total yearly Google searches for the search term 'fire' in South Africa between 2004 and 2017.

^d Total number of fires/fire brigade callouts in South Africa between 2004 and 2017.

^e The HDI values for 2020-2022 were assumed to be constant and equal to the 2019 value. This is based on the likely decline and recovery from the COIVD19 pandemic

3.4. Integrating remarks on the data analysis and comparison with literature

The World Meteorological Organisation reported that the number of wildfires will go up by 14 % between the present and 2030 (WMO, 2022). There will also be a further increase of 50 % by 2050 compared to the current fire numbers (WMO, 2022). For Botswana, Maabong and Mphale (2021) reported that the El-Niño/La-Niña oscillation in Southern Africa can lead to the growth of plants and thus an increase in fuel. That would be followed shortly by the occurrence of wildfires, which ranged from 37 to 938 between 2006 and 2017 in Botswana (Maabong and Mphale, 2021). On a broader time

scale, the number of wildfires in Botswana ranged from about 20 to about 350 between 1994 and 2009, with most of them being of human origin (Maabong and Mphale, 2021). In 2017, a mega-fire hit the area in the Southern Cape and, more specifically the area around the City of Knysna (Kraaij et al., 2018). The triggers for the fire were multi-fold, but the commercial forestry plantations of alien vegetation (namely pine trees) and the fire-prone atmospheric conditions contributed to the severity of the fire losses (Kraaij et al., 2018). Therefore data from this study could indicate that vegetation cover and management will play a key role in the fire DRM in South Africa, as well as in local municipalities such as Makana. The current paper is based on open-source data that is freely available and that can be used to investigate the trends in the fires in South Africa. This is the case in terms of overall number of fires and the factors driving them. The FPASA data base was deemed the most complete in South Africa and was therefore used.

4. CONCLUSIONS

The number of fires and the losses from fires increased between 2004 and 2017. Fires in residential settings, or fires related to rubbish or plant-based fuel, account for a significant majority of the time that fire brigades spent fighting fires in South Africa between 2004 and 2017. Therefore, fuel and waste management, as well as increasing the fire human resilience at the household level, will play a significant role in the fire DRM in South Africa. This will apply to national, as well as local context in local municipalities such as Makana.

ACKNOWLEDGEMENTS

The authors would like to thank the Rhodes University Sandisa Imbewu Fund for supporting the study by supporting the scholarship of Ms. Madondo. Technical University of Liberec and the International Emergency Management Society (TIEMS) are acknowledged for providing technical support for the completion of the study. None of the institutions mentioned above has reviewed any of the study drafts and no formal endorsement by either of those institutions should be inferred.

REFERENCES

- Archer (2022). The 2015-19 multi year drought in the Eastern Cape, South Africa: it's evolution and impacts on agriculture. *Journal of Arid Environments* 196: Paper number 104630. <https://doi.org/10.1016/j.jaridenv.2021.104630>.
- Becker, P. (2009). Grasping the hydra: the need for a holistic and systematic approach to disaster risk reduction. *Jambá: Journal of Disaster Risk Studies* 2(1): Paper number 12. <https://doi.org/10.4102/jamba.v2i1.12>.
- Boston University School of Public Health (2020). PH717 Module 1B - Descriptive Tools Descriptive Epidemiology & Descriptive Statistics: Characteristics of Person, Place, and Time. Available at: https://sphweb.bumc.bu.edu/otlt/MPH-Modules/PH717-QuantCore/PH717-Module1B-DescriptiveStudies_and_Statistics/PH717-Module1B-DescriptiveStudies_and_Statistics3.html (website accessed on 3rd May 2022).
- Burivalová, Z., Butler, R. A., Wilcove, D. S. (2018). Analyzing Google search data to debunk myths about the public's interest in conservation. *Frontiers in Ecology and the Environment* 16(9): 509-514. <https://doi.org/10.1002/fee.1962>.
- Coetzee, C., van Niekerk, D. (2012). Tracking the evolution of the disaster management cycle: A general system theory approach. *Jambá: Journal of Disaster Risk Studies* 4(1): Article number 54. <https://doi.org/10.4102/jamba.v4i1.54>.
- Countryeconomy.com (undated). South Africa - Human Development Index – HDI. Available at: <https://countryeconomy.com/hdi/south-africa> (website accessed on 1st August 2022).

- South African Revenue Service (SARS, 2003-present). Exchange rate USD/ZAR – Table A: Average exchange rates for a year of assessment. Available at: <https://www.sars.gov.za/wp-content/uploads/Legal/Rates/LAPD-Pub-AER-2012-02-Average-Exchange-Rates-Table-A.pdf> (website accessed on 12th May 2022).
- South African Ministry of Cooperative Governance and Traditional Affairs (COGTA, 2020). DEPARTMENT OF CO-OPERATIVE GOVERNANCE NOTICE 515 OF 2020 WHITE PAPER ON FIRE SERVICES XX MONTH 2020, 43734. Available at: https://www.gov.za/sites/default/files/gcis_document/202009/43734gen515.pdf (website accessed on 2nd May 2022).
- Strydom, S., Savage, M. J. (2016). A spatio-temporal analysis of fires in South Africa. *South African Journal of Science* 112(11/12): Paper number 2015-0489. <http://dx.doi.org/10.17159/sajs.2016/20150489>.
- World Meteorological Organisation (WMO, 2022). Number of wildfires forecast to rise by 50 % by 2100. Available at: <https://public.wmo.int/en/media/news/number-of-wildfires-forecast-rise-50-100#:~:text=There%20is%20projected%20to%20be,the%20end%20of%20the%20century.> (website accessed on 19th May 2022).
- Wang, S.-Y. S., Yoon, J.-H., Gillies, R., Hsu, H.-H. (2017). The California Drought: Trends and Impacts (chapter 13). *In book: Climate Extremes: Patterns and Mechanisms*, ISBN: 978-1-119-06784-9, AGU (Wiley), New York, NY, USA. pp. 28.
- World Bank Data (2022). GDP per capita, PPP (current international \$). Available at: <https://data.worldbank.org/indicator/NY.GDP.PCAP.PP.CD> (website accessed on 1st August 2022).
- Xulu, S., Mbatha, N., Peerbhay, K. (2021). Burned Area Mapping over the Southern Cape Forestry Region, South Africa Using Sentinel Data within GEE Cloud Platform. *ISPRS International Journal of Geo-Information* 10(8): Article number 511. <https://doi.org/10.3390/ijgi10080511>.

ACCURACY PERFORMANCE OF SATELLITE-DERIVED SEA SURFACE TEMPERATURE PRODUCTS FOR THE INDONESIAN SEAS

Restu TRESNAWATI^{1,5} , Anindya WIRASATRIYA^{2,4} , Adi WIBOWO³ 

DOI: 10.21163/GT_2022.172.07

ABSTRACT:

The precision of sea surface temperature (SST) from remote sensing data is essential to recognize SST fluctuations prompted by extreme weather conditions due to global climate warming, such as tropical cyclones (TCs). Since 1981 the active remote sensing of satellite-based SST measurements has been around and proliferating to date in Indonesia. However, there has not been much research on the validation of several remote sensing datasets in Indonesia's seas that has limited coverage of buoy observations. Moreover, no studies correspond to which data are the most precise in describing SST fluctuations in tropical storms. In this study, six remote sensing/satellite (Operational Sea Surface Temperature and Sea Ice Analysis (OSTIA), Regional Australian Multi-Sensor SST Analysis (RAMSSA), Global Australian Multi-Sensor SST Analysis (GAMSA), Microwave Infrared Optimally Interpolated (MWIROI), Multi-scale Ultra-high Resolution (MUR), and K10) data are validated and compared to analyze SST fluctuations in TC as a case study. The validation method uses the Haversine distance formula to reach the highest quality iQuam data with satellite data. The comparison analysis is performed by plotting the SST and wind slop in a TC area. Based on the validation, The OSTIA, RAMSSA, GAMSSA, and MWIROI datasets ranked in the top 4 of the smallest RMSEs with values < 0.5. Moreover, in the SST and wind slop in a TC area, TC affects SST cooling as detected in the MUR and K10 datasets where there is a decrease of > 2 °C. In the MWIROI, the decline is more noticeable significant > 3 °C.

Keywords: *Validation, Sea Surface Temperature, Remote Sensing, Tropical Cyclone.*

1. INTRODUCTION

SST is an essential and fundamental parameter in the global oceanic atmospheric system (Xu *et al.*, 2021; Xiao *et al.*, 2019). The SST is used to understand, monitor, and predict heat, gas flow, and momentum at various scales that define complicated interactions between the atmosphere and ocean (O'Carroll *et al.*, 2019; Small *et al.*, 2008). Currently, the global climate change is altering due to human activities, particularly those that generate the release of greenhouse gases from fossil energies (Mcmichael *et al.*, no date). Climate change has significantly affected marine, aquatic, and terrestrial lives. The most noticeable effect is the accumulation of heightened doses of carbon dioxide in the atmosphere, responsible for the greenhouse effect.

¹Faculty of Fisheries and Marine Sciences, Diponegoro University, 50275, Semarang, Indonesia, restutresnawati@students.undip.ac.id, etubowo@gmail.com

²Department of Oceanography, Faculty of Fisheries and Marine Sciences, Diponegoro University, 50275, Semarang, Indonesia, anindyawirasatriya@lecturer.undip.ac.id, aninosi@yahoo.co.id

³Department of Informatics, Faculty of Science and Mathematics, Diponegoro University, 50275, Semarang, Indonesia, bowo.adi@live.undip.ac.id

⁴Center for Coastal Rehabilitation and Disaster Mitigation Studies, Diponegoro University, 50275, Semarang, Indonesia

⁵Semarang Climatology Station, Indonesian Agency for Meteorology Climatology and Geophysics, 50145, Semarang, Indonesia

The oceans have absorbed heat from greenhouse gas emissions, which contribute to the rising SST (Rhein *et al.*, 2013). SST changes can lead to extreme weather and natural disasters, such as droughts and floods, affecting various environmental conditions, dynamics (Herbert *et al.*, 2010), and tropical storms droughts (Upadhyay, 2020; Abounaga, Elwan and Elsharouny, 2019). Thus, recognizing SST fluctuations is the first step in detecting possible climate changes because the SST is an essential variable in climate change studies.

The accurate knowledge of the distribution and time changes of the SST is increasingly essential. Moreover, the SST is the first marine variable to be studied from Earth observation satellites and is easily measured by satellites and in situ sensors (Minnett *et al.*, 2019; Donlon *et al.*, 2007). Moreover, it is required as an input to forecasting systems to determine the modeling of ocean circulation and energy exchange (Donlon *et al.*, 2007).

The dynamic flow of satellite-based SST measures has been around since 1981 (Merchant *et al.*, 2019; O'Carroll *et al.*, 2019; Donlon *et al.*, 2007). Together with the general in situ measurements forming the modern era SST observation system, the numeral and variety of sensors have dramatically expanded and continued to rise (O'Carroll *et al.*, 2019; Martin, 2014). Prior satellite missions donating to the current and current constellation of SSTs have been described by (O'Carroll *et al.*, 2019). SST data were a mature component of observation systems in 1998 and data products with proven capabilities (Bell *et al.*, 2009). However, the availability of these products is limited to large datasets and is challenging to obtain in near real-time (NRT), (Donlon *et al.*, 2007; O'Carroll *et al.*, 2019), while the demand for SST data applications continues to grow.

The Global Ocean Data Assimilation Experiment (GODAE) has defined the minimum data specification for operational marine models as a solution to this problem (Bell *et al.*, 2009). Accordingly Group for High-Resolution Sea Surface Temperature (GHRSSST previously, GODAE High-Resolution Sea Surface Temperature Pilot Project) was formed to address the specifications (Donlon *et al.*, 2009) for SST needs in the global coverage: a minimum spatial resolution of 10 km, updated every 6 hours and minimum accuracy of 0.2 °C (Smith and Koblinsky, 2001).

The large volume of satellite information generated by GHRSSST-Pilot Project (PP) requires, among other things, coordination between data providers (for each satellite sensor) and users, quality control (QC) and archiving methods, and data distribution tools (Robinson, 2004; Robinson, 2010). Jet Propulsion Laboratory (JPL)'s Physical Oceanography Distributed Active Archive Center (PO.DAAC) has developed infrastructure to fulfill the requirements of this project, including NRT (Armstrong *et al.*, 2011; Luquire, 2021). PO.DAAC has also been building a metadata repository since 1993, where the metadata for each L2P product are ingested into an externally accessible database through a web-based search (Armstrong, Bingham and Vazquez, 2004).

They were generated from a wide variety of data by the PO.DAAC as remote sensing SST validation is very important to determine the precision of SSTs in recognizing SST fluctuations in global warming and climate prediction (Hausfather *et al.*, 2017). The accuracy of SSTs from remote sensing data is one of the essential factors in climate and marine analysis (Sukresno, Jatisworo and Hanintyo, 2021). Validating daily remote sensing data with in situ data is required to bring high-quality remote sensing data.

In general, remote sensing SST validation is performed with data in situ measurements from buoys (Castro, Wick and Steele, 2016a; Hao *et al.*, 2017; Reddy *et al.*, 2018). Several studies on remote sensing SST data validation in Indonesia have been conducted (Irawan *et al.*, 2004; Sukresno *et al.*, 2018; Sukresno, Jatisworo and Hanintyo, 2021). However, due to Indonesian waters and limited buoy observation data, SST validation within the Indonesian seas is challenging. Furthermore, Indonesian waters/seas are considered essential as they have different SST characteristics in each region and are located between the Pacific and Indian Oceans, so they are semi-closed (Putra, Karang and Putra, 2019).

The validation of remote sensing SST data is important to determine the best dataset to be used in the Indonesian seas. Validations that have been performed generally only consider the general

state of data and very rarely focus on extreme events. In this study, we want to re-test whether validated data can capture extreme phenomena that quickly take place and whether there is a decrease in the SST caused by a TC event as a case in point. Datasets selected through validation tests and extreme phenomena are expected to describe a phenomenon and can be utilized in the analysis and prediction of extreme weather conditions.

In this study, six-remote sensing/satellite JPL PO.DAAC (Operational Sea Surface Temperature and Sea Ice Analysis (OSTIA), Regional Australian Multi-Sensor SST Analysis (RAMSSA), Global Australian Multi-Sensor SST Analysis (GAMSA), Microwave Infrared Optimally Interpolated (MWIROI), Multi-scale Ultra-high Resolution (MUR), and K10) data were validated. The validation method was carried out by comparing the highest quality iQuam data with satellite data using the Haversine distance formula. An analysis was conducted through an error approach, standard deviation, and bias, where most minor errors and bias values are expected. This study performed the earliest remote sensing SST data validation investigation to identify SST changes that occur due to extreme weather events, such as TCs. The validation and comparison analysis were deployed in an open-source Python language and available at <https://github.com/bowoadi/sst-validation>.

2. DATA AND METHODS

2.1. Data

2.1.1. Dataset SST

Six types of interpolated SST L4 analysis remote sensing datasets were used in this study in 2021 in the coordinates of Indonesia's territory with latitude -12° – 12° and longitude 91° – 147° . The data were acquired from the NASA's JPL Physical Oceanography Distributed Active Archive Center (<http://podaac.jpl.nasa.gov>). The daily dataset is presented in **Table 1**:

Table 1.

Satellite data L4 SST products.				
No	Product Name	Spatial Resolution	Number of Data	Sensor
1	K10 (JPL), 2018)	0.1 ^o	49.056.000	4, 7
2	MWIROI (Systems, 2017)	0.09 ^o	60.555.392	5, 6, 8
3	OSTIA (UKMO, 2012)	0.054 ^o	168.220.274	3, 4, 7, 8
4	RAMSSA (ABOM), 2019b)	0.083 ^o	71.206.895	1, 2, 4
5	GAMSSA (ABOM), 2019a)	0.25 ^o	7.848.960	1,2
6.	MUR (NASA/JPL, 2019)	0.25 ^o	7.848.960	1, 2, 3, 5, 6

1= Buoys GTS	3= AVHRR NOAA	5= MODIS Aqua,Terra	7= Seviri
2= Ships GTS	4= AVHRR MetOp	6= WindSat	8= TMI TRMM

The Naval Oceanographic Office (NAVOCEANO) K10 SST operates satellite data only and merges L2 SST products in the presented average weight to describe the SST at a depth of 1 m, and this is one of the results of L4 that does not use the OI technique. All IR inputs are developed by NAVOCEANO using a separate nonlinear regression qualified against a control-powered GTS float buoy from the previous month. (May *et al.*, 1998).

MW data are excellent at capturing water levels with persistent turbidity where “the all-weather” MW sensor coverage improves accuracy. As shown (in the study by Brasnett (2008), MW and IR data contribute equal measure to the quality analysis for some of these analyses. Hence, the implementation (accuracy) of L4 products compared here, particularly those depending on MW data, is positively compromised.

The Remote Sensing System (REMSS) MWIR (MWIR) SST products use OI analysis and satellite data only (<http://www.remss.com/measurements/sea-surface-temperature/oisst-description>). Inputs are calibrated for daytime use using empirical heating models. The foundation SST product was initially designed for the National Hurricane Center to use the Statistical Hurricane Intensity Projection (SHIPS) model for considering storm intensity. (Castro, Wick and Steele, 2016b). The Operational Sea Surface Temperature and Sea Ice Analysis (OSTIA), (Brasnett, 2008) is assembled daily by the UK Met Office and is used as an operational boundary condition in the NWP and Digital Marine Forecasting in the Met Office and European Centre for Medium-Range Forecasting (ECMWF). OSTIA systems typically imported MW data from AMSR but have limited WindSat SST imports during period gaps using OI analysis. Input data are filtered to eliminate daytime observations with winds < 6 m/s to eliminate probable examples of daytime heating. Although provided at 0.05° (~ 6 km), the OSTIA SST grid is actually in an acceptable design (Donlon *et al.*, 2007).

In high-resolution operations, the Regional Australian Multi-Sensor Sea surface Australia temperature Analysis (RAMSA) has developed Bureau of Meteorology (BOM) within Australia’s Blue-Ocean Ocean project. The new RAMSA system combines SST data from infrared and microwave sensors at spin to produce SST foundation estimates. The main difference between the RAMSA and other analyses of other SST foundation analyses are associated with RAMSA’s methods for implementing advanced systems and determining weights for different data entry streams and bias edits, iFremar, and Met Office analysis systems among all. satellite input data using SST data from the Advanced Along Track Scanning Radiometer (AATSR), (Beggs *et al.*, 2011).

The BOM produces daily SST foundation analysis at a resolution of 0.25° as the Global Australian Multi-Sensor SST Analysis (GAMSSA). It is used as a boundary requirement in the global NWP system and is an extension of the regional L4 product 0.083° (Beggs *et al.*, 2011).

The Multi-scale Ultra-high Resolution (MUR) is produced daily by NASA’s JPL. Unlike other outcomes that use standard OI techniques, the MUR system uses a statistical interpolation method based on wavelet analysis known as the multiresolution variation examination (Mallat, 1989). This multi-scale signal reconstruction technique is excellent for processing multiple spatial resolutions of L2 products used in different satellites’ analysis and irregular swath patterns (Chin, Milliff and Large, 1998). The main contribution of this product is fit spatial resolution (horizontal) and the capability to handle high-resolution SST features such as fronts.

2.1.2. iQuam

iQuam is an in-situ dataset developed by the NOAA Center for Satellite Application and Research (STAR). Measurement data are obtained from ships, drifters, ARGO floats, and tropical mooring data. The data are been processed with strict quality control so that the in situ data obtained are reliable (Sukresno, Jatisworo and Hanintyo, 2021), as presented in **Fig. 1**. The present study used the iQuam dataset obtained from all measurements from ships, drifters, ARGO float, and tropical mooring data in 2021, with 156,152 datasets in total. The iQuam dataset is downloaded through the NOAA: <https://www.star.nesdis.noaa.gov/sod/sst/iquam/data.html> (accessed February 20, 2022). The iQuam dataset used in SST validation has a similar spatial distribution throughout the Indonesian seas.

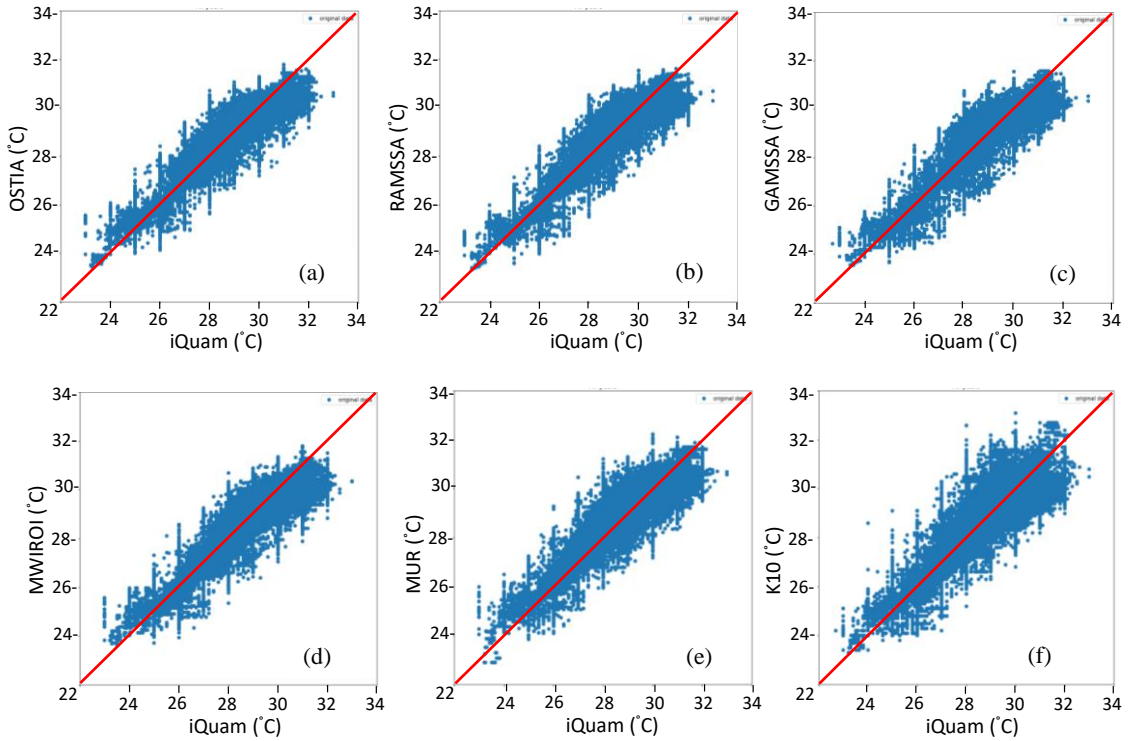


Fig. 1. Scatterplot among the six datasets against iQuam, a) OSTIA, b) RAMSSA, c) GAMSSA, d) MWIROI, e) MUR, f) K10.

2.1.3. Surface Wind

To comprehend the physical pressure of TCs, as an example of a case in the trial on the TC Seroja event, surface wind data from Cross Calibrated Multi-Platform (CCMP) version 2.0 grid analyzed surface winds between March 31 and April 15, 2021 were used. The CCMP used is a level 3 marine wind vector product produced from satellites, mooring buoys, and wind data models. The temporal and spatial resolutions of the surface wind data were 6 h and $0,25^{\circ} \times 0,25^{\circ}$. The CCMP accuracy is more elevated than other wind reanalysis data (Atlas *et al.*, 2011). This dataset can be downloaded from <https://www.remss.com/measurements/ccmp/> (accessed February 25, 2022).

2.2. Methods

The extraction of six SST datasets was carried out in situ according to the data location iQuam at the same spot and time. The filtering process was performed by taking the highest-quality iQuam data. Each of the datasets was positioned with an iQuam dataset on the same acquisition day. The validation employs the Python program language with the following validation algorithm using the Haversine distance formula.

Input:

$$P = \{P_{0,0}, \dots, P_{n-1,m-1}\}, \quad P_{i,j} = (Px_i, Py_j, Pt_{i,j}), \quad i = 0,1 \dots, n-1, \\ j = 0,1 \dots, m-1$$

$$Q = \{Q_0, \dots, Q_{K-1}\}, \quad Q_k = (Qx_k, Qy_k, Qt_k), \quad k = 0,1 \dots, K-1$$

Process:

$$T = \{T_0, \dots, T_{K-1}\}, T_k = -1, \quad k = 0,1 \dots, K-1$$

$$k = 0$$

For each $k < K$:

```

lo = 0
hi = n
While lo < hi do: // Find leftmost value greater than or equal to  $Q_k$  in longitude
    mid = ceil_to_integer( $\frac{lo+hi}{2}$ )
    If  $Px_{mid} < Qx_k$ :
        lo = mid + 1
    Else:
        hi = mid

 $\hat{x} = lo$ 
lo = 0
hi = n
While lo < hi do: // Find leftmost value greater than or equal to  $Q_k$  in latitude
    mid = ceil_to_integer( $\frac{lo+hi}{2}$ )
    If  $Py_{mid} < Qy_k$ :
        lo = mid + 1
    Else:
        hi = mid

 $\hat{y} = lo$ 
lo = 0
hi = n
While lo < hi do: // Find rightmost value less than or equal to  $Q_k$  in longitude
    mid = ceil_to_integer( $\frac{lo+hi}{2}$ )
    If  $Qx_k < Px_{mid}$ :
        hi = mid
    Else:
        lo = mid + 1

 $\check{x} = lo - 1$ 
lo = 0
hi = m
While lo < hi do: // Find rightmost value less than or equal to  $Q_k$  in latitude
    mid = ceil_to_integer( $\frac{lo+hi}{2}$ )
    If  $Qy_k < Py_{mid}$ :
        hi = mid
    Else:
        lo = mid + 1

 $\check{y} = lo - 1$ 
 $d_{\hat{x},\hat{y}}$ 
=  $2 \cdot R$ 
· arcsin (  $\sqrt{\sin\left(\frac{(Py_{\hat{y}} - Qy_k)^2}{2}\right) + \cos(Qy_k) \cdot \cos(Py_{\hat{y}}) \cdot \sin\left(\frac{(Px_{\hat{x}} - Qx_k)^2}{2}\right)}$  )

 $d_{s_{min}} = d_{\hat{x},\hat{y}}$ 
 $t_{selected} = Pt_{\hat{x},\hat{y}}$ 
 $d_{\check{x},\check{y}}$ 
=  $2 \cdot R$ 
· arcsin (  $\sqrt{\sin\left(\frac{(Py_{\check{y}} - Qy_k)^2}{2}\right) + \cos(Qy_k) \cdot \cos(Py_{\check{y}}) \cdot \sin\left(\frac{(Px_{\check{x}} - Qx_k)^2}{2}\right)}$  )

```


$$\begin{aligned}
& \text{If } ds_{min} > d_{\hat{x},\hat{y}}: \\
& \quad ds_{min} = d_{\hat{x},\hat{y}} \\
& \quad t_{selected} = Pt_{\hat{x},\hat{y}} \\
& d_{\hat{x},\hat{y}} \\
& = 2 \cdot R \\
& \cdot \arcsin \left(\sqrt{\sin \left(\frac{(Py_{\hat{y}} - Qy_k)}{2} \right)^2 + \cos(Qy_k) \cdot \cos(Py_{\hat{y}}) \cdot \sin \left(\frac{(Px_{\hat{x}} - Qx_k)}{2} \right)^2} \right) \\
& \text{If } ds_{min} > d_{\check{x},\check{y}}: \\
& \quad ds_{min} = d_{\check{x},\check{y}} \\
& \quad t_{selected} = Pt_{\check{x},\check{y}} \\
& d_{\check{x},\check{y}} \\
& = 2 \cdot R \\
& \cdot \arcsin \left(\sqrt{\sin \left(\frac{(Py_{\check{y}} - Qy_k)}{2} \right)^2 + \cos(Qy_k) \cdot \cos(Py_{\check{y}}) \cdot \sin \left(\frac{(Px_{\check{x}} - Qx_k)}{2} \right)^2} \right) \\
& \text{If } ds_{min} > d_{\tilde{x},\tilde{y}}: \\
& \quad ds_{min} = d_{\tilde{x},\tilde{y}} \\
& \quad t_{selected} = Pt_{\tilde{x},\tilde{y}} \\
& k = k + 1
\end{aligned}$$

\mathbf{P} is the SST satellite data that contain matrix data structures $n \times m$ with value $P_{i,j} = (Px_i, Py_j, Pt_{i,j})$, $i = 0,1 \dots, n-1$, $j = 0,1 \dots, m-1$, where Px_i is the longitude on the line to- i , Py_j is latitude in the column to- j , and $Pt_{i,j}$ is the SST on the line to- i and column to- j . The values Px and Py have been sorted.

\mathbf{Q} is the high-quality iQuam data that contain a flat-array data structure with a size K and value $Q_k = (Qx_k, Qy_k, Qt_k)$, $k = 0,1 \dots, K-1$, where Qx_k is the longitude on the array to- k , Qy_k is the latitude on the array to- k , and Qt_k is the SST on the array to- k .

\mathbf{R} is the estimated radius used in the calculation of distance between points using the formula Haversine distance, which has a value of 6373.

Iterations were performed for each k . The point closest to Q_k , was determined based on four conditions, namely, leftmost point with value Px_i (more than the same as Qx_k as \hat{x}), leftmost point with value Py_i (more than the same as Qy_k as \hat{y}), the rightmost point with the value Px_i (less than the same as Qx_k as \check{x}), and the rightmost point with value Py_i (less than the same as Qy_k as \check{y}). Then the four conditions were combined into four points, namely $\{(\hat{x}, \hat{y}), (\check{x}, \hat{y}), (\check{x}, \check{y}), (\hat{x}, \check{y})\}$ each calculated with distance Qx_k and Qy_k . Then the one that has the shortest distance was selected. The difference in the SST value was obtained by reducing the Qt_k value with SST satellite value from the point with the shortest distance.

2.2.1. RMSE, Standard Deviation, and Bias

Statistical testing to witness the proximity of remote sensing data to iQuam was conducted using RMSE, standard deviation, and bias. The smallest value indicates a better error with observational data (Hidalgo García, 2021).

$$RMSE = \sqrt{\frac{1}{n} \sum_{i=1}^n (SST \text{ In Situ}_i - SST \text{ Satelit}_i)^2} \quad (1)$$

3. RESULTS AND DISCUSSION

3.1. SST Dataset Validation

The initial comparison of six-satellite datasets against the iQuam dataset was carried out by displaying the plot scatter of the six data on 2021 presented in **Fig. 1** and daily data distribution that describes the state of remote sensing and iQuam sorted according to the smallest RMSE values as presented in **Table 2**. Data adjacent to diagonal lines indicates a good distribution of data, as can be seen from root mean square error (RMSE) and slight standard deviation. RMSE, standard deviation, and bias are shown in **Table 2** in the order from the smallest RMSE values. OSTIA has the smallest RMSE and standard deviation values with 0.425 and 0.461, respectively. MUR has the lowest bias value with 0.045.

Table 2.

RMSE values, standard deviations, and biases of six datasets against iQuam.

No	Name	RMSE	Standard Dev	Bias
1	OSTIA	0.425	0.461	-0.079
2	RAMSSA	0.451	0.488	-0.073
3	GAMSSA	0.454	0.489	-0.076
4	MWIROI	0.471	0.529	-0.143
5	MUR	0.516	0.541	0.045
6	K10	0.620	0.648	-0.078

Remote sensing data with an RMSE value of < 0.5 were taken to show the error distribution. The results of the spatial error value interpretation are presented in **Fig. 2**. All Indonesian seas have a reasonably acceptable error value, ranging from -0.5 to 0.5 , symbolized by a bluish-green color. However, the error value is quite significant, ranging from 1 to 2 among the Karimata Strait, Makassar Strait, and around the Aru Sea.

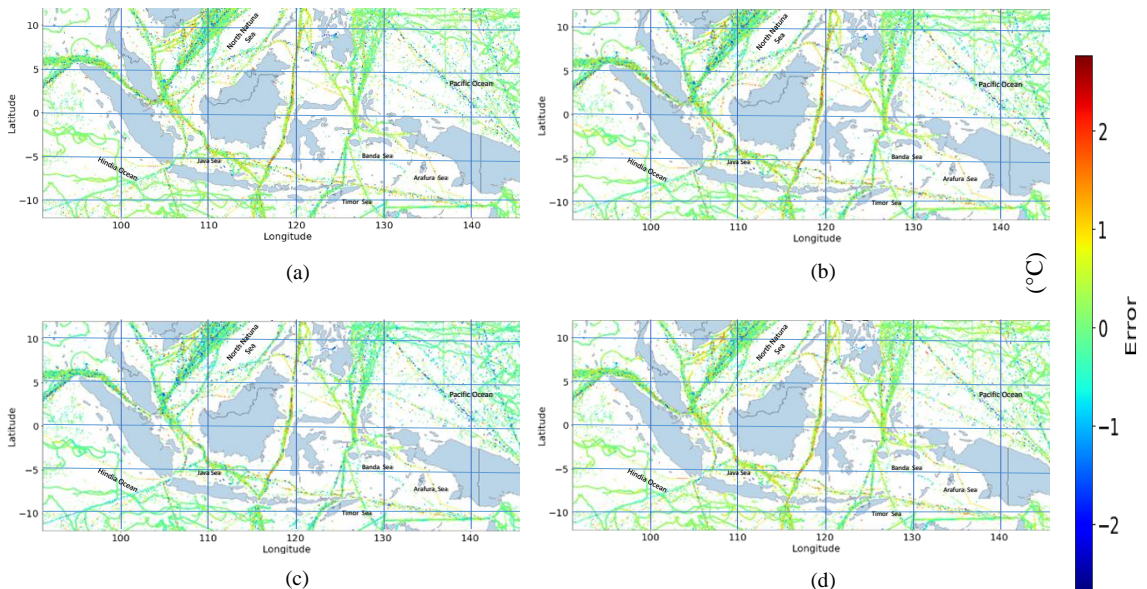


Fig. 2. Distribution of error values in 2021 across Indonesian territorial waters a) OSTIA, b) RAMSSA, c) GAMSSA, and d) MWIROI.

The validation tests concluded that the selected datasets with RMSE values and minor standard deviations were owned on the OSTIA, RAMSSA, GAMSSA, and MWIROI datasets. Similarly, by proving the distribution of error values in 2021, shown in **Fig. 2**, the four datasets have a reasonably small error value in almost all areas of Indonesian waters ranging from -0.5 to 0.5 .

3.2. Sensitivity Tests for Extreme Weather Events

Although Indonesia is an equatorial tropical country, TC events occur pretty often as will be stated in the discussion below. From 2010 to 2021, at least five TCs have had quite an impact on Indonesia. In the previous discussion, the validation results of the six datasets were well known. Nonetheless, we also wanted to know how each SST dataset responded to TC events and whether each dataset captured an extreme weather phenomenon that quickly took place.

The SST is a critical factor in the supply of energy for a TC or storm and affects not only its formation (Gray, 1968; Gray, 1975; Emanuel, 1986; Wang *et al.*, 2007) but also the trace and intensity of the TC (Emanuel, 1999; Schade and Emanuel, 1999; Mei *et al.*, 2015). Even if atmospheric conditions are promising, TC will not develop if the SST is low (Lin *et al.*, 2008) and difficult to occur in SSTs < 26 °C (Emanuel, 2003). In the ocean region bordering the Indonesian seas, especially in the southeastern part of the tropical Indian Ocean, several TCs have occurred, such as Anggrek (October 31 – November 4, 2010), Bakung (December 10 – 13, 2014), Cempaka (November 25 – 27, 2017), Dahlia (November 27 – December 2, 2017), (Paterson, 2012; Gutro, 2014; Samodra *et al.*, 2020; Yang *et al.*, 2020; Aditya *et al.*, 2021) and Seroja ; Latos *et al.*, 2022). TC events can cause critical oceanic phenomena in the form of cooling SSTs (Hazelworth, 1968; Stramma, Cornillon and Price, 1986; Leipper, 1967; Lin *et al.*, 2013). According to (Yang *et al.*, 2020) the effect of TCs on the oceans has changed the thermal stratification of the upper part of the oceans in the southeastern part of the tropical Indian Ocean by decreasing the SST (> 1.5 °C). This paper also sees a decrease in SSTs for TC events in Malakas, Megi, and Chaba (Li *et al.*, 2020), but no studies have specified which remote sensing/satellite data are the most precise in describing SST fluctuations in tropical storm.

As a case study, this research will be indicating the development of TC Seroja using several plot areas on the TC development based on wind and SST data presented in **Figs. 3, 4** and **5**. As shown in **Fig. 3**, on April 1, a strong east wind appeared around the eastern island of Timor. On April 3, wind speeds increased by > 18 m/s in the Sawu Sea (SS) and Northern Australia. The existence of wind patterns on April 3 is the initial stage of the development of TC Seroja, with wind speeds of approximately about $18 - 20$ m/s. The cyclone wind speed of > 23 m/s in the core eye of the TC indicates that TC Seroja fully developed on April 4 and lasted until April 6, 2021. These finding are in line with research (result of Setiawan *et al.*, 2021).

The Validation of six datasets in the TC Seroja case study was also observed through the SST plotting with the wind (**Fig. 4**). SST heating can be an early sign of a fast-paced TC event (65). The heating SST of > 30.5 °C occurred since March 28, 2021, on almost all datasets. Although the heating is quite extreme, an SST 30.8 °C occurred in the K10 and MUR datasets on March 28 – 30, but the dataset could describe the SST condition, which was quite extreme at the time of the full TC development. An increase in the wind speed can cool the surface air temperature during the TC development. The effect of wind occurring in extremes on April 2 – 8, 2021, as explained in **Fig. 4**, along with the decline in SSTs, was very noticeable until the SST reached > 1.5 °C in the MWIROI and MUR datasets, whereas in the other datasets (OSTIA, RAMSSA, GAMSSA, and K10), the SST decrease when wind speed increase was relatively not very noticeable and tend to take place more slowly. Hence, when the wind weakened, the SST of the other datasets only decreased, which is an unnatural thing.

The SST cooling event that occurred during the full development of the TC on April 4 – 6, 2021 is presented in **Fig. 5** to detect the precision of remote sensing SST datasets against TC extreme events. The SST maps, SST temperature and wind line in a latitude of -11 ° are shown for comparison.

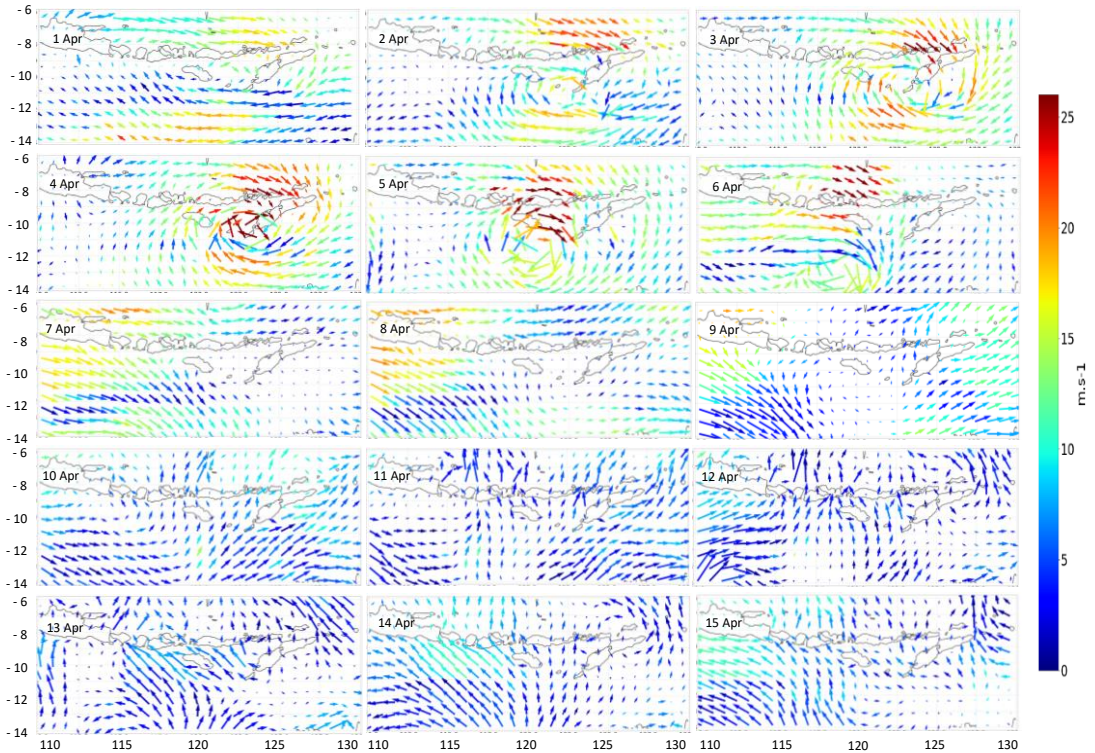


Fig. 3. Wind speed (m/s) on April 1 – 15, 2021.

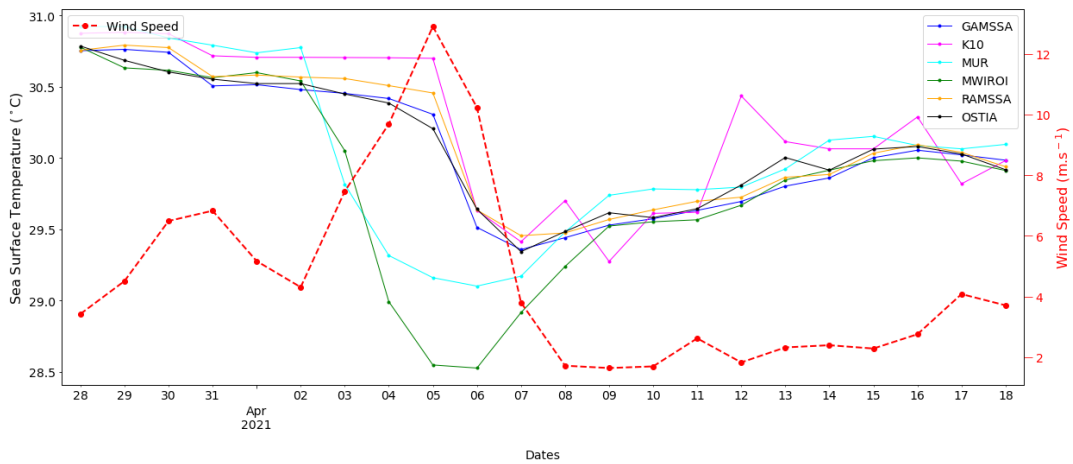


Fig. 4. Time series of the six datasets SST and wind speed of the Savu Sea on March 28 – Apr 31, 2021, (average area is 121 – 125°E; 8 – 11°S similar with the research finding in *Setiawan et al., 2021*).

The strong effect of TC Seroja as presented in **Fig. 5** (top) shows the decrease in the SST in almost all remote sensing data. The wind effect **Fig. 5** (bottom) shown with a slop line during the full TC formation can cause the cooling of SST, as an identification of the precision of remote sensing SST six datasets along with the increase in the wind during the full formation of TC Seroja on April 4 – 6, 2021. On April 4, 2021, a maximum wind speed of approximately > 15 m/s occurred in the longitude 122.5° – 123°, along with a more noticeable decline in SSTs in the MWIROI and MUR datasets.

By contrast, in the other four datasets, the decline in the SSTs is not very noticeable. On April 5, 2021, the maximum wind speed increased to > 22.5 m/s, including the strong gale on the Beaufort scale. Moreover, a relatively sharp decrease in SSTs was observed in the MWIROI and MUR datasets, where there is a drop until 3 °C.

As presented in **Fig. 5** the traces of cyclones of the MUR and K10 datasets are visible on April 5 – 6, 2021, with cold SSTs ranging from 28 °C to 29 °C. OSTIA, RAMSSA, and GAMSSA almost look the same, but the traces of cyclones are not very clear. Meanwhile, in the MWIROI dataset, a visible TC travel since April 4 is characterized by the cold SST ranging of 27.5 °C – 28.5 °C. On April 6, 2021, a maximum wind speed of up to 25 m/s for the decrease in the SST that occurred due to strong winds was most visible in the MWIROI dataset where there was a decrease to > 3 °C from 31.5 °C to 28 °C. Despite the RMSE value, MWIROI’s standard deviation and bias are not the smallest but can better describe the state of the TC, especially at the time of its full development.

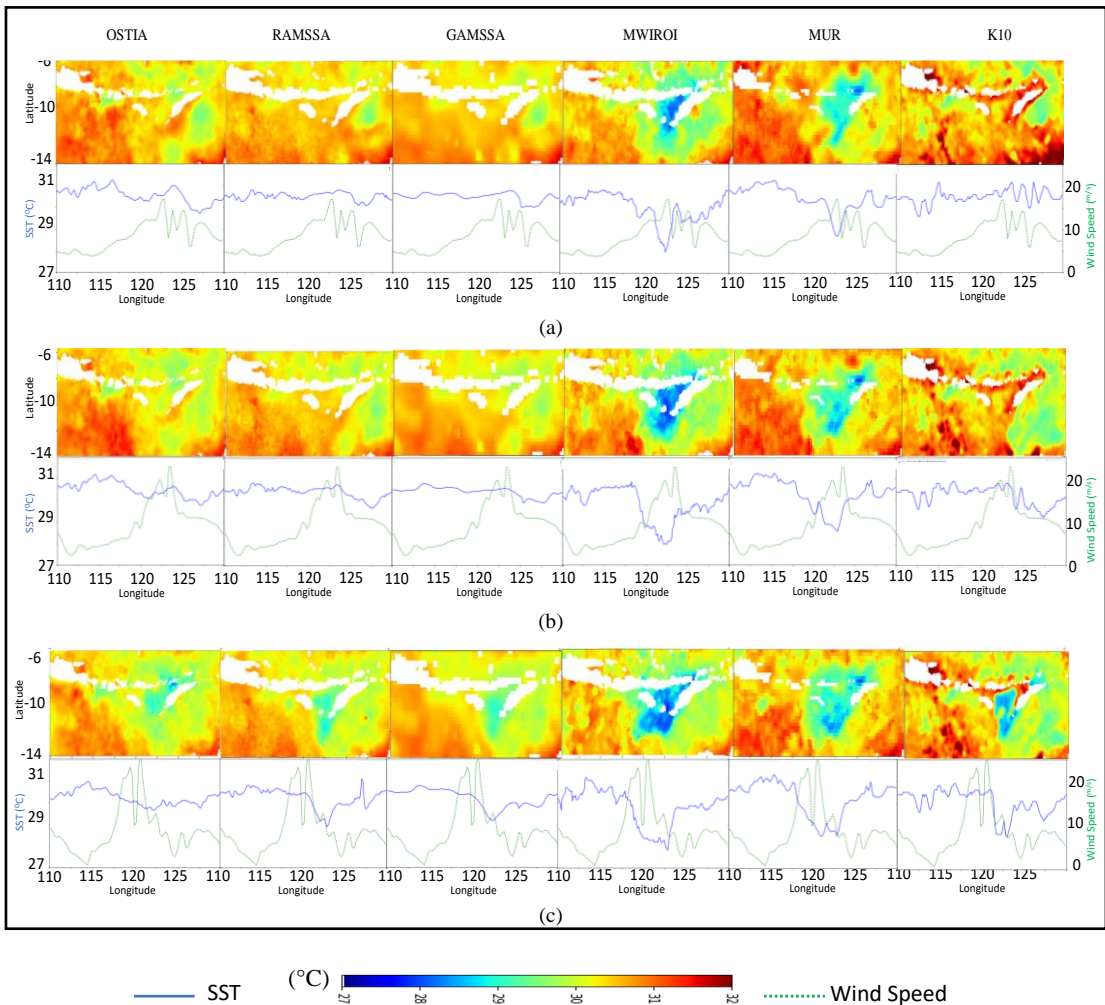


Fig. 5. Plotting SST (°C) (top), SST (°C) and wind (m/s) slope line in latitude of -11°(bottom) in at the time of full TC development; a) April 4, b) April 5 and c) April 6, 2021.

Increased wind speeds from April 3 to 7 and the disappearance of winds toward the southwest can cool the SST, (**Fig. 4** and **5**).

Many factors can describe the total growth and development of TC Seroja in addition to the wind and SST. However, such formations fall outside the scope of this study, which focused on validating the remote sensing SST dataset against iQuam to detect TC Seroja events.

The most visible cyclone trail is shown by MWIROI and MUR, where the decrease in the SST is evident from April 4 to 6, 2021. However, in the OSTIA, RAMSSA, and GAMSSA datasets, the decline in the SST is not very significant, which this happens because both have the same sensor, specifically MODIS Aqua and Terra. The twin-MODIS design aims aimed to optimize cloud-free imaging while minimizing the optical effects of shadows and glares that occur with morning and afternoon sunlight. In three different resolutions, i.e., 250 m, 500 m, and 1 km, MODIS data products help improve our understanding of global environmental processes and dynamics occurring on the land, oceans, and lower atmosphere. The MODIS data records help extend heritage data, such as NOAA's Advanced Very High-Resolution Radiometer, thus ensuring the critical continuity of such collections to support our investigations of short- and long-term global environmental changes. MODIS-derived data products continue to play a vital role in helping develop and validate global Earth system models with sufficient predictive potential to inform and help policymakers address global environmental changes.

The MWIROI dataset is relatively undisturbed by the cloud cover due to the combination of IR data with microwave data that can penetrate the cloud. (Li et al., 2020). In expansion, because this product was initially developed to estimate hurricane intensity, it may be better to capture SST-related ocean extreme events.

4. CONCLUSIONS

In this study, six remote sensing/satellite datasets (OSTIA, RAMSSA, GAMS, MWIROI, MUR and K10) were validated and compared to analyze and validate investigations to identify SST changes that occur due to extreme weather events, such as TCs. The validation method was performed by comparing the highest-quality of iQuam data with satellite data using the Haversine distance formula. The comparison analysis was performed by plotting the SST slope in a TC area. Based on the validation, the OSTIA, RAMSSA, GAMSSA, and MWIROI datasets ranked in the top 4 with the smallest RMSE with a value i.e., < 0.5 . Moreover, in a TC area, the TC Seroja wind speed increased by > 22.5 m/s on April 5, 2021, and SST cooling was detected in the MUR and K10 datasets denoted by a decrease of > 2 °C. For MWIROI, the decline was more noticeably significant as > 3 °C. This finding shows that the MWIROI dataset can describe the extreme conditions of TC Seroja better than other datasets. The most visible cyclone trail is shown by MWIROI and MUR, where the decrease in the SST is highly evident from April 4 to 6, 2021. This happens because both have the same sensor, specifically MODIS Aqua, Terra and WindSat. The twin-MODIS design aim to optimize cloud-free imaging while minimizing the optical effects of shadows and glare that occur with morning and afternoon sunlight. The cyclone's footprint was the most pronounced in MWIROI with a resolution of 0.09° because the product was initially designed to estimate storm intensity. This dataset can be used in future studies, especially for extreme weather or climate analysis.

ACKNOWLEDGMENTS

The authors would like to thank you for the support from PUSDIKLAT BMKG and Diponegoro University. SST L4 analysis remote sensing datasets available at NASA Jet Propulsion Laboratory Physical Oceanography Distributed Active Archive Center (PODAAC, <http://podaac.jpl.nasa.gov>). iQuam is an in-situ dataset developed by the NOAA Center for Satellite Application and Research (STAR) available at <https://www.star.nesdis.noaa.gov/sod/sst/iquam/data.html> CCMP Version-2.0 vector wind from <https://www.remss.com/measurements/ccmp/>

REFERENCES

- (ABOM), A. B. O. M. (2019a) 'GHRSSST Level 4 GAMSSA_28km Global Foundation Sea Surface Temperature Analysis v1.0 dataset (GDS2)'. NASA Physical Oceanography DAAC. doi: 10.5067/GHGAM-4FA1A.
- (ABOM), A. B. O. M. (2019b) 'GHRSSST Level 4 RAMSSA_9km Australian Regional Foundation Sea Surface Temperature Analysis v1.0 dataset (GDS2)'. NASA Physical Oceanography DAAC. doi: 10.5067/GHRAM-4FA1A.
- (JPL), N. J. P. L. (2018) 'GHRSSST Level 4 K10_SST Global 10 km Analyzed Sea Surface Temperature from Naval Oceanographic Office (NAVO) in GDS2.0'. NASA Physical Oceanography DAAC. doi: 10.5067/GHK10-L4N01.
- Aboulnaga, M. M., Elwan, A. F. and Elsharouny, M. R. (2019) 'Global Climate Change Risks: Sectors and Variables' Changes', in *Urban Climate Change Adaptation in Developing Countries*. Springer, pp. 19–48.
- Aditya, H. N. *et al.* (2021) 'Impact of tropical Cyclones Cempaka and Dahlia to the variability of chlorophyll-a and sea surface temperature in the Seas Southern Coast of Java Island', 27.
- Armstrong, E. ~M., Bingham, A. and Vazquez, J. (2004) 'Managing global satellite data: The GHRSSST-PP', in *AGU Fall Meeting Abstracts*, pp. SF33B-07.
- Armstrong, E. M. *et al.* (2011) 'Report on the Global Data Assembly Center (GDAC) to the 12th GHRSSST Science Team Meeting'.
- Atlas, R. *et al.* (2011) 'A cross-calibrated, multiplatform ocean surface wind velocity product for meteorological and oceanographic applications', *Bulletin of the American Meteorological Society*, 92(2), pp. 157–174.
- Beggs, H. *et al.* (2011) 'RAMSSA - An operational, high-resolution, Regional Australian Multi-Sensor Sea surface temperature Analysis over the Australian region', *Australian Meteorological and Oceanographic Journal*, 61(1), pp. 1–22. doi: 10.22499/2.6101.001.
- Bell, M. J. *et al.* (2009) 'GODAE: The Global Ocean Data Assimilation Experiment', *Oceanography*, 22(3), pp. 14–21. Available at: <http://www.jstor.org/stable/24860986> (Accessed: 23 April 2022).
- Brasnett, B. (2008) 'The impact of satellite retrievals in a global sea-surface-temperature analysis', (August), pp. 1745–1760. doi: 10.1002/qj.319.
- Castro, Wick and Steele (2016a) 'Validation of satellite sea surface temperature analyses in the Beaufort Sea using UpTempO buoys', *Remote Sensing of Environment*, 187, pp. 458–475.
- Castro, Wick and Steele (2016b) 'Validation of satellite sea surface temperature analyses in the Beaufort Sea using UpTempO buoys', *Remote Sensing of Environment*, 187, pp. 458–475. doi: 10.1016/j.rse.2016.10.035.
- Chin, T. M., Milliff, R. F. and Large, W. G. (1998) 'Basin-scale, high-wavenumber sea surface wind fields from a multiresolution analysis of scatterometer data', *Journal of Atmospheric and Oceanic Technology*, 15(3), pp. 741–763. doi: 10.1175/1520-0426(1998)015<0741:BShWSS>2.0.CO;2.
- Donlon, C. *et al.* (2007) 'The global ocean data assimilation experiment high-resolution sea surface temperature pilot project', *Bulletin of the American Meteorological Society*, 88(8), pp. 1197–1214.
- Donlon, C. J. *et al.* (2009) 'The GODAE high-resolution sea surface temperature pilot project', *Oceanography*, 22(3), pp. 34–45.
- Emanuel, K. (2003) 'Tropical cyclones', *Annual Review of Earth and Planetary Sciences*, 31(1), pp. 75–104.
- Emanuel, K. A. (1986) 'An air-sea interaction theory for tropical cyclones. Part I: Steady-state maintenance', *Journal of Atmospheric Sciences*, 43(6), pp. 585–605.
- Emanuel, K. A. (1999) 'Thermodynamic control of hurricane intensity', *Nature*, 401(6754), pp. 665–669.
- Gray, W. M. (1968) 'Global view of the origin of tropical disturbances and storms', *Monthly Weather Review*, 96(10), pp. 669–700.
- Gray, W. M. (1975) *Tropical cyclone genesis*. Colorado State University. Libraries.
- Hao, Y. *et al.* (2017) 'Validation of MODIS sea surface temperature product in the coastal waters of the Yellow Sea', *IEEE Journal of Selected Topics in Applied Earth Observations and Remote Sensing*, 10(5), pp. 1667–1680.
- Hausfather, Z. *et al.* (2017) 'Assessing recent warming using instrumentally homogeneous sea surface temperature records', *Science Advances*, 3(1). doi: 10.1126/sciadv.1601207.
- Hazelworth, J. B. (1968) 'Water temperature variations resulting from hurricanes', *Journal of Geophysical Research*, 73(16), pp. 5105–5123.

- Herbert, T. D. *et al.* (2010) 'Tropical ocean temperatures over the past 3.5 million years', *Science*, 328(5985), pp. 1530–1534. doi: 10.1126/science.1185435.
- Hidalgo García, D. (2021) 'Analysis and precision of the Terrestrial Surface Temperature using Landsat 8 and Sentinel 3 images: Study applied to the city of Granada (Spain)', *Sustainable Cities and Society*, 71, p. 102980. doi: <https://doi.org/10.1016/j.scs.2021.102980>.
- Irawan *et al.* (2004) 'STUDI PERBAND. SUHU PERMUKAAN LAUT MENGG. CITRA SATELIT NOAA-AVHRR (Faried Irawan)'.
- Latos, B. *et al.* (2022) 'The role of tropical waves in the genesis of Tropical Cyclone Seroja-one of the first tropical cyclones to significantly impact Indonesian land'.
- Leipper, D. F. (1967) 'Observed ocean conditions and Hurricane Hilda, 1964', *Journal of the Atmospheric Sciences*, 24(2), pp. 182–186.
- Li, J. *et al.* (2020) 'Accurate evaluation of sea surface temperature cooling induced by typhoons based on satellite remote sensing observations', *Water (Switzerland)*, 12(5), pp. 1–16. doi: 10.3390/w12051413.
- Lin, I.-I. *et al.* (2013) 'An ocean coupling potential intensity index for tropical cyclones', *Geophysical Research Letters*, 40(9), pp. 1878–1882.
- Lin, I. I. *et al.* (2008) 'Upper-ocean thermal structure and the western North Pacific category 5 typhoons. Part I: Ocean features and the category 5 typhoons' intensification', *Monthly Weather Review*, 136(9), pp. 3288–3306.
- Luquire, K. (2021) 'A Group for High Resolution Sea Surface Temperature (GHR SST) Level 4 sea surface temperature analysis produced as a retrospective dataset (four day latency) and near-real-time dataset (one day latency) at the JPL Physical Oceanography DAAC using wavelets'. Edited by N. C. for E. I. (U.S.). (NOAA Technical Information Series NESDIS DSMR; 00266). doi: <https://doi.org/10.25923/d47d-0413>.
- Mallat, S. G. (1989) 'A theory for multiresolution signal decomposition: the wavelet representation', *IEEE Transactions on Pattern Analysis and Machine Intelligence*, 11(7), pp. 674–693. doi: 10.1109/34.192463.
- Martin, S. (2014) *An introduction to ocean remote sensing*. Cambridge University Press.
- May, D. A. *et al.* (1998) 'Operational Processing of Satellite Sea Surface Temperature Retrievals at the Naval Oceanographic Office', *Bulletin of the American Meteorological Society*, 79(3), pp. 397–407. doi: 10.1175/1520-0477(1998)079<0397:OPOSS>2.0.CO;2.
- Memichael, A. J. *et al.* (no date) 'Chapter 20 Global climate change'.
- Mei, W. *et al.* (2015) 'Northwestern Pacific typhoon intensity controlled by changes in ocean temperatures', *Science advances*, 1(4), p. e1500014.
- Merchant, C. J. *et al.* (2019) 'Satellite-based time-series of sea-surface temperature since 1981 for climate applications', *Scientific data*, 6(1), pp. 1–18.
- Minnett, P. J. *et al.* (2019) 'Half a century of satellite remote sensing of sea-surface temperature', *Remote Sensing of Environment*, 233, p. 111366. doi: <https://doi.org/10.1016/j.rse.2019.111366>.
- NASA/JPL (2019) 'GHR SST Level 4 MUR 0.25deg Global Foundation Sea Surface Temperature Analysis (v4.2)'. NASA Physical Oceanography DAAC. doi: 10.5067/GHM25-4FJ42.
- O'Carroll, A. G. *et al.* (2019) 'Observational needs of sea surface temperature', *Frontiers in Marine Science*, 6(JUL). doi: 10.3389/fmars.2019.00420.
- Paterson, L. (2012) 'Tropical Low AU1011_01U (Anggrek)', *Bur. Meteorology. Australia*. Accessed, (November 2010).
- Putra, I. N. J. T., Karang, I. W. G. A. and Putra, I. D. N. N. (2019) 'Analisis Temporal Suhu Permukaan Laut di Perairan Indonesia Selama 32 Tahun (Era AVHRR)', *Journal of Marine and Aquatic Sciences*, 5, pp. 234–236.
- R. Gutro (2014) 'Bakung (Southern Indian Ocean)'. NASA's Goddard Space Flight Center. USA. Available at: <https://www.nasa.gov/content/goddard/bakung-southern-indian-ocean/>.
- Reddy, B. *et al.* (2018) 'Comparison of AMSR-2 wind speed and sea surface temperature with moored buoy observations over the Northern Indian Ocean', *Journal of Earth System Science*, 127(1), pp. 1–11.
- Rhein, M. *et al.* (2013) 'Observations: Ocean in Climate Change 2013: The Physical Science Basis. Contribution of Working Group I to the Fifth Assessment Report of the Intergovernmental Panel on Climate Change', *Fifth assessment report of the Intergovernmental Panel on Climate Change*, pp. 255–316.
- Robinson, I. S. (2004) *Measuring the oceans from space: the principles and methods of satellite oceanography*. Springer Science & Business Media.

- Robinson, I. S. (2010) *Discovering the Ocean from Space: The unique applications of satellite oceanography*. Springer Science & Business Media.
- Samodra, G. *et al.* (2020) 'Frequency–magnitude of landslides affected by the 27–29 November 2017 Tropical Cyclone Cempaka in Pacitan, East Java', *Journal of Mountain Science*, 17(4), pp. 773–786. doi: 10.1007/s11629-019-5734-y.
- Schade, L. R. and Emanuel, K. A. (1999) 'The ocean's effect on the intensity of tropical cyclones: Results from a simple coupled atmosphere–ocean model', *Journal of the atmospheric sciences*, 56(4), pp. 642–651.
- Setiawan, R. Y., Susanto, R Dwi, *et al.* (2021) 'Impacts of tropical cyclone Seroja on the phytoplankton chlorophyll-a and sea surface temperature in the Savu Sea, Indonesia', *IEEE Access*, 9, pp. 152938–152944.
- Setiawan, R. Y., Susanto, R. Dwi, *et al.* (2021) 'Impacts of Tropical Cyclone Seroja on the Phytoplankton Chlorophyll-a and Sea Surface Temperature in the Savu Sea, Indonesia', *IEEE Access*, 9, pp. 152938–152944. doi: 10.1109/ACCESS.2021.3125605.
- Small, R. J. d *et al.* (2008) 'Air–sea interaction over ocean fronts and eddies', *Dynamics of Atmospheres and Oceans*, 45(3–4), pp. 274–319.
- Smith, N. R. and Koblinsky, C. (2001) 'The ocean observing system for the 21st Century, a consensus statement', *Observing the Oceans in the 21st Century*, pp. 1–25.
- Stramma, L., Cornillon, P. and Price, J. F. (1986) 'Satellite observations of sea surface cooling by hurricanes', *Journal of Geophysical Research: Oceans*, 91(C4), pp. 5031–5035.
- Sukresno, B. *et al.* (2018) 'Three-Way Error Analysis of Sea Surface Temperature (Sst) Between Himawari-8, Buoy, and Mur Sst in Savu Sea', *International Journal of Remote Sensing and Earth Sciences (IJReSES)*, 15(1), p. 25. doi: 10.30536/ijreses.2018.v15.a2855.
- Sukresno, B., Jatisworo, D. and Hanintyo, R. (2021) 'Validation of Sea Surface Temperature from GCOM-C Satellite Using iQuam Datasets and MUR-SST in Indonesian Waters', *Indonesian Journal of Geography*, 53(1), pp. 136–143. doi: 10.22146/IJG.53790.
- Systems, R. S. (2017) 'GHRSSST Level 4 MW_IR_OI Global Foundation Sea Surface Temperature analysis version 5.0 from REMSS'. PO. DAAC Pasadena, CA, USA.
- UKMO (2012) 'GHRSSST Level 4 OSTIA Global Foundation Sea Surface Temperature Analysis (GDS version 2)'. NASA Physical Oceanography DAAC. doi: 10.5067/GHOST-4FK02.
- Upadhyay, R. K. (2020) 'Markers for Global Climate Change and Its Impact on Social, Biological and Ecological Systems: A Review', *American Journal of Climate Change*, 09(03), pp. 159–203. doi: 10.4236/ajcc.2020.93012.
- Wang, G. *et al.* (2007) 'Tropical cyclone genesis over the South China Sea', *Journal of Marine Systems*, 68(3–4), pp. 318–326.
- Xiao, C. *et al.* (2019) 'Short and mid-term sea surface temperature prediction using time-series satellite data and LSTM-AdaBoost combination approach', *Remote Sensing of Environment*, 233, p. 111358. doi: <https://doi.org/10.1016/j.rse.2019.111358>.
- Xu, Z. *et al.* (2021) 'Long-term evolution of global sea surface temperature trend', *International Journal of Climatology*.
- Yang, Y. *et al.* (2020) 'Diurnal Sea surface temperature response to tropical cyclone Dahlia in the Eastern tropical Indian Ocean in 2017 revealed by the Bailong buoy', *Dynamics of Atmospheres and Oceans*, 92, p. 101163.

GIS-BASED ASSESSMENT OF COASTAL VULNERABILITY IN THE JATABEK (JAKARTA, TANGERANG, AND BEKASI) REGION, INDONESIA

Guntur A. RAHMAWAN^{1*}, Ruzana DHIAUDDIN¹, Ulung J. WISHA², Wisnu A. GEMILANG¹, Agung SYETIAWAN^{3*}, Wiwin AMBARWULAN³ and Ati RAHADIATI³

DOI: 10.21163/GT_2022.172.08

ABSTRACT:

JATABEK (Jakarta, Tangerang, and Bekasi) is a significant area where massive developments are concentrated in the coastal region, becoming the center of industry. Due to the vulnerable coastal area, threats of hazards and disasters are undoubtedly avoided. Therefore, assessing coastal vulnerability is crucial to identifying the potency of coastal damages throughout the JATABEK coastal zone. This study examines six primary parameters (geomorphology, elevation and slope, land use, rigid structure, and coastline changes) to determine the coastal vulnerability in the study area using GIS-based and scoring assessments. The coastline change is quantified based on Modified Normalized Difference Water Index (MNDWI). The scored parameters are then analyzed using Coastal Vulnerability Index (CVI) to gain the distribution of vulnerability levels in the study area. Of particular concern, 42.27% of the JATABEK coastline is categorized as a less vulnerable area. In contrast, 31.59% and 11.45% of the coastal area are categorized as high and very high vulnerability, concentrated in the Bekasi Regency and a little part of Tangerang. The remnant categories are moderate (9.56%), and very low (1.73%) vulnerability observed in the Tangerang and eastern part of Jakarta Bay. The presence of permanent artificial structures, land elevation and slope, and land use changes are the most impactful factors determining coastal vulnerability in the study area. Therefore, mitigation efforts are crucial to stabilize the overwhelming abrasion and deal with tidal flooding events in the vulnerable areas.

Key-words: Coastal vulnerability, JATABEK, scoring assessment, coastal hazards

1. INTRODUCTION

Jakarta is Indonesia's most significant capital city, with a considerable population (more than 9.6 million people registered in 2010) and a total area of 662 km² (Takagi *et al.*, 2016). Skyrocketed developments in the Jakarta coastal area result in various problems. Aside from environmental impacts, it induces coastal damages and vulnerability. Even though the development could enhance the physical growth in the neighboring areas, many coastal issues are reported in the surrounding cities (Tangerang and Bekasi) (Azwar *et al.*, 2013). Furthermore, the urban development is dominated by informal sectors altering the land use in Jakarta and its surroundings.

Due to climate change issues and anthropogenic pressures, Jakarta's coastal area and surroundings are prone to hazards and disasters, such as coastal flooding, sea-level rise, and land subsidence (Takagi *et al.*, 2021). Many solutions, management systems, and environmental-based assessments have been established comprehensively to surmount the impact of rapid urban development (Hakim *et al.*, 2020; Rudianto & Tantu, 2014; Yoo *et al.*, 2014). However, these efforts only encompass several significant areas on the Jakarta coast and did not apply to the surrounding cities. As a result, overwhelming coastal degradation is expected to occur in the Tangerang and Bekasi

¹ Research Institute for Coastal Resources and Vulnerability, Ministry of Marine Affairs and Fisheries, Padang, West Sumatra, 25245. Indonesia. Corresponding author guntura06@gmail.com*, ruzanadhiauddin88@yahoo.com, wisnu.gemilang@yahoo.co.id.

² Research Center for Oceanography, National Research and Innovation Agency (BRIN), Pasir Putih I, Ancol Timur, Jakarta 14430, Indonesia, ulungjantama@gmail.com.

³ Geospatial Research Center, National Research and Innovation Agency (BRIN), Cibinong, West Java, 16911, Indonesia. Corresponding author agungsyetiawan@gmail.com*, wiwini.ambarwulan@brin.go.id, ati.rahadiati@brin.go.id.

Regency. Therefore, a coastal vulnerability assessment is essential to determine the vulnerable areas in the JATABEK (Jakarta, Tangerang, and Bekasi) region (Oloyede *et al.*, 2022).

Coastal management in JATABEK should be regenerated to achieve optimal sustainable development considering environmental awareness (Zacarias *et al.*, 2011). As a preliminary stage, coastal vulnerability assessment in JATABEK needs to be initiated to solicit coastal issues due to urban development in these areas. Several previous studies have proven the overwhelming coastal erosion occurrence in the Jakarta coastal area and its surroundings (Fatimatu Zahroh *et al.*, 2018; Latif, 2022; Prabawa *et al.*, 2021), where sedimentation instability and marine pollution worsen coastal conditions (Breckwoldt *et al.*, 2016; Sindern *et al.*, 2016).

Since earlier studies just analyzed one or two vulnerability factors and did not consider related factors triggering coastal vulnerability (Ningsih *et al.*, 2011; Varrani & Nones, 2018), an integrated assessment of the JATABEK coastal area is crucial to be conducted. Because of many factors that possibly trigger the coastal vulnerability, this study focuses on examining geological and oceanographical aspects using the coastal vulnerability index. A few studies have reported the influence of geo-oceanographical factors on inducing coastal vulnerability (Fatimatu Zahroh *et al.*, 2018; Latif, 2022; Ningsih *et al.*, 2011; Prabawa *et al.*, 2021; Varrani & Nones, 2018), and these aspects should be investigated and re-reviewed. Moreover, the standard scores to assess every parameter are modified and adapted to the natural condition of the study area. Therefore, this study aims to identify and assess the coastal vulnerability in the JATABEK area. This study is expected to be a basis for future decision-making related to coastal management and hazard mitigation in the JATABEK coastal area.

2. STUDY AREA

This study was carried out in the coastal area of JATABEK (Jakarta, Tangerang, and Bekasi), Indonesia, encompassing Bekasi Regency, Bekasi City, North Jakarta Administrative City, Tangerang City, and Tangerang Regency, with a total assessed coastline of 198.06 kilometers (Fig. 1). Generally, the coastal topography of the study area is a lowland formation composed of sedimentary materials developed after the Pleistocene era. According to its slope angle, coastal morphology throughout JATABEK consists of declivous beaches with mangroves and steep beaches with sand-dominated materials (Puspasari & Turni, 2017).

Physio-graphically, JATABEK coastal area is composed of alluvial deposits surrounded by highlands. It is characterized by muddy, sandy, silty sand and sandy silt beaches, commonly found in nearby estuaries (Hidayah & Apriyanti, 2020; Puspasari & Turni, 2017).

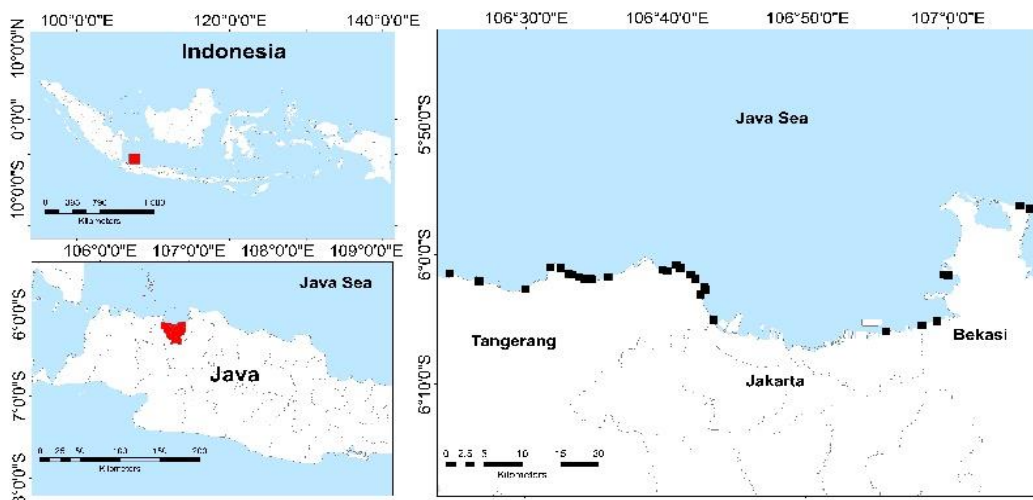


Fig. 1. Details of study area and the observation stations in the JATABEK Region.

3. DATA AND METHODS

3.1. Data Collection and Coastline Changes Identification

The primary data used in this study were collected via field surveys during May 2022 and consisted of several on-site assessments (geomorphological conditions, abrasion and accretion, and coastal structure identification). Thirty-one observation stations were chosen throughout JATABEK Region focused on the area of interest (AOI) (**Fig. 1**). Since the secondary data were remote sensing-based (**Table 1**), it was calibrated by the field measured data to increase the accuracy. The collected data were then analyzed based on the scoring category shown in **Table 1** to determine the vulnerability level of every assessed point. Rigid structures throughout the coastline of the study area were identified using high-resolution imageries (Pleiades and QuickBird) released in 2013-2015 with a spatial resolution of 0.5 meters. In contrast, the coastline change was analyzed using Landsat 8 OLI imagery during 2017 – 2021, with a resolution of 30 meters. On the other hand, the coastline's exact position was quantified from land-water area extraction by applying MNDWI (Modified Normalized Difference Water Index) formula as follows:

$$MNDWI = \frac{\rho_3 - \rho_6}{\rho_3 + \rho_6} \quad (1)$$

where:

ρ_3 = Band 3 of Landsat 8 OLI

ρ_6 = Band 6 of Landsat 8 OLI

Even though the exact coastline is difficult to detect in some cases (Pardo-Pascual *et al.*, 2012), the MNDWI technique uses bands 3 and 6 of Landsat 8 OLI to generate the coastline data (Xu, 2006). The digitized coastlines were then analyzed using DSAS (Digital Shoreline Analysis System) program developed by USGS (Thieler *et al.*, 2000). The transect point was positioned every 500 meters along the baseline, with a total transect of 754.

Meanwhile, the coastline changes rate was calculated using the End Point Rate (EPR) approach (Qiao *et al.*, 2018). Coastline changes are classified as accretion if the EPR is positive and erosion if the EPR is negative. The value in each transect has a specific numbering, easing the spatial detection of coastline change. Rates of erosion and accretion were classified into five categories with values ranging from one to five.

3.2. Coastal Vulnerability Index Assessment

CVI is a calculating method to analyze coastal vulnerability by examining several threatening factors in a region (Gornitz, 1991). The basic calculation of CVI is square-rooting the multiplied parameters and divided by the amount of parameters (Pantusa *et al.*, 2018; Romadhona *et al.*, 2020). The CVI could be calculated using a simple formula as follows (Gornitz, 1991):

$$CVI = \frac{\sqrt{x_1 * x_2 * x_3 * x_4 * x_5 * x_6}}{6} \quad (2)$$

where:

CVI = coastal vulnerability index score

x = variable scores

Table 1 shows the scoring criteria of each parameter used in this study. The vulnerability range of geomorphological parameters was referred to a category previously established (Pantusa *et al.*, 2018). While the vulnerability range of land elevation and the coastal slope was adapted from Irham *et al.* (2021), and the range of land use and coastal area with rigid structures was referred from Romadhona *et al.* (2020).

Table 1.

Vulnerability specification and scoring of each parameter.

No.	Parameter	Category				
		Very Low	Low	Moderate	High	Very High
		1	2	3	4	5
1.	Geomorphology	High cliff, rocky beach	Medium cliff, pebble beach	Low cliff, muddy land	Rocky beach, estuary, lagoon	Barrier beach, sandy beach, brackish swamp, mud, delta, mangrove, coral reefs
2.	Coastal Elevation (m)	≥ 30.10	20.1-30	10.1-20	5.1-10	0-5
3.	Coastal Slope (%)	>1.2	1.2-0.91	0.9-0.61	0.6-0.30	<0.3
4.	Land Use	Dry land	Farm, Bush Land	Vacant land with farm area	Sand area, mangrove, plantation area	Building, Beach, ponds degrade mangrove, swamp, and aquaculture
5.	Artificial Hard Structure-Attached Coastline	80%-100%	60%-80%	40%-60%	20%-40%	0-20%
6.	Coastline Changes	≥ 2.1 Accretion	$\geq 1 - < 2$ Stable	$< 1 - > -1$ Low Erosion	$\leq -1 - > -2$ Moderate Erosion	< -2.0 High Erosion

These six parameters were then divided into a specific vulnerability range, ranging from one to five representing very low, low, moderate, high, and very high vulnerability categories, respectively (Table 2).

Table 2.

Vulnerability classification based on CVI.

Vulnerability class	CVI	Color
Very low	0-4.47	Green
Low	4.48-8.15	Blue
Moderate	8.16-11.83	Yellow
High	11.84-15.51	Orange
Very high	15.52-22.82	Red

4. RESULTS AND DISCUSSIONS

4.1. Coastal Vulnerability Based on Coastline Changes and Coastal Protection

The highest erosion rate of -233.26 m/year was identified in the surrounding Cikeas Estuary and Babelan Coast, Bekasi Regency. This state could be caused by the recent decrease in mangrove forest areas, as reported by (Hidayah & Apriyanti, 2020). The decreased mangrove area is believed to diminish coastal function as a stabilizer from erosion (Walters *et al.*, 2009). More interestingly, the lowest erosion rate was also observed in the Bekasi Regency, with approximately -0.96 m/year concentrated in the surrounding Muara Gembong mangrove forest.

On the other hand, coastal accretion was detected in 175 points scattered in the study area concentrated in North Jakarta. The highest accretion rate was observed in the Pakuhaji - Tangerang Regency (188.29 m/year). The remnant categories, such as low erosion, moderate erosion, and stable, were also identified in the study area though they are not dominant (Table 3). Overall, most of the coastlines in the JATABEK Region are highly vulnerable, with a more than two m/year change rate and approximate cover of 56.97% of the entire study area. Moreover, the highest vulnerability level was detected in the Bekasi Regency, mainly caused by coastline changes.

Coastal vulnerability assessment based on coastline changes in the JATABEK Region is shown in Table 3 and Fig. 2. 56% of the assessed coastline is highly vulnerable (coastline change rate more

than two m/year). Meanwhile, Bekasi Regency is the most vulnerable area with significant erosion (24.45% vulnerable coastline). This state shows the impact of massive developments in Jakarta, worsened by sea-level rise and land subsidence issues (Abidin *et al.*, 2013).

Table 3.

Percentage of coastal vulnerability caused by coastline changes in the study area.

Location	Coastline Vulnerability					Total
	Very Low	Low	Moderate	High	Very High	
Tangerang	0.89%	5.07%	1.47%	0.97%	17.57%	25.97%
Jakarta	0.59%	8.88%	11.50%	1.20%	17.64%	39.80%
Bekasi	0.39%	10.29%	0.71%	1.08%	21.76%	34.23%
Total	1.87%	24.24%	13.68%	3.25%	56.97%	100%

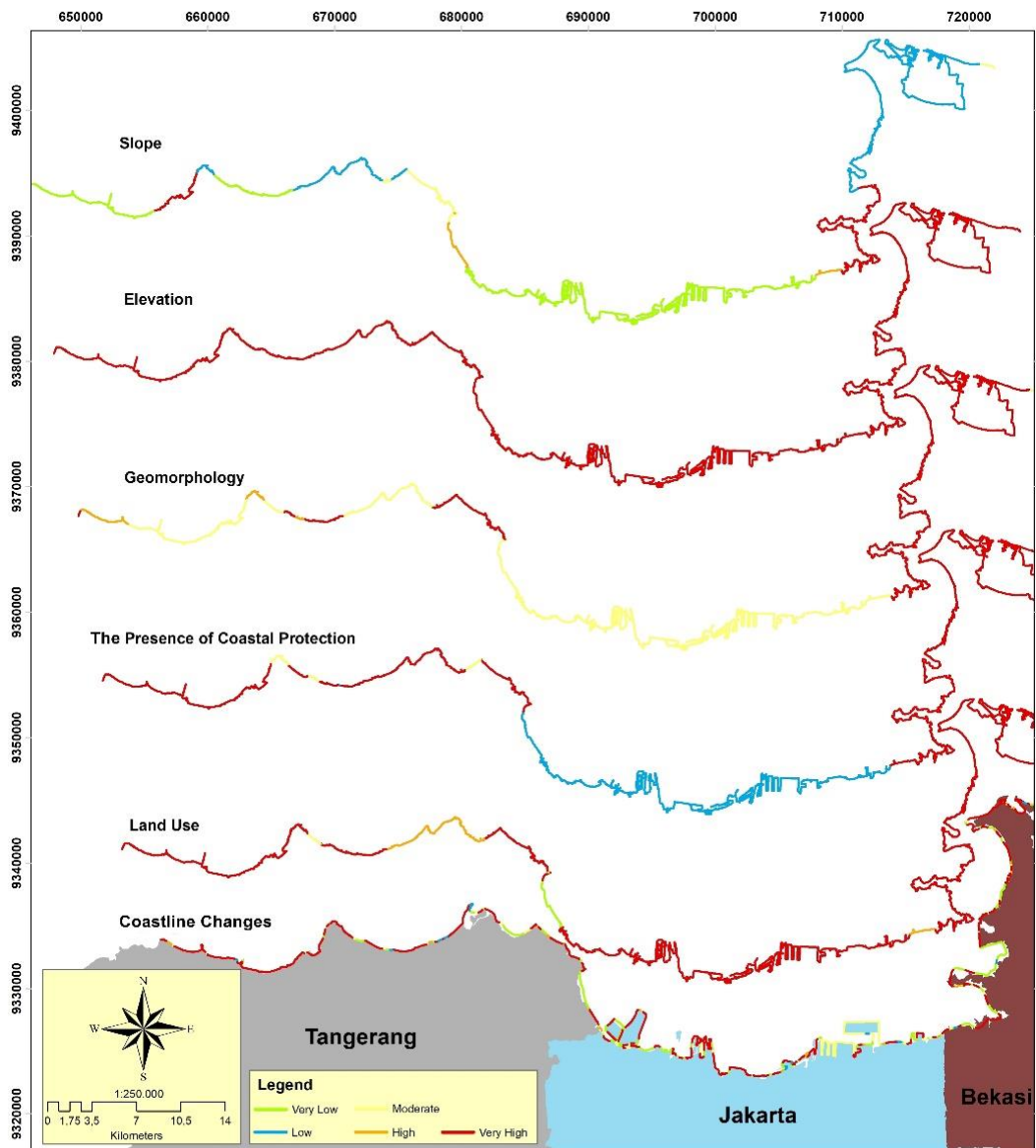


Fig. 2. Coastal vulnerability assessment result of every parameter used in this study.

In addition to coastal erosion, the evidence of erosion in the study area is shown in **Fig. 3**.



Fig. 3. Coastal erosion documented during field survey in 2022. Erosion in Tanjung Anom, Tangerang (a); erosion in Muara Gembong (b); erosion in Pulo Cangkir, Tangerang (c); and erosion in Marunda (d).

The most altered coastline is observed in the Bekasi coastal area, where the absence of coastal protection is the main factor triggering coastline changes. In contrast, Jakarta and Tangerang coastlines tended to be stable because of coastal protection, as El-Mahdy *et al.* (2022) reported that the unstable coastline due to erosion/accretion processes could be overcome using coastal structures. Therefore, coastal protections should be prioritized to protect significant areas from the threats of erosion, sea-level rise, and other coastal hazards and disasters (Hidayat, 2006).

On the other hand, coastal vulnerability assessment based on coastal structures is shown in **Fig. 2** and **Table 4**. A low vulnerability was detected throughout Jakarta coastal area with 36.20%. 80% of the Jakarta coastline is protected by reclaimed islands and coastal breakwater, seawalls, and revetments. Moreover, the local government and third parties have prepared a “Giant Sewall” master plan to protect Jakarta City from tidal flooding (van der Wulp *et al.*, 2016). In contrast, high and very high vulnerability categories were found in Bekasi and Tangerang, where the coastal area is mainly used for aquaculture and tourism. The significant deformation of mangrove forests becoming aquaculture ponds in Muara Gembong - Bekasi results in expanded erosion areas (Oktaviani *et al.*, 2019). Based on the present study analysis, Bekasi Regency experienced a very high erosion with a small area protected by coastal structures (0-20%).

Table 4.

Percentage of coastal vulnerability based on coastline changes and the presence of coastal structures.

Location	Coastal Vulnerability					Total
	Very Low	Low	Moderate	High	Very High	
Tangerang	6.69%	1.67%	1.39%	0.00%	14.15%	23.90%
Jakarta	0.00%	36.20%	0.00%	0.00%	0.00%	36.20%
Bekasi	0.00%	0.00%	0.00%	0.00%	39.90%	39.90%
Total	6.69%	37.87%	1.39%	0.00%	54.05%	100.00%

4.2. Coastal Vulnerability Assessment Based on Coastal Elevation and Slope

Coastal elevation in the study area ranged from 0 to 5 meters. Based on this parameter, the coastal area of JATABEK is highly vulnerable (**Fig. 2**). Land elevation is one indicator determining the area prone to sea-level rise and tidal flooding. A previous study (Dasanto, 2010) predicted that the sea level will rise 0.5 to 1 meter in 2050 and 2100 during flood tides. However, higher sea surface levels and wave inundation contribute to increased coastal hazard potency (Handiani, 2019).

The results of the coastal slope assessment are shown in **Fig. 2** and **Table 5**. The coastal slope ranged from 0.1 to 3.2. The same result is also defined by Dahlia *et al.* (2019), whereby the slope of the Jakarta coastal area is less than five meters. Based on this parameter, the coastal area of JATABEK was predominated by a low vulnerability with 45.70%. The lowest slope was detected in the Bekasi Regency, and the highest slope was identified in the Jakarta coastal area. While, in the Tangerang and Bekasi coastal areas, the slope ranged from 0.1% to 0.25%, categorized as very high vulnerability covering 1.81% and 0.96% of the entire study area, respectively.

Table 5.

Percentage of coastal vulnerability based on slope in the study area.

Location	Coastal Vulnerability					Total
	Very Low	Low	Moderate	High	Very High	
Tangerang	9.50%	5.93%	2.88%	3.67%	1.81%	23.78%
Jakarta	36.23%	0.00%	0.00%	0.00%	0.00%	36.23%
Bekasi	0.00%	26.99%	11.47%	0.54%	0.99%	39.99%
Total	45.73%	32.92%	14.34%	4.20%	2.80%	100.00%

4.3 Coastal Vulnerability Assessment Based on Land Use and Geomorphology

Coastal settings and patterns could minimize the risk of sea-sourced disasters. By contrast, significant land use changes increase hazard and disaster threats in coastal areas (Adnan *et al.*, 2020). Moreover, massive coastal transformation, such as the deformed agriculture area, will cause unstable soil fertility and salinity, eventually affecting the surrounding area's existing buildings (Khan *et al.*, 2015; Lee & Brody, 2018; Rahman *et al.*, 2017). The result of land use analysis in the JATABEK coastal area is shown in Fig. 2 and Table 6.

Table 6.

Percentage of coastal vulnerability based on land use in the study area.

Location	Coastal Vulnerability					Total
	Very Low	Low	Moderate	High	Very High	
Tangerang	1.85%	0.00%	0.58%	5.63%	15.84%	23.90%
Jakarta	0.00%	0.00%	0.00%	0.00%	36.20%	36.20%
Bekasi	0.00%	0.00%	0.00%	0.99%	38.91%	39.90%
Total	1.81%	0.00%	0.55%	5.62%	92.03%	100.00%

Based on land-use parameters, the JATABEK region is highly vulnerable, encompassing more than 90% of the study area. The coastal area of JATABEK is generally used for aquaculture, developed area, and barren zone. On the other hand, the spatial pattern of the JATABEK area complies with the structure and spatial patterns following the main road and highway. A previous study (Nur *et al.*, 2018) defined the increasing tendency of developed areas in the city center, and the development is directed toward the eastern region of Jakarta, including East Jakarta, Bekasi City, and Bekasi Regency. On the other hand, the reclamation area is planned in North Jakarta and Tangerang. 36.20% of the coastline in Jakarta is categorized as a very vulnerable area (Table 6). This region has been experiencing massive and rapid urban development in settlement, industry, open green areas, and agriculture (Mulyaningasih *et al.*, 2018).

In the Tangerang coastal area, a plethora of coastal areas are mismanaged, especially the development of illegal settlement and aquaculture that infringe the spatial regional space regulation (Hidayat, 2006). Nevertheless, a small part of the Tangerang Regency is less vulnerable, with 1.85% empty spaces in the coastal area. In contrast, 38.91% Bekasi coastal zone is categorized as very high vulnerability with the general land use for aquaculture.

Marine-fluvial amalgamation processes generally arrange the land formation of the JATABEK coastal area. The marine process is commonly found in the northern part of the coastal zone. While the fluvial process predominantly influences the middle and the southern areas. These land formations were defined using Digital Elevation Model (DEM), validated by the field assessment. JATABEK coastal area is characterized by low elevation where this region is composed of alluvial lithology (Qa) consisting of clay, silt, sand, and pebble, and beach embankment deposits (Qbr) marked by alluvial lithology, consisting of fine-coarse sand with well-sorted sediment combined with mollusk shell fragments (Turkandi *et al.*, 1992).

Land types in the JATABEK area generally consist of alluvium beaches, beach ridges, the area between ridges, swamps, flooded land, alluvial land, alluvial fan, and riverine channels (Priyatna *et al.*, 2015). The domination of alluvium deposits in the JATABEK Region makes this area prone to puddles and the most vulnerable.

The result of coastal vulnerability assessment based on geomorphology parameters in the JATABEK area is divided into three types of vulnerability; very high, high, and moderate (**Fig. 2**), where the predominant category was very high vulnerability (43.86%) and moderate vulnerability (52.56%) (**Table 7**). The moderately vulnerable area is arranged by silty land formation, related to the fundamental characteristic of the depositional area. In contrast, the highly vulnerable area is arranged by the barrier and sandy beaches, brackish swamp, mud, delta, and mangrove.

Table 7.**Percentage of coastal vulnerability based on the coastal geomorphology parameter.**

Location	Coastal Vulnerability					Total
	Very Low	Low	Moderate	High	Very High	
Tangerang	0.00%	0.00%	14.44%	3.58%	5.88%	23.90%
Jakarta	0.00%	0.00%	36.20%	0.00%	0.00%	36.20%
Bekasi	0.00%	0.00%	1.92%	0.00%	37.98%	39.90%
Total	0.00%	0.00%	52.56%	3.58%	43.86%	100.00%

In addition to the geomorphology of the study area, the alluvium land of JATABEK is composed of uncompacted alluvial deposits. The arranging lithology in the form of younger alluvial deposits and beach embankments consists of sandstone, marl, and limestone deposits, playing a significant role in the basic structure of alluvium, reducing the river runoff (Dahlia *et al.*, 2019). Therefore, the potency of river and coastal flooding could be reduced. In contrast, coastal lithology with sandstone, marl, and limestone triggers flooding area formation. Furthermore, lateral erosion intensity in the coastal area with sand lithology is higher than in the alluvium coast. The high vulnerability of the JATABEK area is worsened by sandy beaches where the sand sediment is easily transported by currents and waves (Serafim *et al.*, 2019).

On the other hand, muddy areas in the surrounding estuaries predominate the center area of study with moderate vulnerability status (**Fig. 2**). The mud (silt) sediment is more solid than the sand texture, thereby minimizing the level of vulnerability. By contrast, the highly vulnerable locations are usually composed of sand (coarse-sized) sediments (El-Mahdy *et al.*, 2022).

4.4 Coastal Vulnerability Index (CVI) in the JATABEK Region

The GIS-based CVI analysis shows that 42.27% of the JATABEK coastline was categorized as lowly vulnerable, concentrated in Tangerang and North Jakarta. Artificial coastal structures could reduce the potency of coastal damages, erosion, and wave overtopping in these areas where it protects almost 80% of the North Jakarta Region. By contrast, the highest vulnerable area is observed in the Bekasi and Tangerang Regency, covering 28.45% and 3.14% of the study area, respectively. The remaining categories are 9.56% moderately vulnerable, 31.59% highly vulnerable, and 11.45% of very high vulnerability (**Table 8** and **Fig. 4**).

Table 8.**Percentage of CVI in the JATABEK Region.**

Location	Coastal Vulnerability Index					Total
	Very Low	Low	Moderate	High	Very High	
Tangerang	1.73%	6.07%	9.56%	3.14%	3.39%	23.90%
Jakarta	0.00%	36.20%	0.00%	0.00%	0.00%	36.20%
Bekasi	0.00%	0.00%	0.00%	28.45%	11.45%	39.90%
Total	1.73%	42.27%	9.56%	31.59%	14.84%	100.00%

The most significant parameter in CVI determination is the land elevation, where the entire study area is characterized by less than 5 meters of elevation. The declivous slope of JATABEK is prone to sea-sourced disaster impacts where in some places, the slope state induces a sudden disaster and increases the coastal zone's vulnerability level (Michoud *et al.*, 2012).

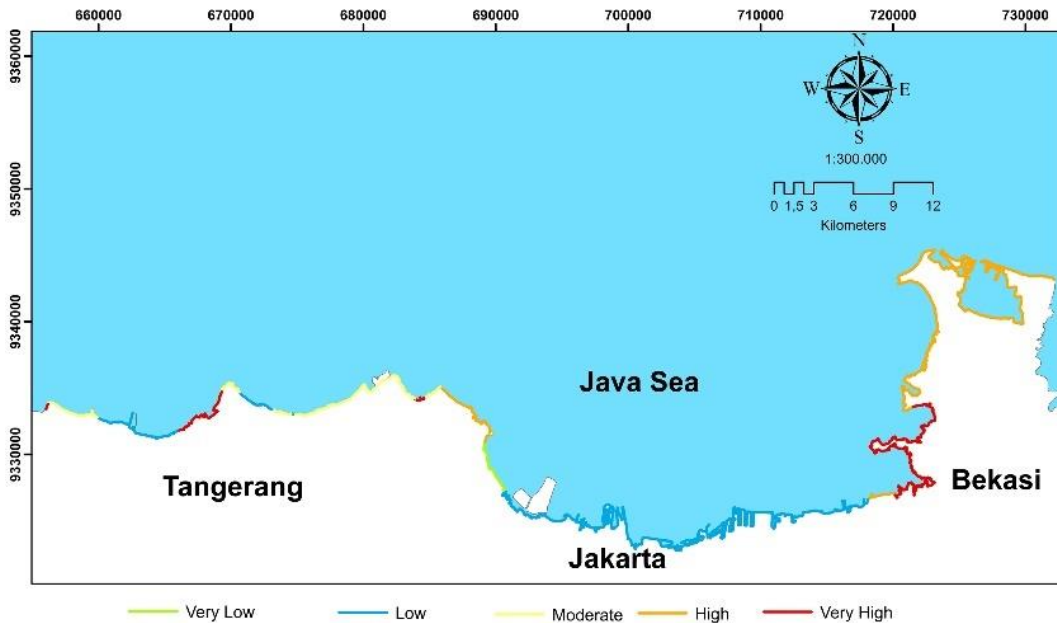


Fig. 4. Coastal vulnerability index in the JATABEK Region.

However, land use in the study area in the form of developed areas and aquaculture ponds also increases the level of vulnerability, generally observed in the Bekasi region with high (28.5%) and very high (11.45%) vulnerability. The coastal destruction in this area is less mitigated, and the massive land use transformation exacerbates the vulnerability status of the Bekasi Regency.

A large scale of coastal vulnerability is caused by the coastal disaster intensity, such as erosion, flooding, and cyclone (Hoque *et al.*, 2022). Vulnerability assessment of a coastal zone is imperative to reduce the impact of coastal hazards. Several scholars prove that many coastline cities are prone to hazards and disasters and eventually impact the socio-economic sectors (Cao *et al.*, 2022; Wang *et al.*, 2021). However, the natural condition of a coastal zone plays a significant role in triggering coastal vulnerability and could trigger other hazardous threats (Yin *et al.*, 2012).

In this study, the use of remote-sensed and field data to generate the CVI analysis complements each other. Land use, elevation, and rigid coastal structure could be remotely observed from satellite images (Elkafrawy *et al.*, 2021). Moreover, satellite data could also cover the gap between field stations (Irham *et al.*, 2021). Therefore, the remote sensing data are significant in determining the vulnerability level in the coastal zone, even though it should be validated using field data to enhance the accuracy of the GIS-based processing results. In addition to the accuracy, the denser field observation station will increase the fidelity of the resulting data (Jana and Bhattacharya, 2013), which is recommended for further studies to extend the observation station during the field survey.

5. CONCLUSIONS

To conclude, based on the GIS-based analyses, the coastal area of North Jakarta is categorized as a less vulnerable area where the presence of artificial coastal protections is significant to preserve this capital area from coastal hazards and disasters. Despite detecting coastal erosion and highly vulnerable areas, several parts of the Tangerang Regency are less vulnerable due to the presence of coastal structures. The most vulnerable area is found in the Bekasi Regency, with high and very high vulnerability categories.

The primary data used in this study was collected from satellite imagery which the lack of accuracy is possible due to the difference in resolution. On the other hand, the field survey could improve the result of GIS-based modeling, where the denser the observation point, the better the data

obtained. We recommend regularly monitoring the coastal zone changes since rapid urban development is still happening in the JATABEK region, which may trigger further coastal alterations and increase the impact of coastal hazards and disasters. A preliminary study is crucial before applying developments in the coastal area since it is now prone to erosion issues.

ACKNOWLEDGMENT

This study is financially funded by Disaster Research seed grant, under the Research Organization of Earth Sciences and Maritime, National Research and Innovation Agency of Indonesia (BRIN) with a grant number of B-676/III/PR.01.03/12/2021 and the field survey is funded by the Expedition and Exploration Funding Program-BRIN with a funding number of 950/II/HK.01.00/4/2022.

REFERENCES

- Abidin, H. Z., Andreas, H., Gumilar, I., Sidiq, T. P., & Fukuda, Y. (2013). Land Subsidence in Coastal City of Semarang (Indonesia): Characteristics, Impacts and Causes. *Geomatics, Natural Hazards and Risk*, 4(3), 226–240. <https://doi.org/https://doi.org/10.1080/19475705.2012.692336>
- Adnan, M. S. G., Abdullah, A. Y. M., Dewan, A., & Hall, J. W. (2020). The effects of changing land use and flood hazard on poverty in coastal Bangladesh. *Land Use Policy*, 99(May), 104868. <https://doi.org/10.1016/j.landusepol.2020.104868>
- Azwar, S. A., Suganda, E., Tjiptoherijanto, P., & Rahmayanti, H. (2013). Model of Sustainable Urban Infrastructure at Coastal Reclamation of North Jakarta. *Procedia Environmental Sciences*, 17, 452–461. <https://doi.org/10.1016/j.proenv.2013.02.059>
- Blasco, F., Saenger, P., & Janodet, E. (1996). Mangroves as indicators of coastal change. *Catena*, 27(3–4). [https://doi.org/10.1016/0341-8162\(96\)00013-6](https://doi.org/10.1016/0341-8162(96)00013-6)
- Breckwoldt, A., Dsikowitzky, L., Baum, G., Ferse, S. C. A., van der Wulp, S., Kusumanti, I., ... Adrianto, L. (2016). A review of stressors, uses and management perspectives for the larger Jakarta Bay Area, Indonesia. *Marine Pollution Bulletin*, 110(2), 790–794. <https://doi.org/10.1016/j.marpolbul.2016.08.040>
- Cao, C., Zhu, K., Cai, F., Qi, H., Liu, J., Lei, G., ... Su, Y. (2022). Vulnerability Evolution of Coastal Erosion in the Pearl River Estuary Great Bay Area Due to the Influence of Human Activities in the Past Forty Years. *Frontiers in Marine Science*, 9. <https://doi.org/10.3389/fmars.2022.847655>
- Dahlia, S., NH, T., & Rosyidin, W. F. (2019). Flood Susceptibility Analysis Using Geomorphology Approach in The Special Capital Region of Jakarta. *Jurnal Alami*, 2(January 2018).
- Dahlia, S., Nurharosono, T., & Rosyidin, W. F. (2018). Analisis Kerawanan Dan Exposure Banjir Menggunakan Citra Dem Srtm Dan Landsat Di DKI Jakarta. *Jurnal Pendidikan Geografi*, 18(1). (In Indonesian)
- Dasanto, B. D. (2010). Assessment of The Impact of Sea Rise On the Coastal Area: A Case Study of Indramayu District. *Jurnal Hidrosfer Indonesia*, 5(2), 43–53.
- El-Mahdy, M. E. S., Saber, A., Moursy, F. E., Sharaky, A., & Saleh, N. (2022). Coastal erosion risk assessment and applied mitigation measures at Ezbet Elborg village, Egyptian delta. *Ain Shams Engineering Journal*, 13(3). <https://doi.org/10.1016/j.asej.2021.10.016>
- Elkafrawy, S. B., Basheer, M. A., Mohamed, H. M., & Naguib, D. M. (2021). Applications of remote sensing and GIS techniques to evaluate the effectiveness of coastal structures along Burullus headland-Eastern Nile Delta, Egypt. *Egyptian Journal of Remote Sensing and Space Science*, 24(2). <https://doi.org/10.1016/j.ejrs.2020.01.002>
- Ewel, K. C., Twilley, R. R., & Ong, J. E. (1998). Different kinds of mangrove forests provide different goods and services. *Global Ecology and Biogeography Letters*, 7(1). <https://doi.org/10.2307/2997700>
- Fatimatuzzahroh, F., Hadi, S. P., & Purnaweni, H. (2018). Mangrove Cultivation for Dealing with Coastal Abrasion Case Study of Karangsong. *E3S Web of Conferences*, 31, 2017–2019. <https://doi.org/10.1051/e3sconf/20183108028>
- Febrianti, N., & Sofan, P. (2014). Ruang Terbuka Hijau Di Dki Jakarta Berdasarkan Analisis Spasial Dan Spektral Data Landsat 8. *Deteksi Parameter Geobiofisik Dan Diseminasi Penginderaan Jauh*, Seminar Nasional Penginderaan Jauh, (April). (In Indonesian)
- Firman, T., Surbakti, I. M., Idroes, I. C., & Simarmata, H. A. (2011). Potential climate-change related vulnerabilities in Jakarta: Challenges and current status. *Habitat International*, 35(2), 372–378. <https://doi.org/10.1016/j.habitatint.2010.11.011>
- Gornitz, V. (1991). Global coastal hazards from future sea level rise. *Palaeogeography, Palaeoclimatology, Palaeoecology*, 89(4), 379–398. [https://doi.org/https://doi.org/10.1016/0031-0182\(91\)90173-0](https://doi.org/https://doi.org/10.1016/0031-0182(91)90173-0)

- Hakim, W. L., Achmad, A. R., Eom, J., & Lee, C. W. (2020). Land Subsidence Measurement of Jakarta Coastal Area Using Time Series Interferometry with Sentinel-1 SAR Data. *Journal of Coastal Research*, 102(sp1), 75–81. <https://doi.org/10.2112/SII02-010.1>
- Handiani, D. N. (2019). Kajian Kerentanan Pesisir Terhadap Kenaikan Muka Air Laut di Kabupaten Subang. *Jurnal Kelautan Nasional*, 14(3), 145–154. <https://doi.org/10.15578/jkn.v14i3.7583> (In Indonesian)
- Hidayah, Z., & Apriyanti, A. (2020). Deteksi Perubahan Garis Pantai Teluk Jakarta Bagian Timur Tahun 2003-2018. *Jurnal Kelautan: Indonesian Journal of Marine Science and Technology*, 13(2), 143–150. <https://doi.org/10.21107/jk.v13i2.7980> (In Indonesian)
- Hidayat, N. (2006). Konstruksi bangunan laut dan pantai sebagai alternatif perlindungan daerah pantai. *Jurnal SMARTEK*, 4(1), 10–16. (In Indonesian)
- Hidayatno, A., Dinianyadharani, A. K., & Sutrisno, A. (2017). Scenario analysis of the Jakarta Coastal Defence Strategy: Sustainable indicators impact assessment. *International Journal of Innovation and Sustainable Development*, 11(1), 37–52. <https://doi.org/10.1504/IJISD.2017.080626>
- Hoque, M. Z., Haque, M. E., & Islam, M. S. (2022). Mapping integrated vulnerability of coastal agricultural livelihood to climate change in Bangladesh: Implications for spatial adaptation planning. *Physics and Chemistry of the Earth*, 125. <https://doi.org/10.1016/j.pce.2021.103080>
- Irham, M., Rusydi, I., Haridhi, H. A., Setiawan, I., Ilhamsyah, Y., Deli, A., ... Siregar, A. M. (2021). Coastal vulnerability of the west coast of aceh besar: A coastal morphology assessment. *Journal of Marine Science and Engineering*, 9(8). <https://doi.org/10.3390/jmse9080815>
- Jana, A., & Bhattacharya, A. K. (2013). Assessment of Coastal Erosion Vulnerability around Midnapur-Balasore Coast, Eastern India using Integrated Remote Sensing and GIS Techniques. *Journal of the Indian Society of Remote Sensing*, 41(3). <https://doi.org/10.1007/s12524-012-0251-2>
- Khan, M. M. H., Bryceson, I., Kolivras, K. N., Faruque, F., Rahman, M. M., & Haque, U. (2015). Natural disasters and land-use/land-cover change in the southwest coastal areas of Bangladesh. *Regional Environmental Change*, 15(2). <https://doi.org/10.1007/s10113-014-0642-8>
- Latif, F. (2022). Technology Transfer as a Strategy for Disaster Risk Reduction Among the Coastal Cities of Asia-Pacific: The Case of Jakarta. *Journal of Community Informatics*, 18(1), 88–103.
- Lee, Y., & Brody, S. D. (2018). Examining the impact of land use on flood losses in Seoul, Korea. *Land Use Policy*, 70. <https://doi.org/10.1016/j.landusepol.2017.11.019>
- Lima, M., Coelho, C., Veloso-Gomes, F., & Roebeling, P. (2020). An integrated physical and cost-benefit approach to assess groins as a coastal erosion mitigation strategy. *Coastal Engineering*, 156, 103614. <https://doi.org/10.1016/j.coastaleng.2019.103614>
- Mazda, Y., Magi, M., Ikeda, Y., Kurokawa, T., & Asano, T. (2006). Wave reduction in a mangrove forest dominated by *Sonneratia* sp. *Wetlands Ecology and Management*, 14(4). <https://doi.org/10.1007/s11273-005-5388-0>
- Michoud, C., Derron, M. H., Horton, P., Jaboyedoff, M., Baillifard, F. J., Loye, A., ... Queyrel, A. (2012). Rockfall hazard and risk assessments along roads at a regional scale: Example in Swiss Alps. *Natural Hazards and Earth System Sciences*, 12(3). <https://doi.org/10.5194/nhess-12-615-2012>
- Mulyaningsih, D., Hendrarto, B., & Muskananfolo, M. R. (2018). PERUBAHAN LUAS HUTAN MANGROVE DI WILAYAH PANTAI INDAH KAPUK, JAKARTA UTARA TAHUN 2010-2015 (The Changing Mangrove Area at Pantai Indah Kapuk, North Jakarta in 2010 – 2015). *Management of Aquatic Resources Journal (MAQUARES)*, 6(4). <https://doi.org/10.14710/marj.v6i4.21334> (In Indonesian)
- Ningsih, N., Suryo, W., & Anugrah, S. (2011). Study on Characteristics of Residual Water Level in Jakarta, Semarang, and Surabaya Waters–Indonesia and Its Relation to Storm Events in November. *J Basic & App Sci*, 11(5), 31–37.
- Nur, I., Juhadi, F., & Indrayati, A. (2018). Fenomena Urban Sprawl Jabodetabek. *Edu Geography*, 6(1). (In Indonesian)
- Oktaviani, S., Yonvitner, ., & Imran, Z. (2019). DAYA DUKUNG OPTIMUM BERBASIS POLA TATA GUNA LAHAN PESISIR DI MUARA GEMBONG KABUPATEN BEKASI. *Jurnal Ilmu Dan Teknologi Kelautan Tropis*, 11(1). <https://doi.org/10.29244/jitkt.v11i1.21600> (In Indonesian)
- Oloyede, M. O., Williams, A. B., Ode, G. O., & Benson, N. U. (2022). Coastal Vulnerability Assessment: A Case Study of the Nigerian Coastline. *Sustainability*, Vol. 14. <https://doi.org/10.3390/su14042097>
- Pantusa, D., D'Alessandro, F., Riefolo, L., Principato, F., & Tomasicchio, G. R. (2018). Application of a coastal vulnerability index. A case study along the Apulian Coastline, Italy. *Water (Switzerland)*, 10(9), 1–16. <https://doi.org/10.3390/w10091218>
- Pardo-Pascual, J. E., Almonacid-Caballer, J., Ruiz, L. A., & Palomar-Vázquez, J. (2012). Automatic extraction of shorelines from Landsat TM and ETM+ multi-temporal images with subpixel precision. *Remote Sensing of Environment*, 123. <https://doi.org/10.1016/j.rse.2012.02.024>

- Prabawa, F. Y., Purbani, D., Sukoraharjo, S. S., Jayawiguna, M. H., & Triwibowo, H. (2021). Mapping the abrasion on Sederhana Beach, Muara Gembong, Bekasi, West Java province for the coastal mitigation purpose. *IOP Conference Series: Earth and Environmental Science*, 925(1). <https://doi.org/10.1088/1755-1315/925/1/012042>
- Priyatna, M., DS, K. A., & Asriningrum, W. (2015). *Pemanfaatan Data Landsat Multitemporal untuk Zonasi Daerah Rawan Banjir di Jakarta Menggunakan Pendekatan Geomorfologi*. (In Indonesian)
- Puspasari, R., & Turni, S. (2017). Di Teluk Jakarta Impact Analysis of Land Reclamation To Environment and Fisheries in Jakarta Bay. *Jurnal Kebijakan Perikanan Indonesia*, 9(November), 85–94.
- Qiao, G., Mi, H., Wang, W., Tong, X., Li, Z., Li, T., ... Hong, Y. (2018). 55-year (1960–2015) spatiotemporal shoreline change analysis using historical DISP and Landsat time series data in Shanghai. *International Journal of Applied Earth Observation and Geoinformation*, 68. <https://doi.org/10.1016/j.jag.2018.02.009>
- Quader, M. A., Khan, A. U., & Kervyn, M. (2017). Assessing risks from cyclones for human lives and livelihoods in the coastal region of Bangladesh. *International Journal of Environmental Research and Public Health*, 14(8). <https://doi.org/10.3390/ijerph14080831>
- Rahman, M. T. U., Tabassum, F., Rasheduzzaman, M., Saba, H., Sarkar, L., Ferdous, J., ... Zahedul Islam, A. Z. M. (2017). Temporal dynamics of land use/land cover change and its prediction using CA-ANN model for southwestern coastal Bangladesh. *Environmental Monitoring and Assessment*, 189(11). <https://doi.org/10.1007/s10661-017-6272-0>
- Romadhona, S., Mutmainnah, L., Wibowo, C., & Setiawati, T. C. (2020). 'assessment of Coastal Vulnerability Index on potential agricultural land-CVI, Banyuwangi Regency'. *E3S Web of Conferences*, 142, 1–8. <https://doi.org/10.1051/e3sconf/202014201002>
- Rudianto, & Tantu, A. G. (2014). An analysis of coastal land conflict in the North of Jakarta coastal area: (A general algebraic modelling system approach). *Journal of Coastal Conservation*, 18(1), 69–74. <https://doi.org/10.1007/s11852-013-0298-4>
- Sakka, Paharuddin, & Rupang, E. (2014). ANALISIS KERENTANAN PANTAI BERDASARKAN COASTAL VULNERABILITY INDEX (CVI) DI PANTAI KOTA MAKASSAR Vulnerability Analysis Based on the Coastal Vulnerability Index (CVI) in Makassar City Coast. *Jurnal Ilmu Kelautan Dan Perikanan*, 24(3), 49–53. (In Indonesian)
- Sathirathai, S., & Barbier, E. B. (2001). Valuing mangrove conservation in Southern Thailand. *Contemporary Economic Policy*, 19(2). <https://doi.org/10.1111/j.1465-7287.2001.tb00054.x>
- Serafim, M. B., Siegle, E., Corsi, A. C., & Bonetti, J. (2019). Coastal vulnerability to wave impacts using a multi-criteria index: Santa Catarina (Brazil). *Journal of Environmental Management*, 230, 21–32.
- Sindern, S., Tremöhlen, M., Dsikowitzky, L., Gronen, L., Schwarzbauer, J., Siregar, T. H., ... Irianto, H. E. (2016). Heavy metals in river and coast sediments of the Jakarta Bay region (Indonesia) — Geogenic versus anthropogenic sources. *Marine Pollution Bulletin*, 110(2), 624–633.
- Takagi, H., Esteban, M., Mikami, T., & Fuji, D. (2016). Projection Coastal Floods Jakarta 2050. *Urban Climate*, 17, 135–145.
- Takagi, H., Esteban, M., Mikami, T., Pratama, M. B., Valenzuela, V. P. B., & Avelino, J. E. (2021). People's perception of land subsidence, floods, and their connection: A note based on recent surveys in a sinking coastal community in Jakarta. *Ocean & Coastal Management*, 211, 105753. <https://doi.org/10.1016/j.ocecoaman.2021.105753>
- Thampanya, U., Vermaat, J. E., Sinsakul, S., & Panapitukkul, N. (2006). Coastal erosion and mangrove progradation of Southern Thailand. *Estuarine, Coastal and Shelf Science*, 68(1). <https://doi.org/10.1016/j.ecss.2006.01.011>
- Thieler, E. R., Pilkey, O. H., Young, R. S., Bush, D. M., & Chai, F. (2000). The use of mathematical models to predict beach behavior for U.S. coastal engineering: A critical review. *Journal of Coastal Research*, 16(1), 48–70.
- Toufique, K. A., & Islam, A. (2014). Assessing risks from climate variability and change for disaster-prone zones in Bangladesh. *International Journal of Disaster Risk Reduction*, 10(PA). <https://doi.org/10.1016/j.ijdr.2014.08.008>
- Turkandi, T., Sidarto, Agustiyanto, D. A., & Hadiwidjoyo, M. M. P. (1992). *Peta Geologi Lembar Jakarta dan Kep Seribu, Jawa*. Bandung. (In Indonesian)
- Vaidya, A. M., Kori, S. K., & Kudale, M. D. (2015). Shoreline Response to Coastal Structures. *Aquatic Procedia*, 4. <https://doi.org/10.1016/j.aqpro.2015.02.045>
- van der Wulp, S. A., Dsikowitzky, L., Hesse, K. J., & Schwarzbauer, J. (2016). Master Plan Jakarta, Indonesia: The Giant Seawall and the need for structural treatment of municipal waste water. *Marine Pollution Bulletin*, 110(2). <https://doi.org/10.1016/j.marpolbul.2016.05.048>
- Varrani, A., & Nones, M. (2018). Vulnerability, impacts and assessment of climate change on Jakarta and Venice.

- In *International Journal of River Basin Management* (Vol. 16).
<https://doi.org/10.1080/15715124.2017.1387125>
- Walters, B. B., Rönnbäck, P., Kovacs, J. M., Crona, B., Hussain, S. A., Badola, R., ... Dahdouh-Guebas, F. (2009). Erratum to 'Ethnobiology, socio-economics and management of mangrove forests: A review' [Aquat. Bot. 89 (2008) 220-236] (DOI:10.1016/j.aquabot.2008.02.009). *Aquatic Botany*, 90(3), 273. <https://doi.org/10.1016/j.aquabot.2008.11.003>
- Wang, X., Zhang, W., Yin, J., Wang, J., Ge, J., Wu, J., ... Lam, N. S. N. (2021). Assessment of coastal erosion vulnerability and socio-economic impact along the Yangtze River Delta. *Ocean and Coastal Management*, 215. <https://doi.org/10.1016/j.ocecoaman.2021.105953>
- Xu, H. (2006). Modification of normalised difference water index (NDWI) to enhance open water features in remotely sensed imagery. *International Journal of Remote Sensing*, 27(14), 3025–3033. <https://doi.org/10.1080/01431160600589179>
- Yin, J., Yin, Z., Wang, J., & Xu, S. (2012). National assessment of coastal vulnerability to sea-level rise for the Chinese coast. *Journal of Coastal Conservation*, 16(1). <https://doi.org/10.1007/s11852-012-0180-9>
- Yoo, G., Kim, A. R., & Hadi, S. (2014). A methodology to assess environmental vulnerability in a coastal city: Application to Jakarta, Indonesia. *Ocean and Coastal Management*, 102(PA), 169–177. <https://doi.org/10.1016/j.ocecoaman.2014.09.018>
- Zacarias, D. A., Williams, A. T., & Newton, A. (2011). Recreation carrying capacity estimations to support beach management at Praia de Faro, Portugal. *Applied Geography*, 31(3), 1075–1081. <https://doi.org/10.1016/j.apgeog.2011.01.020>

HOW THE CLIMATE MIGRATES. CASE STUDY FOR FOUR LOCATIONS IN THE CARPATHIAN-BASIN

Zsolt MAGYARI-SÁSKA¹

DOI: 10.21163/GT_2022.172.09

ABSTRACT:

One of the manifestations of climate change is that the climate of a given location becomes similar to the climate of another location. The detection and investigation of these migration effects is useful in several areas, such as tourism or agriculture. The present study attempts to monitor this location-related climate change. Based on daily temperatures and precipitation at four test sites, using the cosine similarity index shows how the climates of each site migrated in the Carpathian Basin. The study examines the similarity values for each location both for ten- and thirty-years periods. We can see that in most cases the climate not only migrates, but in many cases, it shrinks territorially or largely disappears from the study area. In order to be able to process the large amount of data, we used own developed R scripts, which can be reused and expanded in the context of new data or perhaps a more precise methodology.

Key-words: *Climate change, Climate migration, Modeling, R automatization, Big data, Carpathian-Basin*

1. INTRODUCTION AND AIMS

Climate migration is one of the manifestations of climate change when the climate of a given location becomes similar to the climate of another location. It is important and useful to examine the reality of how the climate of a region has changed/is changing in recent decades (Thompson, 2009), how new, non-native plant cultures appear in certain areas (Gómez-Ruiz and Lacher, 2019), and whether these changes are trend-like or oscillating, because these effects must be analyzed and evaluated according to local characteristics. (Meresá et al., 2017). The change in the climate greatly affects the crops that can be grown on the given area, which is why many studies deal with the investigation of this phenomenon (Mabhaudhi et al., 2019; Malhotra, 2017; Reynolds and Ortiz, 2010). The aim of our research was to develop an automatized, parametrizable software tool which can properly identify areas with similar climate characteristics. This new analysis method and data visualization should be able to track climate change in space and time based on the climate similarity of different areas.

By this having the possibility to study the migration of the climate for several places in the Carpathian-basin, taking into account one of the warmest locations of it, Timișoara (Ács et al., 2020). The climate change in Carpathian basin were studied comparing to global climate change and it was expected to have higher temperature increases (Bartholy et al., 2009) and there are studies which aims to determine and quantify the effects of climate change in that region (Rakonczai, 2011).

To carry out the research a large dataset was necessary. Although the effective amount of data used depends on their spatial and temporal resolution, it was necessary to process a very large amount of data, which is unfeasible without automated analysis. After identifying the usable data source, the next step of the research was to read, aggregate and finally compare the meteorological characteristics for each raster cell (location). For this, a test software analysis module had to be developed, the ultimate goal of which is to be able to determine, for every location, the extent to which the different locations of the test area are similar to each other based on their meteorological characteristics. The parameter of the analysis module is not only the location, but also the test period.

¹ Babeş-Bolyai University, Faculty of Geography, Gheorgheni University Extension, 535000 Gheorgheni, zsolt.magyar@ubbcluj.ro

The software module created in this way provide the opportunity to carry out specific analyses. For this purpose, we selected four locations, namely Sâmboleni (RO), Timișoara (RO), Zagreb (HR) and Győr (HU), examining which of them show the greatest climatic similarity with other locations over time, thereby determining how the climate of the selected location "migrated".

2. DATA AND METHODS

2.1. Data

At the beginning we set up several selection criterions. In order to be able to model the migration of the climate, the temporal extent and temporal resolution of the data series were of primary importance, the longer daily data series were preferred. The second selection criterion was the diversity of the data. Based on the experience of our previous researches (Magyari-Sáska, 2021; Magyari-Sáska and Dombay, 2021, 2022), we would definitely prefer those data sources that, in addition to temperature and precipitation, also contain other weather elements (e.g. humidity, number of sunshine hours, etc.), since these also play a significant role in the examination of climate similarity. The third element that was considered in the selection of the data source was the spatial resolution of the dataset.

Examining the freely available raster-based databases, unfortunately, there was not much possibility to choose, because all four examined databases, which covered the area of the Carpathian Basin, had certain deficiencies in order to achieve the research goal. The WorldClim database contains the data aggregated to the level of months (Fick and Hijmans, 2017), in which it only contains the minimum, maximum and average values, which proved to be insufficient from the point of view of this research, and did not fulfill the first criterion I defined. At the same time, the last year of the available data was 2000, so the data of the last 20 years would have been missing.

The next database examined was the Euro-Cordex, which is a climate modeling database (Jacob et al., 2014), raw data is not available, so it is completely unsuitable for carrying out the type of studies that the present research aims to do. Next came ECLIPS 2, which has a very good spatial resolution (Chakraborty et al., 2021), but which is actually based on Euro-Cordex data, so it presents not raw, but processed, different climate scenarios.

In the end, the selected database was the E-OBS, the temporal extent of which is from 1950 to 2021, the temporal resolution is daily, the spatial resolution is 0.1 x 0.1 degrees, which corresponds to approximately 7-8 km in the examined area (Cornes et al., 2018). The metadata includes several meteorological characteristics, such as daily average, minimum and maximum temperature, rainfall, humidity, air pressure, solar radiation and wind speed. The only weakness of this data source was the spatial resolution, but from the point of view of climate analysis, this is not the most significant, a resolution of roughly 60 km² is acceptable. What is a real disadvantage of the database is the incomplete temporal and spatial coverage of the other characteristics besides temperature and precipitation. In many cases, solar radiation and wind speed are not actually available in the database, so we could not use them in the research. Based on temperature and precipitation data, we used the 30 synthetic indicators to characterize the climate including average values and ratio of values in a given interval, such as the ratio of how many days the average daily temperature was between 10 and 20 degrees.

2.2. Methods

In order to be able to compare the climate of different areas a similarity index must be defined which expresses the joint similarity of the different weather characteristics of two aggregation periods.

The similarity index can be created in such a way that we try to condense the standardized values of the weather characteristics into a single value (e.g. using a linear combination), and then designate the difference between these values as the similarity index. In this case, the question can be raised as to what extent the various characteristics participate in the formation of the weather, what is their information content, is it necessary to weight them, and if so, what would these weights be.

The similarity index can be created without combining the weather characteristics into one value. There are several methods to determine the similarity between two vectors, each consisting of several values (in our case, weather characteristics). One of the most well-known is correlation, but many studies use the Jaccard index, the multidimensional Euclidean, Minkowski or Hamming distance (Thant and Shoe Moe, 2020), and cosine similarity (Tan et al., 2005).

We used the latter, since this indicator is often used in data mining (Han et al., 2012) and shows how much the values of the two vectors have the same orientation (Schubert, 2021). By definition, the cosine similarity index is the cosine of the difference between the resulting vectors defined in a multidimensional (the number of dimensions is the same as the number of features in the vectors) space.

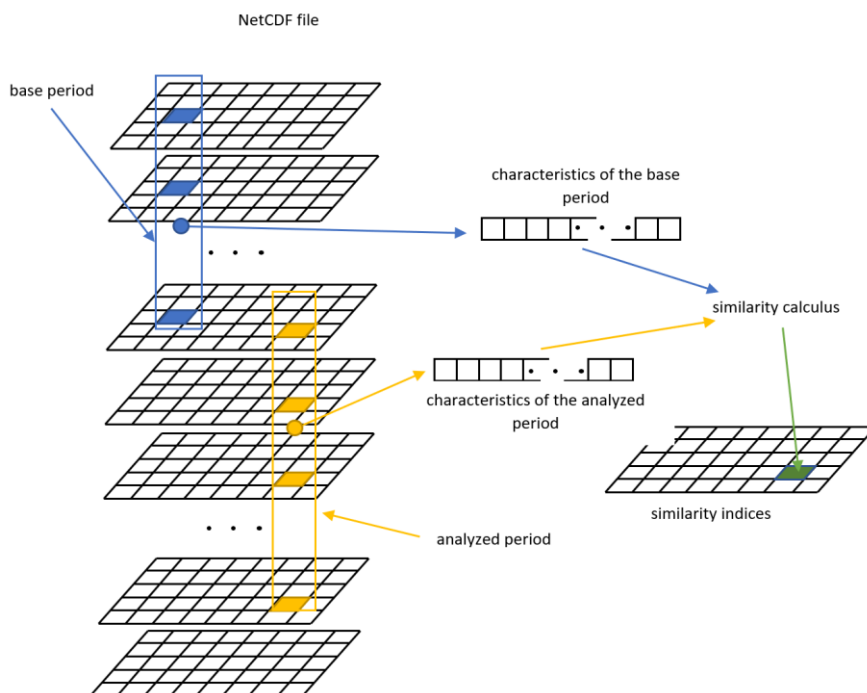


Fig. 1. – Data processing of a NetCDF file for obtaining the similarity value.

The analysis process follows the algorithm shown in **Fig. 1** and it's based on the following steps:

- step 1: a reference location, a reference period which we called the base period, and an examination period are defined. The result of the analysis will show how similar is the climate at different locations during the study period is to the climate of the selected reference location for the base period.
- step 2: for the base period of the reference location, the data of that location are read from the data files, they are aggregated (Kabacoff, 2015) and the 30 indicators that we used are calculated from them.
- step 3: taking the base period into account, the similarity index is calculated for each area unit, this shows how similar the climate was to the reference location in the base period
- step 4: taking the study period into account, the similarity index is calculated for each area unit, thereby showing how similar the climate was to the reference location during the study period, taking into account the climate of the base period.

Based on the data structure and algorithm presented it can be seen that a large amount of data processing is required, and that the analysis itself allows for many parameterizations. It is almost impossible to carry out this research with traditional statistical or geospatial applications through their interactive user interface, since they require continuous human supervision, primarily to set up and

start their repetitive calculations again and again. It was therefore necessary to develop our own analytical toolbox.

One of the most dynamically developing free analysis software of the last decade is R. The command-line application that initially enabled statistical processing (Ihaka and Gentleman, 1996) developed very quickly and gained great popularity among researchers. Today, there are several additional modules for almost every discipline, starting from the life sciences to the fields of geospatial, chemical or remote sensing research and applications.

Since R gives you the opportunity to create your own programmed analysis packages and efficiently manages large data structures, we used this programmable analysis software in this research as well. The created application package can be divided into two parts: the analysis module and the visualization module. We used the following R program packages to create the analysis and data display modules. To manage NetCDF files, we use the `ncdf4` (Pierce, 2021) package. The `rgdal` (Bivand et al., 2022) and `raster` (Hijmans, 2022) program packages were used to manage raster layers, and the `shiny` (Chang et al., 2021) and `shinyjs` (Attali, 2021) packages to create the user interface.

3. RESULTS AND DISCUSSION

The analysis used data aggregated at the annual level. We used the period 1950-1980 as the base period, the climate emerging from the meteorological data of this period was the basis of comparison. For each settlement, we determined the following using the analysis module:

1. the similarity index for each cell based on the climate characteristics of the given settlement using the data between 1950-1980. In the resulting raster layer, a cell value shows how similar the climate of the given area, based on data between 1950-1980, is to the climate of the settlement used, based on data from the same period.

2. the similarity index of each cell based on the meteorological data of five different periods, having as basis for comparison, the climate characteristic of the given settlement in the period 1950-1980. The five examination periods were 1981-1990 / 1991-2000 / 2001-2010 / 2011-2020 and 1990-2000. The first four periods show how the climate has changed in ten-year intervals, while the last study period spans 31 years, just like the base period. Here, based on the 30-year period often used in the study of climate changes, the raster file created for the base period and this 31-year study period serves as the basis for climatic comparisons. In this case a cell value of the raster files obtained as a result, shows how similar the climate of the given area is to the climate of the settlement used for the base period (1950-1980) based on the data of the study period.

In the following map representations, we have marked six categories of similarity: we have depicted the strongest similarity in green, here the value of the similarity index is above 0.998. The four categories that follow use an increasingly lighter shade of blue, where the lower the similarity, the lighter the color is. In these cases, the value difference of the successive similarity categories is 0.002. Areas with a similarity value lower than 0.992 are displayed without coloring.

3.1 Győr as reference location

Based on data from the period 1950-1980, Győr's climate was largely typical of extensive areas of the Carpathian Basin. This settlement is an excellent example for observing the migration of the climate. In the case of the successive decades, it can be clearly seen as if we had blown into the Carpathian basin from the south and south-east (**Fig. 2a**).

In the first decade of investigation, between 1981 and 1990, the number of areas with the greatest similarity in Timișoara region decreases. The area belonging to the highest similarity category is also thinning in the Southern Great Plain of Hungary, and these characteristics are congested to the north from the northern areas of Bosnia and Herzegovina. North of Vienna, in Lower Austria, a small spot also appears, indicating areas with a similarity value higher than 0.998 (**Fig. 2b**).

In the next decade (1991-2000), the impact of this blow will continue to strengthen. The areas in the vicinity of Belgrade that have been until now in the category of the greatest similarity to the climate of the base period, will disappear. This high similarity also disappears from the areas along

the Szolnok, Kiskunfélegyháza and Tompa axes. At the same time, areas with a climate most similar to the climate of Győr's base period appear in the Prekmurje region and the number of areas with these characteristics also increases significantly in the western and northern neighborhoods of Vienna. (**Fig. 2c**).

Between 2001 and 2010, the similarity in most places weakens compared to the climate of the base period. Győr and Vienna are no longer among the locations whose climate is most similar to the climate of the base period. The locations most similar to the climate of the base period can be found in the areas north and south of Vienna. In the north-eastern region of the Carpathian Basin, Satu Mare and its surroundings fall out of the category with the greatest similarity (**Fig. 2d**).

In the last study decade, between 2011-2020, the climate that was typical for Győr and significant areas of the Carpathian Basin in the base period was completely blown out of the inner area of the Carpathian Basin. We only find small spots and islands with the climatic characteristics typical of the base period, such as Prešov, Zalău or Olomuc (**Fig. 2e**). It is also noticeable that outside of the Carpathian basin, in the Eastern parts, the climate of Győr's base period already appears in the period 1991-2000, which extends to larger and larger areas in the following two decades.

3.2. Sâmboleni as reference location

Sâmboleni is a small settlement in the Transylvanian countryside, whose climatic conditions could only be found in three larger areas during the base period. On the one hand, these areas covered the plains of Transylvania and the western Carpathians, but there were similar climatic conditions in the vicinity of the Nógrád and Gömör basins as well. On the western extremities of Hungary, we find similar climate conditions with the base period of Sâmboleni in an even larger area (**Fig. 3a**).

In the next four decades, we can witness the continuous "extinction" of Sâmboleni's climate in the Carpathian Basin. In the period 1981-1990 the areas with the greatest similarity already disappear from Hungary's western part. In the north, the sites in the vicinity of the Nógrád and Gömör basins that belong to the highest similarity category are shrinking, and in Transylvania, these sites are retreating almost exclusively to the Transylvanian plain. In the east, beyond the Carpathian basin, the Pre-Carpathians show similar climatic conditions such as those that characterized Sâmboleni in the base period. In the following decade, between 1991 and 2000 only the climatic conditions of the Gömör basin resemble the climate of the Sâmboleni base period to a large extent. Areas with a high climatic similarity remain in the Transylvanian plain, as in the Pre-Carpathians. The next decade (2001-2010) will bring little change in terms of the similarity of the climatic conditions, the areas in the Târnava ridge that belonged to the highest similarity category will decrease.

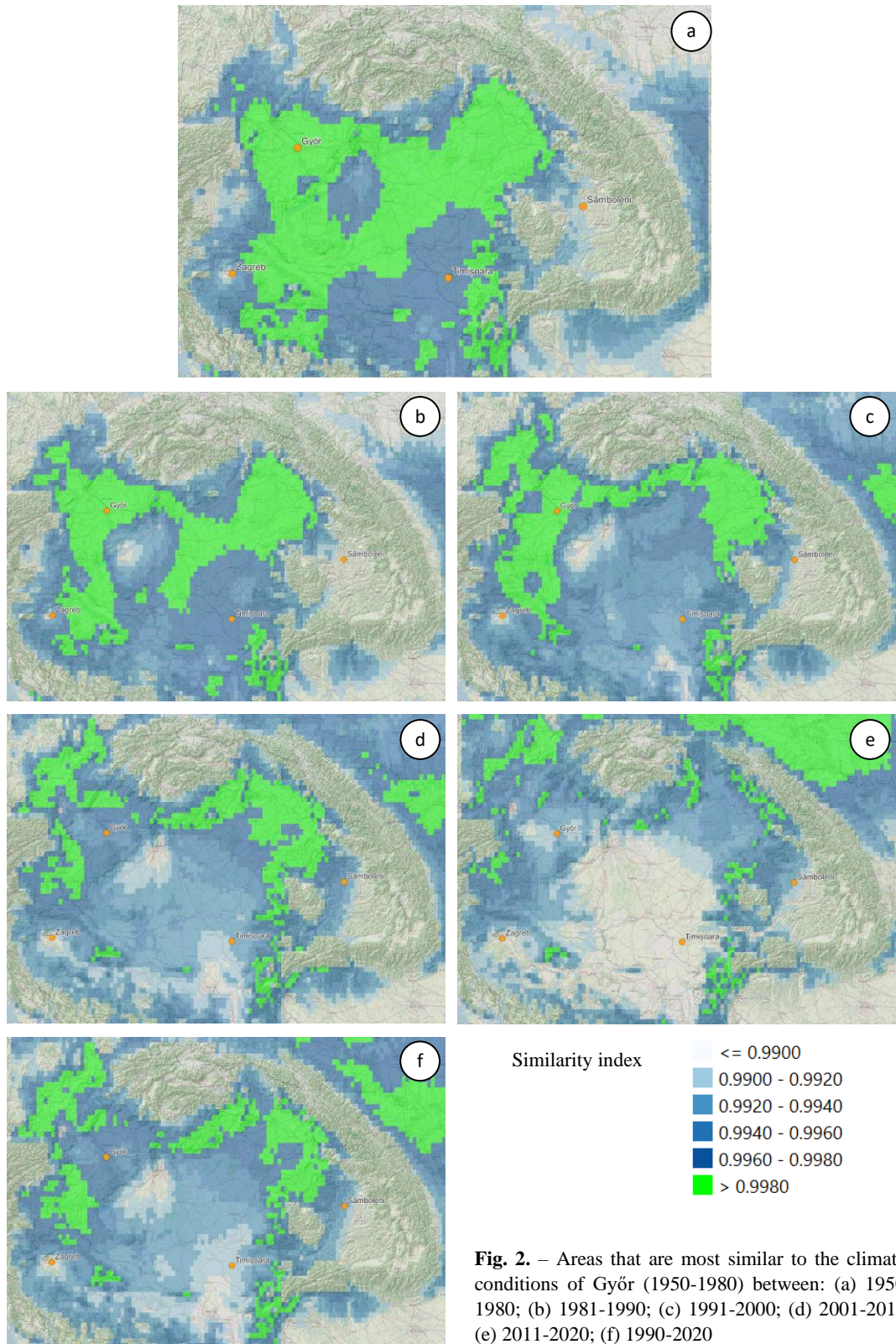
In the last study decade, between 2011-2020, there is already a significant change compared to the climate of the base period. In Transylvania, in the hills of Bistrița-Reghin we find a few more cells that are very similar to the climate of the base period of Sâmboleni. Smaller spots that still have this quality can be found in the north around Râșnov, next to Baia de Arieș, south of Sibiu along the Olt and beyond the Carpathians in the areas of the Pre-Carpathians and Bucovina.

In addition to all of this, it is easy to notice that the climate of Sâmboleni that once characterized the Transylvanian plain has completely disappeared from the Carpathian basin in the last decade. If we look at the climate of the last 30 years, this disappearance is stronger in the northern part of the Carpathian basin and takes place more slowly in the Transylvanian plain (**Fig. 3b**).

3.3. Timișoara as reference location

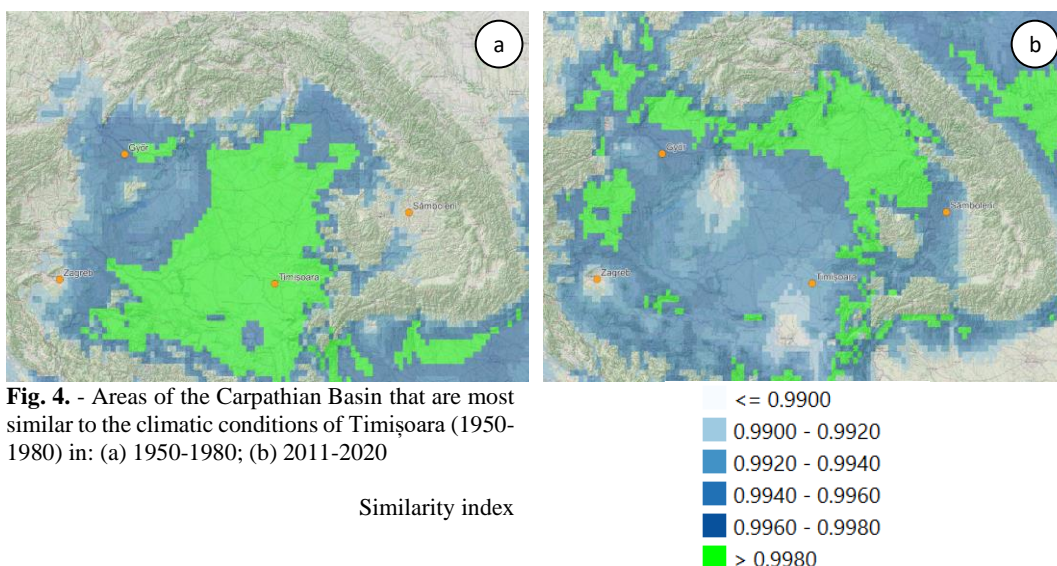
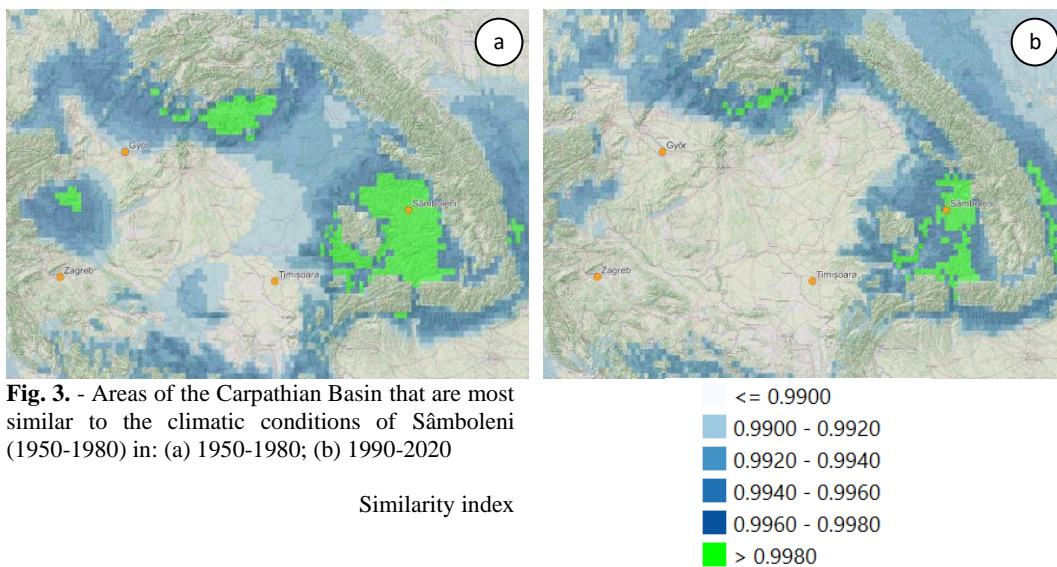
The highest category of similarity indicators calculated for the base period of Timișoara includes the Great Plain, in its eastern extension as far as Satu Mare, the surroundings of Drava and Sava rivers, the surroundings of Komárom, as well as the south Pre-Carpathians (**Fig. 4a**).

In the four consecutive decades of the study period, compared to this base period, we can see the following. There are hardly any changes in the period 1981-1990. The highest similarity value is found in the vicinity of Nyíregyháza and Satu Mare, in the north the area with the highest similarity value is transferred from the vicinity of Komárom to the vicinity of Győr, and in the south beyond the Carpathian basin, the areas of the Oltenian Pre-Carpathians fall into the highest similarity category.



The period 1991-2000 is the period of "expansion". The north-eastern tip of Hungary regains the status of the areas with the greatest similarity, and in the western part of the Carpathian Basin, Győr, Celldömölk, Nagyatád, Bjelovar, Banja Luka, a narrow band appears on the north-south axis, the areas of which have a high similarity with the similarity index calculated for the base period of Timisoara. In the 2001-2010 period, this expansion stalls and the previously unified, connected areas break up. Primarily, the areas of Drava River and Hernád, Timișoara and Cehu Silvaniei, Eger and Kosice, Banja Luka and Doboş come out of the category indicating the greatest similarity.

In the last study decade of 2011-2020, the areas with the highest similarity index show a decrease even more. Primarily, the southern and central parts of the south plain of Hungary and the Danube plain to the east of Pécs lose the status of the highest similarity category. In the south, the climate of the northern slopes of the Southern Carpathians becomes similar to the climate of the base period, in the east, the Moldavian plain and the Hotina ridge are among the areas indicating the highest category of similarity (Fig. 4b).



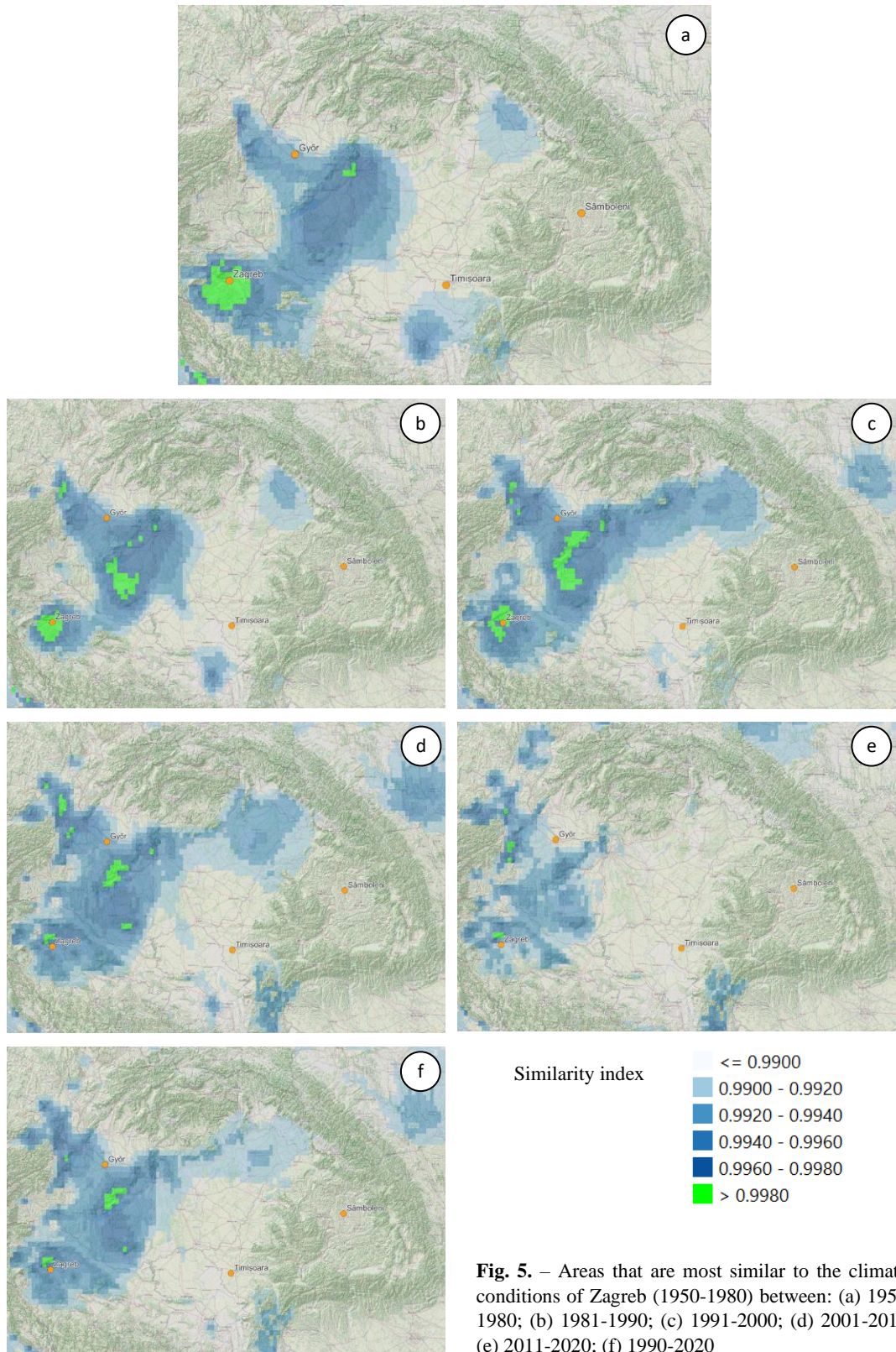


Fig. 5. – Areas that are most similar to the climatic conditions of Zagreb (1950-1980) between: (a) 1950-1980; (b) 1981-1990; (c) 1991-2000; (d) 2001-2010; (e) 2011-2020; (f) 1990-2020

3.4. Zagreb as reference location

The similarity indicators in the highest category calculated for the base period of Zagreb are almost exclusively limited to the surroundings of Zagreb, the Zagreb Basin (**Fig. 5a**). In the period 1981-1990, this area slightly decreases around Zagreb, and a new area appears north of Pécs in the area of the Transdanubia hills, whose similarity index is above 0.998, belonging to the highest similarity category (**Fig. 5b**). In the following decade, between 1991 and 2000, both of the previously mentioned areas migrated a little to the north and even extended in a northerly direction (**Fig. 5c**). In the following decade, the category with the greatest similarity to the base period almost completely disappears near Zagreb, but it appears north of Pécs and Vienna, as well as in the Bakony in the form of a small island (**Fig. 5d**). In the last study period, between 2011-2020, these small islands continue to shrink, and the climate of Zagreb's base period practically disappears from the Carpathian Basin (**Fig. 5e**).

4. CONCLUSIONS

In this research we examined how similar the periods 1950-1980, 1981-1990, 1991-2000, 2001-2010, 2011-2020 and 1990-2020 are to the climate experienced in each settlement between 1950-1980 (base period). We observed where the highest similarity category (above a similarity index of 0.998) appeared in the test periods. In the case of peripheral settlement - Zagreb, the former climate of it practically disappears from the Carpathian basin, and cannot be found in other areas. In the case of the other settlements, we can see primarily a migration, the direction of which basically takes place in the north, north-east direction. It can be clearly observed that in several cases, areas belonging to the highest similarity category also appear beyond the Eastern and North-Eastern Carpathians.

Based on the figures in the base period, the climate of Győr and Timisoara was the most typical among the investigated locations in the Carpathian Basin. Looking at the period 1990-2020 and taking into account the areas that have the greatest similarity compared to the base period, we can say that the climate of Timisoara's base period can still be found to the greatest extent in the Carpathian basin. This is the only settlement whose base period characteristics are present in a larger area today than in the 1950-1980 period.

Examining in percentage terms the extent on which the climate of the base period can be found in the Carpathian Basin in the last 30 years compared to the base period, we can see that the largest decrease occurs in the case of Zagreb. Compared to the base period, the areas which have very similar climate to the base period's is less than 32%. In case of Győr, this number is not much higher, around 38%, and in the case of Sâmboleni it does not reach 40%. As already mentioned, the climate of Timișoara is extending, considering the last 30 years, 105% of the original area has the climate of Timișoara's base period.

Although the present research is a first attempt in assessing the migration of the climate, it clearly shows that we can encounter at least two different situations. There are cases when a specific climate completely disappears from a given region, and there are situations when it conquers larger areas - even if in other locations.

ACKNOWLEDGMENT. The presented research was supported by the DOMUS scholarship program of the Hungarian Academy of Sciences.

R E F E R E N C E S

- Ács, F., Zsákai, A., Kristóf, E., Szabó, A.I., Breuer, H. (2020), Human thermal climate of the Carpathian Basin, *International Journal of Climatology*, 41, S1, E1846–E1859, DOI: 10.1002/joc.6816
- Attali, D. (2021). shinyjs: *Easily Improve the User Experience of Your Shiny Apps in Seconds*. R package version 2.1.0. <https://CRAN.R-project.org/package=shinyjs>
- Bartholy, J., Pongracz, R., Torma, Cs., Pieczka, I., Kardos, P., Hunyady, A. (2009), Analysis of regional climate change modelling experiments for the Carpathian Basin, *International Journal of Global Warming*, 1,(1-3) 238-252

- Bivand, R., Keitt, T., Rowlingson, B. (2022). *rgdal: Bindings for the 'Geospatial' Data Abstraction Library*. R package version 1.5-29., <https://CRAN.R-project.org/package=rgdal>
- Chang, W., Cheng, J., Allaire, J.J., Sievert, C., Schloerke, B., Xie, Y., Allen, J., McPherson, J., Dipert, A., Borges, B. (2021). *shiny: Web Application Framework for R*. R package version 1.7.1. <https://CRAN.R-project.org/package=shiny>
- Cornes, R., G. van der Schrier, E.J.M. van den Besselaar, and P.D. Jones. (2018), An Ensemble Version of the E-OBS Temperature and Precipitation Datasets, *J. Geophys. Res. Atmos.*, 123, doi:10.1029/2017JD028200"
- Debojyoti Chakraborty, D., Dobor, L., Zolles, A., Hlásny, T., Schueler, S. (2021), High-resolution gridded climate data for Europe based on bias-corrected EURO-CORDEX: The ECLIPS dataset, *GeoScience Data Journal*, 8/2, 121-131, <https://doi.org/10.1002/gdj3.110>
- Fick, S.E., Hijmans, R.J. (2017), WorldClim 2: new 1-km spatial resolution climate surfaces for global land areas, *International Journal of Climatology*, 37/12, 4302-4315, <https://doi.org/10.1002/joc.5086>
- Gómez-Ruiz, E.P., Lacher Jr., T.E. (2019), Climate change, range shifts, and the disruption of a pollinator-plant complex, *Scientific Reports*, 9, 14084
- Han, J., Kamber, M., Pei, J. (2012), *Data Mining: Concepts and Techniques*, Elsevier, DOI: 10.1016/C2009-0-61819-5
- Hijmans, R.J. (2022). *raster: Geographic Data Analysis and Modeling*. R package version 3.5-15. <https://CRAN.R-project.org/package=raster>
- Ihaka, R., Gentleman, R. (1996), R: A Language for Data Analysis and Graphics, *Journal of Computational and Graphical Statistics*. 5 (3): 299–314. DOI:10.2307/1390807.
- Jacob, D., Petersen, J., Eggert, B. et al. (2014) EURO-CORDEX: new high-resolution climate change projections for European impact research. *Regional Environmental Change*, 14, 563–578 <https://doi.org/10.1007/s10113-013-0499-2>
- Kabacoff, R.I. (2015), *Aggregation and Restructuring data in R in Action*, Data Analysis and Graphics with R, Manning Publications, ISBN 9781935182399, 472
- Mabhaudhi, T., Chimonyo, V.G.P., Hlahla, S. (2019), Prospects of orphan crops in climate change. *Planta* **250**, 695–708. <https://doi.org/10.1007/s00425-019-03129-y>
- Magyari-Sáska, Z., Dombay, Ş. (2022) Experimental Method to Assess the Looseness or Compactness in Climate Changing for Several Major Cities of Hungary. 2022 "Air and Water – Components of the Environment" Conference Proceedings, Cluj-Napoca, Romania, p. 116-127, DOI: 10.24193/AWC2022_12
- Magyari-Sáska, Z., Dombay, Şt. (2021) Preferential Attachment in Modeling Climate Changes. Test Location: Miercurea-Ciuc, Romania. 2021 "Air and Water – Components of the Environment" Conference Proceedings, Cluj-Napoca, Romania, p. 159-168, DOI: 10.24193/AWC2021_15.
- Magyari-Sáska, Z. (2021), Building and Exploring Network Data Model for a Season Level Climate Change Study for Five Large Cities in Hungary, *Geographia Technica*, 16/2, 183-192, doi: 10.21163/GT_2021.162.15
- Malhotra, S.K. (2017) Horticultural crops and climate change: A review, *Indian Journal of Agricultural Sciences*, 87(1), 12-22
- Meresa, H.K., Romanowicz, R.J., Napiorkowski (2017), Understanding changes and trends in projected hydroclimatic indices in selected Norwegian and Polish catchments, *J.J. Acta Geophys.* (2017) 65: 829. <https://doi.org/10.1007/s11600-017-0062-5>
- Pierce, D. (2021). *ncdf4: Interface to Unidata netCDF (Version 4 or Earlier) Format Data Files*. R package version 1.19. <https://CRAN.R-project.org/package=ncdf4>
- Rakonczi, J. (2011), Effects and Consequences of Global Climate Change in the Carpathian Basin, in *Climate Change, Geophysical Foundation and Ecological Effects*, DOI 10.5772/915
- Reynolds, M.P., Ortiz, R (2010), Adapting Crops to Climate Change: a Summary, in *Climate Change and Crop Production*, CAB International
- Schubert, E. (2021). A Triangle Inequality for Cosine Similarity. In: *Similarity Search and Applications. SISAP 2021. Lecture Notes in Computer Science*, vol 13058. Springer, Cham. https://doi.org/10.1007/978-3-030-89657-7_3
- Tan PN, Steinbach M, Kumar V (2005). *Introduction to Data Mining*. ISBN 0-321-32136-7
- Thant A.A., Soe Moe, A. (2020) Euclidian, Manhattan and Minkowski Distance Methods for Clustering, *International Journal of Scientific Research in Science, Engineering and Technology*, 7/3, doi: 10.32628/IJSRSET2073118
- Thompson D.J., (2009), Shifts in season, *Nature*, 457, 7228
- ***, NetCDF Users Guide v1.1, <https://docs.unidata.ucar.edu/nug/current/>

Joint Distribution And Coincidence Probability Of The Number Of Dry Days And The Total Amount Of Precipitation In Southern Sumatra Fire-Prone Area

Sri NURDIATI ¹, Mohamad Khoirun NAJIB ¹, and Achmad Syarief THALIB ¹

DOI: 10.21163/GT_2022.172.10

ABSTRACT:

El Niño Southern Oscillation (ENSO) and Indian Ocean Dipole (IOD) can affect the increase in rainfall intensity and the number of dry days, also known as dry spells that can cause drought and increase the potential for forest fires. This study examines the effect of ENSO and IOD conditions on the joint distribution of the number of dry days and total precipitation in a fire-prone area in southern Sumatra, Indonesia. The joint distribution is constructed using rotated copulas from several families, including Gaussian, student's t, Clayton, Gumbel, Frank, Joe, Galambos, BB1, BB6, BB7, and BB8. Fire-prone areas are defined using k-mean clustering, while the copula parameters are estimated using the inference of function for margins (IFM) method. Based on the peak of joint probability density functions (PDFs), ENSO and IOD conditions had a significant effect in the dry season but had no significant effect in the rainy season. The peak of joint PDFs is getting to the dry-dry conditions when the ENSO and IOD indexes increase in the dry season. However, based on coincidence probability, ENSO conditions still influence the joint distribution between the number of dry days and total precipitation during the rainy season but not with IOD conditions. The lower the ENSO index, the higher the probability of wet conditions co-occurring in the number of dry days and total precipitation. Meanwhile, ENSO and IOD conditions significantly affect the coincidence probability between the number of dry days and total precipitation. Moderate-Strong El Niño has the most considerable coincidence probability of 68.5%, followed by Positive IOD with 62.6%. The two conditions had similar effects on the joint distribution of the number of dry days and total precipitation. Moreover, the association between the number of dry days and the total precipitation was stronger in the dry season than in the rainy season.

Key-words: *Bivariate copula, Exceedance probability, Rainfall, Risk assessment, Wildfire.*

1. INTRODUCTION

Indonesia - an archipelagic country on the equator flanked by two continents (Asia and Australia) and two oceans (Indian and Pacific Oceans)- has varied climatic conditions. These climatic conditions are influenced by the surrounding oceans, locally and globally. The high precipitation amount in almost all provinces is made possible by an ample supply of water, which comes from the surrounding sea (Nuryanto & Badriyah, 2014). Therefore, local sea conditions will affect the climatic conditions of the surrounding islands. Besides local sea conditions, climatic conditions are also influenced by global ocean conditions around Indonesia, such as the El Niño Southern Oscillation (ENSO) in the Pacific Ocean and the Indian Ocean Dipole (IOD) in the Indian Ocean (Kurniadi et al., 2021).

ENSO is an ocean-atmosphere interaction centered in the equatorial Pacific Ocean that has a global impact on Earth's system (McPhaden et al., 2006). ENSO causes Indonesian seas to be colder during El Niño events and warmer during La Niña events, resulting in increased precipitation during La Niña and decreased precipitation during El Niño (Nur'utami & Hidayat, 2016). Meanwhile, IOD

¹Department of Mathematics, Faculty of Mathematics and Natural Sciences, IPB University, Bogor, Indonesia,

*Corresponding author: nurdiati@apps.ipb.ac.id; mkhourun_najib@apps.ipb.ac.id;
achmad_st@apps.ipb.ac.id

is a phenomenon indicated by differences in sea surface temperature anomalies in the western and eastern parts of the Indian Ocean.

The positive phase of IOD causes a decrease in sea surface temperature in Indonesia, the same as El Niño, accompanied by a reduction in precipitation (Khalidun et al., 2018). Contrary, the negative phase of IOD is like La Niña conditions in the Pacific Ocean. ENSO and IOD phases in each year are not always the same. However, the impact will be more significant if ENSO and IOD are simultaneously in a warm (or cold) phase. For example, the droughts in 1997 and 2015 coincided with ENSO being in an El Niño phase and IOD being in a positive phase (Avia & Sofiati, 2018).

El Niño and positive IOD, which reduce precipitation, indirectly contributed significantly to drought occurrence in several regions in Indonesia, although with different strengths in each area (Ummenhofer et al., 2013). Drought reduces the water content of vegetation, loss of water content in extensive woods, leading to plant death, and increased fire potential (Suharjo & Velicia, 2018). Therefore, precipitation is urgently needed so vegetation's water content can remain within normal limits. The prolonged drought in 1997 caused by the late rainy season due to El Niño and positive IOD climate variability of 1997/1998 has triggered widespread forest fires in the equatorial regions of Sumatra and Kalimantan (Nikonovas et al., 2022).

Previous research has found that forest fires in Kalimantan are more sensitive to ENSO than IOD. Meanwhile, the effect of IOD on forest fires was more pronounced in the southern part of Sumatra because it is located near the Indian Ocean (Nurdiati et al., 2021). Moreover, although it has been mentioned that the lack of precipitation can be a triggering factor for forest fires, the total precipitation is insufficient to characterize forest fires in Indonesia. Other indicators such as the number of dry days, i.e., the number of days with less than 1 mm of precipitation per day (Brown et al., 2010), can better characterize forest fires than total precipitation. Although many experts have investigated the effect of ENSO and IOD on precipitation in Indonesia (Lestari et al., 2018), there has been limited research examining the joint distribution of the number of dry days and total precipitation under different ENSO and IOD phase conditions.

The copula function is the most common method for constructing a joint distribution. The copula is a statistical method that can describe the relationship between variables that is not too tight on distribution assumptions and can clearly show dependency relationships at extreme points (Singh et al., 2020). This method can describe the dependency structure between variables with different marginals and model their tail dependencies (Caraka et al., 2016). Copula has been widely used to address uncertainties in coincidence probability (Yang et al., 2020), conditional probability (H. W. Li et al., 2021), and joint return period analysis (Naeni et al., 2021). However, according to a systematic literature review, the copula is still limited to being applied in forest fire analysis (Najib et al., 2021).

According to the background presented, this study analyzes the joint distribution of the number of dry days and total precipitation in fire-prone areas in southern Sumatra using the copula function. This study begins by identifying fire-prone areas in Sumatra using k-mean clustering based on the burned area dataset. In the specified fire-prone areas, the number of dry days and total precipitation were extracted from 1981 to 2020. After that, the copula function was employed to construct the joint distribution of the number of dry days and total precipitation. The joint distribution is constructed based on the seasonality and phases of ENSO and IOD to analyze the effect of these conditions on the dependencies and coincidence probability. The study results are expected to improve understanding of the dependencies between the variables studied and become an initial provision for further analysis of extreme events such as floods, droughts, and forest fires in the study area.

2. STUDY AREA AND DATASETS

This study focused on southern Sumatra, located at 98°E-107.5°E and 1.5°S-6°S (**Fig. 1**). This study will use four types of data: precipitation, Niño 3.4 index, dipole mode index, and burned area datasets. Precipitation data was derived from Climate Hazards Group Infra-Red Precipitation with Station data (CHIRPS) with a spatial resolution of 0.25°×0.25° in daily and monthly temporal resolutions from 1981 to 2020. Total precipitation data were taken from monthly data, while dry spell

data were extracted using daily data. Moreover, The Niño 3.4 and dipole mode index is time-series data obtained from the average of Hadley Center Sea Ice and Sea Surface Temperature (HadISST1) data. The data was downloaded from the Physical Sciences Laboratory (PSL) of the National Oceanic and Atmospheric Administration (NOAA) from 1981 to 2020. Both are using 1981-2010 as an anomaly in the index calculation. The burned area data uses the fourth generation of the Global Fire Emission Database (GFED4.1s) from 1997-2016 to define fire-prone areas. The GFED4.1s dataset provides monthly global burned area data with a spatial resolution of $0.25^\circ \times 0.25^\circ$ in Hierarchical Data Format version 5 (HDF5).

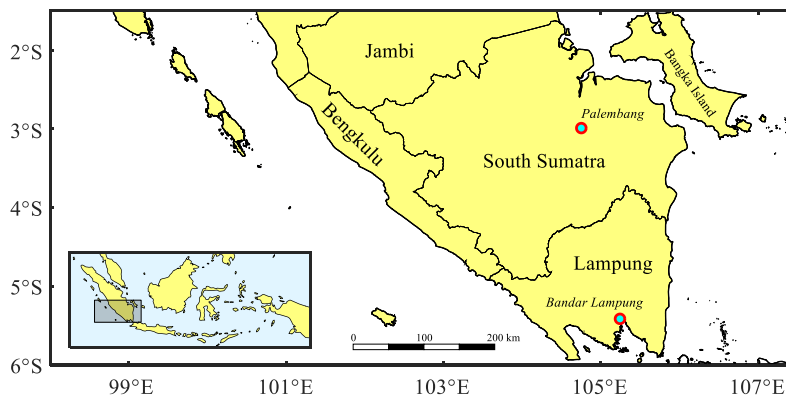


Fig. 1. Location of the southern part of Sumatra on a map of Indonesia

3. METHODS

3.1. k-Means Clustering

This study begins by collecting data from several sources mentioned (*data integration*), then defining fire-prone areas in southern Sumatra using *k*-mean clustering. After that, the number of dry days and total precipitation are extracted and aggregated (*data reduction*). Thus, the time series of the number of dry days and total precipitation are obtained, then partitioned based on seasonality, ENSO, and IOD conditions.

K-means clustering is the most common and popular unsupervised algorithm for clustering. The *k*-means objective can be written in a minimization problem given by

$$\operatorname{argmin}_{\mu_j} \sum_{j=1}^k \sum_{x_j \in D_j'} \|x_j - \mu_j\|^2 \quad (1)$$

where μ_j represent the mean of the *j*-th cluster and D_j' denotes the subdomain of the dataset associated with the *j*-th cluster (Brunton & Kutz, 2022). We use standardization before clustering to provide better, more efficient, and more accurate results (Mohamad & Usman, 2013).

3.2. Correlation Coefficient

Correlation analysis measures the strength of the relationship between two variables, called a correlation coefficient. Three popular correlation coefficients are Pearson (*r*), Spearman (ρ), and Kendall (τ) correlation coefficients (Hauke & Kossowski, 2011). The existence of a correlation between variables is a sufficient condition for copula-based analysis. Because the copula used mostly has a relationship with the Kendall correlation, this study uses the Kendall correlation coefficient to examine the relationship between variables.

3.3. Copula-Based Joint Distribution

The copula is a function that *couples* multivariate distribution functions with one-dimensional marginal distribution functions. In another sense, the copula is a multivariate distribution function whose one-dimensional margin is uniform at the interval (0,1). The copula function can describe dependencies between variables, which is an important step in connecting one climate information to another.

The advantage of the copula function is that each variable is joined by its marginal distribution instead of its original value. Unlike other multivariate distributions, the copula function is flexible in the type of marginal distribution used and does not require input variables to share a similar distribution. Let H be a joint distribution function with F and G as edges, then there is a copula C such that for every $x, y \in R$, so that

$$H(x, y) = C(F(x), G(y)) \quad (2)$$

If F and G are continuous cumulative distribution functions (CDFs), then C is unique (Nelsen, 2006). Assuming the variables are continuously distributed, then C is unique and the joint density function $h(x, y)$ can be written as

$$h(x, y) = c(F(x), G(y)) \cdot f(x) \cdot g(y) \quad (3)$$

where

$$c(F(x), G(y)) = \frac{\partial^2}{\partial F(x) \partial G(y)} C(F(x), G(y)) \quad (4)$$

where f and g are continuous probability density functions (PDFs) and c is a copula density.

3.3.1. Parameters Estimation

This study uses the inference of function for margin (IFM) method to estimate the copula parameters. The first step of this method is to estimate the distribution function used as edges for the copula. There are three continuous distribution functions used, namely generalized extreme value (GEV), normal (N), and lognormal (LN). The fittest distribution function was selected and tested using the Anderson-Darling hypothesis test. After obtaining the fittest distribution function, the second step of the IFM method is estimating the copula parameters. Different copulas have their own characteristics in describing the dependency structure of a pair of variables. There are 11 copulas considered to investigate the dependency structure between the two variables, including Gaussian, Student t, Clayton, Gumbel, Frank, Joe, Galambos, BB1, BB6, BB7, and BB8. The fittest copula function was selected and tested using the Cramer-von Mises hypothesis test (Najib et al., 2022b). Moreover, the first and second steps of the IFM method aim to find the parameter values by maximizing the log of the likelihood of each function. Code for fitting parameter values of univariate distribution and copula functions is available on the GitHub page: <https://github.com/mkchoirun-najiboi/mycopula>.

3.3.2. Coincidence Probability

By dividing the three parts of each edge, each variable's dry, normal, and wet conditions can be determined. Coincidence probability is the probability of dry, normal, and wet conditions of two variables simultaneously, whether the conditions are the same or not (Najib et al., 2022a). It is called synchronous probability if the two conditions are the same (wet-wet, normal-normal, and dry-dry). Conversely, if the conditions are different (wet-normal, dry-wet, etc.), then it is called asynchronous probability (Fig. 2).

ww	nw	dw
wn	nn	dn
wd	nd	dd

Fig. 2. Illustration of the coincidence probability of the number of dry days (x) and total precipitation (y): synchronous probability with blue shading and otherwise asynchronous probability. The subscripts w, n and d mean wet, normal and dry conditions.

4. RESULTS AND DISCUSSION

4.1. Southern Sumatra Fire-Prone Areas

The definition of fire-prone areas using k-mean clustering is done using several choices of the number of clusters. Based on several experiments, clustering with 8 clusters gives the lowest RMSE value compared to the others Fig. 3a. The RMSE in question is the difference between the time series on the data burned area in the fire-prone area and the data burned area in the study area. Fire-prone areas are defined by removing clusters that have low hotspot characteristics. Based on Fig. 3b, clusters A and C from the 8-mean clustering results have low hotspot characteristics.

The results of clustering on the burned area data using 8-means clustering are shown in Fig. 3c. Each color represents eight different clusters named with the letters A to H to avoid misunderstanding if given a name based on numbers. Fire-prone areas are defined by eliminating clusters with low burning area characteristics. Fig. 3d shows the maximum value of the burn fraction in a month that has occurred in an area of $0.25^{\circ} \times 0.25^{\circ}$. The fire-prone areas are focused on three districts in South Sumatra province: Ogan Komering Ilir, Banyuasin, and Musi Banyuasin. The most considerable burn fraction reached 78.6% in the Ogan Komering Ilir district in October 1997. Based on Fig. 3b, the clusters assessed as not prone to fire are clustered C and A, so the other clusters are designated fire-prone areas.

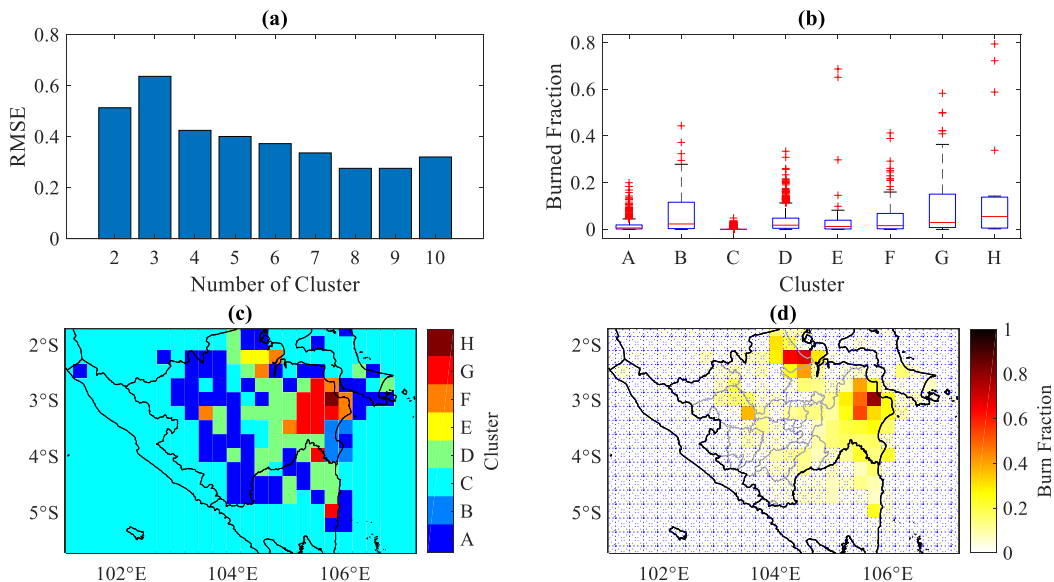


Fig. 3. Definition of fire-prone areas in southern Sumatra: (a) RMSE value from the results of clustering from several choices of the number of clusters, (b) 8-means clustering results (cluster characteristics), (c) 8-means clustering results (cluster location) and (d) maximum burn fraction value for each area.

The area covered by the blue dotted box is the area removed from the fire-prone area. The burned area, precipitation, and the number of dry days data are aggregated to obtain the time series of each data using this fire-prone area.

4.2. Correlation Analysis

This section determines which of the cumulative monthly, 2-monthly, and 3-monthly number of dry days and total precipitation data provides the highest correlation to the burned area data. **Table 1** shows the Kendall correlation value for each condition. In the total rainfall data, the Kendall correlation coefficient shows that the 2-month cumulative variable provides the highest correlation. Meanwhile, the 3-month cumulative variable gives the highest correlation on the number of dry days. Therefore, 2-month and 3-month cumulative variables were selected for total precipitation and the number of dry days data, respectively.

Table 1.

Pearson, Spearman, and Kendall correlation values between climate indicators (the number of dry days and total precipitation) and burned area.

Pair variables	Cumulative Variable		
	1-month	2-month	3-month
Number of dry days and burned area	58.8%	67.0%	67.3%
Total precipitation and burned area	54.6%	63.6%	57.2%

The existence of sufficient correlation is a requirement for using copula-based analysis. The copula parameter has a close relationship with the Kendall- τ correlation coefficient. Therefore, the Kendall- τ correlation coefficient between the variables that have been partitioned by season and phase of ENSO and IOD needs to be considered (**Table 2**).

There are two seasons to consider, i.e., the rainy (Nov-Apr) and dry (May-Oct) seasons. Meanwhile, four ENSO conditions were considered: La Niña (Nino Index ≤ -0.5), Normal ($-0.5 < \text{Nino Index} < 0.5$), weak El Niño ($0.5 \leq \text{Nino Index} < 1$), and moderate-strong El Niño (Nino Index ≥ 1 , for simplicity, will be called strong El Niño). Furthermore, the three IOD conditions consisted of Negative IOD (DMI ≤ -0.4), Neutral IOD (to differentiate from “Normal” terms in ENSO conditions, $-0.4 < \text{DMI} < 0.4$), and Positive IOD (DMI ≥ 0.4).

Table 2.

Kendall- τ correlation coefficient between the number of dry days and total precipitation under different ENSO and IOD conditions.

Season	ENSO Conditions				IOD Conditions		
	<i>La Niña</i>	<i>Normal</i>	<i>Weak El Niño</i>	<i>Strong El Niño</i>	<i>Negative</i>	<i>Neutral</i>	<i>Positive</i>
Rainy	-33.4%	-31.6%	-31.2%	-48.8%	-30.8%	-35.8%	-51.4%
Dry	-59.2%	-65.1%	-76.8%	-81.9%	-35.0%	-66.8%	-84.2%

The Kendall- τ correlation coefficient between the number of dry days and total precipitation has a negative relationship, with the lowest correlation being -30.8% and the highest being -84.2%. The strength of the correlation of each pair-variable ranged from moderate to very strong. Thus, all pair variables can be analyzed using the copula function.

4.3. Parameters Estimation

4.3.1. Distribution Functions

The first step in copula-based joint distribution analysis using the IFM method is to estimate the univariate distribution function of each edge. **Tables 3** and **4** show the fittest distribution functions of the number of dry days and total precipitation in the rainy and dry seasons, respectively. The Anderson-Darling hypothesis test was employed to test the suitability of the distribution. The null hypothesis of this test is that the data comes from a population spread on the selected distribution function. With a p -value of more than the 5% significance level, each of the selected distributions was

in accordance with the data because the hypothesis test failed to reject the null hypothesis. Thus, each selected distribution function can be used as an edge for constructing the copula function.

Table 3.
Fittest distribution functions (i.e., Generalized Extreme Value/GEV, Normal, or Log Normal/LN) with the p-value of the Anderson-Darling hypothesis test (rainy season).

	ENSO Conditions				IOD Conditions		
	<i>La Niña</i>	<i>Normal</i>	<i>Weak El Niño</i>	<i>Strong El Niño</i>	<i>Negative</i>	<i>Neutral</i>	<i>Positive</i>
Number of dry days	GEV (81.7%)	GEV (94.8%)	GEV (85.0%)	GEV (59.7%)	Normal (96.1%)	GEV (73.2%)	GEV (53.4%)
Total Precipitation	LN (74.8%)	LN (84.7%)	GEV (86.7%)	GEV (78.9%)	Normal (88.5%)	Normal (47.2%)	GEV (60.0%)

Table 4.
Fittest distribution functions (i.e., Generalized Extreme Value/GEV, Normal, or Log Normal/LN) with the p-value of the Anderson-Darling hypothesis test (dry season).

	ENSO Conditions				IOD Conditions		
	<i>La Niña</i>	<i>Normal</i>	<i>Weak El Niño</i>	<i>Strong El Niño</i>	<i>Negative</i>	<i>Neutral</i>	<i>Positive</i>
Number of dry days	GEV (86.3%)	GEV (64.2%)	GEV (60.7%)	Normal (27.9%)	LN (71.2%)	GEV (52.1%)	Normal (8.7%)
Total Precipitation	Normal (99.4%)	Normal (99.1%)	GEV (68.9%)	GEV (96.6%)	GEV (99.9%)	GEV (95.3%)	LN (77.2%)

4.3.2. Copula Functions

Some copula functions, such as Clayton, Gumbel, and Joe, can only be constructed on variables that have a positive relationship. By reconsidering **Table 2** that the relationship between the two variables is negative, a rotated copula is needed to obtain a copula function with a negative relationship. Three forms of rotation will be applied, namely 90, 180, and 270 degrees:

$$C_{90^\circ}(u, v|\theta) = v - C(1 - u, v | -\theta) \tag{5}$$

$$C_{180^\circ}(u, v|\theta) = u + v - 1 + C(1 - u, 1 - v|\theta) \tag{6}$$

$$C_{270^\circ}(u, v|\theta) = u - C(u, 1 - v | -\theta) \tag{7}$$

Table 5 shows the fittest copula function with the p-value of the Cramer-von Mises hypothesis test. With a p-value of more than 5% significance level, each of the selected copula functions was appropriate because the hypothesis test failed to reject the null hypothesis. Thus, each chosen copula function can be used to construct the joint distribution between the number of dry days and total precipitation in each condition.

Table 5.
Fittest copula functions with the p-value of the Cramer-von Mises hypothesis test.

Season	ENSO Conditions				IOD Conditions		
	<i>La Niña</i>	<i>Normal</i>	<i>Weak El Niño</i>	<i>Strong El Niño</i>	<i>Negative</i>	<i>Neutral</i>	<i>Positive</i>
Rainy	Joe-90° (53.6%)	BB7-270° (63.6%)	Gumbel-270° (60.3%)	BB8-270° (59.2%)	Clayton° (76.6%)	Galambos-90° (37.3%)	BB8-270° (43.4%)
Dry	Joe-270° (70.6%)	BB1-90° (59.9%)	Gumbel-90° (72.4%)	Frank-270° (64.3%)	Joe-270° (77.5%)	BB8-270° (60.8%)	Frank° (35.4%)

With a variety of copula functions that have been developed and widely used, various characteristics of the relationship between variables can be handled by the copula (Z. Li et al., 2020). As in **Table 5**, each copula function formed for each condition varies from Clayton to BB7 copulas. The various functions of the copula can cope with different relationship behaviors, such as joint behavior in extreme or tail regions.

4.4. Joint Density Functions

After selecting the distribution and copula functions that can represent the data, the joint density function is calculated using Eq. 4, then visualized using a contour plot for each ENSO (**Fig. 4**) and IOD (**Fig. 5**) conditions. Contour levels have been equalized for each condition so that each can be compared with the others. In each plot, nine square areas show each combination of coincidence probability areas.

Based on **Fig. 4**, each ENSO condition in the rainy season has no significant effect on the joint distribution of the number of dry days and total precipitation. This can be seen from the dashed line, which is the peak of the joint probability density functions (PDFs). The peak of joint PDFs in the rainy season does not experience a significant shift and is around normal to wet, with dry days of about 20 days per 3-month and total precipitation of around 600 mm per 2-month. However, some values become outliers and lie in dry conditions during Weak El Niño and Strong El Niño. This outlier occurred in November and December, indicating that there was a delay in the arrival of the rainy season or the prolongation of the dry season during El Niño.

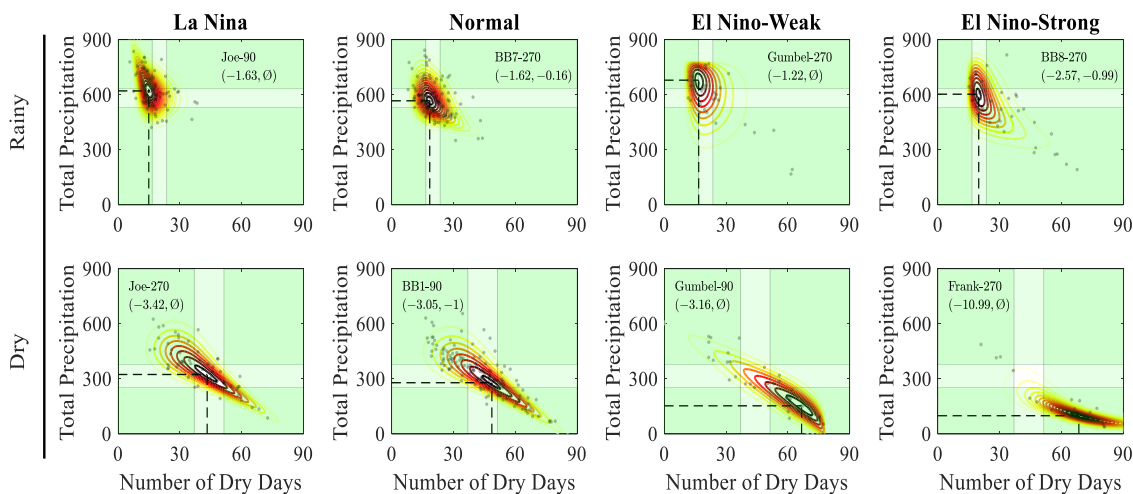


Fig. 4. Contour plot of joint density function for each ENSO condition in the rainy and dry seasons.

Meanwhile, the opposite happened for each ENSO condition in the dry season. The effect of the ENSO condition is discernible from the peak of joint PDFs movement in each condition. The peak of joint PDFs is getting to the dry-dry area when the ENSO index increases. The strong El Niño condition with the highest ENSO index causes the peak of joint PDF to be at the driest state compared to other ENSO conditions in dry seasons, with rainfall intensity of 99 mm in 2-month and the number of dry days of as much as 68.4 days in 3-month.

As before, based on **Fig. 5**, each IOD condition in the rainy season does not significantly affect the joint distribution of the number of dry days and precipitation. In the dry season, it is seen that there is an influence of IOD conditions which makes the peak of joint PDFs of each condition increasingly enters the dry-dry area as the IOD index increases. Positive IOD conditions with the highest IOD index cause the peak of joint PDF to be in the driest state. The peak of joint PDF has a rainfall intensity of 121.5 mm in 2-month and the number of dry days of as much as 65.3 days in three months.

Based on **Figs. 4** and **5** in the dry season, Positive IOD conditions and Strong El Niño have similar effects on the joint PDFs of the number of dry days and total precipitation. Both PDF joints are relatively in dry-dry condition with little probability in normal-dry condition. In contrast, the joint PDFs during Weak El Niño conditions still touch normal-normal conditions, although the peak of the joint PDF is in dry-dry conditions.

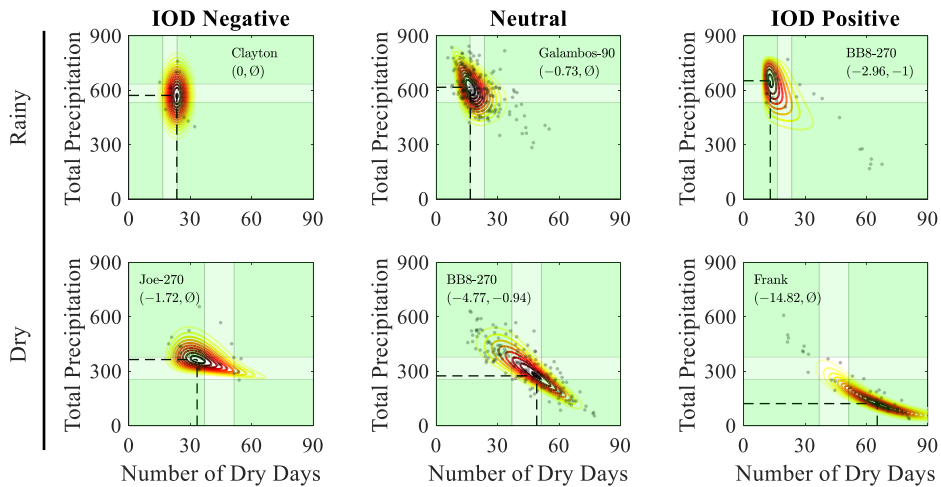


Fig. 5. Contour plot of joint density function for each IOD condition in the rainy and dry seasons.

4.5. Coincidence Probability

Using a suitable copula function, a joint distribution function between climate indicators can be constructed and the joint probability between indicators in dry and wet conditions can be estimated. This probability is often referred to as coincidence or exceedance probability (Wei et al., 2020). Coincidence probability is used to observe the frequency of co-occurrence between the number of dry days and total precipitation under dry, normal, and wet conditions. The values of the synchronous probability are presented in **Tables 6** and **7** for the rainy and dry seasons, respectively. Both also display the total synchronous and asynchronous probability.

Table 6 shows the effect of ENSO on increasing the probability of wet-wet conditions and decreasing the probability of dry-dry conditions as the ENSO index decreases in the rainy season. The lower the ENSO index, the higher the probability of wet conditions co-occurring in the number of dry days and total precipitation. During La Niña, the probability of wet conditions simultaneously is 30.3%. These results indicate that although the ENSO phenomenon does not show a significant effect from the peak of joint PDFs, the effect is clearly seen in the coincidence probability of the number of dry days and total precipitation.

Table 6.
Coincidence probability of the joint PDFs of the number of dry days and total precipitation (rainy season).

Coincidence	ENSO Conditions				IOD Conditions		
	<i>La Niña</i>	<i>Normal</i>	<i>El Niño-Weak</i>	<i>El Niño-Strong</i>	<i>Negative</i>	<i>Neutral</i>	<i>Positive</i>
dry-dry	3.4%	17.8%	19.7%	39.9%	18.5%	13.5%	38.3%
normal-normal	15.3%	17.5%	9.9%	12.9%	15.0%	14.9%	7.6%
wet-wet	30.3%	12.7%	11.4%	2.9%	1.8%	19.8%	13.7%
<i>Total Sync.</i>	<i>48.9%</i>	<i>48.0%</i>	<i>41.0%</i>	<i>55.6%</i>	<i>35.2%</i>	<i>48.3%</i>	<i>59.5%</i>
<i>Total Async.</i>	<i>51.1%</i>	<i>52.0%</i>	<i>59.0%</i>	<i>44.4%</i>	<i>64.8%</i>	<i>51.7%</i>	<i>40.5%</i>

Different things are shown in the IOD conditions, where there is no evident influence from each IOD condition. There is no pattern of decreasing or increasing the probability of co-occurrence when the IOD index increases or decreases. The highest probability for co-occurrence in wet conditions is under Neutral IOD conditions. These results reaffirm that the IOD phenomenon does not significantly affect the joint PDF of the number of dry days and total precipitation in the rainy season.

Table 7.

Coincidence probability of the joint PDFs between the number of dry days and total precipitation (dry season).

Coincidence	ENSO Conditions				IOD Conditions		
	<i>La Niña</i>	<i>Normal</i>	<i>El Niño-Weak</i>	<i>El Niño-Strong</i>	<i>Negative</i>	<i>Neutral</i>	<i>Positive</i>
dry-dry	14.1%	21.7%	48.8%	68.5%	1.0%	22.3%	62.6%
normal-normal	20.9%	21.4%	13.7%	5.1%	19.7%	21.9%	8.9%
wet-wet	35.9%	25.7%	15.0%	4.4%	34.8%	26.7%	8.4%
<i>Total Sync.</i>	<i>70.8%</i>	<i>68.7%</i>	<i>77.5%</i>	<i>78.0%</i>	<i>55.5%</i>	<i>70.8%</i>	<i>80.0%</i>
<i>Total Async.</i>	<i>29.2%</i>	<i>31.3%</i>	<i>22.5%</i>	<i>22.0%</i>	<i>44.5%</i>	<i>29.2%</i>	<i>20.0%</i>

Table 7 shows that ENSO and IOD conditions significantly affect the coincidence probability between the number of dry days and total precipitation, confirming the statement in **Fig. 5**. The higher the ENSO and IOD indexes, the higher the dry condition probability for the number of dry days and total precipitation simultaneously. Strong El Niño and Positive IOD have a coincidence probability of 68.5% and 62.6%, respectively. The two values show almost the same probability, indicating that Strong El Niño and Positive IOD have similar effects on the coincidence probability of the number of dry days and total precipitation. Although the Weak El Niño gives a reasonably high value of 48.8%, this value is still relatively less than the Strong El Niño and Positive IOD conditions. During Strong El Niño, the probability of wet-wet conditions is 4.4%, while the probability of wet-wet conditions in Positive IOD is 8.4%.

Based on the value of total synchronous and asynchronous probability, only Strong El Niño and Positive IOD conditions give a total synchronous probability of more than 50% in the rainy season. In other ENSO and IOD conditions, the total asynchronous probability is higher than the total synchronous probability. This shows that the relationship between the number of dry days and total precipitation is not too high in the rainy season. Thus, the probability of different conditions occurring in the number of dry days and total precipitation is still relatively high, such as the probability of the number of dry days in wet conditions but total precipitation in normal conditions, etc.

Meanwhile, in the dry season, the total synchronic probability is very high, around 70%, which indicates the relationship between the number of dry days and total precipitation is very strong. Only when the IOD condition is negative the total synchronous probability value is 55%, but still higher than the total asynchronous probability. Coincidence probability between the number of dry days and the total amount of precipitation under Moderate-Strong El Niño and Positive IOD is more than 50% in the dry season, which implies that drought and fire potential preparedness should receive greater attention in these conditions.

5. CONCLUSIONS

South Sumatra is an area in Indonesia that is very vulnerable to forest fires with respect to ENSO and IOD events (Putra et al., 2019). Understanding the shared behavior between local climatic conditions such as the number of dry days and the total amount of precipitation is considered important as an early stage to form a probabilistic-based model in the future. The copula model is a very effective way to understand the shared behavior of climate indicators (Dixit & Jayakumar, 2022; Hussain et al., 2022).

This study has defined fire-prone areas in southern Sumatra using k-means clustering. Based on the fire-prone areas, 3-month the number of dry days and 2-month total precipitation gave the highest correlation to the burned area. The joint distribution is constructed using a rotated copula based on ENSO and IOD conditions from these two variables. Based on the peak of joint PDFs, ENSO and IOD conditions did not significantly affect the rainy season but substantially in the dry season. However, based on coincidence probability, ENSO conditions still influence the joint distribution of the number of dry days and total precipitation during the rainy season but not with IOD conditions.

Moreover, the association between the number of dry days and the total precipitation was stronger in the dry season than in the rainy season.

Although the copula is a powerful technique for accessing the joint distribution between variables that are not normally distributed, this method relies heavily on selecting the marginal distribution as the edges of the copula. This study only focuses on time-independent distribution functions, so climate change is not considered in the analysis here. The use of time-varying copula can improve further understanding and make the joint distribution model more precise (Ausin & Lopes, 2010; Xu et al., 2021). In addition, high-dimensional copulas can be used in the same analysis by making the ENSO or IOD index as one of the edges of the copula. This means that the joint distribution model used is no longer divided based on ENSO or IOD categories, but the joint distribution model that is formed can assess the behavior of climate indicators based on the movement of the ENSO or IOD index using tri-variate copulas or more, such as nested Archimedean copula (Zhao et al., 2022).

REFERENCES

- Ausin, M. C., & Lopes, H. F. (2010). Time-varying joint distribution through copulas. *Computational Statistics and Data Analysis*, 54(11), 2383–2399. <https://doi.org/10.1016/j.csda.2009.03.008>
- Avia, L. Q., & Sofiati, I. (2018). Analysis of El Niño and IOD Phenomenon 2015/2016 and Their Impact on Rainfall Variability in Indonesia. *IOP Conference Series: Earth and Environmental Science*, 166(1). <https://doi.org/10.1088/1755-1315/166/1/012034>
- Brown, P. J., Bradley, R. S., & Keimig, F. T. (2010). Changes in extreme climate indices for the Northeastern United States, 1870–2005. *Journal of Climate*, 23(24), 6555–6572. <https://doi.org/10.1175/2010JCLI3363.1>
- Brunton, S. L., & Kutz, J. N. (2022). *Data-driven Science and Engineering: Machine Learning, Dynamical Systems, and Control*. Cambridge University Press.
- Caraka, R. E., Yasin, H., Sugiarto, W., & Ismail, K. M. (2016). Time Series Analysis Using Copula Gauss and Ar(1)-N.Garch(1,1). *Media Statistika*, 9(1). <https://doi.org/10.14710/medstat.9.1.1-13>
- Dixit, S., & Jayakumar, K. V. (2022). Spatio-temporal analysis of copula-based probabilistic multivariate drought index using CMIP6 model. *International Journal of Climatology*, 42(8), 4333–4350. <https://doi.org/10.1002/joc.7469>
- Hauke, J., & Kossowski, T. (2011). Comparison of values of pearson's and spearman's correlation coefficients on the same sets of data. *Quaestiones Geographicae*, 30(2), 87–93. <https://doi.org/10.2478/v10117-011-0021-1>
- Hussain, B., Qureshi, N. A., Buriro, R. A., Qureshi, S. S., Pirzado, A. A., & Saleh, T. A. (2022). Interdependence between temperature and precipitation: modeling using copula method toward climate protection. *Modeling Earth Systems and Environment*, 8(2), 2753–2766. <https://doi.org/10.1007/s40808-021-01256-8>
- Khaldun, M. H. I., Wirasatriya, A., Dwi Suryo, A. A., & Kunarso. (2018). The Influence of Indian Ocean Dipole (IOD) on the Variability of Sea Surface Temperature and Precipitation in Sumatera Island. *IOP Conference Series: Earth and Environmental Science*, 165(1). <https://doi.org/10.1088/1755-1315/165/1/012008>
- Kurniadi, A., Weller, E., Min, S. K., & Seong, M. G. (2021). Independent ENSO and IOD impacts on rainfall extremes over Indonesia. *International Journal of Climatology*, 41(6), 3640–3656. <https://doi.org/10.1002/joc.7040>
- Lestari, D. O., Sutriyono, E., Sabaruddin, S., & Iskandar, I. (2018). Respective Influences of Indian Ocean Dipole and El Niño-Southern Oscillation on Indonesian Precipitation. *Journal of Mathematical and Fundamental Sciences*, 50(3), 257–272. <https://doi.org/10.5614/j.math.fund.sci.2018.50.3.3>
- Li, H. W., Li, Y. P., Huang, G. H., & Sun, J. (2021). Quantifying effects of compound dry-hot extremes on vegetation in Xinjiang (China) using a vine-copula conditional probability model. *Agricultural and Forest Meteorology*, 311. <https://doi.org/10.1016/j.agrformet.2021.108658>
- Li, Z., Shao, Q., Tian, Q., & Zhang, L. (2020). Copula-based drought severity-area-frequency curve and its uncertainty, a case study of Heihe River basin, China. *Hydrology Research*, 51(5), 867–881. <https://doi.org/10.2166/nh.2020.173>
- McPhaden, M. J., Zebiak, S. E., & Glantz, M. H. (2006). ENSO as an integrating concept in earth science.

- Science*, 314(5806), 1740–1745. <https://doi.org/10.1126/science.1132588>
- Mohamad, I. Bin, & Usman, D. (2013). Standardization and its effects on K-means clustering algorithm. *Research Journal of Applied Sciences, Engineering and Technology*, 6(17), 3299–3303. <https://doi.org/10.19026/rjaset.6.3638>
- Naeni, E. M. B., Akhoond-Ali, A. M., Radmanesh, F., Koupai, J. A., & Soltaninia, S. (2021). Comparison of the Calculated Drought Return Periods Using Tri-variate and Bivariate Copula Functions Under Climate Change Condition. *Water Resources Management*, 35(14), 4855–4875. <https://doi.org/10.1007/s11269-021-02965-6>
- Najib, M. K., Nurdianti, S., & Sopaheluwakan, A. (2021). Copula in Wildfire Analysis: A Systematic Literature Review. *InPrime: Indonesian Journal of Pure and Applied Mathematics*, 3(2), 101–111. <https://doi.org/10.15408/inprime.v3i2.22131>
- Najib, M. K., Nurdianti, S., & Sopaheluwakan, A. (2022a). Copula-based joint distribution analysis of the ENSO effect on the drought indicators over Borneo fire-prone areas. *Modeling Earth Systems and Environment*, 8(2), 2817–2826. <https://doi.org/10.1007/s40808-021-01267-5>
- Najib, M. K., Nurdianti, S., & Sopaheluwakan, A. (2022b). Multivariate fire risk models using copula regression in Kalimantan, Indonesia. *Natural Hazards*. <https://doi.org/10.1007/s11069-022-05346-3>
- Nelsen, R. B. (2006). *An Introduction to Copulas* (2nd ed.). Springer Science & Business Media.
- Nikonovas, T., Spessa, A., Doerr, S. H., Clay, G. D., & Mezbahuddin, S. (2022). ProbFire: A probabilistic fire early warning system for Indonesia. *Natural Hazards and Earth System Sciences*, 22(2), 303–322. <https://doi.org/10.5194/nhess-22-303-2022>
- Nur'utami, M. N., & Hidayat, R. (2016). Influences of IOD and ENSO to Indonesian Rainfall Variability: Role of Atmosphere-ocean Interaction in the Indo-pacific Sector. *Procedia Environmental Sciences*, 33, 196–203. <https://doi.org/10.1016/j.proenv.2016.03.070>
- Nurdianti, S., Bukhari, F., Julianto, M. T., Najib, M. K., & Nazria, N. (2021). Heterogeneous Correlation Map Between Estimated ENSO And IOD From ERA5 And Hotspot In Indonesia. *Jambura Geoscience Review*, 3(2), 65–72. <https://doi.org/10.34312/jgeosrev.v3i2.10443>
- Nuryanto, D. E., & Badriyah, I. U. (2014). Sea Surface Temperature Effect to Indonesian Maritime Continent Rainfall on September 2006 (Pengaruh Perubahan Suhu Permukaan Laut Terhadap Curah Hujan Benua Maritim Indonesia Pada September 2006). *Jurnal Meteorologi Dan Geofisika*, 15(3), 147–155.
- Putra, R., Sutriyono, E., Kadir, S., Iskandar, I., & Lestari, D. O. (2019). Dynamical link of peat fires in South Sumatra and the climate modes in the Indo-Pacific region. *Indonesian Journal of Geography*, 51(1), 18–22. <https://doi.org/10.22146/ijg.35667>
- Singh, H., Pirani, F. J., & Najafi, M. R. (2020). Characterizing the temperature and precipitation covariability over Canada. *Theoretical and Applied Climatology*, 139(3–4), 1543–1558. <https://doi.org/10.1007/s00704-019-03062-w>
- Suharjo, B. H., & Velicia, W. A. (2018). The Role of Rainfall Towards Forest and Land Fires Hotspot Reduction in Four Districs in Indonesia on 2015-2016. *Jurnal Silviculture Tropika*, 09(1), 24–30. <https://doi.org/10.29244/j-siltrop.9.1.24-30>
- Ummenhofer, C. C., D'Arrigo, R. D., Anchukaitis, K. J., Buckley, B. M., & Cook, E. R. (2013). Links between Indo-Pacific climate variability and drought in the Monsoon Asia Drought Atlas. *Climate Dynamics*, 40(5–6), 1319–1334. <https://doi.org/10.1007/s00382-012-1458-1>
- Wei, X., Zhang, H., Singh, V. P., Dang, C., Shao, S., & Wu, Y. (2020). Coincidence probability of streamflow in water resources area, water receiving area and impacted area: Implications for water supply risk and potential impact of water transfer. *Hydrology Research*, 51(5), 1120–1135. <https://doi.org/10.2166/nh.2020.106>
- Xu, P., Wang, D., Wang, Y., Qiu, J., Singh, V. P., Ju, X., Zhang, A., Wu, J., & Zhang, C. (2021). Time-varying copula and average annual reliability-based nonstationary hazard assessment of extreme rainfall events. *Journal of Hydrology*, 603. <https://doi.org/10.1016/j.jhydrol.2021.126792>
- Yang, J., Wang, Y., Yao, J., Chang, J., Xu, G., Wang, X., & Hu, H. (2020). Coincidence probability analysis of hydrologic low-flow under the changing environment in the Wei River Basin. *Natural Hazards*, 103(2), 1711–1726. <https://doi.org/10.1007/s11069-020-04051-3>
- Zhao, Z., Wang, H., Shi, Q., & Wang, C. (2022). Study on drought events in China based on time-varying nested Archimedean-copula function. *Water Supply*, 22(1), 795–811. <https://doi.org/10.2166/ws.2021.233>

ALGORITHMS DEVELOPMENT OF THE FIELD MANGROVE CHLOROPHYLL-A BIOMASS, CARBON BASED ON SENTINEL-2A DATA AT CAWAN ISLAND, SUMATERA, INDONESIA

Agus HARTOKO ^{1*}, Aulia RAHIM ¹, Nurul LATIFAH ¹

DOI: 10.21163/GT_2022.172.11

ABSTRACT:

The study develop of algorithms for the tropical mangrove chlorophyll-a, biomass and carbon based on the field data measurements at Cawan Island Sumatera Indonesia and Sentinel-2A satellite data. Samples of mangrove leaf were used for chlorophylla-a measurements using spectrometry method. Field sampling data using purposive sampling method. Data of mangrove tree diameter at breast height (DBH) was processed using allometric equation to estimate the mangrove biomass and carbon content. Algorithms were developed after performing a series of polynomial regressions of field and Sentinel-2A satellite data and then select the highest correlation coefficient. The dominant mangrove is *Rhizophora apiculata*. The field mangrove leaf chlorophyll-a content ranged from 14.03-15.77 mg.ml⁻³, while the estimated chlorophyll-a from algorithm is in the range of 13.714-16 mg.ml⁻³. Calculated field mangrove biomass is in the range of 66.31-85.05 tons.ha⁻¹, while the value from algorithms is in the range of 51-90 tons.ha⁻¹. The highest biomass and carbon storage is in the trunks. This study produces the algorithm of mangrove leaf chlorophyll-a = $0.0002(B_4 + B_2)/2)^2 - 0.057(B_4 + B_2)/2 + 16.79$, with RMSE of 0.072 mg.m⁻³. Algorithm for mangrove biomass = $24.69(B_4/B_2)^2 - 47.41(B_4/B_2) + 36.06$, with RMSE of 0.337 tons/0.2ha and algorithm for mangrove carbon = $10.071(B_4/B_2)^2 - 23.159(B_4/B_2) + 44.233$; with RMSE of 0.235 tonsC/0.2ha. The new insight in this study is that the algorithm developments can be applied for mangrove chlorophyll-a content, biomass and carbon content estimation using any optical satellite data based on its relevant spectral range. This algorithm development is an open approach method based on highest correlation coefficient on regression equation of the field and the satellite spectral value. The algorithms resulted from this study can be applied over wide and in any area in the tropics.

Key-words: Mangrove, Chlorophyll-a, Biomass, Carbon, Sentinel-2A, Algorithm

1. INTRODUCTION

Mangrove is defined as an association of halophytic trees along brackish tropical and subtropical tidal coastlines (Donato et al., 2012). Their physical functions include reducing coastal erosion and sediment trap (Chapman, 1975). The chemical ecological function is to transform CO₂ into organic carbon as greenhouse effect reduction and thus global warming mitigation and adaptation (Hartoko et al. 2010, Lasibani and Eni, 2010). Atmospheric CO₂ generated by burning of fossil oil, coal and vegetation had increased cumulatively (Ramlan, 2008). According to Donato et al., (2011) and Ellison et al., (2015), mangrove ecosystem can reduce atmospheric CO₂ as mangrove biomasses account for 10% of the storage of total atmospheric CO₂ but only 0.7% by the global forest. Atmospheric CO₂ transformed into the trunk, branch and leaves of the mangrove biomass (Alongi, 2012). The organic carbon yield form the atmospheric CO₂ is reported to have organic carbon and CO₂ by ratio of 1 : 3.7 (Chapman, 2018). This can be mainly attributed to the mangrove ecosystem along the tropical coast of Indonesia (Murdiyanto, 2003). Mangrove ecosystem also function as carbon cycles and dissolve organic carbon exporter to other coastal ecosystem of coral reef and seagrass beds (Hartoko, 1989; Afifa et.al.,2020; Ershad et.al.,2020). Indragiri Hilir reGENCY, Riau province in Sumatera is home to one Indonesian's largest area of mangrove forest.

¹ Department of Aquatic Resources Management, Faculty of Fisheries and Marine Science, University of Diponegoro, Semarang, Indonesia. Corresponding author agushartoko.undip@gmail.com, auliarahim6@gmail.com, nurul.latifah@live.undip.ac.id.

In 2003, mangrove coverage in this area is 117.717 ha (Office of Environment. Indragiri Hilir, 2009), which had decreased to 65.534 ha by 2013 (Office of Forestry. Riau Province, 2013). According to Prianto et.al (2006) the decrease in mangrove coverage was due to coastal area developments and land-use changes in coastal areas. The traditional use of mangrove *R.apiculata* as the dominant species at Cawan Island is for household cooking wood (Lubis.et.al, 2018).

Previous studies had focus on the ecological conditions of mangrove, monitoring mangrove area cover with the use of low-resolution satellite imagery, so that the need to use of high-resolution satellite imagery to monitor mangrove area cover is inevitable. There have been some attempts for a more detail study using high resolution satellite imagery for the analysis of normalized difference vegetation index (NDVI) of mangrove leaf, but unfortunately no information's on the species of the mangrove. The information of each mangrove biomass based on each species is important, since each species of mangrove have their own growth characters and different chlorophyll-a, biomass and carbon content. The previous study has developed mangrove algorithms but not differentiated the mangrove biomass and mangrove carbon and without chlorophyll-a (Wicaksono et al, 2016). The use of radar data (Li et.al., 2007), which is fundamentally detect more on the wide of mangrove area based on the electromagnetic reflectance, not the optical satellite data is arguable for biomass estimation. Since mangrove biomass and carbon content is believed as the ecological function of the chlorophyll-a content.

This study develops of spatial algorithms for mangrove biomass and carbon based on step-by-step mangrove biomass and carbon with approach through the chlorophyll-a content. This using the optical data of Sentinel-2A data which is relevant to the reflectance or the spectral value of the mangrove leaf chlorophyll-a data, especially using Band-3 and Band-4. The result of the study with respect to mangrove chlorophyll-a, biomass and carbon has become important model for the sustainable management of the mangrove ecosystem and mitigation of global warming. This study using the field mangrove leaf chlorophyll-a as the first step based on the assumption of the mangrove growth metabolic function into mangrove biomass and carbon. Then to estimate the field mangrove biomass, the study uses the non-destructive method of diameter at breast height (DBH) measurement. The field data then used to develop the spatial mangrove chlorophyll-a, biomass and carbon content. With this approach model can be used for mangrove conditions evaluation more accurately. The spatial algorithms that have been developed based on field allometric and satellite data have enabled efficient data usage and the development of an integrated spatial data base system. The important steps in the satellite data algorithm development are spatial accuracy, information of mangrove species, biomass and carbon content using a non-destructive method of allometric equations based on the field measurement (Hartoko et al., 2015). Important information on mangrove area cover monitoring, is the exact mangrove species based on a field measurement and sampling data. This can be used for mangrove algorithms development for mangrove biomass and ultimately for mangrove carbon estimations over a wide of mangrove area with a more accurate and efficient way.

The aim of this study is to investigate the mangrove species at Cawan Island and measure the chlorophyll-a, biomass, carbon contents and supported with data of total organic content in mangrove sediment. More specifically is to develop the spatial mangrove biomass and carbon algorithm using Sentinel-2A satellite data. The area of study is mangrove trees at Cawan island in Sumatera. Which is a very specific mangrove ecology in respect the only mangrove can grows and reach to 20 m height in 1 m depth of acidic peat-clay substrates. Which is different in comparison to other common mangrove clay substrate in Indonesia or other tropical wetlands of Asia.

2. STUDY AREA

Mangrove field measurement, sampling and ground check located at Cawan Island, along with the same day of the Sentinel-2A satellite data in 24th December 2019 (**Fig. 1**). Cawan Island is located in area extent of 103° 33' 18'' E and 0° 05' 59'' N in the administration of village of Cawan, district of Mandah, Indragiri Hilir regency, Riau province, Sumatera (Lubis et al, 2018). Of its total area of 36.30 km², two thirds of it consists of mangrove vegetation (Riau Bureau of Statistic, 2013).

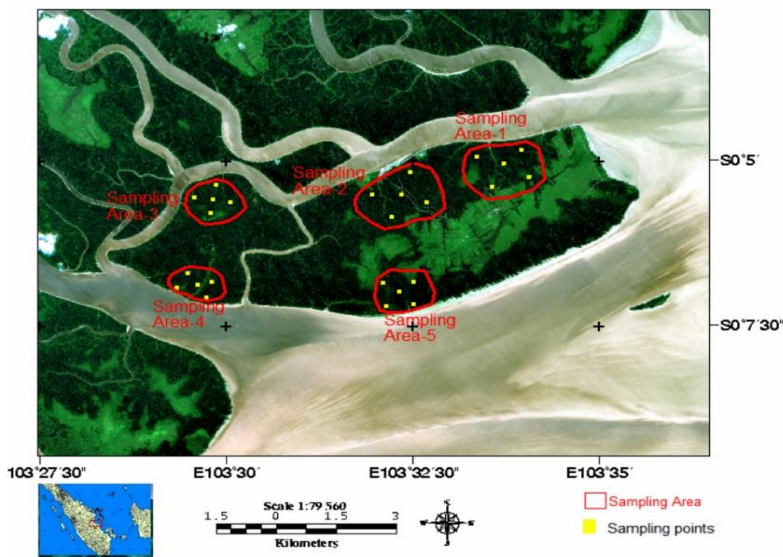


Fig. 1. Five sampling area each with 5 sampling points at Cawan Island.

3. DATA AND METHODS

3.1. Field Sampling

The study established 5 sampling-area, each consist of 5 sampling-points and total of 25 sampling points. In each one sampling-area, there are 1 sampling-point in the centre and 4 sampling-points scattered in the four quarter with 500 m distance as in Fig. 2 (Hutama et al., 2016).

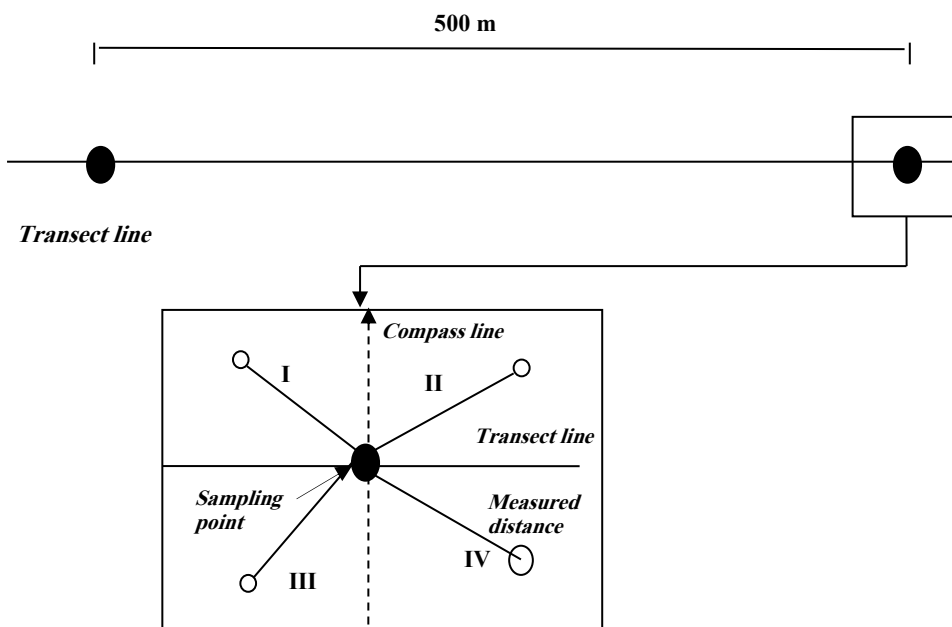


Fig 2. Point Centered Quarter Method (Mitchell, 2007).

This is in order to represent evenly the most area of the mangrove area in the Cawan Island. Each of 25 sampling-points, each have quadrant with size of 20 x 20 m or 400 m², with total of 5 sampling-points thus the wide at each sampling-area is 2,000m² or 0.2 hectares. Field data variables are mangrove species, number of mangroves in each square, sample of mangrove leaves, and measuring diameter at breast height (DBH). The coordinates at each sampling points were taken as mean value using two (a pair) of field GPS, in order to increase the spatial accuracy.

3.2. Sampling Method

Identification of mangrove species is using the textbook of Noor (2012). Field mangrove samplings and measurements were performed using the point centred quarter method (PCQM) which is combination of a line and quadrant sampling. The mangrove vegetation community sampling and analysis using the method developed by Mitchell (2007) as in **Fig. 2**. This method is the best for a spreading mangrove tree conditions. According to Febrianti et.al., 2013 and Ershad et.al., 2020) the PCQ Method has an advantage of easy and quicker for the composition and domination analysis, but with a disadvantage for a vegetation population with higher cluster or groupings or for a homogenous population. In the study area of Cawan Island, twenty-five randomly spreaded sampling points to represent all mangrove vegetations. The distance among sampling stations were not decided homogenously, but more random with consideration to represent for all mangrove species and different densities.

3.3. Method for Mangrove Data Analysis

The field measurement data or ground check is the most important phase for satellite data analysis and validation process. Each species of mangrove leaf samples was macerated, add with acetone and followed with spectrophotometry chlorophyll-a measurement in the laboratory. The mangrove leaf chlorophyll-a content was determined using the UV-Vis spectrometry method of Jeffrey and Humphrey (1975). The organic biomass and carbon content of mangrove leaf were analysed using furnace heating at 550°C for 4 hour and calculate the loss on ignition ash-furnace method (Jeffrey and Humphrey, 1975; Agus et al., 2011). The basic procedure for the Trunk and the branch for mangrove biomass measurement using a 'non-destructive' method. That is measurement of the mangrove trunk diameter so called as diameter at breast height (DBH). Then calculated using the allometric equations (Clough and Scott, 1989; Sutaryo 2009) for the biomass value as in **Table 1**. Based on field survey at Cawan Island that the existing species are *R.apiculata*, *R.mucronata* and *B.gymnorrhiza*, with dominant species is *R.apiculata* then the height for DBH measurements was standardised at height of 1.3 m (Cintron and Noveli, 1984).

Table 1.

The Above Ground Mangrove Biomass Allometric Equations by Species (tons).					
No	Species	(a)Trunk Biomass (WT)	(b)Branch Biomassa (WB)	(c)Leaf Biomass (WL)	Total Biomass (WT+WB+WL)
1.	<i>R.mucronata</i> ,	0.088552 (DBH) ^{2.5621}	0.012726 (DBH) ^{2.6844}	0.013896 (DBH) ^{2.1072}	
2.	<i>R.apiculata</i> and <i>R.stylosa</i>	0.08855 (DBH) ^{2.5621}	0.01272 (DBH) ^{2.6844}	0.01389 (DBH) ^{2.1072}	
3.	<i>B.gymnorrhiza</i>	0.224801 (DBH) ^{2.1407}	0.031535 (DBH) ^{2.2789}	0.013896 (DBH) ^{1.4914}	
4.	<i>C.tagal</i>	0.1468 (DBH) ^{2.3393}	0.01967 (DBH) ^{2.5516}	0.01175 (DBH) ^{2.1294}	

Reference : Clough and Scott (1989); Sutaryo (2009); Akira et.al (2008).

DBH = Diameter at Breast Hight (cm) WT = Trunk Biomass (tons) WB = Branch Biomass (tons)
WL = Leaf Biomass (tons) TB = Total Biomass (WT+WB+WL)

Then the conversion from mangrove biomass into mangrove carbon using constant of 0.5 (Agus et.al.,2011).

3.4. Method for Sentinel-2A Data Analysis

Sentinel-2A satellite data for Cawan Island was extracted on the date of 24 December 2019, which is the same period with the field sampling and measurements 23 – 25 December 2019. The satellite has 12 spectral bands (ESA, 2015) and three bands of red Band-4 with 0.650 – 0.680 μm wavelength, green Band-3 with 0.543 – 0.578 μm wavelength and blue Band-2 with 0.458 – 0.523 μm was used in this study. This is based on consideration that mangrove chlorophyll-a as plant pigment measurement with 0.6 μm in the laboratory and also used for the Senrinel-2A algorithm development. This RGB-432 composite of the satellite data of Band-4, Band-3 and Band-2 have specified spectral reflectance in the wave-length of 0.6 μm which is the best for vegetation chlorophyll-a measurement (Hartoko et al., 2013; Hartoko et al., 2015; Hartoko et.al. 2021). Spectral noise correction was done by means of atmospheric correction using FLAASH method (Hartoko. A., 2019; Esthi Kurnia, D. and B. Trisakti, 2016) that is excluding the digital numbers or spectral below the minimum value. That is known as atmospheric back-scatter and above the maximum real data value known as cloud. Five purposive sampling-area were used to represent distribution of mangrove vegetations at Cawan Island, with GPS coordinates as shown in **Fig. 1**.

Spatial processing and analysis were performed using ER Mapper 7.0. The raw extracted satellite data with wide area coverage of east central Sumatera region, was then polygon cropped along the coastline of the Cawan Island as the area of interest (AOI) for further image processing. This step is important to increase the spectral accuracy to represent only the mangrove chlorophyll-a reflectance (Hartoko et al., 2015). First step, the field measurement coordinates (with its value of chlorophyll-a and biomass at five stations) were overlaid onto the RGB-432 of Sentinel-2A image data. Then pick up the Sentinel-2A satellite numeric data or digital number (DN) at five stations coordinates. To obtain the algorithm with the best fit to the field (chlorophyll-a and biomass) and Sentinel-2A satellite numeric data, a series of polynomial regressions of the field data to the Sentinel-2A satellite data through four combination of spectral values or digital numbers by single-band use of band-4 (B₄), band-3 (B₃), and band-2 (B₂), band-rationing, band-thresholding and band-average methods (Hartoko et al., 2013; Hartoko et al., 2015). The previous studies are usually using the vegetation index (VI) which give a smaller correlation coefficient (r) value in the regression of the field and satellite DN. In this study use a polynomial regression equation of the real field biomass to the satellite DN data which give the highest correlation coefficient (r). Then the equation was selected to be used for the working algorithm based on consideration as indicating the most accurate correspondence between the field and satellite numeric data (Sugiyono. 2016).

The first step is making a multivariate regression equation between the field data of mangrove chlorophyll-a, biomass and carbon should give a significant correlation. This is the basis of the assumption that these three variables are representing the biological function of the mangrove from mangrove leaf chlorophyll-a into the mangrove biomass and carbon. The fundamental concept in the study is developing spatial algorithm (**Fig. 3**) based on the field mangrove chlorophyll-a pigment measurement in the wave-length of 0.5-0.6 μm which is represented by the use band-3, band-4. While for the red-green-blue algorithm use, we can use either band-2 or band-5 of the Sentinel-2A. The field measurement data is incorporated into a 10 m resolution images of B₂, B₃, and B₄ then made the polynomial regression equations. The highest correlation coefficient (r) polynomial regression would be selected as the working algorithm,

$$Y = a + bX + cX^2$$

where

Y = calculated mangrove chlorophyll-a, biomass and carbon

X = numeric data of band-4 (B₄), band-3 (B₃) or band-2 (B₂) of Sentinel-2A

= B₄, B₃ or B₂ : single band method

= (B₄/B₃) : band rationing method

= (B₄ – B₃) : band thresholding method

= (B₄ – B₃)/2 : band average method

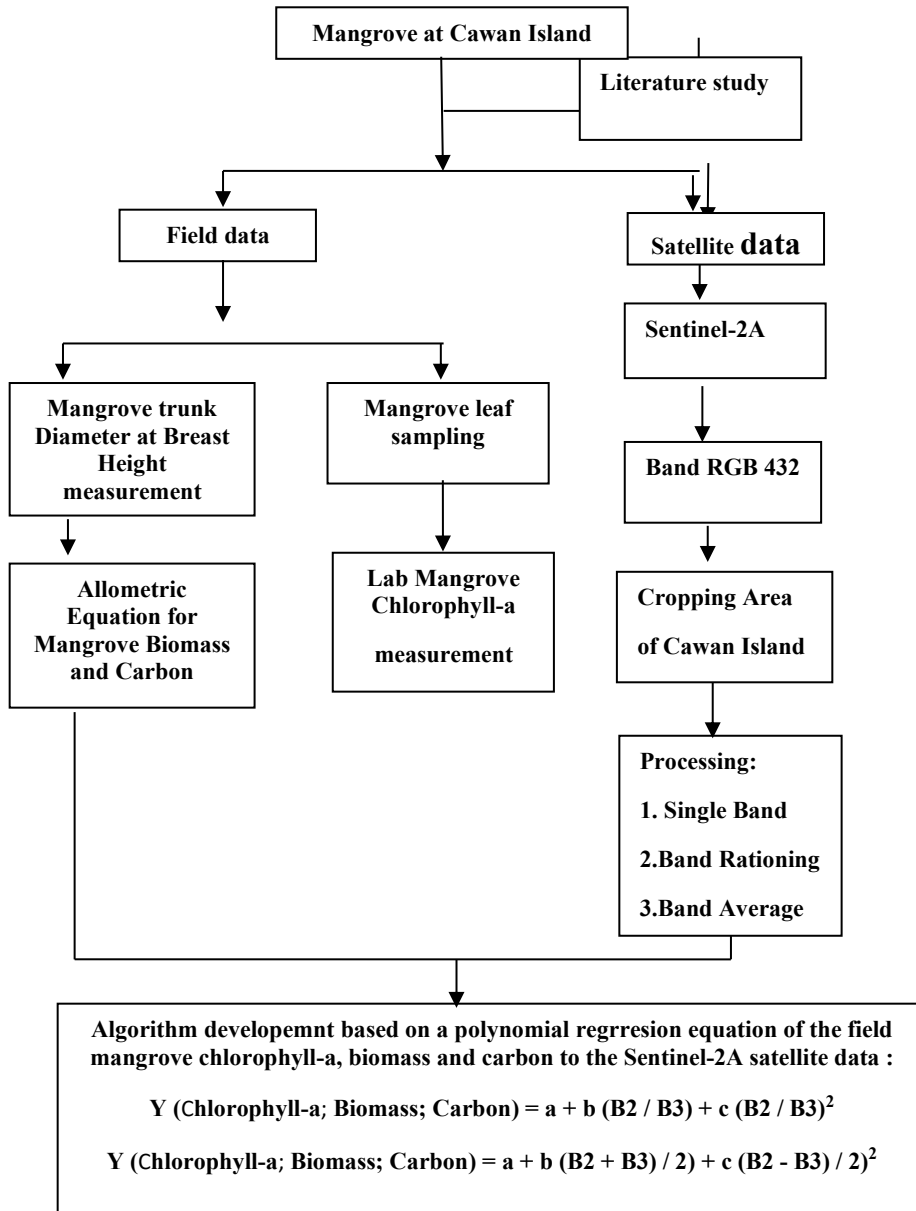


Fig. 3. The working algorithm flow chart.

4. RESULTS AND DISCUSSIONS

4.1. Mangrove Ecosystems

The mangrove species found in Cawan Island are *Rhizophora apiculata*, *Rhizophora mucronata*, *Bruguiera gymnorrhiza* (Rhizophoraceae), *Lumnitzera racemosa* (Combrataceae), *Acrostichum aureum* (Pteridaceae) and *Nypa fruticans* (Arecaceae). None existence of *Avicenia sp* is considered that the species cannot adapt to the acidic peat substrate. The most dominant species is *Rhizophora apiculata* in all twenty-five sampling points. This is considered as the most important species in the ecological community structure of the area (Adip et al.,2014). The assumption for the spatial and

estimate of Chlorophyll-a, biomass and carbon is based on the species of *Rhizophora apiculata*. The average tree height of 20 m and the biggest tree diameters is up to 1.70 m.

4.2. Mangrove leaf chlorophyll-a content

The field mangrove leaf chlorophyll-a content found in this study is in the range of 14.034-15.767 mg.ml⁻³. Flores-de-Santiago et al. (2013) reported that leaves of the red mangrove *Rhizophora mangle* and black mangrove *Avicennia germinans* in Mexico exhibit no seasonal difference in the chlorophyll-a content. Mangrove leaf chlorophyll-a is recognized to be an important parameter for use in the development of spatial algorithms for all kind of satellite data (Febrianti et al., 2013; Hartoko et al., 2015). Hendrawan et.al (2018) performed mangrove monitoring using green pigment and Pranata et al. (2016) utilized the reflectance of the near infrared spectrum as specific optical measurement of chlorophyll-a. The result from field DBH calculation that the mangrove biomass at range is 66.31– 85.05 ton.ha⁻¹, and the carbon ranged from 33.16 – 42.53 tonC.ha⁻¹ (**Table 2**).

Table 2.

Mangrove Biomass and Carbon in Cawan Island, Indragiri Hilir, Riau, Indonesia.

Sampling Area (SA)	Area in Each SA (ha)	Biomass Each SA (ton in 0.2ha)	Carbon Each SA (tonC in 0.2ha)	Biomass (ton.ha ⁻¹)	Carbon (ton.C.ha ⁻¹)
1	0.2	13.26	6.63	66.31	33.16
2	0.2	13.84	6.92	69.21	34.61
3	0.2	15.72	7.86	78.50	39.29
4	0.2	17.01	8.50	85.05	42.53
5	0.2	15.65	7.82	78.25	39.12
Total	1.0	75.48	37.73	377.32	188.71
Average	-	15.09	7.55	75.46	37.74

The individual mangrove biomass as total portion of the trunks, branches and leaves of *Rhizophora apiculata* is in the range of 13.26-17.92 tons and for *Rhizophora mucronata* is 8.92 tons in each sampling-area of 0.2ha. The specific results of the study also revealed that both the value of mangrove biomass and carbon stocks did not always according to the mangrove tree density, this is due to the differences on the individual mangrove trunk and branches. The mangrove tree density range is 390-690 ind.ha⁻¹. Biggest trunk diameter is 1.70 m found in *Rhizophora apiculata*. The peat clay substrate on Cawan Island was found to be acidic with pH range of 4 – 6.5. According to Suryono, et.al (2018) biomass and carbon content are dependent mainly on tree diameter, whereby the bigger is the diameter, the higher biomass and carbon contents. The average of the aboveground mangrove carbon content is 16.4 tons per sampling-area of 0.2 ha, found that the trunks have the biggest portion which is 77.74 % and the lowest is in the leaves (**Fig. 4**).

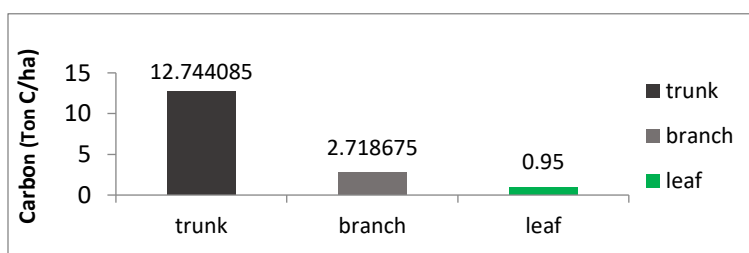


Fig. 4. Average Carbon Proportion of the Trunk, Branch and Leaf (Ton.ha⁻¹) represents of one sampling area of 0.2 ha.

Based on data biomass proportion in the trunk among species, we can be calculate that the trunk biomass ratio of *Bruguiera gymnorrhiza* to *Rhizophora apiculata* was determined to be 1 : 5.4 – 16.69 and ratio of *Rhizophora mucronata* to *Rhizophora apiculata* is 1 : 4.8 - 6.3. The highest total mangrove carbon content at the twenty-five sampling stations for *R. apiculata* was 27. 23 tonC from total of 84 sample trees, which is equivalent to 0.32 tonC for each individual trunk (**Fig. 5**).

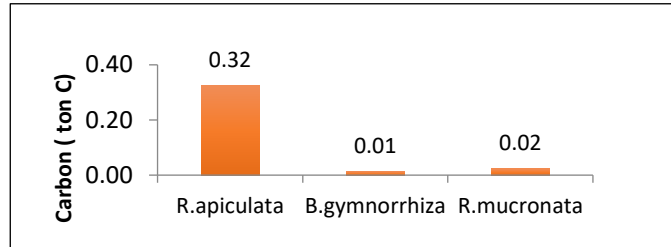


Fig. 5. Carbon contents in the trunks of individual mangrove tree in Cawan Island.

The lowest trunk carbon content was found in *B. gymnorrhiza* with 0.9 tonC from nine sample trees which is equivalent to 0.01 tonC for each trunk. According to Limbong (2009) the high carbon content in the trunks is due to carbon being the main constituent in cellulose cells, lignin and other carbon compound. The study findings revealed that *R. apiculata* had the highest tree carbon content of 0.32 tonC/tree, followed by *R. mucronata* with 0.02 tonC per tree, and the lowest being *B. gymnorrhiza* with 0.01 tonC per tree (**Fig. 6**). Studies by Rachmawati et.al (2014) and Suryono et.al (2018) also found in the genera of Rhizophora to have greater biomass and carbon stock than other species.

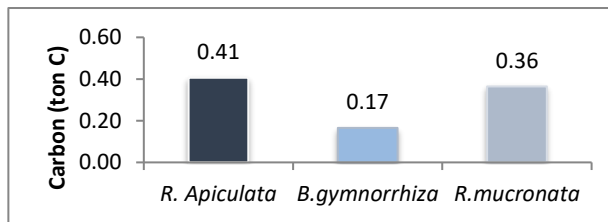


Fig. 6. Total carbon content in individual mangrove trunk, branch and leaf of individual mangrove at Cawan Island.

4.3. Algorithms for Mangrove Leaf Chlorophyll-a, Biomass and Carbon Content

Calculation from field DBH measurement (see Appendix) gives the result that mangrove biomass in 5 sampling areas is 13.26-17.01 tons in each sampling-area of 2000 m² or 0.2 ha. The conversion to biomass and carbon per hectare is found in the range of 66.31-85.05 tons.ha⁻¹ (**Table 2**). The highest biomass found at sampling area-4 with 85.05 ton.ha⁻¹ and carbon content of 42.53 tonC.ha⁻¹. The lowest biomass per hectare was found at sampling-area 1 with 66.31 ton.ha⁻¹ and carbon content is 33.16 tonC.ha⁻¹. The total mangrove biomass and carbon content of the five sampling-area on Cawan Island were determined to be 377.32 ton.ha⁻¹ and 188.71 tonC.ha⁻¹ respectively. This biomass value is higher than that reported by Hartoko et.al (2015) for Karimunjawa Island, which had a total biomass of 182.62 ton.ha⁻¹ as well as that reported by Suryono et.al (2018) for Perancak-Bali region 187.212 ton.ha⁻¹. These allometric results may vary with age, dominant species, and locality.

Globally, tropical mangrove forests are known to have much higher aboveground biomasses than those in temperate areas (Clough and Scott, 1989). The organic carbon content of the mangrove substrate to the depth of 25 cm was determined by first obtaining the organic content from field samples then converting the result using ration 1/1.724 (Agus et.al, 2011). As a supporting data, the study obtained the highest organic content of mangrove substrate is in sampling-area 2 with 16.323 ton.ha⁻¹ and the lowest in sampling-area 3, with 6.793 ton.ha⁻¹. According to Sari et.al (2017), the

organic content of a substrate is a function of the cumulative deposits of mangrove leaves and the rate of its decomposition processes, which can vary from one location to another. Prior to further analysis, a statistically significant proof is performed to test variable correlations among values of chlorophyll-a, biomass, and carbon. The study develops a step-by-step mangrove biomass and carbon with approach the chlorophyll-a content, since the algorithms development are using an optic Sentinel-2A data, which is assumed correlated to the detection of the mangrove chlorophyll-a pigment, especially in Band-3 and Band-4. The result of the analysis of variance (ANOVA) and a multiple regression analysis was carried out. The three main study variables were confirmed to have a significant correlation with F-count of 143504.235 which is higher than the F-table (3.63). Thus, for further Sentinel-2A bands algorithm development steps relating field mangroves variables to Sentinel-2A satellite data is considered to be valuable and significant estimation. This significant test is important step prior the development of spatial algorithms based on the logical numerical analysis, which is often missed in previous study.

The stepwise algorithm is a series of polynomial regressions of the field and the digital number (DN) or the spectral value of the Sentinel-2A satellite data (**Table 3**). This study is mainly using RGB method using band-4, band-3, and band-2 combination, followed with single-band, band-ratoning and band-averaging for the polynomial regression steps. The result with highest correlation coefficient (r) obtained from the polynomial regression is then selected as the operational algorithm to calculate the chlorophyll-a of mangrove leaves, which is the mangrove leaf chlorophyll-a content in its canopy will be represented by the estimated value from the calculated DN of the Sentinel-2A satellite data (Muditha K Heenkenda et al.,2015).

Table 3.
Result of Mangrove Algorithms of Chlorophyll-a, Biomass and Carbon and RMSE Value at Cawan Island, Indragiri Hilir, Riau,Indonesia.

No.	Algorithms	Field Estimation	Satellite Estimation	Threshold	RMSE (ton/0.2ha)
1	Chlorophyll-a (mg.m ³) = 0.0002(B ₄ +B ₂)/2) ² – 0.057(B ₄ +B ₂)/2) + 16.79	SA-1 = 15.77	SA-1 = 15.6.6	0.10	0.115
		SA-2 = 14.62	SA-2 = 14.398	0.22	0.110
		SA-3= 14.95	SA-3= 14.998	-0.04	0.048
		SA-4= 14.45	SA-4= 14.413	0.04	0.050
		SA-5 = 14.03	SA-5 = 14.092	-0.06	0.040
		:			
Average					
2	Biomass (tons.ha ⁻¹) = 24.69(B ₄ /B ₂) ² - 47.41(B ₄ /B ₂)+36.06	SA-1 = 13.26	SA-1 = 13.461	-0.20	0.272
		SA-2 = 13.84	SA-2 = 14.045	-0.21	0.287
		SA-3= 15.72	SA-3= 15.542	0.18	0.309
		SA-4= 17.01	SA-4= 17.510	-0.25	0.500
		SA-5 = 15.65	SA-5 = 15.197	0.45	0.320
		:			
Average					
3	Carbon (tons.ha ⁻¹) = 10.071(B ₄ /B ₂) ² – 23.159(B ₄ /B ₂) + 44.233	SA-1 = 6.63	SA-1 = 6.638	-0.01	0.164
		SA-2 = 6.92	SA-2 = 6.947	-0.03	0.184
		SA-3= 7.86	SA-3= 7.709	0.15	0.212
		SA-4= 8.50	SA-4= 8.904	0.08	0.282
		SA-5 = 7.82	SA-5 = 7.486	0.33	0.334
		:			
Average					

The series of polynomial regression as shown in **Table 4** reveals that the spectral values of band average of B₄ and B₂ has the highest correlation coefficient (r) of 0.966, which means it is the best fit spectral values of Sentinel-2A satellite data for calculating the field mangrove leaf chlorophyll-a content.

Table 4.

Matrix of mangrove leaf chlorophyll-a algorithms.

No	Band	Algorithms	r
1	B ₄	Chlorophyll-a = $-0.0007(B_4)^2 + 0.2355(B_4) - 4.4393$	0.268
2	B ₃	Chlorophyll-a = $0.00024(B_3)^2 - 0.1312(B_3) + 32.451$	0.935
3	B ₂	Chlorophyll-a = $0.0001(B_2)^2 - 0.0373(B_2) + 16.672$	0.886
4	B ₄ /B ₃	Chlorophyll-a = $56.99(B_4/B_3)^2 - 69.90(B_4/B_3) + 35.71$	0.832
5	B ₄ /B ₂	Chlorophyll-a = $3.743(B_4/B_2)^2 - 9.257(B_4/B_2) + 19.95$	0.726
6	B ₃ /B ₂	Chlorophyll-a = $-1.29(B_3/B_2)^2 + 3.648(B_3/B_2) + 12.48$	0.604
7	(B ₄ +B ₃)/2	Chlorophyll-a = $0.0009(B_4+B_3)/2)^2 - 0.410(B_4+B_3)/2) + 60.21$	0.845
8	(B₄+B₂)/2	Chlorophyll-a = $0.0002(B_4+B_2)/2)^2 - 0.057(B_4+B_2)/2) + 16.79$	0.966
9	(B ₃ +B ₂)/2	Chlorophyll-a = $0.00008(B_3+B_2)/2)^2 - 0.021(B_3+B_2)/2) + 15.24$	0.954

The value of RMSE was calculated based on the five class difference of chlorophyll-a value of the field and the estimated algorithm value. The value of RMSE of 0.072 time to the Sentinel-2A pixel size (B₄, B₃, and B₂) of 10 m thus gives 0.72 m of spatial accuracy.

$$\text{Chlo-a (mg.m}^{-3}\text{)} = 0.0002((B_4 + B_2)/2)^2 - 0.057((B_4 + B_2)/2) + 16.79; \text{ RMSE : 0.072}$$

Note :

B₄ : Band-4 (red- band, wavelength : 0.665 μm)

B₂ : Band-2 (blue - band, wavelength : 0.490 μm)

The value and spatial distribution of mangrove leaf chlorophyll-a based on algorithm at Cawan island as presented in Fig. 7, gives the range from 13.714-16 mg.ml⁻³, while the field mangrove chlorophyll-a is in the range of 14-15 mg.ml⁻³. The 'speckle-looks' in the image algorithm indicated only the mangrove leaf chlorophyll-a pigment reflectance had been detected and calculated its digital number, in B₄ and B₂ of Sentinel-2A, with pixel size of 10 m. Will not count the reflectance value of non mangrove leaf such as bushes vegetation in the middle area of the Cawan Island.

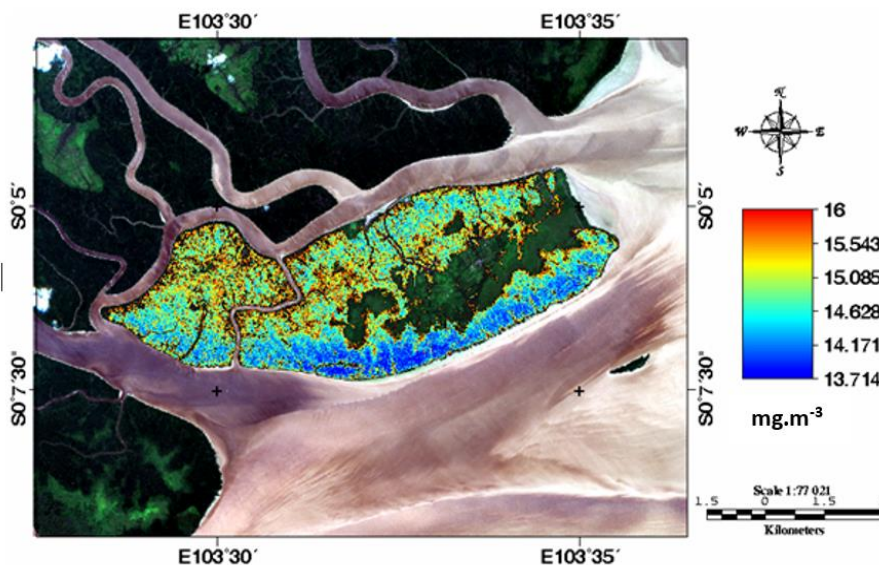


Fig. 7. The content and spatial distribution of mangrove leaf chlorophyll-a at Cawan Island obtained from the algorithm.

Based on the matrix of algorithms shown in **Table 5**, that polynomial regression by the band-ratting of B_4/B_2 of the Sentinel-2A data to the field biomass content had obtained the highest correlation coefficient (r) of 0.94.

Table 5.

Matrix of algorithms for mangrove biomass at Cawan Island.

No	Band	Algorithms	r
1	B_4	Biomass = $0.003(B_4)^2 - 1.116(B_4) + 102.6$	0.738
2	B_3	Biomass = $-0.001(B_3)^2 + 1.103(B_3) - 152.7$	0.906
3	B_2	Biomass = $0.0009(B_2)^2 + 0.3386(B_2) + 46.395$	0.744
4	B_4/B_3	Biomass = $448.0(B_4/B_3)^2 + 472.6(B_4/B_3) + 138.0$	0.901
5	B_4/B_2	Biomass = $24.69(B_4/B_2)^2 - 47.41(B_4/B_2) + 36.06$	0.940
6	$(B_4+B_3)/2$	Biomass = $-0.002(B_4 + B_3)/2)^2 + 0.980(B_4 + B_3)/2) - 106.9$	0.837
7	$(B_4+B_2)/2$	Biomass = $-0.001(B_4 + B_2)/2)^2 + 0.576(B_4 + B_2)/2) - 40.01$	0.593
8	$(B_3+B_2)/2$	Biomass = $-0.0004(B_3 + B_2)/2)^2 + 0.1834(B_3 + B_2)/2) - 13.12$	0.563

As fundamental knowledge that B_4 as red band-4 spectrum with wavelength of $0.650 - 0.680 \mu\text{m}$ is recognized as having the best fit reflectance for the chlororophyll-a pigment algorithm (Hartoko et al., 2013; Febrianti, et.al., 2013).

Biomass (tons.ha⁻¹) = $24.69(B_4/B_2)^2 - 47.41(B_4/B_2) + 36.06$; RMSE : 0.337

where :

B_4 : Band - 4 (red band, wavelength : $0.665 \mu\text{m}$)

B_2 : Band - 2 (blue band, wavelength : $0.490 \mu\text{m}$)

The result of algorithm, the value and spatial distribution of mangrove biomass at Cawan island gives the range of $51-90 \text{ tons.ha}^{-1}$ (**Fig. 8**), while the actual field mangrove biomass in the range of $66.31-85.05 \text{ tons.ha}^{-1}$. This value is based on the dominant mangrove in Cawan Island is *Rhizophora apiculata*.

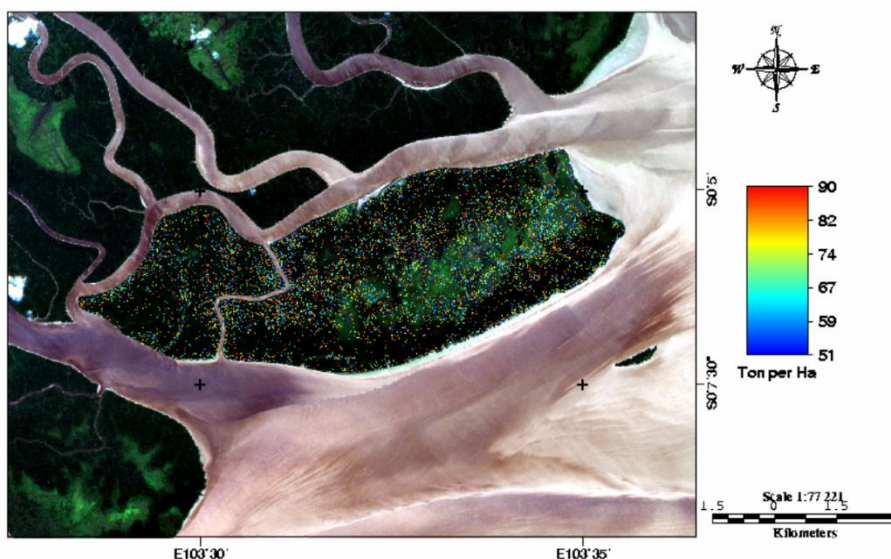


Fig. 8. Mangrove biomass and spatial distribution at Cawan Island (tons.ha^{-1}).

In comparison, earlier study using vegetation index (VI) based on band rationing of 0.740 μm /0.720 μm wavelength hyperspectral data obtained better prediction of chlorophyll-a during the dry season for three species of mangrove (*Rhizophora mangle*, *Avicennia germinans* and *Laguncularia racemosa*) than during the rainy season (Flores-De-Santiago et.al., 2012). This was assumed caused by a better chlorophyll-a reflectance absorption.

The polynomial regression of field carbon to B_4/B_2 band rationing have the highest correlation coefficient (r) of 0.929 (Table 6).

Table 6.

Matrix of algorithms for mangrove carbon at Cawan Island.			
No	Band	Algorithm	r
1	B_4	Carbon = $0.001(B_4)^2 - 0.562(B_4) + 51.62$	0.740
2	B_3	Carbon = $-0.0009(B_3)^2 + 0.5526(B_3) - 76.551$	0.906
3	B_2	Carbon = $0.0004(B_2)^2 - 0.169(B_2) + 23.197$	0.743
4	B_4/B_3	Carbon = $224.7(B_4/B_3)^2 - 237.0(B_4/B_3) + 69.23$	0.901
5	B_4/B_2	Carbon = $10.071(B_4/B_2)^2 - 23.159(B_4/B_2) + 44.233$	0.929
6	$(B_4+B_3)/2$	Carbon = $-0.002(B_4 + B_3)/2)^2 + 0.980(B_4 + B_3)/2) - 106.9$	0.837
7	$(B_4+B_2)/2$	Carbon = $-0.001(B_4 + B_2)/2)^2 + 0.576(B_4 + B_2)/2) - 40.01$	0.593
8	$(B_3+B_2)/2$	Carbon = $-0.0004(B_3 + B_2)/2)^2 + 0.1834(B_3 + B_2)/2) - 13.11$	0.563

This result is attributable to the use of the B_4 red spectrum with wavelength of 0.665 μm for chlorophyll-a reflectance, from which we obtained the biomass and carbon values. Band-2 (B_2) with the shorter wavelength of 0.490 μm was used in the algorithm for its leaf material penetration capability and contrasting spectral values for vegetated and non-vegetated areas.

$$\text{Carbon (tons.ha}^{-1}\text{)} = 10.071(B_4/B_2)^2 - 23.159(B_4/B_2) + 44.233; \text{ RMSE : 0.226}$$

Note :

B_4 : Band 4 (red band, wavelength : 0.665 μm)

B_2 : Band 2 (blue band, wavelength : 0.490 μm)

Fig. 9 shows the carbon content and spatial distribution in mangroves carbon per station (0.2 hectares) at Cawan Island as obtained by the algorithm ranges of 31-42 tonC.ha^{-1} , while actual field mangrove carbon is in the range of 33.16-42.53 tonC.ha^{-1} .

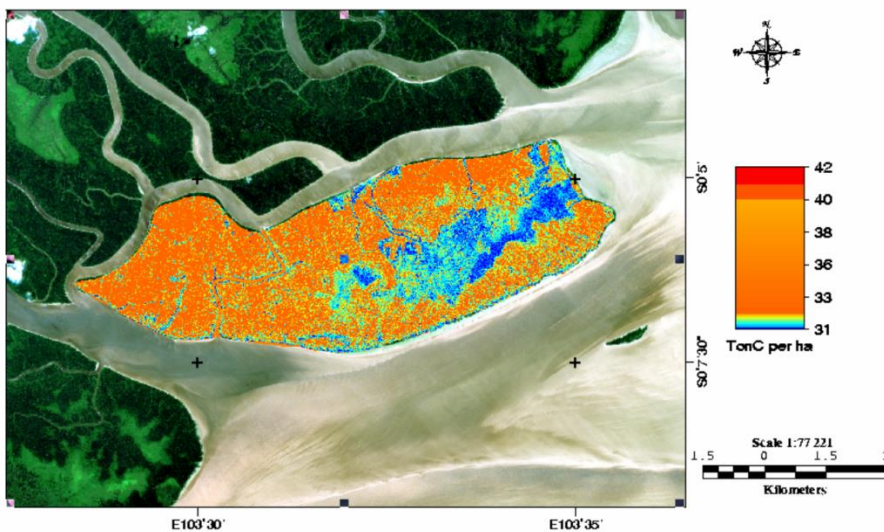


Fig. 9. Carbon content and spatial distribution in mangroves at Cawan Island (tonC.ha^{-1}).

5. DISCUSSION

In the process of algorithm development based on field data with respect to satellite data, the fundamental philosophy is the use wavelength as for the target spectral reflectance. This because satellite units use different name category of bands and its wavelengths. According to Tarigan., et.al. (2013) chlorophyll-a absorbs the visible spectrum of photosynthetic process. Vegetation absorbs spectral wavelengths in the range of 0.400 – 0.700 μm . Wavelength of 0.665 μm for the red band would be accurate for the reflectance for vegetation chlorophyll-a such as the mangrove. Not all light spectrum is absorbed by chlorophyll-a in the photosynthetic process, only 70% of the blue spectrum and 90% of the red spectrum will be absorbed (Jefrey, S.W., and G.F Humphrey, 1975). Flores de Santiago et al., (2015) mention that vegetation index of R_{740}/R_{720} during the dry season measurement give a better mangrove chlorophyll-a estimation. According to Hartoko et.al., (2019) and Hendrawan et.al., (2018), satellite data can be used for field data algorithm development, when the right band wavelengths are used. Furthermore, band combinations such as single-band, band-rationing, band-thresholding or the band- averaging method will lead to identify the algorithm with the best fit.

Statistically based point of view the numeric results any of the above four methods should fit the numeric values of real field data distributions. The band-rationing method will overcome limitation associate with the use of the single-band method. Band-4 and Band-2 rationing (B_4/B_2) can be used to deliniate the vegetation canopy coverage. Algorithms that use a single-band method will have a lower correlation coefficient (r), compared with those that use of two-band combination, the (r) value of which will be much near to a value of one (Hartoko et.al., 2015; Hartoko et.al., 2019). The best regression methods should have a correlation coefficient (r) higher than 0.6 or near to a value of one (Sugiono, 2016).

The use of Sentinel-2A as reliable and controlable image processing for spatio-temporal for effective and countinuesly coastal habitat monitoring. The use of three bands (band-4, band-3 and band-2) of Sentinel-2A data with pixel size of 10 m is in a medium state of spatial accuracy. The research use the Sentinel-2A of B_2, B_3 and B_4 with spatial reslution of 10 m, which is spatially better than the use of the Landsat-TM with pixel size of 30 m as low spatial accuracy. According to Guzman.Julio Pastor et al., (2015) that spectral bands around the red edge (705–753 nm) were more sensitive to mangrove leaf chlorophyll-a content, although Sentinel-2 will improve mangrove monitoring at higher spatial and temporal resolutions. But Sentinel-2A data is spatially still lower accuracy in comparison to other optical satellite data such as IKONOS with 1 m pixel size, Quickbird data with 0.6 m pixel size (Hartoko et.al., 2013; Hartoko et.al., 2015). Thus, the key factor is then to increase the spatial as well as spectral accuracy by means of best fit algorithm of the key field variable such as chlorophyll-a up to a level of mangrove species and satellite data use of 0.6 μm wavelength spectral reflectance of chlorophyll-a. Sentinel-2A data is a choice with free aquisition (with permission) with 10 m pixel size can be used to cover a single of mangrove canopy with diameter of about 10 m by species based on the field sampling coordinates. Since this is an optical data, then a minimum or possibly cloud free images would be a prerequisite for further analysis.

6. CONCLUSIONS

The current study revealed that *Rhizophora apiculata* identified as the dominant species with ecological importance in the mangrove community structure on Cawan Island. The twenty-five sampling points on the island, mangrove leaf chlorophyll-a content is in the range of 14.034-15.767 mg.ml^{-1} . The highest mangrove biomass value is 381.53 ton.ha^{-1} and the highest carbon content is 190.77 tonC.ha^{-1} . Result of algorithms for the mangrove at Cawan Island, Indragiri Hilir, Riau, Sumatera for chlorophyll-a = $0.0002(B_4 + B_2)/2^2 - 0.057(B_4 + B_2)/2 + 16.79$; biomass = $24.69(B_4/B_2)^2 - 47.41(B_4/B_2) + 36.06$; carbon = $10.071(B_4/B_2)^2 - 23.159(B_4/B_2) + 44.233$.

The new insight in this study is that the algorithm developments can be applied for mangrove chlorophyll-a content, biomass and carbon content estimation using any optical satellite data based on its relevant spectral range. This algorithm development is an open approach method based on highest correlation coefficient on regression equation of the field and the satellite spectral value. The algorithms resulted from this study can be applied over wide and in any area in the tropics.

ACKNOWLEDGMENT

The authors would like to express sincere thanks to the European Space Agency (ESA) for the use of the Sentinel-2A satellite data, and to the Institute for the funding support by Research and Community Development, Diponegoro University contract No. 233-39/UN7.6.1/PP/2022 and all parties who had assisted in this study and the writing of the manuscript.

REFERENCES

- Adip, M. S., B. Hendarto and F. Purwanti. 2014. Hue Value of Rhizophora Leaf Its Correlations to Ecological Factors Ringgung Coast, Sidodadi, Padang Cermin District, Lampung. *Diponegoro Journal Of Maquares Management Of Aquatic Resources*, 3 (2): 20–26. <https://ejournal3.undip.ac.id>
- Afifa Hersiana, A Hartoko. Pujiono WP. 2020. Changes and vulnerability of coral reef ecosystem based on field and remote sensing data on Kemujan Island, Karimunjawa Islands, Indonesia. *AACL-Bioflux*. 13(2) : 1016-1026. <http://www.bioflux.com.ro/docs/2020.1016-1026.pdf>.
- Agus, F., K. Hairiah, and A. Mulyani. 2011. Guide for Carbon of Peat Land. World Agroforestry Centre-ICRAF, SEA Regional Office and Balai Besar Penelitian dan Pengembangan Sumberdaya Lahan Pertanian (BBSDLP), Bogor, Indonesia. 58 pp.
- Akira K, J. Ong, and S. Poungparn.2008. Allometry, Biomass and Productivity of Mangrove Forest: Review. *Aquatic Botany*. 89(2) : 128-137
- Alongi, D. M., 2012. Carbon Sequestration in Mangrove Forests. *Carbon Management* ,3 : 313-322.
- Cintron, G. and Novelli, Y.S. 1984. Methods for Studying Mangrove Structure. Editors: Snedaker, S. and Snadaker, J.S. *The Mangrove Ecosystem: Research Methods*. UNESCO. France. <https://www.sciepub.com>
- Chapman, S. 2018. Mangrove Protects the Coastline, Store Carbon and are Expanding with Climate Change. <https://conversation.com>
- Chapman, V.J. (1975). Mangrove biogeography. In: Proc. Int. Symp. Biology and Management of Mangroves (Walsh, G.E., Snedaker, S.C., Teas, H.J., eds.) Univ. Florida Press.
- Clough, B.F and K Scott. 1989. Allometric Relationship for Estimating Aboveground Biomass in Six Mangrove Species. *Forest Ecology Management*. (27) : 117-127
- Donato, D. C., Kauffman, and Murdiyarso. 2012. Mangrove as the Most Rich of Carbon Stock in the Tropic. Center for International Forest Research. Bogor. <https://www.cifor.org>
- Ellison J. C., 2015 Vulnerability assessment of mangroves to climate change and sea-level rise impacts. *Wetland Ecology Management* 23:115-137. <https://link.springer.com>
- Ersad Avisha, A Hartoko, Max Rudolf M. 2020. Algorithm of Seagrass Biomass Based on Sentinel-2A Satellite and Fish Larvae of at Kemujan Island, Karimunjawa, Indonesia. *AACL-Bioflux*. 13(3) : 1511-1521. <http://www.bioflux.com.ro/docs/2020.1511-1521.pdf>
- ESA (2020). European Space Agency. <https://www.esa.int>
- Esthi Kurnia, D and B Trisakti. 2016. Comaprng Atmospheris Correction Methods for Landsat OLI Data. *Int. J. Remote Sensing and Earth Sciences* Vo.13. No.2 : 105-120. DOI: <http://dx.doi.org/10.30536/ijreses.2016.v13.a2472>. <https://jurnal.lapan.go.id>

- Febrianti, D.A., A. Hartoko, and Suryanti. 2013. Algorithm of Mangrove Biomassa and Carbon Field Data and Geoeeye Satellite Data at Parang Island, Karimunjawa Islands. *Journal of Management of Aquatic Resources*, 2 (2): 9-18. <https://ejournal3.undip.ac.id>
- Guzsman, Julio Pastor, Peter M Atkinson, Jadunandan Dash and Rodolfo Rioja-Nieto. 2015. Spatiotemporal Variation in Mangrove Chlorophyll Content Using Langsat 8. *J Remote Sensing*. 7(11) : 14530-14558. DOI: doi.org/10.3390/rs71114530.
- Hartoko, A, 1989. Effects of Plant Species and Agrochemical on Carbon Dynamics in Mangrove Leaf-Detrital Microcosm. Dept of Biology. University of Newcastle upon Tyne. UK.Pp: 63
- Hartoko, A, Indah Susilowaty, Johannes Hutabarat, Tri Winanrmi Agustini. 2010. Adaptation Strategy Towards Climate Change for the Vulnerable Fisheries of Indonesia. CBD. UNEP. Technical Series.No.51.
- Hartoko, A., S.Chayaningrum, D.A.Febriantia , D.Ariyanto and Suryanti. 2015. Carbon Biomass Algorithms Development for Mangrove Vegetation in Kemujan, Parang Island Karimunjawa National Park and Demak Coastal Area – Indonesia. *Procedia Environmental Sciences*, (23) : 39 – 47. <https://doi.org/10.1016/j.proenv.2015.01.007>
- Hartoko, A., A. Febrianto, A. Pamungkas, I. Fachruddin, M. Helmi and Hariadi. 2019. The Myth and Legend of Sadai and Gaspar Straitt Bangka Belitung (Banca-Billiton) and Oceanographic Conditions. *International Journal of GEOMATE*, 17 (62): 212-218. DOI: 10.21660/2019.62.93965
- Hartoko, A., P. Soedarsono and A. Indrawati. 2013. Mangrove Chlorophyll-a, Nitrate and Phosphate Based on Field and Geoeeye Satellite Data at Parang Island, Karimunjawa Islands (In Indonesia). *Journal of Management of Aquatic Resources*, 2 (2): 28-37. DOI: 10.13140/RG.2.2.31599.28324
- Hartoko, A., A Rahim, FH Afifa, Yoan T Sembiring, AF Erzad, Rania WH, N Latifah, MR Muskananfolo, PW Purnomo, B Hendrarto. 2021. Application Sentinel-2A for Data Base of Coastal Habitats (Aplikasi Data Sentinel Untuk Basis Data Spasial Habitat Pesisir). Graha Ilmu. E-Book. ISBN: 978-623-228-855-3
- Hendrawan, J.L. Gaol, and S.B. Susilo. 2018. Density and Mangrove Cover by Satelit Data at Sebatik Island North Kalimantan. *Journal of Tropical Marine Science*, 10 (1): 99-109.
- Heenkenda.K.Muditha, Karen E Joyce, Stefan W Maier, Sytze de Bruin. 2015. Quantifying Mangrove Chlorophyll from High Spatial Resolution Imagery. *ASPRS Journal of Photogrammetry and Remote Sensing*. 108 : 234-244. DOI: [dx.doi.org/10.1016/j.isprs.2015.08.003](https://doi.org/10.1016/j.isprs.2015.08.003)
- Hutama, Y.P., P.W. Purnomo and M. Nitisupardjo. 2016. Mangrove Potential at Tambakbulusan Village Based on Density, C/N Ratio and Total Bakteri. *Journal Of Maquares*, 5(1) : 1-7. <https://ejournal3.undip.ac.id>
- Jefrey, S.W., and G.F Humphrey, 1975. New Spectrophotometric Equations for Determining Chlorophylls a, b, c₁ and c₂ in Higher Plants, Algae and Natural Phytoplankton. *Biochem, Physiol, Pflanzen (BPP)*, Bd. 167: 191-194.<https://agris.fao.org>
- Lasibani S.M., and Ani, K. 2009. Distribution of Mangrove *Rhizophoraceae* Propagules at West Sumatera Coast. *Journal Mangrove and Coastal*, 10 (1):33-38.
- Limbong, H.D.H. 2009. Carbon Potential at the Ex-Burned *Acacia crassicarpa* Peat Land. Postgraduate. Institut Pertanian Bogor.
- Li, X.; Gar-On Yeh, A.; Wang, S.; Liu, K.; Liu, X.; Qian, J.; Chen, X. 2007. Regression and Analytical Models for Estimating Mangrove Wetland Biomass in South China Using Radarsat Images. *Int. J. Remote Sens.*, 28, 5567–5582.
- Lubis, K.M., A. Mulyadi and D. Yoswaty. 2018. Carbon Estimation of *Rhizophora apiculata* and Organic of Sediment at Cawan Island, Indragiri Hilir, Riau. Fac of Fisheries and Marine Science. Universitas Riau.
- Mitchell, K. 2007. Quantitative Analysis by the Point-Centered Quarter Method. Department of Mathematics and Computer Science Hobart and William Smith Colleges Geneva, New York.
- Muditha, Heenkenda.K. Karen E Joyce, Stefan W Maier, Sytze de Bruin. 2015. Quantifying Mangrove Chlorophyll from High Spatial Resolution Imagery. *ASPRS Journal of Photogrammetry and Remote Sensing*. 108 : 234-244. DOI: [dx.doi.org/10.1016/j.isprs.2015.08.003](https://doi.org/10.1016/j.isprs.2015.08.003)
- Murdiyanto, B. 2003. Getting to Know, Maintain and Conserve of Mangrove Ecosystem. Jakarta: *COFISH Project*. 76pp.
- Noor, R.Y., M. Khazali, and I.N.N. Suryadiputra. 2012. Guide for Mangrove in Indonesia. PHKA/WI-IP, Bogor. Office of Forestry. 2013. Mangrove Distribution. Kabupaten Indragiri Hilir. Tembilahan. Office of Environment.2009. Mangrove Ecosystem. Kabupaten Indragiri Hilir. Indragiri Hilir. Tembilahan.
- Pranata, R., A.J. Patandean and A. Yani. 2016. Mangrove Distribution Using Landsat-8 Satellite at Maros Regency. *Journal Sains dan Pendidikan Fisika*, 12 (1): 88-95.<https://ojs.unm.ac.id>
- Prianto, E.,R Jhonnerie, R. Firdaus, T.Hidayat, and Miswadi. 2006. Mangrove Diversity and Ecological Structure Dumai Coastal Area Riau Province. *Biodiversitas*, 7 (4):327-332.<https://ejournal.unsri.ac.id>

- Rachmawati, D, I. Setyobudiandi and E. Hilmi. 2014. Estimation Potential Mangrove Carbon at Muara Gembong Coast. Bekasi Regency (In Indonesian). *Omni-Akuatika*, 10 (2): 85-91. <https://ojs.omniakuatika.net>
- Ramlan, M. 2002. Global Warming. *Journal of Environmental Technology*, 3 (1): 30-32
- Riau Province Bureau of Statistic. 2013. Riau in Numbers. Pekanbaru, Indonesia.
- Santiago. F Flores de, J.M Kovacs, F Flores Verdugo. 2013. The Influence of Seasonality in Estimating Mangrove Leaf Chlorophyll-a Content from Hyperspectral Data. *Wetlands Ecol Management*. 21: 193-207. DOI: 10.1007/s11273-103-9290-x
- Sari, K.W., Yusnafi, and A. Suryanti. 2017. Decomposition of *Rhizophora apiculata* Leaf Litter at Bagan Asahan Tanjung Balai District, Asahan Regency, North Sumatera Province. *Acta Aquatica*, 4 (2): 88-94. <https://ojs.inimal.ac.id>
- Sugiyono. 2016. Quantitative and Qualitative Research Method and Mixed Methods. Bandung: Alfabeta.55pp
- Sutaryo,D. 2009. Mangrove Biomass Calculations for Carbon and Carbon Trades. *Wetlands International Indonesia Programme*. Bogor.<https://www.wetlands.or.id>
- Suryono, N. Soenardjo, E. Wibowo, R. Ario and E. F. Rozy. 2018. Mangrove Biomass and Carbon at Perancak Jembrana Regency, Bali Province. *Buletin Oseanografi Marina*, 7 (1): 1-8. <https://doi.org/10.14710/buloma.v7i1.19036>.
- Tarigan, M.S., and N.N. Wiadnyana. 2013. Monitoring of Chlorophyll-a MODIS Aqua-Terra Satellite Data at Jakarta Bay. *Marine Journal (J Kelautan)*. 8 (2): 81-89.<https://ejournal-balitbang.kkp.go.id>
- Wicaksono, P.; Danoedoro, P.; Hartono; Nehren, U. 2016. Mangrove biomass carbon stock mapping of the Karimunjawa Islands using multispectral remote sensing. *Int. J. Remote Sens.*, 37, 26–52.

Appendix:

Left – DBH measurement, Right – species observation in a deep acidic peat substrate sampling at Cawan Island, Sumatera, Indonesia.



TIDAL FLOOD MODEL PROJECTION USING LAND SUBSIDENCE PARAMETER IN PONTIANAK, INDONESIA

Randy ARDIANTO^{*1,5}, Aris ISMANTO^{2,3}, Joko SAMPURNO⁴, Sugeng WIDADA²

DOI: 10.21163/GT_2022.172.12

ABSTRACT:

Land subsidence is a phenomenon that can exacerbate the impacts of tidal floods in coastal areas, such as disrupting citizen activities, and submerging settlements and public facilities. Therefore, research on tidal floods and their relation to land subsidence was widely studied in coastal areas of Indonesia. However, this study has not yet been carried out in the Pontianak, a dense urban area located in the Kapuas River Delta, West Kalimantan Province. This study aims to analyze the impacts of land subsidence on tidal floods in the city for disaster mitigation and long-term urban planning. We calculated the land subsidence by applying the DInSAR technique to Sentinel-1A imagery. Then, tidal floods were simulated by integrating the DELFT3D hydrodynamic and HEC-RAS hydraulic models. The results showed that the output water level of the DELFT3D model has good agreement with the observation data, which the Nash Sutcliffe Model Efficiency Coefficient (NSE) is 0.83. Furthermore, the maximum land subsidence in Pontianak is ± 1.03 cm/year, where the highest subsidence (between 0.48 - 1.03 cm/year) covers about 28.54% of the total area. Our results showed that shallow inundated areas (water depth less than 0.5 meters) decreased by 23.6%, while deep inundated areas (water depth more than 0.5 meters) increased by 16.9% over the next 50-year. Overall, the depth of the tidal floods within Pontianak that occur in the future will increase by 0.03-0.4 meters and varied in across locations. These analysis results can guide the local water manager in designing a mitigation plan.

Keywords: Tidal flood, DELFT3D, HEC-RAS, Land subsidence, Pontianak

1. INTRODUCTION

Tidal flood occurs due to the movement of sea water to lowland areas which cause inundation (Kurniawan et al., 2021). Tidal flood is detrimental and hampers population activities in coastal and rivers areas are still affected by tides. Inadequate information and analysis on this phenomenon cause delays in disaster mitigation, potentially causing serious problems (Zainuri et al., 2022). The risk factors of tidal flood include rainfall, drainage density, land use, distance to the river, soil type, elevation, slope, sediment transport index, distance to the estuary, and curvature (Chang et al., 2018; Panjaitan et al., 2021).

Pontianak is one of the cities in West Kalimantan Province, Indonesia which is often affected by tidal floods, especially in the riverbank areas (BPIW, 2017; Gultom et al., 2020). Previous studies (Kuntinah et al., 2021; Sampurno et al., 2022a; Sampurno et al., 2022b) have shown that tidal flood in Pontianak often occurs during the high tide seasons from December to February. During this period, the tides reach a maximum height because affected by Asian monsoon (Kästner et al., 2018).

1. Faculty of Fisheries and Marine Sciences, Diponegoro University, 50275, Semarang, Indonesia,

* Corresponding author randy.ardianto@bmkgo.go.id

2. Department of Oceanography, Faculty of Fisheries and Marine Sciences, Diponegoro University, 50275, Semarang, Indonesia, sugengwidada@lecturer.undip.ac.id

3. Center for Coastal Rehabilitation and Disaster Mitigation Studies, Diponegoro University, 50275, Semarang, Indonesia aris109@lecturer.undip.ac.id

4. Department of Physics, Faculty of Mathematics and Natural Sciences, Tanjungpura University, 78124, Pontianak, Indonesia. jokosampurno@physics.untan.ac.id

5. Indonesian Agency for Meteorology Climatology and Geophysics, 10610, Jakarta, Indonesia

The monsoon influences the atmospheric dynamics and potentially causes storm surges and strong westerly winds that impact on the mass movement of estuary water to coastal cities with low-lying topography. The interaction between tides propagation and river streams in downstream area affects the river water level and creating two-directional currents propagation (Acreman, 1994; Pauta, 2017).

According to Sampurno et al. (2022a), the flood hazard along the Kapuas River is delineated into three regions. From the river mouth to 30 km upstream of the river (Pontianak) is the tide-dominated area, where discharge no longer controls the maximum water level, which is correlated to flood hazards. From 30 to 150 km is a transition region, where the flood is triggered by the interaction between tides, surges, and river discharge. Then, from 150 km upstream, the river-dominated area, where tides are no longer capable of triggering floods.

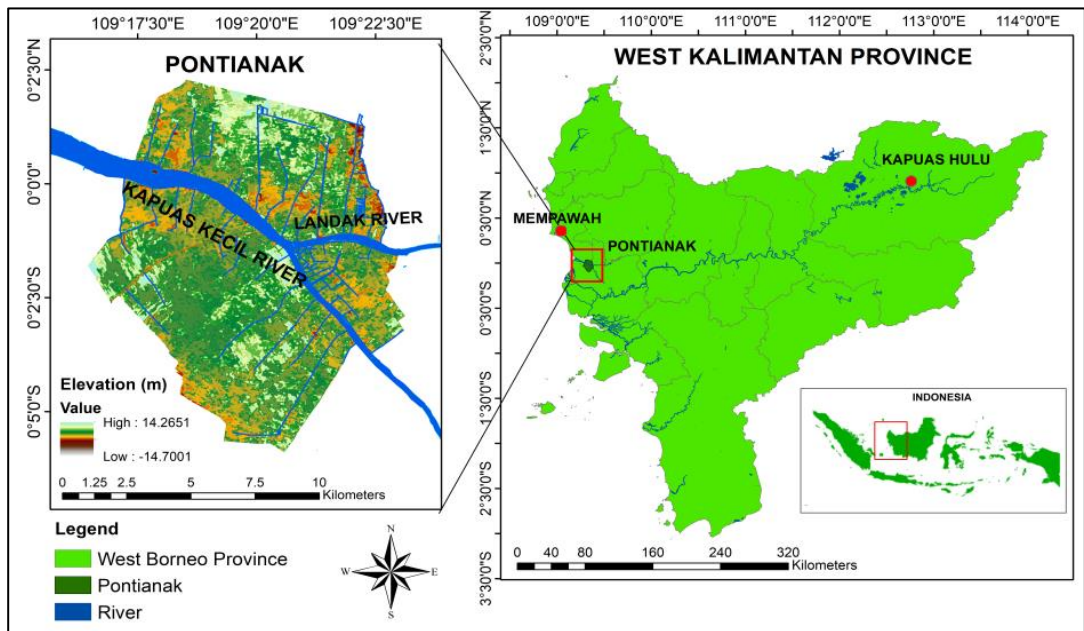


Fig. 1. The DEM of Pontianak, retrieved from the Geospatial Information Agency of Indonesia (BIG), within West Kalimantan Province, Indonesia. The province boundary and waterways maps retrieved from Geofabrik GmbH and OpenStreetMap Contributors | Map tiles: Creative Commons BY-SA 2.0 Data: ODbL 1.0.

The Kapuas River is the longest island river, with a length of 1143 km, stretching from the middle of Borneo Island (Kapuas Hulu Regency) to the western coast (Mempawah Regency). Its river branch stream (The Kapuas Kecil River) flows through Pontianak (Widjonarko et al., 2021). This Kapuas Kecil river stream meets the end of the Landak River in Pontianak, dividing the city into three parts (**Fig. 1**). The Kapuas Kecil River has a width of about 449 - 1977 meters (Lestari et al., 2017), with varying depths from 1 meter (river mouth) to 15 meters (middle stream) (Sampurno et al., 2022a). Potential inundation due to tidal flood within the city through the Kapuas River stream could reached 9.70 km² in Pontianak Kota and Pontianak Barat districts and 4.36 km² in Pontianak Selatan and Pontianak Tenggara districts (Purnomo et al., 2019; Kurnia et al., 2019).

Many factors, such as climate change, land subsidence, and sea-level rise, can exacerbate tidal floods in coastal areas. Those phenomena can increase inundation areas, destroy more infrastructures, and threaten coastal community activities (Takagi et al., 2016; Hidayat et al., 2020; Zainuri et al., 2022). Among those factors, land subsidence is vital in determining the severity of tidal flooding in the long term. Land subsidence is a major cause of environmental degradation (Hamdani et al., 2021).

Land subsidence is decreasing ground-level elevation against a stable reference field, which can occur suddenly or slowly over a long period (Khoirunisa et al., 2015; Islam et al., 2017). According to Whittaker and Reddish (1989) in Kasfari et al. (2019), land subsidence is caused by the extraction of groundwater, heavy loads from human settlement, mining activities, sedimentation of the basin area, and underground cavities that cause sink holes and natural subsidence. Characteristics of land subsidence need to be analyzed for area structuring and planning, including mitigation of tidal flood impacts.

Research on the correlation between land subsidence and the tidal flood has been carried out massively in several parts of Indonesia. In some study areas, they report that land subsidence's effect on tidal floods is more influential than sea level rise (Iskandar et al., 2020). The land subsidence has contributed to the expansion and depth of tidal floods (Marfai and King, 2008; Abidin et al., 2015; Adi and Wahyudi, 2018; Hidayat et al., 2020; Widada et al., 2020).

Unfortunately, tidal floods in the city of Pontianak are still less researched. However, some researchers have studied flood-related topics and the hydrodynamic processes within the city. Kuntinah et al. (2021) used the DELFT3D model to simulate water levels in several flood cases. Sampurno et al. (2022a) used the SLIM model to predict tide-surge-discharge interaction along the Kapuas riverbank. Therefore, this study attempts to simulate the current and the future tidal floods in Pontianak under land subsidence projection scenarios using the DELFT3D model integrated with the HEC-RAS (Hydrologic Engineering Center River Analysis System) model. The results of this study could help the local government prepare disaster mitigation strategies and long-term urban planning.

2. DATA AND METHODS

The land subsidence parameters in this study were calculated using the Differential Interferometric Synthetic Aperture Radar (DInSAR) technique with Sentinel-1 SAR satellite imagery data (Aji et al., 2018; Hidayat et al., 2020). The DInSAR technique is a unique remote sensing approach that can map topography and measure surface changes (Mohammed et al., 2022). The data used was Sentinel 1-A satellite image data on 6 December 2020 as master image and 1 December 2021 as slave image obtained from the Copernicus Open Access Hub (<https://scihub.copernicus.eu/>). Furthermore, the data was processed using the SNAP (Sentinel Application Platform) program (Serco Italia SPA, 2018). SNAP is a tool for processing and analyzing earth observation data developed by the European Space Agency (ESA) (<https://www.esa.int/>). The annual land subsidence is calculated with the formula (adapted from Iskandar et al., 2020) as follows:

$$LS = \frac{DV \times 365}{T' - T} \quad (1)$$

where LS is land subsidence for one year, DV is the displacement derived from the differential phase in the line of sight of Sentinel-1 from DInSAR processing in SNAP Tools. $T' - T$ is the time-lapse of image pair acquisition (in days), here, 6 December 2020 to 1 December 2021.

This study uses the DELFT3D 4.0 model from Deltares (<https://www.deltares.nl/>) to perform flood simulations. DELFT3D is a model that can be used to simulate water dynamics on coasts, rivers, and estuaries (Deltares, 2014). It has been successfully applied to predict water level dynamics (Kuntinah et al., 2021; Madah and Gharbi, 2022). The meteorological data as the input for this model is retrieved from the Global Forecasting System (GFS), which was provided by the National Center for Environment Prediction (NCEP, 2015), with a resolution of $0.25^\circ \times 0.25^\circ$ (data retrieved from $t+0$ to $t+72$ hours). The data comprises pressure and zonal-meridional wind components. Furthermore, the model's boundary conditions were the tidal components obtained from the TPXO 08 global tide model (Egbert and Erofeeva, 2002).

The bathymetry data were obtained from the Indonesian Navy (Kästner et al., 2019) with a resolution of 0.1 x 0.1 km, blended with data from the Geospatial Information Agency with a resolution of 0.18 x 0.18 km. The domain model was drawn from West Kalimantan's coast to the Pontianak to ensure that hydrodynamic and atmospheric phenomena were captured properly (Fig. 2). The average grid resolution was 0.25 x 0.25 km with a computational time step for 60 seconds.

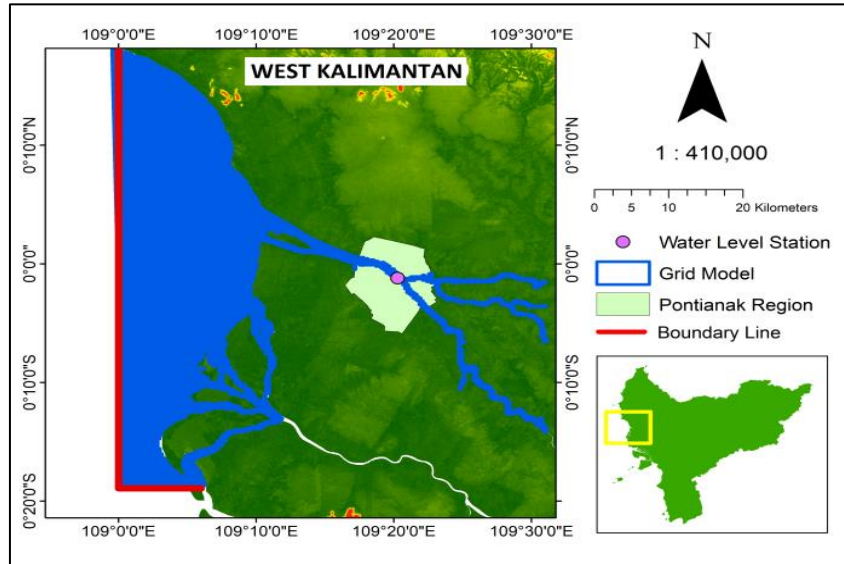


Fig. 2. Domain grid of the DELFT3D model.

The model outputs were validated using hourly observation data from the Pontianak Maritime Meteorological Station (PMMS), with the Nash Sutcliffe Efficiency (NSE) as the goodness of fit indicator. The NSE was developed by Nash and Sutcliffe (1971) and is widely used as a reliable statistic parameter for assessing the goodness of fit of hydrologic models (McCuen et al., 2006). The NSE can be calculated by the following equation:

$$NSE = 1 - \frac{\sum_{t=1}^T (Q_0^t - Q_m^t)^2}{\sum_{t=1}^T (Q_0^t - \bar{Q}_0)^2} \quad (2)$$

where Q_m^t represents the model output, Q_0^t is the observation data, and \bar{Q}_0 is the mean of observation data. The NSE coefficient interpretation is based on the criteria put forward by Motovilov (1999): NSE greater than 0.75 means good, $0.36 < NSE < 0.75$ means sufficient, and NSE less than 0.36 is assumed not sufficient.

The tidal flood inundation within the city was simulated using the HEC-RAS 6.1 model developed by the US Army Corps of Engineers (<https://www.hec.usace.army.mil/>). As the boundary conditions, the water levels and the discharges obtained from the output DELFT3D are imposed. The simulation period started from 6 December 2021 to 9 December 2021, both at 00 UTC, in 10 minutes time steps data. We chose the period because the historical rainfall data is 0 mm (based on data from the Pontianak Maritime Meteorological Station); therefore, the rainfall can be neglected, and the analysis can focus on the interaction of tides and land subsidence. The digital elevation model (DEM) used was provided by the Geospatial Information Agency of Indonesia (BIG) with a 0.27-arcsecond (8.1-meter) resolution. The DEM was corrected with Mean Absolute Error (MAE), retrieved from the benchmark point (yellow dot), which is also obtained from BIG (Fig. 3a). Next, the DEM over dense buildings located around the riverbanks was re-corrected again to remove the impacts of the buildings. Lastly, the river bathymetry was obtained from the Indonesian Navy (Kästner et al., 2019).

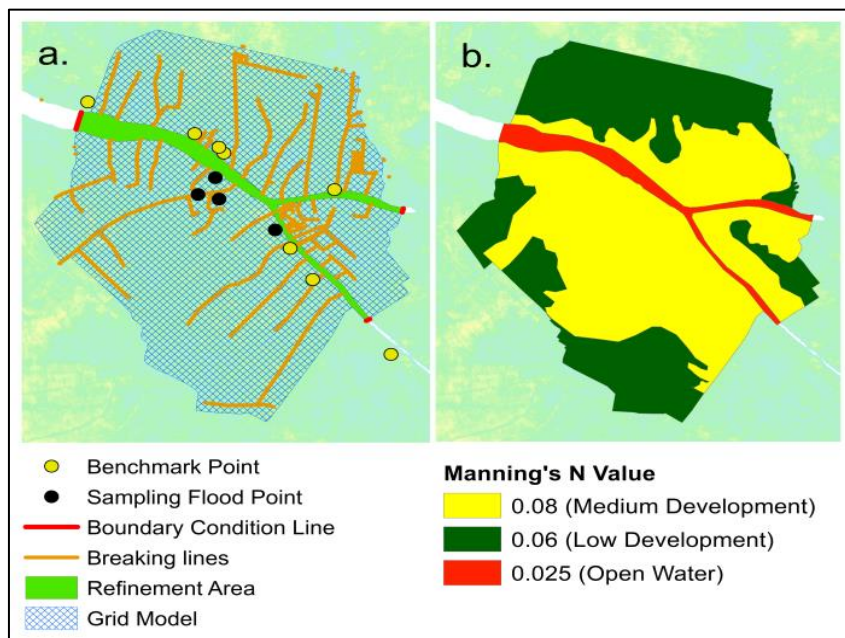


Fig. 3. a) The geometry of the HEC-RAS model. b) Manning's N Values.

The sensitivity of the flood event parameters completely depends on the flood boundary conditions, the DEM resolution, the roughness coefficient, and the 2D cell size (Pathan et al., 2021). Hence, appropriate boundary conditions and high DEM resolution will produce a more accurate model output. In addition, the roughness coefficient will affect the water propagation process. Therefore, the coefficient must be adjusted for every existing land cover. Then, the higher the grid resolution in the domain, the more detailed the model output represents the area. However, a higher grid will cost more computational resources.

The HEC-RAS model domain covered an area of 118 km² with varying resolutions between 10 and 8 meters (**Fig. 3a**). The model was run with a computing time step of 60 seconds. Next, the roughness coefficient was divided into three areas based on the type of land cover (**Fig. 3b**), including rivers (0.025), medium development area (0.08), and low development area (0.06). The coefficients are defined based on the roughness coefficient from the National Land Cover Database 2016 (Dewitz, 2019) and the recommended range of numbers in the HEC-RAS manual (HEC-RAS, 2021). The flood simulation was carried out four times on different DEM data (the current condition in 2021 and the projected conditions due to land subsidence in the next 10 years, 30 years, and 50 years).

3. RESULTS AND DISCUSSIONS

The water level extracted from the DELFT3D model output is close to the observation data (**Fig. 4**). However, there is a small difference where the peak tide's lag time in the model is one hour faster than the observation data, and the lowest ebb generated by the model is also lower than the observation data.

Furthermore, the NSE between the model output and observation is 0.83. It means that the output of the DELFT3D model meets the criteria of good conformity (against the observation) and can be used to represent the real processes. Therefore, we use those outputs as boundary conditions for the HEC-RAS model to estimate the city's tidal flood extent and depth precisely.

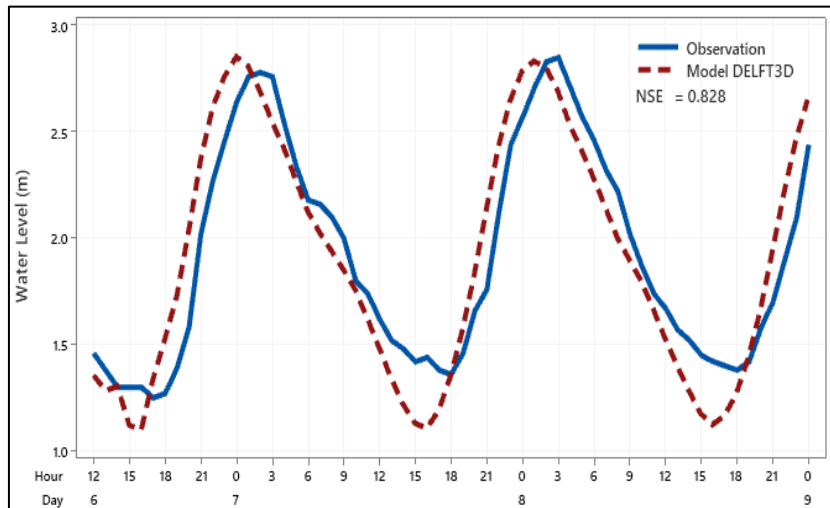


Fig. 4. Comparison between water level from the DELFT3D model output and the observation.

The output of the DELFT3D model shows that the discharge of the Kapuas Kecil ranges from 103 to 1403 m³/s (**Fig. 5a**). However, the observation data from Kästner (2019) shows that from December 2013 to April 2015, the Kapuas discharge at Sanggau (285 km from the estuary, **Fig. 5b**) was between 1000 m³/s (dry season) and 10,000 m³/s (wet season). Then at Rasau (red dot in **Fig. 5b**), 17% of the discharge flows into Kapuas Kecil River (red line), and 83% flows into Kapuas Besar River (blue line). It means the discharge entering the Kapuas Kecil River was between 170 - 1700 m³/s. Since the output of our model is close to the observation, we concluded that the output data of the DELFT3D model is acceptable to represent the real discharge.

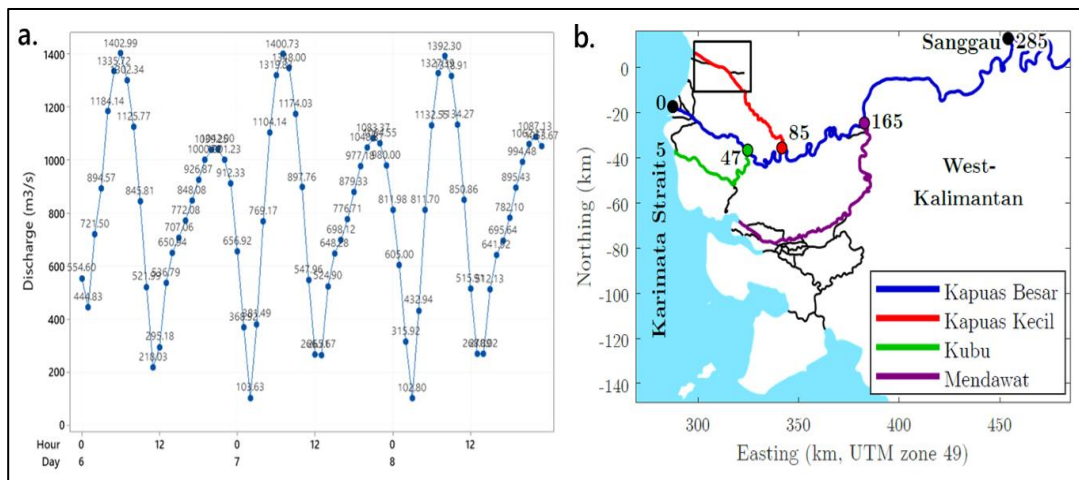


Fig. 5. a) Kapuas River discharge data from DELFT3D model output. The Kapuas River stream and its branches downstream (Kästner, 2019).

The annual land subsidence in Pontianak shows that the maximum is about 1.03 cm/year (**Fig. 6**). The extraction of the maximum land subsidence for each subdistrict in Pontianak: Pontianak Utara 0.71 cm/year, Pontianak Barat 0.89 cm/year, Pontianak Kota 0.99 cm/year, Pontianak Selatan 0.86 cm/year, Pontianak Tenggara 1.03 cm/year, and Pontianak Timur 0.86 cm/year.

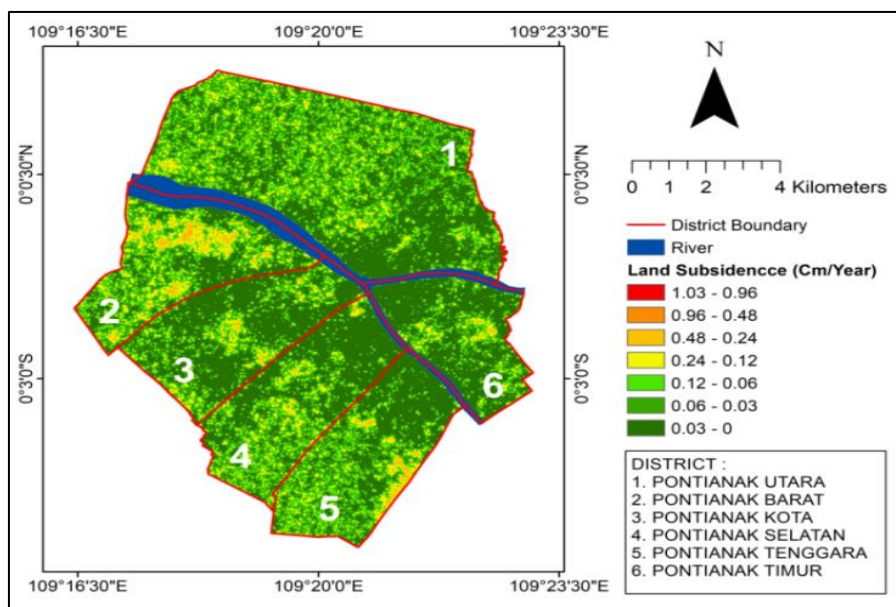


Fig. 6. Land subsidence velocity in Pontianak (cm/year).

Although southeastern Pontianak has high land subsidence, this section area is not directly connected to the river flow. Therefore, we suspect significant changes in tidal flooding for 50 years did not occur in this area. On the contrary, in the western Pontianak, land subsidence areas are directly connected to the river. Consequently, tidal flooding changes in the area will happen in the future. Land subsidence in Pontianak varies over an area of 112.11 km² (Table 1). If the existing domain model is 118 km², there are areas of 5.89 km² without subsidence. The significant land subsidence between 0.48 - 1.03 cm/year occurred over 32 km² (28.54% of the total area).

Table 1.

Land subsidence area of each subdistrict in Pontianak (km²).

Subdistricts/ LS	0 – 0.03 cm/year	0.03 – 0.06 cm/year	0.06 – 0.12 cm/year	0.12 – 0.24 cm/year	0.24 – 0.48 cm/year	0.48 – 0.96 cm/year	0.96 – 1.03 cm/year
Pontianak Utara	14.76	0.01	0.34	3.35	9.34	10.81	0.00
Pontianak Barat	4.04	0.04	0.78	2.59	3.55	3.41	0.00
Pontianak Kota	9.11	0.00	0.01	0.21	1.11	2.31	3.01
Pontianak Selatan	8.23	0.01	0.19	1.36	3.08	3.42	0.00
Pontianak Tenggara	7.02	0.00	0.01	0.37	1.41	3.32	3.72
Pontianak Timur	6.98	0.00	0.11	0.67	1.44	2.01	0.00
Sub Total	50.15	0.05	1.44	8.54	19.93	25.27	6.73
Total Area	112.11						

The simulation of tidal flood projections due to land subsidence aims to see spatial changes over 50 years for existing flood cases. The results of the inundation projection in the scenario of tidal flood cases (Fig. 7-8) show changes in flood extent area and depth.

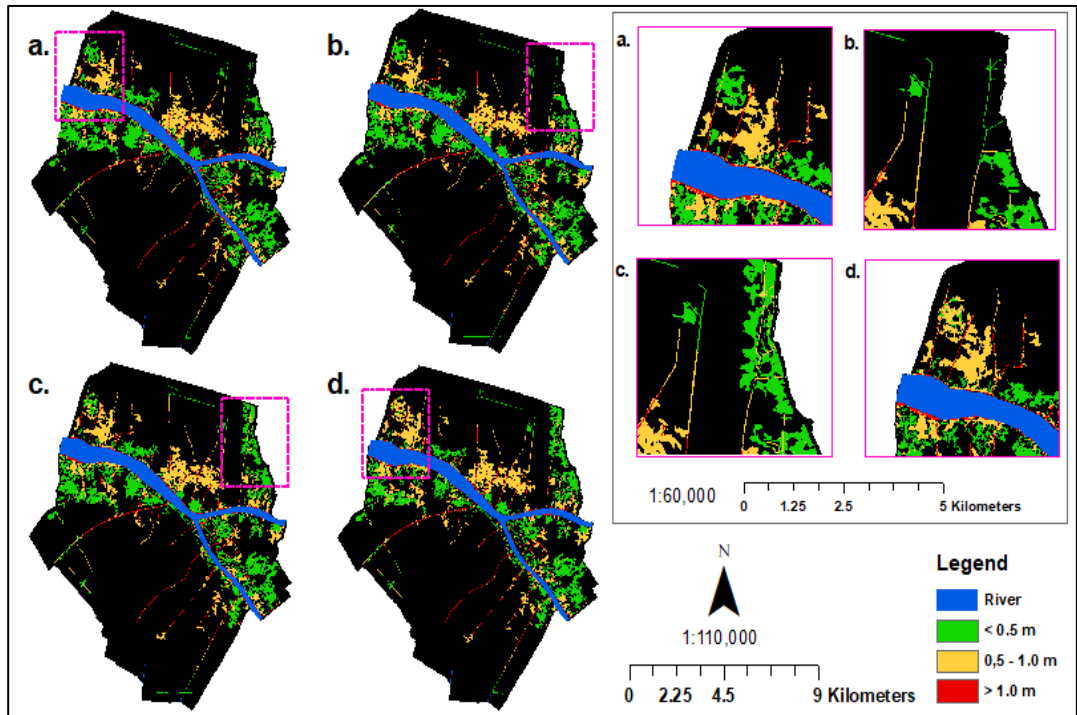


Fig. 7. The inundated areas at the flood's peak on 7 December 2021 at 02.00 UTC in a) current condition, b) 10 years, c) 30 years, and d) 50 years.

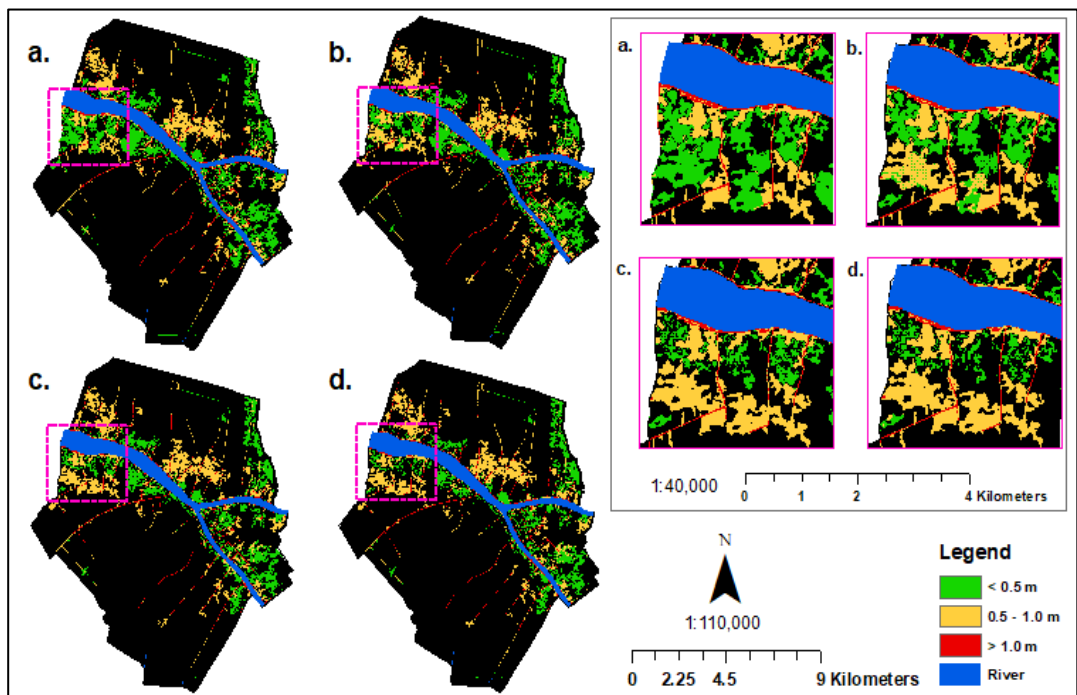


Fig. 8. The inundated areas at the flood's peak on 8 December 2021 at 03.00 UTC in a) current condition, b) 10 years, c) 30 years, and d) 50 years.

For example, northern Pontianak has not been inundated in the current condition and ten years simulations, and then it's become flooded in the next 30 and 50 years. Furthermore, the longer the projection period, the deeper the inundated area in western Pontianak, but its extent narrower (the map color changes from green to yellow).

Table 2.

Inundated areas for each flood's peak scenario (in km²).

7 December 2021				
No.	Simulation Period	Inundation < 0.5 meters	Inundation 0.5 – 1.0 meters	Inundation > 1.0 meters
1.	Current (2021)	10.15	7.07	1.90
2.	10 years	10.01	7.07	1.90
3.	30 years	9.82	7.33	1.92
4.	50 years	8.71	7.68	1.95
8 December 2021				
No.	Simulation Period	Inundation < 0.5 meters	Inundation 0.5 – 1.0 meters	Inundation > 1.0 meters
1.	Current (2021)	10.37	7.93	1.99
2.	10 years	9.29	8.60	2.02
3.	30 years	7.97	8.86	2.16
4.	50 years	7.10	8.95	2.18

Generally, there is a dynamic flood area extent based on their respective depths (**Fig. 7-8**). Based on DEM, we suspect that land subsidence in Pontianak is uneven and clustered. If the land use is constant and the boundary condition is the same, then the inundation depth in some areas will be deepened. **Table 2** shows the inundation projection for the next 50 years based on the scenario of the 7 December 2021 and 8 December 2021 floods. Using the 7 December scenario, we project that the inundated areas with less than 0.5 meters depth decreased by 6.3%, while the inundated areas with a depth between 0.5 - 1.0 meters increased by 4.1%, and then the inundated area with a depth more than 1 meter increased by 1.2%. On the other hand, the flood projection based on the 8 December 2021 flood event shows that the inundated areas with depths lower than 0.5 meters decreased by 23.6%. Meanwhile, the inundated areas with depths between 0.5 - 1.0 meters increased by 10.4%, and inundated areas with depths deeper than 1 meter increased by 6.5% in the next 50 years.

The simulation results showed that the flood depth would be deeper in the future but impacts different sub-areas differently. Location A and D (**Fig. 9a** and **Fig. 9d**) showed that land subsidence increased the depth of the inundation by 0.1 - 0.4 meters. Location B (**Fig. 9b**) showed that in the next 10 years, the flood depth will increase to 0.4 meters, and dry areas in the current scenario will be inundated in future scenarios. Furthermore, for the next 30 and 50 years, while tidal floods subside, waters may remain within the area for two days. The flood dynamic in location C (**Fig. 9c**) is similar to locations A and B but has different depth changes. The simulation for the next 10 years shows that the depth increases by 0.03 meters. Meanwhile, for the next 30 and 50 years, the depth will increase by 0.1 - 0.18 meters.

Overall, we concluded that the impact of land subsidence on tidal flooding in Pontianak varied within each sub-area. The tidal flood depth will increase over the next 50 years due to land subsidence between 0.03 - 0.4 meters. The local government can use this information to plan mitigation strategies for each sub-area within the city.

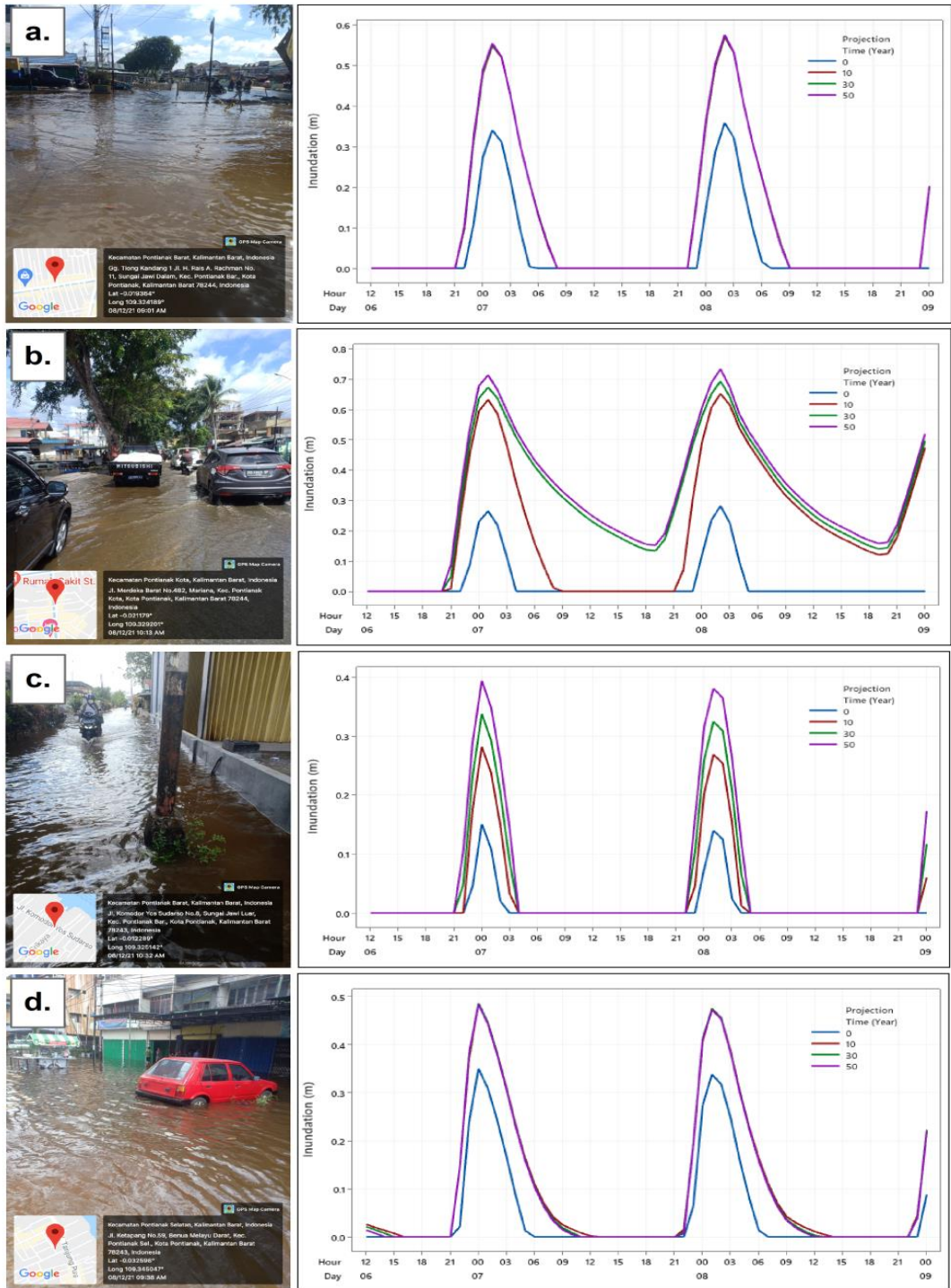


Fig. 9. (a-d) The tidal flood sample locations: documentation of flood events on 8 December 2021 at the different sample locations (left); time-series of flood depth dynamic in the current (0 years) and the future projections (right).

4. CONCLUSIONS

In this study, we successfully built a model that simulates the tidal flood projection due to land subsidence in the study area. The water level validation output of the DELFT3D model shows a good agreement with the observation data, with a NSE of 0.83 (good criteria). Our results showed that land subsidence in Pontianak, which reaches a maximum of ± 1.03 cm/year, will decrease the shallow inundation areas (depth less than 0.5 meters) by 23.6% and increase the deep inundated areas (depth more than 0.5 meters) by 16.9% over a next 50-year. Although the southeastern area of Pontianak has high land subsidence, the area is not directly connected to the river flow. Therefore, tidal flooding in the next 50 years over the area will not be affected. While in the western Pontianak, where the areas are well connected to the river, land subsidence will exacerbate tidal flooding. Overall, the depth of the tidal floods within Pontianak that occur in the future will increase by 0.03 - 0.4 meters and varied in across locations. The local government can use the analysis results to plan proper mitigation to reduce the flood risk.

ACKNOWLEDGMENTS

Randy Ardianto's master degree fellowship was provided by the Center for Human Resource Capacity Development of Meteorological Climatological and Geophysical Agency (PUSDIKLAT BMKG). The sentinel 1-A satellite image was provided by the Copernicus Open Access Hub (<https://scihub.copernicus.eu/>). The Digital Elevation Model (DEM) and BATNAS data (<https://tanahair.indonesia.go.id/>), Benchmark Point data (<https://srgi.big.go.id/>) were provided by the Geospatial Information Agency of Indonesia (BIG).

REFERENCES

- Abidin, H. Z., Andreas, H., Gumilar, I., and Wibowo, I. R. R. (2015). On correlation between urban development, land subsidence and flooding phenomena in Jakarta. *Proceedings of the International Association of Hydrological Sciences*, 370, 15-20. <https://doi.org/10.5194/piahs-370-15-2015>
- Acreman, M. C. (1994). Assessing the joint probability of fluvial and tidal floods in the River Roding. *Water and Environment Journal*, 8(5), 490-496. <https://doi.org/10.1111/j.1747-6593.1994.tb01140.x>
- Adi, H. P., & Wahyudi, S. I. (2018). Tidal Flood Handling through Community Participation in Drainage Management System (A case study of the first water board in Indonesia). *International Journal of Integrated Engineering*, 10(2). <https://doi.org/10.30880/ijie.2018.10.02.004>
- Aji, R.P., Prasetyo, Y., and Awalludin, M. (2018). Lembang Fault Study Using Sentinel-1a Imagery for Monitoring Potential Earthquake Disasters. *Jurnal Geodesi Undip* 7(2), pp. 304-313
- Badan Pengembangan Infrastruktur Wilayah (BPIW) .(2017).<http://perkotaan.bpiw.pu.go.id/n/kota-otonom/40>.(last access: 5 September 2022)
- Chang M.J., Chang H.K., Chen Y.C., Lin G.F., Chen P.A., Lai J.S., and Tan Y.C.(2018). A Support Vector Machine Forecasting Model for Typhoon Flood Inundation Mapping and Early Flood Warning Systems. *Water* 10(12):1734. <https://doi.org/10.3390/w10121734>
- Deltares. (2014). User Manual Delft3DFlow: Simulation of multi-dimensional hydrodynamic flows and transport phenomena, including sediments. Deltares, Delft Netherland.
- Dewitz, J.(2019). National Land Cover Database (NLCD) 2016 Products: U.S. Geological Survey data release, <https://doi.org/10.5066/P96HHBIE>.
- Egbert, G. D., and Erofeeva, S. Y. (2002). Efficient inverse modeling of barotropic ocean tides. *Journal of Atmospheric and Oceanic technology*, 19(2), 183-204.
- Gultom, B. J. B., Jati, D. R., & Andi, A. (2020). Comparison Of Flood Disaster Adaptation In The Kapuas River (Pontianak) Waterfront And Kakap River Area. *Jurnal Pengembangan Kota*, 8(1), 12-22. <https://doi.org/10.14710/jpk.8.1.12-22>

- Hamdani, R. S., Hadi, S. P., & Rudianto, I. 2021. "Progress or Regress? A Systematic Review on Two Decades of Monitoring and Addressing Land Subsidence Hazards in Semarang City" *Sustainability* 13, no. 24: 13755. <https://doi.org/10.3390/su132413755>
- HEC-RAS. (2021). *Creating Land Cover, Manning's N Values, And % Impervious Layers*. US Army Corps of Engineers, Hydrologic Engineering Center, Version 6.0, June 2021
- Hidayat, T.A., Helmi, M., Widada, S., Satriadai, A., Setiyono, H., Ismanto, A., and Yusuf, M. (2020). Processing of Sentinel-1 and Tidal Satellite Data to Study Inundation Areas Due to Tidal Floods in Sayung District, Demak Regency. *Indonesian Journal of Oceanography* 2(4), pp. 01-07
- Iskandar, S.A., Helmi, M., Muslim., Widada, S., and Rochaddi, B. (2020). Geospatial Analysis of Rob Flood Inundation Areas and Its Impact on Land Use in 2020-2025 in Pekalongan City, Central Java Province. *Indonesian Journal of Oceanography* 2(3), pp. 73 - 84
- Islam, L.J.F., Prasetyo, Y and Sudarsono, B. (2017). Analysis of Land Subsidence (Land Subsidence) of Semarang City Using Sentinel-1 Image Based on Dinsar Method in Snap Software. *Jurnal Geodesi* 6(2), pp. 29-36
- Kasfari, R., Yuwono, B. D., dan Awaluddin, M. (2018). Observation of Land Subsidence in Semarang City in 2017. *Jurnal Geodesi*, 7(1), pp. 120-130
- Kästner, K., Hoitink, A. J. F., Torfs, P. J. J. F., Vermeulen, B., Ningsih, N. S., and Pramulya, M.(2018). Prerequisites for accurate monitoring of river discharge based on fixed-location velocity measurements. *Water Resources Research*, 54, pp. 1058- 1076. <https://doi.org/10.1002/2017WR020990>
- Kästner, K.(2019). *Multi-scale monitoring and modelling of the Kapuas River Delta*. Wageningen University. <https://doi.org/10.18174/468716>
- Kästner, K., Vermeulen, B., Hoitink, T., and Geertsema, T. J. (2019). Data underlying "Multi-Scale monitoring and modelling of the Kapuas River Delta" . Wageningen University & Research. <https://doi.org/10.4121/uuid:b163813a-a893-47ae-b4db-a2c7eeb06596>
- Khoirunisa, R., Yuwono, B.D., Wijaya, and A.P. (2015). Analysis of Land Subsidence in Semarang City in 2015 Using Gamit 10.5 Software. *Jurnal Geodesi* 4(4), pp. 341-350
- Kuntinah., Nugraheni, I. R., and Ardianto, R. (2021). The Simulation of Water Level Using Delft3D Hydrodynamic Model to analyze the case of coastal Inundation in Pontianak. *Innovative Technology and Management Journal*, 4, pp. 32-44
- Kurnia, M.I., Mulki, G.Z., and Firdaus H. (2019). Mapping of Flood Hazards in South Pontianak and Southeast Pontianak Districts Based on Geographic Information Systems (GIS). *JeLAST : Jurnal PWK, Laut, Sipil, Tambang* 6(2) <http://dx.doi.org/10.26418/jelast.v6i2.34343>
- Kurniawan, D., Prasetyo, S., and Fibriani, C. (2021). Distribution of Vegetation in Areas with Potential for Coastal Flood Disasters (Rob) Semarang City. *Indonesian Journal of Computing and Modeling*, 4(1), pp. 10-13. <https://doi.org/10.24246/icm.v4i1.4653>
- Lestari, A. D., Pramadita, S., & Simatupang, J. M. (2017). Sedimentation in the Kapuas Kecil River, Pontianak, West Kalimantan Province. *Prosiding Semnastek*.
- Madah, F., and Gharbi, S. H. (2022). Numerical Simulation of Tidal Hydrodynamics in the Arabian Gulf. *Oceanologia*. doi: 10.1016/j.oceano.2022.01.002.
- Marfai, M. A and King, L. (2008). Tidal inundation mapping under enhanced land subsidence in Semarang, Central Java Indonesia. *Natural hazards*, 44(1), 93-109. <https://doi.org/10.1007/s11069-007-9144-z>
- McCuen, Richard & Knight, Zachary & Cutter, A. (2006). Evaluation of the Nash-Sutcliffe Efficiency Index. *Journal of Hydrologic Engineering - J HYDROL ENG*. 11. 10.1061/(ASCE)1084-0699(2006)11:6(597).
- Mohamed, S. A., Nasr, A. H and Keshk, H. M. (2022). Three-Pass (DInSAR) Ground Change Detection in Sukari Gold Mine, Eastern Desert, Egypt. *In Pervasive Computing and Social Networking* (pp. 653-662). Springer, Singapore. https://doi.org/10.1007/978-981-16-5640-8_49
- Motovilov, Y.G., Gottschalk, L., Engeland, K.,and Rodhe, A. (1999). Validation of a Distributed Hydrological Model Against Spatial Observations. *Elsevier Agricultural and Forest Meteorology* 98. pp. 257-277 [https://doi.org/10.1016/S0168-1923\(99\)00102-1](https://doi.org/10.1016/S0168-1923(99)00102-1)
- National Centers for Environmental Prediction/National Weather Service/NOAA/U.S. Department of Commerce. 2015, updated daily. NCEP GFS 0.25 Degree Global Forecast Grids Historical Archive. Research Data Archive at the National Center for Atmospheric Research, Computational and Information Systems Laboratory. <https://doi.org/10.5065/D65D8PWK>. Accessed † April 1, 2022.

- Nash, J. E., & Sutcliffe, J. V. (1970). River flow forecasting through conceptual models part I—A discussion of principles. *Journal of hydrology*, 10(3), 282-290. [https://doi.org/10.1016/0022-1694\(70\)90255-6](https://doi.org/10.1016/0022-1694(70)90255-6)
- Panjaitan, M., Mulia, A.P., and Nasution, Z.P. (2021). North Medan Rob Flood Mapping Using Artificial Neural Network and Gis for Mitigation Steps. *Jurnal Syntax Admiration*, 2(8), pp. 1512-1526.
- Pathan, A.I., Agnihotri, P.G., and Patel, D. (2021). Identifying the efficacy of tidal waves on flood assessment study – a case of coastal urban flooding. *Arab J Geosci* 14, 2132. <https://doi.org/10.1007/s12517-021-08538-6>
- Pauta, D. F. M. (2018). Tidal influence on the discharge distribution at two junctions of the Kapuas River (West Kalimantan, Indonesia) (Doctoral dissertation). <http://hdl.handle.net/10316/47412>
- Purnomo, S., Mulki, G.Z., and Firdaus, H. (2019). Mapping of Flood Prone in West Pontianak District and Pontianak City Based on Geographic Information System (GIS). *JeLAST: Jurnal PWK, Laut, Sipil, Tambang* 6(2). <http://dx.doi.org/10.26418/jelast.v6i2.34829>
- Sampurno, J., Vallaey, V., Ardianto, R., and Hanert, E. (2022a). Modeling interactions between tides, storm surges, and river discharges in the Kapuas River delta, *Biogeosciences* (19) pp. 2741-2757, <https://doi.org/10.5194/bg-19-2741-2022>
- Sampurno, J., Vallaey, V., Ardianto, R., Hanert, E. (2022b). Integrated hydrodynamic and machine learning models for compound flooding prediction in a data-scarce estuarine delta. <https://doi.org/10.5194/npg-2021-36>.
- Serco Italia SPA. (2018). Land Subsidence with Sentinel-1 using SNAP (version 1.2). Retrieved from RUS Lectures at <https://rus-copernicus.eu/portal/the-rus-library/learn-by-yourself/> Accessed † April 4, 2022
- Takagi, H., Thao, N & T A, Le. (2016). Sea-Level Rise and Land Subsidence: Impacts on Flood Projections for the Mekong Delta's Largest City. *Sustainability*. Pp 8-15. <http://dx.doi.org/10.3390/su8090959>
- Widada, S., Zainuri, M., Yulianto, G., Satriadi, A., Wijaya, Y. J., and Helmi, M. (2020). Mitigation of floodwaters inundation due to land subsidence in the coastal area of Semarang City. *IOP Conference Series: Earth and Environmental Science* (Vol. 530, No. 1, p. 012006). IOP Publishing.
- Widjonarko, W., Ardi, I. A., & Hidayati, S. R. (2021). Multi-Hazard Disaster in the Kapuas River Basin, West Kalimantan. *Reka Ruang*, 4(2), 95-105. <https://doi.org/10.33579/rkr.v4i2.2756>
- Zainuri, M., Helmi, M., Novita, M. G. A., Kusumaningrum, H. P., & Koch, M. (2022). Improved Performance of Geospatial Model to Access the Tidal Flood Impact on Land Use by Evaluating Sea Level Rise and Land Subsidence Parameters. *Journal of Ecological Engineering*, 23(2). <http://dx.doi.org/10.12911/22998993/144785>

DAILY STREAMFLOW FORECASTING USING EXTREME LEARNING MACHINE AND OPTIMIZATION ALGORITHM. CASE STUDY: TRA KHUC RIVER IN VIETNAM

Huu Duy NGUYEN ¹ 

DOI : 10.21163/GT_2022.172.13

ABSTRACT:

Accurate prediction of streamflow plays an important role in water resource management and sustainability. Recent years have seen increased interest in data-based models, compared to the more established physics-based models, due to the accuracy of their predictions. Better results mean greater support for those who are tasked with formulating strategies and writing policy around water resource management. The objective of this study is the development of a state-of-the-art streamflow prediction method based on extreme learning machine (ELM), optimized by both hunger games search (HGS) and social spider optimization (SSO) to make accurate predictions for the Tra Khuc River in Vietnam. Rainfall and flow from 2000 to 2020 at Son Giang station on the Tra Khuc River were used to build the streamflow prediction model. The statistical indices root-mean-square error, mean absolute error, and the coefficient of determination (R^2) were applied to assess the predictive ability of the proposed models. The results showed that both optimization algorithms successfully improved the ELM model to predict the streamflow for one day and six days ahead by using data from one day and three days before the day in question. Of the proposed models, the ELM-SSO model scored highest, with $R^2=0.891$ for the one-day-ahead prediction and $R^2=0.701$ for six days ahead. Second was ELM-HGS ($R^2=0.889$ and $R^2=0.699$ for one day and six days respectively), and third was ELM ($R^2=0.883$, $R^2=0.696$). The results demonstrate ELM to be a robust data-driven method for simulating time series regimes that is appropriate for various hydrological applications. The models proposed in this study can be generalized to predict streamflow in rivers around the world.

Key-words: ELM-SSO, ELM-HGS, Streamflow, Machine learning, Tra Khuc river.

1. INTRODUCTION

Streamflow prediction plays an important role in water resource management. It is required in the optimization of water resource distribution, water quality assessment, and agriculture and industrial development (Adnan et al., 2022; Lin et al., 2021; Parisouj et al., 2020). The streamflow process is very complicated because it is influenced by multiple parameters, such as precipitation, temperature, evaporation, and land use. It is also characterized by a nonlinear relationship between flow rates and characteristics of the watershed. Therefore, accurate prediction of streamflow is difficult (Ahmed et al., 2021; Parisouj et al., 2020).

The literature broadly consists of two sets of streamflow prediction models: physics-based and data-based. Physics-based models are developed only using real-life streamflow data (Khosravi et al., 2021; Rahimzad et al., 2021). Although this method has been proven effective in predicting the streamflow of rivers around the world, the development of such models is very complicated and time-consuming. In addition, physical-based models require detailed data like topography, precipitation, and land use/land cover to calibrate model parameters, and these models can also be negatively affected when watershed data do not respond well to water balance constraints (Khosravi et al., 2021). The uncertainty of precipitation and hydrology data also greatly influences streamflow prediction,

¹ Faculty of Geography, University of Science, Vietnam National University, Hanoi, Vietnam, nguyenduynh@hus.edu.vn

and physics-based models suffer in data-limited regions (Krzysztofowicz, 2002). Such models may be replaced by more robust automated techniques.

In recent years, data-driven models have received increasing attention from the worldwide scientific community. They enjoy low input-data requirements and are easy to use. There are two main groups: statistical models and machine learning models. Statistical models include logistic regression (Long et al., 2022), fuzzy logic (Kothari and Gharde, 2015), autoregressive integrated moving average model (Ab Razak et al., 2018; Singh et al., 2020), and autoregressive model (Özgür, 2005; Terzi and Ergin, 2014). These models assume a linear relationship between input and output data, so they cannot explain the nonlinear relationship of hydrological processes. This limits performance.

Machine learning has proven more effective than statistical models in solving the problem of nonlinearity when predicting streamflow. Such models include support vector machine (Guo et al., 2011; Kisi and Cimen, 2011), random forest (Wang et al., 2021a), extreme learning machine (ELM; Yaseen et al., 2016; Yaseen et al., 2019), artificial neural network (Ali and Shahbaz, 2020; Ghimire et al., 2021), and long short-term memory network (LSTM; Ghimire et al., 2021; Hunt et al., 2022). However, traditional models use samples discretely, including input and output data, so the performance of these models often deteriorates if the input data contains some degree of error (Rahimzad et al., 2021; Tikhamarine et al., 2020). Additionally, several studies have pointed out that data-driven models have limited effectiveness in streamflow prediction because they require time-series information and produce temporal dependence on the data (Adnan et al., 2021a; Ahmed et al., 2021). To overcome these shortcomings, several studies have demonstrated how prediction accuracy can be improved by developing hybrid models, eliminating the weak points of individual models (Bui et al., 2020; Nguyen, 2022a; Pham et al., 2020).

Adnan et al. (2022) integrated the adaptive neuro-fuzzy inference system (ANFIS) model with five optimization algorithms, namely gradient-based optimization (GBO), particle swarm optimization (PSO), genetic algorithm (GA), differential evolution, ant colony optimization, and gray wolf optimization (GWO) to predict streamflow in Pakistan. ANFIS-GBO was shown to perform better than the other models in predicting streamflow. Adnan et al. (2021b) combined the ELM model with PSO, GWO, and gravitational search algorithm (GSA) to predict the streamflow in the Mangla watershed of northern Pakistan. The ELM-PSOGWO model was superior to the other models (ELM, ELM-PSO, ELM-GWO, and ELM-PSOGSA). Kilinc and Haznedar (2022) used LSTM network and GA to predict the streamflow in the Euphrates River in western Asia. The LSTM-GA model outperformed the LSTM model. Al-Juboori (2021) combined K-nearest neighbor (KNN) with random tree (RT) to predict the monthly streamflow in three rivers in Iraq. The results saw the hybrid KNN-RT model outperform the individual KNN and RT models.

These models can be divided into three main approaches: ensemble framework, evolutionary algorithm, and swarm-based algorithm. Of the three approaches, swarm-based algorithms are the most popular and have been shown to be effective in predicting the streamflow in previous studies (Nguyen et al., 2021). These approaches can solve global optimization problems through the process of exploration and exploitation. However, according to the no-free-lunch theory, there are no methods that can solve all problems in all regions, due to differences in climatic, hydrological, and environmental conditions and in human activities (Bui et al., 2020). Because of this, the selection process is always subject to significant bias. Moreover, the overfitting problem looms large when using machine learning (although models can perform well in the training process because they learn the targets based on the samples in the past to predict streamflow in the future, in many cases, if the data is limited, these models may not perform well in the validation process (Mosavi et al., 2018).

The objective of this study is the development of state-of-the-art models based on the ELM, hunger games search (HGS), and social spider optimization (SSO) algorithms to predict streamflow in the Tra Khuc River. This study is different from previous studies because it is the first time the ELM model has been combined with HGS and SSO to predict streamflow. In recent years, streamflow in the study area has been strongly influenced both by climate change and human activity, particularly in the dry season.

2. STUDY AREA AND DATA USE

The Tra Khuc River is over 160 km long and is located in the Central region of Vietnam (**Fig. 1**). Its source is in the east of the Truong Son Mountain range and it flows into the sea at Quang Ngai. The basin has an area of about 3703 km². The basin's complex topography generally lowers from west to east. There are four main terrain types: plateau, high mountains, plains, and sandy coast. The plateau has an elevation of between 1100 and 1300 m and accounts for about 5% of the basin area. The high mountains have an average elevation of 500 to 700 m and account for about 70% of the study area. The plain runs from north to south, close to the sea; it has an altitude of 20–10 m and covers about 20% of the study area. The sandy coastal area consists of sand dunes distributed in a narrow strip, running along the coast, with an average width of about 2m.

The Tra Khuc River basin is located in a tropical monsoon region and sees an average annual rainfall of about 2960 mm. The climate of the study area is characterized by two main seasons: a rainy season from September to January – which accounts for 70–75% of total annual rainfall – and a dry season from February to August, where severe drought is not uncommon.

The hydrological system in the Tra Khuc River is characterized by short rivers and steep slopes. The river has nine main branches: Daclang, Nuoc Lac, Dacseco, Tam Dinh, Xa Dieu, Tam Rao, Song Giang, Song Phuoc, and tributary number 9. Their combined length is 195 km. The average flow rate of the Tra Khuc River (calculated over several years) is 176 m³/s. The flood season figure is 13 L/s/km². The uneven distribution of flows between the rainy and dry seasons is considered to be one of local authorities' greatest challenges. During each rainy season, the basin floods an average of between five and seven times, while in the dry season, the river flow is depleted enough to cause severe drought, with significant effects on economic development.

Water resource management is considered one of the major challenges of local government in the study area. In recent years, reservoirs have been built upstream of the Tra Khuc river, which cause negative effects on the water resource downstream: the water level of the river downstream tends to become drier and drier in dry season and increase rapidly in the rainy season. Therefore, streamflow prediction is an important task to build appropriate strategies for water resource management and agriculture development.

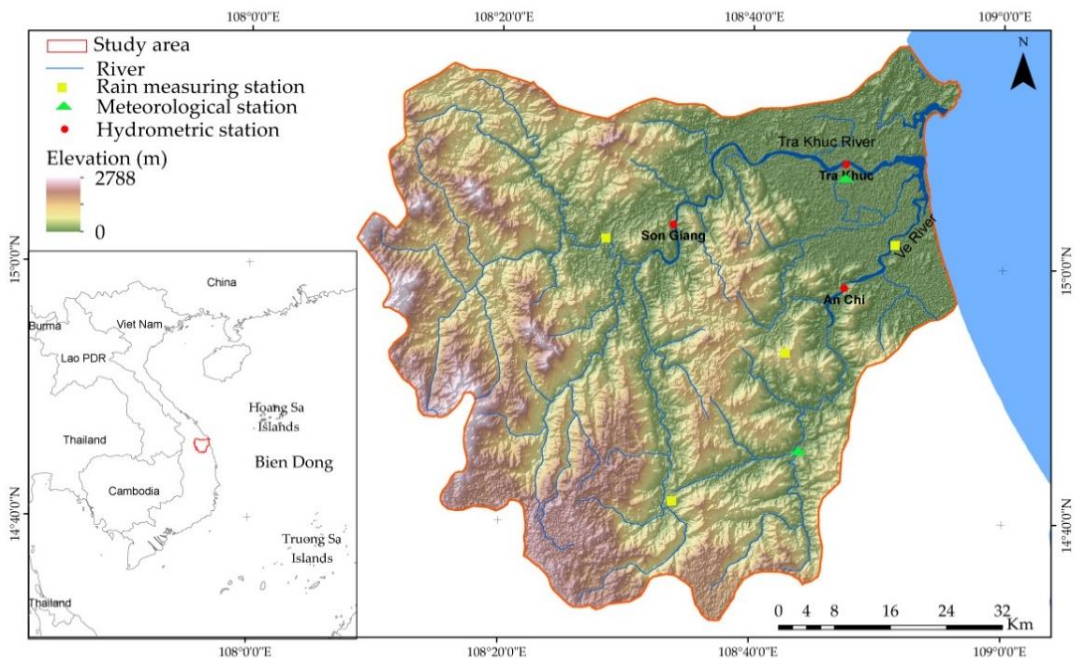


Fig. 1. The location of Tra Khuc River in Vietnam.

In this study, daily rainfall and streamflow data at Son Giang station on the Tra Khuc River from the period 2000–2020 were used to construct streamflow predictions for one day and six days ahead. These data were divided into two parts: 90% were used to calibrate the model parameters, while the remaining 10% were used to evaluate model performance (**Fig.2**).

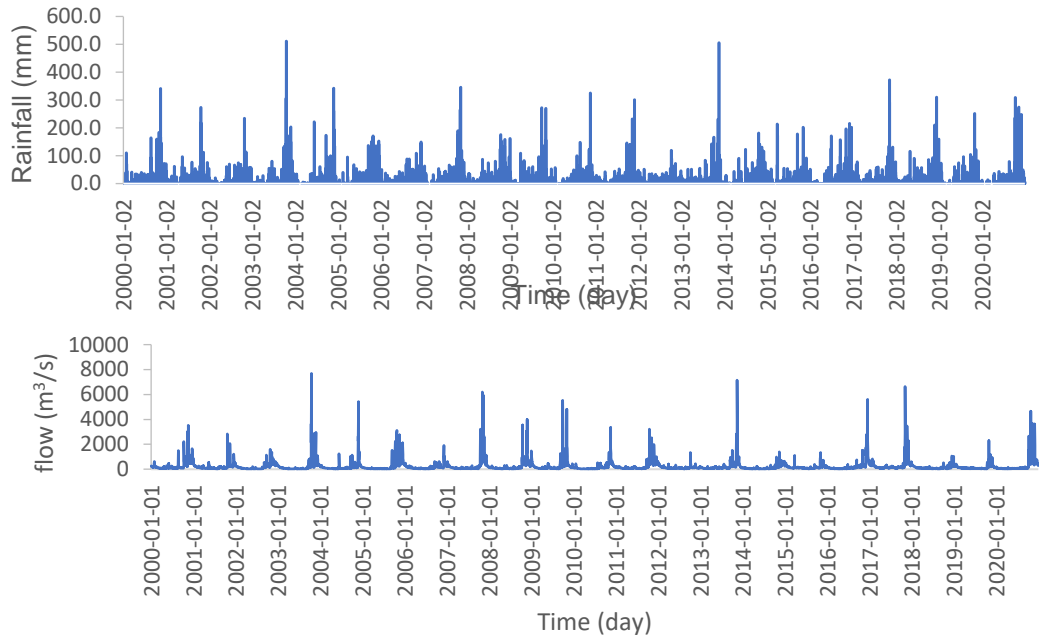


Fig. 2. Rainfall (top) and flow (bottom) at Son Giang, 2000–2020.

To make the model input data consistent and increase convergence in the model training process, precipitation and flow were normalized before being input into the model. There are several normalization techniques, such as nominal, ordinal, ratio, and min-max normalization. In this study, min-max normalization was used to prepare the data. In this technique, the original values of the precipitation and flow data were kept, but the input database was normalized using the ranges of similar measurements. The min-max was calculated by the following equation:

$$D_{normalised} = \frac{(D_i - D_{min})}{(D_{max} - D_{min})}$$

3. METHODS

This study can be divided into four main steps: i) data collection, ii) model building, (iii) model validation, and iv) streamflow prediction (**Fig. 3**).

i) Data collection

Precipitation and flow data at Son Giang station were collected to build the streamflow prediction models. Precipitation and flow data from the past one and three days were used to predict the streamflow for one day and six days ahead. Although multiple hydro-meteorological factors affect streamflow – including temperature, evaporation, and change in land cover – we considered only precipitation, as the development of an accurate prediction model using limited information is very useful, especially in regions where data is not available, and because the study region is located in a mountainous region with low average temperature, so temperature and evaporation may not play as important a role in streamflow prediction as they usually do.

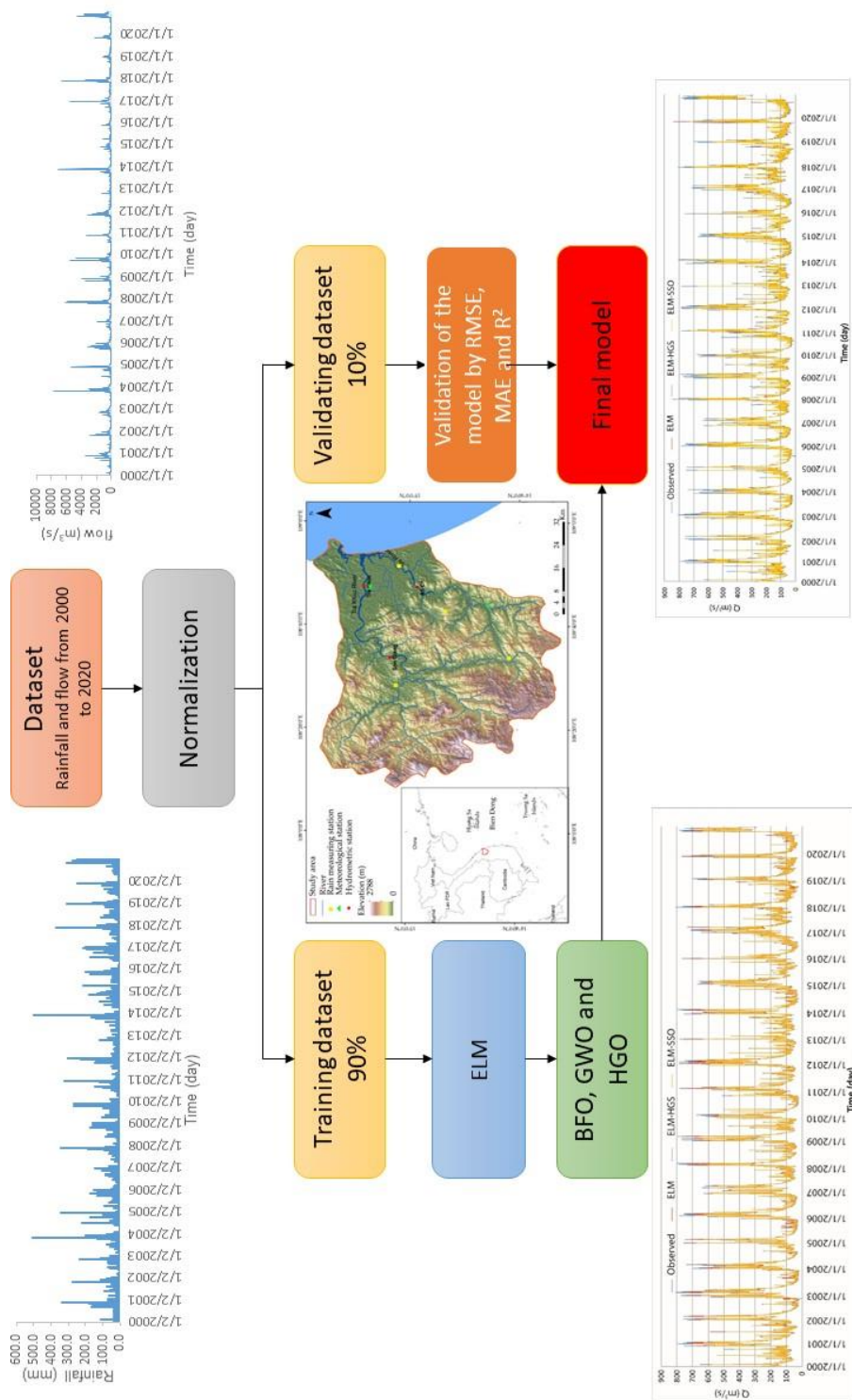


Fig. 3. Flowchart of the models ELM, ELM-HGS, and ELM-SSO.

The model used in this study is based on neural networks, which have the advantage of describing non-linear relationships between the input and output variables of a system. Initially, an analysis of the data obtained made it possible to highlight the information necessary to define the input variables of the network. Then, we identified the weights or parameters assigned to network connections. For this, the data was divided into two parts. As there are no universal guidelines for splitting data, we tried several different rates. The best results were obtained by using 90% of the data to build the models and 10% of the data to validate.

Precipitation and flow data were not normally distributed; therefore, before use, these data were normalized to improve the predictive ability of the models.

ii) Model construction

HGS and SSO were used to improve the prediction ability of the ELM model. The model construction process was divided into two main steps: the first was the initialization of the ELM model parameters using the trial-and-error method. The second was the determination of the optimal parameters of the hybrid models.

ELM is a feed-forward neural network for predicting the streamflow with a single layer of hidden nodes, where the weights connecting the inputs to the hidden nodes are randomly distributed and never updated. The weights between the hidden nodes and the outputs are learned in a single step, which is essentially the same as learning a linear model. In this study, the initialization of the neural network parameters included 256 weight values. 256 represents – for example – the position of the spider in the web for SSO or the number of animals in the hungry state for HGS.

iii) Model validation

The statistical indices RMSE, MAE, and R^2 were used to validate the streamflow model. These indices have been shown to be effective in previous studies.

iv) Use model

Predict streamflow at Son Giang station on the Tra Khuc River.

3.1. ELM

ELM is a feed-forward neural network, which means that the data only traverses the series of layers in one direction (Ding et al., 2014). The structure of ELM includes three layers of neurons: the input layer, the hidden layer, and the output layer (Wang et al., 2021b). The input layer gets the information from the input data, while the output layer gets a linear one without any transformation function. The hidden layer plays a role of linking the input layer and the output layer. Extreme learning machines use the concept of random projection and early perceptron patterns to do specific types of problem solving (Huang et al., 2006). In the ELM model, rather than adjusting all the weights of a neural network to emulate a function, the neural network is made up of a large number of neurons in the inner layer. Input weights are randomly initialized once and stay with that value. The adaptation, which is also done in one go, therefore only concerns the weights of the output layer (Qu et al., 2021; Wang et al., 2021b).

The output function of the ELM model is computed by the following equation:

$$Y = \sum_{i=1}^m B_i f(w_i x_j + b_i), j \in [1, n]$$

where m is the number of hidden nodes, B is the vector of output weights, x is the output vector of the hidden layer, and f is the activation function.

Compared with conventional models, the hidden node parameters in ELM are not only independent from the training data, but also from each other. Additionally, ELM can generate node parameters before considering formation

3.2. HGS

HGS is a swarm-based optimizer algorithm, first introduced by Yang et al. (2021). This algorithm is inspired by the behavior of animals in a state of starvation. In order to find food and improve their survival, animals tend to cooperate with each other. Stronger animals have a greater heart capacity to obtain food than weak animals (Yang et al., 2021).

In nature, animal behavior is influenced by many different factors, a primary one being hunger. When the food source is limited, it leads to competition between animals – a “hunger game.” The HGS algorithm is divided into two stages: the first stage simulates the process of cooperation between animals to find a food source; the second step describes the animals’ activities in a state of starvation (Abu Shanab et al., 2021; Yang et al., 2021). The HGS algorithm has proven effective in the technical assessment and analysis of natural hazards (Nguyen, 2022b).

3.3. SSO

SSO is a swarm-based optimization algorithm first developed in 2015 (Cuevas et al., 2013). It is inspired by the foraging behavior of spiders (Bui et al., 2020). In nature, spiders often live in groups and cooperate with each other in search of food. The spider web is considered as an n-dimensional search space where each node is a solution to the optimization problem. Spiders are agents that search by moving through the area (web) from node to node in search of the optimal solution (Humaidi et al., 2021). Spiders are divided into male and female groups. Each spider receives a weight value that corresponds to the solution it represents. The movement of each spider generates vibrations that propagate through the search space. Other spiders receive vibrations and rely on capacitive dynamics to determine the size of the spider and how far away it is. The spider's current position is affected by the current positions of all other spiders in the colony and their previous positions (Ochoa et al., 2017). The SSO algorithm solves the optimization problem by performing the following steps (Klein et al., 2015; Luque-Chang et al., 2018):

- i) The optimization process starts by collecting information from random locations on the spider web.
- ii) Spiders are divided into two groups (60-90% of spiders in the colony are female; the rest are male).
- iii) The weight of each spider is determined by the objective function.
- iv) Identify the best spider in the herd, the best female, and the spider in the center position.
- v) The position of each spider is continuously updated after each loop.
- vi) Male and female spiders within the mating radius will mate to produce new spiders.
- vii) New spiders will replace weak spiders if they have better weight.

3.4. Performance assessment

In this study, to assess the accuracy of machine learning technique in the training and validation process, the statistical indices RMSE, R^2 , and MAE were used. These indices have been shown to be effective in previous studies (Parisouj et al., 2020; Rasouli et al., 2012).

RMSE and MAE are used to measure the errors between observation values and prediction values (Chicco et al., 2021). They are calculated by the following equations:

$$RMSE = \sqrt{\frac{1}{n} \sum_{i=1}^n (Y_{predicted} - Y_{observed})^2}$$

$$MAE = \frac{1}{n} \sum_{i=1}^n |Y_{predicted} - Y_{observed}|$$

where n is the number of samples, $Y_{predicted}$ is the prediction value at sample i , and $Y_{observed}$ is the observation value at sample i .

R^2 is a statistical indicator that measures the strength and weakness of the relationship between the observation and prediction streamflow value (Meshram et al., 2022; Pirzado et al., 2021).

The value of R^2 varies from 0 to 1. The closer R^2 is to 1, the more accurate the streamflow prediction model is.

4. RESULTS

4.1. Evaluation of the number of previous days

Table 1 presents the accuracy of the proposed models in predicting the streamflow for one day and six days ahead. In general, when data from three days ago was used, the performance of the models increased. In the case of the one-day-ahead prediction, for the ELM model, the value of RMSE decreased from 52.707 to 51.373, MAE decreased from 25.261 to 24.995, and R^2 increased from 0.883 to 0.891. For the ELM-HGS model, the value of RMSE decreased from 51.165 to 50.301. MAE value decreased from 24.721 to 23.206. R^2 value increased from 0.889 to 0.896. For the ELM-SSO model, the value of RMSE decreased from 50.74 to 50.233. MAE value decreased from 24.667 to 23.199. While the R^2 value increased from 0.891 to 0.901.

In the case of six days ahead, for the ELM model, the RMSE value decreased from 84.763 to 83.815. MAE value decreased from 41.141 to 40.742. While the R^2 value increased from 0.696 to 0.699. For the ELM-HGS model, the RMSE value decreased from 84.337 to 39.333. MAE value decreased from 40.274 to 39.333. R^2 value increased from 0.699 to 0.705. For the ELM-SSO model, the value of RMSE decreased from 84.17 to 83.289. MAE value decreased from 40.161 to 39.245. While the R^2 value increased from 0.701 to 0.707.

In general, the ELM-SSO model performed better than the other models in predicting one-six days ahead using the one and three previous days, followed by ELM-HGS, ELM, respectively. The results also showed that two optimization algorithms were successfully improved to predict the streamflow in the Tra Khuc river.

Table 1.

Performance of the models for one-six days ahead using one and three previous days.

One previous day						
	For one day ahead			For six days ahead		
	RMSE	MAE	R^2	RMSE	MAE	R^2
ELM	52.707	25.261	0.883	84.763	41.141	0.696
ELM-HGS	51.165	24.721	0.889	84.337	40.274	0.699
ELM-SSO	50.74	24.667	0.891	84.17	40.161	0.701
Three previous days						
ELM	51.373	24.995	0.891	83.815	40.742	0.699
ELM-HGS	50.301	23.206	0.896	83.302	39.333	0.705
ELM-SSO	50.233	23.199	0.901	83.289	39.245	0.707

4.2. Evaluation of the one-day and seven-day ahead

To assess the prediction capacity of the proposed models, this study used two prediction scenarios (for one day ahead and six days ahead). In general, as the number of prediction days increases, the accuracy of the models is decreased in both cases of using one previous day and three previous days. Fig. 4 and 5 showed the value of R^2 for the proposed models for one and six days ahead using one and three previous days.

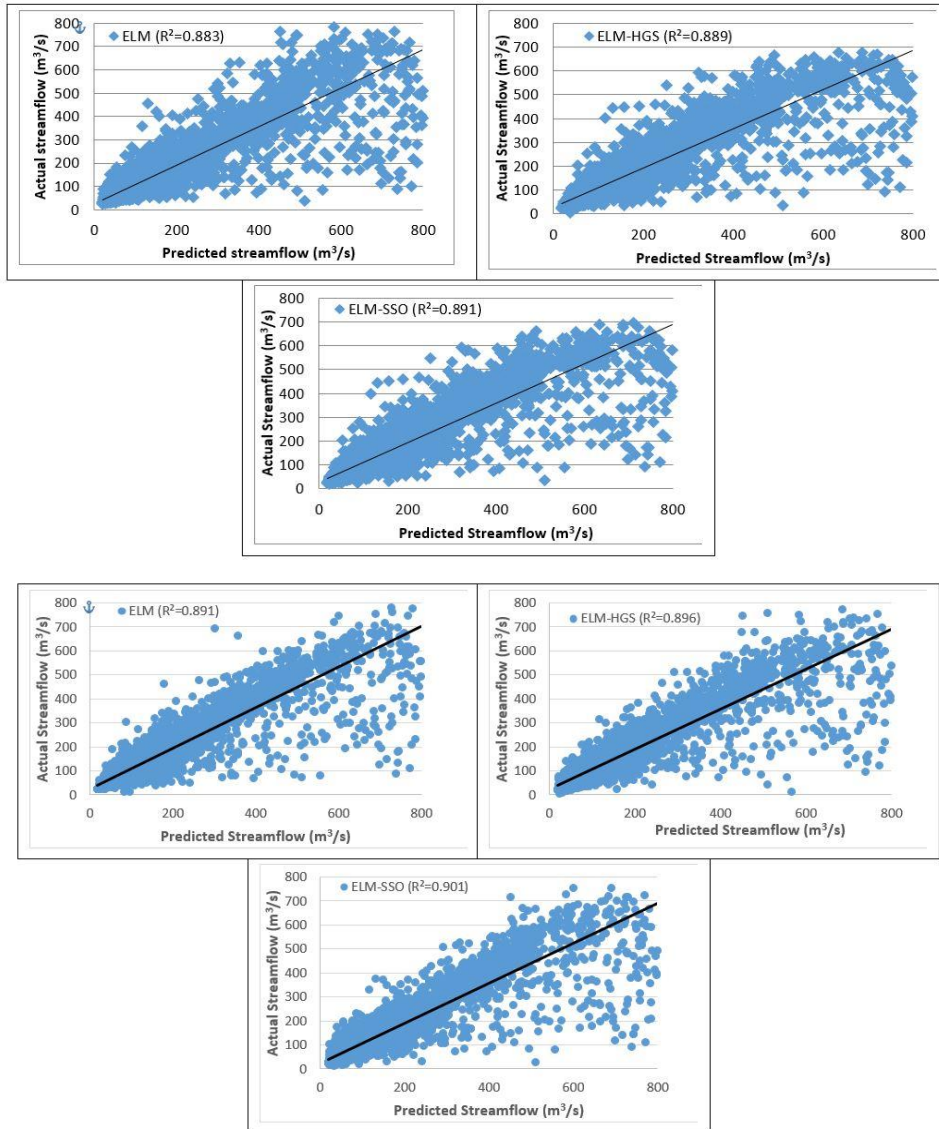


Fig. 4. R^2 value for one day ahead using one (top) and three (down) previous days.

For one previous day, for the ELM model, the value of RMSE increased from 52.707 to 84.763 when the day ahead increased from one to six days. The same, the value of MAE increased from 25.261 to 41.141. While the R^2 value decreased from 0.883 to 0.696. For the ELM-HGS model, the value of RMSE increased from 51.165 to 84.337 and from 24.721 to 40.274 for MAE. The R^2 value decreased from 0.889 to 0.699. For the ELM-SSO model, the RMSE value increased from 50.74 to 84.17 and from 24.667 for MAE. While the R^2 value decreased from 0.891 to 0.701.

For three previous days, the value of RMSE increased from 51.373 to 83.815 and from 24.995 to 40.742 for the value of MAE. While the value of R^2 decreased from 0.891 to 0.699 for the ELM model. For the ELM-HGS model, the value of RMSE increased from 50.301 to 83.302 and from 23.206 to 39.333 for the value of MAE. While the R^2 value decreased from 0.896 to 0.705. For the ELM-SSO model, the value of RMSE increased from 50.233 to 83.289 and from 23.199 to 39.245 for the value of MAE. The R^2 value decreased from 0.901 to 0.707.

It can be seen on the above figures that by increasing the number of previous days to forecast the flow, the observed and predicted values tend to concentrate along the regression line, and to approach each other. Therefore, the accuracy of the model increases.

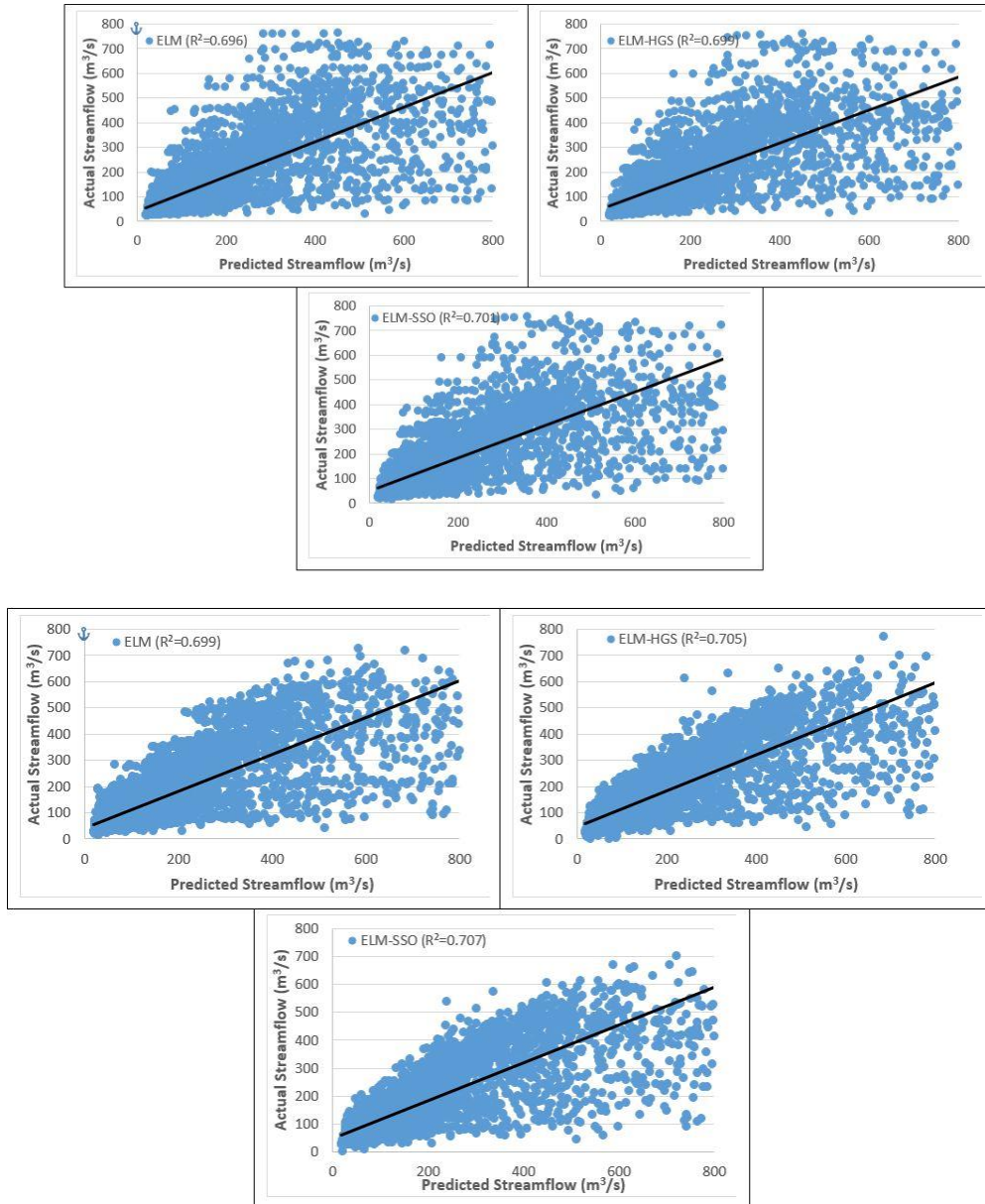


Fig. 5. R^2 value for six days ahead using one and three previous days.

On the contrary, by increasing the number of forecast days from 1 to 6 days, the values of observations and forecasts tend to be further from the regression line and further out. As a result, the accuracy of the model decreases.

Fig. 6 and **7** show the throughput value for one and six days ahead using one and three previous days. For one day ahead using one and three previous days, in general, the predicted streamflow value follows the observed streamflow value. However, the predicted streamflow value during major flooding tends to be lower than the observed streamflow value. Meanwhile, for six days ahead using one and three previous days, not only the streamflow value at large floods is lower than the observed value, but also at small and medium floods.

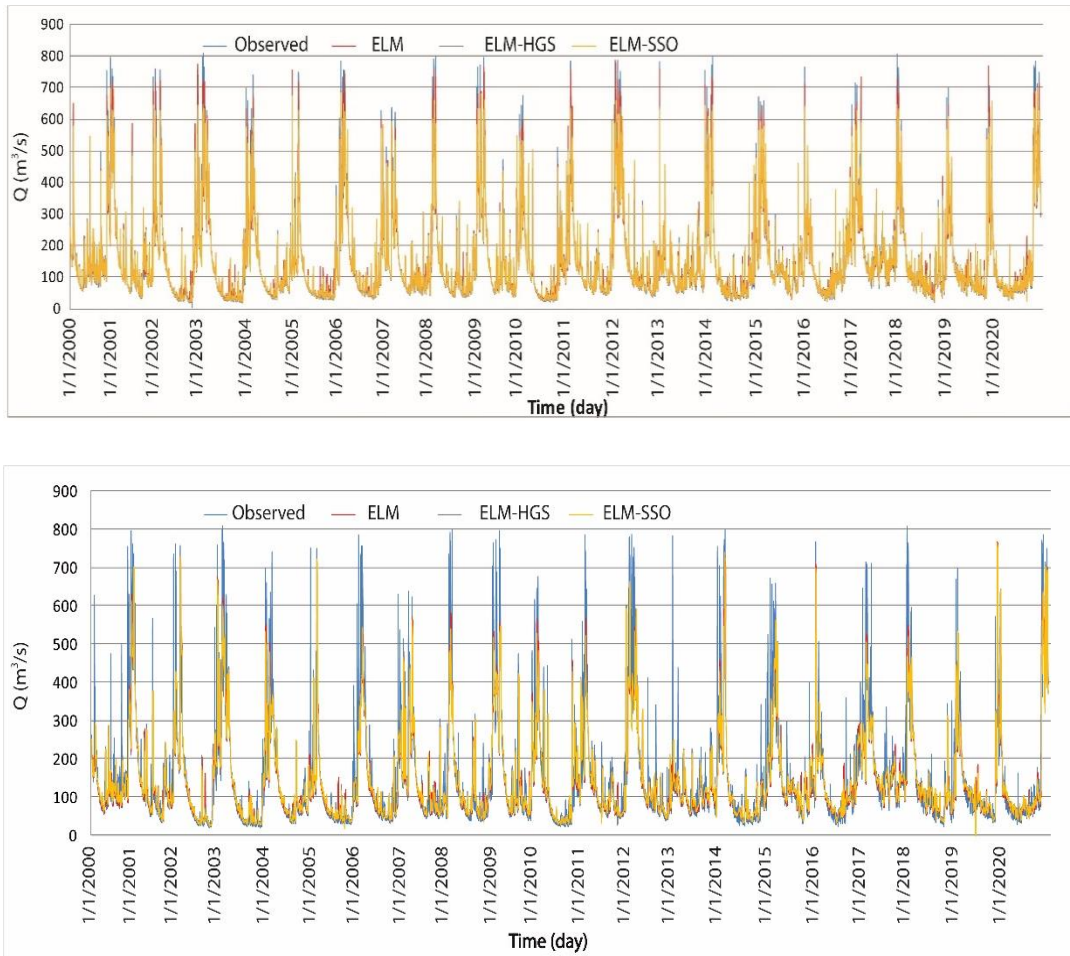


Fig. 6. The streamflow for one (top) and six (down) days ahead using one previous day.

Fig. 6 and **7** show the throughput value for one and six days ahead using one and three previous days. For one day ahead using one and three previous days, in general, the predicted streamflow value follows the observed streamflow value. However, the predicted streamflow value during major flooding tends to be lower than the observed streamflow value. Meanwhile, for six days ahead using one and three previous days, not only the streamflow value at large floods is lower than the observed value, but also at small and medium floods.

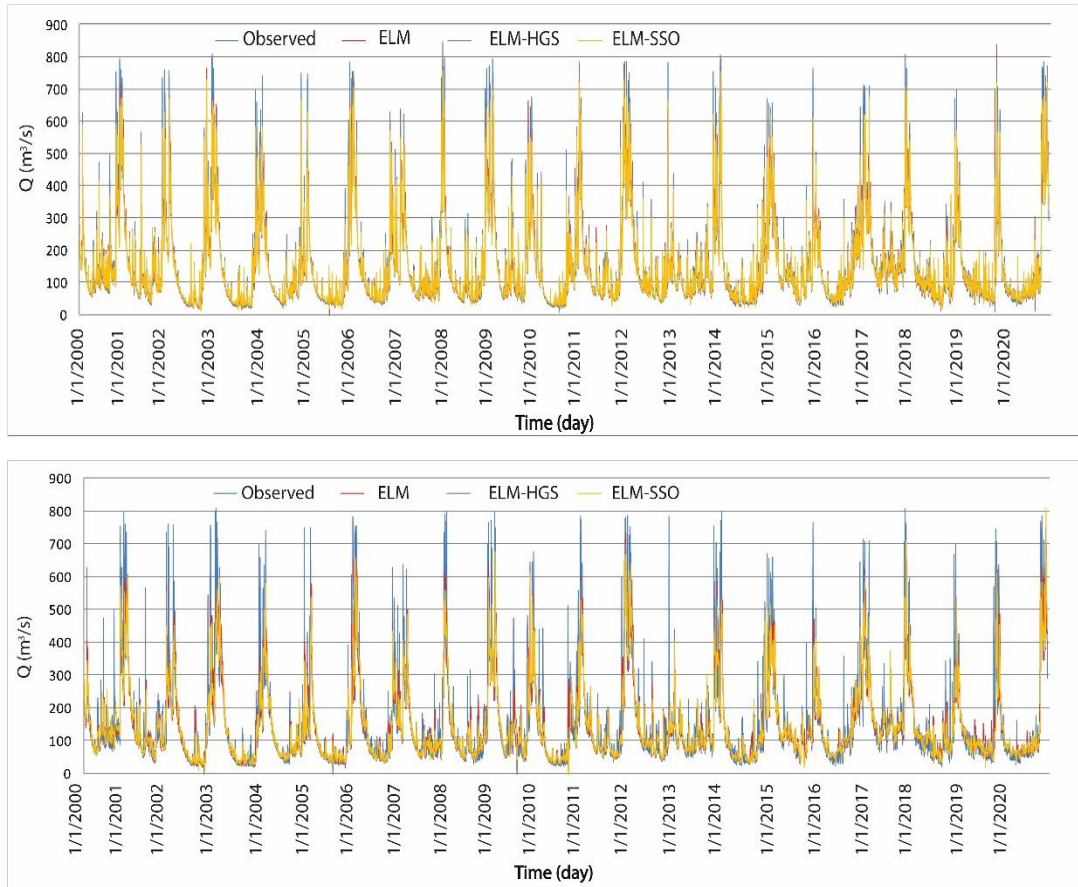


Fig. 7. The streamflow for one and six days ahead using three previous days.

5. DISCUSSION

The accurate prediction of short- and long-term streamflow plays an important role in water-resource management, operation, and planning. While short-term prediction (on hourly, multi-hour, or daily timescales) is used to provide information on flood forecasting, long-term prediction (over weeks, months, seasons, or years) provides important information for planning reservoir operations and for water resource management in general (Liu et al., 2022; Mohammadi, 2021; Rahimzad et al., 2021). However, both are difficult, due to the stochastic and nonlinear characteristics of the flow process at long time scales (Mendoza et al., 2017). Therefore, in recent years, great effort has been made in the development of automated control and monitoring methods. Using artificial intelligence techniques as a basic tool for decision support can generate more detailed answers.

ELM stands out from other tools due to its capacity and its speed of learning. In addition, it has the advantage of being able to intrinsically describe non-linear relationships between the input variables and the output variables of a system (Adnan et al., 2021a; Anmala and Turuganti, 2021; Gholizadeh et al., 2022).

The results confirmed that two optimization algorithms (HGS and SSO) successfully improved the prediction ability of the ELM model. Among the proposed models, ELM-SSO performed best, with $R^2 = 0.891$ (one day ahead) and 0.701 (six days ahead), followed by ELM-HGS with $R^2 = 0.889$ (one day ahead) and 0.699 (six days ahead), and then ELM with $R^2 = 0.883$ (one day ahead) and 0.696 (six days ahead).

SSO has advantages regarding the balance between the processes of exploration and exploitation. Compared with traditional methods, the learning and convergence speed of SSO is faster (Luque-Chang et al., 2018; Mirjalili et al., 2015). HGS is based on a population with a factor that transforms randomly, so it can enrich the ability of exploration and exploitation in the process of foraging. Moreover, HGS has advantages on the adaptive and time-varying mechanism, so this algorithm can solve the local optimization problem (Yang et al., 2021).

In recent years, streamflow has been strongly influenced by human activities such as dam construction and land-cover change. This causes difficulties in streamflow prediction, especially in extreme conditions such as flooding. Although several previous studies have shown the data-based approach to be better than other approaches (Tran et al., 2021; Tran and Kim, 2022), there is still debate around the effectiveness of machine learning and deep learning in streamflow prediction under the aforementioned conditions. This may be resolved if the amount of data to train the data is sufficient.

This study encountered general limitations. Several studies have pointed out that the water level at the station is considered an important factor in predicting streamflow; however, in the study area, the water level is very difficult to measure. So, in future research, we will try to collect more data to improve the predictive ability of the proposed models. Additionally, as mentioned above, streamflow has been influenced by human and climatic activities. This topic needs to be explored in greater depth.

6. CONCLUSIONS

Streamflow prediction with high precision can play a crucial role in optimizing the distribution of water resources, the development of agriculture, and in industry more generally. Therefore, the objective of this study is the development of state-of-the-art method based on ELM and two optimization algorithms, namely HGS and SSO to predict the daily streamflow in the Tra Khuc river of Vietnam.

In this study, two optimization algorithms were successfully proven to improve the prediction ability of the ELM model to predict the streamflow in the Tra Khuc River. The complete proposed models can be generalized to predict the streamflow in the other river in Vietnam, especially in data-limited regions. The use of machine learning can support decision makers in building appropriate strategies and policies for water resource management.

The hydrological regime of the Tra Khuc River was recorded during the process of ELM, ELM-HGS, ELM-SSO model formation, with an accuracy of +0.8. Of the proposed models, the ELM-SSO model performed best. The results highlighted that the prediction of the extreme discharge values of the proposed models is still limited and the accuracy of prediction results decrease when increasing the number of prediction days. The results of this study can be an effective tool to analyze and develop water resource management strategies in Vietnam in particular and in the whole world in general. The methodology used in this study can also be developed to predict the natural hazard such as salinity prediction.

REFERENCES

- Ab Razak, N., Aris, A., Ramli, M., Looi, L. & Juahir, H. (2018) Temporal flood incidence forecasting for segamat river (malaysia) using autoregressive integrated moving average modelling. *Journal of Flood Risk Management*, 11, S794-S804.
- Abushanab, W.S., Abd Elaziz, M., Ghandourah, E.I., Moustafa, E.B. & Elsheikh, A.H. (2021) A new fine-tuned random vector functional link model using hunger games search optimizer for modeling friction stir welding process of polymeric materials. *Journal of materials research and technology*, 14, 1482-1493.
- Adnan, R.M., Mostafa, R.R., Elbeltagi, A., Yaseen, Z.M., Shahid, S. & Kisi, O. (2022) Development of new machine learning model for streamflow prediction: Case studies in pakistan. *Stochastic Environmental Research and Risk Assessment*, 36 (4), 999-1033.

- Adnan, R.M., Mostafa, R.R., Kisi, O., Yaseen, Z.M., Shahid, S. & Zounemat-Kermani, M. (2021a) Improving streamflow prediction using a new hybrid elm model combined with hybrid particle swarm optimization and grey wolf optimization. *Knowledge-Based Systems*, 230, 107379.
- Adnan, R.M., R. Mostafa, R., Kisi, O., Yaseen, Z.M., Shahid, S. & Zounemat-Kermani, M. (2021b) Improving streamflow prediction using a new hybrid elm model combined with hybrid particle swarm optimization and grey wolf optimization. *Knowledge-Based Systems*, 230, 107379.
- Ahmed, A.M., Deo, R.C., Feng, Q., Ghahramani, A., Raj, N., Yin, Z. & Yang, L. (2021) Deep learning hybrid model with boruta-random forest optimiser algorithm for streamflow forecasting with climate mode indices, rainfall, and periodicity. *Journal of Hydrology*, 599, 126350.
- Al-Juboori, A.M. (2021) A hybrid model to predict monthly streamflow using neighboring rivers annual flows. *Water Resources Management*, 35 (2), 729-743.
- Ali, S. & Shahbaz, M., (2020) Streamflow forecasting by modeling the rainfall–streamflow relationship using artificial neural networks. *Modeling Earth Systems and Environment*, 6 (3), 1645-1656.
- Anmala, J. & Turuganti, V. (2021) Comparison of the performance of decision tree (dt) algorithms and extreme learning machine (elm) model in the prediction of water quality of the upper green river watershed. *Water Environment Research*, 93 (11), 2360-2373.
- Bui, Q.-T., Nguyen, Q.-H., Nguyen, X.L., Pham, V.D., Nguyen, H.D. & Pham, V.-M. (2020) Verification of novel integrations of swarm intelligence algorithms into deep learning neural network for flood susceptibility mapping. *Journal of Hydrology*, 581, 124379.
- Chicco, D., Warrens, M.J. & Jurman, G. (2021) The coefficient of determination r-squared is more informative than smape, mae, mape, mse and rmse in regression analysis evaluation. *PeerJ Computer Science*, 7, e623.
- Cuevas, E., Cienfuegos, M., Zaldívar, D. & Pérez-Cisneros, M. (2013) A swarm optimization algorithm inspired in the behavior of the social-spider. *Expert Systems with Applications*, 40 (16), 6374-6384.
- Ghimire, S., Yaseen, Z.M., Farooque, A.A., Deo, R.C., Zhang, J. & Tao, X. (2021) Streamflow prediction using an integrated methodology based on convolutional neural network and long short-term memory networks. *Scientific Reports*, 11 (1), 1-26.
- Gholizadeh, R., Yılmaz, H. & Danandeh Mehr, A. (2022) Multitemporal meteorological drought forecasting using bat-elm. *Acta Geophysica*, 70 (2), 917-927.
- Guo, J., Zhou, J., Qin, H., Zou, Q. & Li, Q. (2011) Monthly streamflow forecasting based on improved support vector machine model. *Expert Systems with Applications*, 38 (10), 13073-13081.
- Humaidi, A.J., Najem, H.T., Al-Dujaili, A.Q., Pereira, D.A., Ibraheem, I.K. & Azar, A.T. (2021) Social spider optimization algorithm for tuning parameters in pd-like interval type-2 fuzzy logic controller applied to a parallel robot. *Measurement and Control*, 54 (3-4), 303-323.
- Hunt, K.M., Matthews, G.R., Pappenberger, F. & Prudhomme, C. (2022) Using a long short-term memory (lstm) neural network to boost river streamflow forecasts over the western united states. *Hydrology and Earth System Sciences Discussions*, 1-30.
- Khosravi, K., Golkarian, A., Boojj, M.J., Barzegar, R., Sun, W., Yaseen, Z.M. & Mosavi, A. (2021) Improving daily stochastic streamflow prediction: Comparison of novel hybrid data-mining algorithms. *Hydrological sciences journal*, 66 (9), 1457-1474.
- Kilinc, H.C. & Haznedar, B. (2022) A hybrid model for streamflow forecasting in the basin of euphrates. *Water*, 14 (1), 80.
- Kisi, O. & Cimen, M. (2011) A wavelet-support vector machine conjunction model for monthly streamflow forecasting. *Journal of Hydrology*, 399 (1-2), 132-140.
- Klein, C.E., Segundo, E.H., Mariani, V.C. & Coelho, L.D.S. (2015) Modified social-spider optimization algorithm applied to electromagnetic optimization. *IEEE Transactions on Magnetics*, 52 (3), 1-4.
- Kothari, M. & Gharde, K. (2015) Application of ann and fuzzy logic algorithms for streamflow modelling of savitri catchment. *Journal of Earth System Science*, 124 (5), 933-943.
- Krzysztofowicz, R. (2002) Bayesian system for probabilistic river stage forecasting. *Journal of hydrology*, 268 (1-4), 16-40.
- Lin, Y., Wang, D., Wang, G., Qiu, J., Long, K., Du, Y., Xie, H., Wei, Z., Shangguan, W. & Dai, Y. (2021) A hybrid deep learning algorithm and its application to streamflow prediction. *Journal of Hydrology*, 601, 126636.

- Liu, J., Yuan, X., Zeng, J., Jiao, Y., Li, Y., Zhong, L. & Yao, L. (2022) Ensemble streamflow forecasting over a cascade reservoir catchment with integrated hydrometeorological modeling and machine learning. *Hydrology and Earth System Sciences*, 26 (2), 265-278.
- Long, Y., Lv, Q., Wen, X. & Yan, S. (2022) Bayesian logistic regression in providing categorical streamflow forecasts using precipitation output from climate models. *Stochastic Environmental Research and Risk Assessment*, 1-12.
- Luque-Chang, A., Cuevas, E., Fausto, F., Zaldívar, D. & Pérez, M. (2018) Social spider optimization algorithm: Modifications, applications, and perspectives. *Mathematical Problems in Engineering*, 2018.
- Mendoza, P.A., Wood, A.W., Clark, E., Rothwell, E., Clark, M.P., Nijssen, B., Brekke, L.D. & Arnold, J.R. (2017) An intercomparison of approaches for improving operational seasonal streamflow forecasts. *Hydrology and Earth System Sciences*, 21 (7), 3915-3935.
- Meshram, S.G., Meshram, C., Santos, C.a.G., Benzougagh, B. & Khedher, K.M. (2022) Streamflow prediction based on artificial intelligence techniques. *Iranian Journal of Science and Technology, Transactions of Civil Engineering*, 46 (3), 2393-2403.
- Mirjalili, S.Z., Saremi, S. & Mirjalili, S.M. (2015) Designing evolutionary feedforward neural networks using social spider optimization algorithm. *Neural Computing and Applications*, 26 (8), 1919-1928.
- Mohammadi, B. (2021) A review on the applications of machine learning for runoff modeling. *Sustainable Water Resources Management*, 7 (6), 1-11.
- Mosavi, A., Ozturk, P. & Chau, K.-W. (2018) Flood prediction using machine learning models: Literature review. *Water*, 10 (11), 1536.
- Nguyen, H.D. (2022a) Gis-based hybrid machine learning for flood susceptibility prediction in the nhat le-kien giang watershed, vietnam. *Earth Science Informatics*, 1-18.
- Nguyen, H.D. (2022b) Hybrid models based on deep learning neural network and optimization algorithms for the spatial prediction of tropical forest fire susceptibility in nghe an province, vietnam. *Geocarto International*, 1-25.
- Nguyen, H.D., Nguyen, Q.-H., Du, Q.V.V., Nguyen, T.H.T., Nguyen, T.G. & Bui, Q.-T. (2021) A novel combination of deep neural network and manta ray foraging optimization for flood susceptibility mapping in quang ngai province, vietnam. *Geocarto International*, 1-25.
- Ochoa, A., Juárez-Casimiro, K., Olivier, T., Camarena, R. & Vázquez, I. (2017) Social spider algorithm to improve intelligent drones used in humanitarian disasters related to floods. *Nature-inspired design of hybrid intelligent systems*, 457-476.
- Özgür, K. (2005) Daily River flow forecasting using artificial neural networks and auto-regressive models. *Turkish Journal of Engineering and Environmental Sciences*, 29 (1), 9-20.
- Parisouj, P., Mohebzadeh, H. & Lee, T. (2020) Employing machine learning algorithms for streamflow prediction: A case study of four river basins with different climatic zones in the united states. *Water Resources Management*, 34 (13), 4113-4131.
- Pham, Q.B., Afan, H.A., Mohammadi, B., Ahmed, A.N., Linh, N.T.T., Vo, N.D., Moazenzadeh, R., Yu, P.-S. & El-Shafie, A. (2020) Hybrid model to improve the river streamflow forecasting utilizing multi-layer perceptron-based intelligent water drop optimization algorithm. *Soft Computing*, 24 (23), 18039-18056.
- Pirzado, A.A., Sutahar, S.K., Sutahar, V., Qurashi, N.A., Jatoi, I.K., Khaskeli, S.A., Chandio, R.A., Aarain, K. & Peerzado, M.B. (2021) Checking the significance of correlation coefficient from the regression analysis using wheat yield. *Journal of Applied Research in Plant Sciences*, 2 (2), 132-141.
- Rahimzad, M., Moghaddam Nia, A., Zolfonoon, H., Soltani, J., Danandeh Mehr, A. & Kwon, H.-H. (2021) Performance comparison of a lstm-based deep learning model versus conventional machine learning algorithms for streamflow forecasting. *Water Resources Management*, 35 (12), 4167-4187.
- Rasouli, K., Hsieh, W.W. & Cannon, A.J. (2012) Daily streamflow forecasting by machine learning methods with weather and climate inputs. *Journal of Hydrology*, 414, 284-293.
- Singh, S., Parmar, K.S., Kumar, J. & Makkhan, S.J.S. (2020) Development of new hybrid model of discrete wavelet decomposition and autoregressive integrated moving average (ARIMA) models in application to one month forecast the casualties' cases of covid-19. *Chaos, Solitons & Fractals*, 135, 109866.
- Terzi, Ö. & Ergin, G. (2014) Forecasting of monthly river flow with autoregressive modeling and data-driven techniques. *Neural Computing and Applications*, 25 (1), 179-188.

- Tikhmarine, Y., Souag-Gamane, D., Ahmed, A.N., Kisi, O. & El-Shafie, A. (2020) Improving artificial intelligence models accuracy for monthly streamflow forecasting using grey wolf optimization (gwo) algorithm. *Journal of Hydrology*, 582, 124435.
- Tran, T., Tran, V. & Kim, J. (2021) Improving the accuracy of dam inflow predictions using a long short-term memory network coupled with wavelet transform and predictor selection. *Mathematics*, 9, 551.
- Tran, V. & Kim, J. (2022) Robust and efficient uncertainty quantification for extreme events that deviate significantly from the training dataset using polynomial chaos-kriging. *Journal of Hydrology*, 609, 127716.
- Wang, J., Bao, W., Gao, Q., Si, W. & Sun, Y. (2021) Coupling the xinjiang model and wavelet-based random forests method for improved daily streamflow simulation. *Journal of Hydroinformatics*, 23 (3), 589-604.
- Yang, Y., Chen, H., Heidari, A.A. & Gandomi, A.H. (2021) Hunger games search: Visions, conception, implementation, deep analysis, perspectives, and towards performance shifts. *Expert Systems with Applications*, 177, 114864.
- Yaseen, Z.M., Jaafar, O., Deo, R.C., Kisi, O., Adamowski, J., Quilty, J. & El-Shafie, A. (2016) Stream-flow forecasting using extreme learning machines: A case study in a semi-arid region in iraq. *Journal of Hydrology*, 542, 603-614.
- Yaseen, Z.M., Sulaiman, S.O., Deo, R.C. & Chau, K.-W. (2019) An enhanced extreme learning machine model for river flow forecasting: State-of-the-art, practical applications in water resource engineering area and future research direction. *Journal of Hydrology*, 569, 387-408.

HEIGHT MEASUREMENT AND OIL PALM YIELD PREDICTION USING UNMANNED AERIAL VEHICLE (UAV) DATA TO CREATE CANOPY HEIGHT MODEL (CHM)

Nayot KULPANICH^{1*}, Morakot WORACHAIRUNGREUNG¹,
Katawut WAIYASUSRI¹, Pornperm SAE-NGOW¹, Dusadee PINASU²

DOI: 10.21163/GT_2022.172.14

ABSTRACT:

Oil palms are currently in high demand, which tend to increase even higher as a source of alternative energy for humans, especially in Southeast Asian countries. This leads to the study that focuses on the height measurement, using an unmanned aerial vehicle (UAV), and age analysis of oil palm trees planted within the experimental plots in order to predict their yield. The methodology described in the paper provides using Canopy Height Model (CHM) for height measurement and prediction of the oil palm yield by multiple linear regression. The results indicated that the errors caused by overlapping age ranges were found in 3 out of 12 experimental plots. Furthermore, the primary factors influencing the oil palm yield prediction included the age (9 years and above) and canopy density (over 41% of the area), while the secondary factors supporting more accuracy included the total plot area, canopy area, and canopy height, with the coefficient of determination or R-squared at 0.98. In this study, we learned that the aforementioned factors could be concluded from the data collected by an UAV, which reduced the time for measuring the height of each tree manually, resulting in more accurate yield prediction.

Key-words: *Oil palm yield, Unmanned Aerial Vehicle, Canopy Height Model, Height measurement*

1. INTRODUCTION

The energy generated from fossil fuels—such as petroleum, natural gas, and coal—is non-renewable and deemed non-eco-friendly, causing environmental pollution to the earth. Alternative or renewal energy, therefore, becomes an efficient solution to address this issue. Becoming a source of alternative energy and bioenergy for transportation and industry development (Fitrianto et al., 2017; Sumathi et al., 2008), oil palms have been vastly cultivated across Southeast Asia (Chong et al., 2017; Zheng et al., 2021; Farobie & Hartulistiyoso, 2022). Ranked the third of the world after Indonesia and Malaysia, respectively (FAO, 2020), the oil palm plantations in Thailand cover the area of 9,405 square kilometers, 283.16 of which is found in the western region, especially in Prachuap Khiri Khan where the oil palm plantations spread across the area of 218.18 square kilometers. In Bang Saphan Noi, a district located in this province, the oil palm plantations cover the area of 81.59 square kilometers (Agricultural Product Data, 2018).

As a result of technological advance, the popular remote survey has been applied to agricultural industry in terms of mapping, locating suitable areas for oil palm cultivation (Shaharum et al., 2020), monitoring and improving agricultural yield (Dansagoonpon & Tripathi, 2013, Amirruddin et al., 2020; Shen, et al., 2022), predicting yield (Piekutowska, et al., 2021) and carbon emission of each type of crops (Kiew et al., 2020). During the past 20 years the technology of unmanned aerial vehicle (UAV) has been applied to a number of studies in various fields, including environment, forestry and ecosystem, and wildfire effect. For agriculture, UAVs have been used to develop the precision agriculture (Akhtman, et al., 2017; Tsouros et al., 2019; Zheng, et al., 2021; Velusamy, et al., 2022) and analyze crop health (Izzuddin et al., 2020; Kurihara et al., 2022).

¹Suan Sunandha Rajabhat University, Faculty of Humanities and Social Sciences, Geography and Geoinformatics Program, Bangkok, Thailand, Corresponding author * nayot.ku@ssru.ac.th, Morakot.wo@ssru.ac.th, katawut.wa@ssru.ac.th, pornperm.sa@ssru.ac.th.

²National Science and Technology Development Agency (NSTDA), Technology and Informatics Institute for Sustainability (TIIS), Bangkok, Thailand, dusadee.pin@ncr.nstda.or.th.

Satellite images and LiDAR have been also applied to the digital elevation model (DEM), digital surface model (DSM), and canopy height model (CHM) in order to analyze the areas for slope indication and water flow planning. In this regard, Ahmad et al. (2017) reported the high accuracy of the data generated from the DEM, DSM, and CHM using LiDAR. In addition, the photogrammetry was applied to the study of Lisein et al. (2013) in order to create the CHM with the images taken by the UAV along with the data from LiDAR and linear regressions to classify the high and outstanding canopies in the forest area from the CHM.

This study of oil palm yield prediction in Bang Saphan Noi, Prachuap Khiri Khan, has the objectives to measure the oil palm height by using the UAV and analyze the oil palm age within the experimental plots. The results can provide the accurate yield prediction (Hernández et al., 2022) for further yield efficiency improvement to the plots (Fawcett et al., 2019). The analysis of the data collected by the UAV can lead to the planning and implementation of agricultural policies in provincial level, as well as the efficiency improvement to low yield plots for future production and marketing planning by the agriculturists.

2. STUDY AREA

As the last district before entering the southern region of Thailand, Bang Saphan Noi is one of the districts in Prachuap Khiri Khan, located at $11^{\circ}4'30''\text{N}$ to $11^{\circ}2'57''\text{N}$ and $99^{\circ}16'39''\text{E}$ to $99^{\circ}17'03''\text{E}$ (Fig. 1). The west of the study area is the Tenasserim Range, forming a barrier between Thailand and Myanmar from north to south. With the Gulf of Thailand in the east, a coastal undulating plain, covering the area of 671.97 square kilometers is situated in the center of the study area, divided into 5 subdistricts: Pak Phraek, Bang Saphan, Sai Thong, Chang Raek and Chaiyarat. The area of 448.28 square kilometers (66.71% of the total area) is utilized for agricultural purposes, 105.47 square kilometers (23.53% of the total agricultural area) of which is covered by oil palm plantations, equivalent to 15.69% of the total area of Bang Saphan Noi (Land Development Department, 2018).

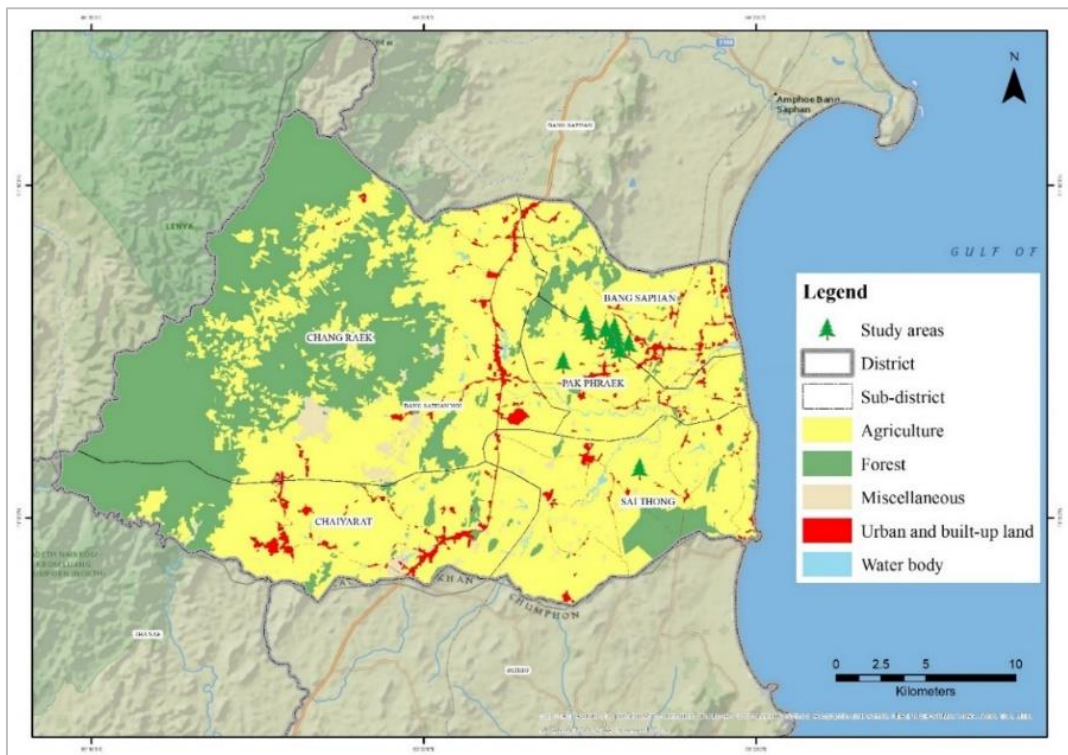


Fig. 1. Land Utilization Map of Bang Saphan Noi, Prachuap Khiri Khan.

3. DATA AND METHODS

3.1. Data Collection

The data was collected from 12 experimental plots following the purposive sampling and after obtaining permission to fly a UAV for data collection within the plots between August and September in the study areas. The selected UAV was DJI Phantom 4 Pro V 2.0, with the key features comprising: GPS/GLONASS satellite positioning systems; flying distance up to 7 kilometers; service ceiling up to 500 meters; wind speed resistance up to 36 kilometers/hour; operating frequency at 2.40-5.85 GHz; 1-inch CMOS camera (12.80 × 9.60 mm) with effective pixel of 20 MP (megapixels), FOV at 84°, f/2.8-f/11, auto focus at 1 meter-∞; and 3-axis stabilization (pitch, roll, yaw) (DJI, 2018). The RGB color model applies to the captured images which are in JPEG format. The double grid flight path at 90-meter height was employed with the side lap at 70% and overlap at 80%, resulting in the ground sample distance in the images of 2.47 centimeters. Flight planning is very important to image quality and the results of this study are very important. In this study, image position overlays were used side lap at 70% and overlap at 80% to avoid overlaying of images that affect processing. Moreover, the high altitude at 90 meters has a huge effect on image quality. However, in this study was conducted from the height of oil palm trees with a GSD of 2.47 meters. From this quality, it was explained that the object could be separated at 2.47 meters, which was considered a high image quality.

In addition, the suitable flight period for this area was between 10.00 hours to 15.00 hours due to calm wind, resulting in the most appropriate images for this study.

3.2. Methodology

To measure the height of the oil palm trees in the study area, the UAV photogrammetry was applied, as well as the orthorectification which is the process of eliminating the relief and tilt displacement by using the terrain data and referring to the Universal Transverse Mercator (UTM). This resulted in more accurate position, size and shape of the objects presented in the adjusted images in accordance with the photogrammetric principle. Therefore, the orthoimages, digital terrain model (DTM) and digital surface model (DSM) were produced.

The DTM and DSM were then used to calculate the canopy height model (CHM) by analyzing the data with the geographic information system (GIS) using the raster calculator as presented in Equation 1 (Ve'ga & St-Onge, 2009; Mohan et al., 2017; Wang et al., 2021).

The formula is expressed as follows:

$$CHM = DSM - DTM \quad [m] \quad (1)$$

where:

CHM = Canopy Height Model

DSM = Digital Surface Model

DTM = Digital Terrain Model

As a result of the above equation, the CHM provided the characteristics and height of the oil palm trees within the study area. The results from the model were used to identify the canopy shapes by converting the data from the raster images to vector graphic, which was then used to indicate the canopy density in the study area. Regarding the age analysis, 4 age ranges were classified seed, 0-3 years; young, 3-8 years; teen, 9-14 years; and mature, 15-25 years. The data collected by the questionnaire during a ground survey was later used to verify such age ranges, as presented in table 1.

Table 1.**Analysis of Age Ranges and Canopy Density.**

Group	Class	Age Range	Canopy Density (%)
1	Seed	0-3	Less than 10
2	Young	3-8	10 – 40
3	Teen	9-14	41 – 80
4	Mature	15-25	More than 81

Source: Fitrianto et al. (2017).

The oil palm yield prediction in Bang Saphan Noi, Prachuap Khiri Khan was subject to 5 influencing factors, consisting of: canopy area, canopy density, canopy height, age, and total plot area. They were the independent variables while the yield of each plot was the dependent variable. Then the yield prediction was calculated using the multiple linear regression as presented in Equation 2 (Liu et al., 2021; Abrougui et al., 2019).

$$y = \beta_0 + \beta_1x_1 + \beta_2x_2 + \dots + \beta_ix_i + \varepsilon \quad (2)$$

where:

β = Coefficient of Estimation

x = Variable Influencing Oil Palm Yield in Experimental Plot

y = Yield of Experimental Plot

The result from the above multiple linear regression was later used to verify the data collected from each experimental plot. The accuracy and reliability of such data was assessed by the coefficient of determination or R-squared (Abrougui et al., 2019).

$$R^2 = \frac{RSS}{TSS} \quad (3)$$

$$RSS = \sum_{i=1}^n (f_i - \bar{f})^2 \quad (4)$$

$$TSS = \sum_{i=1}^n (Y_i - \bar{Y})^2 \quad (5)$$

where:

RSS and TSS coefficients represent the sum of squares and the total sum of squares where f and Y are the means of the predicted values (f_i) and observed data (Y_i). The entire process is shown in **Figure 2**.

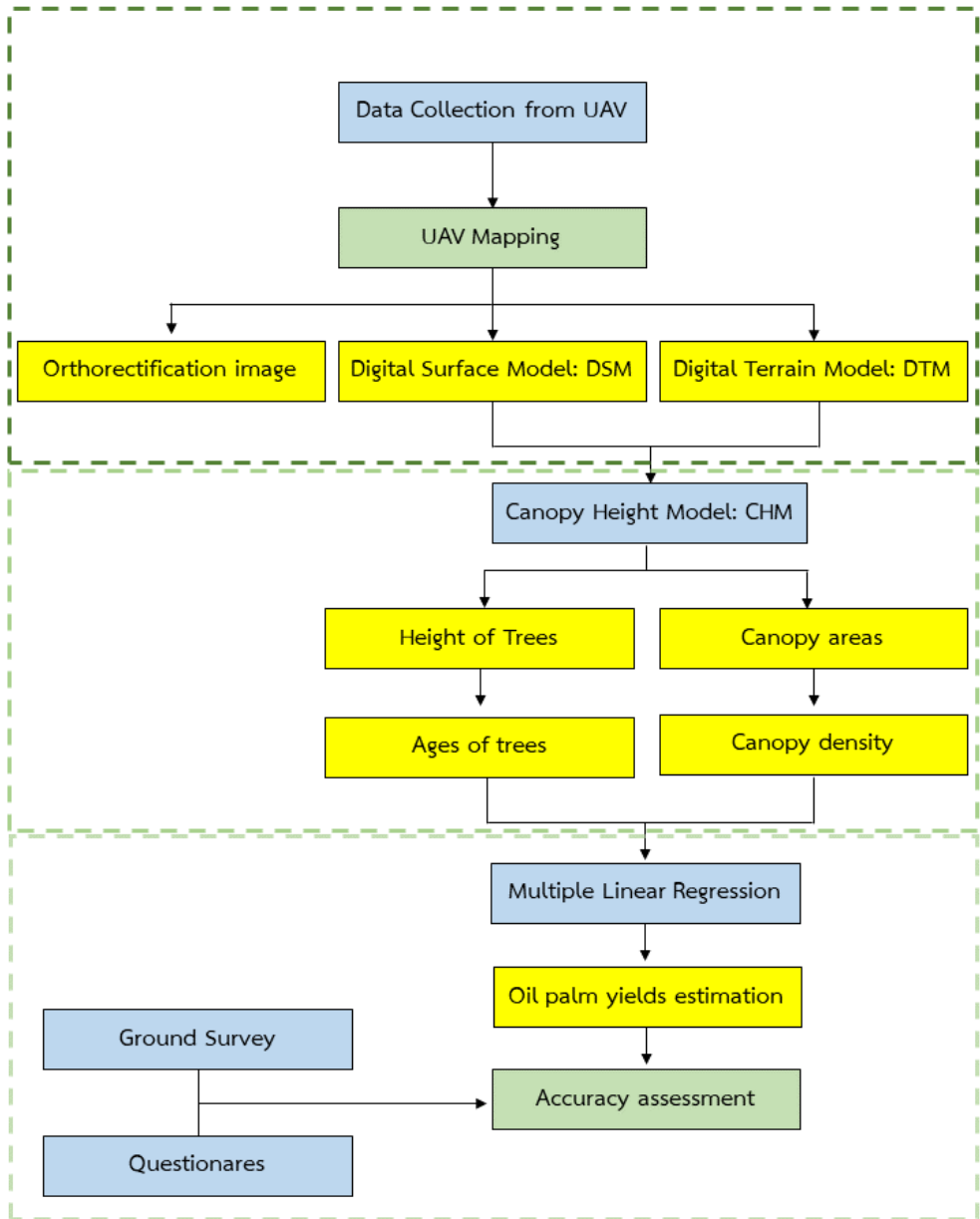


Fig. 2. Conceptual Framework Summarizing the Methodological Steps Used in This Research.

4. RESULTS AND DISCUSSIONS

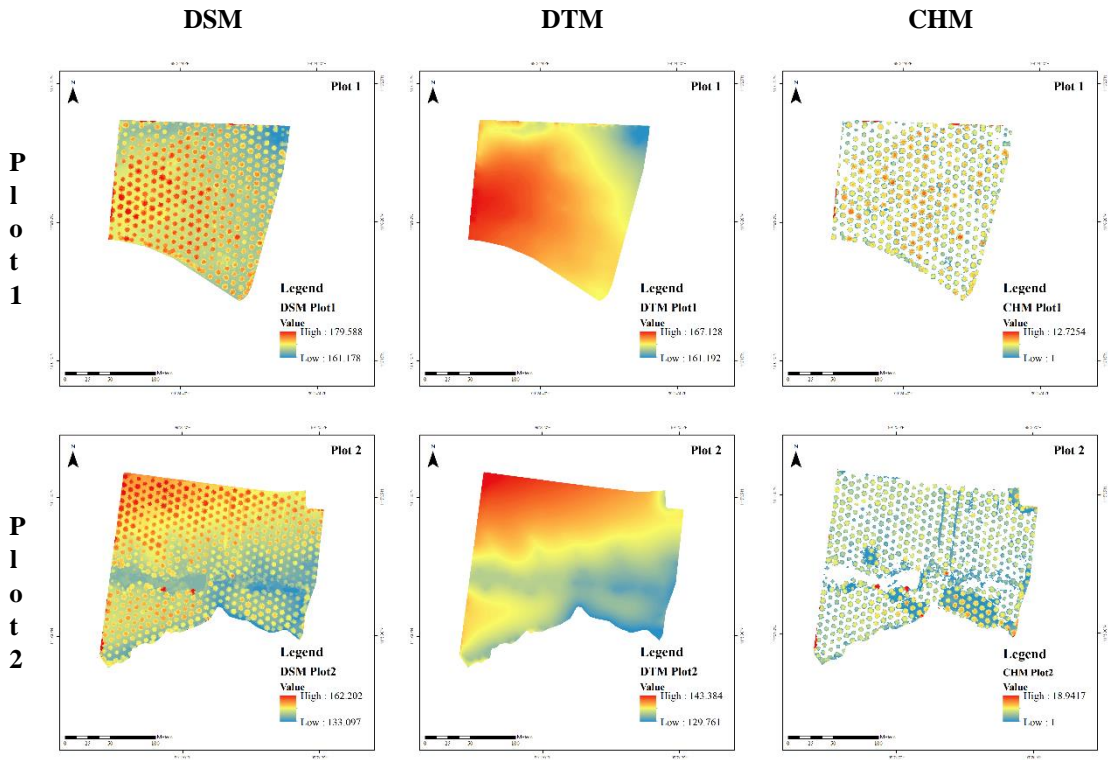
4.1. Analysis of Canopy Height Model Using Unmanned Aerial Vehicle

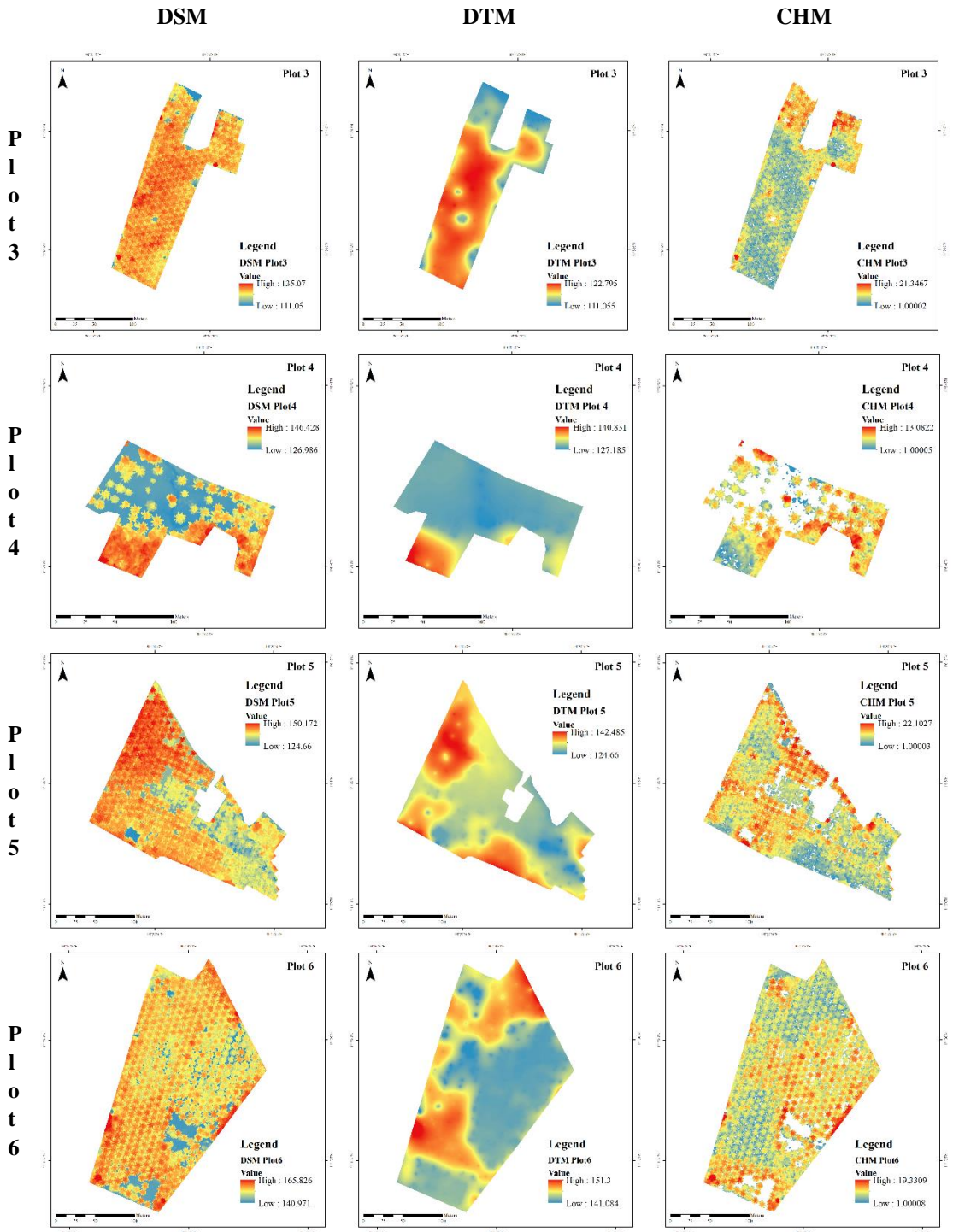
This study was to create the canopy height model (CHM), digital surface model (DSM) and digital terrain model (DTM) using the data collected from 12 experimental plots by an unmanned aerial vehicle (UAV). The results are presented in **Table 2** and **Figure 3** below (12 plots on the next 4 pages).

Table 2

Analysis Result of CHM in Experimental Plots.

Experimental Plot	Digital Surface Model (DSM) (m)			Digital Terrain Model (DTM) (m)			Canopy Height Model (CHM) (m)	
	Lowest	Average	Highest	Lowest	Average	Highest	Average	Highest
1	161.18	165.71	179.59	161.18	164.25	164.25	3.31	12.72
2	133.10	139.24	162.20	129.76	137.64	143.38	3.08	18.94
3	111.04	123.91	135.07	111.05	118.06	122.79	6.09	21.35
4	126.98	134.78	146.43	127.18	130.64	140.83	6.56	13.08
5	124.66	141.09	150.17	124.66	142.49	134.92	6.69	22.10
6	140.97	151.49	165.83	141.08	144.92	151.30	7.17	19.33
7	128.26	138.76	148.92	128.26	130.62	138.73	8.97	17.50
8	136.19	150.3	159.86	135.99	144.71	151.54	5.85	17.06
9	137.04	149.73	168.90	137.63	146.94	154.67	3.72	18.48
10	121.89	136.2	160.96	122.45	125.71	133.04	12.70	34.78
11	111.99	121.36	130.84	111.99	113.29	118.45	10.38	18.15
12	146.94	159.43	171.56	147.14	151.98	160.00	8.85	23.27



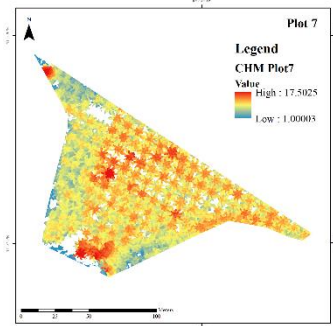
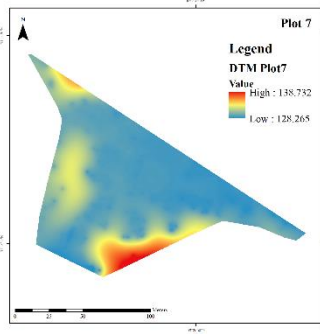
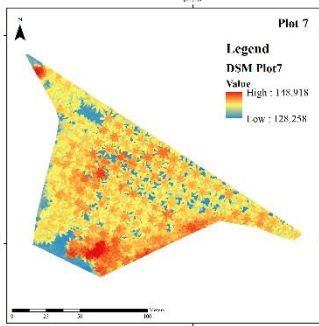


DSM

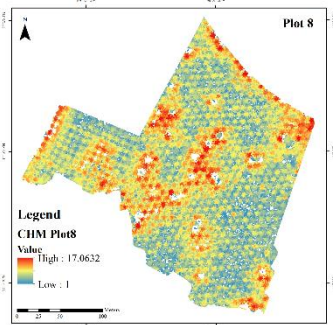
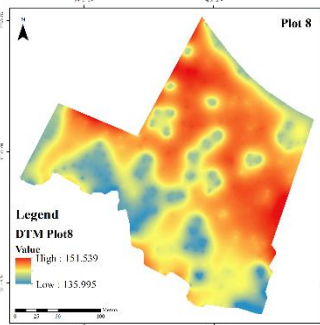
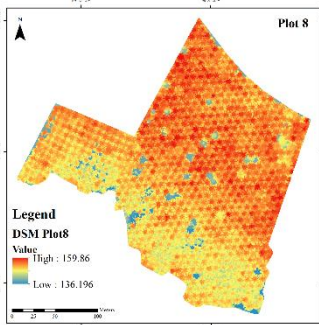
DTM

CHM

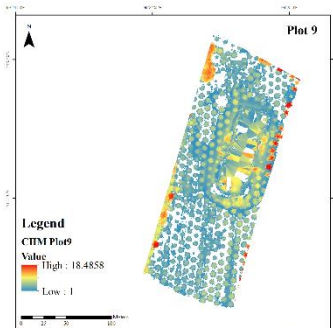
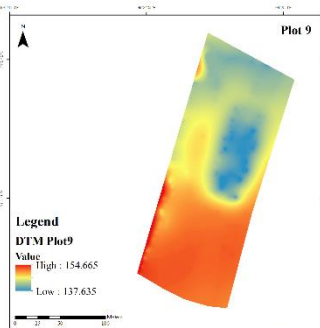
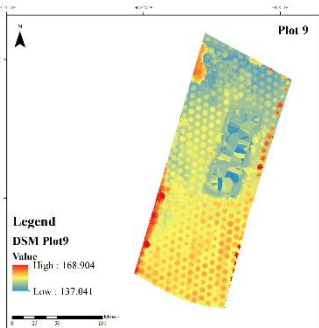
P
l
o
t
7



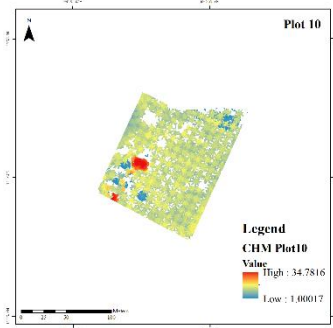
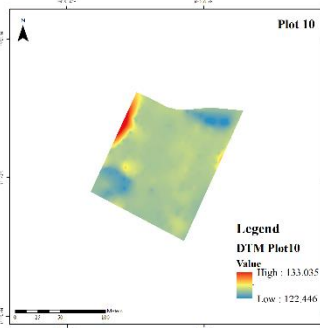
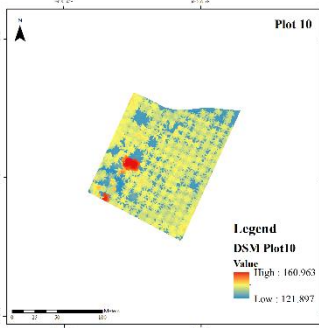
P
l
o
t
8



P
l
o
t
9



P
l
o
t
10



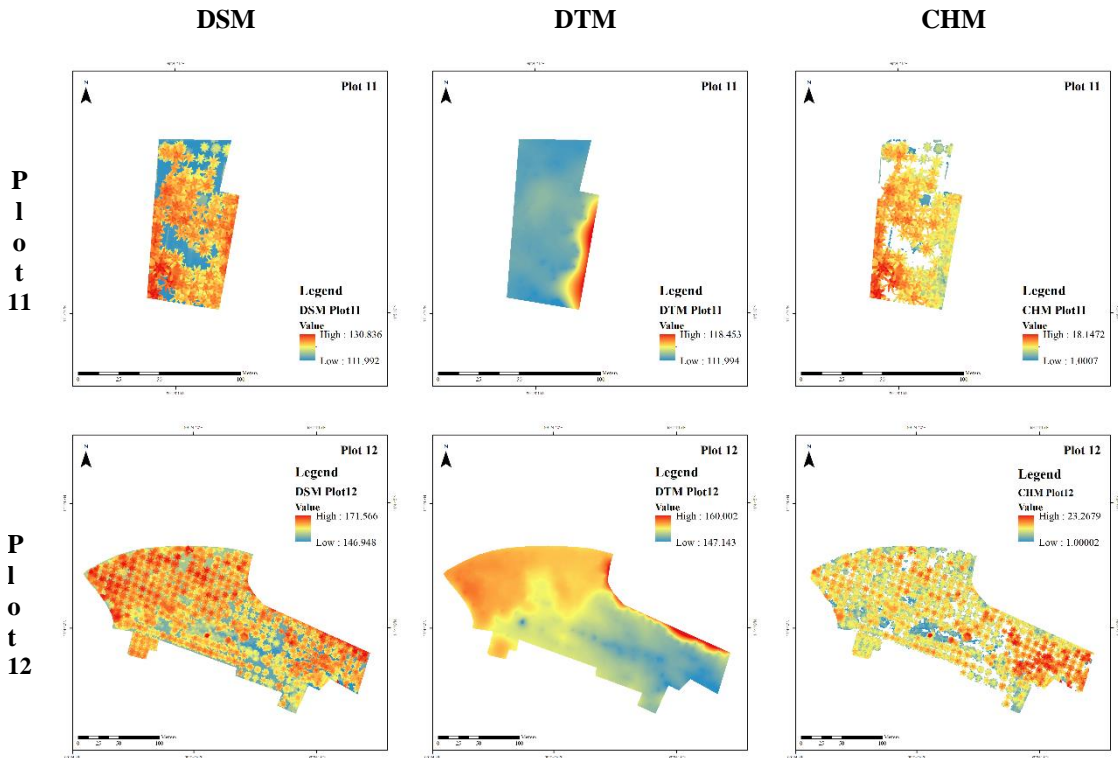


Fig. 3. Maps Presenting Analysis Result of CHM in Experimental Plots.

4.2. Correlation Analysis of Age and Canopy Density

Age Analysis Using UAV – The result indicated that the average density correlated to the standard age, consistent with the following ground survey results and as presented in **Table 3**.

Table 3.

Correlation Analysis of Age and Canopy Density.

Plot	Plot Area (sq.m.)	Canopy Area (sq.m.)	Canopy Density (%)	Canopy Height (m.)	Standard Age (Years)	Observed Age (Years)
1	28,748.77	11,334.23	39.43	3.31	3-8	3-8
2	37,161.50	13,110.29	35.28	3.08	3-8	3-8
3	18,748.27	17,985.79	95.93	6.09	15-25	15-25
4	9,609.61	5,931.07	61.72	6.56	9-14	9-14
5	29,750.12	24,921.43	83.77	6.69	15-25	15-25
6	40,522.48	34,493.05	85.12	7.17	15-25	15-25
7	13,648.26	12,087.24	88.56	8.97	15-25	15-25
8	56,106.23	53,468.95	95.28	5.85	15-25	15-25
9	28,954.94	12,124.31	41.87	3.71	9-14	3-8
10	15,688.13	12,912.50	82.31	12.70	15-25	9-14
11	4,714.09	3,555.78	77.43	10.38	9-14	15-25
12	34,854.01	27,963.56	80.23	8.85	15-25	15-25

Young oil palms trees, in the age range of 3-8 years, were found in Plots 1, 2 and 9 with more details as follows:

- Plot 1 covered the total area of 28,748.77 square meters, 11,334.23 of which was the canopy area with the canopy density of 39.43% and average canopy height of 3.31 meters. Compared to the age analysis table, the oil palm trees in this plot were in the age range of 3-8 years or young class.
- Plot 2 covered the total area of 37,161.50 square meters, 13,110.29 of which was the canopy area with the canopy density of 35.28% and average canopy height of 3.08 meters. Compared to the age analysis table, the oil palm trees in this plot were in the age range of 3-8 years or young class.
- Plot 9 covered the total area of 28,954.94 square meters, 12,124.31 of which was the canopy area with the canopy density of 41.87% and average canopy height of 3.71 meters. However, compared to the age analysis table, the oil palm trees in this plot were in the age range of 9-14 years. The plot owner informed that the trees were planted 8 years ago; thus they were classified as young trees.

Teen oil palms trees, in the age range of 9-14 years, were found in Plots 4 and 10 with more details as follows:

- Plot 4 covered the total area of 9,609.61 square meters, 5,931.07 of which was the canopy area with the canopy density of 61.72% and average canopy height of 6.56 meters. Compared to the age analysis table, the oil palm trees in this plot were in the age range of 9-14 years or teen class. The plot owner informed that the trees were planted 12 years ago.
- Plot 10 covered the total area of 15,688.13 square meters, 12,912.50 of which was the canopy area with the canopy density of 82.31% and average canopy height of 12.7 meters. Compared to the age analysis table, the oil palm trees in this plot were in the age range of 9-14 years or teen class.

Mature oil palms trees, in the age range of 15-25 years, were found in Plots 3, 5, 6, 7, 8, 11 and 12 with more details as follows:

- Plot 3 covered the total area of 18,748.27 square meters, 17,985.79 of which was the canopy area with the canopy density of 95.93% and average canopy height of 6.09 meters.
- Plot 5 covered the total area of 29,750.12 square meters, 24,921.43 of which was the canopy area with the canopy density of 83.77% and average canopy height of 6.69 meters.
- Plot 6 covered the total area of 40,522.48 square meters, 34,493.05 of which was the canopy area with the canopy density of 85.12% and average canopy height of 7.17 meters.

- Plot 7 covered the total area of 13,648.26 square meters, 12,087.24 of which was the canopy area with the canopy density of 88.56% and average canopy height of 8.97 meters.
- Plot 8 covered the total area of 56,106.23 square meters, 53,468.95 of which was the canopy area with the canopy density of 95.28% and average canopy height of 5.85 meters.
- Plot 11 covered the total area of 4,714.09 square meters, 3,555.78 of which was the canopy area with the canopy density of 77.43% and average canopy height of 10.38 meters. The plot owner informed that the trees were planted 15 years ago.
- Plot 12 covered the total area of 27,963.56 square meters, 34,854.01 of which was the canopy area with the canopy density of 80.23% and average canopy height of 8.856 meters. The plot owner informed that the trees were planted between 15 and 25 years ago.

4.3. Oil Palm Yield Prediction Using UAV

In this study, the oil palm yield prediction in Bang Saphan Noi, Prachuap Khiri Khan was subject to 5 influencing factors, which were the independent variables, consisting of: canopy area, canopy density, canopy height, age, and plot area. However, it was found from the ground survey that Plot 1 has not yielded yet, thus only the data collected from the remaining 11 experimental plots could be used for analysis by multiple linear regression with the coefficient of determination or R-squared at 0.98. Therefore, it was suggested that the aforementioned influencing factors correlated with the yield per plot as follows:

Given the p-value level, the most influencing factor was the age, with the p-value of 0.006, followed by the canopy density, with the p-value of 0.026; the total plot area, with the p-value of 0.055; canopy area, with the p-value of 0.112; and canopy height, as the least influencing factor, with the p-value of 0.498. The multiple linear regression predicted the oil palm yield in the experimental plots as presented in **Table 4** and **Figure 4** below.

Table 4.

Yield Prediction of Experimental Plots.

Plot	Plot Area (sq.m.)	Canopy Area (sq.m.)	Canopy Density (%)	Canopy Height (m.)	Ages (Year)	Observed Product (kg.)	Predict Product (kg.)	Residuals
2	37,161.50	13,110.29	35.28	3.08	6	2,500.00	2,617.39	-117.389
3	18,748.27	17,985.79	95.93	6.09	21	2,500.00	2,493.88	6.118406
4	9,609.61	5,931.07	61.72	6.56	11	750.00	735.92	14.0846
5	29,750.12	24,921.43	83.77	6.69	16	2,700.00	2,678.77	21.22832
6	40,522.48	34,493.05	85.12	7.17	17	4,000.00	3,905.15	94.84679
7	13,648.26	12,087.24	88.56	8.97	19	2,000.00	1,940.13	59.86357
8	56,106.23	53,468.95	95.28	5.85	20	5,700.00	5,772.21	-72.2105
9	28,954.94	12,124.31	41.87	3.71	8	2,500.00	2,346.16	153.8367
10	15,688.13	12,912.50	82.31	12.70	14	1,200.00	1,079.27	120.7219
11	4,714.09	3,555.78	77.43	10.38	15	450.00	659.72	-209.722
12	34,854.01	27,963.56	80.23	8.85	14	2,700.00	2,771.38	-71.3783

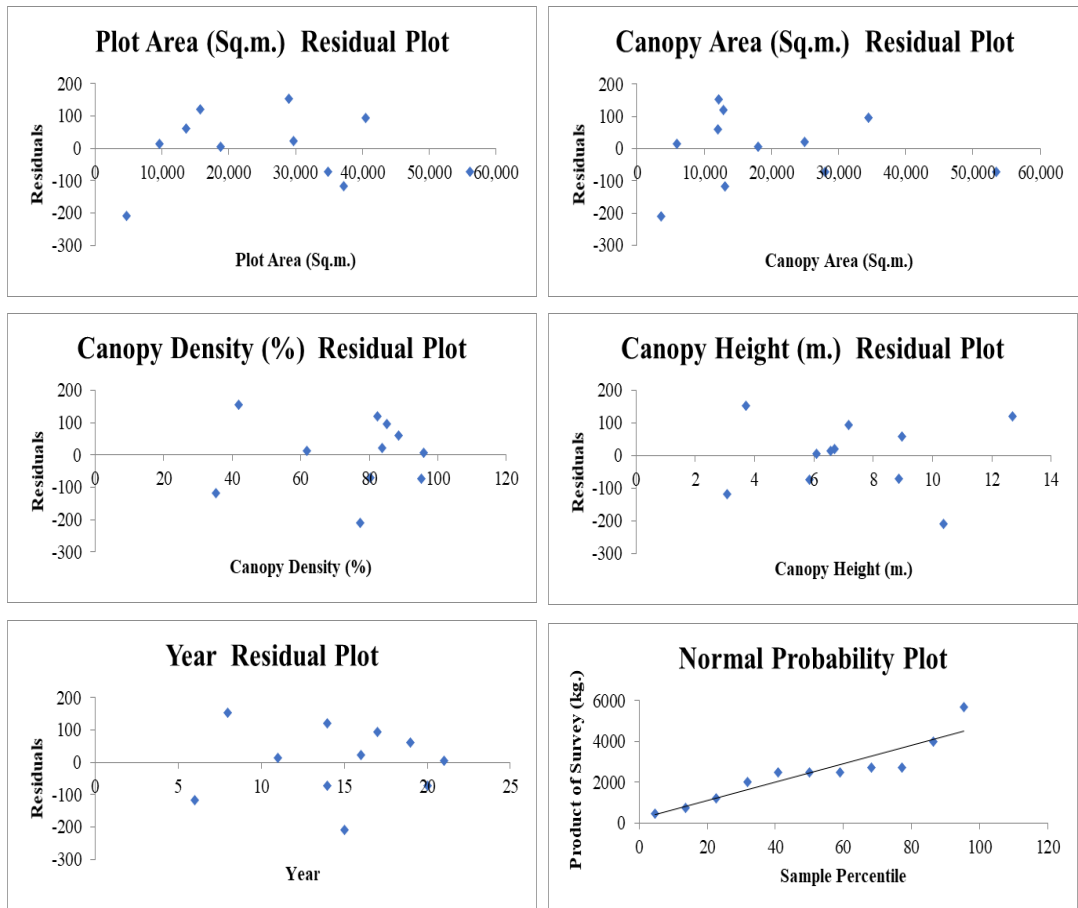


Fig. 4. Scatter Plot of Residual Factor of Estimate Oil Palm Production and Normal Probability Plot.

5. DISCUSSION

According to the results presented above, it is suggested that the oil palm yield prediction can be conducted via remote survey due to its efficiency (Chong et al., 2017), while the canopy height model (CHM) is used for analysis (Fawcett et al., 2019) of the data collected by various tools, including satellite images (Veiga & St-Onge, 2009) suitable for large areas due to the limitation on image resolution which is subject to the type of satellite. Another key tool is the light detection and ranging (LiDAR), providing high accuracy (Lisein et al., 2013) although it requires high costs for production and analysis. Therefore, in case of small plots, it is suggested to use an unmanned aerial vehicle (UAV) due to lower cost than the satellite images and LiDAR.

It was indicated that the most influencing factor in this study was the age of the oil palm trees as it affected the yield; the oil palm trees in the age range of 9-14 years (teen) yield the most, followed by 15-25 years (mature), and 3-8 years (young), during which the trees require more nutrients for growth. However, the trees with no yield are in the age range of 0-3 years (seed) (Fitrianto et al., 2017). Another influencing factor was canopy density, as a result of the agriculturists' behaviors, such as trimming the canopy before or after harvesting, and controlling height for easy maintenance and harvesting. The secondary or supporting factors included the total plot area, canopy area, and canopy height.

However, the limitation of this study is overlapping age ranges and behaviors during harvesting, such as trimming the canopy, affected the canopy size, causing the inaccurate canopy density. Therefore, it is suggested that the physical factors and environmental and economic characteristics should be applied in any further studies to obtain more complete and accurate results.

6. CONCLUSIONS

The development of agricultural technology is becoming very popular nowadays, especially the use of data to forecast yields (Precision agriculture). Unmanned aerial vehicles are a powerful tool for storing data and can be processed. In this study, the application of an UAV for oil palm yield prediction and age classification in this study, it was indicated that the errors caused by overlapping age ranges were found in 3 out of 12 experimental plots. Regarding the oil palm yield, the most influencing factor was the age (9 years and above), followed by the canopy density canopy density (over 41% of the area), total plot area, canopy area, and canopy height, respectively, with the coefficient of determination or R-squared at 0.98. We learned that the aforementioned factors could be concluded from the data collected by an UAV, which reduced time for measuring the height of each tree manually, resulting in more accurate yield prediction. In addition, this study can be applied to agriculture which is an important product of Thailand and Southeast Asian countries. this research can be used to determine the growth of plants within the plot. And can use such methods to increase the productivity of farmers in the region.

ACKNOWLEDGEMENTS

We would like to express our appreciation to the owners of all 12 experimental oil palm plots and Geography and Geoinformatics Program, Department of Social Sciences, Faculty of Humanities and Social Sciences, Suan Sunandha Rajabhat University, for the support on data collection tools and facilitation throughout this research.

REFERENCES

- Ve'ga, C., & St-Onge, B. (2009). Mapping site index and age by linking a time series of canopy height models with growth curves. *Forest Ecology and Management*, 3(257), 951-959. doi:10.1016/j.foreco.2008.10.029
- Abrougui, K., Gabsi, K., Mercatoris, B., Khemis, C., Amami, R., & Chehaibi, S. (2019). Prediction of organic potato yield using tillage systems and soil properties by artificial neural network (ANN) and multiple linear regressions (MLR). *Soil & Tillage Research*(109), 202-208. doi:10.1016/j.still.2019.01.011
- Ahmad, F., Goparaju, L., & Qayum, A. (2017). Natural Resource Mapping Using Landsat and Lidar towards Identifying Digital Elevation, Digital Surface and Canopy Height Models. *International Journal of Environmental Sciences & Natural Resources*, 1-8. doi:10.19080/IJESNR.2017.02.555580
- Akhtman, Y., Golubeva, E., Tutubalina, O., & Zimin, M. (2017). Application of hyperspectral images and ground data for precision farming. *GEOGRAPHY, ENVIRONMENT, SUSTAINABILITY*, 10(4), 117-128. doi:10.24057/2071-9388-2017-10-4-117-128

- Amirruddin, A. D., Farrah, M. M., Ismail, M. H., Ismail, M. F., Tan, N. P., & Karam, D. S. (2020). Hyperspectral remote sensing for assessment of chlorophyll sufficiency levels in mature oil palm (*Elaeis guineensis*) based on frond numbers: Analysis of decision tree and random forest. *Computers and Electronics in Agriculture*, *169*, 105221. doi:10.1016/j.compag.2020.105221
- Chong, K. L., Kanniah, K. D., Pohl, C., & Tan, K. P. (2017). A review of remote sensing applications for oil palm studies. *Geo-spatial Information Science*, *2*(20), 184-200. doi:10.1080/10095020.2017.1337317
- Dansagoonpon, S., & Tripathi, N. K. (2013). Modeling Site Suitability for Oil Palm Plantations in Southern Thailand. *GIScience & Remote Sensing*, *43*(3), 252-267. doi:10.2747/1548-1603.43.3.252
- DJI. (2018). *Phantom 4 Pro and Pro Plus Series User Manual*.
- FAO. (2020). *FAOSTAT*. Retrieved from FAO: <http://www.fao.org/faostat/en/?#data/>
- Farobie, O., & Hartulistiyoso, E. (2022). Palm Oil Biodiesel as a Renewable Energy Resource in Indonesia: Current Status and Challenges. *BioEnergy Research*(15), 93-111. doi:10.1007/s12155-021-10344-7
- Fawcett, D., Azlan, B., Hill, T. C., Kho, L. K., Jon, B., & Anderson, K. (2019). Unmanned aerial vehicle (UAV) derived structure-from-motion photogrammetry point clouds for oil palm (*Elaeis guineensis*) canopy segmentation and height estimation. *International Journal of Remote Sensing*, *19*(40), 7538-7560. doi:10.1080/01431161.2019.1591651
- Fitrianto, A. C., Tokimatsu, K., & Sufwandika, M. (2017, มกราคม 1). Estimation the Amount of Oil Palm Trees Production Using Remote Sensing Technique. *IOP Conference Series: Earth and Environmental Science*, *98*, p. 012016. Yogyakarta, Indonesia. doi:10.1088/1755-1315/98/1/012016
- Hernández, F. W., Calderón, N. G., & da Silva, P. R. (2022). Oil Palm Yield Estimation Based on Vegetation and Humidity Indices Generated from Satellite Images and Machine Learning Techniques. *AgriEngineering*(4), 279–291. doi:10.3390/agriengineering4010019
- Izzuddin, M. A., Hamzah, A. B., Nisfariza, M. N., & Idris, A. (2020). Analysis of multispectral imagery from unmanned aerial vehicle (UAV) using object-based image analysis for detection of ganoderma disease in oil palm. *Journal of Oil Palm Research*, *3*(32), 497-508. doi:10.21894/jopr.2020.0035
- Kiew, F., Hirata, R., Hirano, T., Xhuan, W. G., Aries, E. B., Kemudang, K., . . . Melling, L. (2020). Carbon dioxide balance of an oil palm plantation established on tropical peat. *Meteorology, Agricultural and Forest*, *295*, 108189. doi:10.1016/j.agrformet.2020.108189
- Kurihara, J., Koo, V.-C., Guey, C. W., Lee, Y. P., & Abidin, H. (2022). Early Detection of Basal Stem Rot Disease in Oil Palm Tree Using Unmanned Aerial Vehicle-Based Hyperspectral Imaging. *Remote Sensing*, *3*(14), 799. doi:10.3390/rs14030799
- Land Development Department. (2018). Land use information. Bangkok, Thailand.
- Lisein, J., Pierrot-Deseilligny, M., Bonnet, S., & Lejeune, P. (2013). A Photogrammetric Workflow for the Creation of a Forest Canopy Height Model from Small Unmanned Aerial System Imagery. *Forests*, *922-944*.
- Liu, M., Hu, S., Ge, Y., & Heuvel, G. B. (2021). Using multiple linear regression and random forests to identify spatial poverty determinants in rural China. *Spatial Statistics*, *42*, 100461. doi:10.1016/j.spasta.2020.100461
- Mohan, M., Silva, C. A., Klauberg, C., Jat, P., Catts, G., Cardil, A., . . . Dia, M. (2017). Individual Tree Detection from Unmanned Aerial Vehicle (UAV) Derived Canopy Height Model in an Open Canopy Mixed Conifer Forest. *Forests*, *9*(8), 340. doi:10.3390/f8090340
- Office of Agricultural Economics. (2018). *Agricultural Product Data*. Retrieved from Office of Agricultural Economics, Ministry of Agriculture and Cooperatives: <http://www.oae.go.th/>
- Piekutowska, M., Niedbała, G., Piskier, T., Lenartowicz, T., Pilarski, K., Wojciechowski, T., . . . Kosacka, A. C. (2021). The Application of Multiple Linear Regression and Artificial Neural Network Models for Yield Prediction of Very Early Potato Cultivars before Harvest. *Agronomy*, *5*(11), 885. doi:10.3390/agronomy11050885
- Shaharum, N. S., Shafri, H. Z., Ghani, W. W., Samsatli, S., Al-Habshi, M. M., & Yusuf, B. (2020). Oil palm mapping over Peninsular Malaysia using Google Earth Engine and machine learning algorithms. *Remote Sensing Applications: Society and Environment*, *17*, 100287. doi:10.1016/j.rsase.2020.100287
- Shen, Y., Mercatoris, B., Cao, Z., Kwan, P., Guo, L., Yao, H., & Cheng, Q. (2022). Improving Wheat Yield Prediction Accuracy Using LSTM-RF Framework Based on UAV Thermal Infrared and Multispectral Imagery. *Agriculture*, *6*(12), 892. doi:10.3390/agriculture12060892

- Sumathi , S., Chai, S. P., & Mohamed, A. R. (2008). Utilization of oil palm as a source of renewable energy in Malaysia. *Renewable and Sustainable Energy Reviews*, 9(12), 2404-2421. doi:10.1016/j.rser.2007.06.006.
- Tsouros, D. C., Bibi, S., & Sarigiannidis, P. G. (2019). A Review on UAV-Based Applications for Precision Agriculture. *information*(10), 349. doi:10.3390/info10110349
- Velusamy, P., Rajendran, S., Mahendran, R. K., Naseer, S., Shafiq, M., & Choi, J. G. (2022). Unmanned Aerial Vehicles (UAV) in Precision Agriculture: Applications and Challenges. *Energies*(15), 217. doi:10.3390/en15010217
- Wang, C., Morgan, G., & Hodson, M. E. (2021). sUAS for 3D Tree Surveying: Comparative Experiments on a Closed-Canopy Earthen Dam. *Forest*, 695. doi:10.3390/f12060659
- Zheng, J., Fu, H., Li, W., Wu, W., Yu, L., Yuan, S., . . . Kanniah, K. D. (2021). Growing status observation for oil palm trees using Unmanned Aerial Vehicle (UAV) images. *ISPRS Journal of Photogrammetry and Remote Sensing*(173), 95-121. doi:10.1016/j.isprsjprs.2021.01.008

NIGHTTIME AND DAYTIME POPULATION ESTIMATION FROM OPEN DATA

Nelson MILEU ¹, Margarida QUEIRÓS ¹

DOI: 10.21163/GT_2022.172.15

ABSTRACT:

Most of the studies on population loss and damage, due to earthquakes or any other natural or anthropogenic catastrophe rely on methodologies that usually make use of the resident population counted in the latest census. However, the need for disaggregated data for high extensions of territory and the increasing availability of open data opens new possibilities for the construction of population exposure models. Essential to emergency planning is determining where people are likely to be located, which varies from day to night, from weekdays or weekends and / or seasonally. Focusing on variations from day to night, using addresses open data, night populations are estimated at building level. To determine daytime population estimates, points of interest representing the locations of each business together with administrative and statistical data are used to establish how many people are employed or study on each building. The result for daytime population is 19% higher than the nighttime population confirming the commuting official values.

Key-words: *Population distribution, Population exposure, Open data, Earthquake.*

1. INTRODUCTION

Worldwide, there are a raising number of large disasters and among the variety of causes for such an increase we can list climate change, the rise of population densities in specific hazard-prone areas (especially in coastal regions and in areas at mountain slopes), and the susceptibility of the aging building stock (Vora *et al.*, 2008). It has also been argued that the magnitude and frequency of extreme events are increasing (Bosher *et al.*, 2009; O'Brien, 2008). Some authors suggest that several recent extreme natural events resulted in great humanitarian tragedies because of weak preventive disaster management (Ismail-Zadeh & Takeuchi, 2007), mitigation, and the lack of knowledge about the size, nature and geographical distribution of the present population potentially in danger. For instance, earthquake risk analysis involves quantitative estimation of damage, casualties and costs within a specified geographic area over a certain period of time (Vora *et al.*, 2008). Obviously, estimation of the human damage and loss is highly relevant (Smith & Petley, 2009). Wenzel, *et al.* (2007) point out that during the last decade there has been an increasing potential for large scale disasters caused by severe earthquakes in regions with high population densities (for instance, around 6,000 deaths in Kobe, Japan, and 20,000 deaths in Izmit, Turkey, in 1995 or, recently, Japanese death count surpass 11,000 as a result of earthquake and tsunami in 2011).

Population exposure refers to human occupancy near or presence within the hazard-prone area and thus the population that would be potentially affected by an event (Freire & Aubrecht, 2012; Mileu & Queirós, 2018). In metropolitan areas due to densely populated areas and commuting (also due to tourism), the distribution of people depends on the time of a 24h day. Realistic earthquake loss estimations depend on reliable population exposure models. This is also a reason why “population exposure” estimation is increasingly important on the research and political agendas: to identify the potential population loss because of the present population exposed to hazardous events.

Exposure is simply defined as the number of people or amounts of assets (e.g., physical, economic, social, environmental, historical, cultural, etc.) exposed to a hazard (Kamranzad *et al.*, 2020). Having accepted this definition, exposure can be evaluated based on observed (census) or estimated data (Kamranzad *et al.*, 2020).

¹University of Lisbon, Centre of Geographical Studies, Institute of Geography and Spatial Planning, 1600-276 Lisbon, Portugal; nmileu@campus.ul.pt, margaridav@campus.ul.pt.

In this research we estimate population exposure at the building level based on open data, and considered daily dynamics. This means population exposure in the perspective of its variations along daily periods, in time and space. We use this expression to underline the human dimension, which means drawing attention on population and not on buildings, roads, etc. Our core research is about understanding territorial and temporal patterns of people distribution. In this particular case, night and day population, and its occurrence during a journey is fundamental to risk science and critical for the region where the present population is permanent (residents) or temporarily (for labour or touristic reasons) located, particularly if it is a seismic area.

The estimation of the present population is however a methodologically difficult and controversial procedure (see a short but accurate identification of these problems in Chapter Two of *Tools and Methods for Estimating Population at Risk* (NRC, 2007). For instance, the estimates based in the lighted settlement and high-resolution imagery constitute important improvements in this research field, but they are uneven and static proxies, and with high levels of uncertainty.

Most of the studies on population loss and damage, due to earthquakes or any other natural (Tavares *et al.*, 2016; Santos *et al.*, 2016) or anthropogenic catastrophe rely on methodologies that usually make use of the resident population counted in the latest census. An area's resident population consists of those persons usually resident, where they stay most of the time (USCB, 2000). Nevertheless, only roughly can we consider these estimates based on residents, wrongly equated with the population present at nighttime, as an adequate estimate of present population. Current research in earthquake modelling (scenario or probabilistic) using the software program HAZUS for loss estimation usually doesn't consider population data about present population, which in both conditions of highly seismic and metropolitan areas should be crucial.

The estimation of the population exposure based on the census datasets usually overestimates or underestimates the present population and do not even consider the mobility during a daily or a weekly period. As we show in this paper, the present population is most often much higher than the resident population officially known.

Several approaches have been used to study the distribution of the population during daytime and nighttime and we can mention some of the more relevant for our purposes. Qi *et al.* (2015) established a relationship model for the three components of 'population, land use and time (daytime or night)' to explore the temporal and spatial characteristics of different types of population, and to estimate urban population during the day and night (and to analyse their spatial characteristics at a grid scale). In addition to population data aggregated in statistical areas, there are other geographic representations in the population distribution. Using a dasymetric mapping technique, Freire and Aubrecht (2012) obtained the population census data for daytime and nighttime in the metropolitan area of Lisbon, Portugal, to analyse variable spatiotemporal exposure of the population to earthquake hazard. Supported by a framework for modelling population distribution in space and time based on the integration of available information from census and administrative sources Renner *et al.* (2018) created high-resolution population data for different points in time for the region of the Autonomous Province of Bolzano. At the building level, Ara (2014) modelled total daytime and nighttime population based on the datasets from the Comprehensive Disaster Management Program and used a relationship between the occupancy classes and average space. Based on land use and land cover classes from different datasets, Freire (2007, 2020) modelled nighttime population using street centerlines to derive residential streets and allocating population in each census block group. The same author (2007; 2020), to model the daytime worker population georeferenced the addresses of private businesses and public services (including health care facilities and schools) and respective workforce. More recently, Ma *et al.* (2017) developed a model to estimate hourly dynamic changes in population at the community level based on subway smart card data exploring the possibilities given by big data.

When developing instruments for emergency planning, the knowledge of the difference between night and day population at building level is critical (ANPC, 2020), as the potential of human loss on a basis of the present estimated population (whether resident, worker, tourist or other) that really is in a specific area in a given moment (hour, day, week, month...), is more accurate than the official data

for potential human loss. Our research demonstrates this closeness. Also, we suggest a new conceptual and methodological application, supported by the ratio referring to the number of employees per economic activity classification and administrative workforce data. For each building we established the day occupation with the purpose of establishing the population mobility between day and night periods. For the night period, we propose the use of open address data to estimate the resident population at the building level. The referred methodology allows the estimation of the potential human loss based on the present estimated population, which is the population that is in a specific area in each moment of a 24h day. Thus, the aim of this article is to estimate the people occupying buildings at different times of the day (day and night) based on open data. For our case study we choose the municipality of Oeiras in the Lisbon Metropolitan Area.

2. STUDY AREA

The municipality of Oeiras is located in the Lisbon Metropolitan Area, Portugal (**Fig. 1**). Given its location in the western Iberian Peninsula on the Atlantic Ocean, the Lisbon Metropolitan Area is susceptible to offshore earthquakes occurring on the Africa-Eurasia plate boundary, particularly in the Gorringe Bank region (Tang *et al.*, 2012). This region has been affected by severe historical earthquakes, like the emblematic 1755 Lisbon earthquake with $M_w = 8.5 - 9.0$ (Costa *et al.*, 2009).



Fig. 1. Study area location.

The seismic hazard in this region has also a contribution of onshore, moderate to strong intraplate earthquakes on inherited crustal fractures like the Lower Tagus Valley fault zone (Vilanova e Fonseca, 2004). Oeiras is a predominantly urban municipality with a population of 172,167 inhabitants and a high economic development associated with medium-sized and large-sized business parks, mainly associated to higher tertiary activities. In the last years, Oeiras municipality has a positive growth rate of the locally employed population (INE, 2003). Due to the existence of several business parks and offices, Oeiras municipality attracts population from the contiguous municipalities of Sintra, Lisbon, Cascais and Amadora. It showed a significant increase in the employment polarization index and in

the rate gross employee attraction and a decrease in the repulsion rate of employees (INE, 2003; INE, 2018), constituting for these reasons a case study with the necessary characteristics of a municipality with a high number of intra and inter-municipal commutes and located in a critical seismic region in Portugal. Additionally, the Oeiras city council was interested in an emergency plan focusing on the topic.

3. DATA AND METHODS

3.1. Dynamics of Present Population and Commuting

Information on the expansion or contraction experienced by different places in terms of nighttime and daytime populations is important for many planning purposes, including those dealing with disaster relief operations (NRC, 2007; Freire, 2020). If in every seismic risk assessment, the seismic hazard computation for the studied area is a key issue (Sleeter & Wood, 2006) it is also true that the identification of people location and the consideration of its movement are crucial. Interactions between resident, working (and other reasons) population are critical factors on the overall human dynamics of a metropolitan area. This frequently leads to consider the importance of the forces responsible for temporal mobilities, often difficult to determine. There are also conceptual and methodological challenges to estimate the timeframe period and place specific location of a population. It is known that in metropolitan areas the population fluctuates and commuters (those who travel some distance to work and/or study reasons on a regular basis) are often in higher numbers than residents. An identified problem related to this increase of population is its variation according to the time of the day, week, and season. To be able of producing data on these dynamics of present population will substantially help disaster relief efforts.

For our purposes it is relevant that every worker or student (or even a tourist/visitor) that shows up in one place in a functional metropolitan area, might have started the day in another place. Thus, some places experience a daytime decline as people depart, while others have population peaks late in the day. Following the Openquake Platform exposure model (GEM, 2022) we assume two periods for the buildings' number of occupants (Fig. 2): night and day.

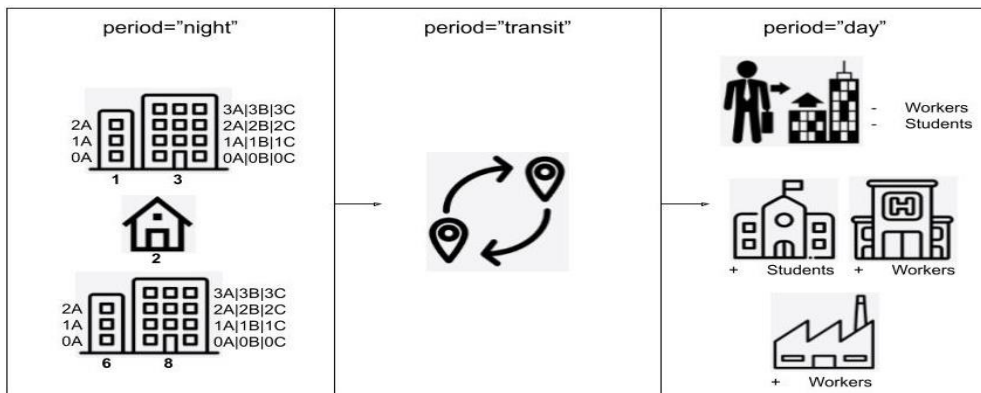


Fig. 2. Overview of three periods considered in population exposure model.

The integration of population data as an exposure layer into risk assessments for sudden hazard events needs to account people mobility (Renner *et al.*, 2018). Due to the lack of open traffic data, this period was not considered in this work. There is a certain relationship of this method with methodologies using satellite images (Sutton *et al.*, 2001; Deichmann *et al.*, 2011), extrapolations of Resident Population, or the administrative data available (Kamranzad *et al.*, 2020). Nevertheless, while these are mainly static methodologies, the method applied in this research is based on the powerful idea of flows between places (spatial interaction) using simple formulas that make estimates with an acceptable accuracy.

3.2. Data

Table 1 lists open data sets used in this work. They comprise building polygons, points of interest (POIs that include workplaces, schools, health facilities, touristic accommodations, restaurants), addresses and the enumeration units for the municipality of Oeiras. All these items are openly accessible, making it possible to build models of exposure of the population on a building scale.

Table 1.

Summary of geographic data used.

Dataset name	Source	Year
Buildings	OpenStreetMap	2021
POIs	OpenStreetMap	2021
Addresses	Statistics Portugal	2011
Enumeration units	Statistics Portugal	2011

Fig. 3 shows the geographic information layers used in the work, where the urban and metropolitan context of the case study can be verified.

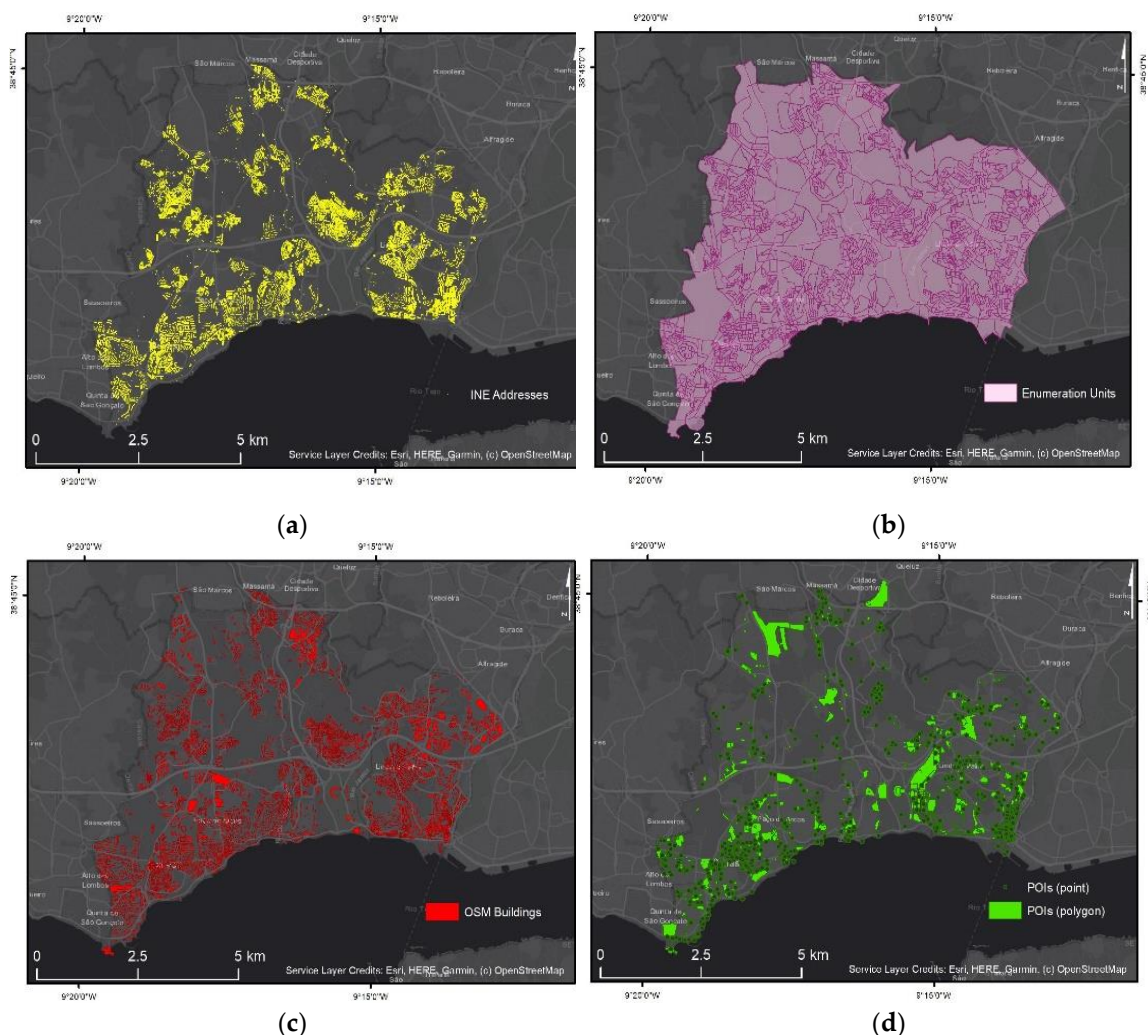


Fig. 3. (a) INE Addresses point layer; (b) INE Enumeration units (polygon layer); (c) OSM building layer (polygon layer); (d) OSM points of interest layer (polygon and point layer).

In addition to geographic data, administrative information was used to obtain the number of workers or students, such as a list of schools with the number of students, teachers and staff, health facilities, or administrative buildings. For establishments where it was not possible to determine the number of workers from the lists, this value was obtained from a rate value calculated from the information published by Statistics Portugal regarding the persons employed by establishments by geographic localization and economic activity classification division (**Table 2**) or subdivision. The economic classification codification by division or subdivision was critical to associate the number of workers to the establishment(s) in the building(s).

Table 2.**Number of workers per establishment by division of economic classification.**

Economic Classification Division	Workers/Establishments (workers per building)
Agriculture, animal production, hunting, forestry and fishing	1.5
Extractive industries	1.0
Manufacturing industries	9.9
Electricity, gas, steam, hot and cold water and cold air	1.8
Collection, treatment and distribution of water; sanitation, waste management and depollution	29.6
Construction	7.0
Retail trade; car and motorcycle repair	6.6
Transport and storage	5.4
Accommodation, restaurants and similar	4.1
Information and communication activities	10.2
Real estate activities	1.4
Consulting, scientific, technical and similar activities	3.0
Administrative and support services activities	3.8
Education	1.9
Human health activities and social support	3.5
Artistic, show, sporting and recreational activities	1.6
Other service activities	1.6

Source: Statistics Portugal (INE)

3.3. Nighttime Population Estimation

Data on the resident population are traditionally aggregated to the statistical areas and do not exist at the building scale. For this reason, a methodology was established for calculating the resident population from open data on addresses (**Fig. 4**). The building-scale resident population is calculated using open address data and enumeration units (polygons).

To determine the number of residents per building, the number of people per housing unit was calculated for all enumeration units. This value is associated with each existing housing unit in the building, making it possible to calculate the resident population through the sum of the average population of the housing unit in each building.

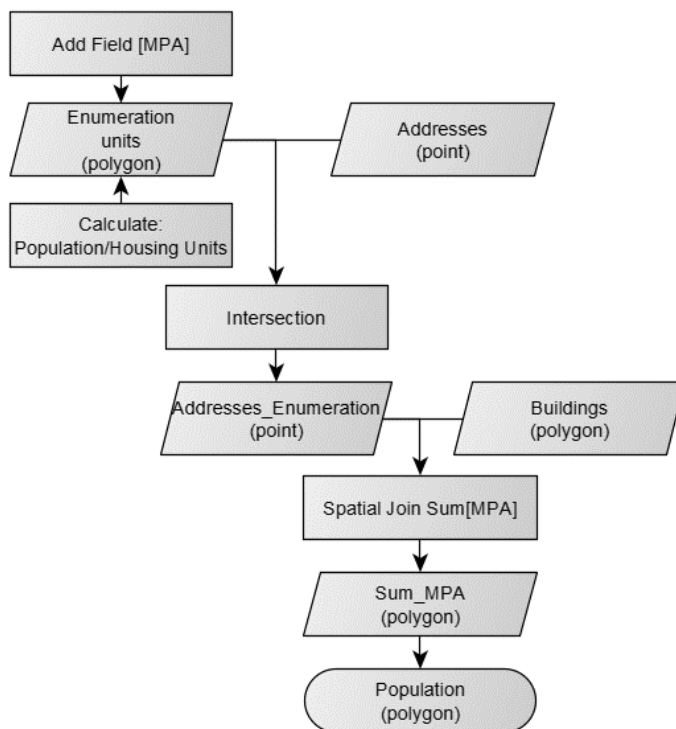


Fig. 4. Flowchart to calculate nighttime population for buildings.

3.4. Daytime Population Estimation

The methodological approach for estimating the present population, at the building scale, followed an adaptation of the methodology proposed by Sleeter & Wood (2006). The daytime population estimation considered total in-commuters (workers and students) and total out-commuters to each building. The estimation of the daytime population was performed using 3 iterations (Fig. 5).

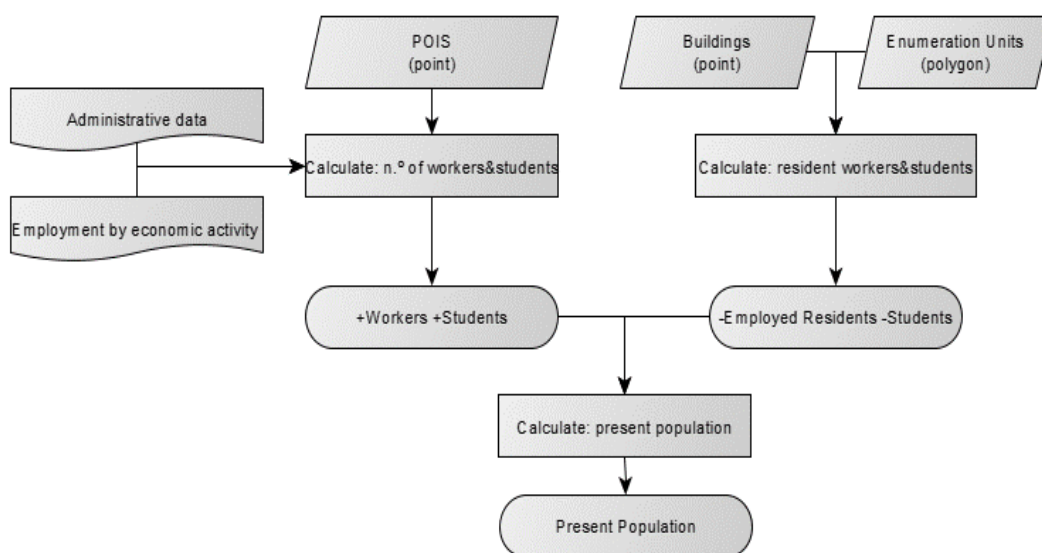


Fig. 5. Flowchart to calculate daytime population for buildings.

The first iteration represents all persons who are not employed or in school and who are assumed to remain in the household. As these data do not exist at the building scale, they were obtained through the statistical data available in the enumeration unit, allocating to each building the average value obtained per housing unit. In the second iteration, administrative data is used regarding the number of employees/students that are associated with each record in the points of interest layer. For the commercial and services where it was not possible to establish the number of workers, an average value was established, obtained from the employment by economic activity statistics. The third iteration estimates for each building the diurnal population through the difference between the mobile population (workers and students), without-going trips and the mobile population with incoming trips. This approach does not focus on the destination of the worker or student, but rather on the fact that the worker or student leaves home. Once the worker or student is determined away from home, the worker or student gets subtracted from the building.

4. RESULTS AND DISCUSSIONS

4.1. Aggregated Night and Day Population Distribution

According with the methodology described in the previous section, it was estimated the resident (night) and present (day) population for all the buildings in Oeiras municipality. These data were stored in a point layer where we can retrieve the population for both periods, by building, or by any aggregate administrative unit like places or parishes. **Fig. 6** illustrates the estimation of night population, for 2011, aggregated in a hexagonal tessellation. This aggregation demonstrates the possibility of obtaining an exposure model aggregated to different geographic units and the distribution of the resident population.

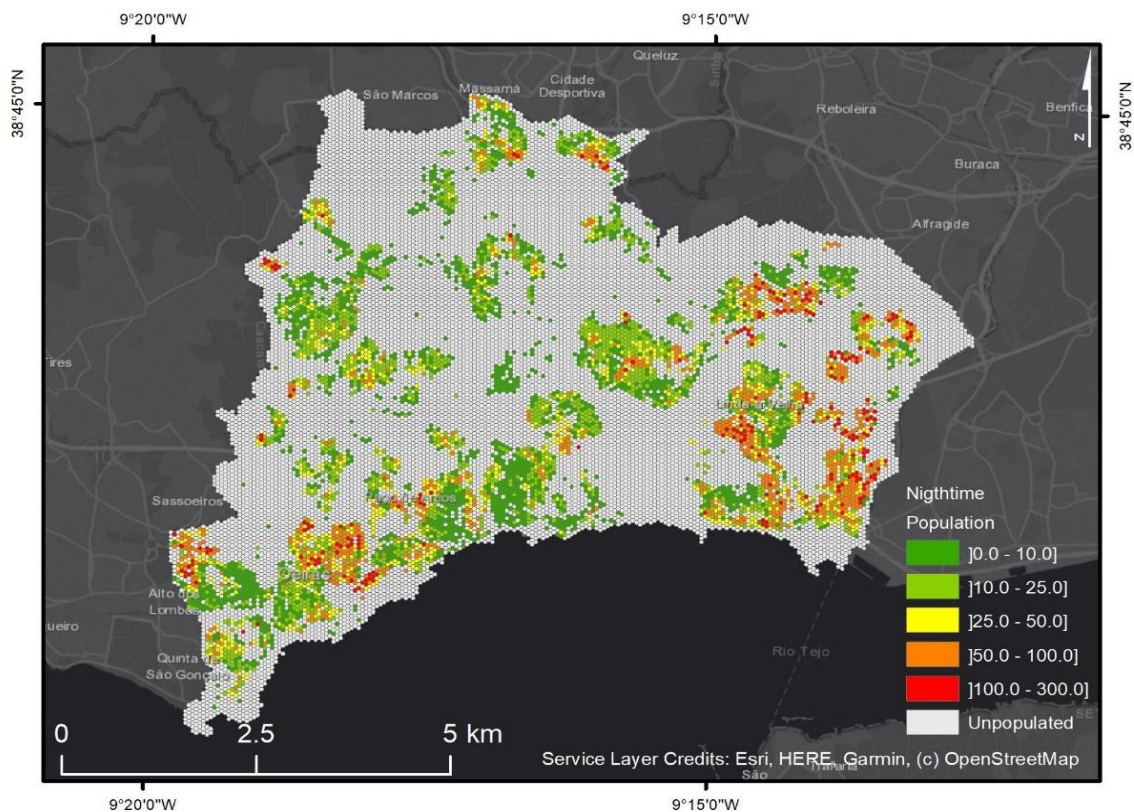


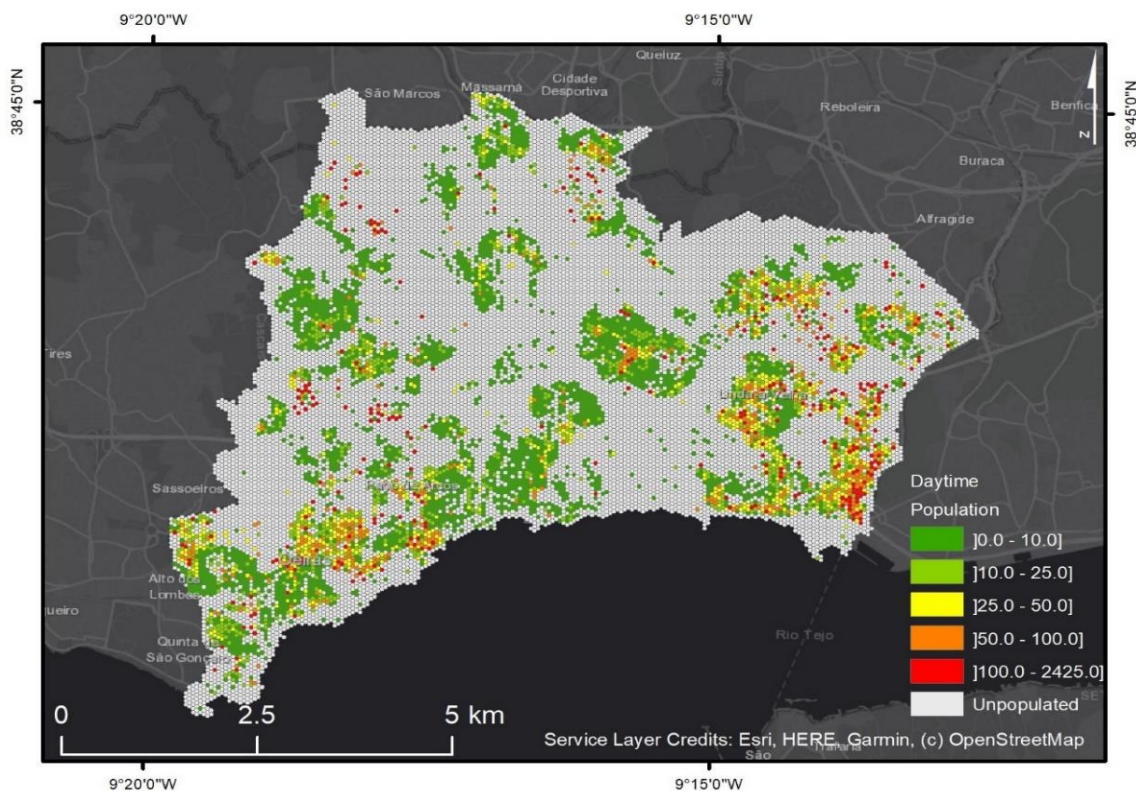
Fig. 6. Aggregated night population distribution (data).

The resident population is unevenly distributed across the territory, with low-density residential neighbourhoods (as it happens in Valejas, Gandarela, Quinta da Moura, Linda-a-Pastora neighbourhoods), as opposed to more densely populated residential urban areas, located mostly on the Algés-Miraflores-Carnaxide axis. According to the population exposure model, in 2011, the estimated total population for the night period was 165,614 residents (**Table 3**). The parishes with the largest number of residents are the coastal ones – Algés, Linda-a-Velha and Cruz Quebrada-Dafundo. The parishes with the lowest number of residents are located north of the A5 motorway – Porto Salvo and Barcarena.

Table 3.

Night population by parish.	
Parish	Population
Union of parishes of Oeiras and São Julião da Barra, Paço de Arcos and Caxias	56219
Union of parishes of Algés, Linda-a-Velha and Cruz Quebrada-Dafundo	46504
Union of parishes of Carnaxide and Queijas	34928
Porto Salvo	14625
Barcarena	13338
TOTAL	165614

Fig. 7 illustrates the estimation of day population, for 2011, aggregated in a hexagonal tessellation.

**Fig. 7.** Aggregated day population distribution (data).

This figure shows a predominance of the residential function in all urban areas, including in those where there is some importance of employment, such as Algés or Oeiras. The employment centres clearly stand out from the other areas, namely the business parks of Taguspark, Lagoasparque, Quinta da Fonte, Outurela/Portela, the industrial area of Carnaxide, the office parks of Miraflores and the

industrial area of Queluz de Baixo. At the same time, school, and university areas such as the Faculty of Human Motricity, Atlantic University or Instituto Superior Técnico stand out. On the other hand, there are some areas where there is a mixture of residential and employment components, namely Linda-a-Velha, Dafundo or Miraflores. According to the population exposure model, in 2011, the estimated total population for the day period was 197,076 people (**Table 4**). All parishes have a population in the day period higher than the night period. It is important to highlight the high attractiveness of this municipality as a destination for commuters in the Lisbon Metropolitan Area, particularly from the neighbouring municipalities of Lisbon, Cascais, Sintra and Amadora. The parish of Porto Salvo registers the biggest difference between the two periods (+69%), this value being explained by the fact that it constitutes an employment centre through a set of office parks. The parishes of Barcarena, Carnaxide and Queijas, register the smallest difference between the night and day period.

Table 4.**Day population by parish.**

Parish	Population
Union of parishes of Oeiras and São Julião da Barra, Paço de Arcos and Caxias	64576
Union of parishes of Algés, Linda-a-Velha and Cruz Quebrada-Dafundo	55737
Union of parishes of Carnaxide and Queijas	37289
Porto Salvo	24787
Barcarena	14687
TOTAL	197076

4.2. Night and Day Population Distribution by Building

Fig. 8 illustrates the estimation of exclusive day population and residential or mixture of residential and employment components, for 2011, by building.

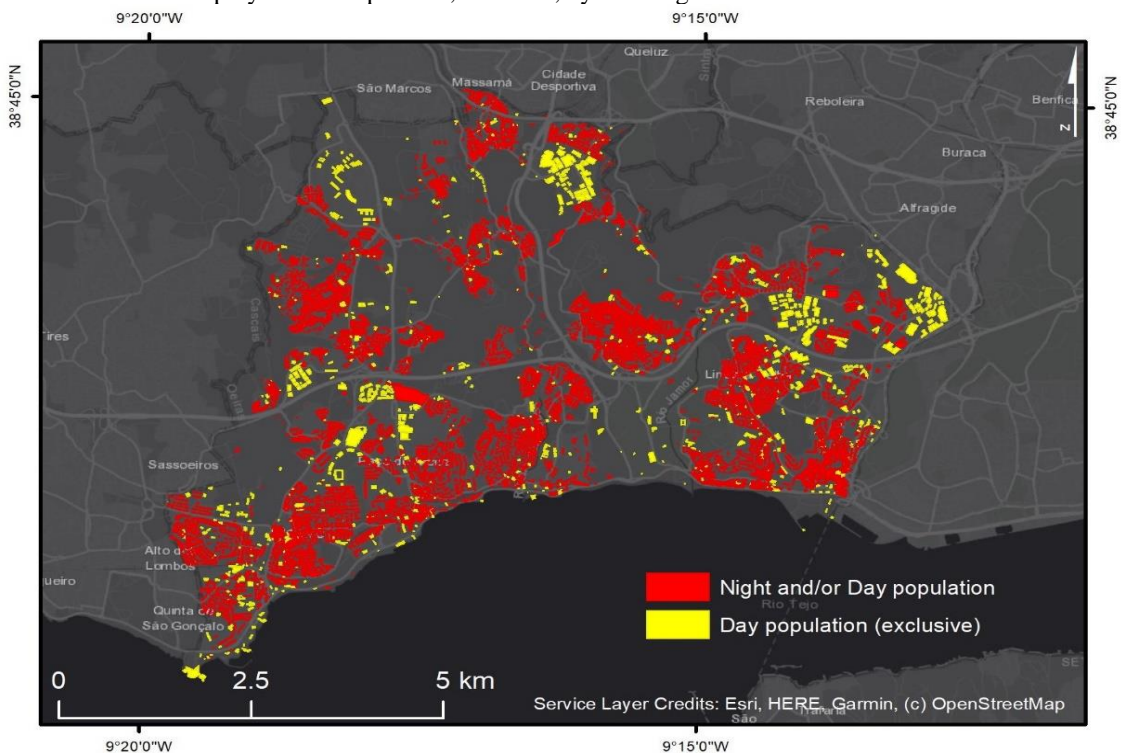


Fig. 8. Building distribution classified by exclusive day population and night and/or day population.

This figure shows a predominance of the residential or mixed function in all urban areas. The business parks stand out from the other areas, namely Taguspark, Lagoasparque, Quinta da Fonte, Outurela/Portela, the industrial area of Carnaxide, the office parks of Miraflores and the industrial area of Queluz de Baixo. In a more dispersed way, we can observe buildings with an exclusively daytime population, such as schools, hospitals, shopping centers or cultural buildings.

In **Fig. 9**, the result of the population distribution for the day and night period in two locations can be observed. In the first, corresponding to Algés, the distribution of the population by buildings shows a predominance of the residential function. As it is an area with some expression of proximity commerce, it is possible to verify the relevance of this use in some buildings. In the second location, corresponding to the Lagoaspark business centre, the distribution of the population by buildings allows checking the exclusive use during the day in some of the office buildings.

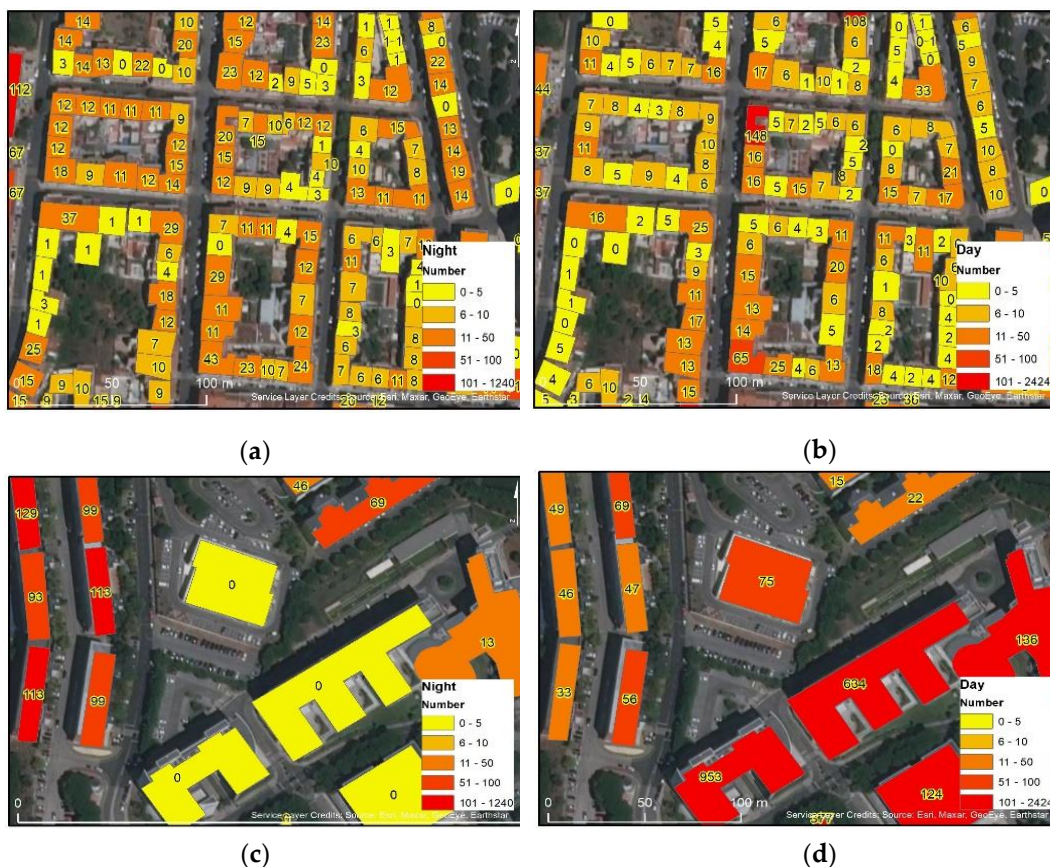


Fig. 9. (a) Night population by building in Algés; (b) Day population by building in Algés; (c) Night population by building in Lagoas Park Business Park; (d) Day population by building in Lagoas Park Business Park (data).

5. DISCUSSION

This paper presents the results of a building-scale population exposure model based on open data for earthquake loss estimation. The results of the analysis reveal that with some effort and additional work in associating the number of employees from administrative sources or from the average number of workers obtained from statistical sources to buildings polygons, is possible to locate the employed population for all buildings and create a population day exposure model. For the night period, the location and quantification of the resident population per building was possible to determine from a

source of open addresses. These results represent an enhancement to existing population data sets such as the official data set (enumeration units) provided by Statistics Portugal since they allow its use with models of physical vulnerability (buildings) for two periods: day and night. The results obtained for the two periods allowed the identification of several limitations and problems associated with the methodology and open data. Most of these issues are related with inaccuracies and incompleteness on the building and points of interest datasets. For the building dataset we observed that some polygons do not have a geographic correspondence with the addresses layer. The geometry of buildings assumes aggregations and disaggregations that do not correspond to reality. It was also verified the inexistence of some polygon geometries of the OSM buildings dataset. The POIs layer is not exhaustive of the set of economic activities existing in the municipality, which is reflected in the underestimation of the present population in some buildings.

In this study, for the day period, the approach does not consider the different occupations during the day (e.g. markets, shops) or during the week or month (e.g. hotels), assuming the maximum capacity of the establishments as a principle. Due to commuting movements highly relevant in metropolitan areas, the determination of the population exposed in transit is of great importance. However, its inclusion in this work was not possible due to the lack of open data, being one of the aspects to be evaluated in future works.

The validation of the results allows to verify for the night period, a difference of 6506 inhabitants for the total of residents counted in the 2011 censuses. In the absence of an open dataset for the buildings with the true value for the resident population, an aggregation of the results of the night exposure model was carried out, which allowed a comparison with the enumeration units of the censuses. This comparison showed that in 28% of the enumeration units the model population coincides with the resident population and in 50% of the enumeration units the error varies between -2 to 2.

For the day period the results allow us to confirm Oeiras municipality as a generator/attractor of travels. For a basic quantitative validation daytime model results were compared against the total number of workers in various business parks. For example, in Quinta da Fonte business park we observed a difference of -63 workers. However, in Lagoaspark or Taguspark business parks the differences are more significant (-1469 and -1217). These differences can be explained by the completeness of the points of interest dataset representing the economic establishments, since they directly influence the calculation of the number of workers in the buildings.

Since that one of the verified difficulties related with the implementation of the methodology was the time spent in the search for administrative or auxiliary information related to the number of workers, in future works the possibility of integrating these data into open data datasets should be considered. This finding was also stated by Renner *et al.* (2018) in his work where the preparation of the diverse input datasets for the spatiotemporal models resulted in a time-consuming and cost-effective task.

6. CONCLUSIONS

There are many potential benefits in the use of the presented methodology based on open data. The empirical outcomes we used, as an application example, clearly demonstrate that there is an obvious difference between the night population and the day population.

By 2011, the official resident population in Oeiras was about 172 120. Our estimated present population for the municipality, was 197 076, more than 14% times the official resident population.

According to the differences found in this study, we concluded that the population exposure in metropolitan contexts is a dynamic concept as the night and day population change significantly. These findings are in agreement with the study carried out by Freire (2020) in the Lisbon Metropolitan Area. In risk assessments these differences emphasize the importance of considering daytime complementary to nighttime population, as traditional administrative census data are only based on a static perspective/view of resident population. It is also fair to consider that “while it is generally true that any data are better than no data in an emergency situation, the best decisions are those made with the best data... (p.66)” (NRC, 2007).

There are significant outcomes in the calculation of present population deriving from the use of indirect techniques, as those that apply satellite images, but the uncertainty of these estimates and the limited information they produce make them insufficient methods to support emergency and mitigation plans.

We also keep in mind that the present population is not a static variable since it moves in time and space. According to the presented methodology, the use of open data like addresses and points of interest is a useful contribution to build population exposure models that can be integrated in software tools for assessment of earthquake risk, like OpenQuake Platform.

The dimension of the differences we found concerning the size of the resident population makes clear the necessity of enlarging the debate about traditional methods and the application of new ones, which can integrate innovative elements and processes of calculation, to estimate the dimension and space-time nature of population exposition. Despite the growing possibility of mapping the distribution and dynamics of the population based on Big Data and on sources such as mobile phones, the difficulty in accessing this data and the need for information at the building level to model earthquake loss estimation only emphasize the relevance of the methodology used in this research.

Beyond this contribution to the debate, we are sure that the improvement of estimations of the exposed present population will allow the production of better preventive plans for emergency situations, an improved efficiency of the reactive protocol, and an adequate foundation for infrastructure, equipment, and management of human resources.

REFERENCES

- Ara, S. (2014) Impact of Temporal Population Distribution on Earthquake Loss Estimation: A Case Study on Sylhet, Bangladesh. *Int J Disaster Risk Sci*, 5, 296–312 (2014). <https://doi.org/10.1007/s13753-014-0033-2>
- Autoridade Nacional de Protecção Civil – ANPC (2010) Estudo do Risco Sísmico e de Tsunamis do Algarve, Direcção Nacional de Planeamento de Emergência / Núcleo de Riscos e Alerta. ISBN: 978-989-8343-06-2
- Bosher L, Dainty A, Carrillo P, Glass J, Price A. (2009) Attaining improved resilience to floods: a proactive multi-stakeholder approach. *Disaster Prevention and Management*, Vol.18(1), 9-22.
- Codermatz R, Nicolich R, Slejko D. (2003) Seismic risk assessments and GIS technology: applications to infrastructures in the Friuli–Venezia Giulia region (NE Italy). *Earthquake Engineering and Structural Dynamics*; 32, 1677–1690.
- Costa, A.C., Sousa, M.L., Carvalho, A. E Coelho, E. (2009) Evaluation of seismic risk and mitigation strategies for the existing building stock: Application of LNECloss to the metropolitan area of Lisbon, *Bulletin of Earthquake Engineering* 8(1):119-134.
- Deichmann, U., Ehrlich, D., Small, C., and Zeug, G. (2011) Using high resolution satellite data for identification of urban natural risk. European Union and World Bank.
- Freire, S. (2007) Modeling Daytime and Nighttime Population Distributions in Portugal using Geographic Information Systems, Master of Arts Thesis in Geography, University of Kansas.
- Freire, S. (2020) Modeling of Population Distribution in Space and Time to Support Disaster Risk Management, PhD Dissertation, University of Twente. DOI 10.3990/1.9789036549998
- Freire, S.; Aubrecht, C. (2012) Integrating population dynamics into mapping human exposure to seismic hazard, *Nat. Hazards Earth Syst. Sci.*, 12, 3533–3543. <http://dx.doi.org/10.5194/nhess-12-3533-2012>
- GEM (2022) The OpenQuake-engine User Manual. Global Earthquake Model (GEM) OpenQuake Manual for Engine version 3.13.0, 204 pages. doi: 10.13117/GEM.OPENQUAKE.MAN.ENGINE.3.13.0
- Instituto Nacional de Estatística – INE (2003) Movimentos pendulares e organização do território metropolitano: área metropolitana de Lisboa e área metropolitana do Porto: 1991/2001 [Commuting movements and organization of the metropolitan territory: metropolitan area of Lisbon and metropolitan area of Porto: 1991/2001], Instituto Nacional de Estatística [National Statistics], Portugal.
- Instituto Nacional de Estatística – INE (2018) Mobilidade e funcionalidade do território nas Áreas Metropolitanas do Porto e de Lisboa 2017 [Mobility and functionality of the territory in the Metropolitan Areas of Porto and Lisbon 2017], Instituto Nacional de Estatística [National Statistics], Portugal.

- Ismail-Zadeh A, Takeuchi K. (2007) Preventive disaster management of extreme natural events. *Nat Hazards*, 42, 459–467.
- Kamranzad, F.; Memarian, H.; Zare, M. (2020) Earthquake Risk Assessment for Tehran, Iran. *ISPRS Int. J. Geo-Inf.*, 9, 430. <https://doi.org/10.3390/ijgi9070430>
- Ma, Yunjia, Wei Xu, Xiujuan Zhao, and Ying Li. (2017) Modeling the Hourly Distribution of Population at a High Spatiotemporal Resolution Using Subway Smart Card Data: A Case Study in the Central Area of Beijing *ISPRS Int. J. Geo-Inf* 6, no. 5: 128. <https://doi.org/10.3390/ijgi6050128>
- Mileu, N.; Queirós, M. (2018) Integrating Risk Assessment into Spatial Planning: RiskOTe Decision Support System. *ISPRS Int. J. Geo-Inf.*, 7, 184. <https://doi.org/10.3390/ijgi7050184>
- National Research Council – NRC (2007) Tools and methods for estimating populations at risk from natural disasters and complex humanitarian crises. Washington, DC: National Academies Press (NAP).
- O'Brien G. (2008) UK emergency preparedness: a holistic response? *Disaster Prevention and Management*, Vol.17(2), 232-243.
- Qi, W.; Liu, S.; Gao, X.; Zhao, M. (2015) Modeling the spatial distribution of urban population during the daytime and at night based on land use: A case study in Beijing, China. *J. Geogr. Sci.*, 25, 756-768.
- Renner, K.; Schneiderbauer, S.; Pruß, F.; Kofler, C.; Martin, D.; Cockings, S. (2018) Spatio-temporal population modelling as improved exposure information for risk assessments tested in the Autonomous Province of Bolzano, *International Journal of Disaster Risk Reduction*, Volume 27. <https://doi.org/10.1016/j.ijdr.2017.11.011>
- Santos, A., Tavares, A. O., Queirós, M. (2016) Numerical modelling and evacuation strategies for tsunami awareness: lessons from the 2012 Haida Gwaii Tsunami, *Geomatics, Natural Hazards and Risk*, 7:4, 1442-1459, DOI: 10.1080/19475705.2015.1065292.
- Sleeter, R.; Wood, N. (2006) Estimating daytime and nighttime population density for coastal communities in Oregon. Urban and Regional Information Systems Association Annual Conference Proceedings, p. 973+. Gale Academic OneFile, Accessed 15 Sept. 2020.
- Smith K., Petley DN. (2009) Environmental Hazards: Assessing Risk and Reducing Disaster. 5th Revised Ed. London: Routledge.
- Sutton, P., Roberts, D., Elvidge, C., Baugh, K. (2001) Census from Heaven: an estimate of the global human population using night-time satellite imagery. *International Journal of Remote Sensing*, 22(16): 3061 -3076.
- Tang, Y, Y. Yin, K. Hill, V. Katiyar, A. Nasser, and T. Lai. (2012) Seismic Risk Assessment of Lisbon Metropolitan Area under a Recurrence of the 1755 Earthquake with Tsunami Inundation. 15th World Conference on Earthquake Engineering.
- Tavares, A. O., Barros, J.L., Santos, A. (2016) Multidimensional Approach for Tsunami Vulnerability Assessment: Framing the Territorial Impacts in Two Municipalities in Portugal, *Risk Analysis*, Version of Record online: 5 SEP 2016, DOI: 10.1111/risa.12678
- US Census Bureau – USCB (2000) Available at: <http://www.census.gov/main/www/cen2000.html> - <http://www.census.gov/population/www/cen2000/maps/respop.html>, Accessed on 19 March 2019.
- Vilanova S., Fonseca J. (2004) Seismic hazard impact of the Lower Tagus Valley FaultZone (SW Iberia). *J Seimol.* 8(3):331-345.
- Vora M, Lee ZH, Pong W. (2008) The cost of seismic structural damage and preventive action. *Disaster Prevention and Management*, Vol.17(5), 601-621.
- Wenzel F, Bendimerad F, Sinha R. (2007) Megacities – megarisks. *Nat Hazards*, 42, 481–491.

A NEAR FUTURE CLIMATE CHANGE IMPACTS ON WATER RESOURCES IN THE UPPER CHAO PHRAYA RIVER BASIN IN THAILAND

Naphol YOOBANPOT¹  and Weerayuth PRATOOMCHAI² * 

DOI: 10.21163/GT_2022.172.16

ABSTRACT:

This paper focused on regional climate change impacts on hydro-meteorological variables in the Upper Chao Phraya River basin located in northern Thailand. The five global climate models were used with a number of 15 experiments to assess near future water resources over the period 2026-2040. The impacts of climate change were quantified in percentages relative to a retrospective period (1986-2000). On average, the surface temperature tends to increase by 1.45, 1.48, and 1.80 °C under the lowest (RCP2.6), intermediate (RCP4.5), and highest (RCP8.5) CMIP5 greenhouse gas emission scenarios, respectively. Mathematical model called H08 was used, the coupling of three modules did a very good job on mimicking river discharge with high Nash-Sutcliffe and Index of Agreement. The projections of rainfall and its response to surface runoff and groundwater recharge exhibit relatively uneven distributions. The upper basin tends to face extremely heavy rainfall and taking place of serious flood, while the lower areas are expected to cope with drought. Based upon ensemble averages over the entire area, relative changes of -1.7% (-6.4%), -0.1% (-5.2%), and -2.0% (-9.3%) in the mean annual rainfall (groundwater recharge) are shown under the RCP2.6, RCP4.5, and RCP8.5 scenarios, respectively. This study included a groundwater recharge assessment indicating potential available groundwater use, which is considered to be a key resource for climate change adaptation. Based on these findings, implementing such an artificial groundwater recharge system is needed in order to harvest surplus water and making for coping with water stress in the dry season.

Key-words: *Climate change, Drought, Flooding, Groundwater recharge, Water resources management*

1. INTRODUCTION

Climate change is real and is now an international problem. It has a broad and spatially distributed impact on multiple sectors. Observations of air temperature rises and a number of extreme hydrological events, for example 2022 drought across Europe, 2022 Pakistan flood as well as people's perceptions on the impacts of climate change show an increasing trend (Kiguchi et al., 2021; IPCC, 2018; Magramo, 2022; Hansen et al., 2010; Heim, 2015; Manandhar et al., 2015; Pratoomchai et al., 2015b). The consequences of climate change impacts on hydro-meteorology related to water variability and hazard are complicated. In addition, these impacts are uncertain and difficult to predict. Therefore, understanding how potential climate change effects alter the distribution and availability of hydro-meteorological variables at a regional or basin scale is crucial and necessary to frame resilient measures to provide and formulate better water resource management such as conjunctive water use.

In Thailand, extreme floods and droughts are common (Pavelic et al., 2012 and Kiguchi et al., 2021). During the period 1991-2011, approximately 8,300 million US dollars were spent toward flooding damage (Department of Disaster Prevention and Mitigation, 2011). On the other hand, the depletion of river discharge and widespread drought-affected areas were reported, for example, in 1986, 1987, 1990, 1993, 1998, 2003, 2005, 2012, 2015 and 2018.

¹ King Mongkut's University of Technology North Bangkok, Faculty of Engineering, Department of Civil Engineering, Bangkok, Thailand, naphol.y@eng.kmutnb.ac.th

²* King Mongkut's University of Technology North Bangkok, Faculty of Engineering, Department of Civil Engineering, Bangkok, Thailand, weerayuth.p@eng.kmutnb.ac.th

More recently, over two consecutive years (2014 and 2015), the annual rainfall over Thailand was 8% and 12%, respectively, below the 30-year average (from 1981-2010). Because of the hydrological conditions in Chao Phraya River basin, changes on the order of a few percentages of rainfall can lead to a significant impact on the runoff volume (Kotsuki and Tanaka, 2013). In this case, the volume of water storage in major reservoirs was low in an approximately 30-year return period; therefore, irrigation water was not allocated to grow rice during the dry season, which had a large impact on more than ten million people who were primarily farmers.

Regarding the potential of climate change impact studies, Kotsuki et al. (2014), Pratoomchai et al. (2014), and Watanabe et al. (2014) noted that both flooding and drought periods in the Chao Phraya River basin tend to be amplified adversely compared to the last decade. The number of rainy days might decrease, but the amount and intensity of precipitation tend to increase. Hydrologically extreme events and their aftermath, e.g., extreme precipitation-induced landslides, are likely to be exacerbated (Kuraji et al., 2009; Limsakul and Singhruck, 2016; Ono et al., 2015). Thorough assessments are consequently needed with a high horizontal resolution (Kiguchi et al. 2021). It will be more practical and useful if an assessment provides information at a sub-basin scale or at monitoring/warning points, e.g., main gauging stations. Furthermore, groundwater is rarely studied in Thailand, but its potential is now being considered as a buffer for the available water supply to cope with water stress. Thus, a projection of climate change impacts, including impacts with regard to groundwater flux (recharge), is needed to evaluate basin threats and resilience. Therefore, investigating the temporal and spatial distributions of hydro-meteorological variables affected by climate change to provide scientific, region-based information for adaptation options is mandatory for intensive agriculturally based countries such as Thailand. Key hydro-meteorological variables, i.e., surface temperature, rainfall, runoff, river discharge, and groundwater recharge, were subjected to investigation in this study to reveal hydro-meteorological changes at a sub-basin and grid-based scale as well as at monitoring gauging stations. Accordingly, decision makers, community leaders, and people who are interested in how anthropogenic climate change might shape future water resources can benefit from this paper.

2. THE UPPER CHAO PHRAYA RIVER BASIN

Thailand is a country that plays a significant role in supplying agricultural products such as rice, which is a staple food for global food demand. However, the trend in the rice yield is currently decreasing because of an increasing number of hot days (≥ 37.5 °C, Pratoomchai et al., 2015, 2020) and less water for allocating to irrigation area. The Upper Chao Phraya River basin (UCP), which is associated with the Ping, Wang, Yom, and Nan sub-basins (comprising 12 provinces) in the northern part of the country shown in **Fig. 1a**, is a major source for rice growth. Its basin covers a total massive land area of approximately 109,973 km². The altitude varies from that of a mountain range (the upper region) with a maximum elevation of approximately 2,570 m (above mean sea level, msl) to that of a lowland area at approximately 14 m (msl) at the basin outlet.

The basin lies in a tropical zone that is usually dominated by two distinct monsoon seasons: the rainy southwest monsoon (May-July) and the northeast monsoon (August-October), wherein approximately 82% of the average annual rainfall occurs during the rainy season. On average, the base-wide annual rainfall is 987 mm. Kuraji et al. (2009) showed that the annual high-altitude rainfall reaches approximately 1,300 mm and demonstrates an increasing trend. Flooding is the most severe natural disaster threat over the lowland area. Based on satellite image data that were analyzed by the Geo-Informatics and Space Technology Development Agency (GISTDA) of Thailand, the area of maximum flood inundation varied between 1,455 km² and 9,490 km². The light-blue shaded area (**Fig.1b**) represents the extent of maximum flood inundation of the 2011 extreme flood event. Deforestation, especially in the headwaters of the Nan sub-basin, is expected to accelerate and contribute to an increased flood volume downstream.

Generally, the river delineation and flow are from north to south, which is the same direction of the storm paths. The Wang River merges with the Ping River, the Yom River joins with the Nan River, and the Ping and Nan Rivers have a confluence at the C.2 gauging station in the Nakhon Sawan

Province with an observed mean river discharge of $734 \text{ m}^3 \text{ s}^{-1}$ (during the 2011 event, the maximum daily peak was $4,686 \text{ m}^3 \text{ s}^{-1}$, or approximately $1,200 \text{ m}^3 \text{ s}^{-1}$ over its channel capacity). Overall, approximately 82% of the annual rainfall is evaporated back into the atmosphere (Pratoomchai et al., 2015).

There are 2 major artificial storages (i.e., the Bhumibol reservoir on the Ping River, which is not far upstream from the Ping-Wang confluence, and the Sirikit reservoir on the Nan River, **Fig. 1b**) with a total storage of approximately 23 km^3 within the basin. Both reservoirs were considered in this study. However, other artificial storages that are also situated within the upper Ping and Wang sub-basins were not considered in our assessment because their capacities are relatively small compared with those of the Bhumibol and Sirikit reservoirs.

There are a couple of reasons to select UCP as the study area. First, based on statistical data, the content of the UCP basin tends to increase in terms of both magnitude and frequency with both flooding and droughts (e.g., Ekkawatpanit et al., 2013; Kuraji et al., 2009; Mateo et al., 2014; Pavelic et al., 2012; Pratoomchai et al., 2014, 2015a; Gopalan et al., 2021). Second, approximately 80% of the agricultural areas that are mainly used for rice in the basin are rain-fed. There is explicit plan to develop new irrigation areas in these rain-fed that requiring more water budget (Royal Irrigation Department, 2010). Furthermore, there has been very strong and aggressive protesting from the local populace on the construction of a new reservoir in the Yom sub-basin because of natural and environmental concerns. Nevertheless, prior to a couple of years ago, groundwater irrigation promoted and played a distinguished role in the growth of rice (Department of Groundwater Resources, 2012; National Research Council of Thailand, 2022). Therefore, the abovementioned factors will push the UCP into a critical hydro-meteorological state that will eventually impose negative impacts upon the residents.

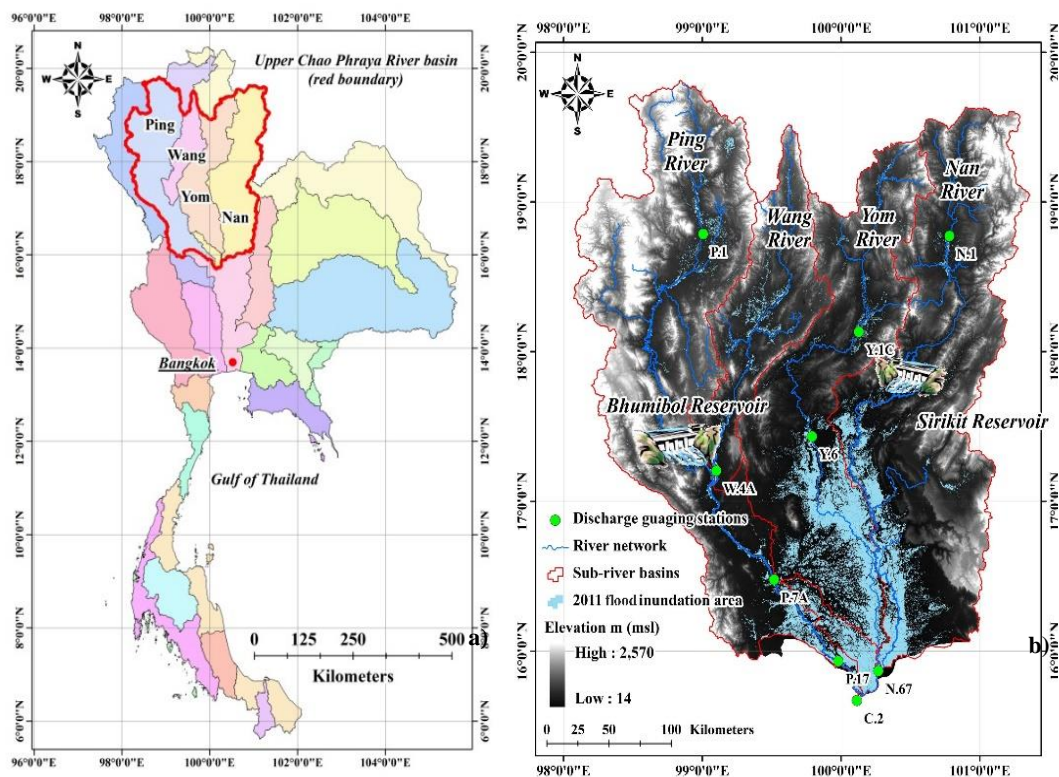


Fig. 1. Study area: a) the main river basins in Thailand and b) the Upper Chao Phraya River basin.

3. METHODOLOGY AND DATA

3.1. Mathematical model

This study took advantage of the Integrated Study Project on Hydro-Meteorological Prediction and Adaptation to Climate Change in Thailand (the IMPAC-T project, <http://impact-www.eng.ku.ac.th/cc/>), which downscaled the water resource model known as H08 (Hanasaki et al., 2008) from a $1.0^\circ \times 1.0^\circ$ to a $5' \times 5'$ spatial resolution that is more reasonable for a regional-scale assessment (Hanasaki and Mateo, 2012; Hanasaki et al., 2014). Three modules of the H08 model, i.e., land surface, river routing, and reservoir operation modules, were conducted in this study (Fig. 2). The technical details and limitations of H08 are available in Hanasaki et al., 2014; Mateo et al., 2014. However, a brief description of each particular module will be outlined below.

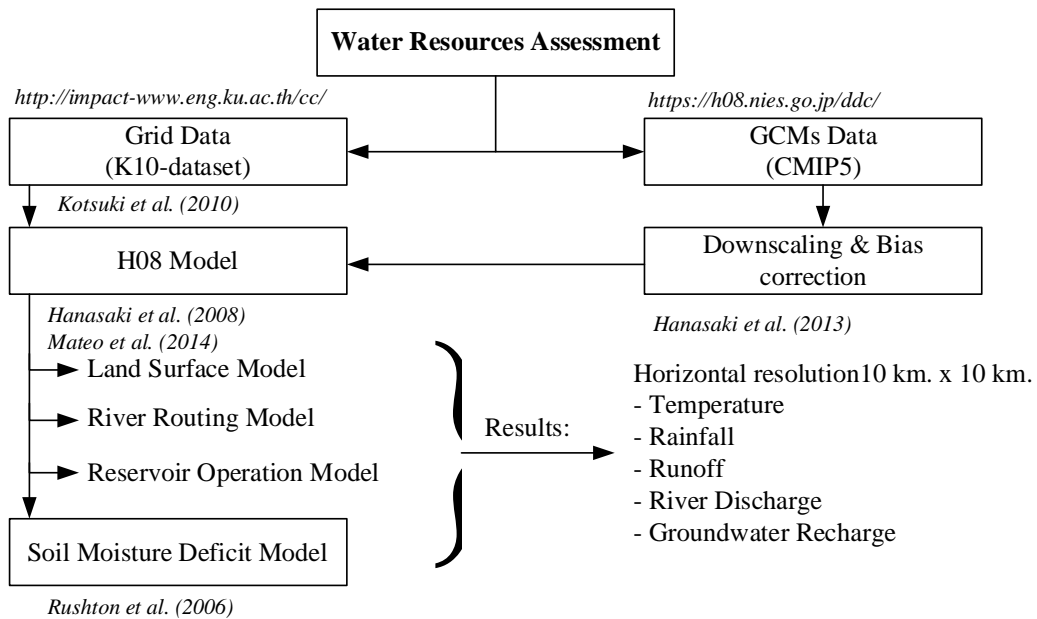


Fig. 2. Schematic diagram of methodology.

First, the land surface module (LSM) was constructed under a soil water balance concept (Hanasaki et al., 2008), which is able to simulate a diurnal soil-surface water balance. Second, a virtual straight-line river element concept from the Total Runoff Integration Pathways (TRIP) model, which was developed by Oki and Sud (1998), was implemented into the river routing module. Lastly, a simple reservoir operation module, consisting of the mean seasonal released flows (i.e., of the wet and dry seasons), was determined from historical operating data (Bhumibol and Sirikit reservoirs) for normal regulation. In extreme circumstances (i.e., droughts and flooding), the module will output a zero-discharge value if the storage volume is less than the dead reservoir storage (i.e., 3.80 and 2.85 km³ for the Bhumibol and Sirikit reservoirs, respectively) and will output more discharge to maintain the water level in the reservoir below that which is allowed by the upper rule curve if a large amount of runoff volume flows into the reservoirs (Hanasaki and Mateo, 2012; Mateo et al., 2014).

To provide groundwater recharge calculations, we simplified an approach known as the soil moisture deficit (SMD) method and focused on the distribution of groundwater recharge as driven by rainfall (Rushton et al., 2006). Groundwater recharge is generated on days when the SMD estimate reaches a negative value. If the SMD becomes zero, it represents the state wherein the soil is at 100% saturation and ready to free the recharged volume. Groundwater recharge is therefore the quantity of water in excess of that required to saturate the soil. The model structure, calculation steps, and parameters as well as the initial conditions can be found in Pratoomchai et al. (2014 and 2015a).

There were some limitations of our model. Only the Bhumibol and Sirikit reservoirs were included in the reservoir operation module while small reservoirs in the Ping, Wand, and Nan sub-basins were not considered. Land use land cover in the UCP for the projected climate change period (2026-2040) and reference period (1986-2000) was assumed the same, no land use change. The study focused on only climate change impacts on water resources, socio-economic changes did not include.

3.2. Forcing climate data

Kotsuki et al. (2010, 2014) collected observed data (1981 to 2004) from the Thai Meteorological Department (TMD) and Royal Irrigation Department (RID) and created the 10 km. x 10 km. horizontal resolution in binary format. This data-set known as K10-data and contributed (**Table 1**), free of charge, for researchers under the international IMPAC-T project (<http://impact-www.eng.ku.ac.th/cc/>). To simulate the LSM, K10-dataset was used for the model input. The observed river discharge provided by RID were used for model calibration and validation.

Table 1.

Forcing climate data for the H08 model.

Data	Grid size	Temporal resolution	Sources
Surface air temperature	10 km. x 10 km.	Daily	K10-data set (http://impact-www.eng.ku.ac.th/cc/)
Specific humidity	10 km. x 10 km.	Daily	
Wind speed	10 km. x 10 km.	Daily	
Surface air pressure	10 km. x 10 km.	Daily	
Short-wave downward radiation	10 km. x 10 km.	Daily	
Long-wave downward radiation	10 km. x 10 km.	Daily	
Rainfall	10 km. x 10 km.	Daily	
River discharge	Gauging stations	Daily	Royal Irrigation Department

3.3. Global climate model (GCM) selection, climate change scenarios, and bias correction of GCMs

As a consequence of an incomplete knowledge of the earth’s systems and an unforeseeable future (e.g., Hanasaki et al., 2013; Jackson et al., 2011), there is no universally applicable GCM that is recommended for conducting studies to assess climate change. Applying an increased number of GCMs is common for projecting climate change impacts because each GCM has been developed and treated using a different technique. The results obtained from multiple GCMs might reflect and encompass a broader possible range of the future assessment.

In this paper, 5 GCMs were selected, namely, 1) MIROC-ESM-CHEM (MIROC), 2) HadGEM2-ES (HadEM), 3) GFDL-ESM2M (GFDL), 4) IPSL-CM5A-LR (IPSL), and 5) NorESM1-M (NorESM), which were selected from the World Climate Research Program’s Coupled Model Inter-Comparison Project phase 5 (CMIP5). All of these GCMs are earth system models, the results of which were cross-checked in the Inter-Sectoral Impact Model Intercomparison Project (<http://www.isi-mip.org/>). These 5 GCMs from different climate research institutes were selected to reflect uncertainties within the models. Three scenarios (i.e., representative concentration pathways, or RCPs), including low (RCP2.6), intermediate (RCP4.5), and high (RCP8.5) levels of emissions, were used to project the future climate for the period 2026-2040, which represents the near future, in order to ignore the effects of land use change. Since multiple GCMs and scenarios were considered, a plausible range and pattern of hydro-meteorological variables due to the forcing of climate change should be revealed.

For the projection and simulation of climate change, the systematic biases from 3 variables (i.e., temperature, rainfall, and longwave downward surface radiation) that were collected from the GCMs were corrected. A shifting and scaling technique previously used by researchers, including Hanasaki et al. (2013), was applied to remove the systematic bias of the 3 variables. This is one of the simplest and most popular techniques for GCM bias correction. In short, a time series of current climate data can be modified by adding or multiplying climate elements that are affected by climate change in order to create a new climate variable time series under a particular scenario or set of climate change conditions.

4. RESULTS AND DISCUSSION

4.1. Surface temperature and rainfall changes

Fig. 3a shows the spatial average of the mean annual surface air temperature variations over the entire UCP in 2026-2040. It shows the differences between the projection period and the reference period (1986-2000), which had a 25.38°C mean annual surface air temperature (**Fig. 3b**). In general, these projections show good agreement with the degree of greenhouse gas emissions. There were changes (anomaly) of 1.45, 1.48, and 1.80°C under the RCP2.6, RCP4.5, and RCP8.5 scenarios, respectively, which all exhibit an increasing trend. All scenarios projected a rising trend in every single area. The projected results show good agreement with the forcing conditions, which are the lowest in the RCP2.6 scenario and the highest in the RCP8.5 scenario. In fact, the values shown above were averaged from the 5 GCMs for each scenario to express a general trend and overcome the uncertainty within the GCMs (e.g., Jackson et al., 2011).

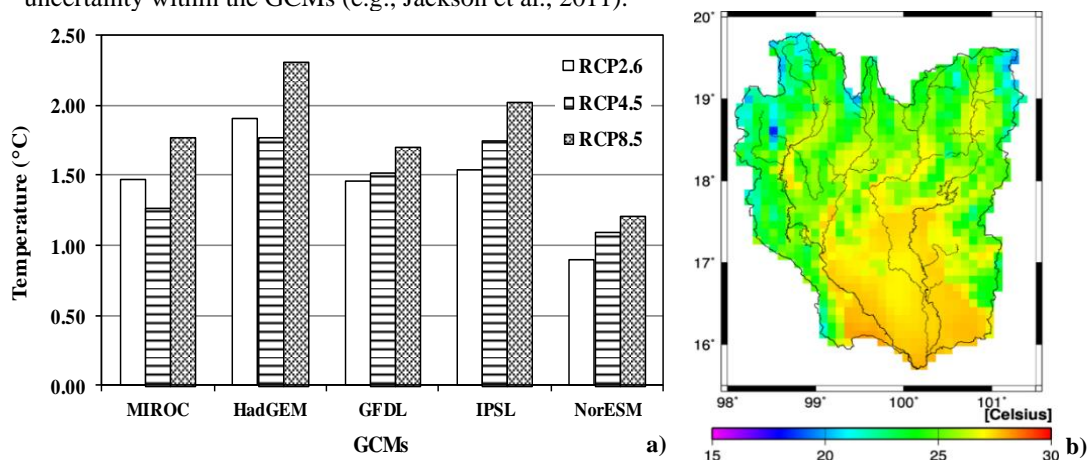


Fig. 3. a) Projection of annual surface air temperature changes in 2026-2040 and b) spatial distribution of the past mean annual temperature (1986-2000).

All of the GCMs were also applied to project the spatial mean annual rainfall, runoff, and evaporation, as shown in **Table 2**. The GCMs and scenarios that revealed decreasing trends are presented in *italics*. In general, we observe that the projected trends depended upon the GCMs rather than the scenarios. The MIROC and NorESM GCMs showed an increasing trend for all variables. Rainfall acts like an input into the system, for which the projected variability or ranges from -10.5 to +7.5%, -11.5 to +6.4%, and -10.2 to +10.2% corresponding to the RCP2.6, RCP4.5, and RCP8.5 scenarios, respectively, relative to the reference period (987 mm). Using a simple average among the GCMs for each particular scenario, we can quantify potential -1.7%, -0.1%, and -2.0% changes in the mean annual rainfall under the RCP2.6, RCP4.5, and RCP8.5 scenarios, respectively. Based on the projected results, rainfall tends to decrease, and the other variables (runoff and evaporation) are associated with rainfall.

Table 2.

**Mean annual rainfall, runoff, and evaporation in 2026-2040
under the modeled climate change conditions.**

Scenarios	GCMs	Mean annual projections					
		Rainfall		Runoff		Evaporation	
		mm	% changes	mm	% changes	mm	% changes
RCP2.6	MIROC	1,057.50	7.14	189.20	6.89	868.30	7.20
	HadGEM	883.30	-10.51	137.10	-22.54	746.10	-7.89
	GFDL	925.20	-6.26	161.80	-8.59	763.40	-5.75
	IPSL	923.30	-6.45	144.00	-18.64	779.20	-3.80
	NorESM	1,060.60	7.46	196.80	11.19	863.80	6.64
RCP4.5	MIROC	1,045.10	5.89	188.20	6.33	856.90	5.79
	HadGEM	938.90	-4.87	153.60	-13.22	785.30	-3.05
	GFDL	873.00	-11.55	138.80	-21.58	734.20	-9.36
	IPSL	1,032.90	4.65	186.50	5.37	846.40	4.49
	NorESM	1,049.80	6.36	188.10	6.27	861.70	6.38
RCP8.5	MIROC	1,088.20	10.25	205.60	16.16	882.60	8.96
	HadGEM	885.90	-10.24	135.70	-23.33	750.30	-7.37
	GFDL	904.40	-8.37	152.00	-14.12	752.40	-7.11
	IPSL	888.40	-9.99	140.80	-20.45	747.60	-7.70
	NorESM	1,070.50	8.46	201.10	13.62	869.40	7.33

Fig. 4 shows the spatial distributions of the average annual rainfall, runoff, and evaporation. The figures show the spatial average from the past (left, 1986-2000), the ensemble average using the 5 GCMs under the RCP8.5 scenario (middle, 2026-2040), and the difference between the projected and reference periods (right). Both increases and decreases in the projected rainfall changes are observed, except within the projection under the RCP4.5 scenario. This scenario demonstrates that rainfall over the entire basin might be reduced by 20 mm to 50 mm relative to the period 1986-2000. However, all scenarios showed agreement that the lower part of the UCP is likely to be subject to a reduction in the amount of rainfall, especially in the lower Ping sub-basin. On the other hand, RCP2.6 suggests that rainfall will increase in the Ping sub-basin in the future. The spatial distributions of evaporation and runoff show the same patterns as rainfall because the rainfall is the input into the system. More rainfall means more available water for evaporation, while the rest contributes to runoff.

However, the results based on the 5 GCMs can be changed when we consider a greater number of GCMs, but there is no rule of thumb on this matter. Since the projections were focused on the near future to avoid the effects of land use change, the signals of climate changes may not be clearly observable within the projected period. However, the projected models imply that the first monsoon tends to decrease, while the second monsoon season shows an increasing trend. This interannual variability might induce both drought (i.e., an insufficient water supply for good crop growth over the period from May to July) and flooding during the second monsoon.

4.2. River discharge changes

Fig. 5 shows a comparison between river discharge rates (i.e., from observation and simulation) at the selected 8 gauging stations over the period 1986-2000 as a result of the coupling of 3 modules (LSM, river routing, and reservoir operation) in a daily time-step. Two objective functions, i.e., the Nash-Sutcliffe coefficient (Ef) and index of agreement (IOA), were applied to quantitatively show the model performance. Both the Ef and IOA are likely close to unity; thus, we note that our model very capably predicted the river discharge rates at the various observed stations. Thus, adapting the validated model to assess the river discharge under different climate change conditions should be reasonable.

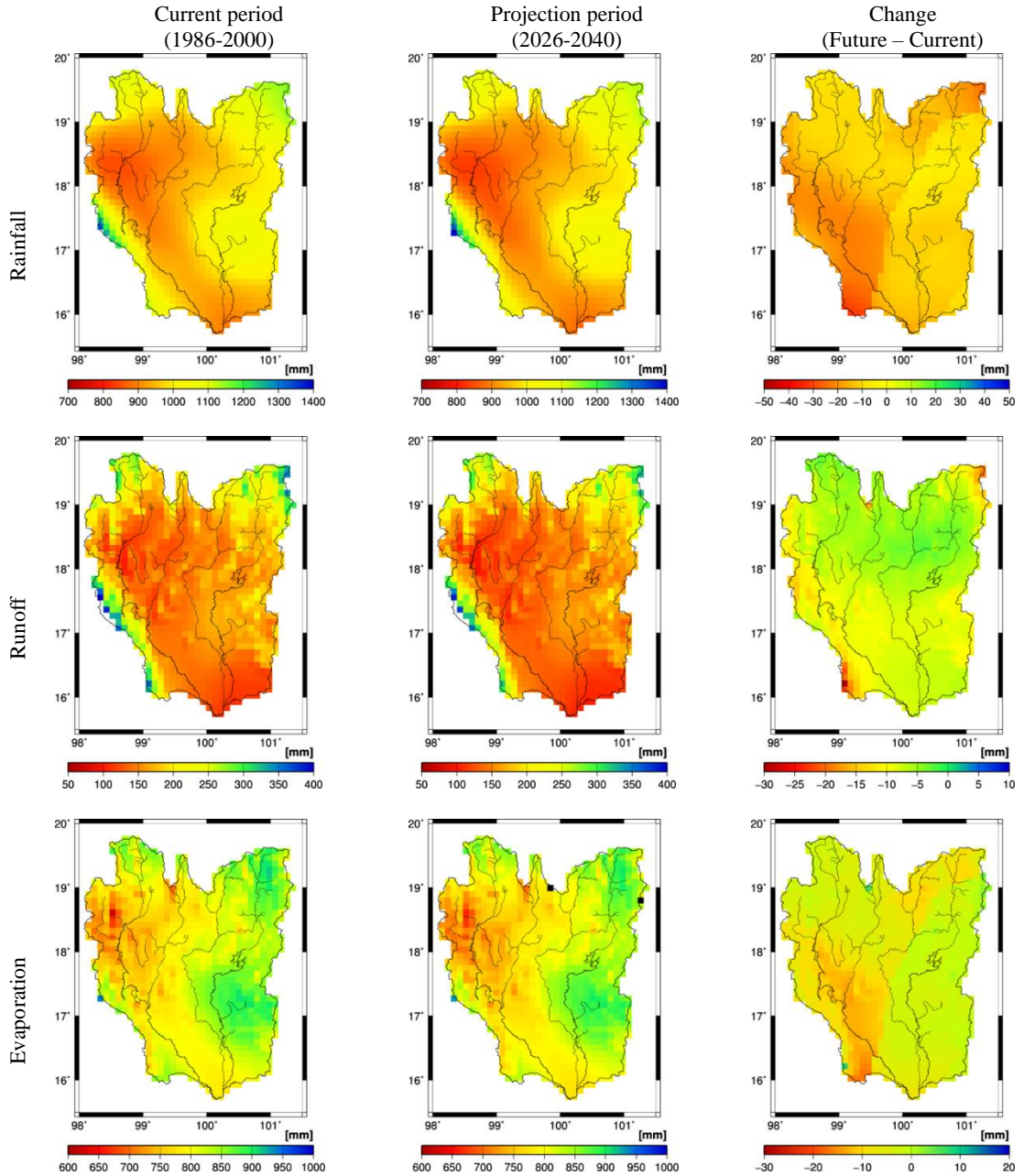


Fig. 4 Spatial distribution of average annual rainfall, runoff, and evaporation under the RCP8.5 scenario using the ensemble average from the 5 GCMs.

As shown in the figure, Ef and IOA were not calculated for the P.17 and N.67 stations because of incomplete observed data. For the IOA values (0.89 – 0.98), the model did a very good job on mimicking discharge observation. The other objective function (Ef) also showed good performance on producing model results with Ef values between 0.76 and 0.95. However, W.4A station (Outlet of the Wang sub-basin), Ef coefficient (0.49) revealed relatively low due to the fact that there are two dams in this sub-basin but we did not consider in our model since their total capacity is very small compare to the Bhumibol and Sirikit reservoirs.

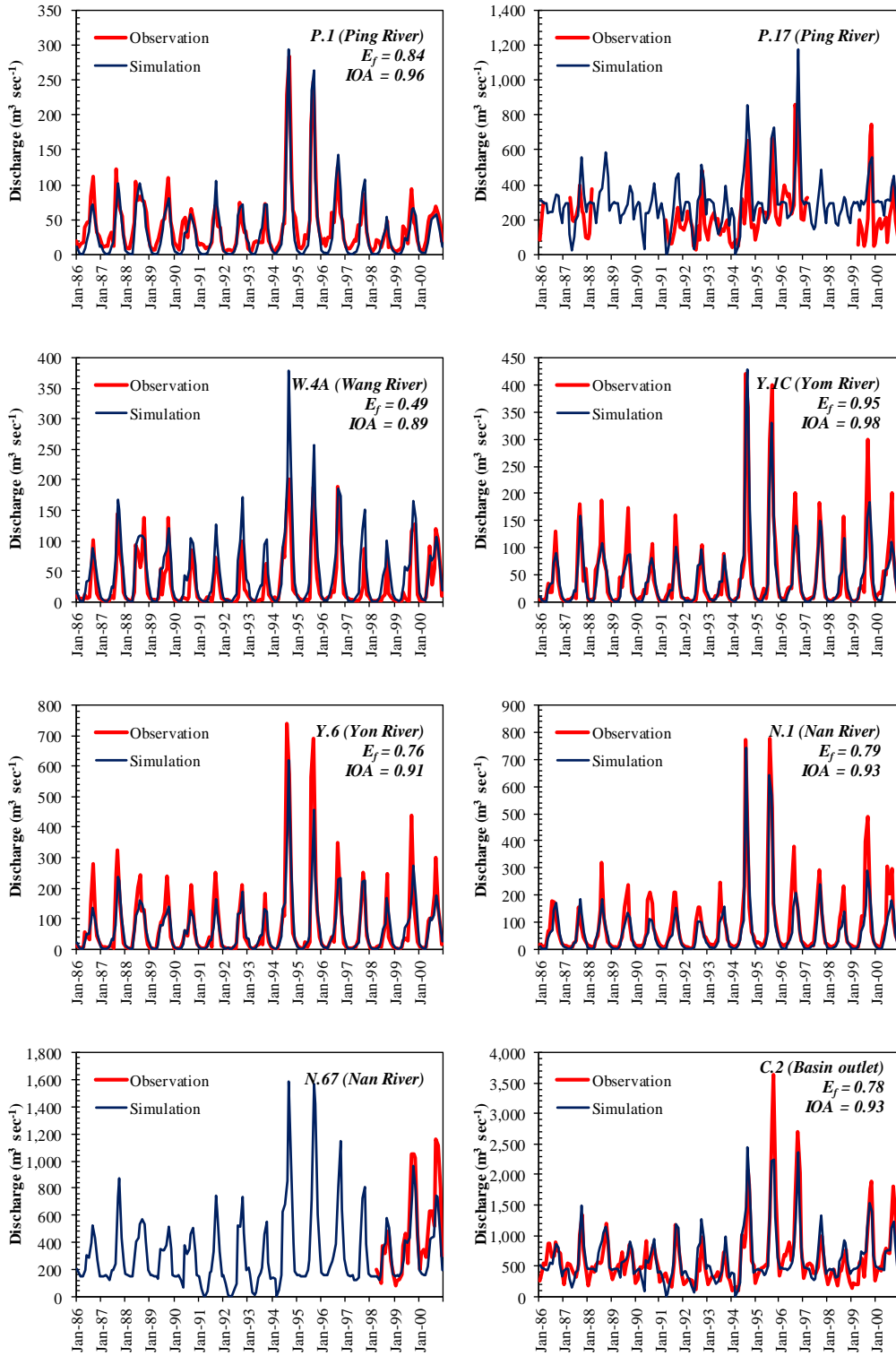


Fig. 5. Comparison of monthly river discharge rates at the main gauging stations in the UCP.

Overall, the model performance able to capture the general patterns of river discharge in the UCP. It was confirmed by model result at C.2 station (UCP outlet), 0.78 and 0.93 for the Ef and IOA, respectively. However, for an extreme event (1995 flood event), the model did not capture the peak well (under estimate) because of special reservoir operation policy and it is a limitation of our model. Under the climate change conditions (**Fig. 6**), at the basin outlet (station C.2), the black dashed line was quite stable from January to May (approximately $390 \text{ m}^3 \text{ sec}^{-1}$) because this period was governed by reservoir operations.

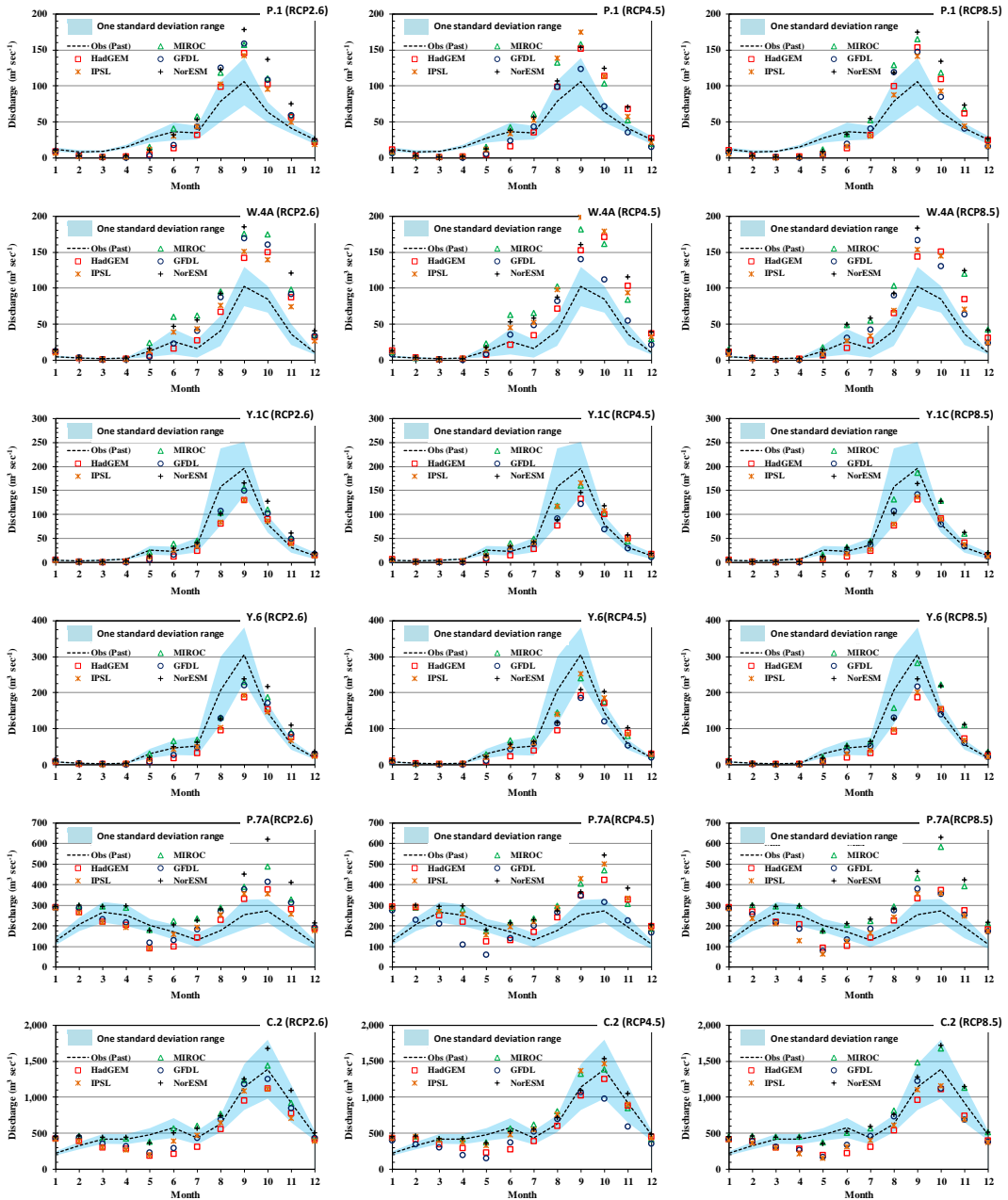


Fig. 6. Comparison of past (1986-2000) and projected (2026-2040) river discharge rates. The light blue shaded area represents a band of one standard deviation using the observed data for analysis.

During the wet season (May to October), the river discharge at the basin outlet station reached its peak in October (approximately $1,400 \text{ m}^3 \text{ sec}^{-1}$ from an average of 15 years), but the rainfall reached a maximum in September. It can be roughly estimated that the travel time of surface water in the UCP is approximately 1 month. However, for the stations that are not subject to reservoir effects, almost zero discharge was observed during the dry season. From January to May, the projections of river discharge rates resulting from the multiple GCMs and scenarios were decreased for these stations (i.e., P.1, W.4A, Y.1C, and Y.6). In contrast, during the second monsoon period (August to October), the river discharge rates in the upper area (i.e., the mountainous region) showed a significant increase, as their projected results (e.g., for stations P.1 and W.4A) exceeded the one standard deviation range.

NorESM GCM projected the highest discharge while HadGEM GCM showed relatively low discharge rate for all scenarios. The degree of climate change impact on river discharge in the UCP is not much difference between climate change scenarios, for example, projected maximum monthly discharge at P.1 (headwater) and C.2 (UCP outlet) stations are approximately 180 and $1,600 \text{ m}^3 \text{ s}^{-1}$, respectively. For the sub-basin scale, the Ping, Wang, and Nan sub-basins showed increasing in runoff volume but the Yom sub-basin yielded less discharge compared to the based-period. These projected patterns showed consistency for all scenarios.

In addition, an increasing trend of rainfall in the upper Ping region has been observed (Kuraji et al., 2009). To alleviate the expected flood volume, a reservoir operation option was modeled and simulated by Mateo et al. (2014), the results of which revealed that, because of the operation of the Bhumibol and Sirikit reservoirs, approximately 8.6 billion m^3 of the 2011 downstream flood volume was reduced. Further adaptations of the reservoir rule curves were examined. If the proper rule curve had applied during the flood, approximately 2.4 billion m^3 would have been further reduced.

In terms of their spatial distributions, the projections show an increasing river discharge in the upper basin with a decreasing trend in the lower area. This is especially clear if we look at the spatial distributions of the runoff. It is optimistic that the lower basin can take advantage of the reservoir storage capacities (i.e., the Bhumibol and Sirikit reservoirs), and therefore, climate change impacts on river discharge rates might not much change except for within the Yom sub-basin.

4.3. Groundwater recharge changes

Based on the model results, nearly 100% of the recharge occurred between May and October. The maximum groundwater recharge time frame for both the reference and projected periods occurred during August-September, which was coincident with the second monsoon period. Approximately 93 mm of the mean annual groundwater recharge accounted for 9.4% of the mean annual rainfall (1986-2000). Meanwhile, there is no observation of groundwater recharge within the UCP or in Thailand. However, the amount of the calculated groundwater recharge was consistent with amounts reported in other studies, such as Ramnarong and Wongsawat, 1999, Döll (2009), and Koontanakulvong et al. (2010). The future projections show a large range in the mean annual groundwater recharge from 70.8 mm (a -24% decrease) to 105 mm (a +13% increase). These findings are consistent with the results of Döll (2009), who obtained a range in the projected changes in groundwater recharge in Thailand from -30% (decrease) to +10% (increase) by 2050 under the ECHAM4 and HadCM3 models with scenarios A2 and B2. Overall, we note that the projections varied predominantly according to the GCM utilized rather than by the scenario. This emphasizes that the projections are sensitive to the GCMs used (e.g., Döll, 2009; Jackson et al., 2011).

Fig. 7 shows the spatial distributions of the mean annual groundwater recharges over the projected period. In addition, the ensemble averages (Jackson et al., 2011) of the spatial distributions for each scenario are presented. Decreases of 87.0 (-6.4%) mm, 88.1 (-5.2%) mm, and 84.3 (-9.3%) mm relative to the reference period were observed for the RCP2.6, RCP4.5, and RCP8.5 scenarios, respectively. The maximum projected decrease in the mean annual groundwater recharge is approximately -22.2 mm (24%), which was obtained under the HadGEM model for the RCP8.5 scenario corresponding to the extreme decrease in the projected rainfall. On the other hand, the same experiment (RCP8.5) under the MIROC model projected a 13% increase in the mean annual groundwater recharge relative to the period 1986-2000.

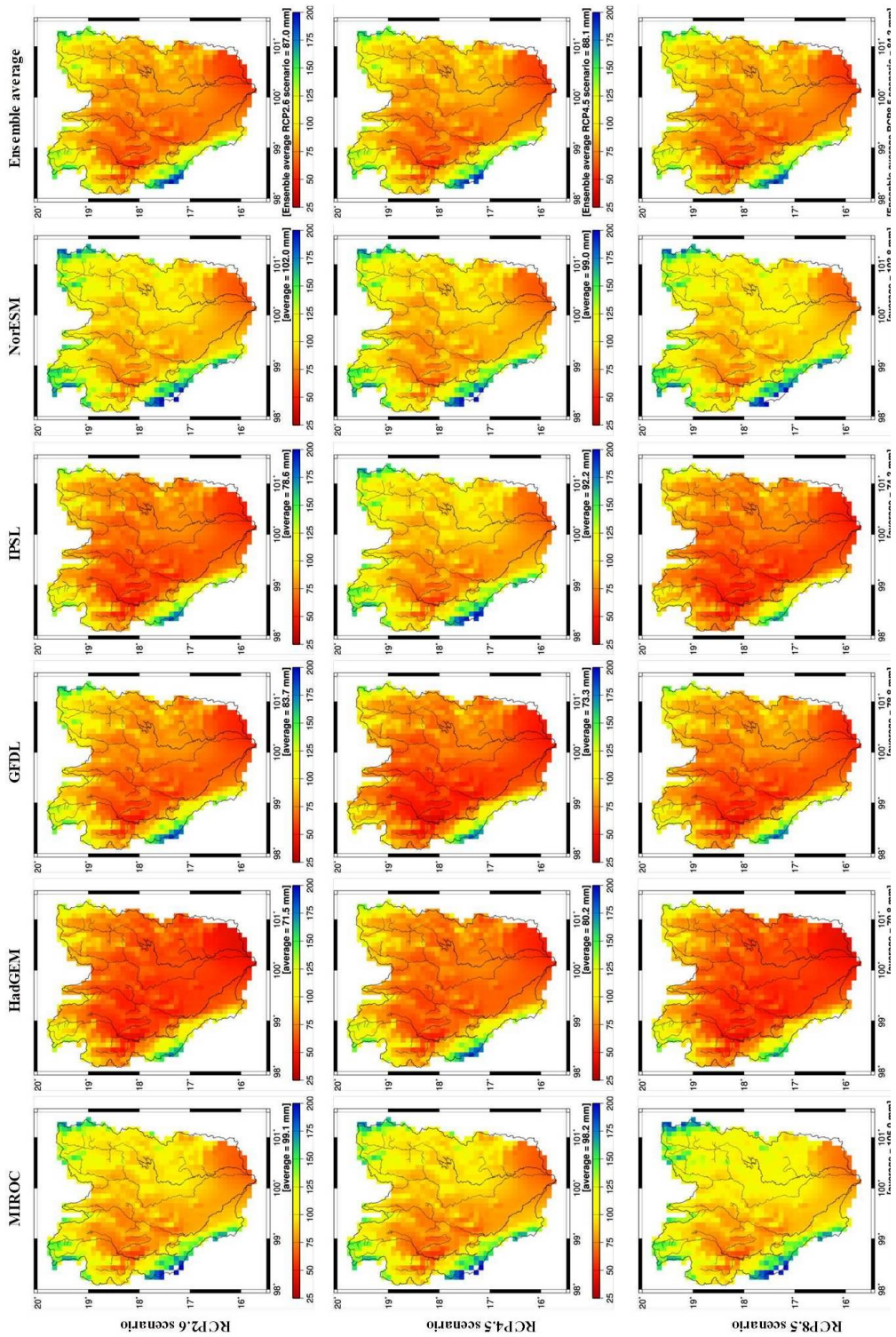


Fig. 7. Spatial distribution of the average annual groundwater recharge rates under different climate change conditions.

However, it should be noted that the decreasing rate of groundwater recharge is evidence of the effect of evaporation that is driven by increasing surface air temperatures. If we compare the range of the projected changes in the mean annual rainfall (from -11.5% to +10.2%) with those of the groundwater recharge (from -24% to +13%), we see that the range in the projected change of the groundwater recharge is larger.

There is a clear interrelationship between flood inundation and induced groundwater in a floodplain area (e.g., Kazama et al., 2007). Thus, a flood harvesting scheme should be implemented in order to take advantage of this phenomena to buffer droughts during the dry season. As suggested by Pavelic et al. (2012), the allocation of areas ranging from 70 km² to 340 km² (depending on the infiltration rate) in the lower Yom and Nan sub-basins should be considered for constructing infiltration ponds. In fact, groundwater use is now playing an important role in alleviating surface water shortage (National Research Council of Thailand, 2022). However, the observed fluctuations of groundwater levels in the wet and dry seasons showed a larger range during consecutive years given the high volume of extracted groundwater (Pratoomchai et al., 2015b). Thus, a measure to induce additional groundwater recharge to compensate for high groundwater drafting is needed to avoid groundwater depletion.

5. CONCLUSIONS

Key hydrological variables, i.e., temperature, rainfall, runoff, river discharge, and groundwater recharge, were projected under different climate change conditions over the near period 2026-2040 because it was reasonable to ignore the effects of land use change. An increased temperature ranges from 1.45-1.80 °C was expected relative to the period 1986-2000. Rainfall was projected to increase under the MIROC and NorESM GCMs, but the HadGEM, GFDL, and IPSL GCMs suggested a decrease in the rainfall trend. Using ensemble averages, the future annual rainfall was expected to decrease by approximately 20 mm under the highest greenhouse gas emission scenario (RCP8.5). In terms of its spatial distribution, only the upper Ping sub-basin showed an increasing rainfall trend. The rest of the basin, the majority of which is the UCP, was subjected to decreasing rainfall; therefore, the runoff and groundwater recharge, on average, were projected to show 5.6% (10 mm) and 9.3% (8.7 mm) reductions under the RCP8.5 scenario. Among the 4 sub-basins, the Yom sub-basin is the most vulnerable area and going to face with drought because of pronounced climate change impacts, low river discharge and groundwater recharge, and a lack of artificial storage, e.g., a reservoir. Therefore, a structural measure to secure flood water in the wet season and release downstream in the dry season is now not available for this area.

Climate change might cause or induce more flooding (e.g., the upper Ping and Wang sub-basins during the second monsoon) and drought (e.g., the lower basin, especially in the Yom sub-basin). Considering the advantages of reservoir storage and their proper operation is one possible option to alleviate the problems related to flooding (Mateo et al., 2013, Gopalan et al., 2021). On the other hand, enhancing the use of groundwater is one possible option to cope with drought (Pratoomchai et al., 2015a). However, to ensure that groundwater will not be depleted and thereby induce other problems, increasing the groundwater recharge rate by means of floodwater harvesting schemes (i.e., allocating low-lying areas in the lower Yom and Nan sub-basins for temporary natural flood ponds) is recommended during the second monsoon (September-October). In addition, a law or policy to control groundwater extraction should be implemented.

Further suggestions and projections with an uncertainty analysis are a crucial component to improve the qualitative understanding of potential climate change impacts on water resources at a local scale. A number of small reservoirs in the Ping and Wang sub-basins and land-use/land-cover changes should be included in the mathematical model. Moreover, an integrated assessment between climate change and socio-economic change impacts on water sector will provide a clearer picture for what should do to cope with the era of changing climate (Kiguchi et al. 2021). Finally, we hope that this study will provide useful guidance for decision makers managing of water resources in helping to secure and alleviate water problems induced by climate change in the UCP.

ACKNOWLEDGEMENTS

The authors are very pleased with and appreciate the funding provided by Faculty of Engineering, King Mongkut's University of Technology North Bangkok, under grant number ENG-64-108.

REFERENCES

- Department of Disaster Prevention and Mitigation (2011) Statistics of flood and droughts in Thailand (in Thai). Bangkok, Thailand.
- Department of Groundwater Resources (2012) Groundwater and sustainable agriculture in Thailand (in Thai). Bangkok, Thailand.
- Döll P. (2009) Vulnerability to the impact of climate change on renewable groundwater resources: a global scale assessment. *Environmental Research Letters* 4: 035006.
- Ekkawatpanit C, Kazama S, Sawamoto M, Sarukkalige P. (2013) Evaluation of the inequality of water resources. *Water Management* 166: 303-314.
- Green TR, Taniguchi M, Kooi H, Gurdak JJ, Allen DM, Hiscock KM, Treidel H, Aureli A. (2011) Beneath the surface of global change: impact of climate change on groundwater. *Journal of Hydrology* 405: 532-560.
- Gopalan S.P., Hanasaki N., Champathong A., Tebakari T. (2021) Impact assessment of reservoir operation in the context of climate change adaptation in the Chao Phraya River basin. *Hydrological Processes*. <https://doi.org/10.1002/hyp.14005>
- Hanasaki N, Mateo CM. (2012) H08 regional application: Case study of the Chao Phraya River. H08 supplemental documentation 1.
- Hanasaki N, Kanae S, Oki T, Masuda K, Motoya K, Shirakawa N, Shen Y, Tanaka K. (2008) An integrated model for the assessment of global water resources Part1: Model description and input meteorological forcing. *Hydrology and Earth System Sciences* 12: 1007-1025.
- Hanasaki N, Fujimori S, Yamamoto T, Yoshikawa S, Masaki Y, Hijioka Y, Kainuma M, Kanamori Y, Masui T, Takahashi K, Kanae S. (2013) A global water scarcity assessment under shared socio-economic pathways - Part2: Water availability and scarcity. *Hydrology and Earth System Sciences* 17: 2393-2413.
- Hanasaki N, Saito Y, Chaiyasaen C, Champathong A, Ekkawatpanit C, Saphaokham S, Sukhapunnaphan T, Sumdin S, Thongduang J. (2014) A quasi-real-time hydrological simulation of the Chao Phraya River using meteorological data from the Thai Meteorological Department automatic weather stations. *Hydrological Research Letters* 8(1): 9-14.
- Hansen J, Ruedy R, Sato M, Lo K. (2010) Global surface temperature change. *Reviews of Geophysics* 48: RG4004
- Heim RR. (2015) An overview of weather and climate extremes - products and trends. *Weather and Climate Extremes* 10: 1-9.
- IPCC (2018). In V. Masson-Delmotte, et al. (Eds.), *Global Warming of 1.5° C*. An IPCC Special Report on the impacts of global warming of 1.5° C above pre-industrial levels and related global greenhouse gas emission pathways, in the context of strengthening the global response to the threat of climate change, sustainable development, and efforts to eradicate poverty.
- Jackson CR, Meister R, Prudhomme C. (2011) Modelling the effects of climate change and its uncertainty on UK Chalk groundwater resources from an ensemble of global climate model projections. *Journal of Hydrology* 399: 12-28
- Kiguchi et al. (2021) A review of climate-change impact and adaptation studies for the water sector in Thailand. *Environmental Research Letters* 16 023004
- Kazama S, Hagiwara T, Ranjan P, Sawamoto M. (2007) Evaluation of groundwater resources in wide inundation areas of the Mekong River basin. *Journal of Hydrology* 340: 233-243.
- Koontanakulvong S, Suthidhummajit C, Roodpai S. (2010) The assessment report impact of climate change to irrigation and groundwater: Case study in Plaichumpol Irrigation Project. Final report (in Thai), Chulalongkorn University, Bangkok, Thailand.
- Kotsuki S, Tanaka K, Kojiri T, Hamaguchi T. (2010) The water budget analysis with land surface model in Chao Phraya River basin. In *Proceedings of Japan Society of Hydrology and Water Resources*, 23rd annual conference, 44-45.

- Kuraji K, Mei G, Kowit P. (2009) Inter-annual and spatial variation of altitudinal increase in rainfall over Mount Inthanon and Mae Chaem watershed, Northern Thailand. *Hydrological Research Letters* 3:18-21.
- Magramo K. (2022) A third of Pakistan is underwater amid its worst floods in history. Here's what you need to know. CNN (access September 2022)
- Manandhar S, Pratoomchai W, Ono K, Kazama S, Komori D. (2015) Local people's perceptions of climate change and related hazards in mountainous areas of northern Thailand. *International Journal of Disaster Risk Reduction* 11: 47-59.
- Mateo CM, Hanasaki N, Komori D, Tanaka K, Kiguchi M, Champathong A, Sukhapunphan T, Yamazaki D, Oki T. (2014) Assessing the impacts of reservoir operation to floodplain inundation by combining hydrological, reservoir management, and hydrodynamic models. *Water Resources Research* 50: 7245-7266.
- Oki T, Sud YC. (1998) Design of total runoff integrating pathways (TRIP)-A global river channel network. *Earth Interact* 2: 1-37.
- Pavelic P, Srisuk K, Saraphirom P, Nadee S, Pholkern K, Chusanathas S, Munyou S, Tangsutthinon T, Intarasut T, Smakhtin V. (2012) Balancing-out floods and droughts: Opportunities to utilize floodwater harvesting and groundwater storage for agricultural development in Thailand. *Journal of Hydrology* 470-471: 55-64.
- Prajamwong S, Supparatarn P. (2009) Integrated flood mitigation management in the Lower Chao Phraya River basin. Expert group meeting on innovative strategies towards flood resilient cities in Asia-Pacific.
- Pratoomchai W, Kazama S, Ekkawatpanit C, Komori D. (2015a) Opportunities and constraints in adapting to flood and drought conditions in the Upper Chao Phraya River basin in Thailand. *International Journal of River Basin Management* 13: 1-15.
- Pratoomchai W, Kazama S, Hanasaki N, Ekkawatpanit C, Komori D. (2014) A projection of groundwater resources in the Upper Chao Phraya River basin in Thailand. *Hydrological Research Letters* 8(1): 20-26.
- Pratoomchai W, Kazama S, Manandhar S, Ekkawatpanit C, Saphaokham S, Komori D, Tongduang J. (2015b) Sharing of people's perceptions of past and future hydro-meteorological changes in the groundwater use area. *Water Resources Management* 29: 3807-3821.
- Ramnarong V, Wongsawat S. (1999) Groundwater resources in Thailand (in Thai). *Thai Hydrologist Association Journal*, vol. 1.
- Royal Irrigation Department Thailand (2010) The system of irrigation plan under the framework of 60 million Rai. Summary report (in Thai), Bangkok, Thailand.
- National Research Council of Thailand (2022) Drought risk assessment and crop damage using geographic information system (in Thai), Bangkok, Thailand.
- Rushton KR, Eilers VHM, Carter RC. (2006) Improved soil moisture balance methodology for recharge estimation. *Journal of Hydrology* 318: 379-399.

MAPPING OF *SUBAK* AREA BOUNDARIES AND SOIL FERTILITY FOR AGRICULTURAL LAND CONSERVATION

Ida Bagus Putu BHAYUNAGIRI^{1*}  and Moh SAIFULLOH² 

DOI: 10.21163/GT_2022.172.17

ABSTRACT:

Soil fertility is the most crucial aspect of the sustainability of agricultural land productivity. As an agricultural country, Indonesia is closely related to agricultural activities and soil fertility. This scientific paper analyzed the boundary of *subak*, soil fertility condition, which will later be used as a guide for agriculture land conservation. *Subak* is a traditional Balinese farmer organization that aims to manage water irrigation and rice cropping patterns in paddy fields. Boundary *subak* agricultural land is determined by participatory mapping method, involving farmers. Soil fertility data were analyzed through field and laboratory surveys. The condition of the limiting factors for soil fertility in each mapping unit is then used as the basis for managing and conserving agricultural land. The result showed that area of *subak* in agriculture land is 2,177.33 ha divided into 65 Subaks. Soil fertility status in each Subak is grouped into two soil fertility statuses (medium and high). Therefore, it is necessary to carry out integrated soil conservation, such as returning plant residues into the soil periodically and adding organic matter and fertilizers containing P and K elements in single fertilizers and compound fertilizers. Adding P and K compound fertilizers is needed to support optimal land productivity and increase the CEC value of the soil. Types of organic matter can be applied to the soil by returning crop residues, manure, and composting.

Key-words: GIS, Conservation, Mapping, Soil Fertility, Subak, Bali-Indonesia.

1. INTRODUCTION

Subak is a traditional Balinese farmer organization that primarily aims to manage water irrigation and rice cropping patterns in paddy fields (Sumiyati et al., 2017; W. Windia et al., 2018). *Subak* is a traditional organization that is already known abroad. As an organization that deals with conventional irrigation systems, *Subak* also has a unique attraction for tourists, namely terraced rice fields, generally composed of terraced rice fields or terraces resembling unsized steps; this view presents tourists with both local and local. Furthermore, foreign countries visit Bali (Suasih et al., 2018). United Nations Education, Scientific, and Cultural Organization (UNESCO), on June 12, 2012, designated *Subak* as a world cultural heritage in the cultural landscape category.

One of the challenges currently facing *Subak* is the shrinking of irrigated paddy fields due to conversion to non-agricultural activities. In the last five years, rice fields in Bali have decreased by more than 1000 ha/year (Widia & Wiguna, 2013). Land conversion occurs in many urban areas because it is triggered by land prices that continue to soar, so farmers in urban areas are very tempted by very high price offers. The land-use change is thought to be due to the low productivity of agricultural land, one of which occurred in *Subak* in Sawan District, Buleleng Regency, Bali-Indonesia Province.

In agriculture, especially in plant cultivation, soil conditions and their management are essential factors determining whether the growth and yield of plants to be cultivated are optimal. This is because the soil is a production factor that acts as a growing medium for plants, a supplier of nutrients, and a water supply indispensable for plant growth (Subedi, 2018). Therefore, the ability of the soil to support plant growth will be determined by the state of soil fertility. As far as fertility is concerned, soil productivity can be improved and enhanced by specific technological inputs.

^{1*} Land Resources Laboratory, Faculty of Agriculture Udayana University, 80234 Denpasar, Indonesia, Corresponding author*, bhayunagiri@unud.ac.id

² Spatial Data Infrastructure Development Center Udayana University, 80234 Denpasar, Indonesia, moh9saifulloh@gmail.com

Soil fertility is the ability of the ground to provide balanced amounts of nutrients for plant growth and production. Planting crops can cause the loss of essential nutrients in the soil because, during harvesting, essential nutrients are transported out of the land, mainly if they are cultivated continuously (Kome et al., 2019; Bayu, 2020; Prabakaran et al., 2021). Thus, soil fertility will decrease until it reaches a state where the addition of nutrients through fertilization is necessary to obtain profitable agricultural products.

The boundaries of the *subak* agricultural area are not currently available spatially. The data is essential, especially in the management of *subak* agricultural land, irrigation arrangements, and the distribution of fertilizer subsidies by the government so that they are right on target and in the right location. *Subak* land mapping and quantification of soil properties were carried out using a Geographic Information System (GIS). Previous researchers used GIS technology to map landslide hazards (Diara et al., 2022; Trigunasih & Saifulloh (a), 2022), monitor changes in vegetation index and urban air quality (Sunarta & Saifulloh, 2022), as well as spatial analysis of relationships between flooding and soil infiltration in urban areas (Trigunasih & Saifulloh (b), 2022). We use GIS to analyze and map the spatial distribution of agricultural subaks, and soil properties, which are used as the basis for future *subak* land conservation.

Evaluation of fertility status to assess and monitor soil fertility is essential to identify deficiencies or obstacles in terms of nutrients possessed by the land. One way that is often used to assess the soil's fertility is through soil analysis or soil testing. Soil analysis or testing is a relatively more objective approach to determining soil fertility status. Assessment of soil fertility status is essential because if no fertilization action is under the soil's needs over time and land use, then soil fertility will decrease. This research was conducted to know the spatial distribution of *Subak* land, analyze soil fertility status, and provide recommendations for land conservation based on soil fertility properties.

2. STUDY AREA

The case study of this research is administratively located in Sawan District, Buleleng Regency, Bali, Indonesia. Geographically, Sawan Regency is located at $8^{\circ} 5' 14'' - 8^{\circ} 14' 45''$ South Latitude and $115^{\circ} 6' 55'' - 115^{\circ} 11' 1''$ East Longitude (Fig. 1). This is because it has varied topography and slopes. *Subak* agriculture stretches widely from the upstream area with an altitude of > 2000 m asl to the northern coastal area with an altitude of < 5 m asl. The slope of the slope also varies, from flat (0-8%) to very steep ($> 45\%$). Rainfall in the upstream area reaches > 2500 mm/yr, while in coastal areas, it ranges from 1000-1500 mm/yr.

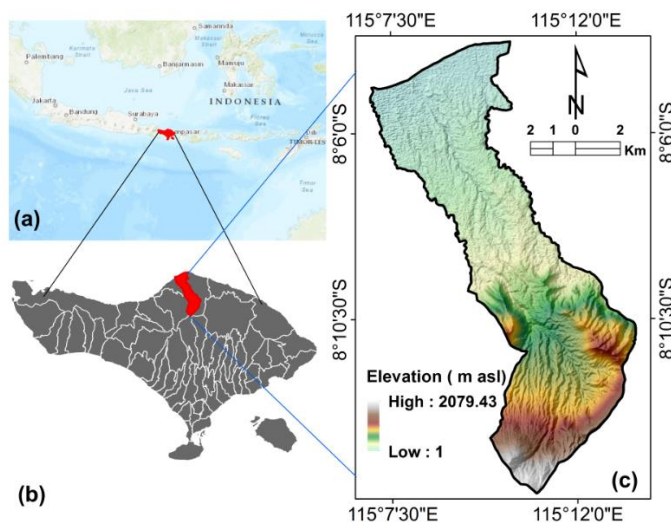


Fig.1. The research location is viewed from a low scale (left, a and b), the research location appears to be on a larger scale (right).

The *subak* area in this study focuses on wetlands ie rice fields. Based on field observations, the period of the rice cropping pattern on the land is 2 times a year, depending on the conditions of the availability of rainwater and irrigation. This condition is assumed to affect the chemical variability and soil fertility of *subak* agricultural land. On steep slopes to steep, it was easily leaching nutrients due to being washed away by rainwater in the upstream to downstream areas.

3. DATA AND METHODS

3.1. Tools and Materials

The materials used to analyze soil samples in the laboratory are chemical substances as reagents for soil analysis. The materials used for analysis in the laboratory include HCl 25%, NH₄OAc pH 7 1N, 80% alcohol, 50% NaOH, concentrated H₂SO₄, liquid paraffin, concentrated H₃PO₄, K₂Cr₂O₇, FeSO₄ 1N, DPA, Whatman 42 filter paper, an indicator of methyl red and aqua dust. The maps are the image of the research area from Google Earth in 2020, a slope map, a land map, subak map. The tools needed in this research are: tools in the laboratory include an oven, pH meter, Erlenmeyer, pipette, burette, Kjeldahl flask, and Kjeldahl distillation device. The tools needed in the field include a Belgian drill, dagger, meter, plastic bag, label paper, Garmin Montana 6.80 Hand GPS and stationery.

3.2. Methods and stages of research

This research was conducted using survey methods and soil test methods which were analyzed at the Laboratory of Soil and Environmental Sciences, Faculty of Agriculture, Udayana University. The chemical properties of the soil determined were Cation Exchange Capacity (CEC) and Base Saturation (NH₄OAc Extraction pH 7 1N), total P₂O₅ and total K₂O content (25% HCl), C-Organic content (Walkley and Black, 1934), pH (H₂O 1: 2.5), then the levels are determined based on the criteria for soil chemical properties (PPT, 1995). Determination of soil fertility status using technical instructions for evaluation of soil fertility-Indonesia (PPT, 1995). The criteria for assessing soil chemical properties are presented in **Table 1**.

Table 1.

Criteria of several chemical properties of the soil.

Criteria	Very Low	Low	Moderate	High	Very High
C Organic (%)	< 1.00	1.01-2.00	2.01-3.00	3.01-5.0	>5.00
P ₂ O ₅ Bray I (ppm)	< 10	10-15	16-25	26-35	>35
P ₂ O ₅ (ppm), Olsen, 1954	< 10	10-25	26-45	46-60	>60
K ₂ O (me/100 g)	< 0.1	0.1-0.2	0.3-0.5	0.6-1.0	>10
Base Saturation (%)	< 20	20-35	36-50	51-70	>70
CEC (me/100 g)	< 5	5-16	17-24	25-40	>40
pH	4.5-5.5 Sour	5.6-6.5 Bit Sour	6.6-7.5 Netral	7.6-8.5 Bit Base	>8.5 Alkaline/base

The stages of the research started with delineating the mapping unit, field survey, and soil analysis in the laboratory. Delineation of mapping units based on land map overlays, slope maps, and subak maps. Determination of subak boundaries is done by participatory mapping, involving farmer groups who own the land. Farmers have a main role in this activity, while researchers are GIS operators who direct the mapping of the boundaries of the subak area. From the results of overlaying several maps, a map of the mapping unit can be obtained, which is used as an observation unit in soil sampling. Making a unit mapping using a QGIS 3.22 LTR applications. The spatial distribution of mapping units is presented in the next sub-chapter. Field surveys are carried out by checking the correctness of the boundaries of the mapping unit, then adjusting to the conditions in the field. Furthermore, soil

samples were taken with a depth of 0-30 cm in the mapping unit following the irrigation canal from upstream, middle, and downstream with a purposive sampling method and then composited. A Belgian drill and GPS assisted this soil sampling for geo-tagging the location.

Soil analysis in the laboratory was carried out after taking soil samples in the field. The chemical properties of the soil analyzed included pH, CEC, Base Saturation, K-total, P-total, and C-organic. The results of soil analysis are used to assess soil fertility status. After obtaining soil chemical properties data, tabulated using the QGIS 3.22 LTR application by entering soil chemical properties data into a table to make it easier to view soil chemical properties data and determine soil fertility status. Evaluation of fertility status is determined based on the chemical properties of the soil, which is matched with the criteria for soil fertility status (PPT, 1995). Determination of land conservation based on soil fertility status and limiting factors on low and medium soil fertility. After obtaining the results of laboratory analysis, a determination is made by classifying the status of soil fertility according to the criteria for assessing chemical properties (Sardiana et al., 2017; Siregar et al., 2021).

4. RESULTS AND DISCUSSIONS

4.1. Mapping of Subak Land

Subak is a community organization that regulates the irrigation system used in rice cultivation in Bali, Indonesia. *Subak* generally has a temple called *Pura Uluncarik* or *Pura Bedugul*, specially built by landowners and farmers. According to Balinese beliefs, the temple is dedicated to *Dewi Sri*, the goddess of prosperity and fertility. This irrigation system is managed by a traditional leader (*Pekaseh*), a farmer in Bali. The *subak* system has become one of the characteristics of Balinese society. This irrigation system develops under the influence of solid Hindu religious values . It forms a pearl of local wisdom, which allows farming communities in Bali to be in harmony with nature to obtain optimal yields (Windia & Wiguna, 2013). Based on the participatory mapping, the area of *Subak* land in Sawan District is 2,177.33 ha, which is divided into 65 *Subaks*. *Subak* with an area of 75-100 ha, there are 4 *Subaks*, including the Landahan Kerobokan, Guliang and Babakan Jagarag. *Subak* above 100 ha there is only one *Subak*, namely Kloncing with an area of 102.24 ha. The graph of the difference in the area of *Subak* from the mapping is presented in **Fig. 2**.

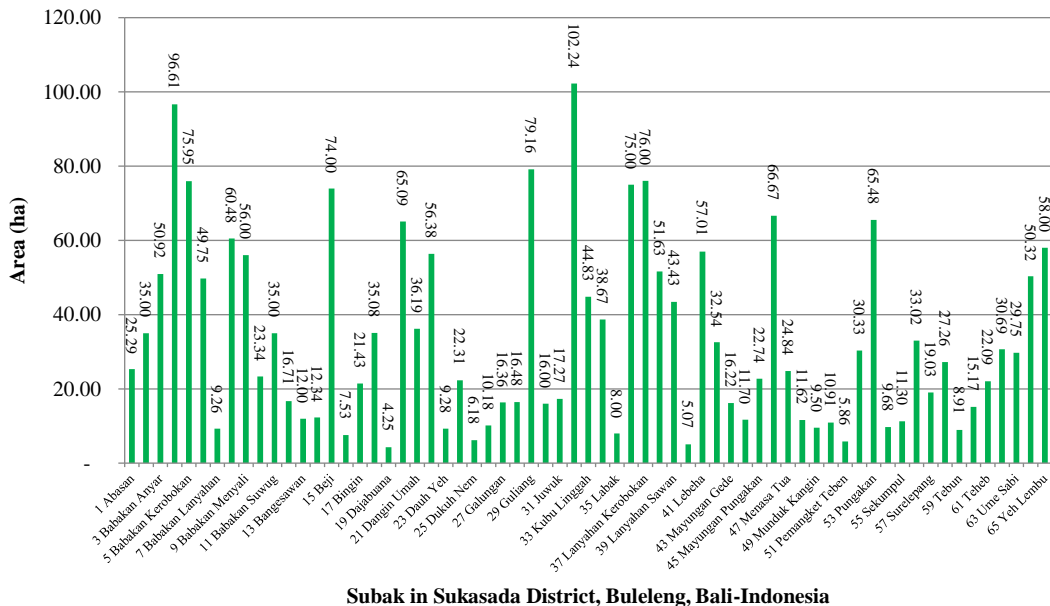


Fig. 2. The graph of the difference in the area from the mapping of Subak.

The boundaries of the *subak* area are determined based on irrigation canals and natural boundaries, namely rivers. *Subak* does not follow administrative boundaries because the subak area existed before the government set administrative boundaries, such as villages or sub-districts (Aryastana et al., 2020; Norken et al., 2016; Trigunasih & Saifulloh (c), 2022). Based on **Fig. 3**, the Tukad Sungsit (river) is a barrier between the Subak Beji area and Subak Dangin Yeh, which is spatially located on the north coast of Bali Province.



Fig. 3. Spatial distribution of Subak area as seen from the Bing World Imagery Satellite.

This research focuses on *Subak* rice fields (wetlands). Spatially, 65 Subaks in Sawan District are presented in **Fig. 4**. The northern coastal area contains Subak Labak, Beji, Dangin yeh Guliang, and Yangai with flat slopes (0-8%). The southern part has steep slopes (25-45% spatially), Subak Bingin, Bangesawan, and Galungan. The previous mapping of the *Subak* boundary was carried out by (Lanya & Manalu, 2021; Lanya et al., 2017; Lanya & Subadiyasa, 2016).

Protection of *Subak* land is essential to control land conversion into built-up land. The conversion of *Subak* land is not only detrimental to farmers. It is also detrimental to the tourism sector because *Subak* in Bali is not only for agricultural activities but also for a destination for tourist attraction (Budiasa et al., 2015; Norken et al., 2016; Sunarta et al., 2019; Sunarta et al., 2021), so Subak land resources need to be preserved. One of the sustainable *Subaks* in Bali namely Subak Jatiluwh.

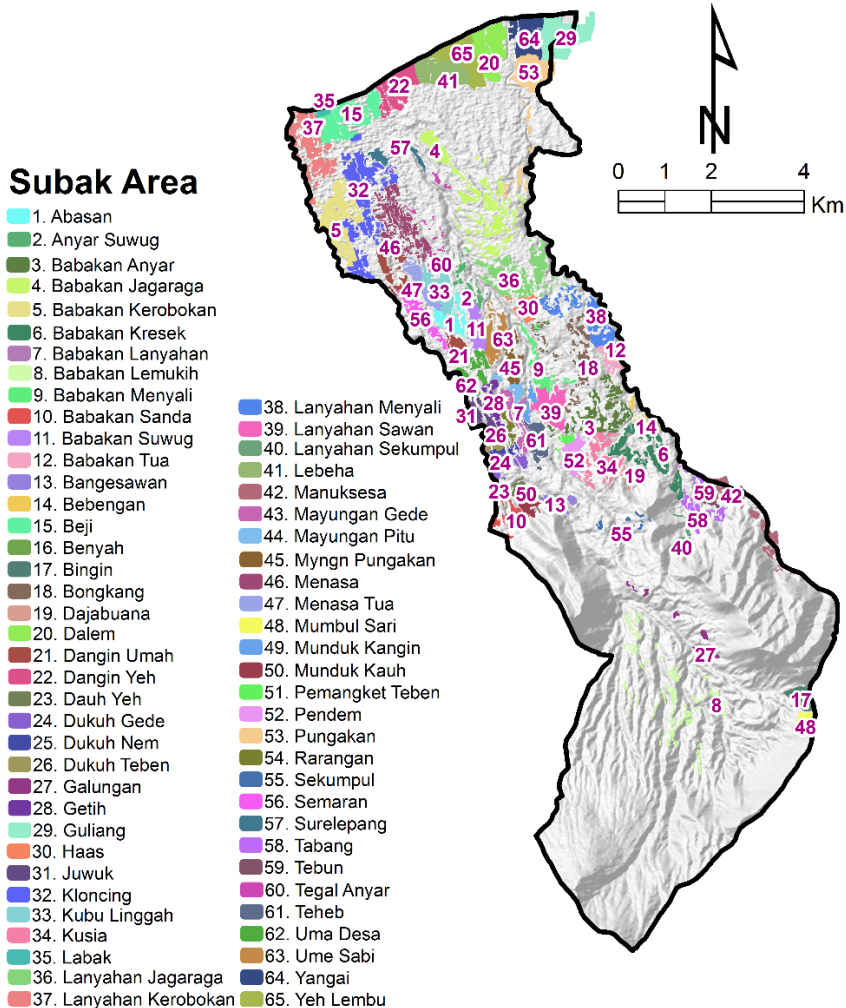


Fig. 4. Spatial distribution of the Subak land.

Subak Jatiluwih, located in Penebel District, Tabanan Regency ($8^{\circ}22'6.68''\text{S}$, $115^{\circ}8'12.64''\text{E}$), has become one of the role models in the management of Subak rice fields in Bali (**Fig. 5**). Apart from being an agricultural activity, the Subak land is a mainstay tourist destination in Bali, which domestic and foreign tourists know. The *Subak* area is located on a steep slope, but water availability for each rice field is still met. This condition is due to managing irrigation water with one inlet and one outlet system, which the *Subak* organization has managed. Even though it is on a steep slope, Subak Jatiluwih is safe from erosion and landslides. This condition is due to the terracing system on sloping land. Terraces can minimize runoff due to high rainfall, retain coarse material from upstream areas and minimize sedimentation.

The traditional *Subak* land conservation efforts can be duplicated in other areas by considering each region's local wisdom. This research reviews conservation actions through agricultural land management based on soil fertility conditions. Effective management is right on target and in the right location to be effective and efficient. With the findings in this study, practitioners in agriculture carry out land management (especially in terms of chemistry) with different chemical compositions of fertilizers. Based on the soil fertility conditions that have been analyzed in each land unit.



Fig. 5. Map of Subak Jatiluwih rice fields (left) sourced from the Tabanan Regency Agriculture Service, Natural panorama of Subak Jatiluwih terraces (right), sourced from <https://www.klook.com>.

4.2. Land Unit Mapping

Land units (LU) are delineated based on the slope and soil type. The soil types in the research location include brown regosol, gray brown regosol, and yellowish-brown latosol (**Fig. 6a**). The slopes at the study site ranged from 0-8%, 8-15%, 15-25%, and 25-45% (**Fig. 6b**). As well as the green map, which shows the spatial distribution of *Subak* land in Sawan District (**Fig. 6c**). Based on the overlay, the land unit (**Fig. 6d**) can be obtained, which is used as a working map in soil sampling and a basis for determining Subak land management through soil fertility analysis. The land unit is the basis for the researchers' consideration in analyzing soil fertility data because the soil sample represents the condition of the soil properties in the field. The soil formation is influenced by parent material, slope, climate, and others (Jáuregui et al., 2018; Minasny et al., 2008; Phillips, 2017). The basis for taking soil samples using Land units has also been carried out by previous researchers (Sardiana et al., 2017; Beisel et al., 2018).

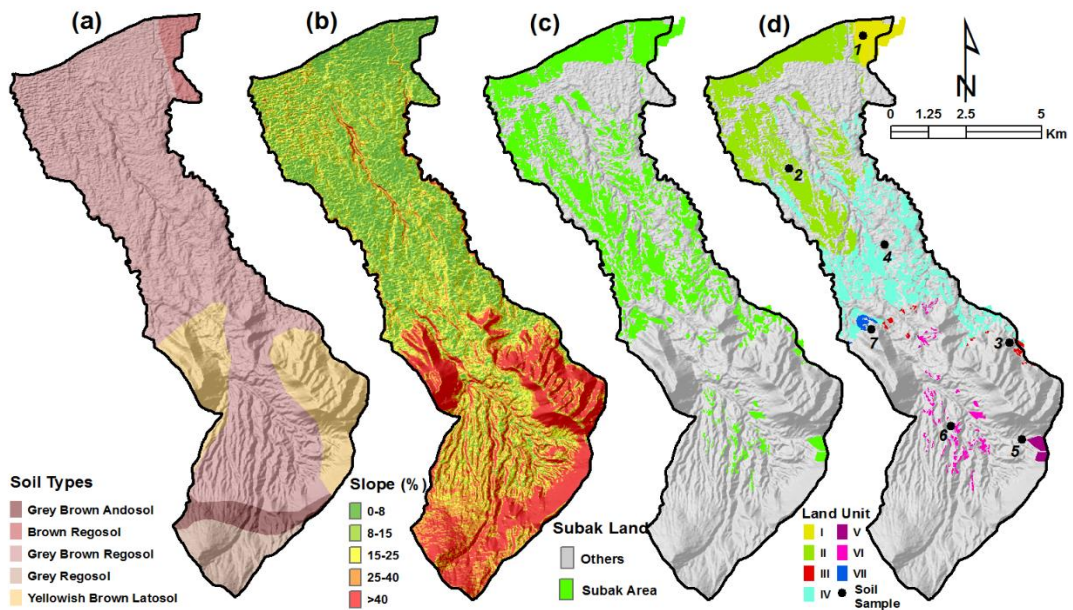


Fig 6. Thematic map of soil types (a), slope (b), Subak area (c), land units and soil sampling location on field (d).

4.3. Mapping of Soil Fertility

The chemical properties of the soil in this study consisted of CEC, base saturation, organic matter, total P, total K, and pH as supporting data on soil fertility status (**Table 2**).

Table 2.
The results of the analysis of soil chemical properties through the Laboratory and Adjustment to Soil Fertility.

LU	CEC (me/100 g)	Base Saturation (%)	C-Organic (%)	P ₂ O ₅ (mg/100g)	K ₂ O (mg/100 g)	pH H ₂ O	Soil Fertility
I	22.62 (M)	99.04 (VH)	4.03 (H)	50.79 (H)	143.31 (VH)	6.64 (N)	Moderate
II	27.42 (H)	95.99 (VH)	3.68 (H)	37.01 (M)	202.93 (VH)	6.50 (N)	High
III	26.47 (H)	93.33 (VH)	3.70 (H)	50.99 (H)	142.28 (VH)	6.66 (N)	High
IV	26.38 (H)	96.55 (VH)	3.81 (H)	91.11 (VH)	47.98 (H)	6.55 (N)	High
V	19.32 (M)	93.33 (VH)	3.60 (H)	49.32 (H)	107.38 (VH)	6.30 (BS)	Moderate
VI	27.49 (H)	91.05 (VH)	3.75 (H)	36.91 (M)	118.47 (VH)	6.60 (N)	High
VII	28.77 (H)	93.75 (VH)	6.79 (VH)	21.83 (M)	13.48 (L)	6.58 (N)	Moderate

Data Source: Laboratory Analysis, 2021:(L)Low, (M)Medium, (H)High, (VH)Very High, (N)Neutral, (BS)Base.

CEC is one of the chemical properties of the soil that is closely related to the availability of nutrients for plants and is an indicator of soil fertility. The higher the CEC of the soil, the greater the ability of the soil to absorb and exchange nutrients. Based on the soil analysis results, the soil's CEC value at the research site, according to the assessment criteria used, is classified as high to moderate (**Fig. 7a**). The higher the pH value of the soil, the higher the CEC value of the soil. On the other hand, hydrolysis does not occur at low pH values, so the soil's CEC value is low (Nadeau & Sullivan, 2015).

Based on the analysis results of the base saturation value in each land units at the research location, the observed criteria are classified as very high (**Fig. 7b**). Base saturation is related to releasing these cations into the soil solution. The higher the cation saturation, the easier it is to release the cation into the soil solution. In other words, the more readily available the cation is to plants (Utomo et al., 2016). The high value of base saturation at the research site reflects that there are still many basic cations in the soil.

Based on the results of the C-Organic analysis of the soil in each land unit in the research location, it was classified as high to very high criteria (**Fig. 7c**). Giving organic matter into the soil not only adds nutrients to plants but also creates conditions suitable for plant growth and can improve water holding capacity, facilitate root penetration, improve aeration, increase soil pH, CEC, and nutrient uptake (Meimaroglou & Mouzakis, 2019; Wei et al., 2020). One of the primary sources of soil organic matter is plant debris that is returned to the soil. Adding organic matter into the soil will liberate the elements it contains, such as N, P, K, Ca, Mg, and so on, and increase its availability for plants (Antonkiewicz et al., 2019). Soil organic matter plays a vital role in exchanging cations and, at the same time, providing nutrients for plants. Soils with high organic matter have a higher CEC than soils with low organic matter (Wei et al., 2020). Organic matter can increase the adsorption capacity and cation exchange capacity. This can happen because the weathering of organic matter will produce humus (organic colloid), a source of negative soil charge, so it has a surface that can hold nutrients and water.

Based on the P-Total value of the soil in each land unit, it is classified as medium, high to very high criteria (**Fig. 7d**). The availability of P in the soil is closely related to soil acidity (soil pH). According to (Basha, 2020; Sirsat et al., 2017), most soils with a maximum total P-value can be found at a neutral pH range between 6.0 – 7.0, so the availability of P will decrease if the pH is below 6.0 or above 7.0. According to (Montaño et al., 2021; Papangelou & Mathijs, 2021), the form of equilibrium is in the form of fixation or dissolution with other nutrients. P in soil is found in various compounds, most of which are unavailable to plants. Most of the fertilizer applied to the soil cannot

be utilized by plants because it has reacted with cations, so the efficiency of P fertilization is generally low to very low.

Based on the results of the K-Total analysis of the soil in each land unit in the research location, it was included in the criteria of very high, high to low (Fig. 7e). The high value of soil CEC can affect the soil solution to be able to release potassium and can reduce the potential for leaching of potassium in the soil (Nakhli et al., 2017). The K-Total value of the soil at the research site, which is included in the very high, high, and low criteria, is because the CEC value at the research location is classified as high to moderate. A high soil CEC value can increase the soil's ability to hold K nutrients so that the soil solution is slow to release K nutrients and reduce leaching potential. The straw, the rest of the harvest, is also the primary source of K and Si (Silicate). About 80% of plants' nutrient K is contained in the straw. Therefore, returning crop residues to the soil can slow down the impoverishment of K and Si nutrients. Returning crop residues to paddy fields has the potential as K fertilizer, either in fresh form, composted, or burned. According to (Si et al., 2018), in addition to replacing K fertilizer at a specific dose, straw also plays an essential role in improving the productivity of paddy fields, increasing fertilization efficiency, and ensuring production stability.

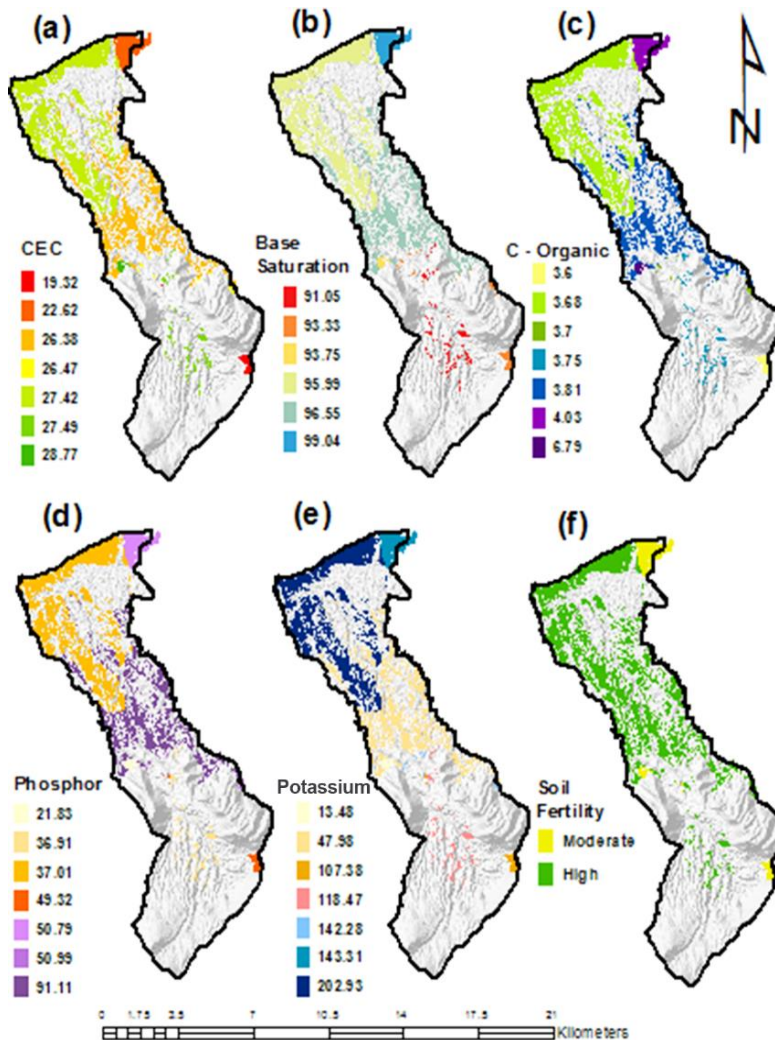


Fig 7. Spatial distribution of the CEC map (a), Base Saturation (b), Soil Organic Mater (c), Phosphor (d), Potassium (e) and Soil fertility status (f).

The limiting factors for soil fertility status (**Fig. 7f**) found at the research sites were CEC which was classified as moderate, P-Total, which was classified as moderate, and K-Total, which was classified as low. Therefore, it is necessary to carry out integrated soil management, such as regularly returning crop residues to the soil and adding organic matter and fertilizers containing P and K elements in the form of single fertilizers and compound fertilizers. Adding P and K compound fertilizers is needed to support optimal land productivity and increase the soil's CEC value. According (Chenu et al., 2019; Scotti et al., 2015). Types of organic matter can be applied to the soil by returning crop residues, providing manure, and compost. In addition to maintaining the content of organic matter in the soil, adding organic matter can also increase P nutrients in the soil.

5. CONCLUSIONS

The area of Subak land in Sawan District is 2,177.33 ha, divided into 65 Subaks. This research is one of the efforts to manage Subak land to survive sustainably. The conservation through soil fertility management on Subak land. The limiting factors for fertility status found at the research sites were CEC which was classified as moderate, P-Total, which was classified as moderate, and K-Total, which was classified as low. Therefore, it is necessary to carry out integrated soil conservation, such as regularly returning crop residues to the soil and adding organic matter and fertilizers containing P and K elements in the form of single fertilizers and compound fertilizers. Adding P and K compound fertilizers is needed to support optimal land productivity and increase the soil's CEC value. Types of organic matter can be applied to the soil by returning crop residues, providing manure, and compost. In addition to maintaining the content of organic matter in the soil, adding organic matter can also increase P nutrients in the soil.

REFERENCES

- Antonkiewicz, J., Kuc, A., Witkiewicz, R., & Tabak, M. (2019). Effect of Municipal Sewage Sludge on Soil Chemical Properties and Chemical Composition of Spring Wheat. *Ecological Chemistry and Engineering S*, 26 (3), 583-595.
- Arenas-Montañó, V., Fenton, O., Moore, B., & Healy, M. G. (2021). Evaluation of the fertiliser replacement value of phosphorus-saturated filter media. In *Journal of Cleaner Production*, 291(125943), 1-18.
- Aryastana, P., Yujana, C. A., & Ardantha, I. M. (2020). Irrigation Water Management by Using Remote Sensing and GIS Technology to Maintain the Sustainability of Tourism Potential in Bali. *Journal of Infrastructure & Facility Asset Management*, 2(1), 63-72.
- Basha, S. J. (2020). Management of phosphorus and potassium in bidi tobacco (*Nicotiana tabacum* L.) under rainfed conditions. *Annals Of Plant And Soil Research*. 22(4), 420-424.
- Bayu, T. (2020). Review on contribution of integrated soil fertility management for climate change mitigation and agricultural sustainability. *Cogent Environmental Science*, 6(1), 1823631, 1-21.
- Beisel, N. S., Callahan, J. B., Sng, N. J., Taylor, D. J., Paul, A. L., & Ferl, R. J. (2018). Utilization of single-image normalized difference vegetation index (SI-NDVI) for early plant stress detection. *Applications in Plant Sciences*, 6(10), 1-10.
- Budiasa, I. W., Setiawan, B. I., Kato, H., Sekino, N., & Kubota, J. (2015). The role of the Subak system and tourism on land use changes within the Saba watershed, Northern Bali, Indonesia. *Journal of the International Society for Southeast Asian Agricultural Sciences*, 21(2), 31-47.
- Chenu, C., Angers, D. A., Barré, P., Derrien, D., Arrouays, D., & Balesdent, J. (2019). Increasing organic stocks in agricultural soils: Knowledge gaps and potential innovations. *Soil and Tillage Research*, 188. <https://doi.org/10.1016/j.still.2018.04.011>
- de Lourdes Figueroa Jáuregui, M., Menez, M. R. M., Solorio, C. A. O., & Reynoso, D. F. (2018). Influence of factors of soil formation in the properties of soils in Mixteca, Oaxaca, México. *Terra Latinoamericana*, 36(3), 287-299.

- Diara, I. W., Suyarto, R., & Saifulloh, M. (2022). Spatial Distribution Of Landslide Susceptibility In New Road Construction Mengwitani-Singaraja, Bali-Indonesia: Based On Geospatial Data. *Geomate Journal*, 23(96), 95-103.
- Norken IN, Suputra IK, & Arsana IGNK. (2016). Challenges to the Conservation of Subak System as World Cultural Heritage in Bali. *Journal of Agricultural Science and Technology B*, 6(4), 1-9.
- Kome, G. K., Enang, R. K., Tabi, F. O., & Yerima, B. P. K. (2019). Influence of Clay Minerals on Some Soil Fertility Attributes: A Review. *Open Journal of Soil Science*, 09(09), 155-188.
- Lanya, I., & Manalu, T. J. (2021). Remote sensing and GIS application for mapping data base of sustainable agriculture land in Denpasar City. *IOP Conference Series: Earth and Environmental Science*, 648(1), 1-11.
- Lanya, Indayati, & Netera Subadiyasa, N. (2016). Role of Remote Sensing and Geographyc Information System Mapping for Protected Areas Land Rice Field Subak, Buffer Zones, and Area Conversion (Case Studies in Gianyar Regency, Bali Province). *IOP Conference Series: Earth and Environmental Science*, 47(1). 1-11.
- Lanya, Indayati, Subadiyasa, N. N., & Hutauruk, J. (2017). Subak Land Information System Based On Remote Sensing And Geographic Information System In Denpasar City. *Geoplanning: Journal of Geomatics and Planning*, 4(2). 1-12.
- Liu, C., Qin, Y. S., & Zhao, X. L. (2020). Long-term effect of fertilization on accumulation and availability of heavy metal in a calcareous paddy soil. *Journal of Agro-Environment Science*, 39(7), 1494-1502.
- Meimaroglou, N., & Mouzakis, C. (2019). Cation Exchange Capacity (CEC), texture, consistency and organic matter in soil assessment for earth construction: The case of earth mortars. *Construction and Building Materials*, 221, 27-39.
- Minasny, B., McBratney, A. B., & Salvador-Blanes, S. (2008). Quantitative models for pedogenesis - A review. *In Geoderma*, 144, 140-157.
- Nadeau, M. B., & Sullivan, T. P. (2015). Relationships between Plant Biodiversity and Soil Fertility in a Mature Tropical Forest, Costa Rica. *International Journal of Forestry Research*, 2015, 1-13.
- Nakhli, S. A. A., Delkash, M., Bakhshayesh, B. E., & Kazemian, H. (2017). Application of Zeolites for Sustainable Agriculture: a Review on Water and Nutrient Retention. *Water, Air, and Soil Pollution*, 228(12), 1-34.
- Nicoleta, M., Mihail, D., Carmen, S., & Traian, C. (2018). The influence of n and p fertilization on some chemical characteristics of the soil. *International Multidisciplinary Scientific Geo Conference Surveying Geology and Mining Ecology Management, SGEM*, 18(3.2), 575-582.
- Olsen, S. R. (1954). Estimation of available phosphorus in soils by extraction with sodium bicarbonate (No. 939). *US Department of Agriculture*.
- Papangelou, A., & Mathijs, E. (2021). Assessing agro-food system circularity using nutrient flows and budgets. *Journal of Environmental Management*, 288, 1-22.
- Phillips, J. D. 2017. Soil Complexity and Pedogenesis. *In Soil Science*. 182 (4), 117-127.
- Prabakaran, G., Vaithiyathan, D., & Ganesan, M. (2021). Soil fertility review using fuzzy logic. *In Journal of Engineering Research (Kuwait)*, 9, 192-202.
- PPT (1995). Guidelines for analysing soil chemical properties in Indonesia. *Soil Research Center Department, Bogor-Indonesia*. <http://balittanah.litbang.pertanian.go.id/ind/>
- Sardiana, I. K., Susila, D., Supadma, A. A., & Saifulloh, M. (2017). Soil Fertility Evaluation and Land Management of Dryland Farming at Tegallalang Sub-District, Gianyar Regency, Bali, Indonesia. *IOP Conference Series: Earth and Environmental Science*, 98(1), 1-11.
- Scotti, R., Bonanomi, G., Scelza, R., Zoina, A., & Rao, M. A. (2015). Organic amendments as sustainable tool to recovery fertility in intensive agricultural systems. *In Journal of Soil Science and Plant Nutrition*. 15(2). 333-352.
- Si, L., Xie, Y., Ma, Q., & Wu, L. (2018). The short-term effects of rice straw biochar, nitrogen and phosphorus fertilizer on rice yield and soil properties in a cold waterlogged paddy field. *Sustainability (Switzerland)*, 10(2), 1-17.
- Siregar, E. G., Adi, I. G. P. R., & Supadma, A. N. (2021). Mapping the Fertility Status of Rice Fields Based on Geographic Information Systems in Subak Buaji and Subak Padanggalak, East Denpasar District. *Jurnal Agroteknologi Tropika*, 10(1). 1-10.
- Sirsat, M. S., Cernadas, E., Fernández-Delgado, M., & Khan, R. (2017). Classification of agricultural soil parameters in India. *Computers and Electronics in Agriculture*, 135, 269-279.
- Suasih, N. N. R., Darma, I. K., & Sara, I. M. (2018). The Role of Subak (Traditional Farmers Institution In Bali) To Farmers Welfare After The Cultural Landscape of Subak Inscribed As A World Heritage. *Russian Journal of Agricultural and Socio-Economic Sciences*, 75(3), 36-47.
- Subedi, T. 2018. Analysis of plant nutrient elements of soil in Pokhara. *Himalayan Biodiversity*, 6, 58-62.

- Sumiyati , Windia, I. W., & Tika, I. W. (2017). Operation and maintenance of subak irrigation network in Tabanan Regency. *Jurnal Kajian Bali (Journal of Bali Studies)*, 7(1).
- Sunarta, I. N., Adikampana, I. M., & Nugroho, S. 2019. The Existence of Subak inside the Northern Kuta Tourism Area, Bali. *IOP Conference Series: Earth and Environmental Science*, 313(1), 1-8.
- Sunarta, I. Nyoman, Nugroho, S., & Adikampana, I. M. (2021). Spatial Transformation of Subak in Northern Kuta Tourism Area, Bali: From Agricultural to Cultural-Service. *South Asian Journal of Social Studies and Economics*, 9(1), 26-38.
- Sunarta, I. N., & Saifulloh, M. (2022). Coastal Tourism: Impact For Built-Up Area Growth And Correlation To Vegetation And Water Indices Derived From Sentinel-2 Remote Sensing Imagery. *GeoJournal of Tourism and Geosites*, 41(2), 509-516.
- Trigunasih, N.M., & Saifulloh. M. (a). (2022). Spatial Distribution of Landslide Potential and Soil Fertility: A Case Study in Baturiti District, Tabanan, Bali, Indonesia. *Journal of Hunan University Natural Sciences*, 49(2).
- Trigunasih, N. M., & Saifulloh, M. (b). (2022). The Investigating Water Infiltration Conditions Caused by Annual Urban Flooding Using Integrated Remote Sensing and Geographic Information Systems. *Journal of Environmental Management and Tourism*, 13(5), 1467-1480.
- Trigunasih, N. M., & Saifulloh, M. (c). (2022). Correlation between soil nitrogen content and NDVI derived from sentinel-2A satellite imagery. *Jurnal Lahan Suboptimal: Journal of Suboptimal Lands*, 11(2), 112-119.
- Walkley, A., & Black, I. A. (1934). An examination of the Degtjareff method for determining soil organic matter, and a proposed modification of the chromic acid titration method. *Soil science*, 37(1), 29-38.
- Wei, H., Liu, Y., Xiang, H., Zhang, J., Li, S., & Yang, J. (2020). Soil ph responses to simulated acid rain leaching in three agricultural soils. *Sustainability (Switzerland)*, 12(1), -12.
- Windia, I. W., & Wiguna, W. A. A. (2013). *Subak world cultural heritage*. Udayana University Press.
- Windia, W., Suamba, I. K., Sumiyati, S., & Tika, W. (2018). Subak System for Environmental Development Based on Tri Hita Karana. *SOCA: Jurnal Sosial Ekonomi Pertanian*. 118-132.

CATEGORIZING THE CAUSES OF OCCURRENCE OF CHATEAU BROWNFIELDS: A CASE STUDY ON THE CZECH REPUBLIC

*Kamila TURECKOVA*¹ 

DOI: 10.21163/GT_2022.172.18

ABSTRACT:

In the European space, chateau buildings and sites represent an important historical, urban and social element of the cultural landscape, which refers to the continuity of the present and the past in the space of urban and rural settlements. However, it is a sad fact that many of these buildings are now abandoned and dilapidated. The aim of this paper is to identify, against the background of a synthesis of both theoretical and actual knowledge, a group of reasons why this is the case, using the example of the Czech Republic. Due to the political and property changes implemented in the first half of the 20th century, two original groups of market and non-market causes and four categories of causal factors have been determined (inappropriate purpose; ownership problem; operational (investment) inefficiency and extraordinary events), which have their parallel in the analysis of the causes of occurrence specific chateau brownfields in the Moravian-Silesian Region.

Key-words: Brownfield, Chateau, Cause of origin, Czech Republic, Categorization.

1. INTRODUCTION

Chateaux, or aristocratic manors, manorial courts or manorial residences represent an important architectural and historical monument that have been an integral part of the predominantly European rural, and later urban landscape since the early modern period, and refer to their administrative, economic, representative and residential function (Turečková et al., 2022a, Pluskowski et. al., 2019 or Magnussen, 2018). Chateau buildings, like other real estate, are subject to processes of renewal, development, decline or extinction after their creation and may also be for a certain period of time a brownfield, which refers to the status of a building or premises that is without any use, is empty and structurally and technically desolate, dilapidated and decaying.

The intention of this paper is to try to identify the causes of occurrence of chateau brownfields on a pilot basis and to categorize them against the background of an inductive approach resulting from the analysis of the actual causes of abandonment of chateau sites in the Moravian-Silesian Region. Considering the historical milestones of the last century in the Czech Republic, especially the formation of an independent republic after the First World War, the forced administration of the territory by fascist Germany during 1938-1945, the Benes Decrees and the onset of communism after the end of the Second World War, it is necessary to look for potential causes of the subsequent non-use of chateau buildings here as well. The above also applies to the recovery of family property after 1989, especially in the form of restitution. Other countries of the so-called Visegrad Four, or other Eastern Bloc countries, have undergone similar processes of forced (political) interruption (abolition) of property rights to their (chateau) property in the form of seizure, nationalisation or confiscation. From this point of view, the presented classification of the causes of occurrence of chateau brownfields is also applicable to countries other than the Czech Republic, and as a result it is generalized to such an extent that it can be used universally.

¹ School of Business Administration in Karvina, Silesian University in Opava, Univerzitni Nam. 1934/3, 733 40 Karvina, Czech Republic, tureckova@opf.slu.cz

The issue of chateau brownfields has not yet been directly addressed scientifically, and therefore it is impossible to conduct a relevant literature search and critical discussion on the topic. The majority of the text is based on the author's synthesis of information from brownfield theory, history, social geography and urbanism, her own experience and factual findings obtained from the analysis of identified chateau brownfields in the Moravian-Silesian Region.

The basic definition of a chateau brownfield was elaborated in Turečková et al. (2022a) and Turečková et al. (2022b), and a chateau brownfield is defined here as a specific type of brownfield that represents a completely or partially abandoned dilapidated property originally serving as a chateau residence (an originally permanently inhabited feudal residence of the modern period, typical of its representative, residential, economic and/or administrative function) for which no meaningful functional use has been found within the specified period (**Fig. 1**).



Fig. 1. Example of chateau brownfield (Chateau Dolní Lutyně, region Karviná), (*Source: own*).

In the context of the general definitions of brownfield sites (see for example Kunc et al., 2014; Turečková & Duda, 2020; Alker et al., 2000; Ferber et al., 2006; Yount, 2003; Krzystofik et al., 2013; Thomas, 2003; Tang & Nathanail, 2012; Greenberg et al., 2000, De Sousa, 2003 or Martinát et al., 2016), where contamination and regeneration potential are emphasized, we should add that in this case the restoration of chateaux is more time-consuming and economically demanding due to their architectural specifics, whereas the probability of contamination is quite low to none. The status of cultural monument assigned to the building may also be a constraint on regeneration plans. The chateau brownfield can be perceived in both narrower and broader terms, with the narrower term referring only to the main building of the chateau itself, which forms the very core of the entire chateau complex, while the broader definition reflects the chateau's hinterland, i.e. the entire chateau complex including outbuildings, park, utility and ornamental gardens, physical infrastructure, greenhouses, etc. (Turečková et al., 2022b).

2. METHODOLOGY AND DATA

Determination of the causes of occurrence of chateau brownfields and their subsequent categorization is based on the analysis of actual and objectively identifiable reasons for the abandonment of chateau settlements found in a pilot sample of 32 brownfields identified among physically existing 52 chateau buildings in the Moravian-Silesian Region (without region Nový Jičín) what is more than 61%.

Relevant information was traced and verified from several possible publicly available sources as National monument institute, official pages of individual chateaus, websites of municipalities and “freely” on the Internet. A number of relevant data were difficult to find, or the data differed between partial sources. There is also possible future additions of other chateau objects or specify present information. The spatial specification of their location within the Moravian-Silesian Region is shown in **Figure 2** and **Figure 3**.

For the purpose of fulfilling the objective defined in this paper, the specific causes behind the loss of functionality and abandonment of the identified chateau brownfields were traced. The individual reasons have been generalised into four broad categories, so as to reflect the very cause of the brownfields on the one hand, and at the same time to generalise them as far as possible.

Selected regions of the Moravian-Silesian Region	Chateau in total	of which chateau brownfields	
Karviná	11	7	
Ostrava City	7	7	
Frýdek Místek	12	5	
Bruntál	10	7	
Opava	12	6	

Fig. 2. Identified chateau and chateau brownfields in Moravian-Silesian Region

(Source: data own and map: www.czso.cz).

Note: Region Nový Jičín is missing due to missing information at the time of article preparation.

Table 1 lists the names of the chateaux that have had the status of chateau brownfield for some time and which have been the subject of research. The information in the table is supplemented by castle buildings without brownfield status and which were the objects of our research. **Figure 3** shows the geographical distribution of all identified chateaux and chateau brownfields in individual regions of the Moravian-Silesian Region.

Table 1.

Chateau in Moravian-Silesian Region.

Region	Ostrava City	Karviná	Frýdek Místek	Opava	Bruntál
Chateau Brownfields	Rothschild Chateau, Zábřeh, Poruba, Polanka nad Odrou, Stará Ves nad Ondřejnicí, Klimkovice, Hošťálkovice	Petrovice u Karviné, Chotěbuz, Doubrava, Rychvald, Dolní Lutyně, Šumbark, Životice	Paskov, Hukvaldy, Ropice, Hnojník, Střítež	Deštné, Dolní Benešov, Hlučín, Kravaře, Litultovice, Štáblovice	Janovice, Dívčí hrad, Brantice, Bruntál, Linhartovy, Slezské Pavlovice, Slezské Rudoltice
Chateau without statut Brownfield	---	Fryštát, Larisch Chateau Těrlicko, New Chateau Horní Suchá, Dolní Bludovice	Frýdek, Kanská, Trinec, Horní Tošanovice, Dolní Tošanovice, Bílá, Hartisov	Stěbořice, Hradec nad Moravicí, Opava, Raduň, Velké Heraltice, Velké Hoštice	Jindřichov, Hošťálkovy, Krnov

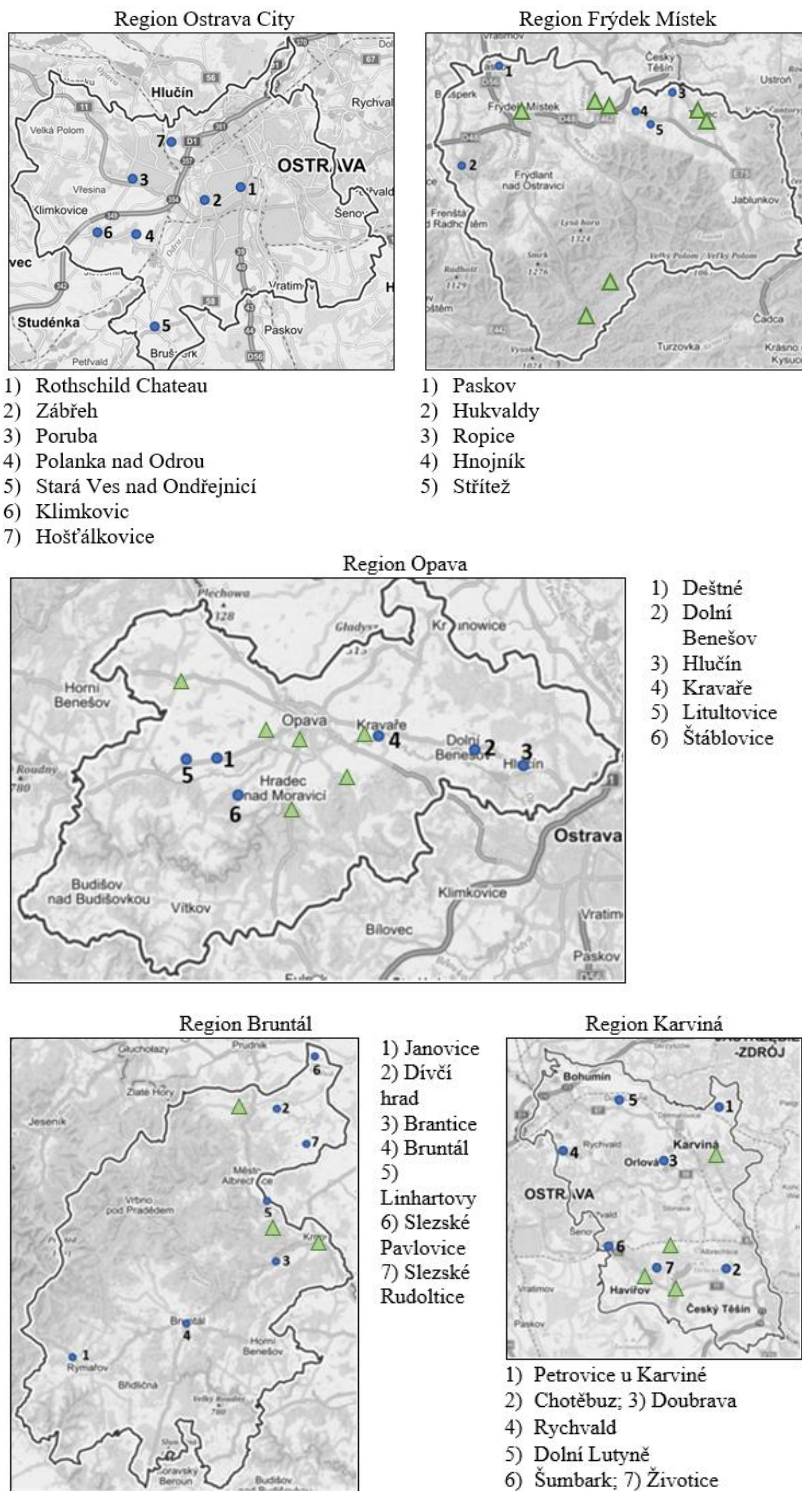


Fig. 3. Identified chateau and chateau brownfields in Moravian-Silesian Region and their localization in regions (Source: own, www.mapy.cz).

Note: ● chateau brownfields and its name; ▲ chateaux without statut brownfield

From their localization and knowledge of the spatial characteristics of places, a logical conclusion can be drawn that chateau brownfields reflect the density of population in the given territory and, with reference to the distribution of all chateau objects, they do not tend to be specifically concentrated, i.e. their distribution within the network of chateaux is completely random (from the point of view of spatial phenomena, the localization of chateau brownfields among all identified chateaux is accidental).

3. CATEGORIZING THE CAUSES OF OCCURRENCE OF CHATEAU BROWNFIELDS

In the context of the historical events of the first half of the 20th century associated with the aforementioned forced changes of ownership rights to chateau residences in the Czech Republic, we can also indirectly refer to the original (hidden) causes of occurrence of chateau brownfields, which have a parallel in these political decisions.

The chateaux were then usually (on the basis of a directive) used for purposes for which they were not suitable at all in terms of the layout and character of the building, their operation was underfinanced, especially due to the increased demands on the operation (e.g. this concerned the heating of the chateau buildings) and therefore they were abandoned after a while and the activities carried out were relocated to completely different buildings (Poruba Chateau, Zábřeh Chateau, Ropice Chateau, etc.). Non-market causes can also include extraordinary events such as the devastation of the building by fire or war conflict (Chateau Chotěbuz, Chateau Klimkovice or Chateau Zámek Stará Ves nad Ondřejnicí), etc. Apart from these non-market causes, which are characteristic of Central and Eastern European countries in varying degrees and manifestations, it is logical to identify market causes that refer to the natural processes of the creation of chateau brownfields associated with changes in the functional use of real estate in general.

By analysing the specific causes of occurrence of 32 chateau brownfields in the Moravian-Silesian Region, four categories were explicitly formulated, which are general enough to both capture the essence of the abandonment of the objects and at the same time encompass all the identified reasons. These are causes having an analogy in (1) inappropriate purpose; (2) ownership problem; (3) operational (investment) inefficiency; and (4) extraordinary events.

The combinations of the original causal factors with the four specific categories of causes of occurrence are elaborated in **Table 2** for better visualization and briefly introduced and described later in the text of the paper.

The extraordinary causes of occurrence of chateau brownfields are related to unusual events of a one-off but fundamental nature originating outside the chateau building itself. These are exogenous phenomena (explosion, war conflict, fire, flood, mining tremors, earthquakes, sabotage, other natural disasters, etc.) that led to the unplanned and sudden abandonment of the chateau site, the potential restoration of which is financially and temporally very demanding.

The abandonment of a chateau for an inappropriate purpose is the most common reason for the creation of a brownfield in the Czech Republic. By this we mean that activities were inappropriately (decided without proper knowledge of the issue) placed in the chateau's buildings that were not suitable for the chateau at all due to its architecture, layout, orientation and accessibility of rooms, size of rooms, basic technical infrastructure (heat, water, electricity, sanitation). The accumulation of problems associated with inappropriately implemented activities (purpose) together with the unwillingness to invest in these buildings gradually led to their devastation and dilapidation, which resulted in their final abandonment. This reason for the creation of chateau brownfields is related to the property-ownership changes of the first half of the 20th century mentioned earlier.

The third identified reason behind the emergence of chateau brownfields is related to ownership problems and property disputes, which include the so-called "post-Soviet" restitution processes. In a number of cases when the chateau belonged to more than one owner, there was no agreement between them on the future fate of the building, and often the buildings change ownership because they are the subject of speculation and financial intrigue. We can also include here the problem of determining the inheritance, finding the rightful heir, or the owners' lack of interest in their property.

Table 2.

Categorizing the causes of occurrence of chateau brownfields.

Original causative factors	Specific categories of causes	Explanation
Non-market character	exceptional	one-off harmful effects of forces and phenomena caused by human activity, natural influences, as well as accidents that significantly limit the use of the chateau object and its existence
	inappropriate purpose	the useful function implemented in the chateau building is not compatible with its urban design and the location of the chateau in the longer term (the useful function of the chateau does not reflect its nature and is determined "from above, by a directive decision from the table")
Market character	problem with ownership	from a legal point of view, the concrete owner is not clear, there is a dispute over ownership or the owner does not show interest in the chateau property
	operational (investment) inefficiency	the functional use of the chateau is not effective in the long term (economic costs exceed the economic benefits), or the return on investment is not attractive for investors and/or the use of the chateau is not profitable

Operational or investment inefficiency is behind the creation of brownfields at the moment when the economic costs exceed the economic benefits and the operation of the chateau itself is not financeable in terms of resources and their return. In other words, from the point of view of cost-benefit analysis, the solution in question, whatever it is in the context of the use of the chateau, is inefficient, uneconomic and not meaningful. Let us add that in such a case it is not only the direct, implicit effects that are assessed, but also the indirect costs and benefits, which are explicit and not always concrete, must be taken into account.

In some cases, it is not easy to determine whether the occurrence of chateau brownfield was caused by the inappropriate use of the building or by operational inefficiency, or it is problematic to establish the mutual causality between these two categories of causes and to determine which preceded the other. It is then necessary to use one's own experience, analogy with a similar chateau brownfield site or additional information retrieval. In a number of cases, in our set of chateau brownfields in the Moravian-Silesian region, it was possible to use the logic that it is obvious that using a chateau building as a healthcare facility is not a happy solution (inappropriate purpose). It was only ex post that the problems of financing the operation and the necessary investments related to the care of the property itself emerged.

The identification and classification of the causes of the formation of chateau brownfields, it can be added that, logically, it will also apply in the context of the causative factors of the formation of brownfields in general, i.e. also for other types of abandoned and unused buildings and areas.

4. CONCLUSION

Chateau settlements have been, are, and will certainly continue to be an important historical, urban and social element of the European territory and our cultural landscape. It is therefore socially desirable to support in every possible way the restoration of such buildings which are empty, dilapidated and without use, not only because they are places associated with a concentration of negative externalities (Turečková and Chmielová, 2018), but also because they represent untapped

and often hidden potential for the development of the area. This is not only manifested on the economic level (positive impact on regional economic growth, employment, the amount of investment, etc.), but especially in the deepening of general prosperity and stability, in the improvement of living conditions and its quality, safety and aesthetics of places, cleanliness, the availability of places for recreational and leisure activities, the diversity of landscape use and environmental protection.

The aim of this paper was to pilot the causes of occurrence of the 32 identified chateau brownfields on the basis of the induction of the identified facts and then to categorize them. Such a categorization of the causes of occurrence of brownfields is completely new and has no parallel in any other scientific work. Due to the historical realities resulting from the forced ownership and property changes in the first half of the last century, it was necessary to objectively search for the subsequent causes of occurrence of chateau brownfields here as well. Therefore, two groups of initial causal factors, specifically market and non-market factors, and four specific category groups relating directly to the identified cause of the abandonment of the chateau site were determined (Figure 3). These sub-causes can be logically linked to the loss of the use of the chateau in question, to problems related to the determination of ownership, to economic reasons related to operational (and/or investment) efficiency and to causes of an exceptional nature.

Given that this is a pilot finding and the categorization of the causes of occurrence of brownfields is based on the knowledge from the Czech Republic only, it is possible that in the future the categorization will have to be modified to take into account the need for generalization within a wider spatial dispersion. In the next step of the scientific research work we will try to determine and quantify the importance of individual causal factors and complement this with appropriate regeneration solutions based on good practice examples. This synthesis of the understanding of the causes and condition that followed the chateau's overcoming of its brownfield status can help to potentially restore existing unused chateau buildings as well as those that may be abandoned in the future. It would also seem highly desirable, as part of further research, to identify the tangible and intangible benefits of regenerated chateau buildings and sites to regional development and society as a whole. Finally, it should be added that the presented categorisation scheme is so universal that it is very likely to be transferable and applicable to other types of brownfield sites than the chateau ones. From this point of view, this paper may also contribute to deepening the theoretical concept of brownfields in general terms, or enrich the scientific discussion with substantive criticism.

ACKNOWLEDGMENT

This paper (research) was supported by the project SGS/25/2022 "Regenerative potential of brownfields in the Czech Republic with a focus on chateaux and mansions".

REFERENCES

- Alker, S., Joy, V., Roberts, P. & Smith, N. (2000) The definition of brownfield. *Journal of Environmental Planning and Management*, 43 (1), 49-69. ISSN: 0964-0568. DOI 10.1080/09640560010766
- De Sousa, C. A. (2003) Turning brownfields into green space in the City of Toronto. *Landscape Urban Planning*, 62 (4), 181-198.
- Ferber et al. (2006) Sustainable brownfield regeneration: CABERNET network report. Nottingham: University of Nottingham.
- Greenberg, M., Lowrie, K., Solitare, L. & Duncan, L. (2000) Brownfields, toads, and the struggle for neighbourhood redevelopment: a case study of the State of New Jersey. *Urban Affairs Review*, 35 (5), 717-733.
- Krzystofik, R., Kantor-Pietraga, I. & Spórna, T. (2013) A Dynamic Approach to the Typology of Functional Derelict Areas (Sosnowiec, Poland). *Moravian Geographical Reports*, 21 (2), 20-35.

- Kunc, J., Navrátil, J., Tonev, P., Frantál, B., Klusáček, P., Martinát, S., Havlíček, M. & Černík, J. (2014) Perception of urban renewal: Reflexions a coherences of socio-spatial patterns (Brno, Czech Republic). *Geographia Technica*, 9 (1), 66-77.
- Magnussen, S. 2018: Form Follows ‚Fürst‘? A Study on the Uses of Analogies in Castle Research by Reference to Valdemar I and Erik VI of Denmark. In MAGNUSSEN, S. and KOSSACK, D. ed. *Castles as European Phenomena. Towards an international approach to medieval castles in Europe. Contributions to an international and interdisciplinary workshop in Kiel. Frankfurt am Main (Peter Lang)*, 177–195.
- Martinát, S., Dvořák, P., Frantál, B., Klusáček, P., Kunc, J., Navrátil, J., Turečková, K. & Reed, M., (2016) Sustainable urban development in a city affected by heavy industry and mining? Case study of brownfields in Karvina, Czech Republic. *Journal of Cleaner Production*, 118 (1), 78–87.
- Pluskowski, A., Banerjea, R. & García-Contreras, G. (2019) Forgotten Castle Landscapes: Connecting Monuments and Landscapes through Heritage and Research. *Landscapes*, 20(2), 89-97. DOI: <http://dx.doi.org/10.1080/14662035.2020.1857909>.
- Tang, Y. T. & Nathanail, C. P. (2012) Sticks and Stones: The Impact of the Definitions of Brownfield in Policies on Socio-Economic Sustainability. *Sustainability*, 4 (5), 1-23. DOI: <https://doi.org/10.3390/su4050840>
- Thomas, R. M. (2003) Brownfield Redevelopment: Information Issues and the Affected Public. *Environmental Practice*, 5(1), 62-68. DOI: <https://doi.org/10.1017/S1466046603030175>.
- Turečková, K. & Chmielová, P. (2018) Brownfieldy v regionálním rozvoji a v externalitní teorii. In: XXI. mezinárodní kolokvium o regionálních vědách. Brno: MU ESF Brno, 302-308. ISBN 978-80-210-8969-3
- Turečková, K. & Duda, D. (2020) Existence brownfieldů jako příčina nižšího výnosu daně z nemovitých věcí v obecních rozpočtech: případová studie na Českou republiku. In: *Mezinárodní vztahy 2020: Aktuální otázky světové ekonomiky a politiky*. Bratislava (EUBA), 706-720.
- Turečková, K., Nenička, L. & Glacová, K. (2022b) Chateau brownfields: Causes of their formation in the context of the historical specificities of the Czech Republic. In: *Mezinárodní vztahy 2022: Aktuální otázky světové ekonomiky a politiky*. (in print)
- Turečková, K., Nenička, L. & Příkrylová, K. (2022a) Teoretický koncept zámeckých a panských brownfieldů v České republice. In: XXV. mezinárodní kolokvium o regionálních vědách. Brno (MU ESF Brno), 173-178. DOI: <http://dx.doi.org/10.5817/CZ.MUNI.P280-0068-2022>.
- Yount, K. R. (2003) What are brownfields? Finding a conceptual definition. *Environmental Practice*, 5 (1), 25-33. DOI: <https://doi.org/10.1017/S1466046603030114>.

Aims and Scope

Geographia Technica is a journal devoted to the publication of all papers on all aspects of the use of technical and quantitative methods in geographical research. It aims at presenting its readers with the latest developments in G.I.S technology, mathematical methods applicable to any field of geography, territorial micro-scalar and laboratory experiments, and the latest developments induced by the measurement techniques to the geographical research.

Geographia Technica is dedicated to all those who understand that nowadays every field of geography can only be described by specific numerical values, variables both of time and space which require the sort of numerical analysis only possible with the aid of technical and quantitative methods offered by powerful computers and dedicated software.

Our understanding of **Geographia Technica** expands the concept of technical methods applied to geography to its broadest sense and for that, papers of different interests such as: G.I.S, Spatial Analysis, Remote Sensing, Cartography or Geostatistics as well as papers which, by promoting the above mentioned directions bring a technical approach in the fields of hydrology, climatology, geomorphology, human geography territorial planning are more than welcomed provided they are of sufficient wide interest and relevance.

Targeted readers:

The publication intends to serve workers in academia, industry and government. Students, teachers, researchers and practitioners should benefit from the ideas in the journal.

Guide for Authors

Submission

Articles and proposals for articles are accepted for consideration on the understanding that they are not being submitted elsewhere.

The publication proposals that satisfy the conditions for originality, relevance for the new technical geography domain and editorial requirements, will be sent by email to the address editorial-secretary@technicalgeography.org.

This page can be accessed to see the requirements for editing an article, and also the articles from the journal archive found on www.technicalgeography.org can be used as a guide.

Content

In addition to full-length research contributions, the journal also publishes Short Notes, Book reviews, Software Reviews, Letters of the Editor. However the editors wish to point out that the views expressed in the book reviews are the personal opinion of the reviewer and do not necessarily reflect the views of the publishers.

Each year two volumes are scheduled for publication. Papers in English or French are accepted. The articles are printed in full color. A part of the articles are available as full text on the www.technicalgeography.org website. The link between the author and reviewers is mediated by the Editor.

Peer Review Process

The papers submitted for publication to the Editor undergo an anonymous peer review process, necessary for assessing the quality of scientific information, the relevance to the technical geography field and the publishing requirements of our journal.

The contents are reviewed by two members of the Editorial Board or other reviewers on a simple blind review system. The reviewer's comments for the improvement of the paper will be sent to the corresponding author by the editor. After the author changes the paper according to the comments, the article is published in the next number of the journal.

Eventual paper rejections will have solid arguments, but sending the paper only to receive the comments of the reviewers is discouraged. Authors are notified by e-mail about the status of the submitted articles and the whole process takes about 3-4 months from the date of the article submission.

Indexed by: **CLARIVATE ANALYTICS**
SCOPUS
GEOBASE
EBSCO
SJR
CABELL

ISSN: 1842 - 5135 (Print)
ISSN: 2065 - 4421 (Online)

